Subglacial rhyolite volcanism at Torfajökull, Iceland

Thesis

Subglacial rhyolite volcanism at Torfajökull, Iceland

A thesis presented in fulfilment of the requirements for the degree of Doctor of Philosophy by

Hugh Tuffen
MA (Cantab) 1997
DEA (Clermont-Ferrand) 1998
FGS

Department of Earth Sciences
The Open University

Environmental Science Department
Lancaster University

October 2001

everything in this book may be wrong

Abstract

Subglacial rhyolite eruptions at Torfajökull, Iceland have produced a variety of volcanic edifices during the last glacial period (115-11 ka). These range from small-volume (<0.1 km^3) volcanoes, such as Bláhnúkur and Dalakvíslfell, to larger volume (~1 km^3) flat-topped tuyas such as South-east Rauðufossafjöll. Lithofacies associations at each volcano record distinct phases of volcano-ice interaction beneath temperate glaciers at least 350 m thick.

All eruptions began with the construction of a pile of glassy fragmental material within a subglacial cavity. Fragmentation at Bláhnúkur was primarily caused by quenching, when rising magma encountered meltwater. Fragmentation at South-east Rauðufossafjöll was apparently more energetic, and generated phreatomagmatic ash over 300 m thick. Dalakvísl is intermediate between the other two localities. Most fragmental deposits are massive, suggesting that a sustained meltwater lake did not develop during eruptions, in contrast with evidence from many basaltic volcanoes. Instead, meltwater drained away in a number of discrete channels, some of which have been identified. The eruption at Bláhnúkur apparently terminated before the glacier surface had been pierced, whereas the eruption at South-east Rauðufossafjöll produced a cap of flat-lying subaerial lava flows about 1.5 km in length.

Numerical models are presented, in which simple patterns of ice melting and deformation are used to simulate the evolving size of subglacial cavities during eruptions. The radius of the cavity is compared to the radius of the growing subglacial volcano. The models predict that, at low magma discharge rates and beneath thick ice, cavities will become completely filled with volcanic debris and the eruption will be dominantly intrusive, forming the types of lithologies observed at Bláhnúkur. Cavities never become filled at higher magma discharge rates, and an explosive phreatomagmatic eruption is predicted, which would form the types of lithologies observed at South-east Rauðufossafjöll.

Acknowledgements

I am indebted to Dave McGarvie for the amount of time, energy and enthusiasm he has put in to help this project work, and for first becoming intrigued by subglacial rhyolite way back in the early 80's. He has given me a great deal of encouragement over the three years. I'm grateful to Jennie Gilbert and Harry Pinkerton for always having time for me even when they've been inundated with work, for their ideas, organisation, flapjacks, trekking poles, expertise and interest in subglacial volcanoes. Thanks to Richard Brooker at Bristol University for his help with the FTIR, Andy Tindle at the OU for help with the microprobe, and Naomi Williams at the OU for help with the SEM. I'd like to thank John Smellie, Magnús Tumi Guðmundsson and Bruce Houghton for sharing their knowledge, and the following people who have provided useful discussions: Lionel Wilson, Steve Lane, Steve Sparks, John Eichelberger, Kathy Cashman, Ian Skilling, David Lescinsky, Carl Benson, Mary Chapman, Ben Edwards and Thom Wilch. The examiners, John Smellie and Steve Blake, painstakingly picked their way through this mammoth thesis, and their comments have greatly improved the clarity of the text.

Thanks to Mike, Graham, Katy, John, Jane and Sas for being star-like office-mates, and to the administration staff at Environmental Science in Lancaster for all their help. It was good to feel welcome on my occasional foray to OU Earth Sciences at MK, for which I thank the postgrads, including Steve 'menu lobber' Smith, Steve Donegan, Andy Macmillan, Mark Davies, Helen Williams, Yvonne Smit and Siobhan McGarry; the staff, including Steve Blake, Hazel Rymer, and John Murray; and also Yvette, Lynne and Neil and Emma.

Thanks to Paul Bradbury for providing me with a house, blues music and the odd bike, and thanks or hi to Sara, Helmut, Pamela, Claire, Flo, David, Jael, Johan, Carole, Martin, Nina, Matteo, Megan, John, Emma, Stuart, Sandra, Jo, Becky, Anna and everyone who helped make Lancaster a place.

Hey up Derwent, Suzza, Magalie, Johnny Mac, Beff, Ruth, Mark O (the muse), Tamsin, Gilli, Shaun P, Hannah, Jules, and all you lovely people out there. In Iceland is was great to meet Chris, Kirsty, Binna, Finnur E., Glóey, Sædis, Herdís, Jökull, Svala, Davið, Sacha, Lauriane, Krystel, Björk, Ásta, Ilya, Hlif Una, Disa, Finnur P. and Lars amongst others.

Thanks to the following people for helping me on the perilous path towards a doctorate: Graham Tomlinson, the late Richard Bossingham, David Pyle, James Jackson, Sally Gibson, Tim Druitt and Michael Higgins. Thanks to Wes Hildreth, John Smellie, Ian Skilling, Andy Russell, Armann Hoskuldsson, Magnús Tumi Guðmundsson and Ben Edwards for their reviews of my papers, which greatly strengthened the science and focussed my ideas.

Thanks to Antonin Dvorak, JS Bach, the Coen Brothers, Serge Gainsbourg, Jean-Luc Godard, Franz Kafka, Bertrand Russell, Egon Schiele and the grape growers of Chile for providing unnecessarily pleasant things to play, watch, listen to, read, look at and drink, and also thanks to.....

On a more personal level, thanks to my family, and *Maia*, well, what can I say?

Aims of the PhD

The aims of the PhD are to provide the first modern volcanological study of subglacial rhyolite volcanoes. Three contrasting volcanoes have been selected, at which patterns of volcano-ice interaction were markedly different. It is hoped that, in describing these differences and speculating about their origins, some of the key parameters which control the course of events during subglacial eruptions will be identified. Another goal is to compare the lithofacies architecture of subglacial rhyolite at Torfajökull with subglacial basalt described by Smellie and others in Antarctica, and thus evaluate the predictions of Hoskuldsson & Sparks (1997) about the difference between subglacial rhyolite and basalt eruptions. During fieldwork many unusual (and some previously undocumented) rhyolitic lithologies were found, some of which are described and analysed in detail. These physical volcanological 'subchapters' are intended to complement the aspects dealing with volcano-ice interaction.

Along with the fieldwork, highly simplified mathematical models of melting and ice deformation during eruptions have been constructed, to explore ways in which the response of glaciers to basal melting can potentially affect eruption mechanisms. The non-equilibrium, non-ductile deformation of glacial ice is poorly understood and little studied, hence this part of the PhD (Chapter 5) is merely a speculative first attempt.

Table of contents

Chapter 1.

Introduction to subglacial rhyolite volcanism.....1

Chapter 5.
Numerical models of volcano-ice interaction 255

List of figures

Chapter 1.

Chapter 2.

Chapter 3.

Chapter 4.

Chapter 5.

List of tables

Chapter 1.
Introduction to subglacial rhyolite volcanism

1.1. A general introduction to terrestrial subglacial volcanism

This first section provides a brief overview of subglacial volcanoes worldwide, in which I outline where they are found, why it is important to study them, and how they are recognised in the field. In this chapter and the rest of the thesis I will make frequent use of many terms (e.g. subglacial, hyaloclastite, jökulhlaup). A glossary listing the terms and definitions used throughout the thesis is provided in Appendix A.

It is only in the last century that the products of ancient subglacial volcanic eruptions have been recognised in the field (Pjetursson 1900). Since then, field studies have investigated the characteristics and mode of origin of two main types of ancient subglacial volcanoes: those constructed within ice sheets (these are dominantly basaltic, although some are rhyolitic), and glacier-capped stratovolcanoes (dominantly basaltic to dacitic). Volcano-ice interaction at these two main types of subglacial volcano is very different, with contrasting eruption mechanisms, resultant hazards and volcanic products.

Basaltic volcanoes constructed within ice sheets are comparatively well-studied and understood [section 1.2], whereas rhyolitic volcanoes have been largely ignored, despite growing

evidence for Quaternary rhyolitic eruptions in Iceland [section 1.10.4.]. In section 1.4 I summarise the field evidence gathered to date for volcano-ice interaction at stratovolcanoes. Noteworthy observations of subglacial eruptions are described in section 1.5.

Sections 1.6-1.9 deal with the mechanics of volcano-ice interaction, the complex system is pulled apart as I consider melting of ice [section 1.7], meltwater drainage [section 1.8] and deformation of ice [section 1.9]. Section 1.10 aims to put subglacial rhyolite into perspective, by comparison with subglacial basalt and subaqueous rhyolite, and considers the distribution of subglacial rhyolite formations in Iceland, as well as subglacial rhyolite in the tephrochronological record.

In section 1.11 I introduce the area in which my field studies were conducted, Torfajökull central volcano in Iceland, and outline the methodology and aims of the PhD.

1.1.1. Global distribution of subglacial volcanoes

Volcano-ice interaction occurs wherever active volcanoes are entirely or partially covered by ice (Smellie 1999), firn (Kiver & Steele 1975) or seasonal snow fields (Major & Newhall 1989, Walder 2000a). Subglacial eruptions are typically defined as those fed by vents or fissures that are initially entirely covered by ice (Smellie 1999), and which may or may not pierce the ice surface, terminating with a subaerial phase. Ancient and active volcanoes with a history of interaction with ice are found in Iceland, Alaska, Cascades, Mexico, Ecuador, Chile, Antarctic Peninsula, and Kamchatka (Fig. 1.1). Volcanoes at high latitudes (in Antarctica and Iceland) have

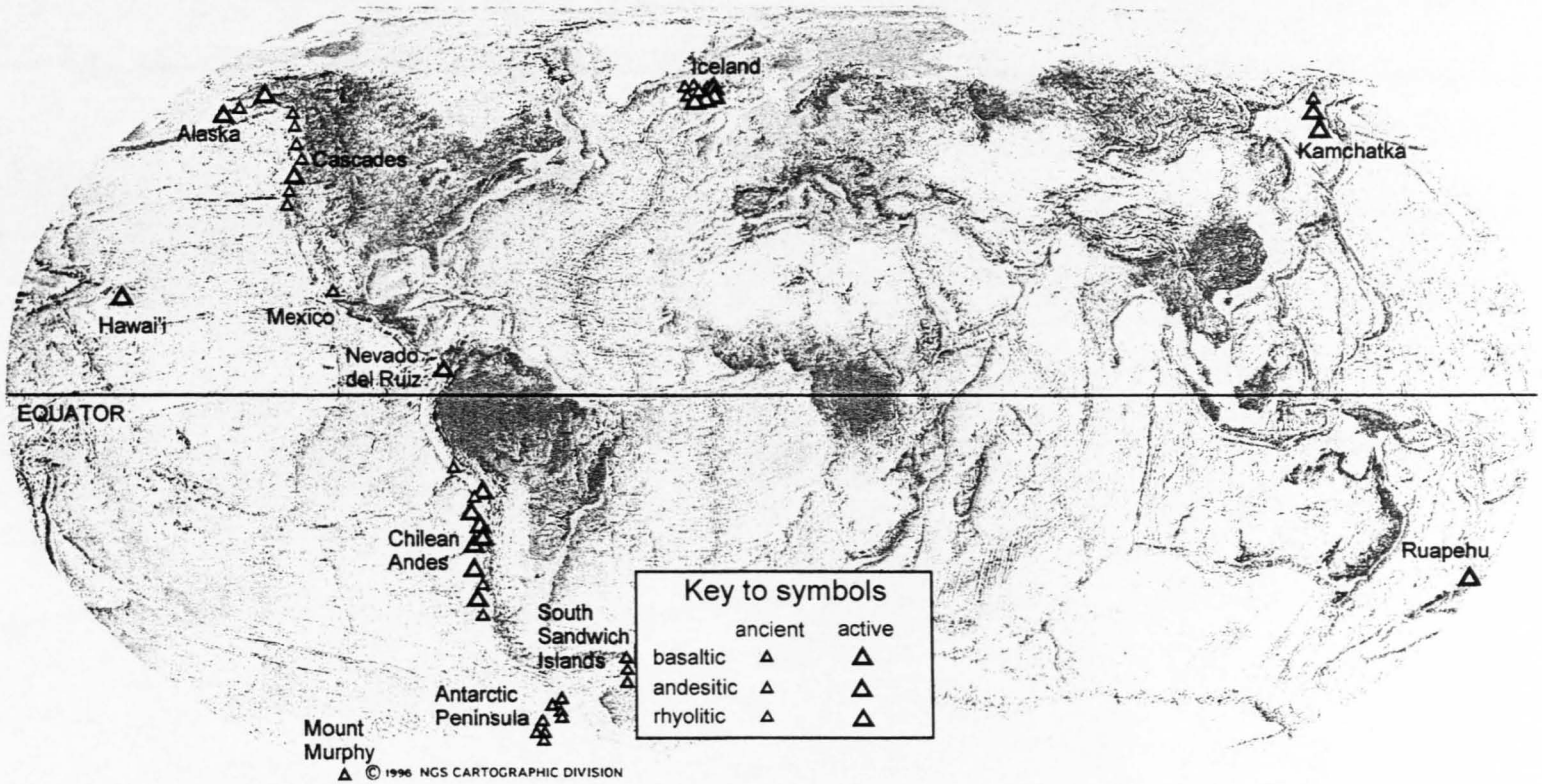

Fig. 1.1. The global distribution of volcanoes where volcano-ice interaction has either been observed during eruptions, or has been inferred from ancient sequences. It is thought to be only in Iceland and Antarctica that volcanoes have been constructed entirely within ice; all volcanoes elsewhere are stratovolcanoes with flank glaciers and snowfields. Basaltic and andesitic volcanoes are comparatively widespread, whereas the only documented rhyolitic volcanoes are in Iceland.

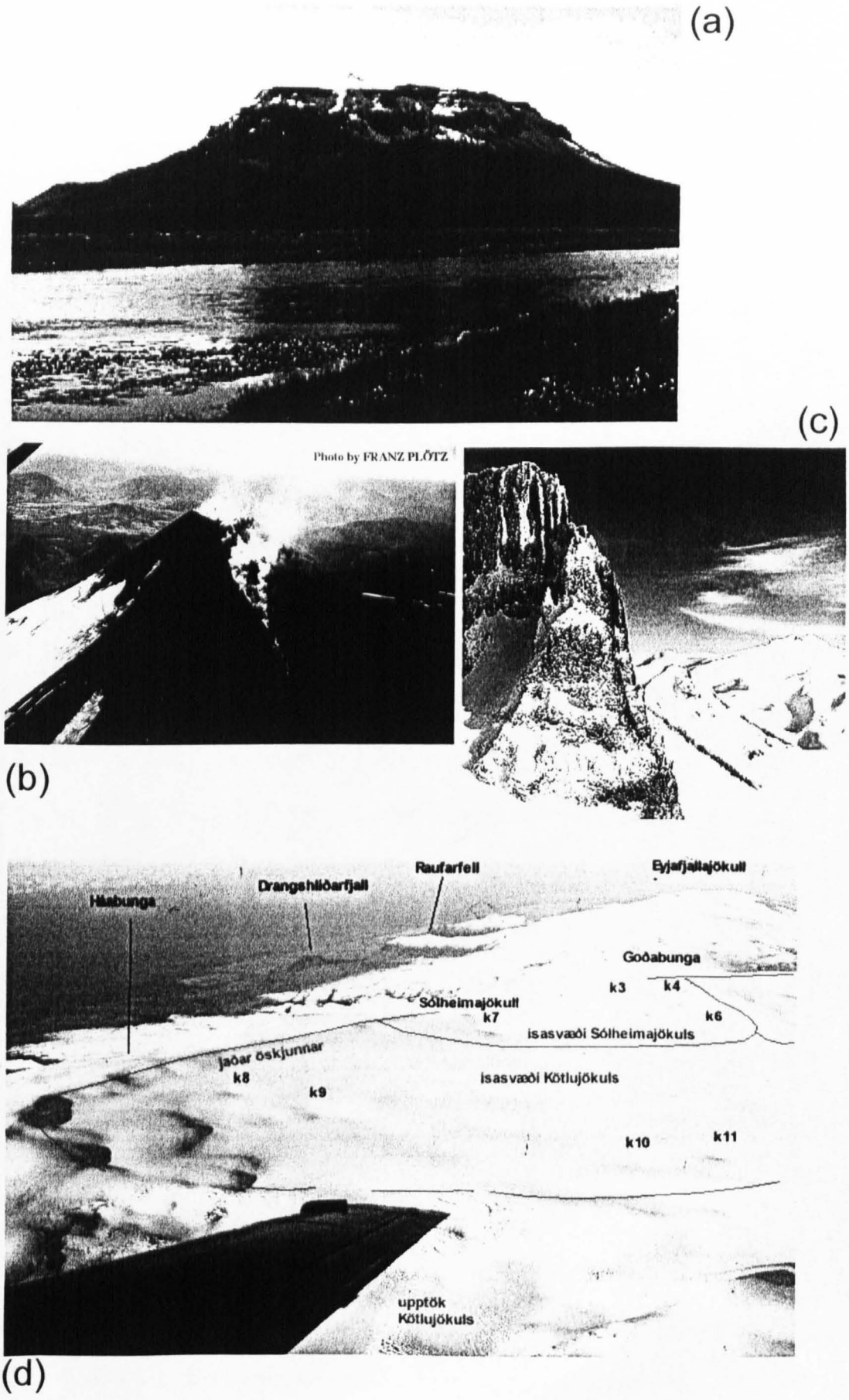
(a)
(c)
Photo by FRANZ PLÖTZ
(b)
Raufarfell
Eyjafjallajökull
Drangshlíðarfjall
Hlíðarenga
Goðabunga
k3
k4
Sólheimajökull
k7
k6
ísasvæði Sólheimajökuls
Jaðar öskjunnar
k8
ísasvæði Kötlujökuls
k9
k10
k11
upptök
Kötlujökuls
(d)

Fig. 1.2.

Fig. 1.2. Some contrasting volcanic landforms. **(a)** Herðubreið, a subglacial basaltic tuya in northern Iceland. It is a flat-topped edifice that rises some 1100 m above its base, and was formed in the subglacial equivalent to a shield-building eruption during the last glacial period (Werner et al. 1996). **(b)** The ice-clad summit cone of Villarrica, an andesitic stratovolcano in Chile, during the 1971 eruption. *Black areas* are where the ice has been covered by lava flows, tephra and avalanche debris. Steam is rising from the margins of a lava flow which originated in the ice-free summit crater and is advancing within a channel melted into the ice. Photo by Franz Plötz, courtesy of the POVI website. (www.povi.org). **(c)** The Table, a flat-topped volcano that consists almost entirely of andesitic lava flows (Mathews 1951), the cliffs are c. 350 m high. The volcano was probably surrounded by ice walls during its construction. **(d).** The caldera of Katla volcano, southern Iceland, viewed from the air. The caldera rim is indicated (red line). The ice is up to 600 m thick within the caldera. Numerous circular depressions in the ice surface (labelled k3-k11) formed during subglacial melting in 1999 (Table 1.2a). Photograph by M.T. Guðmundsson.

---

been constructed within large ice sheets typically 400-1500 m thick, and some volcanic edifices have been built entirely within the ice. By contrast, ice only occurs at high elevation (>2km) in mid-and low-latitude regions such as the Andes, Mexico and Kamchatka, where it commonly forms thin valley-type glaciers on the upper slopes of stratovolcanoes and ponded ice within some summit calderas (e.g. Gilbert et al. 1996). As will be discussed, the mechanism of volcano-ice interaction is markedly different in these two types of ice-covered volcano and contrasting landforms are produced (Fig. 1.2).

The greatest concentration of subglacial volcanoes is in Iceland, due to its long history of glaciation in the Quaternary and late Tertiary (Duncan & Helgason 2001) and high rate of magma production and volcanism since the early Tertiary (Jakobsson 1979). Around 90% of the magma generated in Iceland is basaltic, the remaining 10 % is rhyolitic. Subglacial volcanoes within the Andes, Cascades, Alaska and

Kamchatka are mostly basaltic to andesitic stratovolcanoes, whereas those in Antarctica are dominantly basaltic in composition, with minor trachyte and phonolyte.

1.1.2. Why study subglacial volcanoes?

There are many scientific and socio-economic reasons to study subglacial volcanoes.

Firstly, active ice-covered volcanoes can be extremely hazardous (Major & Newhall 1989), posing the double threat of explosive phreatomagmatic eruptions and catastrophic meltwater floods (jökulhlaups). Melting of summit ice at Nevado del Ruiz, Columbia, during the eruption of October 1985 generated lahars that swept down the volcano flanks, destroying villages in their paths (Pierson et al. 1990). The lahars claimed the lives of 23 000 people, the fourth largest recorded death toll from a volcanic eruption. The 1996 Gjálp eruption beneath Vatnajökull in Iceland was of modest volume (~0.4 km^3 of basaltic magma was erupted), yet approximately 4 km^3 of meltwater was discharged in a jökulhlaup whose peak discharge rate exceeded 40 000 $m^3 s^{-1}$ (Guðmundsson et al. 1997). Despite the precautions made, the force of the jökulhlaup was sufficient to destroy major sections of the national ring road. The eruption also generated a plume of ash and steam up to 9 km high (Fig. 1.3). Although only relatively small explosive subglacial eruptions have been observed in Iceland in the twentieth century (Guðmundsson, submitted), tephra layers formed by subglacial and subaerial eruptions in Iceland are distributed over much of northern Europe (e.g. Dugmore et al 1995, Lacasse et al. 1998), and may have been formed in much larger eruptions.

Secondly, identification and dating of subglacial volcanic sequences can be used to reconstruct past glacier fluctuations over millions of years (LeMasurier et al. 1994, Helgason & Duncan 2001) and provide a proxy record of climate change. This

may be particularly useful, when it is considered that other climatic reconstruction techniques rely on organic matter such as pollen and fossils, which are scarce both in glaciated regions, and at high elevations and latitudes. Work currently being undertaken at Nevados del Chillan (Chile) and Mount Murphy (Antarctica) aims to reconstruct glacier fluctuations using high-resolution dating and identification of subglacial and subaerial lithofacies at volcanoes with a long history of glaciation and eruption.

Furthermore, field discrimination between subglacial and subaerial volcanoes has provided estimates of the magma production rate in the Icelandic Eastern Volcanic Zone during glacial and interglacial periods (Jull & McKenzie 1996). The discovery that thirty times more magma was produced at the end of the last glacial period (c. 10 ka) has lead to new models of magma generation and ascent within the Icelandic crust (Slater et al. 1998, Maclennan et al. 2001).

Recent research has identified a possible link between subglacial volcanic activity and glacier instability, both of alpine glaciers on stratovolcanoes (Sturm 1995, Walder & Driedger 1995) and the more extensive ice sheets of modern-day Antarctica (Blankenship et al. 1993) and Pleistocene Iceland (Bourgeois et al. 2000).

In addition, the study of active and ancient subglacial volcanoes may aid understanding of physical volcanology. Abrupt variations in subglacial pressure (Hooke 1984, Kavanaugh & Clarke 2000), meltwater availability (see reviews by Hubbard & Nienow 1997, Fountain & Walder 1998) and mechanical constraint by ice walls (e.g. Vinogradov & Murav'yev 1988) may occur during subglacial eruptions. If changes in the eruptive environment are more rapid than the response time of the magmatic system (governed by processes such as conduction and diffusion), then there is scope for non-equilibrium eruptive phenomena (e.g. degassing and

Fig. 1.3. Ash and steam plume rising 3-4 km above the main vent of the basaltic Gjálp eruption on October 2nd 1996, the day that the glacier surface was first pierced. The eruption style is surtseyan, with pulses of magma forming dark 'cocks tails' that contrast with the white steam plume behind. Note the cracks on the glacier surface. Photograph by F. Sigmarsson, taken from the Nordic Volcanological Institute website - www.norvol.is.

vesiculation, Gardner et al. 1999). Study of the products of such eruptions may be a unique source of information on the non-equilibrium, non-linear processes that operate during the rise and fragmentation of magma at shallow crustal levels. Finally, the melting rate of ice above a volcano can be used as a calorimeter, providing accurate estimates of geothermal heat output (Björnsson & Guðmundsson 1993), and volatiles released by a degassing subglacial volcano may be trapped within an intraglacial lake, allowing determination of time-integrated volatile fluxes (Ágústsdóttir & Brantley 1994), that can only be estimated by other means.

1.1.3. Evidence for subglacial volcanism in the geological record

Many subglacial eruptions have occurred in regions that were previously glaciated but are now devoid of ice. Some or all of the following criteria can be used to deduce that a given set of lithofacies was erupted in a subglacial environment:

1. Evidence for magma-water interaction (such as perlitised obsidian, blocky ash shards, peperitic lavas, matrix vesicles, pillow lavas) in a region where there is no evidence for the existence of a palaeotopography which could have confined a non-glacial lake (Jones 1970, Smellie & Skilling 1994, Smellie & Hole 1997).

2. The lack of marine fossils can be used to reject a submarine eruptive setting. The current elevation of the volcanic sequence may also be used to reject a submarine setting if it is significantly greater than accepted values of global sea level change and there are no tectonic structures consistent with localised uplift (e.g. Smellie 1999).

3. Columnar jointing patterns within lava bodies that suggest they chilled against steeply inclined sub-planar surfaces. Such jointing patterns, which have not been found in subaqueous or subaerial lavas, are best explained by the chilling of lavas against ice walls (Lescinsky & Sisson, 1998).

4. The intercalation or intimate association between volcanic lithofacies and non-volcanic glacial deposits such as tills, which contain facetted or striated clasts.

5. The presence of striated surfaces within the lithofacies sequence, created by flowing ice (Smellie 1999).

6. A known history of glaciation in the region at time of eruption (only possible if rocks have been dated and there is a well-constrained palaeoclimatic record).

1.2. Field studies of ancient basaltic subglacial volcanoes

1.2.1. Early volcanological studies

Basaltic volcanoes constructed within ice sheets occur in Iceland (e.g. Jones 1968), Antarctica (e.g. Smellie et al. 1993) and British Columbia (e.g. Mathews 1947). Early work (Pjetursson 1900, Noe-Nygaard 1940) established the subglacial eruptive setting of widespread Quaternary basaltic formations in Iceland, known collectively as móberg (literal translation: brown rock). These occur as linear ridges (tindars), dominated by palagonitised hyaloclastite, and flat-topped table mountains, also known as stapar (Icelandic term) and called tuyas throughout this thesis. Tindars have

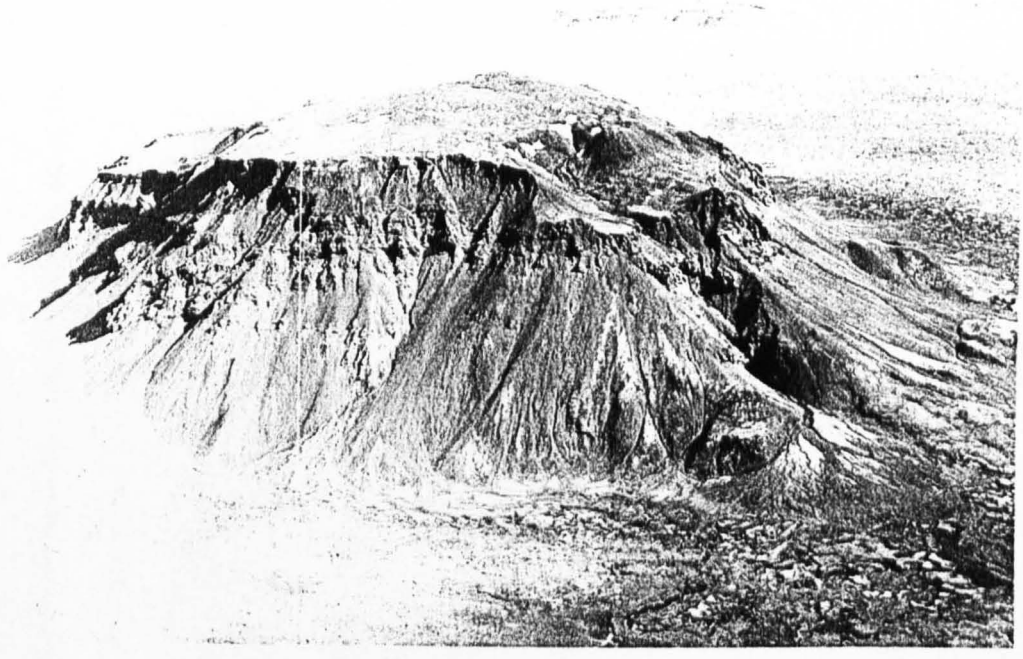

(a)

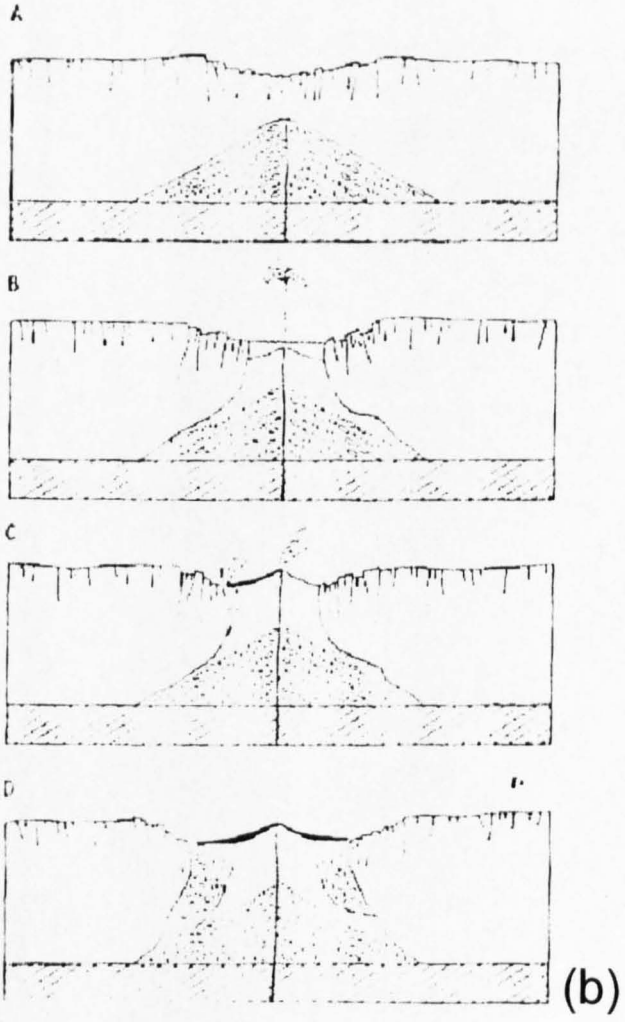

(b)

Fig. 1.4.

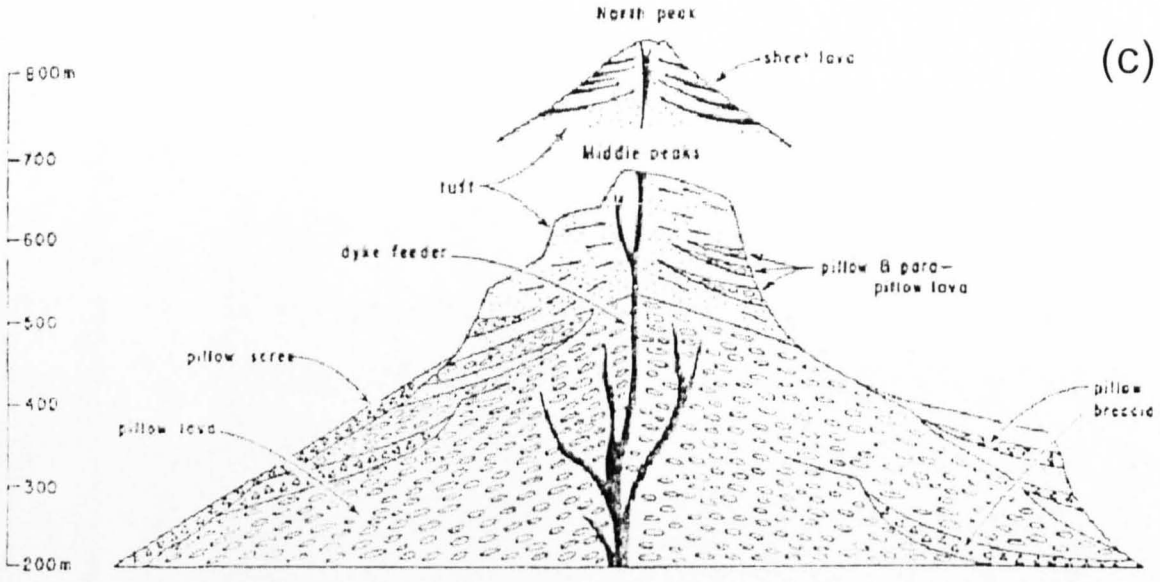

Fig. 1.4. **(a)** Aerial view of Hloðufell basaltic tuya in southwest Iceland. Pillow lavas at the base of the volcano are mostly concealed by scree, and are overlain by broken cliffs of hyaloclastite breccias. The flat top is formed by flat-lying subaerial lava flows. Note the prominent bench on the right hand flank of the edifice - this is a lower subaerial lava unit, suggesting that the succession is more complex than the 'idealised' tuya. Vertical distance from base to top ~ 500 m. Photograph by I. Skilling. **(b)** The classic cartoon of Jones (1970) showing his interpretation of the events that formed Kalfstindar in southwest Iceland. A - Subglacial eruption, pillow lavas formed and an ice cauldron develops. B - The ice roof is broken and hyaloclastite is formed increasingly explosively within a meltwater lake. C - The edifice has now built above lake level and subaerial lavas are formed, which are constrained by the walls of the ice cauldron. D - Melting of the surrounding ice leads to instability and slumping of the volcano flanks. **(c)** Schematic cross section of Kalfstindar, after Jones (1970). Note that a large proportion of the edifice is made of pillow lavas, and that sheet lavas are intercalated with hyalotuffs at the top of the sequence, suggesting a cyclic eruption mechanism, possibly linked to fluctuations in the lake level. No vertical exaggeration.

Fig. 1.4. continued

formed on fissures parallel to the local rift direction, and are typically 5-20 km long and 200-300 m high. Tuyas form in the subglacial equivalent to shield-building eruptions, and are between 400 and 1100 m high, with basal diameters of 4-10 km. Fig. 1.4a shows Hloðufell, a typical basaltic tuya in southwest Iceland.

W.H. Mathews discovered similar flat-topped basaltic tuyas in British Columbia, Canada. His observations and interpretations (Mathews 1947) have since provided a benchmark for subsequent studies of subglacial basaltic volcanoes. He reported that tuyas are flat-topped edifices in which basal pillow lava is overlain by inclined beds of hyaloclastite, which are in turn overlain by near-horizontal subaerial lavas. In his model, an eruption within an ice-enclosed 'intraglacial' lake commenced with the quiet effusion of pillow lavas, became increasingly energetic and explosive, and terminated with the effusion of subaerial lavas once the edifice had built above the level of the intraglacial lake. He noted that the subaerial lavas do not drape over the hyaloclastite flanks of the tuyas, and inferred that flowing lavas were confined by ice walls. He suggested that the level of the intraglacial lake depended upon the flux of meltwater draining from it, and speculated that lake levels may drop during ice sheet retreat. Finally, he suggested that bedding in the hyaloclastite was deltaic, and would have required a sustained meltwater lake to be present.

Fieldwork by J.C. Jones in the 1960's focussed on basaltic tuyas and tindar ridges in the Laugarvatn region of south-west Iceland, and led to a series of seminal papers on volcano-ice interaction (Jones 1966, 1968, 1970). This built upon the work of Mathews, and made numerous advances. Jones's classic model of the various stages of basaltic tuya construction (Fig. 1.4b), based on field mapping of Kalfstindar, has long been used in textbooks. Notably, greater attention was paid to the sedimentary structures and clast types present in the fragmental lithologies, which led

to refined models of magma-water interaction during the construction of a basaltic edifice within an intraglacial meltwater lake (Jones 1970). Observations from the 1963-64 eruption of Surtsey (Thorarinsson 1967) provided an invaluable perspective on volcanic processes during subaqueous-to-emergent eruptions. Jones used the term 'passage zone', taken from deltaic sedimentology, to describe the contact between hyaloclastite and the overlying subaerial lavas, and suggested that its elevation may indicate the approximate palaeo-water level in the meltwater lake at this phase of the eruption (Fig. 1.4b). He noted that the vesicularity of pillows increased upwards within a 250 m-thick sequence at Kalfstindar, and that pillows were fed by numerous dykes, parallel to the ridge orientation (Fig. 1.4c). Furthermore, he suggested that the explosivity of an eruption within an intraglacial lake is likely to be controlled by the eruption rate. Numerous slumped blocks of hyaloclastite and pillow breccias on tuya and tindar flanks were interpreted as deposits that were initially emplaced upon the glacier surface, and subsequently collapsed and rotated during ice sheet recession.

Allen et al. (1982) compared tuya landforms in British Columbia to those in Iceland. No novel field observations were made, but the theoretical models of Allen (1980), which dealt with volume changes during subglacial basaltic eruptions, were applied to the observed sequences. Since the overall volume of the volcano-ice-water system would decrease if all the thermal energy of basaltic magma were used to melt ice, Allen et al. (1982) suggested that a water-filled vault at the glacier base would expand upwards and laterally during the subglacial phase of the eruption. Roof collapse would lead to the establishment of an intraglacial lake. Since Heiken (1972) had recognised that the morphology of ash shards is related to the mechanism of magma fragmentation, Allen et al. (1982) suggested that the blocky, low-vesicularity

ash shards within the hyaloclastite indicated fragmentation during explosive magma-water interaction.

1.2.2. Modern volcanological studies

A significant development in the study of ancient subglacial volcanoes has come in the last decade, with detailed field studies of well-exposed Antarctic volcanoes by J. L. Smellie and co-workers at the British Antarctic Survey (BAS). Increasingly detailed investigation of the sedimentology of fragmental deposits has been used to deduce emplacement environments (Smellie et al. 1993, Smellie & Skilling 1994, Smellie & Hole 1997, Smellie 1999, Smellie 2001). Furthermore, interpretation of the three-dimensional lithofacies architecture, combined with insights into glacier structure and hydrology, has led to improved models of volcano-ice interaction (reviewed in Smellie 1999). Based upon the lithofacies associations, subglacial basaltic volcanoes have been grouped into two categories: those emplaced beneath thick ice (≥200 m) and thin ice (<150 m).

Eruptions beneath thick ice (≥200 m)

A complete example of a typical succession formed beneath thick ice is the classic 'tuya succession' (Jones 1968, 1970; Smellie 1999), although volcanoes may lack the subaerial lava cap if the eruption terminated prior to a subaerial effusive phase. Pillow lavas up to 500 m thick at the base of the subglacial volcanic sequences are overlain by subaqueous-to-emergent Surtseyan sequences, as described by Skilling (1994) at Brown Bluff, Antarctica (Fig. 1.5). The hyaloclastite delta at the top of the subaqueous sequence is overlain by one or more sheet-like columnar-jointed lava flows and subaerial pahoehoe lava flows (e.g. Brown Bluff, Skilling 1994).

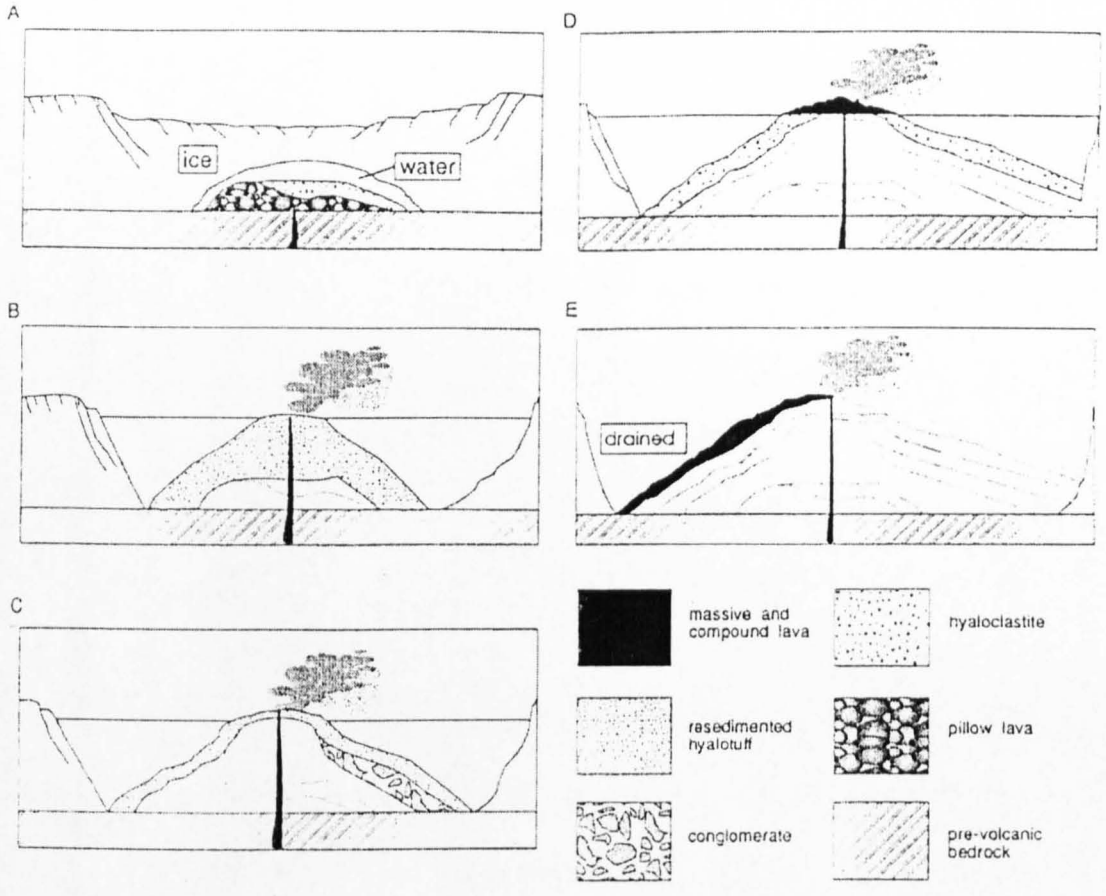

Fig. 1.5. Cartoon illustrating the current interpretation of the sequence of events at Brown Bluff, Antarctica, after Smellie & Skilling (1994). A - subglacial eruption within water-filled cavity, as an ice cauldron forms on the ice surface above. Pillow lavas formed. B - construction of a subaqueous-to-emergent edifice within an intraglacial lake. Hyaloclastite formed close to the vent slumped down the edifice flanks. C - transition to explosive eruptions at depths 150 m below the contemperaneous water level. This is best explained by a dramatic fall in lake level. Slopes are unstable, and sector collapse occurred. D - Emplacement of a subaerial lava cap on top of hyaloclastite foreset beds. E - Effusion of subaerial lavas which drape over the edifice flanks follows a dramatic drop in the level of the lake. After Smellie & Skilling 1994.

Inward-dipping bedding planes within some delta sequences (first observed by Jones 1970) are best explained by 'stacking' of sediments against a confining ice wall (Skilling 1994). Slumped breccias commonly occur on volcano flanks (e.g. Skilling 1994), some of which contain deformed 'pillow stringers', suggesting syn-eruptive collapse of portions of the subaqueously-emplaced edifice (Smellie & Hole 1997). Sequences are seldom as simple as this type example, there being often multiple pillow units and subaerial lavas overlain by hyaloclastites (e.g. Smellie & Skilling 1994). Werner et al. (1996) observed similar complexities at the basaltic tuya Herðubreið in Iceland.

The new observations from Antarctica have led to the following refinements to the tuya construction model:

1. The level of the intraglacial lake may abruptly decrease by up to 75 m, based on the intercalation of subaerial and subaqueous lithofacies at Brown Bluff (Smellie & Skilling 1994). This is thought to be triggered by sudden subglacial drainage of the lake (jökulhlaup), due to flotation of the surrounding glacier by the intraglacial lake (Nye 1976, Björnsson 1988, Fowler 1999). Thermal erosion of the surrounding ice by heated meltwater may also trigger or accelerate sudden drainage (Clarke 1982). Lake levels may thus be highly variable during the course of tuya construction. Therefore, caution must be applied when using the elevation of passage zones as an indicator of the palaeo-ice level - as the lake level may be significantly lower than the level of the surrounding ice surface.

2. Edifice collapse and slumping may be triggered by withdrawal of supporting water during jökulhlaup drainage, withdrawal of supporting ice walls from the edifice during melting, constructional oversteepening or fluidisation of water-saturated breccias during seismic events (Smellie & Hole 1997).

3. Turbidite units within lacustrine hyaloclastite sequences may record discrete explosion events and jets of tephra during an emergent Surtseyan eruption (Smellie & Hole 1997, White & Houghton 1999).

4. Stable lake levels during the delta-building phase may be maintained by englacial or supraglacial drainage - through or over permeable firn and snow in the upper 20-70 m of the glacier (Smellie 1999, Smellie 2001).

Eruptions beneath thin ice (<150 m)

Volcanic sequences inferred to have been emplaced beneath thin ice are markedly different from tuya sequences (Smellie & Skilling 1994). The best-studied basaltic sequence, at Mount Pinafore, was emplaced within a palaeo-valley beneath <150 m of ice (Smellie et al. 1993). Fig. 1.6 shows their reconstruction of the main phases of eruption. Pillow lavas are absent, and the base of the succession comprises fragmental deposits (tills and hyaloclastites) which have been emplaced in running water, probably within a channelised subglacial meltwater stream. Lava flows and associated hyaloclastites were then emplaced within the tunnel incised by the meltwater stream. Intense phreatomagmatic activity at the vent area created a hyalotuff cone, indicating that some meltwater accumulated at this phase of the eruption. Smellie et al (1993) speculate that drainage within the subglacial tunnel may have been impeded by the lava and hyaloclastite, allowing meltwater accumulation at the vent. Independent evidence from Redoubt volcano, Alaska during the 1989-1990 eruptions, indicates that subglacial meltwater drainage channels may indeed become temporarily blocked by volcanic debris or blocks of ice (Trabant et al. 1994).

1.2.3. Geochemical studies

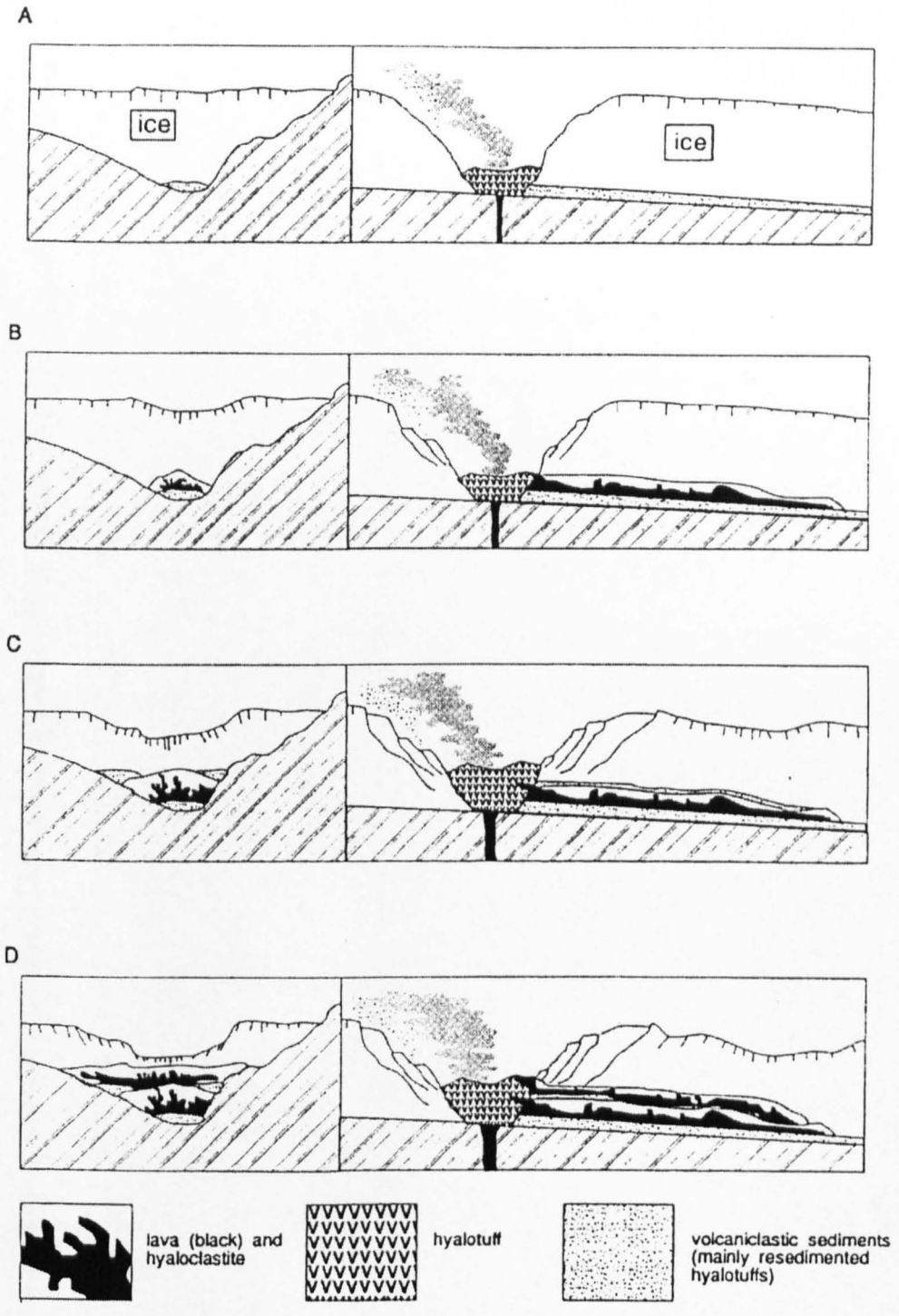

Fig. 1.6. Inferred sequence of eruptive events at Mount Pinafore, Antarctica, where a basaltic eruption occurred beneath ice 100-150 m thick. A - The eruption has rapidly melted through to the ice surface, and phreatomagmatic interaction between magma and meltwater is forming a mound of hyalotuff. Meanwhile, tephra is reworked as meltwater flushes down thermally-enlarged subglacial tunnels. B - Phreatomagmatic eruption continues; meanwhile lava flows within a subglacial drainage channel, where it interacts with meltwater to form a hyaloclastite carapace. C - Continued eruption, meltwater now drains on top of the lava flow, and a new subglacial tunnel is formed, which is subsequently exploited by a second lava flow (D). After Smellie & Skilling (1994).

In addition to straightforward field mapping of deposits, analysis of the geochemistry of magma within tuyas can yield useful information on patterns of volcano construction. Detailed sample analysis of Herðubreið, a 1100 m-high basaltic tuya in the eastern rift zone of Iceland (Fig. 1.2a), has led to contrasting models of tuya construction (Moore & Calk 1991, Werner et al. 1996). Moore & Calk (1991) determined the sulphur content of glass from various lithologies within the tuya sequence. Sulphur degassing patterns of basaltic lavas from submarine volcanoes (e.g. Sakai et al. 1982, Gerlach 1986) vary systematically with the confining pressure of emplacement. Moore & Calk found sulphur-rich pillows intercalated with hyaloclastites and inferred that the water level had risen approximately 300 m during the eruption, based on the stratigraphic association with the lowest subaerial lava unit. Werner et al. (1996) questioned this model, and suggested that tuya construction occurred in three distinct phases, during which the regional glacier level fluctuated by hundreds of metres. The debate cannot be fully resolved until all the deposits have been accurately dated. Nevertheless, the systematic measurement of magmatic volatile concentrations, first applied to subglacial volcanoes by Moore & Calk (1991), is a highly promising technique. A subsequent study of degassing and magmatic evolution within basaltic tuyas in British Columbia (Moore et al. 1995) was less successful, due to inadequate exposure of different lithologies.

There is increasing evidence that the presence of an overlying glacier may affect the generation and rise of magma. The weight of several hundred metres of ice may act as a 'lid' - for example by inhibiting production of basaltic magma within the mantle (Sigvaldasson et al. 1992, Jull & McKenzie 1996, Slater et al. 1998). Furthermore, the eruption of dense, unevolved magmas from shallow chambers may

be suppressed until fractionation has generated more buoyant magmas capable of rising through the shallow crust (Moore et al. 1995, Edwards 1997).

1.3. Field studies of ancient intermediate and silicic subglacial volcanoes

Silicic volcanoes constructed within ice sheets are less widespread and less well studied than their basaltic counterparts (Fig. 1.1; Smellie 1999). To date, subglacial rhyolite deposits have been identified in Iceland (Fridleifsson 1970, 1973; Sæmundson 1972, Grönvold 1972, Sæmundsson & Noll 1974, Einarsson 1975, Furnes et al. 1980, Jónasson 1994, Smellie 1999) and a subglacial andesite volcano has been described in British Columbia (Mathews 1951). Sæmundson (1972) and Grönvold (1972) described flat-topped rhyolitic 'table mountains' at Torfajökull and Kerlingarfjöll respectively, thought to have been erupted within ice-bounded lakes with water depths of 200-300 m before terminating with the effusion of subaerial lavas – an eruptive sequence analogous to the evolution of basaltic tuyas proposed by Jones (1968, 1970). The first detailed study of the structure of fragmental deposits (rhyolitic hyaloclastite) was that of Furnes et al. (1980), who described sequences at Bláhnúkur, Torfajökull and mentioned similar deposits elsewhere in Iceland. This paper is summarised in the next section.

1.3.1. Observations and interpretations of Furnes et al. (1980)

Furnes et al. divided the subglacial rhyolite of Bláhnúkur into three lithologies: type 1 hyaloclastite, type 2 hyaloclastite and lava lobes. Their observations and interpretations are summarised in Table 1.1. In their model (Fig. 1.7), the initial phase of the eruption was explosive, with considerable exsolution of magmatic volatiles, forming pumiceous type 1 hyaloclastite. Variable degrees of interaction with meltwater created variable eruption styles, within the range strombolian-surteyan-subplinian-plinian. This was succeeded by an intrusive style of eruption, in which lava lobes were emplaced within the growing pile of wet hyaloclastite, some reaching the contact between the hyaloclastite and the meltwater above. The transition from an explosive to an intrusive eruption style was thought to have been triggered by the exhaustion of magmatic volatiles and the emplacement of degassed magma. However, more volatile-rich magma was thought to have formed the vesicular lobe interiors, leading to overpressure and failure of the outer carapace of some lobes. Furnes et al. made two important advances: the recognition that the generation of rhyolitic hyaloclastite and lava lobes is closely linked, and that the style of eruption may be highly variable, with scope for differing fragmentation mechanisms during magma-water interaction and the emplacement of variably degassed magma.

Deposit name	Description	Interpretation
Type 1 hyaloclastite	Poorly-sorted units up to 40 m thick. Dominated by spherical- to-elongate pumice fragments 0.1 mm to 50 cm long, some are perlitised.	Formed by the initial explosive phase of the subglacial eruption, fragmentation dominated by degassing of magmatic volatiles, and variable degrees of interaction with meltwater.
Type 2 hyaloclastite	Thick, poorly-sorted units contain angular fragments of obsidian, flow-banded/flow-folded pumice and rhyolite from 1 mm to >40 cm in length. Grade into lava lobes.	Vesicle-poor lava lobes intruded the water-saturated pile of debris, and the vesicle-poor margins quenched. Subsequent intrusion of vesicle-rich magma into the lobes triggered disaggregation, forming type 2 hyaloclastite.
Lava lobes	Ellipsoidal to irregular lava bodies, typically 7 m in length. Contain an outer vesicle-poor obsidian zone 20 cm-5 m thick, a highly vesicular flow-banded zone up to 1 m thick and a microcrystalline rhyolite interior with columnar jointing.	Volatile-poor magma emplaced and quenched, forming outer zone. More volatile-rich magma injected within obsidian, forming flow-banded zone. Bursting of the carapace allowed 'budding' of a new lobe, and the process was repeated until the magma supply was extinguished.

Table 1.1. Descriptions and interpretations of subglacial rhyolite lithologies at Bláhnúkur, Iceland by Furnes et al. (1980).

1.3.2. Mathews 1951: The Table, British Columbia

The first published account of a silicic volcano constructed within an ice sheet was that of Mathews (1951), who described The Table, a spectacular andesitic volcano in British Columbia (Fig. 1.2c). It consists of near-vertical cliffs of lava 300 m high, beneath a near-horizontal cap 300 m long and 200 m wide. Talus derived from the cliffs conceals most of the underlying lithologies. The lava consists of three superimposed units, each of which comprises a ~3 m thick basal layer cut by vertical columns 50 cm wide, overlain by a 30-80 m thick upper section with more slender vertical columns, 15-20 cm wide (Fig. 1.8). Flow banding, where observed, is near-horizontal in the central parts of the lavas, and normal to columnar joints. The edges of lava bodies have steeply-inclined flow banding, normal to gently dipping columnar joints, and appear to have draped over the flank of the edifice (Fig. 1.8). One lava flow draping over the edifice flank directly overlies glacial till.

Mathews interpreted The Table as a volcano emplaced within a steep-sided, well-drained vault melted into a glacier >300 m thick. He suggested that each lava unit was a discrete cooling body, with a basal colonnade overlain by an upper entablature section, and that the relative thicknesses of the upper and lower sections approximately indicated the relative cooling rates of the top and base of the lavas. The tops of lavas were rapidly cooled (cooling rate 10-25 times that of the base), possibly by glacial meltwater, and the edges of lavas may have flowed within bergshrunds – gaps between the edifice and the encapsulating ice walls. Mathews was the first to recognise that the configuration of columnar joints in lava bodies, which indicates the

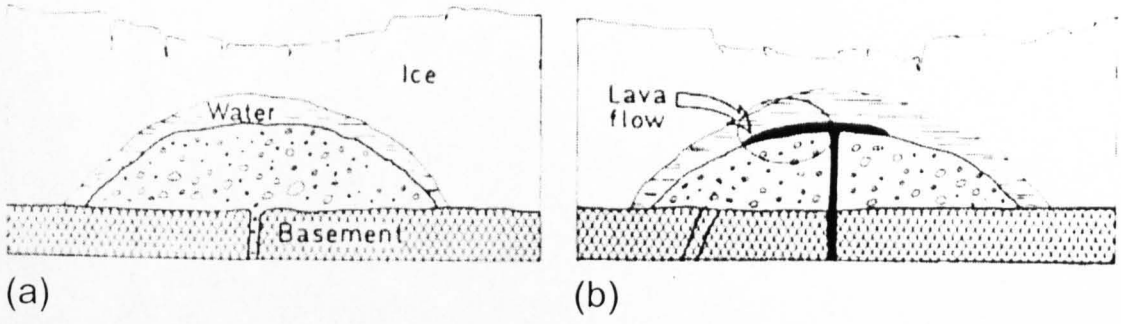

Fig. 1.7. The eruption model of Furnes et al. (1980) for the subglacial rhyolite volcano Bláhnúkur, at Torfajökull, Iceland. A - Violently explosive magma-water interaction within a water-filled subglacial cavity creates pumiceous (sic) type 1 hyaloclastite. B - Intrusion of volatile-poorer magma within hyaloclastite, some of which reaches the meltwater-hyaloclastite interface.

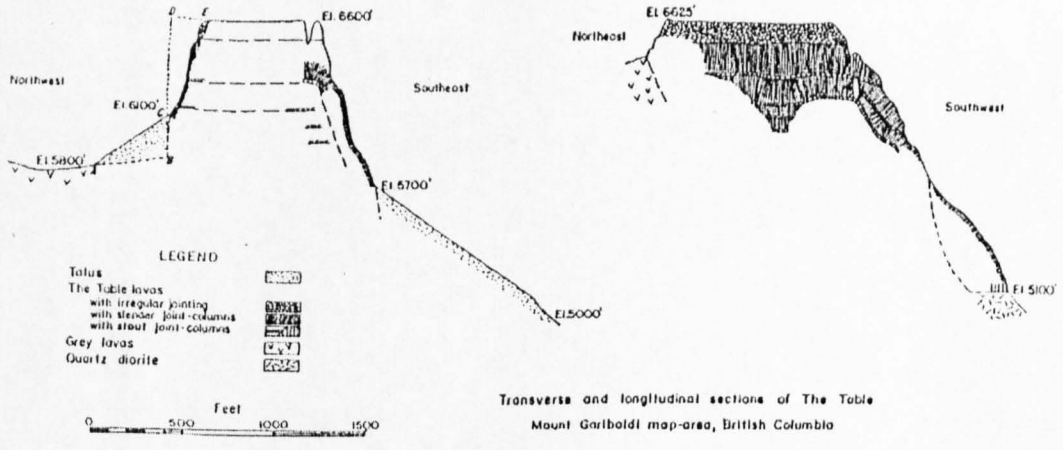

Fig. 1.8. Cross-section of The Table, a subglacial andesitic volcano in British Columbia. Note the steepness of the edifice, which appears to be built almost entirely of lava. One lava body has 'dribbled' over the flank of the edifice, and directly overlies older till and basement rock on the southeast side of the volcano. After Mathews (1951).

orientation of cooling surfaces (e.g. Degraff et al. 1989), may be used in a subglacial context to infer the position of ice walls during an eruption (since applied by Lescinsky & Sisson 1998). He added that the mechanism of heat transfer between lava (or magma) and ice would determine the geometry of melting. The elevation of the lava cap of The Table lies 60 m below a glacial 'tide mark' – the highest extent of striae formed by contemporaneous glaciation in the region. Mathews suggested that, if emplacement of The Table coincided with the period of thickest ice cover, the lavas built a pile that reached within 60 m of the palaeo-ice surface. Another important observation was that the axis of elongation of the lava cap of The Table exactly coincides with the orientation of glacial striae in the region – suggesting that the shape of the subglacial cavity within which The Table was emplaced may have been influenced by patterns of glacier flow.

1.4. Field evidence for volcano-ice interaction at stratovolcanoes

Many stratovolcanoes, even those at mid- and low latitudes, have been partly covered by glaciers for much or part of their history (Major & Newhall 1989). In tropical or subtropical climatic zones, only stratovolcanoes of 4000 m elevation or more currently host permanent snow and ice fields (e.g. Nevado del Ruiz, Columbia at 5389 m). This decreases to <1000 m in temperate and sub-polar zones (e.g. Unmak, Alaska). Glaciers on volcano flanks are typically <100 m thick (e.g. Redoubt, Mount Rainier), whereas summit calderas may contain ponded ice 600 m thick (Sollipulli, Chile; Gilbert et al. 1996), or even 1 km thick (Mount Wrangell, Alaska; Benson & Follett 1986). The mode of volcano-ice interaction on the flanks of stratovolcanoes is markedly different from volcanic eruptions beneath more extensive, thicker ice sheets

- partly due to the thinner ice cover on the volcano flanks, but also due to the steeper bedrock topography, which prevents substantial meltwater accumulation (Smellie 1999). Evidence for volcano-ice interaction during ancient eruptions of stratovolcanoes has been found at Hoodoo Mountain, British Columbia (Edwards 1997), Sollipulli, Chile (Gilbert et al. 1996), Nevados del Chillan, Chile (Dixon et al. 1999), Mount Rainier, Washington (Lescinsky & Sisson, 1998), Redoubt volcano, Alaska (Till et al. 1994) and Mont-Dore, France (Morel et al. 1992).

The most common evidence for volcano-ice interaction at stratovolcanoes is the presence of columnar-jointed lava flows (Morel et al. 1992, Till et al. 1994, Gilbert et al. 1996, Edwards 1997, Lescinsky & Sisson 1998, Dixon et al. 1999), commonly found within valleys incised in the volcano flanks by glacial erosion or flowing meltwater. Columnar jointing *per se* is not evidence for a subglacial eruptive setting, since columns also form in lavas emplaced within river valleys and inundated by water (Sæmundsson 1970). Glacial melting can be inferred as the most likely source of water at many stratovolcanoes, whose elevation is far above any palaeo-lake or river channel. Columns are thought to develop during cooling contraction of lavas, and column axes develop perpendicular to the plane of cooling (Degraff et al., 1989). Thus the orientation of columnar joints within a lava body gives an indication of the geometry of heat loss from the lava. The arrangement of columnar joints in subglacial or ice-contact lavas (Fig. 1.9) is distinct from that of other, non-glacial lavas (Lescinsky & Sisson 1998). This reflects the geometry of cooling - the sides of lavas appear to have cooled and chilled against ice walls, typically near-planar and steeply inclined, whereas the top of lavas may lack columnar joints and appear subaerial, or be cut by near-vertical joints. Observations of recent eruptions at the ice-covered

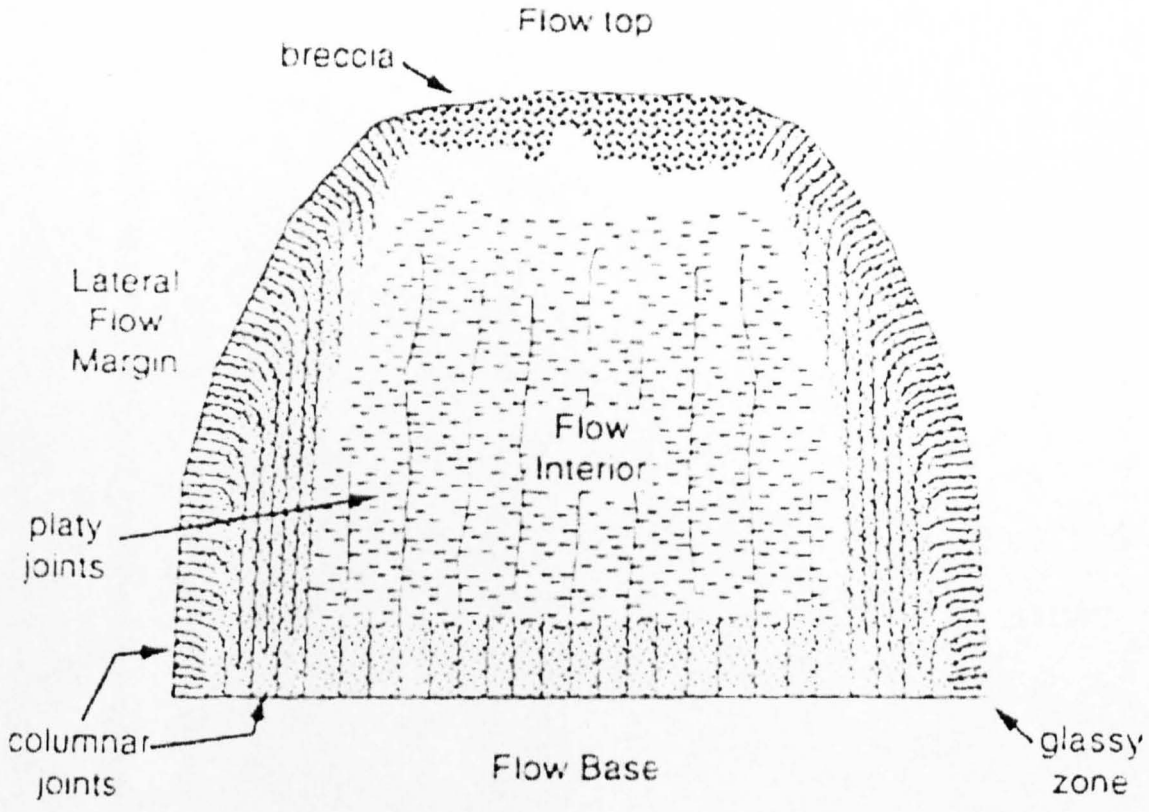

Fig. 1.9. Idealised cross-section of an ice-marginal dacite lava flow on Mount Rainier, from Lescinsky & Sisson 1998. Section normal to long axis of flow.

stratovolcanoes Llaima, Chile (Moreno & Fuentealba 1994), Kluivekovsky, Kamchatka (Vinogradov & Murav'yev 1988) and Villarrica, Chile (Gonzalez-Ferran 1984, 1985) have confirmed that lava flows may be deflected by, and chilled against, steeply-inclined ice walls (Fig. 1.2b).

Fragmental lithologies at some stratovolcanoes are also interpreted as the products of volcano-ice interaction: including 'hyaloclastites', debris flow deposits and peperites (Morel et al. 1992, Gilbert et al. 1996, Edwards 1997). Although similar deposits may also form in subaqueous conditions, glacial melting is, in each case, the most plausible source of meltwater. Many stratovolcanoes have erupted over periods of tens or hundreds of thousands of years, which have spanned glacial and interglacial conditions, and there are frequently subaerial deposits intercalated with subglacial units (e.g. Edwards 1997). A consistent theme at stratovolcanoes is the absence of evidence for deposition of fragmental material within a standing body of meltwater (c.f. Skilling 1994). Limited accumulation of meltwater will reduce both the potential for explosive magma-water interaction and for the generation of high-magnitude jökulhlaups, but nevertheless rapid melting of ice and snow during eruptions may generate damaging lahars (e.g. Pierson et al. 1990, Trabant et al. 1994, Walder 2000a).

1.5. Observations of volcano-ice interaction during eruptions

Many observations of volcano-ice interaction have been made in the twentieth century, chiefly in Iceland, the Andes and Alaska. Observed eruptions are predominantly basaltic and rarely andesitic, whereas rhyolitic eruptions have yet to be observed.

Major and Newhall (1989) provide a comprehensive summary of recorded historical eruptions. There have been numerous examples of volcano-ice interaction in the twelve years since Major & Newhall's review was published, and eruptions are becoming increasingly well documented and monitored. The largest-volume subglacial eruption in the twentieth century was at Katla in 1918, when ~1 km^3 of basalt was erupted, but unfortunately details of the course of events are incomplete (Guðmundsson, submitted). Eruptions at least an order of magnitude larger in volume have occurred in Iceland during the Quaternary (e.g. Werner et al. 1996).

Observations and interpretations from a selection of important twentieth-century eruptions in which volcanoes interacted with ice are given in Tables 1.2a (Iceland) and Table 1.2b (rest of the world). The tables are accompanied by a selection of photographs and diagrams of eruptions (Fig 1.10), which are mostly taken from the internet. By far the best-observed subglacial eruption was that of Gjálp, Iceland in 1996. This was an extremely important eruption for the study of volcano-ice interaction, and so a detailed chronology is provided in Table 1.2c.

Volcano name, type and glacier type	Date, duration	Observations	References
Katla Basaltic stratovolcano, 11 x 14 km ice-filled caldera. Temperature ice 200-700 m thick	July 1999 Few hours	Eruption/melting beneath 450 m ice. Ice cauldron 2 km diameter, 50 m deep formed in ~1 day, small jökulhlaup. Ten smaller ice cauldrons formed in subsequent month close to caldera walls (Fig. 1.2d).	Guðmundsson, submitted NVI website
Grímsvötn Basaltic stratovolcano, 6 x 8 km caldera contains meltwater lake, covered by ice shelf ≤250 m thick	December 1998 10 days	Eruption beneath 50-150 m ice. Earthquakes followed by subglacial phase of <20 minutes, then surtseyan eruption, column to 10 km. Continued melting in weeks after eruption. Total magma volume ~0.05 km^3	Guðmundsson, submitted NVI website
Gjálp ~6 km long basaltic fissure, ice 450-750 m thick.	Sept-Oct 1996 13 days	Eruption beneath 450-750 m ice. See Table 1.2c for detailed description of events	Guðmundsson et al. 1997, for others see Table 1.2c.
Katla For description see above	 1955 Few hours	Eruption beneath 400-450 m ice. Earthquakes 5 hours duration, jökulhlaup 1 hour later. 2 ice cauldrons formed, 1 km diameter and 80 m deep. Cauldron volume ≈ jökulhlaup discharge. Subglacial mound at melting site 60 m high and 300 m diameter observed in 2000.	Björnsson et al. 2000 Guðmundsson, submitted
Grímsvötn For description see above	1934 14 days	Eruption beneath 100-150 m ice. Subglacial phase <20 minutes. Surtseyan eruption, craters 5-10 m above openings in ice shelf 0.3-0.6 km across. Total volume <0.05 km^3 magma. Possibly triggered by 80-90 m drop in lake level during (non-geothermal) jökulhlaup.	Guðmundsson, submitted
Katla For description see above	1918 24 days	Earthquakes followed by plume 2 hours later, 400 m ice melted in 2 hours. Surtseyan plume to 14 km. Jökulhlaup began at same time as plume, reached 3 × 10^5 m s^{-1}, total discharge 1-8 km^3 water, 1 km^3 magma. Much erupted material carried by meltwater. Ice cauldrons formed	Guðmundsson, submitted NVI website

Table 1.2a Observations of volcano-ice interaction during notable twentieth century eruptions in Iceland.

Table 1.2b Observations of volcano-ice interaction during notable twentieth century eruptions outside of Iceland.

Mount Rainier, USA Andesitic stratovolcano with alpine glaciers on flanks and firn 120 m thick in summit crater	c. 1850 to present day	Fumaroles at rim of summit crater have melted 1.8 km long firn cave system. Size balance between melting and roof deformation. All meltwater drains into permeable bedrock. Caves steep-sided, air circulates at 4 °C.	Kiver & Steele 1975, Zimbelman et al. 2000
Llaima Basaltic stratovolcano with 8 km caldera and glacier-covered flanks	1994	Sub-plinian eruption from summit vent. Waning phase generated spatter-fed lava flows which travelled beneath ice on upper flank, subsequent melting triggered lahars. Explosions and steam from glacier downslope of lava entry indicated subglacial lava-ice interaction	GVP website
Westdahl, Aleutian Islands Basaltic stratovolcano	1991	Explosive eruptions generated 18 km ash plume, jökulhlaups followed 3-4 hours later. Ice cauldrons 300 m across, lahars generated, lavas flowed beneath and over ice	AVO website
Redoubt, Alaska Basaltic-andesitic stratovolcano with 1.8 km diameter ice-filled caldera Ten alpine glaciers on steep flanks	1989-1990	Pyroclastic flows and rock avalanches generated during paroxysmal plinian eruption remove 0.08 km^3 snow and ice from caldera and flank glaciers, generating jökulhlaups with discharges of 1-7 × 10^4 m^3 s^{-1}. Episodic dome growth adjacent to ice, inward ice deformation and explosive steam formation (Fig. 1.10c). Ice canyons on flanks melted at 10^{-3} m s^{-1} by meltwater.	Till et al. 1994, Trabant et al. 1994, Waitt et al. 1994
Nevado del Ruiz, Columbia Andesitic stratovolcano, ice-filled summit crater 1 km diameter, 240 m deep.	1985	5-15 % of summit ice cap melted by minor pyroclastic flows and surges, total volume 3-6 × 10^6 km^3. Lahars up to 4.7 × 10^4 m^3 s^{-1}, killed 23 000 people.	Major & Newhall 1989, Pierson et al. 1990, GVP website
Villarrica, Chile Basaltic stratovolcano, <100 m thick temperate ice on steep flanks	1984	Lava flows descended ice-covered flanks beneath summit crater (Fig. 1.2b), flowed within channels 30-40 m deep, 50 m wide and 1 km long melted into ice. Steam plumes at flow front where lavas in contact with steep ice walls. Fissures in ice adjacent to channels. Minor mudflows: most of meltwater evaporated or flowed into bedrock.	Major & Newhall 1989, www.povi.org, GVP website
Veniaminof, Alaska Basaltic stratovolcano with 8 × 11 km ice-filled caldera, intracaldera cone above ice	1983	Lava flows from the intracaldera cone and adjacent subglacial activity melted ~0.15 km3 of the caldera ice field, forming a 0.9x2 km water-filled ice pit approximately 120 m deep The ice pit subsequently was partially filled by an estimated 0.04 km3 of lava.	Yount et al. 1985, Yount et al. 1987 GVP website
Cerro Hudson, Chile Basalt-andesite stratovolcano, 9 km diameter caldera, 40 m thick temperate ice ponded in crater	1973	70 % of ice within crater melted, lahars travelled 70 km, killing 2 people.	GVP website

Deception, South Shetland Isles 8-10 km caldera flooded by sea. Island supports extensive snow and ice fields.	1969	Short-lived basaltic andesite eruption on 5 km long fissure beneath ice ~100 m thick. Cylindrical ice chimneys formed, which overflowed with meltwater, sudden jökulhlaup generated, eroding channels on ice surface	Major & Newhall 1989, GVP website, Smellie (personal communication)
Mount Wrangell, Alaska Basaltic shield volcano with ice-filled 4 × 6 km summit caldera Ice frozen-based, >1 km thick	1965-	Geothermal activity increased in 1965 after nearby earthquake, melting 43×10^6 m^3 of summit ice (Fig. 1.10d). Ice deformation into regions of melting. No jökulhlaups, since ice frozen-based.	Benson et al. 1975, Benson & Follett 1986
Calbuco, Chile Stratovolcano	1961	Lava dome melted through summit glacier, generating lahars up to 3000 m^3 s^{-1}. Lava effusion during following two months. Eruption terminated with violent explosive eruption, generating 15 km high ash plume.	MTU Chilean website

Table 1.2b Observations of volcano-ice interaction during a selection of twentieth century eruptions outside Iceland. Website addresses quoted: AVO (Alaska Volcano Observatory) website: http://www.avo.alaska.edu/, GVP (Global Volcanism Program) website: http://www.nmnh.si.edu/gvp/volcano/index.htm, MTU (Michigan Tech University) Chilean website: http://www.geo.mtu.edu/~boris/Chilehome.html, NVI (Nordic Volcanological Institute) website: http://www.norvol.hi.is.

Date	Observations	Interpretation and significance	References
Sept 29 1996	*10:48* Magnitude 5.4 earthquake in Barðarbunga	Structural changes in shallow crust	Zobin 1999
Sept 30	*22:00* Continuous eruption tremor at Gjálp	Onset of eruption	Guðmundsson et al. 1997
Oct 1	*am* Two 1-2 km wide ice cauldrons observed during overflight (Fig. 1.10e), deepen and enlarge throughout day, two additional bowls form on fissure 5-6 km long. Original ice thickness 450-750 m. Northeastern bowl deepens 50 m in four hours. Ice surface initially smooth, concentric fractures form in ice as bowls deepen. Level of ice cover of Grímsvötn lake 15 km south rises 10-15 m, shallow linear subsidence structure develops from eruption site to Grímsvötn.	Subglacial melting focussed at four points on fissure, deformation and collapse of roofs of subglacial cavities. Rapid melting due to fragmentation and meltwater convection. Meltwater draining from eruption site into Grímsvötn lake in subglacial tunnel, melting of walls.	Description of events: Guðmundsson et al. 1997, GVP website, NVO website. Monitoring of ice deformation: Alsdorf & Smith 1999, Björnsson et al. 2000. Fracturing: Malthe-Sorenssen et al. 1998
Oct 2	*04:47* Onset of subaerial 'surtseyan' eruption, rhythmic explosions through water column ~50 m deep form black ash clouds, tephra deposited on glacier surface nearby, plume 4-5 km high (Fig. 1.3), opening in glacier surface several hundred metres wide. *pm* New ice cauldron formed to north.	Complete melting and collapse of ice roof above main vent, magma-water interaction during eruption through water locally ponded at eruption site. New locus of activity to north.	Description of events: Guðmundsson et al. 1997, GVP website, NVO website Monitoring of ice deformation: Alsdorf & Smith 1999, Björnsson et al. 2000.
	Northern bowl now 2 km wide, periodic explosive eruptions	Continued melting on subglacial parts of	

Oct 3	from main vent, water level 50-200 m below original ice surface. Opening in glacier surface further enlarged, ice cover continues to rise at Grímsvötn. Ice subsidence over area 8-9 km long and 2-3 km wide. Surface drainage of meltwater within ice canyon 150 m deep, 3.5 km long at southern part of fissure (Fig. 1.10f).	fissure. Continued eruption at main vent, deformation of ice into cauldrons exceeded by melting. Despite drainage into Grímsvötn, overspill of meltwater indicates that some ponding at vent occurred, possibly due to damming of drainage channels by erupted material.	Description of events: Guðmundsson et al. 1997, GVP website, NVO website. Monitoring of ice deformation: Alsdorf & Smith 1999, Björnsson et al. 2000.
Oct 10	Continued eruption, intensity decreasing. Size of opening in glacier surface constant. Main vent still water-covered, black ridges of basaltic hyaloclastite protrude above water level. Grímsvötn lake level continues to rise	Deformation rate of ice into vent area now equal to melting rate. Eruption rate dwindling, continued meltwater drainage into Grímsvötn.	Description of events: Guðmundsson et al. 1997, GVP website, NVO website.
Oct 13	Eruption tremor ceases, 3 km^3 of meltwater now accumulated in Grímsvötn lake	End of eruption. Continued meltwater drainage into Grímsvötn	Description of events: Guðmundsson et al. 1997, GVP website, NVO website.
Oct 18	Ridges of hyaloclastite rise tens of metres above meltwater level in main vent area. Continued melting of ice, level of Grímsvötn lake continues to rise.	Residual heat in erupted products causes melting, meltwater continues to drain subglacially into Grímsvötn.	Guðmundsson et al. 1997.
Nov 4	*21:30* Seismic tremor detected at Grímsvötn	Probably reflects ice fracture and movement as ice barrier pierced	NVO website.
Nov 5	*08:30* Onset of jökulhlaup on Skeiðarársandur, 50 km south of Grímsvötn. *am* Meltwater bursts out of crevasses beneath ice 200 m thick (Fig. 1.10g), delta built to sea by transported sediments. *pm* Destruction of bridges on coastal plain, many icebergs carried by floodwater. *23:00* Peak water flow of 45 000 $m^3 s^{-1}$	Subglacial meltwater transport, rapid enlargement of drainage channels and melting due to thermal and kinetic energy of meltwater. Subglacial pressures considerably higher than glaciostatic, triggering brittle failure of ice 200 m thick.	Guðmundsson et al. 1997, Fowler 1999, Maria et al. 2000, Smith et al. 2000, Roberts et al. 2001, Russell et al. 2001, Waller et al. 2001.
Nov 6	*13:00* Small eruption in Barðarbunga, 20-30 minutes duration, eruption column to 4 km	Intrusion of magma triggered by decompression during drainage of Grímsvötn	NVO website.
Nov-Dec	Total meltwater volume discharged 4 km^3.	Only 75 % of melting occurred during eruption, hence 25 % of magma thermal energy released gradually	Guðmundsson et al. 1997.
June 1997	Radio echo soundings indicate that 6 km long ridge up to 500 m high formed, of volume 0.7 km^3 (c. 0.4 km^3 DRE). Ridge broad and flat to north, where ice thickest (c. 750 m). Exposed part of ridge 300 m long, composed of altered, glassy hyaloclastite of	Morphology of edifice similar to numerous Quaternary basaltic tindars in Iceland. Broad shape of northern part due to thicker ice, but unclear why: higher water pressures?	Guðmundsson et al. 1997, Langley 2000, Steinthorsson et al. 2000, Guðmundsson, submitted.

	basaltic andesite-icelandite composition		
1997-1998	Ice canyons gradually filled by lateral ice flow, closure of ice around main vent area	Ductile deformation of ice acts to even out irregularities in ice surface. Ice will eventually heal, and nunatak will disappear.	Aðalgeirsdóttir et al. 2000

Table 1.2c Summary of observations and interpretations of events during and after the 1996 Gjálp subglacial basalt eruption.

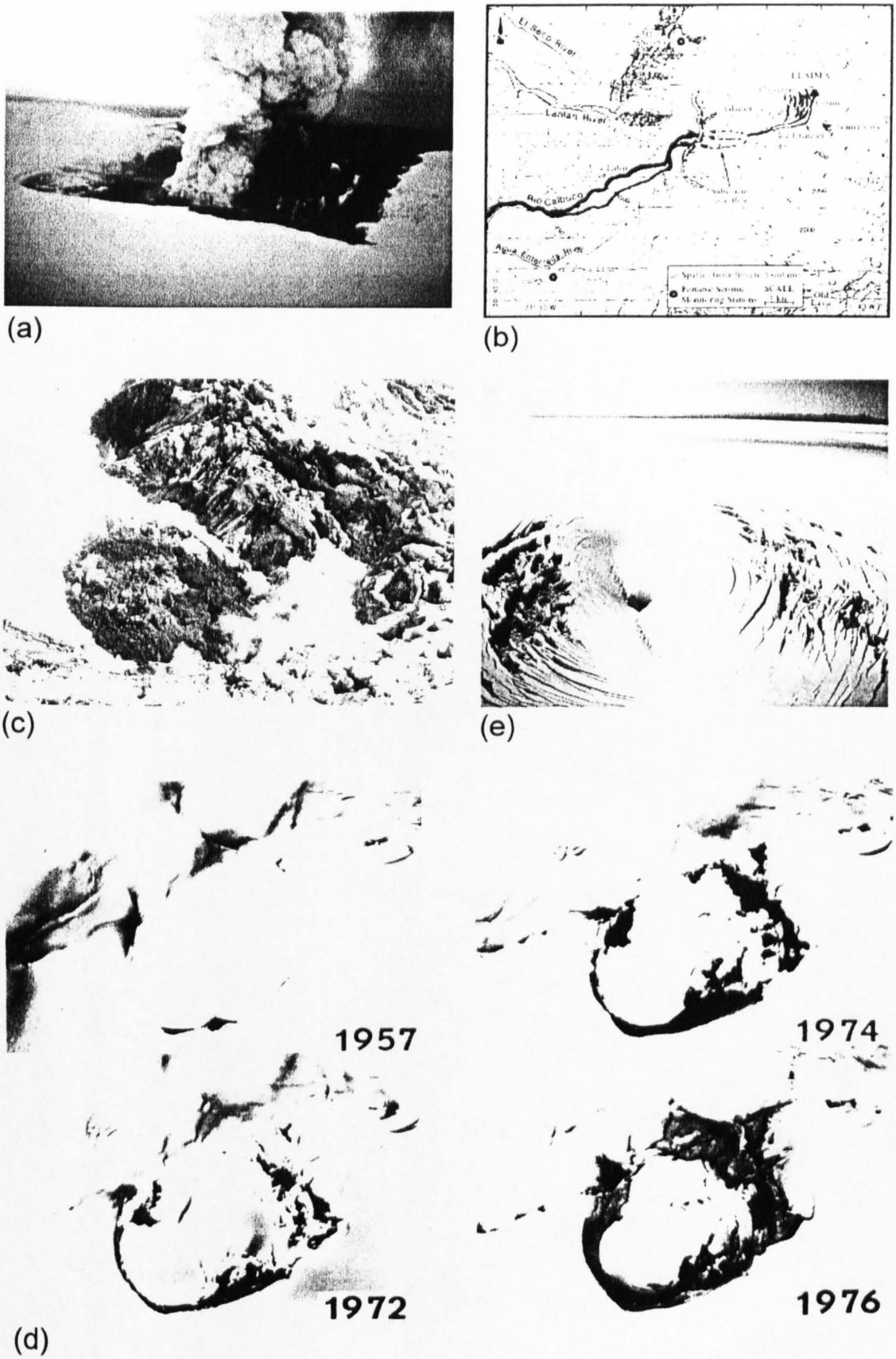

Fig. 1.10.

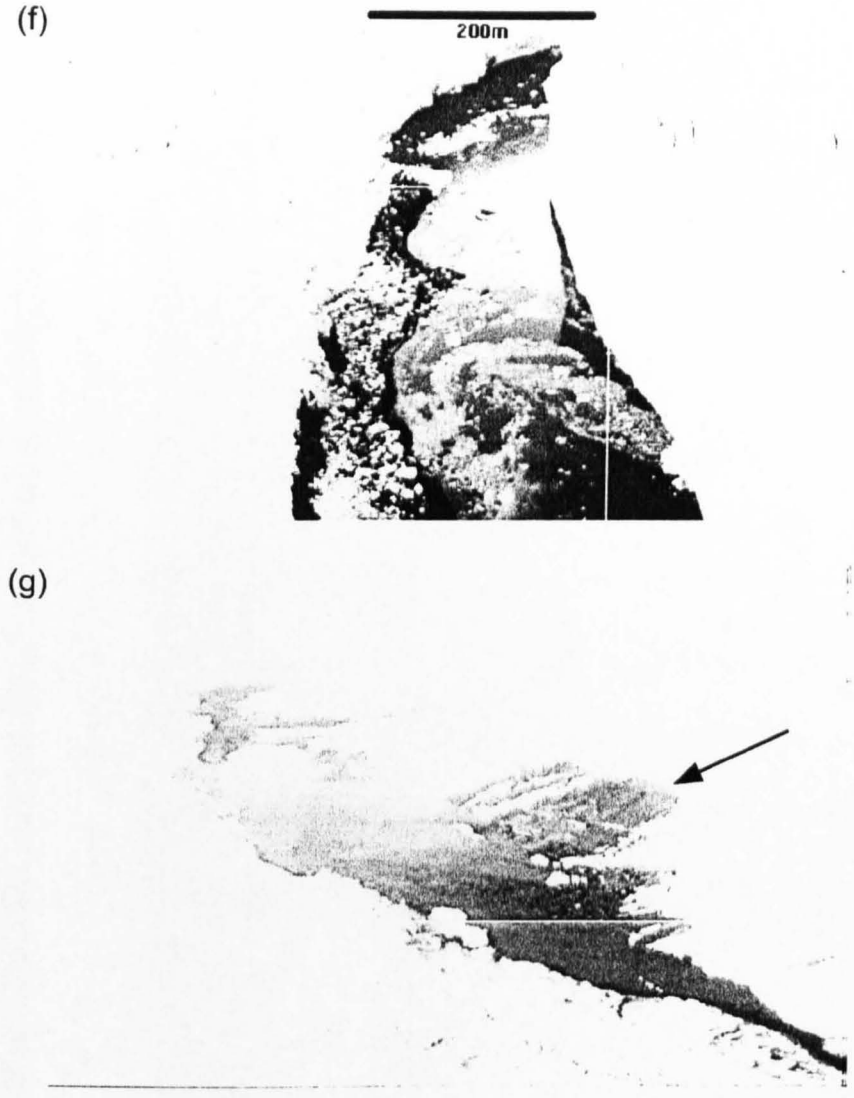

Fig. 1.10. (a) The steam-and-ash plume rising from the vent area of the 1998 Grímsvötn eruption. Note the blanket of black tephra covering part of the glacier surface. Photograph by Freysteinn Sigmundsson. **(b)** Sketch map of the Chilean volcano Llaima in the aftermath of its 1994 eruption. *Arrows* indicate the subglacial trajectory taken by the lava, the areas devastated by lahars created during the eruption are shaded black. Drawing by H. Moreno. **(c)** Lava dome at Redoubt volcano on June 9th 1990. The dome (dark grey, left centre of picture) is surrounded by clouds of steam that rise from its outer margin, where the dome is in contact with heavily fractured ice. From Miller (1994). **(d)** Photographs of the north crater of Mount Wrangell before and after the 1965 earthquake. The crater is approximately 1 km in diameter. After Benson & Motkya 1978. **(e)** An ice cauldron above the main vent of the 1996 Gjálp eruption, pictured on October 1st, approximately 15 hours after the onset of the eruption. At this stage, the bowl is approximately 100 m deep and 1 km in diameter. Photograph by M. T. Guðmundsson. **(f)** The ice canyon that formed on the surface of Vatnajökull above the southern part of the Gjálp eruptive fissure. Meltwater is flowing south towards Grímsvötn lake. Photograph by M. T. Guðmundsson.**(g)** The outlet glacier, Skeiðarárjökull, during the November 1996 jökulhlaup that was triggered by the Gjálp eruption. The jökulhlaup burst through the glacier snout beneath ice some 200 m thick (Roberts et al. 2000), the fractures formed are linear (arrow). The dark area down-glacier from the fractures is a veneer of sediment that was entrained in the jökulhlaup and deposited on the glacier surface. This photograph was taken by M. T. Guðmundsson ~1 hour after water started to emerge from this part of the glacier.

Fig. 1.10. continued

1.5.1. Style of observed eruptions

The style of a subglacial eruption depends upon the magma type, magma discharge rate, ice thickness, structure of ice and bedrock slope. Volcano-ice interaction can profoundly affect the eruption mechanisms, as, for example, explosive magma-water interaction may occur in the subglacial equivalent of lava-producing fissure eruptions. Eruptions of basaltic magma beneath thick ice (>200 m, e.g. Katla 1918, Gjálp 1996) begin with a subglacial eruption, with rapid melting. Hours or days later, the ice surface is pierced, and a Surtseyan-type eruption ensues, with ash and steam plumes reaching 4-18 km in height (Fig. 1.3).

Eruptions beneath thinner ice (<150 m) with near-horizontal bedrock, e.g. Grímsvötn 1998, typically have a much shorter subglacial phase (minutes), followed by a Surtseyan eruption (Fig. 1.10a). The volume of Surtseyan products is much smaller than that formed beneath thicker ice, probably due to less meltwater being available at the vent area.

Eruptions at stratovolcanoes have often been characterised by a period of explosive activity, with an ash plume originating from a vent in the summit crater, followed by effusive activity, in which lava flows are generated. Lava flows have been observed to flow within channels melted into ice on the steep volcano flanks (e.g. Villarrica 1984, Llaima 1994), and to be deflected by ice walls, as occurred during the 1983 eruption of Klyuchevskoi (Vinogradov & Murav'yev 1988). There is little magma-water interaction, and the presence of ice does not significantly affect the eruption mechanism.

Pyroclastic flows passed over snow and ice on the upper slopes of Nevado del Ruiz during the 1985 eruptions, caused rapid melting, and generated devastating

lahars and mudflows. However, the *eruption mechanism* itself was not significantly affected by the presence of ice, as rising magma did not interact with ice or meltwater.

1.5.2. Melting rates during observed eruptions

The following rates of subglacial melting can be estimated from twentieth cenutry Icelandic eruptions: 0.06 m s^{-1} during Katla 1918 (400 m ice), >0.04 m s^{-1} during Grímsvötn 1998 (50-150 m ice) and 10^{-3} m s^{-1} during Gjálp 1996 (450 m ice). These estimates are based on the length of time from the onset of volcanic tremor to the first observed subaerial eruption (Guðmundsson, submitted). Brittle failure of ice above the vent will dramatically reduce the time taken for the glacier surface to be pierced, and will have a larger effect if much of the ice is prone to brittle fracture (i.e. thin ice). Thus the apparent high melting rate during Grímsvötn 1998 may be mostly due to brittle fracture of thin ice. These melting rates are orders of magnitude more rapid than predictions of melting during cooling of basaltic pillows (Hoskuldsson & Sparks 1997), suggesting that more rapid magma-ice energy exchange occurred. It has been proposed that this was due to fragmentation and turbulent convection of a heated meltwater-pyroclast mixture (Guðmundsson et al. 1997).

The melting rate of the glacier surface during the 1989-1990 eruption of Redoubt was approximately 10^{-3} m s^{-1}, which is comparable to that during Gjálp 1996. At Redoubt 1989-1990, melting was dominated by mechanical scouring of sediment-laden meltwater as it flowed rapidly over the ice surface, and was observed to slow significantly once the initially crevassed surface became smoothed (Trabant et al. 1994). This indicates that the *roughness of the ice surface* (e.g. the surface area of ice available for melting) is a first-order effect in determining the melting rate, along with the *mechanism* of melting.

1.5.3. Meltwater drainage patterns

Meltwater is thought to have drained away from the eruption site during both Icelandic eruptions observed beneath thick ice (Katla 1918 and Gjálp 1996), at approximately the same rate as it was formed close to the vent (Guðmundsson et al. 1997, Guðmundsson, submitted). However, the subaerial phase of the Gjálp 1996 eruption emerged from meltwater >50 m thick that had ponded at the vent. A likely explanation is that, although subglacial meltwater drainage was possible (the 'leaky vault' scenario of Smellie 1999), the rate of meltwater generation exceeded the rate at which meltwater could escape. Partial or complete blockage of subglacial drainage channels by volcanic debris may periodically reduce the rate of meltwater escape during eruptions (Trabant et al. 1994), especially when meltwater is sediment-laden (e.g. Tómasson 1996, Maria et al. 2000). Continuous meltwater drainage contradicts established models for the hydrology of thick temperate glaciers, in which meltwater escape is prevented by the development of ice cauldrons (Nye 1976, Björnsson 1988); and may reflect subglacial thermal erosion by heated meltwater (Clarke 1982, Smellie 1999).

Meltwater *accumulated* at the vent area during the 1969 Deception eruption, beneath thin ice – again contradicting conventional hydrological models, which suggest that meltwater accumulation is unlikely (Smellie & Skilling 1994). In this case, the thin glacier was formed predominantly of impermeable ice and acted hydraulically like a thicker glacier (Smellie, in press). In addition, the escape of meltwater may have been prevented by blockage of meltwater drainage channels by volcanic debris (Smellie, in press).

Negligible meltwater accumulation has been observed during eruptions at stratovolcanoes, largely because eruptions have occurred in summit craters, and

meltwater has readily drained down the steep upper slopes of the volcanoes. Meltwater discharge rates may either be similar to melting rates (e.g. Llaima 1994), or considerably lower, possibly due to evaporation and percolation into permeable bedrock (Villarrica 1984). Minor meltwater accumulation during the emplacement of a subglacial lava flow at Redoubt probably occurred when the subglacial channel became temporarily blocked (Trabant et al. 1994).

Although there has been considerable geothermal melting at Mount Wrangell (Alaska) since 1965, no jökulhlaups have been generated – since the glacier base is frozen, and any meltwater is likely to have been refrozen before travelling a significant distance subglacially (Benson & Follett 1986).

1.5.4. Ice deformation patterns

Ice cauldrons form on the surface of thick glaciers during subglacial melting. The sizes of bowls formed in glaciers 400-750 m thick are fairly consistent: widths vary between 1-2 km and depths between 50-150 m. The ice surface remains smooth during the initial period of bowl formation, indicating ductile deformation (Guðmundsson, personal communication 2001), and concentric fractures then develop as bowls deepen (Malthe-Sorenssen et al. 1998). This may reflect the strain-rate dependent rheology of ice, which initially deforms in a ductile manner at low strain rates and fails brittly when strain rates increase (Jones 1982). Flow of ice into depressions in the ice surface occurs both during and after eruptions. This has two effects: firstly, the diameter of an opening in the ice surface may be limited by inward ice deformation (e.g. Guðmundsson et al. 1997). This would suggest that only high-magnitude, prolonged eruptions are capable of producing a sizeable subaerial lava cap. Secondly, inward ice deformation after the eruption may 'heal' the opening in the

ice surface around the vent, thus burying and eroding tephra that was deposited in a subaerial eruption.

Thinner ice may also deform during eruptions, and it also forms concentric fractures (e.g. Calbuco 1961, Deception 1969, Redoubt 1989-1990). However, ice deformation rates are much slower. Only minor ice deformation occurs on thin glaciers on the flanks of stratovolcanoes, although crevasses have been observed in ice adjacent to channels cut in ice on Villarrica's summit in 1984 - indicating brittle ice deformation. Rapid post-eruptive accumulation of snow may play an important role in burying ice-contact lava flows on Villarrica and other stratovolcanoes.

1.5.5. Summary of observations

Observations of subglacial eruptions in the twentieth century have shed light on the response of glaciers: both the geometry and rate of ice melting and deformation. Although great thicknesses of ice can be melted with surprising rapidity, ice walls are capable of containing and deflecting flowing lava, explaining why lava flows with 'ice-moulded' characteristics are found on some glaciated stratovolcanoes. Patterns of meltwater drainage are at odds with most theoretical predictions, suggesting a role for blockage of drainage channels by volcanic debris, which may allow temporary accumulation of meltwater.

1.6. Overview of the volcano-ice system

> *Observations of eruptions and interpretation of ancient subglacial deposits have led to [a limited] understanding of volcano-ice interaction and the behaviour of the volcano-ice system. In the*

forthcoming sections 1.7, 1.8 and 1.9, I will use different pieces of evidence from the 'pure' glaciological literature to predict the response of the glacier to subglacial melting, and the effects of this response upon the eruption mechanisms and resultant products. But first it is useful to summarise the geometry and organisation of the volcano-ice system that is being considered. This brief section uses schematic diagrams to illustrate the system, and points out some of the uncertainties in its behaviour that will be mentioned later in this chapter and in Chapter 5.

There are three types of volcano-ice system dealt with here: eruptions beneath thick glaciers (the most relevant to this thesis); eruptions beneath thin glaciers; and eruptions at glacier-clad stratovolcanoes.

1.6.1. Subglacial eruptions beneath thick temperate glaciers

The following sequence of events are likely to occur during an eruption beneath a thick temperate glacier:

In the initial phase of the eruption, which may be of hours or days duration, subglacial melting forms a cavity at the glacier base. Meltwater is likely to escape from the cavity, leading to the formation of an ice cauldron on the glacier surface above. Escape of meltwater may be reduced or entirely stopped by ice deformation, and thus the cavity may become completely water-filled (Fig. 1.5a). Aided by fracturing of the surface, the thinning ice roof will collapse and rapidly melt, leading to the onset of a subaerial eruption through a meltwater lake. Deformation of ice into

the vent area limits the size of opening melted in the glacier surface. The level of meltwater will be determined by the relative rates of meltwater formation (melting) and meltwater loss by subglacial drainage. The eruption style will become increasingly explosive as the height of the water column above the growing edifice reduces, until a subaerial eruption ensues (Fig. 1.5b). The lake level may become stabilised at this stage if meltwater can drain away through permeable firn, although the lake may 'float' the surrounding ice barrier if the firn layer is thin, leading to a jökulhlaup and a dramatic drop in the lake level (Fig. 1.5e).

A meltwater lake will not develop at the eruption site if meltwater drains away at the same rate as it is formed during the eruption. In this instance, the subglacial cavity may be filled with steam, and collapse of the roof will occur once it is thinned beyond a critical (and undetermined) point. A phreatomagmatic eruption will then occur, with dwindling magma-water interaction as the edifice grows and available meltwater diminished, and finally a subaerial lava cap will be formed.
Key questions include:

- *what is the mechanism of heat transfer from magma to ice?*
- *what is the geometry of melting?*
- *at what stage will the roof collapse?*
- *will meltwater accumulate or escape?*

In order to answer these questions, it is necessary to discuss the likely mechanisms of magma-ice heat transfer, the melting and deformation of ice, and aspects of glacial hydrology.

1.6.2. Subglacial eruptions beneath thin temperate glaciers

The sequence of events contrasts with that of eruptions beneath thicker ice, in that the subglacial phase is much shorter, little meltwater accumulates at the eruption site, ice deformation is less important, and advancing lavas may be moulded within subglacial drainage tunnels, or channels cut into the ice surface (Vinogradov & Murav'yev 1988; Fig. 1.2b, Fig. 1.6).

1.6.3. Volcano-ice interaction at stratovolcanoes

If an eruption occurs within an ice-filled summit caldera of a stratovolcano, it may be classed as an eruption beneath thick ice (section 1.6.1). However, many stratovolcanoes, such as Villarrica or Nevados del Ruiz, have little ice around the eruptive vent, but glacier-clad flanks. In this case, rapid melting may occur if hot volcanic debris comes into contact with the glacier surface, and lahars may be generated (Fig. 1.11). Lavas may flow and be moulded within channels earlier melted in the ice (Fig. 1.11). No or little meltwater accumulation occurs (e.g. Trabant et al. 1994).

1.7. Melting of ice during subglacial eruptions

The mechanism, rate and geometry of ice melting during volcano-ice interaction will play an important role in determining the style of eruption and morphology of its products, as well as controlling the generation of meltwater. Melting during volcano-ice interaction

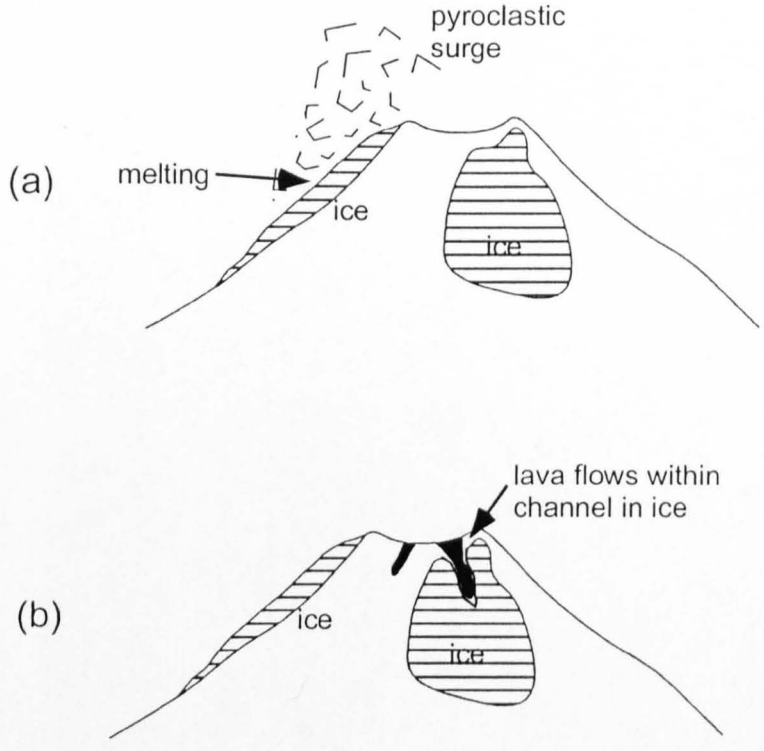

Fig. 1.11. Cartoon illustrating possible events during eruption of a glacier-clad stratovolcano. **(a)** Pyroclastic surges travel over the glacier surface, causing rapid melting and forming lahars. **(b)** The eruption is now effusive, and lava flows within channels etched into the glacier surface.

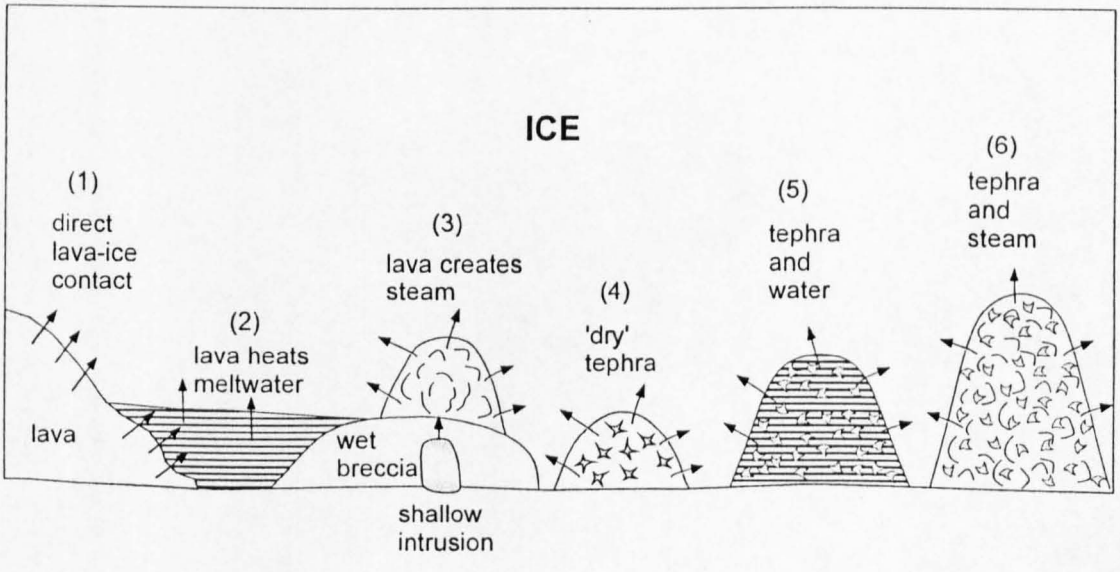

Fig. 1.12. Schematic diagram illustrating various possible mechanisms of energy exchange between magma and ice. More details of each mechanism are given in Table 1.3.

occurs in two principal patterns: firstly, and most importantly for the present study, the glacier base can be melted by a subglacial eruption, where the eruptive vent is initially entirely covered by ice (e.g. Gjálp 1996, Guðmundsson et al. 1997). Secondly, the products of volcanic eruptions (e.g. lavas and pyroclastic flows) can travel over a glacier or snowfield, melting its surface (e.g. Pierson & Janda 1994). In this case, the eruptive vent need not necessarily be ice-covered (Major & Newhall 1989). I will first examine models and observations of subglacial melting, before briefly discussing surface melting.

1.7.1. Energy transfer from magma to ice

The mechanism of energy transfer from magma to ice can be divided into two parts, although each is connected: (1) the loss of heat from the magma and (2) the thermal or mechanical erosion of the ice. Magma may cool in direct contact with the ice, within water or within steam (Fig. 1.12). The rate of cooling is mediated by the mechanical state of the magma as it cools - whether it fragments or remains in a coherent body. The first order effect that fragmentation has upon cooling rates is to increase the surface area available for energy transfer to the surrounding medium (air, water, steam or ice). Table 1.3 lists a number of possible mechanisms of magma-ice energy transfer, and cites research that has attempted to put quantitative constraints on each. This energy exchange is investigated in more detail in section 5.2.

	Energy exchange mechanism	Probable products	Observed during an eruption?	Ancient examples	Required conditions	References (modelling)	References (ancient examples)
no fragmentation	lava → ice	Columnar-jointed lava bodies with minor massive breccias. .	Yes, at Kluivescky, Villarrica, Llaima and elsewhere, but products of historical eruptions not studied	Lava flows on Mount Rainier and elsewhere	Subglacial: effusive eruption within air-filled subglacial cavity (meltwater drainage). Ice-contact: effusive eruption forms lava flows which chill against ice	Chapter 5 (this study)	Lescinsky & Sisson 1998 Lescinsky & Fink 2000
no fragmentation	lava → water → ice	Lava bodies with associated vesicle-poor glassy breccias which display evidence for deposition within water.	No	Pillow lavas at the base of basaltic tuya and tindar successions	*Subglacial:* effusive eruption with water-filled subglacial cavity. Pressure sufficiently high to prevent fragmentation of magma. Meltwater accumulation. Ice-contact: highly unlikely	Einarsson 1966 Allen 1982 Hoskuldsson & Sparks 1997	Jones 1970 Fridleifsson et al. 1982 Moore & Calk 1991 Skilling 1994
no fragmentation	lava → steam → ice	Variable. If lava intrudes shallow wet sediments, may produce pumiceous peperitic lavas. Evidence for fluxing by steam.	Possibly at Redoubt 1989-90, Villarrica 1984, Llaima 1994, but ice-contact, not subglacial, and inefficient.	Bláhnúkur lava lobes (Chapter 2)	*Subglacial:* drainage of meltwater from cavities into permeable bedrock. Intrusion of waterlogged material at the glacier base by lava bodies. *Ice-contact:* steam plumes form around lavas. Favoured by meltwater drainage (high magma/water ratio)	none	Kiver & Steele 1975 This study: Chapter 2, Chapter 5.9
fragmentation	tephra → ice	Variable. If tephra emplaced on ice surface, may produce poorly-sorted debris flow deposits with evidence for fluidisation. If tephra emplaced subglacially, may produce massive deposits of vesicular ash.	Many: e.g. Mt St Helens 1980, Nevado del Ruiz 1985 (Major & Newhall 1989)	Lahars generated during pyroclastic flows over snow and ice	The kinetic energy and thermal energy of tephra is transferred to ice during collision with the ice or emplacement on the ice. There is little magma-water interaction and little steam is generated. If subglacial, requires a drained cavity.	Walder 2000a, Walder 2000b	summarised in Rodolfo 1999

ragmentation						
tephra → water → ice	Low-vesicularity tephra, possibly displaying evidence for deposition within water (e.g. turbidites, laminated sandstones, local channels)	Not directly observed but inferred during Gjálp 1996	Bedded vesicle -poor 'hyaloclast - ites' at basaltic tuyas	Explosive magma-water interaction within a water-filled cavity. Thermal and kinetic energy transferred to ice. No 'air gap' for steam formation.	none	Jones 1970 Skilling 1994 Smellie 1999
tephra → steam → ice	Structureless low-vesicularity tephra if not subsequently reworked	No	Chapter 3, Chapter 4 (this work)	Subglacial: explosive eruption within a partly water-filled cavity. Requires drainage of meltwater from cavity, and possibly percolation into growing pile of debris	None	None

Table 1.3. Energy exchange mechanisms during magma-ice interaction.

1.7.2. Structure and distribution of terrestrial glaciers

Glaciers on earth vary from vast ice sheets over a kilometre thick (e.g. the West Antarctic ice sheet, Blankenship et al. 1993) to alpine glaciers, which may be <100 m thick and are commonly confined to valleys less than a kilometre wide (Bennett & Glasser 1996). Bodies of ice in the coldest climatic zones (Antarctica, Greenland and the mountains of Alaska and Yukon) are entirely colder than the pressure melting point (Paterson 1994 p. 12), and are termed 'frozen-based' glaciers, whereas ice within glaciers elsewhere is at the melting point throughout (temperate glacier). An important difference between these two glacier types is that temperate glaciers have meltwater at their bases, whereas frozen-based glaciers do not. Snow that accumulates on the glacier surface is compacted, and converts to firn and polycrystalline hexagonal ice I_h (Hooke 1998). In temperate glaciers, the thickness of the upper firn and snow layer is variable, but typically falls within the 40-70 m range (Paterson 1994). Snow and firn are permeable, contain significant trapped air bubbles, and have densities in the range 50-300 and 400-830 kg m^{-3}, respectively. Ice is impermeable, with a typical density of 917 kg m^{-3} (Paterson 1994, p. 9). As subglacial eruptions in Iceland are thought to have occurred beneath temperate glaciers, I will limit my discussion of eruptions beneath frozen-based glaciers to brief speculation in Appendix I.

1.7.3. Mathematical models of subglacial melting

In a typical subglacial eruption, subglacial melting forms a cavity within which a pile of volcanic debris accumulates, and meanwhile meltwater is formed (e.g. Guðmundsson et al. 1997). Although such a model may appear simple, the mechanisms of volcano-ice interaction and, specifically, magma-ice heat transfer

remain poorly constrained. It is necessary to determine 1) the mechanism of heat transfer between magma and ice, 2) the geometry of melting and resultant ice deformation, and 3) the volume and pressure changes that accompany magma emplacement and melting. To date, only three papers have directly addressed these topics.

An early investigation of magma-heat transfer by Einarsson (1966) suggested that melting during the pillow-forming phase of a subglacial basaltic eruption could not keep pace with the rate of magma injection, and the eruption would be suppressed by the weight of the overlying ice. Sluggish melting was thought to be due to the insulating effect of the chilled margins of pillows, although at the time, no robust quantitative models of pillow cooling had been published (the breakthrough paper appeared ten years later - Moore, 1976). According to Einarsson, Icelandic tuyas cannot have been formed subglacially, and tectonic uplift was proposed as an alternative. Einarsson's ideas have been largely forgotten, as compelling and consistent evidence for the subglacial origin of tuyas has accumulated in the last 35 years (e.g. Jones 1970). Nevertheless, Einarsson raised some important questions about rates of heat transfer and the influence of confining pressure upon magma ascent which are still pertinent today.

Allen (1980) revisited the problem of energy exchange between basaltic magma and ice at the base of a glacier. He considered the energy flux released from cooling pillow lavas during the initial phase of an eruption beneath a thick (500 m) temperate glacier, and used field observations of subglacial basalt in Iceland as an example (Jones 1970, Allen 1979). His pillow cooling model assumed that meltwater is abundant throughout, and that a water-filled cavity will exist at the glacier base prior to the onset of any subglacial eruption, due to increased heat flux in the vent

region prior to the first effusion of magma. Allen estimated the heat flux from pillows of 0.15 m radius and 1.5 m long, and considered the time taken for a pillow to become entirely solidified (assumed to occur when the magma temperature drops from its initial 1200 °C to 1065 °C, the solidus temperature of Icelandic basalt samples, Allen 1979). Without justification, he postulated that the rate of heat loss will greatly reduce once the pillow is completely solidified, and predicted that each pillow would have already released sufficient heat to melt four times its own volume of ice when it became entirely solid. He mentioned the insulating effect of a chilled carapace (e.g. Moore 1976), and that it is countered by the development of brittle fractures, which increase the surface area for energy exchange. Moore et al. (1973) found that the temperature of seawater only a few centimetres from advancing submarine pillow lavas is only 2.5 °C. Allen thus argued that little of the thermal energy of the magma is stored in heated meltwater, and that the heat power causing melting is equal to the heat flux released from the pillows. The magma discharge rate was estimated at 10^3 m s^{-1}, and pillows were assumed to be emplaced in layers, each of which is buried by the successive layer after $\sim 10^5$ s, long enough for most of the thermal energy to have already been released. Heat loss from pillows during cooling from 1065 °C to 0 °C is not considered.

Allen assumed that heat loss from magma during the explosive tuff-producing phase of subglacial basalt eruptions is instantaneous, and that a unit volume of magma can melt 9.1 times its volume of ice. He did not consider variably vesicular magma, incomplete heat exchange, or the partition between thermal and kinetic energy of pyroclasts (since examined by Wohletz 1983, 1986). Furthermore, his study did not consider the thermodynamics of energy exchange between meltwater and ice.

The thermodynamic aspects of subglacial volcanism were addressed by Hoskuldsson & Sparks (1997), who considered the emplacement of effusive lava pillows within a subglacial cavity filled with convecting meltwater. They assumed that the subglacial hydrological system was 'closed' and no meltwater could escape, and they considered the overall volume changes brought about by melting. This model predicts that positive volume changes will accompany effusion of rhyolitic magma, due to its relatively low initial temperature, whereas volume changes may be negative during effusion of basaltic magma, providing at least 80 % of the thermal energy of the magma causes melting of ice (Fig 1.13). Positive volume changes will favour drainage of meltwater, and may cause localised uplift of the glacier. Negative volume changes, accompanied by the development of ice cauldrons, are thought to favour meltwater accumulation in a subglacial or ice-marginal lake (Hoskuldsson & Sparks 1997).

Hoskuldsson & Sparks estimated the rates of heat exchange between lava pillows and meltwater, and between meltwater and ice, although they did not attempt to incorporate the two rates into an 'energy sink' model, which could have provided solutions for time-dependent meltwater temperatures. However, they suggested that the heat flux from the cooling pillows should be sufficient to maintain the meltwater at a mean temperature of 5-50 °C. Cooling times of lava pillows were estimated at 10^5 s using the cooling half-space model of Carslaw & Jaeger (1959), although the individual effects of marginal chilling and fracture were not assessed quantitatively. The melting rate of ice was estimated using Huppert & Sparks' 1988 model, which assumed turbulent convection of a hot fluid. It led to low estimates of ice melting rates: 10^{-5} m s^{-1} in basaltic and 10^{-6} m s^{-1} in rhyolitic eruptions. In contrast, considerably higher melting rates of 10^{-3} m s^{-1} during the 1996 Gjálp eruption in

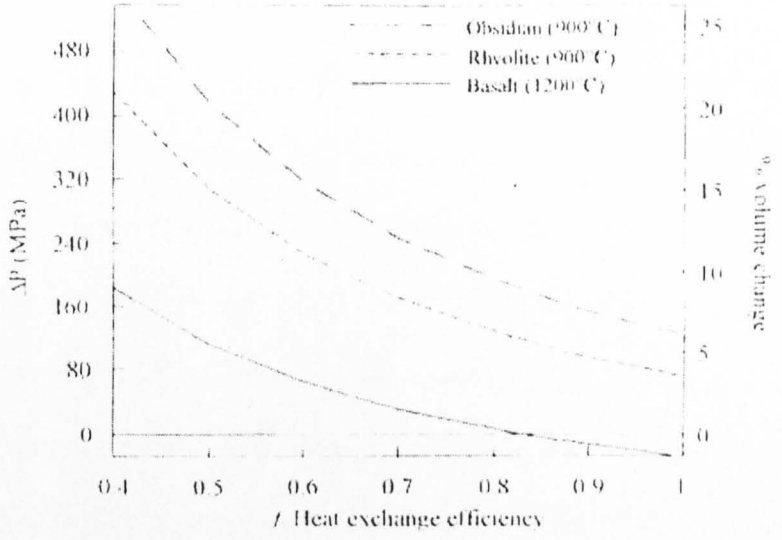

Fig. 1.13. Predicted pressure changes (proportional to volume changes) in a closed magma-ice-meltwater system within a subglacial cavity, from Hoskuldsson & Sparks (1997). Negative volume changes are possible during eruption of basaltic magma, providing >80 % of its thermal energy causes melting, which may favour meltwater accumulation and ice cauldron formation. In contrast, effusion of rhyolitic magma is always predicted to cause positive volume (pressure) changes, which may either deform the ice walls of the subglacial cavity, or pump meltwater out of the cavity.

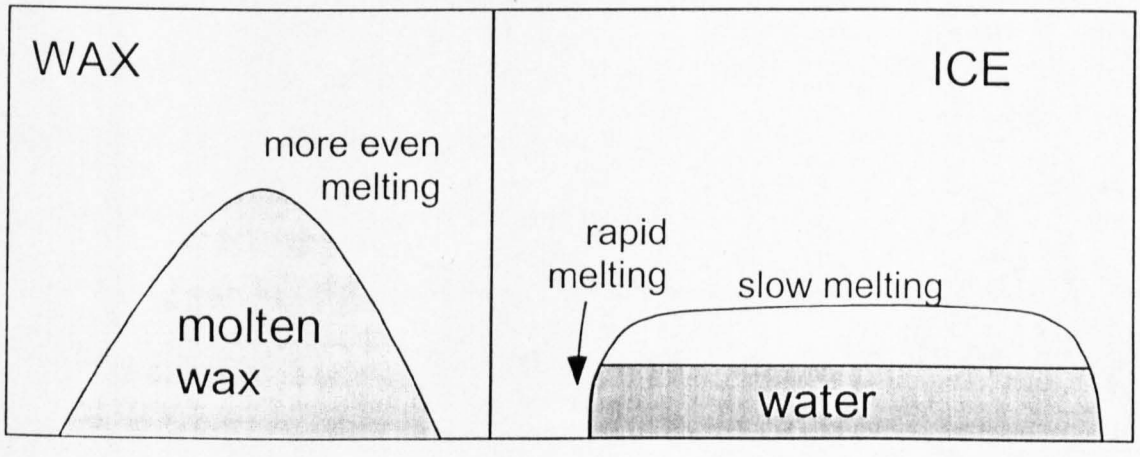

Fig. 1.14. Shapes of cavities formed by the melting experiments of Hoskuldsson & Sparks (1997). Melting of ice (right hand side) causes a reduction in volume, so an air gap develops in the cavity, there being no ice deformation on this scale. Thus melting is more rapid on the walls than the roof, and a low, broad cavity shape develops. There is negligible volume change upon melting wax (left hand side), and a higher, conical cavity develops.

Iceland are attributed to turbulent convection of a meltwater-ash mixture (Guðmundsson et al. 1997).

Although this paper constitutes significant progress, being the first to attempt to quantify melting rates and energy exchange rates, it fails to address the geometry of melting, ice deformation, non-glaciostatic water pressure, fragmentation, the effects of marginal jointing, the permeability of the bedrock, the evolving size of the subglacial cavity or any aspect of subglacial hydrology. Hoskuldsson & Sparks cite the development of ice cauldrons during the 1996 Gjálp basaltic subglacial eruption as evidence for negative pressure changes, which their model predicts. However, Guðmundsson et al. (1997) state that meltwater drained from the eruption site, making the 'closed system' model of Hoskuldsson & Sparks inappropriate. Furthermore, negative volume changes are only predicted if energy exchange were more than 80 % efficient, whereas it is estimated at 75 % for the initial phase of the Gjálp eruption (Guðmundsson et al. 1997; Guðmundsson, submitted).

Little is known about the thermodynamics of alternative melting mechanisms (e.g. convecting steam or abrasion of ice by ash particles during subglacial explosions), and there is clearly much more work to be done in this field. Chapter 5 is an attempt to enhance these existing models by incorporating aspects of ice deformation and of subglacial hydrological patterns.

1.7.4. Experimental simulations of subglacial melting

Hoskuldsson & Sparks (1997) used blocks of ice and PEG wax and a basal heat source to simulate the formation of subglacial cavities during volcanic eruptions. Cavities entirely filled with convecting meltwater had conical morphologies, whereas those in which an air gap developed became 'pancake-shaped' (Fig. 1.14). This

reflects slower melting rates of ice in contact with air than ice in contact with convecting meltwater. In another study, finite element analysis was used to investigate the evolution of a subglacial conduit carrying a variable meltwater flux (Cutler 1998). During periods of high meltwater discharge, conduits may become only partially filled with meltwater. This acts to focus melting low on the walls, forming broad, low conduits (c.f. Hooke 1984). Pressure in conduits may become atmospheric, if a hydrological connection is established with the glacier snout. High, narrow conduits are expected to enlarge more rapidly, since they have a greater 'wetted area'. Thus, the initial shape of a conduit may influence its subsequent evolution. To date, no study has addressed the melting behaviour of a steam-filled ice cavity.

1.7.5. Observations of cavities melted by geothermal heat

Useful insights into melting patterns and cavity morphologies can be gained from glacier-bearing volcanoes currently in a quiescent phase. Fumarole-melted ice and firn caves are known to exist at Mount Rainier (Washington), Mount Baker (Washington), Mount Wrangell (Alaska) and Mount Erebus (Antarctica) (Kiver & Steele 1975). Of these, the summit firn caves of Mount Rainier are by far the best documented (e.g. Kiver & Mumma 1971, Kiver & Steele 1975, Zimbelman et al. 2000). Although the rheology of firn differs from that of glacier ice (e.g. Paterson 1994), melting and deformation patterns are broadly similar to those of ice during subglacial melting. At Mount Rainier, a cave system totalling 1.9 km in length has been mapped within the summit craters (Fig. 1.15), beneath snow and firn up to 120 m thick. Kiver & Steele (1975) made the following observations:

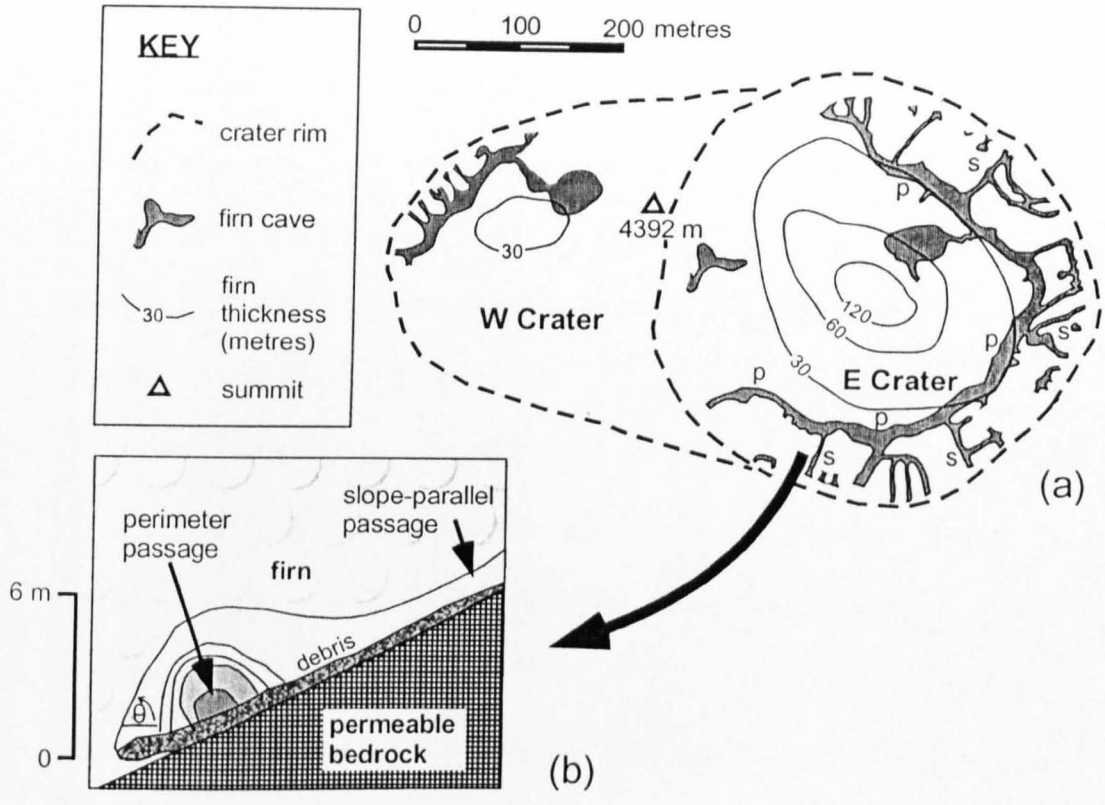

Fig. 1.15. (a) Map showing the extent of the firn cave system so far discovered within the summit craters of Mount Rainier, Washington. Slope-parallel passages (s) occur on slopes dipping into the craters at up to 35°. Perimeter passages (p) are roughly normal to the slope and are sub-parallel to the crater walls. Redrawn from Kiver & Steele (1975). **(b)** Cross-section of a typical firn cave at Mount Rainier, showing an inclined bedrock slope, an air-filled cavity and a firn wall dipping steeply downslope (angle θ). Redrawn from Kiver & Steele (1975).

1. Meltwater drips almost continuously from ice walls and ceilings, but percolation into permeable bedrock appears to prevent the accumulation of standing water.
2. Rates of cavity closure by firn deformation and enlargement by fumarolic melting were in approximate equilibrium during the period 1970-1974. Deformation and melting rates were estimated at 2-3 m per year ($\sim 10^{-7}$ m s^{-1}).
3. The position of cavities is strongly influenced by the spatial distribution of basal heating, with individual cavities related to single fumaroles. However, some sections of cavities appear to be maintained by motion of warm air.
4. Cavities occur as slope-normal 'perimeter passages' and slope-parallel cavities (Fig. 1.15a). Both types are roughly semi-circular in cross section and bounded by steep, scalloped ice walls. There is well-established airflow from one cavity to the next.
5. Talus on cavity floors is close to the angle of repose (30-40°), and highly unstable.
6. Smooth-walled conical 'steam cups' develop above the most powerful fumaroles.

Implications for melting patterns during subglacial eruptions

An important conclusion gained from Mount Rainier is that subglacial melting may be strongly heterogeneous, and controlled by the distribution of heat at the glacier base. Furthermore, meltwater accumulation within subglacial cavities may be prevented if the bedrock is sufficiently permeable (c.f. Hoskuldsson & Sparks 1997). This would favour the development of low-pressure, steam-filled cavities during some eruptions, possibly even beneath much thicker glacier ice.

1.7.6. Melting of the glacier surface

Major and Newhall (1989) collected many observations of melting and disruption of ice and snow during volcanic eruptions worldwide. Melting occurs due to the thermal (Walder 2000a) and mechanical (e.g. Pierson et al. 1990, Pierson & Janda 1994) effects of pyroclastic flows, pyroclastic surges, lava flows, hot blasts and hot-rock avalanches crossing the ice surface, also lavas flowing against ice, heating of the base of an ice cap (subglacial melting during eruptions or geothermal events), or eruptions through crater lakes (see Major & Newhall for list of observed eruptions up to 1989). Melting rates during eruptions can be estimated from the rate of deepening of channels incised into Drift Glacier by flowing meltwater, pyroclastic flows and mixed avalanches of ice and rock generated by the 1989-1990 eruption of Redoubt volcano, Alaska, as detailed in Trabant et al (1994). A 40 m-deep ice canyon was eroded in 24 hours, giving an average melting rate of 5×10^{-4} m s^{-1}, which is comparable to the subglacial melting rate during the first 36 hours of the 1996 Gjálp eruption in Iceland (10^{-3} m s^{-1}).

1.8. Subglacial hydrology: water flow through temperate glaciers

The water that flows through temperate glaciers may come from a variety of sources: in 'normal', non-volcanic regions, water may be formed by surface ablation, by frictional heating where the glacier base overrides the bedrock, or by mechanical erosion of the walls of drainage channels by flowing meltwater (reviewed by Fountain & Walder 1998). Also, in geothermally or volcanically active

areas, melting may be caused by elevated bedrock temperatures (Björnsson et al. 1982, Salamatin et al. 2000), injection of jets of steam beneath thin ice or firn (Kiver & Steele 1975), high-temperature meltwater at the glacier base, or injection of hot magma and associated volcanic gases (e.g. Guðmundsson et al. 1997).

Classical theories of glacial hydrology and meltwater drainage patterns have been developed for 'normal', i.e. non-volcanic regions with meltwater at the pressure melting point throughout (e.g. Hooke 1984, Fountain & Walder 1998), and need to be adjusted for glaciers in volcanic regions (Björnsson 1988). Nevertheless, useful insight into water flow during subglacial eruptions can be gathered from a review of the standard glaciological literature.

The dominant mechanism of meltwater transport within temperate glaciers is by flow at the glacier base (subglacial drainage, reviewed in Fountain & Walder 1998), although some meltwater may be transported englacially or as surface run-off (Fountain & Walder 1998), by permeable flow within the bedrock (Bennett & Glasser 1996), or within permafrost channels in the bedrock (Kumpulainen 1994). Subglacial drainage may occur in one or both of two different modes: either within Rothlisberger channels, which are conduits incised upwards into the ice; or within Nye channels, which are incised into the bedrock (Fig. 1.16, see also reviews by Fountain & Walder 1998, Hooke 1998).

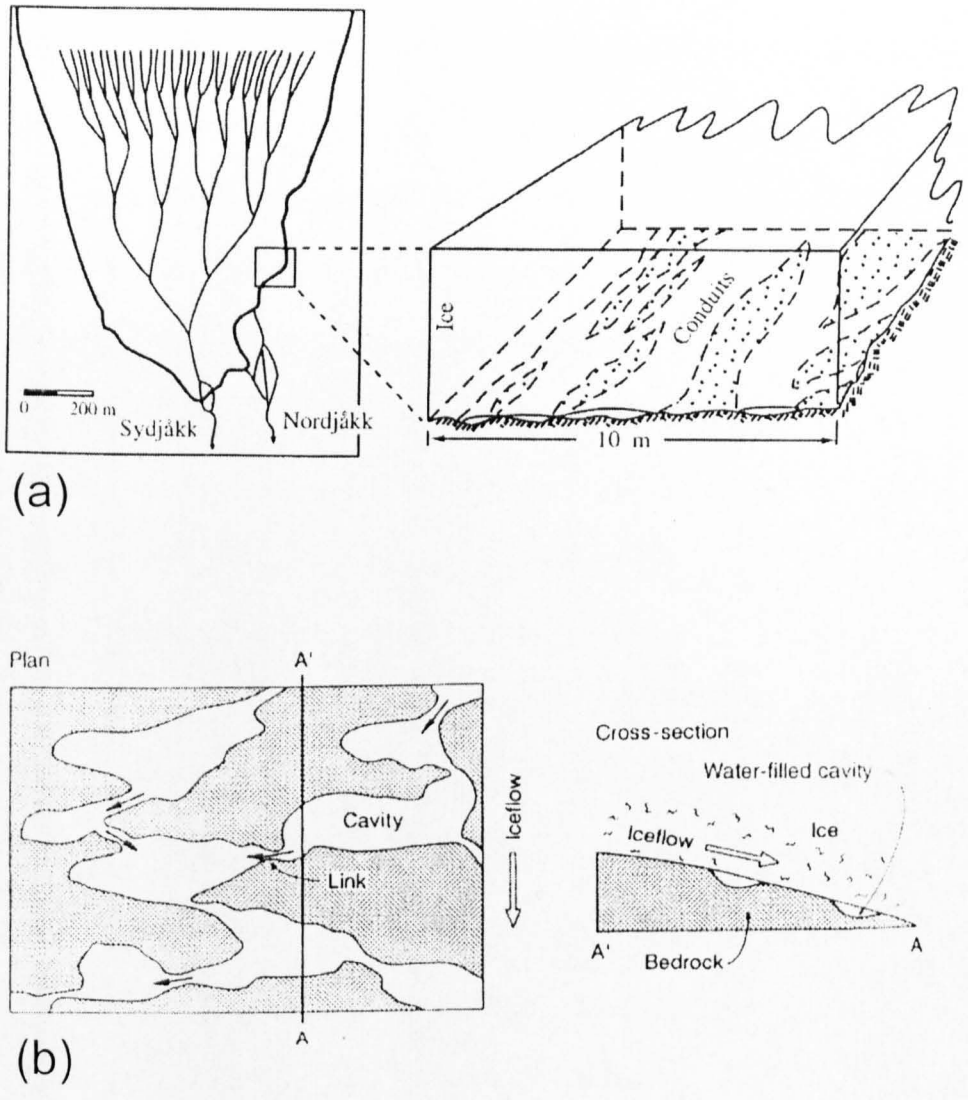

Fig. 1.16. The two types of drainage system that may exist beneath temperate glaciers. **(a)** Röthlisberger channels form a branching network that are cut upwards into the basal ice. Diagram of Storglaciaren after Hooke (1998). **(b)** Nye channels are more irregular and cut into the bedrock. From Bennett & Glasser (1996).

1.8.1. Rothlisberger channels

Rothlisberger channels (hitherto referred to as R channels) form a branching network that typically converges to one or more 'master channels' at the glacier snout (Fig. 1.16a). Pressure within R channels is likely to fall into the range between near-glaciostatic (in water-filled parts of the system far from the glacier snout), to atmospheric (close to the glacier snout and beneath thin ice, where channels are only partly filled with meltwater and there is a hydrological connection with the glacier surface; Hooke 1984, Hooke 1998). R channels are typically broad smooth-walled arches in cross-section, and may range from less than 5 m to at least 10 m in radius (Fountain & Walder 1998). In general, R channels develop in spring, when the supply of meltwater to the glacier base is greatly increased by surface ablation, and facilitated by flow within crevasses, moulins and englacial conduits (Fountain & Walder 1998). R channels reach their maximum size in late summer, and collapse in the winter when meltwater discharge is low (e.g. Bennett & Glasser 1996). R channels rarely survive from one year to the next unless they are close to the glacier snout. The size of R channels is a balance between enlargement by melting and deformation by creep closure (e.g. Nye 1953, Hooke 1984, Cutler 1998). In most cases, melting is dominated by the viscous drag of flowing meltwater on the ice walls (Shreve 1972), but the thermal effect of heated meltwater greatly increases the melting rate, possibly by an order of magnitude (e.g. Clarke 1982). Hooke (1984) derived approximate solutions for the melting rate and creep closure rate of idealised R channels, and arrived with the critical discharge rate

$$Q_c = \left[\frac{h^3}{B \sin^{7/5} \beta} \right]^5 \qquad (1)$$

where Q_c is the critical meltwater discharge, h is the glacier thickness, β is the bedrock slope in degrees and B is an ice viscosity parameter. This result assumes that meltwater is at the pressure melting point, that melting is entirely due to the mechanical effects of flowing meltwater, and that cavity deformation obeys Nye's law. At meltwater discharge rates above Q_c, the rate of melting exceeds that of deformation, and R channels may contain an air gap ('open' channels, potentially at atmospheric pressure). However, this will only occur if there is hydrological connectivity with the glacier snout along R channels, or with the glacier surface through crevasses and moulins. Without connectivity, an air gap may not develop, and the pressure is likely to be near-glaciostatic (Hooke 1984). If a low-pressure 'open' regime were to develop at a region of steep bedrock slope, thin ice or high meltwater discharge, backfilling may occur from connected parts of the system which are at much higher (near-glaciostatic) pressures (Hooke 1984, Björnsson 1988). For example, the bedrock slope is so gentle (< 5 degrees) beneath much of Vatnajökull icecap, Iceland that most R channels are likely to be below the critical meltwater discharge, and hence water-filled and at near-glaciostatic pressure (Björnsson 1988). However, there are considerably steeper bedrock slopes (~20-30 degrees) in the vicinity of subglacial volcanic edifices, and R channels may here be expected to be 'open', with an air gap. A vexed question is the extent to which backfilling from adjacent regions of shallower bedrock slope will increase the channel pressure, and prevent the formation of open channels by 'pumping' of meltwater into them, possibly up the steep bedrock slope. Channels carrying a meltwater discharge below Q_c are likely to be entirely filled with meltwater, and at near-glaciostatic pressure.

If R channels are 'open', the direction of water flow is controlled by the bedrock slope only, whereas water flow in 'filled' channels is governed by the water

potential field, which is a function of the ice surface and bedrock slope, as explained in section 1.83. These different controls on the orientation of 'open' and 'filled' channels is demonstrated by the orientation of eskers (fossilised R channels) at Burroughs Glacier, Alaska (Syverson et al. 1994): eskers are parallel to the bedrock slope near the glacier snout, where R channels are observed to be 'open', but parallel to the potential gradient in other regions, where channels are presumably water-filled.

1.8.2. Nye channels

Nye channels (hitherto called N channels), also known as 'linked cavities' (Fountain & Walder 1998), are eroded into the glacier substrate (Fig. 1.16b). Although their shape may be influenced by local weaknesses in the bedrock, the direction of water flow is, like filled R channels, controlled by the water potential gradient (Bennett & Glasser 1996). N channels may persist from year to year and, despite being less efficient carriers of meltwater than R channels, much of the winter and early spring meltwater discharge is carried within them (reviewed in Fountain & Walder 1998). N channels are anastamosing, irregular and do not necessarily converge towards the glacier snout (Sharp et al. 1993, Fountain & Walder 1998).

There are thus two different types of subglacial drainage system, which may coexist. Recent dye tracer and borehole experiments on Alpine glaciers have investigated the relative roles of R and N channels during periods of fluctuating meltwater discharge, both seasonal and diurnal (e.g. Nienow et al. 1996a, Nienow et al. 1996b, Hubbard & Nienow 1997, Gordon et al. 1998). Gordon et al. (1998) studied the changing drainage patterns of part of the Haut Glacier d'Arolla, Switzerland during the summer of 1993. Early in the summer, before a subglacial drainage channel had formed, the subglacial cavity system consisted of 'hydraulically

impermeable patches interspersed with storage spaces, and transmitted a very low water flux'. A rapid increase in the supply of meltwater and rainfall then allowed an incipient channel to connect to a well-established channelised drainage system down-glacier, and drainage became more efficient. Changes in water pressure within the channel were in phase with changes in discharge, typical of 'open' R channels (Fountain & Walder 1998). However, pressure and discharge were out of phase in boreholes several metres from the channel, as they were connected to the channel by a 'resistant' drainage system. These observations illustrate that changes in subglacial water pressure and drainage patterns can be brought about by changes in the input of water to the glacier base, which would clearly occur during a subglacial eruption.

1.8.3. Water potential at the glacier base

The water potential is defined as the height (or piezometric head) of meltwater that could be sustained above the glacier base at a given position on a glacier (e.g. Björnsson 1988, and illustrated schematically in Fig. 1.17).

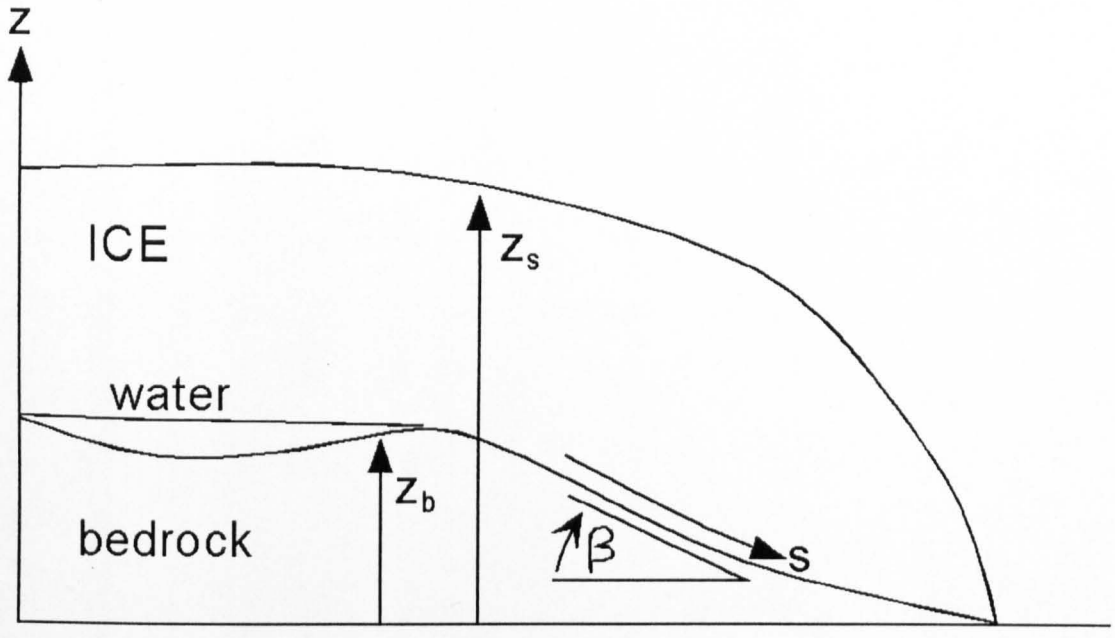

Fig. 1.17. Schematic cross-section of a glacier showing the different parameters referred to when water potential is discussed. Explanation of symbols: *s* is a coordinate parallel to the glacier base, z_b is the elevation of the glacier base, z_s the elevation of the ice surface and β is the bedrock slope in degrees.

The water potential ϕ_b (in J m^{-3}) is given by

$$\phi_b = \rho_w g z_b + P_w \qquad (2)$$

where ρ_w is the density of water, g is gravitational acceleration, z_b is the height above the glacier snout and P_w is the local water pressure. Equation (2) is thus the sum of the gravitational potential (first term on the right hand side) and local pressure P_w. The local pressure P_w is, for filled cavities, equal to $P_i + \Delta P$, where P_i is the ice overburden pressure and ΔP is a local pressure effect determined by the balance between ice wall deformation and melting (Björnsson 1988). P_i is defined by

$$P_i = \rho_i g(z_s - z_b) \tag{3}$$

where s is an axis parallel to the glacier base, z_s is the elevation of the ice surface at a given position on the glacier surface, and z_b is the elevation of the subglacial cavity (Fig. 1.17). Equations (2) and (3) can be combined and rearranged to give

$$\phi_b = z_b g(\rho_w - \rho_i) + z_s g \rho_i + \Delta P \tag{4}$$

which shows that the water potential is dominantly controlled by z_s, the ice surface elevation, rather than z_b, the bedrock elevation.

Water flow in water-filled subglacial conduits is driven by the negative potential gradient $-d\phi_b/ds$ (Fig. 1.17). The potential gradient is acquired by differentiating equation (4) with respect to s, which gives

$$\frac{d\phi}{ds} = g(\rho_w - \rho_i)\frac{dz_b}{ds} + g\rho_i \frac{dz_s}{ds} + \frac{d\Delta P}{ds} \tag{5}$$

where dz_b/ds and dz_s/ds are the bedrock and ice surface slope respectively. The ratio of the influence of bedrock topography and ice surface topography is thus equal to $(\rho_w-\rho_i)/\rho_i$, which is approximately 83/917, or roughly 1:11. This result thus illustrates that the direction of water flow in filled subglacial conduits is towards areas of low ice surface elevation. Notable exceptions occur if 1) the ice surface is near-horizontal, but the bedrock topography is steeply inclined, or 2) cavities are not filled with meltwater, in which case flow is down the bedrock slope (Björnsson 1988, Hooke 1998). Elegant proof of the second exception comes from the aforementioned study of

esker orientations beneath Burroughs Glacier, Alaska (Svyerson et al. 1994). Eskers are mostly parallel to the potential gradient (and hence approximately parallel to the ice surface slope), except near the snout, where the ice is less than 100 m thick, and eskers follow the bedrock slope. This is due to subglacial cavities close to the snout being only partially filled with meltwater, as predicted by Hooke (1984) for cavities beneath thin ice.

The formation of ice cauldrons can thus create a 'potential well', a localised minimum in the water potential, due to the lowering of the ice surface (Björnsson 1988). Meltwater within filled cavities in this potential well will thus drain *towards* the ice cauldron, favouring the formation of a subglacial lake. This can continue, with growth of the subglacial lake (termed *englacial* by Smellie 1999 and others), until the ice surface is pierced, and an intraglacial lake is formed (Fig. 1.5). Continued increase in the level of the lake may then cause the surrounding ice to 'float' (Nye 1976, Björnsson 1988, Fowler 1999, Smellie 1999), releasing a catastrophic jökulhlaup. Field observations from Iceland (section 1.2.2, 1.2.3) suggest that individual jökulhlaup events may lower the level of an intraglacial lake by 300 m (Moore & Calk 1991). However, a jökulhlaup will only be generated if the level of the intraglacial lake can become deep enough to float the surrounding ice. There are two scenarios that may prevent this. Firstly, high meltwater temperatures in the intraglacial lake may cause rapid thermal erosion of subglacial conduits (Clarke 1982); and sustain 'open' conduits, with an air gap, throughout the life of the lake. In this case, meltwater would drain down the bedrock slope, and a 'potential trap' could not develop. Secondly, meltwater may drain englacially, within the permeable firn and snow part of the glacier, and prevent the lake from becoming deep enough to float the surrounding ice (Smellie 1999). This will only occur if the firn and snow layer

constitutes >25% of the total glacier thickness (Smellie 2001), and is thus likely to be confined to glaciers <400 m thick. However, it is questionable whether the permeability of firn is high enough to sustain a sufficient meltwater flux, although permeable flow of meltwater within firn has been reported at Storglaciaren, Sweden (Schneider 1999).

An important caveat to the above analysis is that local pressure effects are ignored when considering potential gradients. High magnitude, localised perturbations in subglacial water pressure may occur during subglacial eruptions, which may further complicate hydrological patterns prior to the piercing of the ice surface. These are discussed further in Chapter 5.

1.8.4. Observations of subglacial water pressure

There is a growing body of evidence that subglacial water pressures within filled conduits may vary rapidly, triggered by fluctuations in the meltwater discharge rate. Subglacial water pressures have been measured directly in boreholes, which penetrate from the glacier surface to the glacier base (e.g. Iken et al. 1983, Kavanaugh & Hooke 2000).

Iken et al. (1983) found that maximum water pressures beneath Unteraargletscher (an alpine glacier in Switzerland) occurred in early spring, just as the input of meltwater was increasing, but there had been insufficient time for the subglacial cavities to sufficiently enlarge (i.e. the R-channel system was immature). Thus, the subglacial cavity system was overwhelmed by a sudden increase in meltwater discharge. Similarly, Warburton & Fenn (1994) inferred that the cavity system of Bas Glacier d'Arolla, Switzerland was overwhelmed in 1987 during heavy rainstorms. It is interesting that the period of maximum subglacial pressure at

Unteraargletscher corresponded to an uplift of the glacier surface of some 0.4 m, thought to be triggered by the increase in subglacial pressure (Iken et al. 1983). Similarly, Hooke et al. (1985) found that the base of Bondhusbreen glacier, Norway became detached from the bedrock in the early spring, increasing the transported sediment load, as subglacial pressure increased due to a rise in meltwater discharge. Kavanaugh & Clarke (2000) detected a brief period (minutes) of exceptionally high water pressure (15 times the ice overburden pressure) beneath Trapridge Glacier, Yukon in summer 1996. Curiously, there was no significant change in meltwater discharge during this period, and the dramatic overpressure was attributed to abrupt ice motion, which may have altered the volume of the subglacial hydraulic system. In this specific case, the degree of overpressure may have been controlled by the bulk modulus of water (Blake 1981, Hoskuldsson & Sparks 1997), that was compressed within an isolated, non-connected cavity.

It has long been established that ice motion and the existence of pressurised subglacial cavities are closely linked (e.g. Lliboutry 1968, Iken & Bindschadler 1986, Harbor et al. 1997), and large-scale patterns of ice motion may be related to melting triggered by geothermal heat and volcanic eruptions (Bourgeois et al. 2000).

Meltwater flowing beneath Skeiðarárjökull, Iceland during the November 1996 jökulhlaup escaped from the glacier several hundred metres from the snout (Roberts et al. 2001, Waller et al. 2001), apparently through a system of fractures which cut ice approximately 200 m thick. Brittle fracture of such thick ice is unusual, and is best explained by extreme pressurisation of subglacial cavities, which may have occurred due to extremely rapid increase in the meltwater flux during the early stages of the jökulhlaup.

1.8.5. Meltwater temperature during subglacial eruptions

Heating of meltwater may have a significant influence on, as well as being a consequence of, subglacial eruption mechanisms. The temperature of meltwater will determine 1) rates of ice melting via conduction and convection of thermal energy from water, 2) the volume of ice melted per unit volume of magma, and thus the overall pressure balance (Hoskuldsson & Sparks 1997), and possibly 3) the drainage characteristics (or 'leakiness') of any subglacial or intraglacial lake, given that the 'ice barrier' may be etched through much more rapidly by heated meltwater, possibly prior to flotation (Clarke 1982, Fowler 1999). Indeed, Björnsson (1992) has applied Clarke's 1982 jökulhlaup drainage model to twentieth century jökulhlaups from Grímsvötn, Iceland, and has found that discharge rates in the majority of jökulhlaups are consistent with meltwater temperatures of 0.2 °C. However, more rapid drainage during the 1938 jökulhlaup is attributed to elevated meltwater temperature (4 °C), caused by a raised geothermal heat flux prior to the 1938 eruption (Björnsson 1992).

It is not easy to predict meltwater temperatures during subglacial eruptions, since the magma-meltwater and meltwater-ice heat fluxes must be determined to acquire the amount of heat stored in the liquid phase. A critical point is that conductive heat transfer within ice is negligible (Salamatin et al. 2000), hence all thermal energy transferred to ice can be assumed to trigger melting. No study has yet provided time-dependent solutions for meltwater temperature during a subglacial volcanic event. However, meltwater temperatures have been measured and estimated during three subglacial eruptions.

Guðmundsson et al. (1997) compared the volume of ice cauldrons at the site of the 1996 Gjálp eruption (assumed to equal the volume of ice melted beneath) to the volume of meltwater discharged into Grímsvötn lake. The amount of melting

estimated during transfer of meltwater from the eruption site to Grímsvötn is consistent with meltwater leaving the eruption site at a temperature of 15-20 °C. However, this method of estimation may be highly misleading, as the volume of ice cauldrons and meltwater drained are not necessarily equal (Chapter 5). Meltwater leaving the snout of Skeiðarárjökull in the November jökulhlaup was at a temperature of ~1 °C (Guðmundsson et al. 1997), and meltwater draining north was at 1.6 °C (Kristmannsdóttir et al. 1999). These lower exit temperatures indicate that considerable cooling of meltwater occurred during transport from the eruption site to the glacier snout, probably caused by melting the walls of subglacial channels. The temperature of meltwater within Grímsvötn lake has been independently estimated at 8 °C (Björnsson 1987) and measured at 0-4 °C in 1991 (Ágústsdóttir & Bentley 1994).

The temperature of meltwater draining down Drift Glacier valley during the 1989-1990 eruption of Redoubt Volcano, Alaska was measured at 80 °C (Trabant et al. 1994). Meltwater released during magma-snow and magma-ice interaction on Hekla in 1947 was estimated at 30-40 °C (Major & Newhall 1989). It was the surface of steeply inclined snow or ice that was melted in these last two examples, which may explain the considerably higher meltwater temperatures than that inferred at Gjálp 1996, since drainage was rapid, reducing time for interaction between heated water and ice. The Gjálp 1996 eruption most relevant to this study, since it occurred beneath 'thick' ice.

1.9. Ice deformation during subglacial eruptions

Deformation of ice occurs during subglacial eruptions, as observed during Gjálp 1996, when the shape of the glacier is disrupted by melting. Patterns and rates of ice deformation may have profound effects on eruption mechanisms and the volcanic landforms created, and are discussed in this section. This follows a brief review of the deformation behaviour of ice and, specifically, the creep closure of subglacial cavities.

1.9.1. Deformation of glacier ice

Ice within terrestrial glaciers is dominantly of the form I_h, the rheology, microstructure and deformation behaviour of which is comprehensively reviewed in Hooke (1998). Only a brief summary will be given here. The initial response of ice I_h to an applied load is elastic, with inhomogeneous stress on a microscopic scale, as unfavourably aligned crystals glide to take up stress. At strain above ~1%, dynamic recrystallisation occurs: in which growth of new crystals acts to equilibrate stress throughout the ice. At strain above ~10 %, the crystalline texture has adjusted sufficiently to be in equilibrium with the applied stress, and ice enters the deformation regime known as steady-state tertiary creep (Budd & Jacka 1989). This deformation regime is also known as power-law creep, since the strain (creep) rate is proportional to the stress to the power of n, where $n>1$. The standard power-law creep relationship for isotropic ice, defined by Glen (1955), is

$$\dot{\varepsilon}'_e = \left[\frac{\sigma_e}{B}\right]^n \qquad (6)$$

where ε_e' is the effective strain rate, σ_e the applied stress, B is an ice viscosity parameter and $n \sim 3$. Glen's law is only useful if an appropriate value of B can be chosen to approximate the viscosity of the entire (heterogeneous?) ice body considered. B is influenced by the pressure, temperature and water content of ice. Large-scale flow patterns of a glacier depend upon the bedrock and ice surface topography, the viscosity and thickness of ice and the accumulation rate on the ice surface. Although these large-scale flow patterns may influence the overall morphology of subglacially emplaced volcanoes (Mathews 1951); local, transient ice deformation caused by localised subglacial melting (e.g. Aðalgeirsdóttir et al. 2000, Salamatin et al. 2000) is of more interest to the present study. In order to consider this, it is necessary to consider the idealised scenario during a subglacial-to-emergent volcanic eruption (Fig. 1.18).

In phase 1 (Fig. 1.18a), a cavity forms at the glacier base due to localised melting of ice above a volcanic vent (e.g. Jones 1970, Skilling 1994). For simplicity, the cavity is assumed to be semicircular in cross-section, although a variety of cavity morphologies are possible. During this early phase, the cavity radius $r << h$, the ice thickness, and the ice roof of the cavity deforms in accordance with Nye's law (Nye 1953),

$$r' = r\left(\frac{\Delta P}{nB}\right)^n \tag{7}$$

where r' is the roof deformation rate, r is the cavity radius, ΔP is the pressure difference $P_c - P_g$ between the cavity pressure P_c and the confining glaciostatic pressure of the ice roof ($P_g = \rho_i g h$, where ρ_i is density of ice, g is acceleration due to

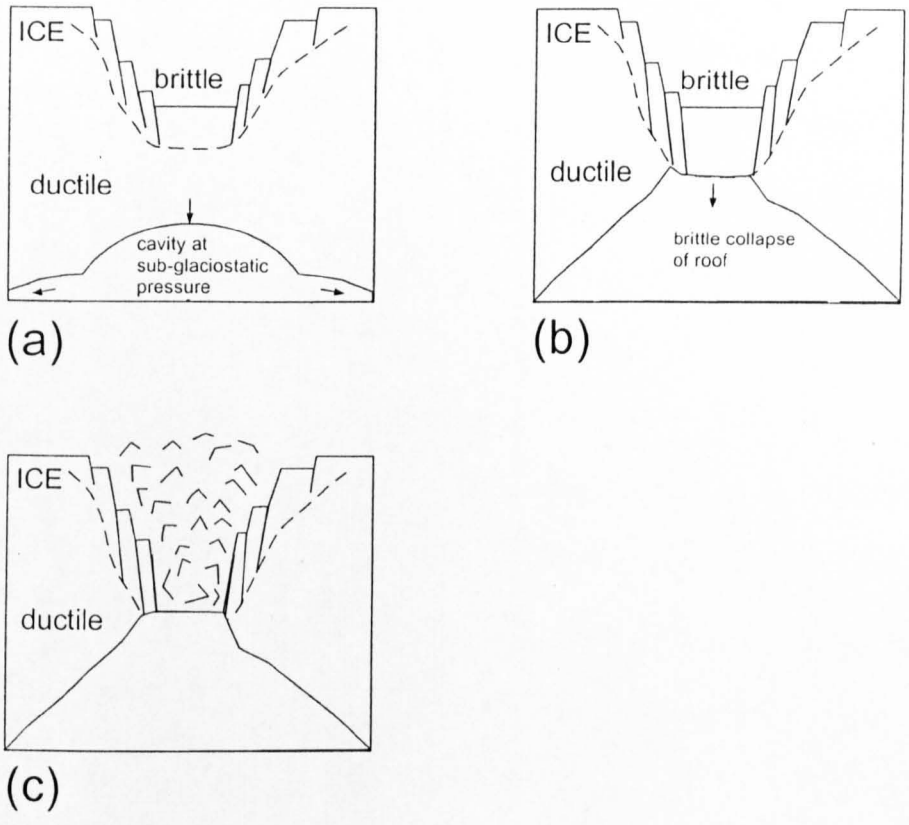

Fig. 1.18. Schematic diagram illustrating the likely configuration of zones of brittle and ductile ice deformation during a subglacial eruption. **(a)** When the cavity radius is small relative to the glacier thickness, its walls deform in a ductile manner, obeying Nye's law. However, brittle fractures develop in snow, firn and shallow ice at the glacier surface. **(b)** As the subglacial cavity increases in size, Nye's law breaks down and the roof fails brittly. **(c)** The roof has been melted through and a subaerial eruption has commenced. Ice deformation into the vent will be brittle at the glacier surface, with spalling of crevasse-bound blocks, but may still be ductile at deeper levels in the glacier.

gravity and h is the overlying ice thickness). Parameter n is of value ~3 and $B \sim 1.6 \times 10^5$ Pa $a^{1/3}$, ~500 Pa $s^{1/3}$ (Hooke 1984). Note that the pressure difference between the ice roof and the cavity exerts a strong influence on the rate of ice deformation.

The strengths of Nye's law are that it is simple, and that it can be used to approximate the closure rate of subglacial conduits and cavities. When estimates of closure rates are combined with rates of conduit/cavity enlargement by melting, it is possible to estimate the time-dependent variation in cavity radius (e.g. Hooke 1984). The weaknesses of Nye's law are that it applies only to cavities with a semicircular cross-section, and that it can only be applied to cavities significantly smaller than the glacier thickness. Furthermore, it is necessary to know the pressure in the cavity. More recent models of deformation and melting at subglacial cavities (Cutler 1998) use three-dimensional finite element techniques to improve predictions of the evolving shape of irregular conduits at varying pressures.

In phase 2 (Fig. 1.18b), continued melting has resulted in a much larger cavity, such that $r \sim h$. Nye's law can no longer be used to estimate rates of ice deformation, as higher strain rates lead to brittle deformation of the upper part of the ice, as observed during subglacial eruptions in Iceland (Guðmundsson, submitted). Roberts et al. (2001) have found that ice up to 200 m thick near a glacier snout may be cut from base to surface by brittle fractures during periods of extreme overpressure at a glacier base triggered by a jökulhlaup. Brittle deformation of the upper part of a glacier is also favoured by the presence of firn and snow, which are less prone to ductile deformation than polycrystalline ice (Paterson 1994). Experiments have found that ductile ice deformation is favoured by high pressures and low strain rates, whereas brittle deformation is more likely at low pressures and high strain rates (e.g. Jones 1982). In order to account for and model the brittle-ductile ice deformation patterns

during a subglacial eruption, it would be necessary to resolve three main problems: (1) to construct a three-dimensional 'map' of stress and strain rates during this phase of cavity evolution; (2) to place well-constrained limits on the threshold between ductile and brittle ice deformation; and (3) to account for the varying rheology at different depths in the glacier. These problems still constitute a major challenge, and no robust models of ice deformation during subglacial eruptions have yet been constructed. In the meantime, application of Nye's law may provide a useful first approximation to ice deformation patterns (Chapter 5).

In phase 3, the ice roof of the cavity has collapsed and melted, leaving a growing volcanic edifice within an intraglacial lake (Fig. 1.18c). There may be flow of ice into the vent area, as observed during Gjálp 1996 (Guðmundsson et al. 1997) and Redoubt 1989-90 (Miller 1994). The significance of this is discussed in Chapter 5.

1.9.2. Effects of ice deformation on glacier hydrology

Downsag of the ice surface above the region of ice deformation occurs during phases 1 and 2 (Fig. 1.18a,b), forming an ice cauldron (e.g. Björnsson 1988, Branney 1995, Guðmundsson et al. 1997, Alsdorf & Smith 1999). The reason for this deformation can be conceptualised if one considers the ice overlying the cavity to be an undeformable piston, hence the rate of surface deformation equals the rate of ice roof deformation at depth. In reality, these two rates are unlikely to be identical, as some internal deformation within the ice roof is almost inevitable, and indeed, complex three-dimensional flow fields may be established (Aðalgeirsdóttir et al. 1999, Salamatin et al. 2000). Ice cauldrons formed on the surface of Icelandic glaciers 500-

700 m thick are typically 1-2 km in diameter and vary from ~50 m to 150 m in depth (Guðmundsson, submitted). This local perturbance in the glacier surface topography leads to horizontal and vertical deformation of the surrounding ice to fill the depression (Aðalgeirsdóttir et al. 1999). Rates of 'healing' of ice cauldrons by inward ice flow are thought to be fastest where there is thick ice and a large 'catchment area' from which incoming ice can originate. The size and shape of ice cauldrons is likely to be related to the ice thickness, melting rate, glacier structure and horizontal ice flow, but the influence of each individual factor is currently unknown.

The formation of ice cauldrons, in altering the surface topography of the glacier, may cause important changes in the patterns of meltwater drainage from around the growing subglacial volcano (section 1.8.3.). Thus, ice deformation may prevent meltwater escape and allow the development of an intraglacial lake, although this depends upon the thickness of the ice, bedrock slope, glacier structure and possibly meltwater temperature (section 1.8.3.).

1.10. Subglacial rhyolite in perspective

1.10.1. Predicted differences between subglacial rhyolite and subglacial basalt

Hoskuldsson & Sparks (1997) presented a simplified heat-exchange model for subglacial effusive eruptions, which calculates the volume of ice melted per unit volume of magma erupted, and the resultant volume (and pressure) changes. This model assumes that all the energy from the cooling magma is transferred to the ice via convecting meltwater, and does not account for ice deformation. It provides a useful prediction of the hydrological patterns that may develop during eruptions of rhyolite

Property of eruption	Subglacial rhyolite	Subglacial basalt	Implications
Magma temperature[1]	800-900°C	1100-1200°C	Less energy released as rhyolite is quenched
Melting potential[1]	≤ 8 times own volume of ice	≤ 14 times own volume of ice	Positive pressure changes during rhyolite eruption, negative during basalt
Pressure changes during eruption[1]	positive	negative	Rhyolite: meltwater tends to drain away Basalt: meltwater tends to collect at vent
Magma viscosity[1]	10^6-10^7 Pa s	10^3-10^4 Pa s	Rhyolite eruptions tend to be more explosive, larger aspect ratio lava flows
Effusion rate[1]	10^1-10^2 $m^3 s^{-1}$	10^1-10^4 $m^3 s^{-1}$	Inward ice creep[2] more significant during rhyolite eruptions because edifice growth is slower[1]
Distribution[3]	Iceland, mostly at central volcanoes	Antarctica, Iceland, British Columbia	Basalt much better studied than rhyolite
Recent eruptions	None observed	Gjálp 1996, Iceland[3]	Insight gained on basaltic eruptions, not on rhyolitic.

Table 1.4a. Major differences between subglacial rhyolite and basalt eruptions. [1]Hoskuldsson & Sparks 1997, [2]Guðmundsson et al. 1997, [3]Smellie 1999. After Tuffen et al. (2001).

Property of eruption	Subglacial environment	Subaqueous environment	Implications
Edifice constraint	Constraint by ice walls during subglacial stage[1]	No constraint	Subglacial edifices likely to be steeper, with greater risk of flank collapse if ice recedes
Effective pressure	Varies from glaciostatic to atmospheric, depending upon meltwater discharge rate[2]	Variable, but hydrostatic	Style of subglacial eruptions likely to be more variable: effusive and explosive
Water/ magma ratio	Variable, depending upon drainage patterns	Consistently high, although steam envelopes may 'shield' magma[3]	Subglacial sequences may include 'dry' units with little evidence for magma-water interaction

Table 1.4b. Major differences between subaqueous and subglacial eruptions. [1]Skilling 1994, [2]Hooke 1984, [3]Kokelaar 1982. After Tuffen et al. (2001).

and basalt under temperate glaciers (Table 1.4a). The model suggests that meltwater accumulation is likely in a basaltic eruption. This is due to the high temperature of basaltic magma (~1200 °C), which is capable of melting up to 14 times its own volume of ice, which is more than sufficient to accommodate the volume of magma added. This is expected to cause a pressure reduction, which will encourage meltwater

accumulation. Rhyolitic magma has a lower temperature (~850 °C) and can thus melt only <10 times its own volume of ice. Positive pressure changes are predicted, which will favour drainage of meltwater.

Eruptions of rhyolitic and basaltic magmas under ice are thus likely to produce contrasting suites of lithofacies, due to differences in the physical environment. The contrasting physical properties of the magmas are also likely to influence subglacial eruption dynamics and the nature of the products (Table 1.4a).

1.10.2. Predicted differences between subglacial and subaqueous/submarine rhyolite successions

Various authors have conducted detailed lithofacies analysis of subaqueously emplaced rhyolite (Yamagishi & Dimroth 1985, Cas et al. 1990, Hanson 1991, Scutter et al. 1998, Hunns & McPhie, 1999). These studies have shed light on mechanisms of rhyolite lava-water interaction (e.g. Yamagishi & Dimroth 1985, Hunns & McPhie 1999), and as thus provide a useful perspective on the less-studied products of subglacial eruptions. However, eruptions under ice are likely to differ from eruptions under water because of significant differences in the physical environment, which are summarised in Table 1.4b.

1.10.3. Subglacial rhyolite in Iceland

Approximately 10 % of the magma produced in Iceland is rhyolitic (Jakobsson 1979), and subglacial rhyolitic formations are widespread, occurring both at Quaternary central volcanoes (e.g. Torfajökull, Kerlingarfjöll, Katla, Öræfajökull, Tindfjallajökull, Krafla) and at smaller, isolated volcanoes (e.g. Hágöngur, Prestahnúkur). Central volcanoes are long-lived (hundreds of thousands to millions of years), and typically produce a spectrum of magma types between basalt and rhyolite

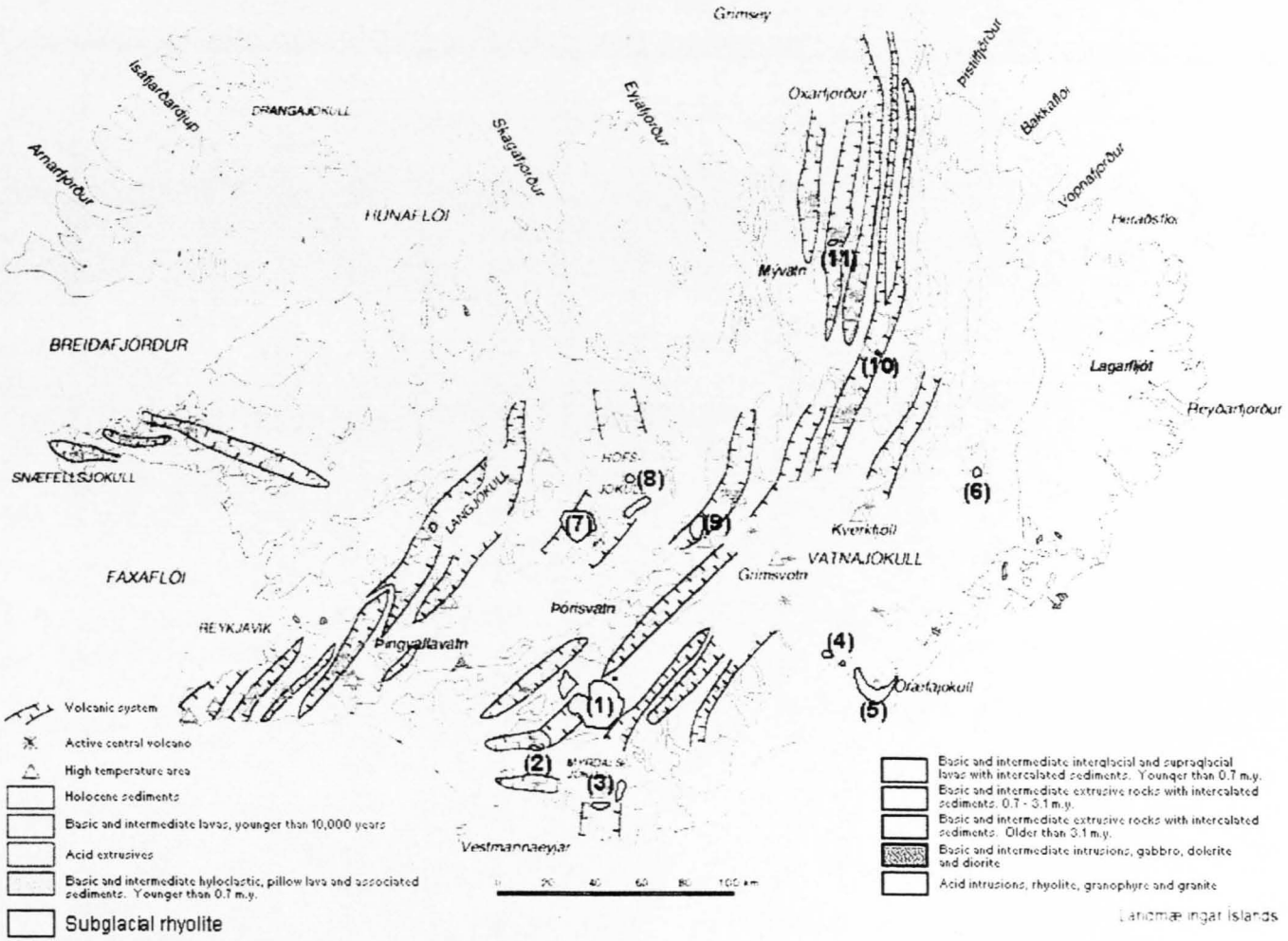

Fig. 1.19. Simplified geological map of Iceland, indicating the distribution of subglacial rhyolite lithologies that have been recognised to date. Redrawn from A. Newton (unpublished map on Tephrabase website, run by Edinburgh University Geography department).

(1) Torfajökul. (2) Tindfjallajökull. (3) Mýrdalsjökull. (4) Skaftafellsfjöll. (5) Oræfajökull. (6) Snæfell. (7) Kerlingarfjöll. (8) Armafell and Hásteinar. (9) Hágöngur. (10) Eggert. (11) Hliðarfjall.

(e.g. Blake 1984, McGarvie 1984, Furman et al. 1992, Hards et al. 2000). Torfajökull has produced the most rhyolitic magma of any Quaternary central volcano in Iceland – in excess of 250 km^3 (McGarvie 1985). Ancient central volcanoes have been identified in off-axis parts of western and eastern Iceland, which are of Quaternary and Tertiary age (e.g. Furman et al. 1992, Jónasson et al. 1992). Magmas generated at central volcanoes may be of an alkaline or tholeiitic affinity, depending upon the relative influence of crustal remelting and 'primitive' basalts (e.g. McGarvie 1984, Macdonald et al. 1990, Gunnarsson et al. 1998). Based upon the geological map of Iceland published by Náttúrufræðistöfnun Íslands (Jóhannesson & Sæmundsson 1998), field observations by H. Tuffen between 1996 and 2001, D. W. McGarvie between 1982 and 2001 and personal communication from K. Sæmundsson and K. Jónasson, Figure 1.19 indicates the distribution of known subglacial rhyolite formations in Iceland. A vexed question is whether the rate of generation of rhyolitic magma in Iceland is influenced by the extent and thickness of ice cover – in a manner similar to that which affects rates of mantle melting and the composition and production rate of basaltic magma (Sigvaldasson et al. 1992, Jull & McKenzie 1996, Slater et al. 1998, Maclennan et al. 2001).

1.10.4. Icelandic rhyolite in the tephrochronological record

Silicic tephra layers in Greenland ice cores are thought to originate from rhyolite eruptions in Iceland (e.g. Zielinski et al. 1997), due to geochemical similarities with Icelandic rhyolite, many were erupted during glacial periods (e.g. Lacasse & Garde-Schönberg 2001). A similar origin has been attributed to tephra layers in Icelandic glaciers (Larsen et al. 1998), on the Atlantic sea floor (Lacasse et al. 1996) and in Scottish peat (Dugmore et al. 1995). The majority of ash shards are vesicle-poor and

blocky, and <100 μm in diameter – morphologies and sizes that are consistent with phreatomagmatic fragmentation (Heiken & Wohletz 1985). Hafliðason et al. (2000) found quantitative differences in the morphology of basaltic ash shards formed in subglacial eruptions (blocky, equant) from those formed in subaerial eruptions (more irregular, elongate). This is thought to indicate that fragmentation during subglacial eruptions is influenced by explosive magma-water interaction, whereas fragmentation in subaerial eruptions is dominantly triggered by magmatic degassing. No similar patterns have been identified in the morphology of rhyolitic ash shards, partly due to a much smaller sample of eruptions. Some of these tephra layers were probably generated by initially subglacial eruptions that pierced the surface of the ice and formed an eruption column (phreatoplinian, subplinian or plinian). It has not been possible to determine eruption column heights from isopachs, and vent-proximal air-fall deposits during glacial periods are unlikely to be preserved in the geological record, being susceptible to redeposition during deglaciation (Lacasse et al. 1996, Geirsdóttir et al. 2000). A key question is whether ice above a rhyolitic volcano will diminish or decrease the explosivity of eruptions – this will be discussed in Chapter 5.

1.11. The field area: Torfajökull central volcano, Iceland

Torfajökull is the largest active silicic centre in Iceland (e.g. McGarvie 1985), and predominantly rhyolitic magmas cover an area in excess of 400 km^2 (e.g. Blake 1984). In the following section, I will outline the geological setting, overall structure and

eruptive history of Torfajökull, and the current understanding of the physical volcanology of its eruptions.

1.11.1. Geological setting

Torfajökull central volcano is located in south-central Iceland, within a non-rifting segment of unusually thick crust at the southern terminus of the active Eastern Rift Zone (Fig. 1.20 a,b). It is the largest active silicic complex in Iceland, measuring 18 by 12 km with a total area in excess of 400 km^2, and has erupted >250 km^3 of alkaline rhyolite and subordinate transitional alkalic basalt since activity began in the late Quaternary (Sæmundsson 1972, Sæmundsson 1988, McGarvie et al. 1990, Macdonald et al. 1990). Central volcanoes in Iceland are long-lived (10^5-10^6 years) and active examples are within or adjacent to the active rift zones (Fig. 1.20c). However, silicic and basaltic plutonic rocks of Tertiary age far from the active rift zones (e.g. Austurhorn, Furman et al. 1992) are thought to represent the roots of earlier generations of central volcanoes, which may therefore have developed throughout much of the c. 50 Ma history of volcanism in Iceland. Central volcanoes (e.g. Jakobsson 1979, Guðmundsson 2000) may generate magmas of a predominantly basaltic (e.g. Grímsvötn), intermediate (e.g. Hekla) or silicic composition (e.g. Torfajökull).

1.11.2. Structure of Torfajökull

The Torfajökull area is a highly dissected upland plateau, at a base elevation of approximately 600 m, from which numerous peaks, some flat-topped, rise to elevations of 924 to 1235 m above sea level (Fig. 1.21). Curved ridges form

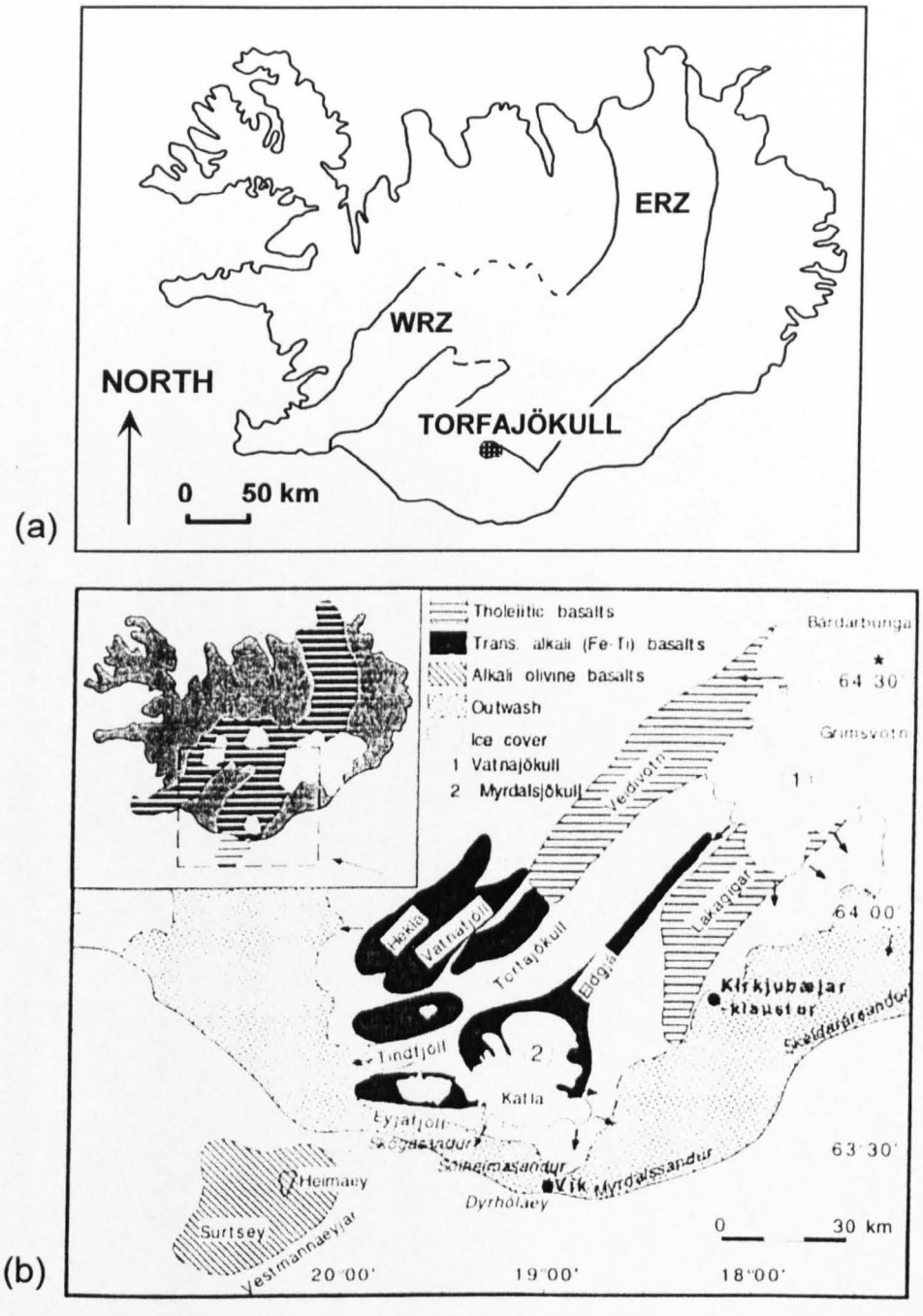

Fig. 1.20. (a) Map of Iceland, indicating the location of Torfajökull at the southern terminus of the Eastern Volcanic Zone (ERZ). **(b)** Simplified geological map indicating the principal volcanic systems of the Eastern Rift Zone of Iceland, and the current ice cover. From Lacasse et al. 1998.

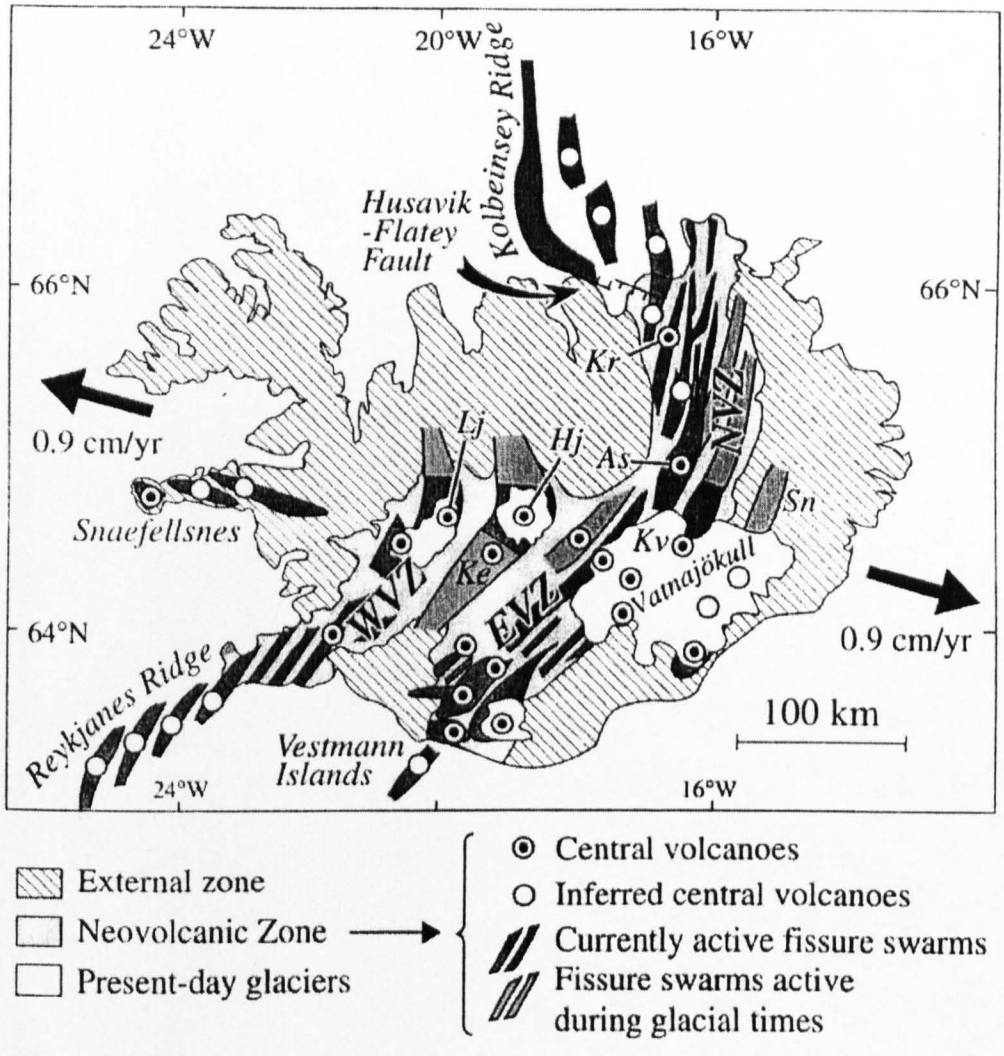

Fig. 1.20. (c) Map of Iceland indicating the distribution of central volcanoes and active volcanic zones, after Bourgeois et al. 1998.

Fig. 1.20. continued

discontinuous ring structures, which are prominent in aerial photographs and indicated in Fig. 1.21. The topography of the northern fringe of Torfajökull and the adjacent region to the north is dominated by southwest-northeast trending subglacial basaltic ridges and Holocene crater rows of the Veiðivötn fissure swarm within the actively spreading Eastern Rift Zone.

1.11.3. Eruptive history

Pre-Holocene activity The oldest mapped rocks at Torfajökull are subaerial metaluminous rhyolites (68-69 % SiO_2, Sæmundsson 1972). Subsequent activity has been dominated by the effusion of peralkaline rhyolite magmas, with minor transitional basalt (McGarvie 1984), which constitutes the bulk of the magma erupted at Torfajökull.

Subglacial eruptions have formed distinctive, commonly flat-topped volcanoes around the periphery of the volcanic complex (Figs. 1.21 and 1.22), which reach 924-1235 m in elevation and rise 300-550 m above the surrounding topography. On the basis of their geochemistry and field relationships, these subglacial volcanoes fit into two distinct groups: the Jökulgil formation and the Kirkjufell formation (McGarvie 1984, Ivarsson 1992). Each formation has involved the eruption of >10 km^3 of rhyolitic magma. The magma of each formation has a restricted compositional range, suggesting that that each was emplaced in a single eruptive episode (McGarvie 1984, McGarvie 1985), which might, however, have had a duration of thousands of years. Furthermore, both formations consist of several discrete edifices that were erupted on vents separated by up to 25 km (Fig. 1.21). McGarvie (1984) has proposed that the Kirkjufell formation was erupted on a ring fissure from a single magma chamber. Indeed, fissure orientations within the three southern volcanoes are arcuate and are

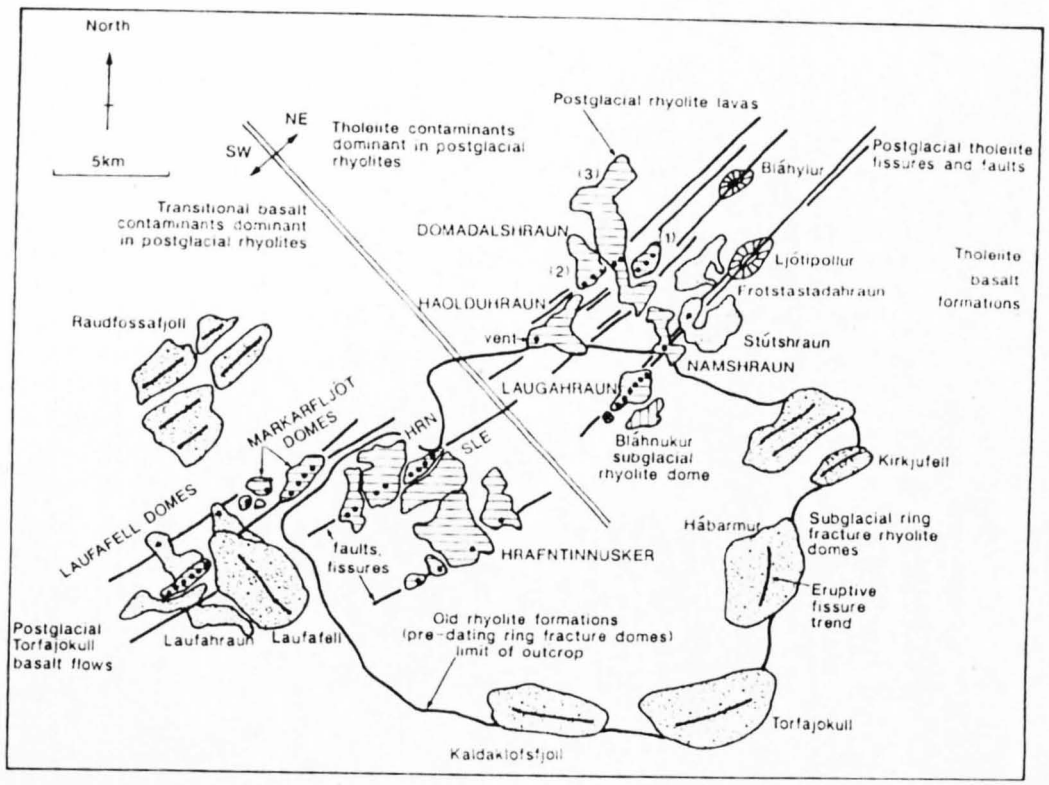

Fig. 1.21. Simplified geological map of Torfajökull, indicating the rhyolitic tuyas of the Kirkjufell formation, eruptive fissures, and postglacial lavas. Laugahraun, Namshraun, Stútshraun and Ljótipollur all formed during the c. 1477 eruptions. Tholeiitic basalts have been erupted from fissures in the northeast of Torfajökull, whereas transitional basalts have been erupted to the southwest. After Macdonald et al. (1990).

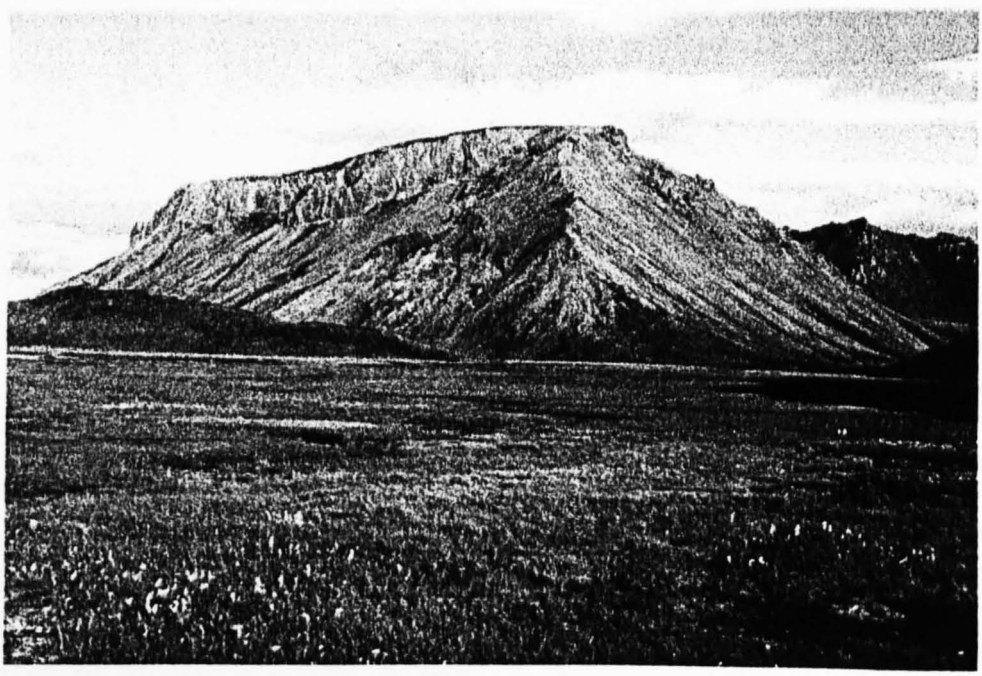

Fig. 1.22. Kirkjufell, a typical rhyolite tuya at Torfajökull (see Figure 1.21 for location). The gently inclined summit is formed by a lava flow over 100 m thick. Note that the flanks are mostly covered by scree derived from the summit lava. Vertical distance from base to top: 370 m. Photograph by D. W. McGarvie.

consistent with a single ring-like fracture, however, fissures within the three northern volcanoes are aligned parallel to the Holocene Veiðivötn fissure swarm (Fig. 1.21). These northern volcanoes are thought to be the oldest rhyolites at Torfajökull to contain inclusions of tholeiitic basalt from the Veiðivötn fissure system (McGarvie 1984), and the eruption of rhyolite may have been triggered by lateral intrusion of Veiðivötn tholeiite (see also Blake 1984).

Holocene activity

Patterns of activity during the Holocene are markedly different from those during glacial periods, with frequent small-volume eruptions rather than infrequent large-volume eruptions. Torfajökull has erupted 11 times in the Holocene, most recently in 1477, producing rhyolitic lava flows with a combined volume of ~2 km^3 (McGarvie 1985). All postglacial rhyolite lavas at Torfajökull were erupted from southwest-north-east trending fissures, thought to indicate the increasing tectonic influence of the Veiðivötn fissure system as the Eastern Volcanic Zone has propagated southwards.

1.11.4. Evidence for past glaciation at Torfajökull

Conclusive proof that rhyolitic volcanoes at Torfajökull were erupted beneath glaciers hundreds of metres in thickness can be obtained from examination of the volcanic lithofacies, which show compelling evidence for eruption beneath thick ice (Chapters 2-4). However, it is useful to cite independent evidence for the former presence of extensive glaciers over the Torfajökull central volcano:

1. Tills and diamicts of subglacial derivation are widely distributed throughout the Torfajökull area (Sæmundsson 1972, Sæmundsson 1988, Chapter 4.13, Chapter 4.14). Glacial landforms such as truncated spurs, U-shaped valleys and moraines are also widespread.

2. Small ice caps are present today at Torfajökull (from which the complex derives its name) and Kaldaklofsjökull (Fig. 1.21). These are in recession and terminal moraines are located tens of metres from the current snout, indicating that the ice cover was considerably more extensive in the recent past.

3. Modern palaeoclimatic reconstructions indicate that much of inland Iceland was covered by ice up to 1000 m thick in the last glacial period (see Bourgeois et al. 1998, Bourgeois et al. 2000), including the Torfajökull area (Fig. 1.23).

1.11.5. Choice of localities at Torfajökull for detailed study

Chapters 2-4 each deal with a specific subglacially erupted rhyolite volcano at Torfajökull. Their distribution is indicated on Fig. 1.24. They were chosen for the following reasons:

a) *Bláhnúkur* (Chapter 2). This accessible volcano was the product of a small-volume effusive eruption and apparently failed to melt through to the glacier surface (Furnes et al. 1980, Tuffen et al. 2001). It is easily reached from Landmannalaugar campsite and parts of the succession are well exposed in stream cuttings. Bláhnúkur was studied in August 1998 and July-August 1999.

b) *South-east Rauðufossafjöll* (Chapter 3). This more remote volcano was the product of a much larger-volume eruption than Bláhnúkur, and it will be argued that the eruption melted through to the glacier surface. The lithofacies are more complicated

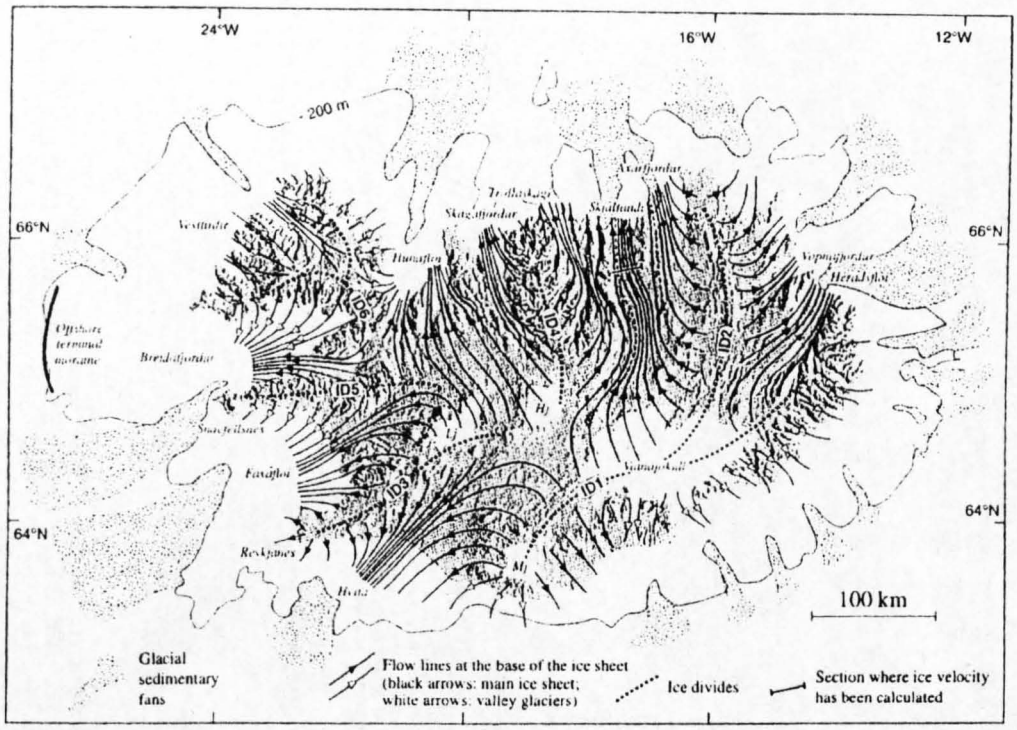

Fig. 1.23. Glacial extent and flow patterns in Iceland during the last glacial period. Inland areas, which include Torfajökull, were covered by ice hundreds of metres thick. After Bourgeois et al. (2000).

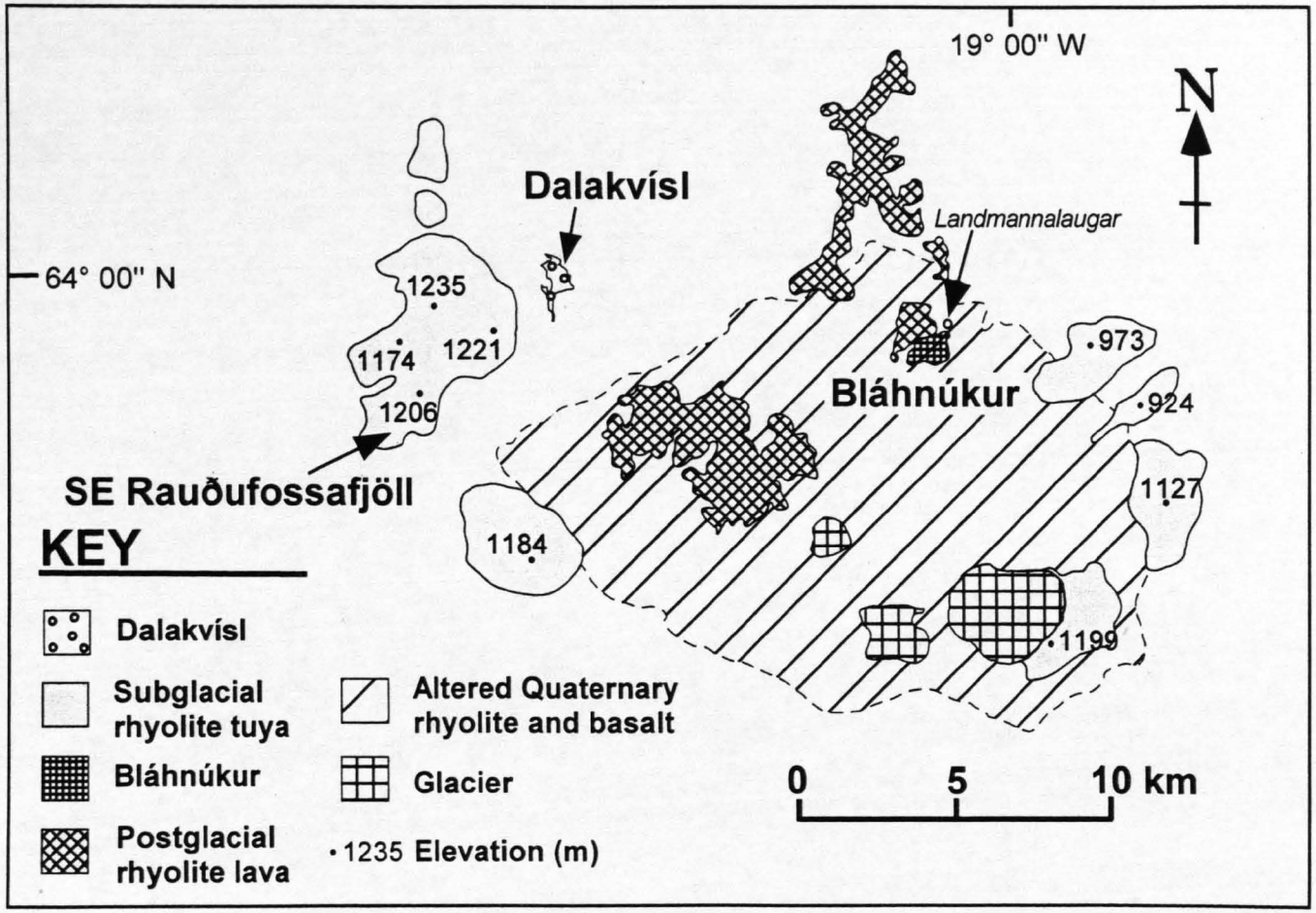

Fig. 1.24. Map of Torfajökull, indicating the location of the three volcanic sequences studied in detail.

than at Bláhnúkur and the terrain is more challenging. Exposure is locally good at the foot of the edifice. It was studied in July 1999 and July-August 2000.

c) *Dalakvísl* (Chapter 4). The intriguing deposits of Dalakvísl are transitional in nature between those of Bláhnúkur and South-east Rauðufossafjöll. It is perhaps the most difficult to interpret, and puts the other two field areas into perspective. Dalakvísl was studied in July-August 1999 and July-August 2000.

1.11.6. Fieldwork methodology and sample analysis

Mapping of each volcano, which encompass areas of c. 2-7 km^2, was conducted mostly at 1:10 000, but up to 1:500 in areas of complex geology. The nomenclature and classification of lithologies used follows that of McPhie et al. (1993). Samples of ash were collected for scanning electron microscope (SEM) analysis, and the technique of microscopy is outlined in Appendix F1. Samples of obsidian and rhyolite lava and pumice were collected, and unpolished 30 μm thin sections cut at the Open University. Selected sections were analysed by microprobe at the Open University, the analytical techniques are described in Appendix C1. A number of samples were analysed using Fourier Transform Infra-red Analysis (FTIR) at Bristol University, analytical techniques are described in Appendix D1.

Chapter 2.
Bláhnúkur: the product of an effusive subglacial rhyolite eruption

2.1. Overall structure of Bláhnúkur

Bláhnúkur is a prominent, isolated rhyolitic edifice close to Landmannalaugar in the north of the Torfajökull volcanic complex (Fig. 2.1). It rises 350 m above a dissected plain of altered Quaternary rhyolite. Roughly pyramidal in form, it has a core of older rhyolite draped by a veneer of younger subglacial rhyolite, henceforth called the Bláhnúkur rhyolite (Fig. 2.2, Fig. 2.3). The drape adds approximately 50 m to its height (Fig. 2.2). Geomorphologically, Bláhnúkur consists of four distinct linear ridges, whose orientations vary between WSW-ENE to NW-SE (Fig. 2.3). These ridges are both parallel and non-parallel with the NE-SW regional tectonic trend. The base of the Bláhnúkur rhyolite is locally underlain by massive orange-brown diamicton, which locally exceeds 20 m in thickness and contains cobbles of altered basalt and rhyolite lava set in a mud-grade matrix. The Bláhnúkur rhyolite, which differs from the subglacial rhyolite of neighbouring volcanoes in both its freshness and chemistry (Sæmundsson 1972, Ivarsson 1992), appears to be the product of an isolated, small-volume effusive eruption during the last glacial period (i.e. 115-11 ka ago). It contains a minor proportion of basaltic inclusions, a feature also typical of postglacial rhyolite lava flows at Torfajökull (McGarvie, 1984).

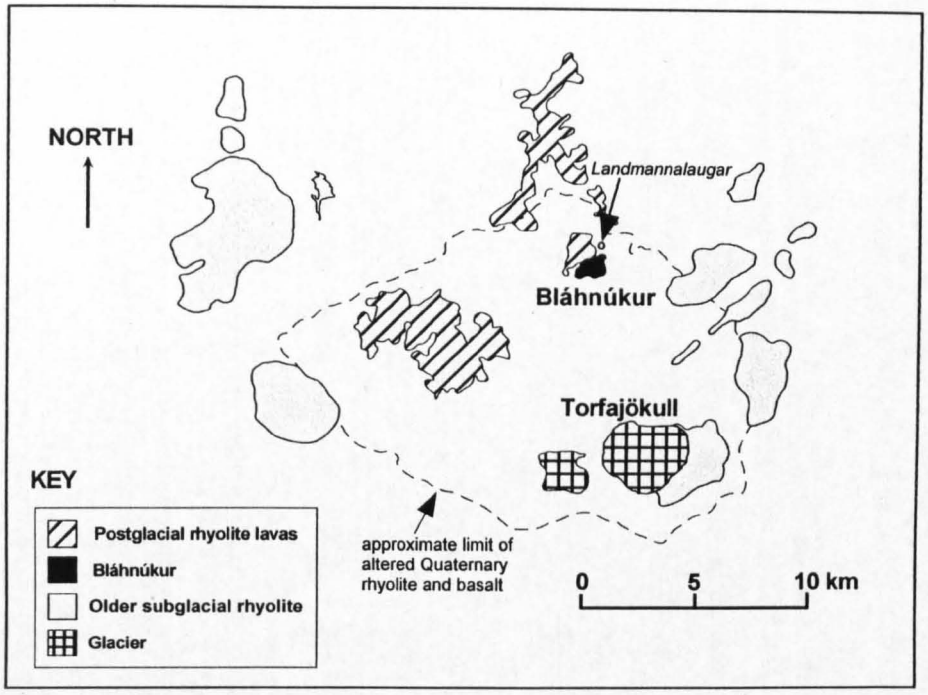

Fig. 2.1. Simplified geological map of the Torfajökull volcanic complex, showing the location of Bláhnúkur. The dotted line indicates the approximate extent of Quaternary altered rhyolite and basalt.

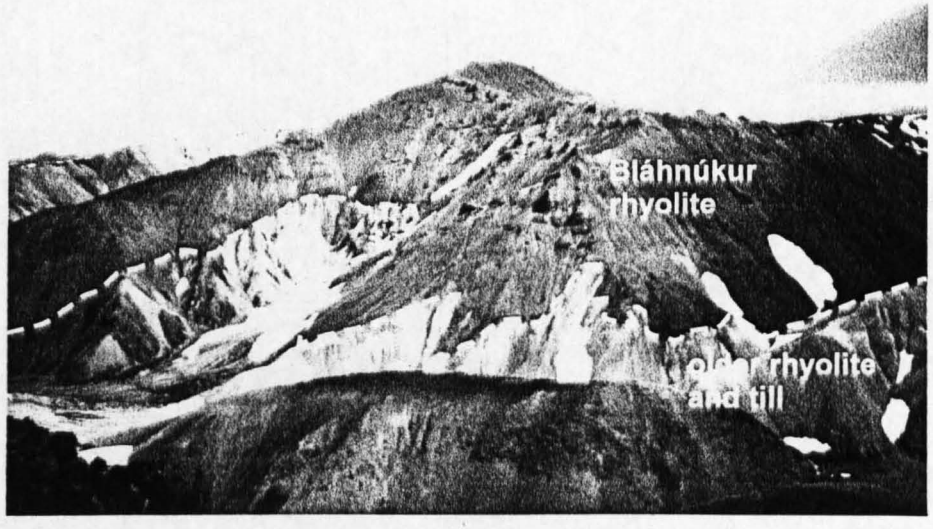

Fig. 2.2. View of Bláhnúkur from the west. A veneer of young subglacial rhyolite overlies older rhyolite and till. Vertical distance from base to summit: 350 m.

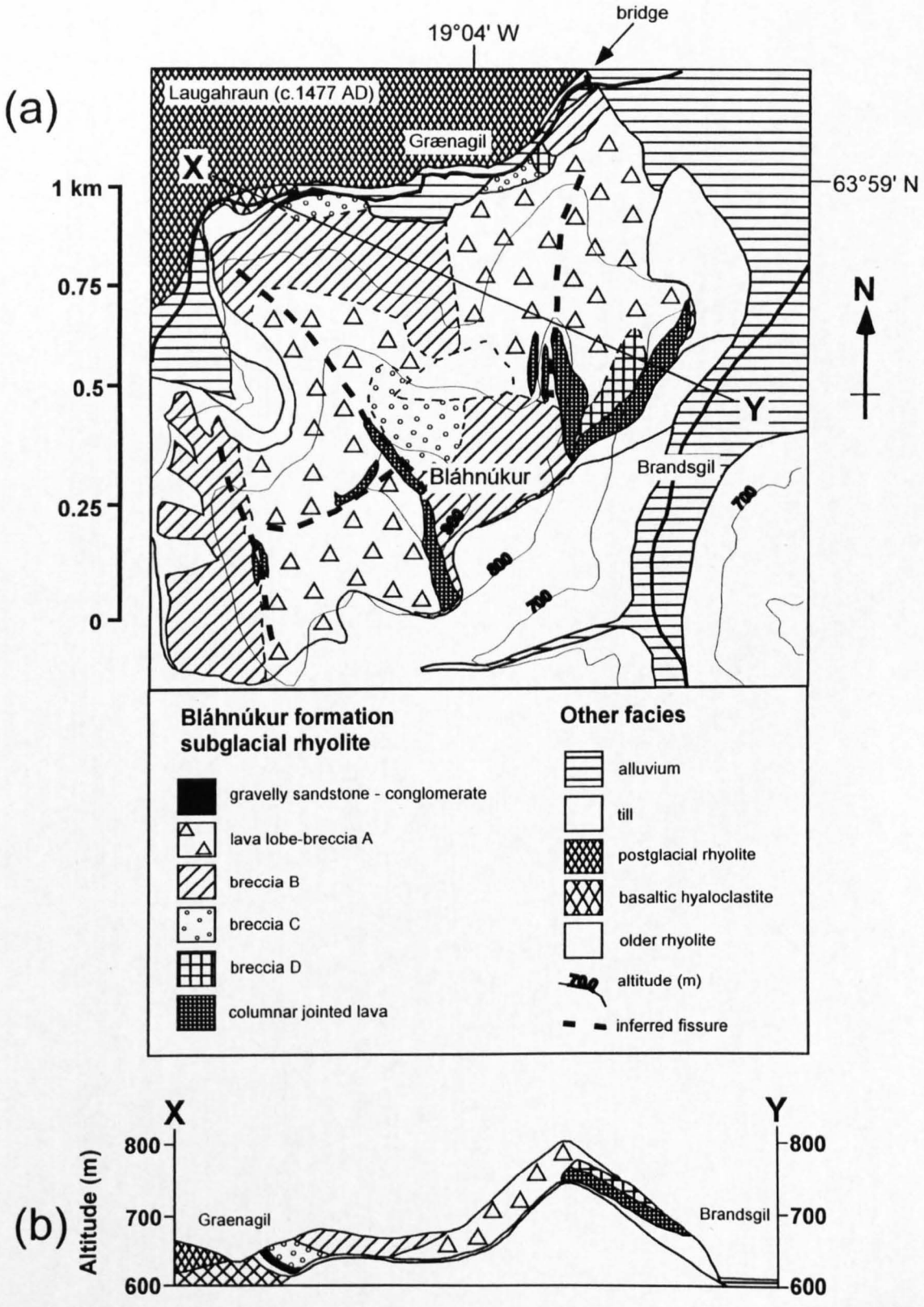

Fig. 2.3. (a) Simplified geological map of Bláhnúkur. Bláhnúkur is bounded to the north and east by the streams Grænagil and Brandsgil respectively. The postglacial rhyolite lava flow Laugahraun crops out on the north side of Grænagil. (b) Simplified cross section.

Fig. 2.3. (a) Simplified geological map of Bláhnúkur. Bláhnúkur is bounded to the north and east by the streams Grænagil and Brandsgil respectively. The postglacial rhyolite lava flow Laugahraun crops out on the north side of Grænagil. (b) Simplified cross section.

2.2. Evidence for a subglacial environment

Although there is no single feature that provides unambiguous evidence for a subglacial eruptive setting, the following features, when taken together, suggest that Bláhnúkur rhyolite was erupted under ice:

(1) Much of the sequence consists of breccias, which show evidence for magma-water interaction (perlitised obsidian, blocky ash shards, fines-rich veins, matrix vesicles). There is no evidence for the existence of a palaeotopography which could have confined a non-glacial lake (c.f. Jones 1970, Smellie & Skilling 1994, Smellie & Hole 1997). In fact, the reverse is true - the Bláhnúkur rhyolite was emplaced upon an existing topographic high. The lack of fossils, as well as the current elevation of 600-945 m in the absence of any tectonic structures consistent with uplift, precludes a submarine setting. Glacier melting is thus the most likely source of the water with which the magma interacted.

(2) Columnar jointing patterns suggest that many lava bodies in the sequence chilled against steeply inclined, sub-planar surfaces. Such jointing patterns, which have not been found in subaqueous or subaerial rhyolite lavas (e.g. Fink 1983, Scutter et al. 1998) are best explained by the chilling of lavas against ice walls (Lescinsky & Sisson, 1998).

(3) One lithology within the gravelly sandstone-conglomerate contains rounded, facetted clasts and a mud matrix consistent with a subglacial derivation.

2.3. Lithological descriptions and interpretations

Volcaniclastic lithologies were distinguished in the field using bedding characteristics, together with the type, size, and morphology of clasts (McPhie et al., 1993). The crystallinity, morphology, vesicularity, and jointing patterns of coherent volcanic lithologies are also described. 'Juvenile' is used to refer to products of the (subglacial) Bláhnúkur rhyolite eruption, whereas 'lithic' refers to clasts derived from the underlying basement - of altered Quaternary rhyolite, minor basalt and fluvioglacial deposits.

Of the following lithologies, gravelly sandstone-conglomerate (section 2.4.) contains both juvenile and lithic material, whereas all other lithologies (sections 2.5. - 2.9.) consist of entirely juvenile material.

2.4. Gravelly sandstone and conglomerate

2.4.1. Description

The gravelly sandstone and conglomerate lithology occurs as a 5-14 m thick sequence on the southern bank of Grænagil 1 km upstream of the bridge (Fig. 2.3, Fig. 2.4). At the base, a 0.5-5 m thick unit of orange-brown massive to planar-bedded matrix-supported lithic conglomerate lies in an inclined erosive channel cut into basaltic pillow breccia. Upper and lower surfaces are sharp, the channel pinching out laterally over ~ 100 m. The conglomerate contains sub-rounded to rounded, facetted cobbles of altered aphyric rhyolitic and basaltic lava up to 30 cm in diameter in a mud-grade orange-brown matrix. It is devoid of juvenile material.

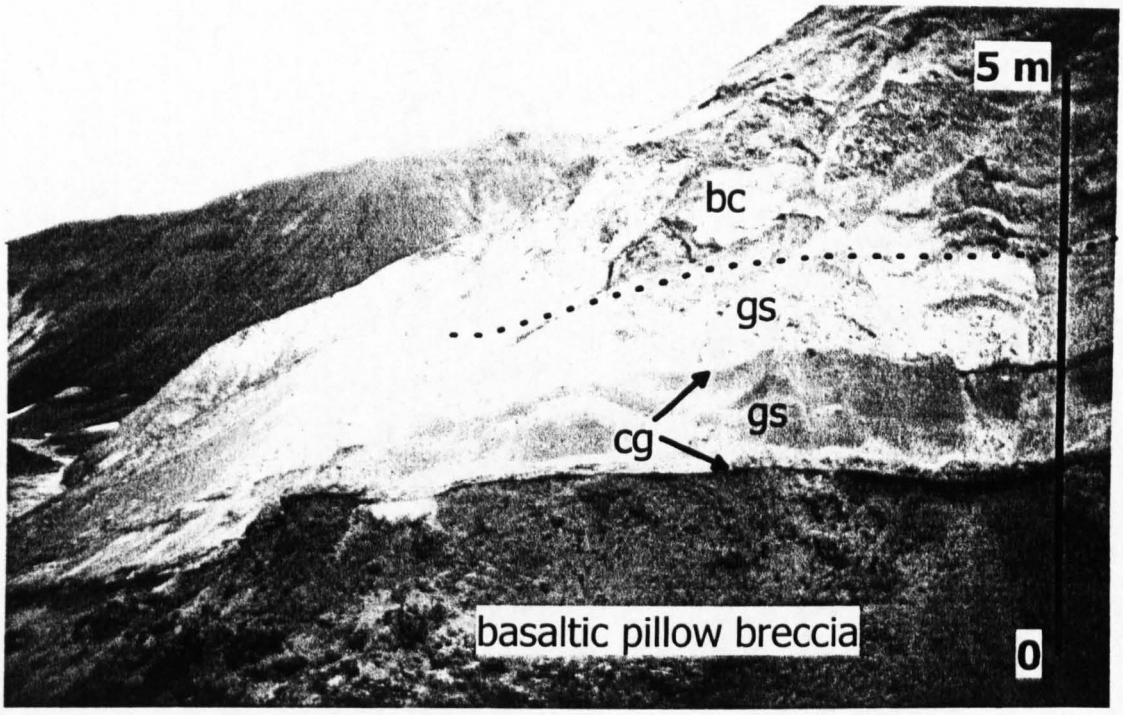

Fig. 2.4. 10 m-high outcrop on the south bank of the stream Grænagil, 1 km upstream of the bridge. Gravelly sandstone and conglomerate unconformably overlie basaltic pillow breccia. The gravelly sandstone is overlain by breccia C (upper 6 m of section). Key: cg - conglomerate, gs - gravelly sandstone, bc - breccia C. From Tuffen et al. (2001).

A 1-6 m thick gravelly sandstone unit overlying the conglomerate (Fig. 2.4) is moderately well sorted and laterally continuous over at least 100 m. In general, the gravelly sandstone comprises sub-planar beds 10-30 cm thick. However dune-like cross-stratification is also developed, with a wavelength of ~ 3 m. Over 95 % of clasts consist of juvenile phenocryst-rich black obsidian and grey perlitised vesicular obsidian (i.e. the Bláhnúkur rhyolite). Clasts are angular to sub-angular and 0.5-2 cm across. Sub-rounded 0.5-1 cm diameter lithic clasts of altered aphyric rhyolite and basalt lava make up the remainder of the deposit. The matrix consists of sand-grade angular clasts of juvenile obsidian.

A 3 m-thick brown breccia and conglomerate unit is locally present at the top of the sequence, comprising 10-20 cm thick matrix-supported lithic-rich breccia horizons intercalated with 3-10 cm thick beds of unconsolidated conglomerate. This unit is overlain by 1 m of cemented brown conglomerate. At the northern limit of this exposure, lithics in the gravelly sandstone disappear 3 m above the erosive base (Fig. 2.4). It is overlain by poorly-sorted juvenile breccias (breccia C).

2.4.2. Interpretation

The channelised, poorly-sorted conglomerate is similar to units on Mt Pinafore, Alexander Island, Antarctica (Smellie et al., 1993; Smellie & Skilling, 1994), which were interpreted as meltout tills formed by the redeposition of till by meltwater within a subglacial cavity. A similar interpretation is made here. The sorting, horizontal and cross stratification, and sharp boundaries of the gravelly sandstone units suggest deposition from a traction current (Smellie et al., 1993). The presence of interbedded lithic- and juvenile-dominated units suggests that pulses of juvenile material entered the subglacial cavity, probably washed from the vent area by a flowing stream of

volcanically-generated meltwater. This syn-eruptive lithology crops out 350 m vertically below the highest Bláhnúkur rhyolite deposits. It only crops out at the base of the subglacial eruptive sequence at one locality - suggesting localised meltwater flow drainage. Hence it can be inferred that localised, channelised meltwater drainage occurred during the eruption beneath a glacier at least 350 m thick.

2.5. Lava lobe-breccia A

2.5.1. Description

This lithology dominates the western flank of Bláhnúkur (Fig. 2.3, Fig. 2.5a). It is best exposed about 250 m north-west of the summit and on the south bank of Grænagil between 100 and 150 m upstream of the bridge. It consists of 5-20 m dark, irregularly to cylindrically-shaped obsidian and microcrystalline rhyolite lobes set in pale grey breccia. Lobes can be subdivided into flow lobes and feeder lobes.

Flow lobes are commonly cylindrical to prismatic in shape, with the long axis aligned parallel to the modern day slope (Fig. 2.5b, 2.5c, Fig. 2.6a). They consist of a black obsidian carapace 0.05-0.5 m thick that envelops a pale grey microcrystalline rhyolite interior. A banded zone up to 0.2 m thick at the obsidian-microcrystalline rhyolite contact consists of sheared blebs of pale crystalline lava 0.01-0.1 m long enclosed within dark crystal-poor obsidian.

The obsidian carapace of the upper part of flow lobes is frequently cut by columnar joints. Columns are 0.07-0.1 m wide, and normal to a steeply inclined near-planar surface (Fig. 2.5c, Fig. 2.6a). The orientations of 58 of these near-planar surfaces were measured and these are plotted in Fig. 2.6b. Over 90% of the columnar-jointed surfaces dip at between 45 and 80° from the horizontal (Fig. 2.6c). It is also

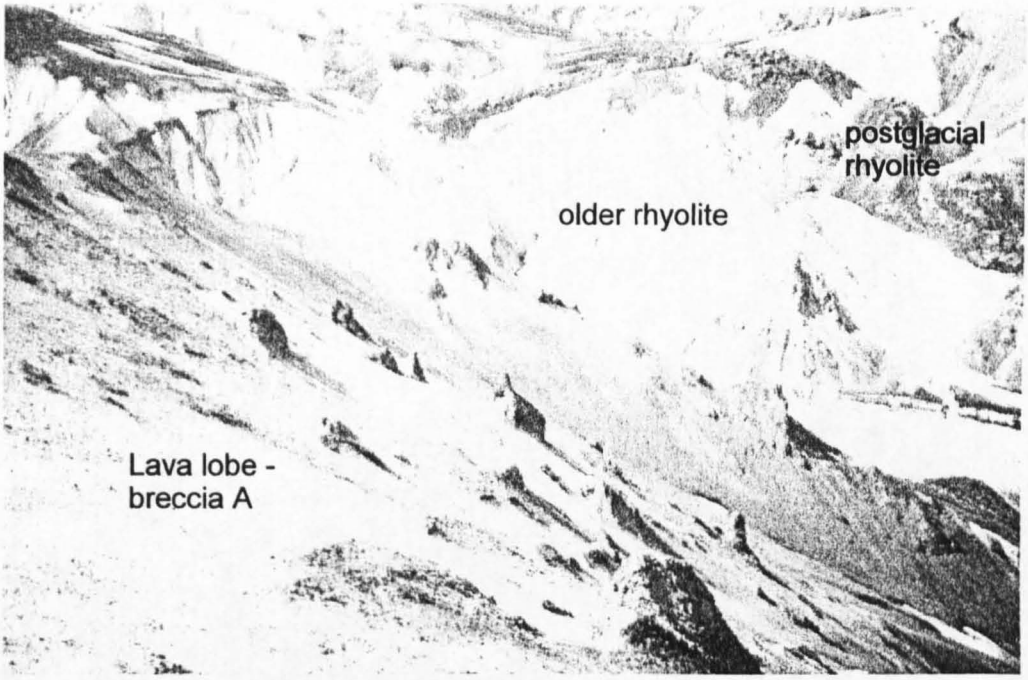

Fig. 2.5a. Overview of the west flank of Bláhnúkur (foreground), showing lava lobes (dark bodies) within poorly consolidated breccias (pale material). Lobes are randomly distributed. The pale material in the background is pre-Bláhnúkur rhyolite.

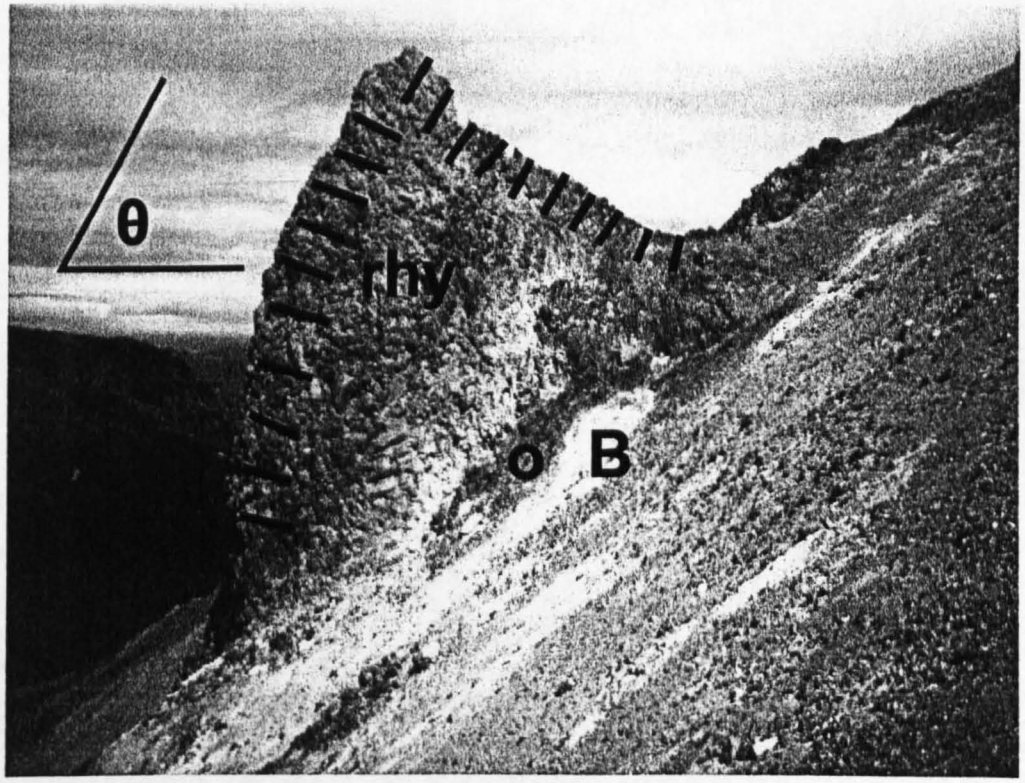

Fig. 2.5b. Photograph of a typical flow lobe on the west flank of Bláhnúkur. Dark grey obsidian at the base (O) grades downwards into pale grey breccia (B). The lobe interior is mid-grey microcrystalline rhyolite (rhy). Columnar joints on the upper surfaces are indicated. The dip angle of the surface normal to columnar joints is indicated (θ).

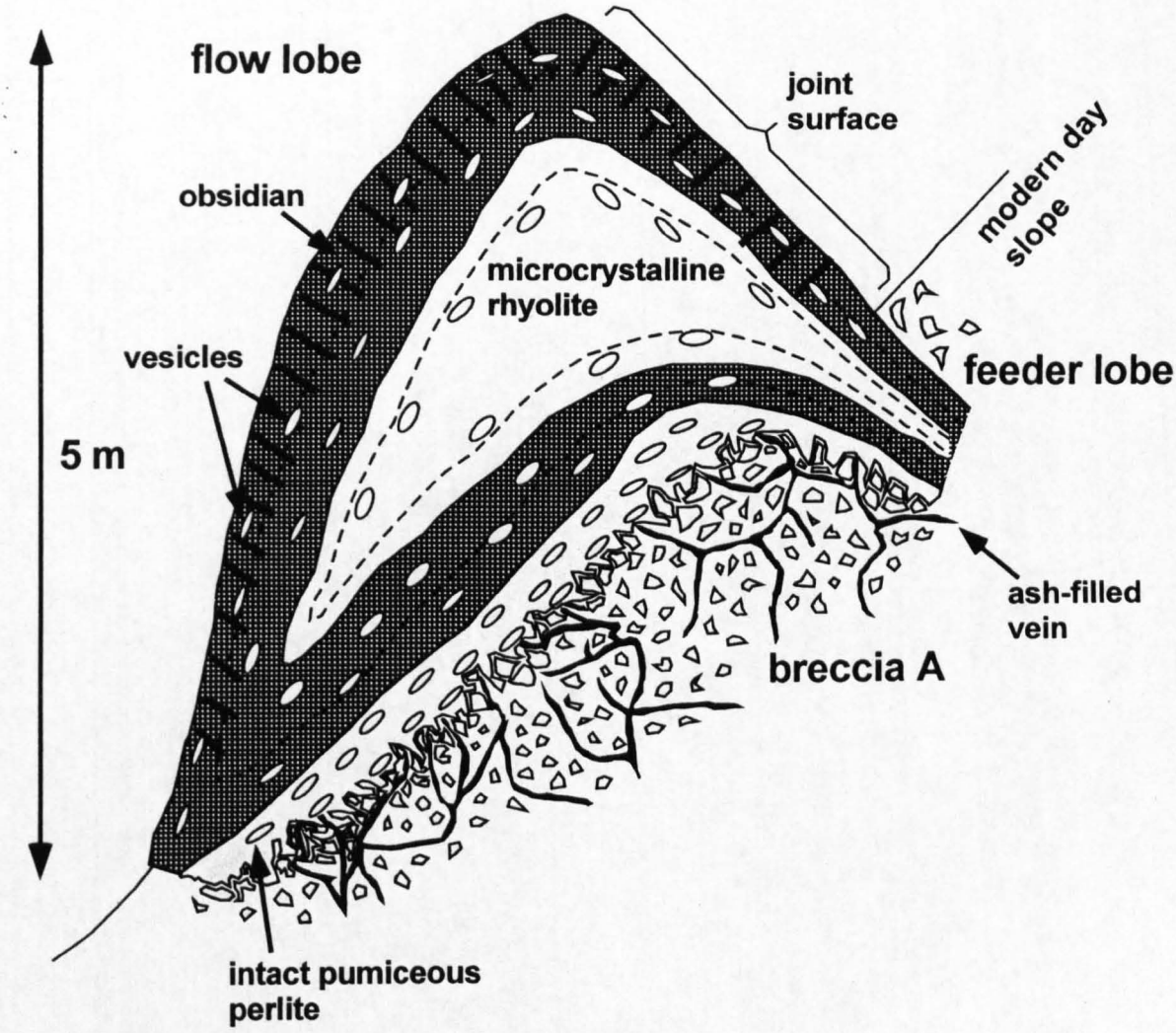

Fig. 2.5c. Schematic diagram showing the characteristics of an idealised lava lobe. Modified from Tuffen et al. (2001).

notable that the dip directions of the columnar-jointed surfaces are mostly near-parallel to the modern-day slope. Joints penetrate into the microcrystalline rhyolite core of most flow lobes. Intact black obsidian at the bases of flow lobes grades downward into grey, highly-fractured, perlitised obsidian, which becomes increasingly fragmented and grades downward into massive, poorly-sorted breccia (Fig. 2.5c). Columnar joints are absent.

The breccia consists of 0.5-30 cm wide angular clasts of pale grey perlitised obsidian in an ash matrix. Ash shards are typically 10-100 μm in diameter, glassy, and have blocky morphologies (Fig. 2.11a). The breccia is cut by an anastamosing network of veins 5-30 mm wide and up to 10 m in length (Fig. 2.8a). These are entirely filled by ash, which contains spherical to elongate vesicles up to 20 mm in length. Veins terminate at the intact obsidian of the lower margin of flow lobes (Fig. 2.5c). Vesicularity varies from <5% in the microcrystalline rhyolite cores of the lava lobes to 15-40% in the perlitised lower carapace and breccias.

Feeder lobes are irregular to sheet-like, oriented roughly perpendicular to flow lobes, and typically 5-20 m across. Where exposed, feeder lobes are seen to be linked to one or more flow lobes (Fig. 2.8b). Feeder lobes have hackly-jointed, microcrystalline cores and 0.1-0.5 m thick obsidian margins, which grade outwards into the massive breccias described above. The banded obsidian-microcrystalline transition zone common in flow lobes is absent. Vesicularity is generally less than 5%.

The orientation of flow banding within 111 flow lobes and feeder lobes was measured and is indicated in Fig. 2.7. Flow banding in flow lobes is typically near-parallel to the local modern-day slope, and thus dips down-slope on either side of ridges. Flow banding in feeder lobes generally dips into the local modern-day slope.

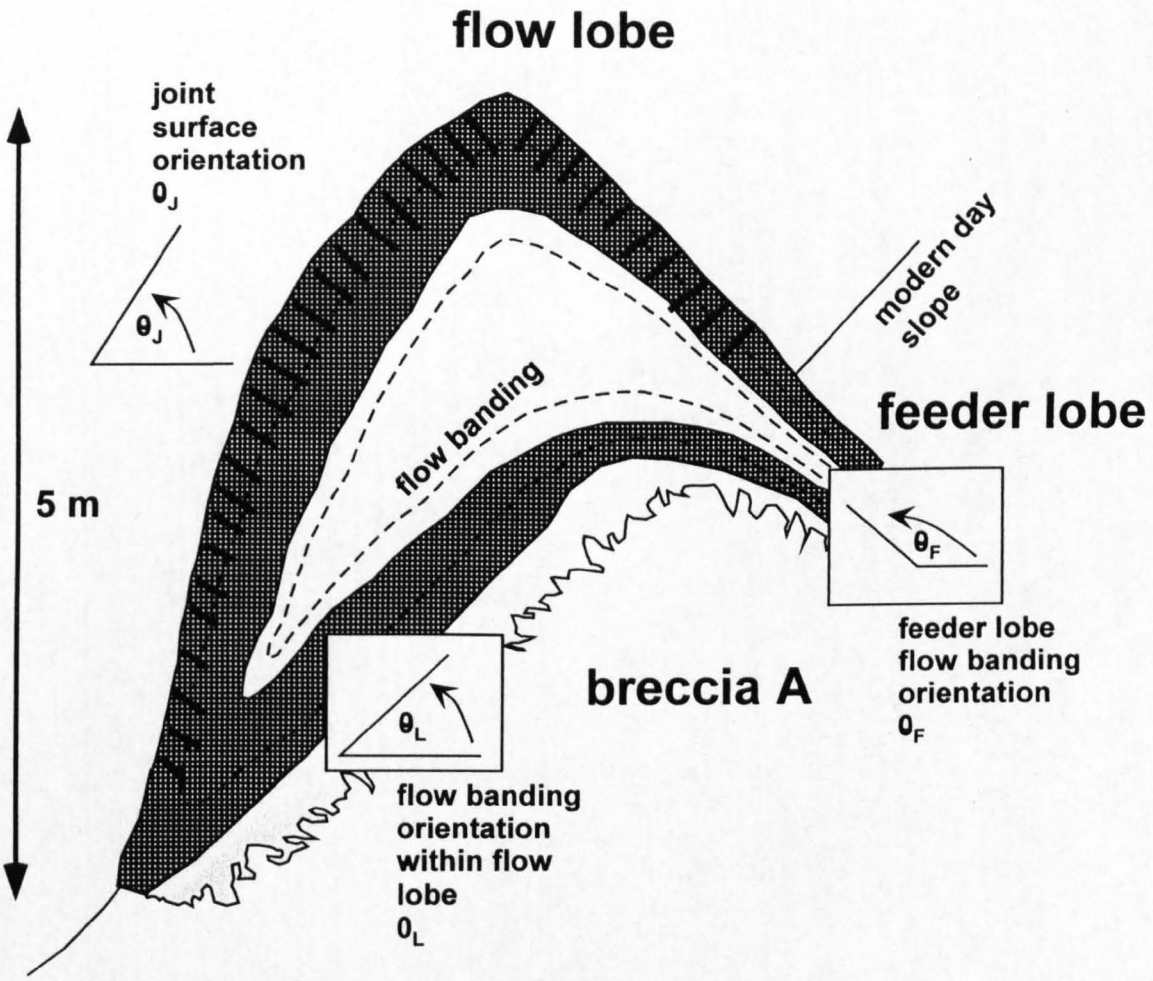

Fig. 2.6a. Simplified, schematic diagram of a typical lava lobe, indicating the orientation of columnar joint surfaces and flow banding. Thin dashed line - flow banding. Thick black line - columnar joint.

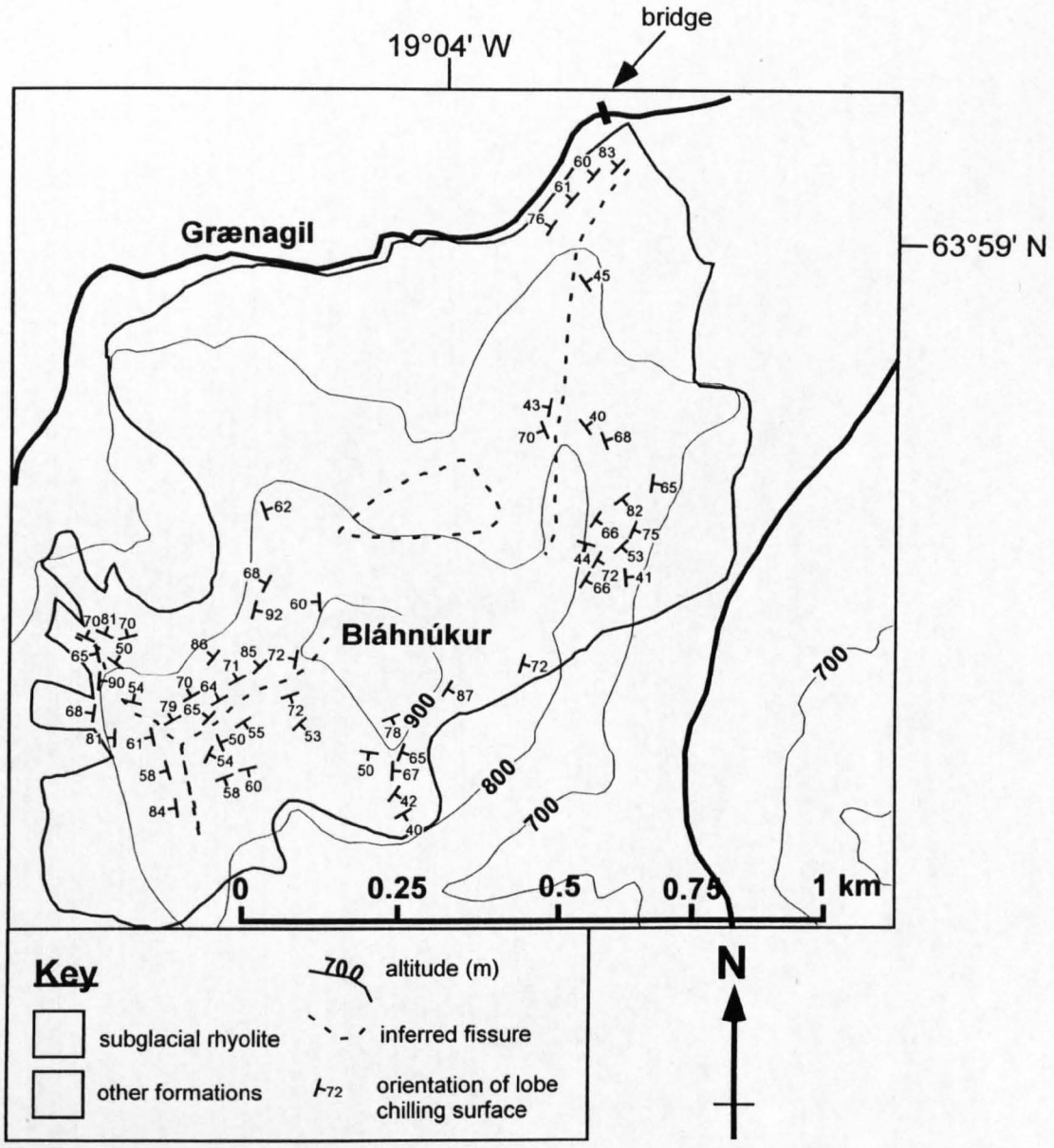

Fig. 2.6b. Simplified geological map of Bláhnúkur. Orientations of columnar-jointed surfaces of lava lobes are indicated (degrees from horizontal). These surfaces, which are interpreted as chilling surfaces, are measured normal to the long axis of columnar joints. Note that most chilling surfaces dip approximately down the modern-day slope.

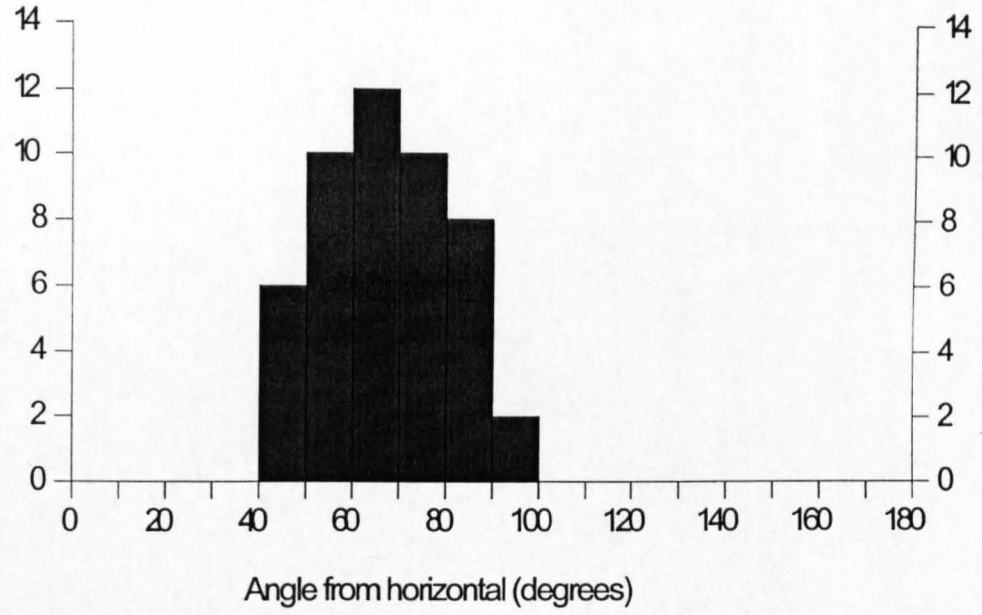

Fig. 2.6c. Histogram showing the orientation θ_J of 58 chilling surfaces on Bláhnúkur lava lobes. The vast majority of surfaces are inclined at between 50∘ and 80∘ from the horizontal.

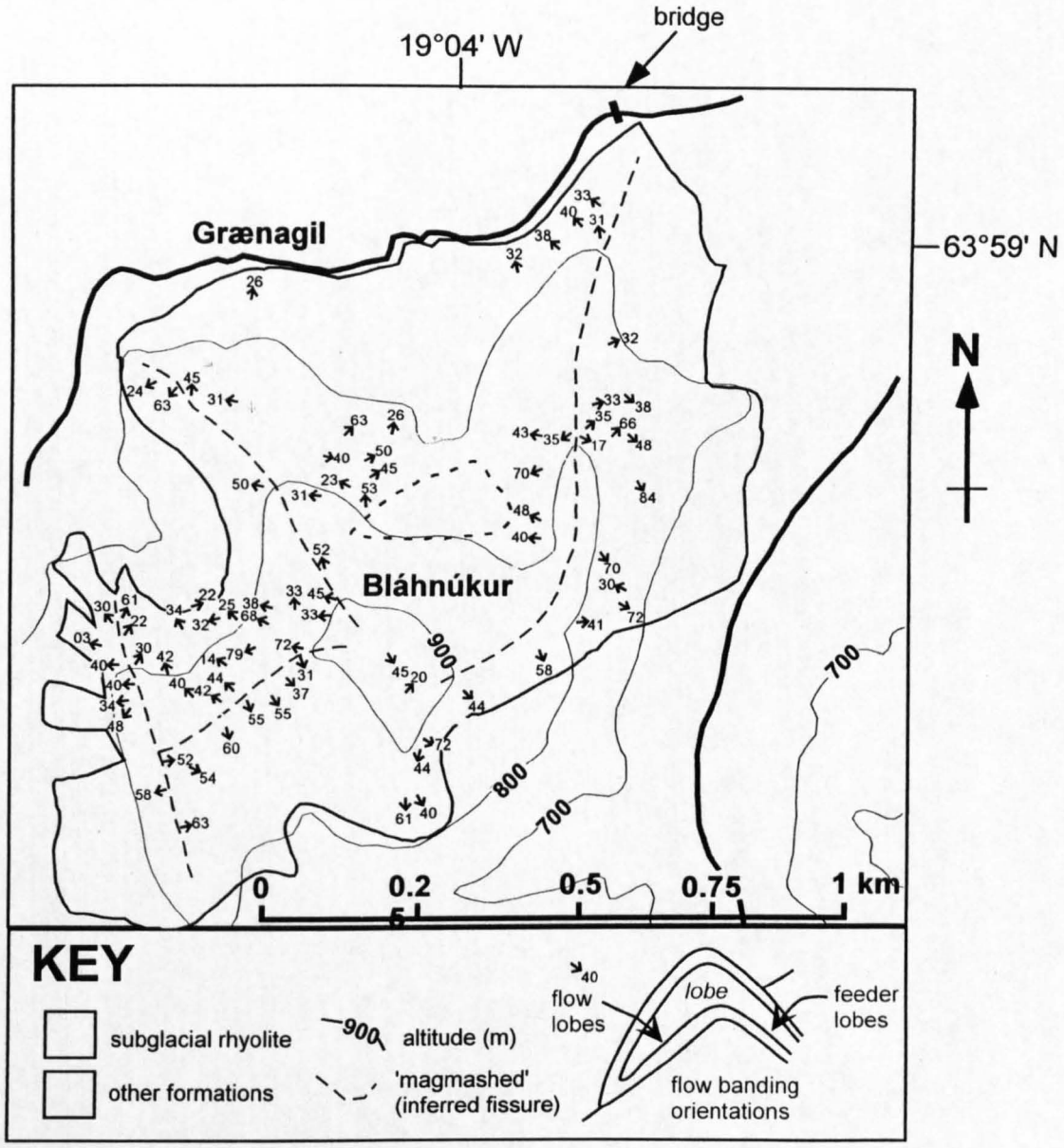

Fig. 2.7. Simplified geological map of Bláhnúkur. Orientations of flow banding planes are indicated (degrees from horizontal). Flow banding in most flow lobes (black) dips approximately down the modern slope, whereas flow banding in most feeder lobes (red) dips approximately into the edifice.

Fig. 2.8a. Ash-filled veins within poorly-sorted breccia A in Grænagil. The veins are anastamosing, locally sub-planar, and typically 5-30 mm wide. They are interpreted as vapour-escape pipes (see text). Ice axe is 0.5 m long.

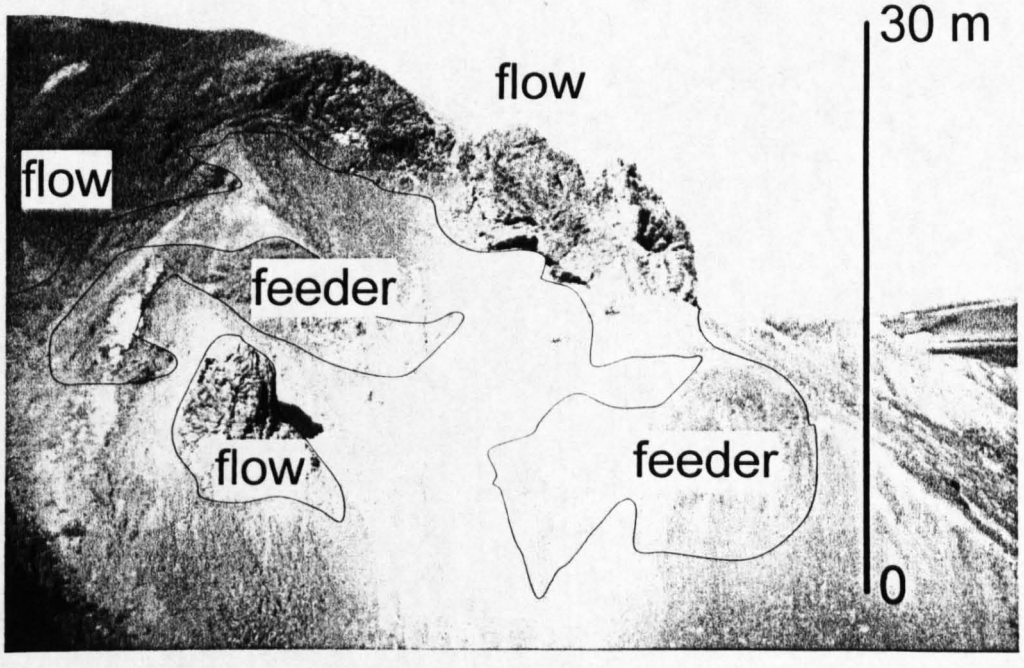

Fig. 2.8b. Lava lobes within a subglacial rhyolite formation at Dalakvísl, Torfajökull. In this highly dissected exposure, feeder lobes and flow lobes are clearly connected. The pale material is poorly-sorted perlitised breccia with an ash-grade matrix. This example from elsewhere has been chosen because the incision of a stream valley has revealed the relationship between feeder lobes and flow lobes more clearly than any exposure at Bláhnúkur. Otherwise, this lithology (lava 3, Chapter 4) shares many characteristics with the lava lobe-breccia A lithology at Bláhnúkur.

2.5.2. Interpretation

The gradational contact between the base of flow lobes and breccia suggests *in situ* fragmentation of the lobes. Pumiceous, perlitised clasts and ash were created at lobe bases, which were in contact with earlier-formed breccia. A similar suite of textures occurs in rhyolitic pumiceous peperite emplaced in a submarine setting at Mt. Chalmers Queensland, Australia (Hunns & McPhie 1999). The increase in vesicularity from the core to rim of lobes (Furnes et al. 1980) suggests that magmatic volatiles diffused outward from the lobe interior. Furnes et al. (1980) labelled this lithology type 1 hyaloclastite, and suggested that fragmentation was driven by magma vesiculation. This interpretation in questionable, since the blocky morphology of ash shards suggests that fragmentation was dominantly phreatomagmatic and driven by quenching, rapid glass contraction and steam explosivity (Heiken & Wohletz, 1985). Dehydrative decrepitation (Mungall et al. 1996) may have also contributed to fragmentation. Instead, it is suggested that the lava lobes represent the subglacial equivalent of an effusive rhyolite eruption, in which fragmentation due to volatile exsolution was minimal. Furthermore, perlitic alteration is an indication that water interacted with lobe margins, and vesiculated ash may indicate that a vapour phase was present (Lorenz, 1974, Hunns & McPhie 1999).

The orientation of columnar joints in lavas indicates the direction of heat loss during cooling (DeGraff et al. 1989). The upper carapaces of flow lobes thus appear to have chilled against steeply-inclined, near-planar surfaces. One interpretation is that the flow lobes were emplaced at the base of a glacier, where they flowed and chilled against the walls of cavities melted into the basal ice (c.f. Furnes et al. 1980). There is strong corroborative evidence for a subglacial eruptive setting, such as the presence of facetted clasts within diamicton in the volcanic sequence at Bláhnúkur.

Similar columnar-jointed lava flows elsewhere are interpreted as an ice-contact feature (Lescinsky & Sisson 1998). The position of flow lobes suggests that the subglacial cavities were randomly distributed. The consistently steep orientation of a number of inferred cavity walls suggests a common melting mechanism.

It is therefore inferred that lobes rose towards the glacier base within poorly-consolidated, water-saturated breccias. Flow lobes reached the glacier base and show ice-contact features, whereas feeder lobes solidified within the breccia. Water released during the melting of subglacial cavities may have possibly percolated into the permeable breccias, thus it is possible that an air-filled cavity developed, similar to the fumarole-melted firn caves in the summit crater of Mount Rainier (Kiver & Steele 1975). The cavities at Bláhnúkur were probably beneath considerably thicker ice (>350 m, compared to <120 m at Mount Rainier), and thus the possibility that cavities were water-filled cannot be eliminated. However, the poorly-sorted breccias lack evidence for aqueous reworking, supporting the view that standing bodies of meltwater did not accumulate in cavities. This may explain the inferred steepness of the ice walls, since a cavity partially filled with meltwater is expected to develop a broad, low shape (Hoskuldsson & Sparks 1997, Cutler 1998). Steam-filled cavities (steam cups) on Mount Rainier have smooth, steeply inclined walls (Kiver & Steele 1975), as do cavities entirely filled with meltwater (Hoskuldsson & Sparks 1997). Melting mechanisms and the possible accumulation of meltwater in these cavities is discussed in greater detail in section 5.9.

Ash-filled veins are interpreted as vapour-escape pipes, which formed during brittle failure of poorly consolidated breccia. Veins were filled by the ash matrix of the breccia, which was remobilized by rising steam. Vapour escape was probably accompanied by the development of numerous fumaroles, as observed in ignimbrites

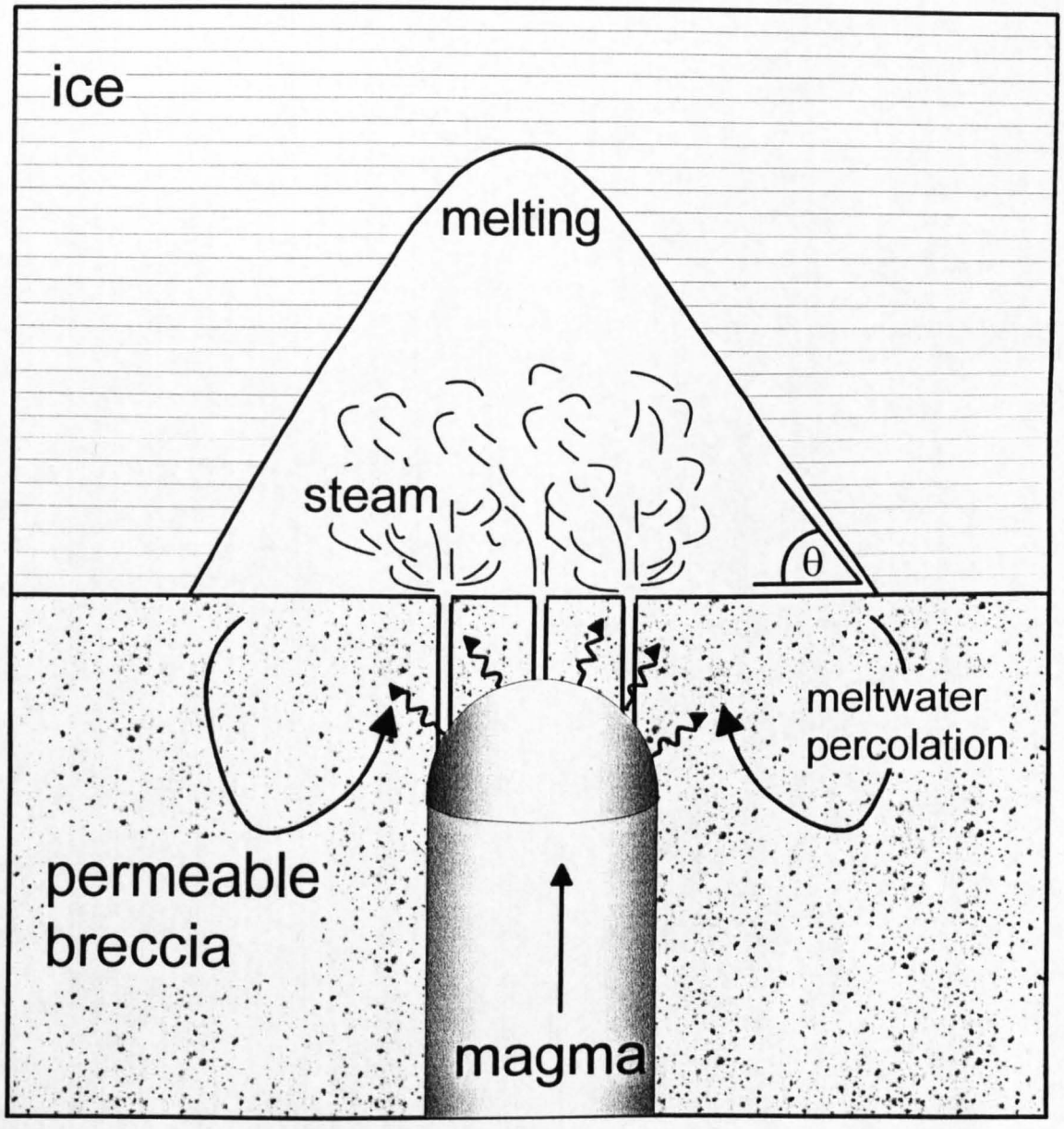

Fig. 2.9. Cartoon illustrating the preferred model for the emplacement of flow lobes at the glacier base. θ = orientation of ice wall. Heat from the rising lobe boils water in the surrounding permeable breccia, creating steam that fluxes through the breccia along pathways of preferential permeability (vapour-escape pipes). This causes localised melting of the glacier base, forming a steep-walled steam-or water- filled cavity (a steam-filled cavity is illustrated here). Meltwater drains into the breccia, and recharges the cooling system.

(Sheridan 1970). The position of fumaroles would have been highly localised, being concentrated close to the heat source (an individual magma body). It is proposed that cavities may have melted in the ice above a rising magma body during the last ~10 metres of its ascent to the glacier base, which is the maximum length of vapour-escape pipe observed (see section 5.9). Rapid, focussed transfer of heat from magma to ice by convecting steam within vapour-escape pipes facilitated melting ahead of the advancing magma (Fig. 2.9). Cavities acted as moulds for the advancing magma, which flowed and chilled against the ice walls. This melting mechanism is modelled numerically in section 5.9. The ability of ice to deflect moving lava flows has been observed during a basaltic eruption in Alaska (Vinogradov & Murav'ev 1988).

The orientation of the long axes of lobes is bimodal, with feeder lobes dipping into the modern-day slope and flow lobes dipping at an angle parallel to the modern-day slope. Ridge crests at Bláhnúkur appear to have been 'magmasheds', with flow lobes dipping down either side (Fig. 2.7). A similar bimodal pattern was seen in subaqueous rhyolite hyaloclastite in Japan (Yamagishi & Dimroth 1985). The interpretation at Bláhnúkur is that magma rose in sheets or fingers to the base of the glacier, where it flowed a limited distance down-slope within cavities over water-saturated breccias, before freezing against constraining ice walls (Furnes et al. 1980). Rising magma locally stalled within the breccia, forming irregular intrusions. The ridges are considered to constitute eruptive fissures. Thus Bláhnúkur was constructed by effusion along four or more short (<1 km) fissures (Fig. 2.3), which are both parallel and non-parallel to the regional tectonic trend (NE-SW). This configuration of fissures is consistent with the location of Bláhnúkur, close to the northern margin of Torfajökull. In this region, there is a transition between NE-SW fissures to the north,

parallel to the Veiðivötn fissure swarm, and arcuate fissures to the south, many of which are tangential to the margins of the near-circular Torfajökull complex (Fig. 1.21).

2.5.3. Internal structure of lava lobes

Many lava lobes of Bláhnúkur display common patterns of textural zonation that are visible in the field as concentric bands of distinct colour. The typical zonation pattern is illustrated in Fig. 2.10. The principal features of the different textural zones, which vary in width both between and within lobes, are listed in Table 2.1 and illustrated in Fig. 2.11.

2.5.4. Lava lobe microtextures

The characteristics of each textural zone are summarised in Table 2.1. Fig. 2.10 shows the outcrop-scale distribution of textural zones, whereas thin section and SEM photographs of typical samples from different zones are provided in Fig. 2.11. The proportions of vesicles and microlites are estimated from thin sections. Although this is a qualitative study, the relative orientation of microstructural elements (phenocrysts, microlites, vesicles, fractures) allows the chronology of microtextural evolution to be unravelled. Similar studies have been applied to the orientation of crystals in obsidian (Vernon 1987, Manga 1998) and flow banding in obsidian (Seaman et al. 1995). Marti et al. (1999) used vesicle deformation patterns in tube pumice to reconstruct changing glass rheology during shear and fragmentation. Yamagishi & Dimroth (1985) described similar patterns of crystallinity and vesicularity within subaqueous rhyolitic lava lobes of similar size, but did not describe the relative orientation of textural features. A 'metamorphic philosophy' is applied here, and the relative timing of events (vesiculation, microlite crystallization,

Zone	Appearance	Homo-geneous?	Vesicles	Microlites	Deformation	Comments
A	Fine-grained pale grey ash. Blocky shards 10-100 μm long with hydrated surfaces. Zone is >1 m thick beneath lobes (see Fig. 2.11a).	Yes.	Elongate, smooth-walled, c. 20%, sizes not estimated.	Aligned parallel to vesicles, acicular, 5-10 μm. Abundance not estimated.	Ductile shear followed by brittle fracture.	Fragmentation probably triggered by magma-meltwater interaction.
B	Mid-grey crumbly obsidian 5-20 cm thick at base of flow lobes. Mostly microlite-poor (1), ~5% microlite rich (2).	No. Elongate microlite-rich 'blebs' 1-4 mm long.	(1) c. 10%, elongate, pointed corners, coalesced, 0.1-2 mm. (2) c. 20%, equant, rough, <0.5 mm.	(1) ~5%, aligned parallel to vesicles, acicular. (2) ~15%, poorly aligned or random, acicular.	Ductile shear followed by folding and minor brittle fracture.	Blebs possibly scavenged from feeder walls. Fracture due to meltwater?
C	Dark grey-black homogeneous obsidian 5-50 cm thick.	Yes.	c. 20%, 0.2-5 mm, elongate, smooth-walled, pointed corners.	~5-10%, aligned parallel to vesicles, acicular.	Ductile shear followed by folding and compression.	Glass has folded into vesicle spaces during compression.
D	Dark grey obsidian (1), contains irregular to rounded pale grey 'blebs' 10-100 mm long (2). 3-10 cm thick zone.	No. Irregular pale microlite-rich 'blebs' 10-100 mm long.	(1) c. 15% smooth-walled, elongate 0.1-2 mm. (2) 10-30% equant, rough, coalesced, 0.1-1 mm.	(1) ~15-20%, weakly aligned parallel to vesicles, acicular. (2) ~50%, randomly orientated, acicular.	Ductile shear followed by magma mixing and further ductile shear.	Blebs possibly scavenged from vent walls. Boundary layer between core + rim.
E	Pale grey microcrystalline rhyolite 0.1-2 m thick.	Yes.	<10 % irregular, rough walls, associated with phenocrysts, <1 mm.	~60-80%, aligned in 'kink bands' 0.1-1 mm wide, not parallel to vesicles, acicular.	Ductile shear followed by highly viscous compression.	Probable Bingham rheology due to high crystallinity.
F	Mid grey microcrystalline rhyolite 0.5-5 m thick (1). Rare vesicle-rich blebs (2).	No. <5% vesicle-rich blebs 1-2 mm long.	(1) c. 5%, rough, <0.5 mm. (2) c. 20%, rough, coalesced, 0.1-1 mm.	(1) ~50%, aligned in 'kink bands'. (2) ~50%, randomly oriented.	Ductile shear followed by magma mixing and highly viscous compression.	Vesicle-rich blebs possibly scavenged from earlier vent walls.

Table 2.1. Summary of characteristics of textural zones within lava lobes at Bláhnúkur. See Fig. 2.10 for a schematic diagram of these zones.

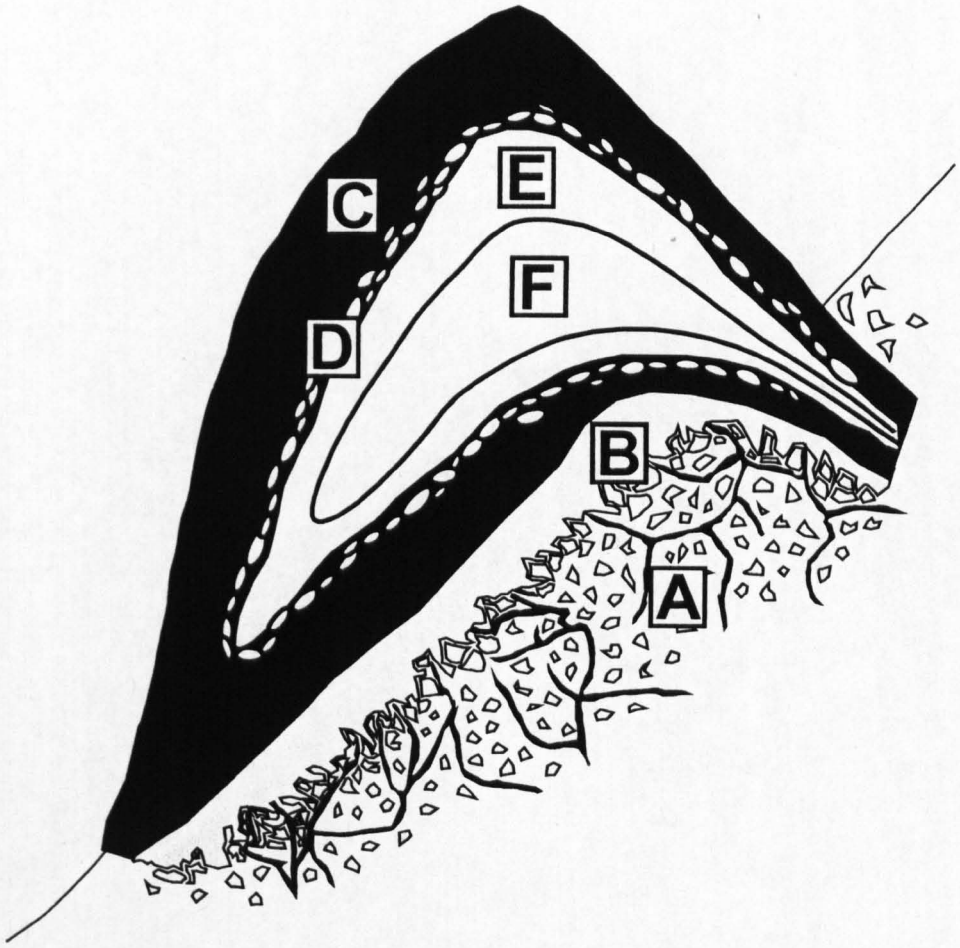

Fig. 2.10. Simplified, schematic diagram of a typical lava lobe, indicating the patterns of textural zonation. Although many lobes display this zonation, some have repeated zonations and highly complex internal structures. See Table 2.1 for details of zones A-F. Modified from Tuffen et al. (2001).

magma mixing, ductile deformation, brittle fragmentation) has been reconstructed and is presented in Fig. 2.12. The emplacement scenario envisaged for a typical lobe, illustrated in Fig. 2.13, involves:-

(a). The outer carapace of ductile, microlite-poor magma is emplaced (lobe zones A-C). The magma contains rare 'rags' of microcrystalline magma which have been scoured from the crystallising feeder walls. The outer margin of the carapace becomes quenched by interaction with meltwater, and fragments.

(b) The last of the microlite-poor ductile magma collects increasing quantities of microcrystalline magma from the feeder walls, and a mixed 'boundary layer' is emplaced (lobe zone D).

(c) Finally, high-viscosity, microlite-rich magma is intruded into the core of the lobe (zones E-F). Its emplacement causes deformation of the outer carapace, with the vesicles in still-ductile magma being flattened, whereas more chilled magma may fragment brittly. Furnes et al. (1980) envisaged this mode of formation for the vesicle-poor type 2 hyaloclastite.

One explanation for this chain of events is that individual flow lobes have been fed by progressively crystallising feeder lobes. Initially, the low-crystallinity (and less viscous) interior of feeder lobes was tapped, followed by increasingly crystalline, more viscous magma. A similar textural zonation was observed within numerous different flow lobes, implying that a common mechanism probably operated. This may be due to the accumulation of magma within shallow-level feeder lobes close to the glacier base, which acted as 'mini magma chambers', within which the suite of microtextures seen in flow lobes was developed. Indeed, there is evidence elsewhere that intrusive lava bodies fed one or more ice-contact flow lobes (Fig. 2.8b).

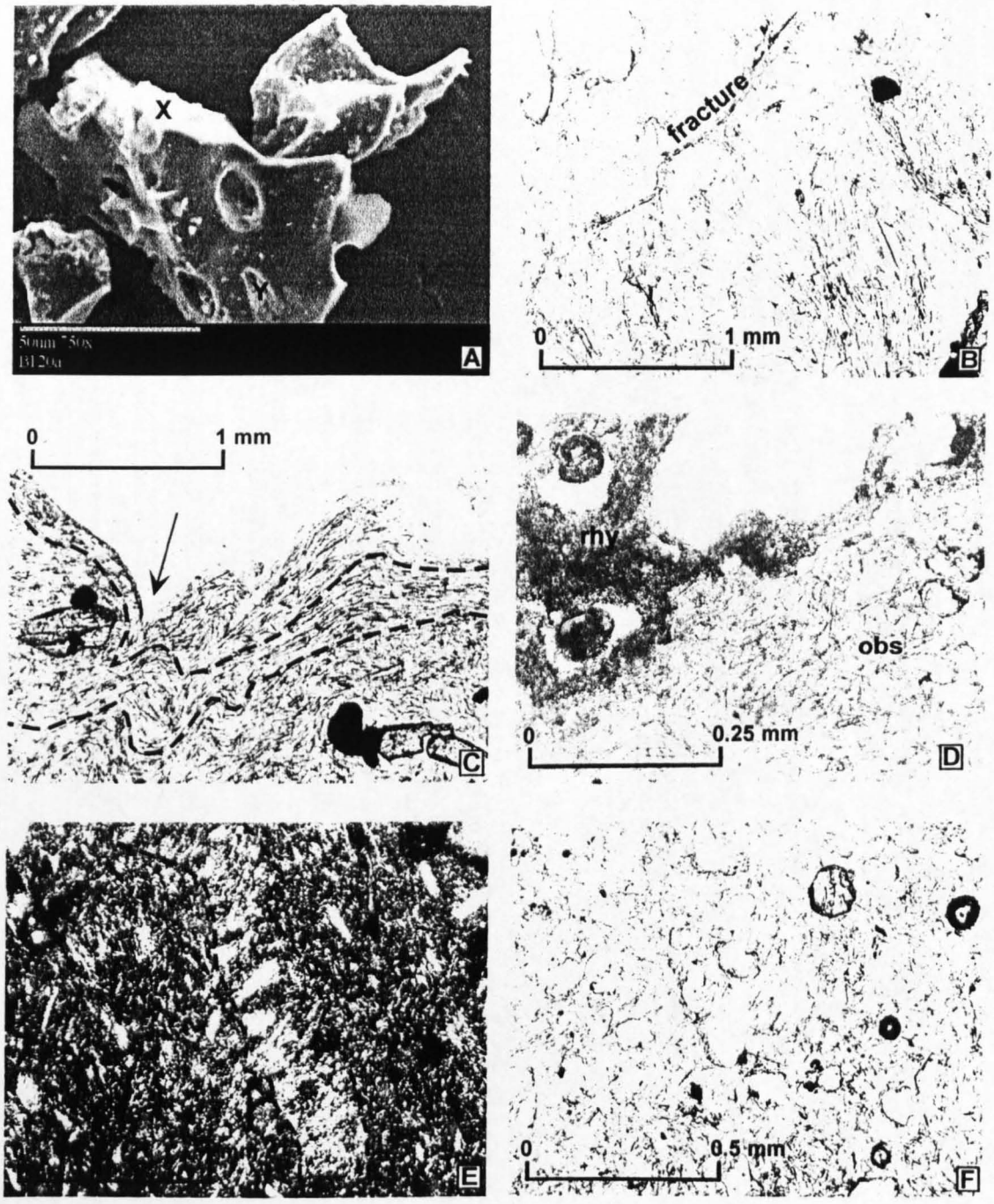

Fig. 2.11

Fig. 2.11. **(a)** SEM image of a glassy ash shard from poorly-sorted breccia at the lower margin of a flow lobe. The shard is blocky in morphology, with < 20% elongate vesicles (Y), and has pitted, altered surfaces (X). **(b)** Photomicrograph of fractured obsidian (lobe zone B) in plane polarised light. A fracture plane (indicated) cuts obsidian. Note the domains of both well-aligned microlites and more randomly distributed microlites. **(c).** Photomicrograph of crenulated obsidian (lobe zone C). The orientation of microlites describes a well-formed lineation, which has been folded (red lines). Folding of vesicle walls has resulted in angular embayments (arrow). Plane polarised light. **(d)** Photomicrograph of mixed zone (lobe zone D). A dark microlite-rich region (top left) contains near-equant, rough-walled vesicles. The pale microlite-poor region (bottom right) contains smooth-walled vesicles. Plane polarised light. **(e)** Photomicrograph of outer microcrystalline rhyolite (lobe zone E), with crossed polars. Microlites are arranged in 'kink bands' (indicated). **(f)** Photomicrograph of inner microcrystalline rhyolite (lobe zone F) in plane polarised light. Microlites are randomly oriented, whereas vesicles are near-equant and rough-walled.

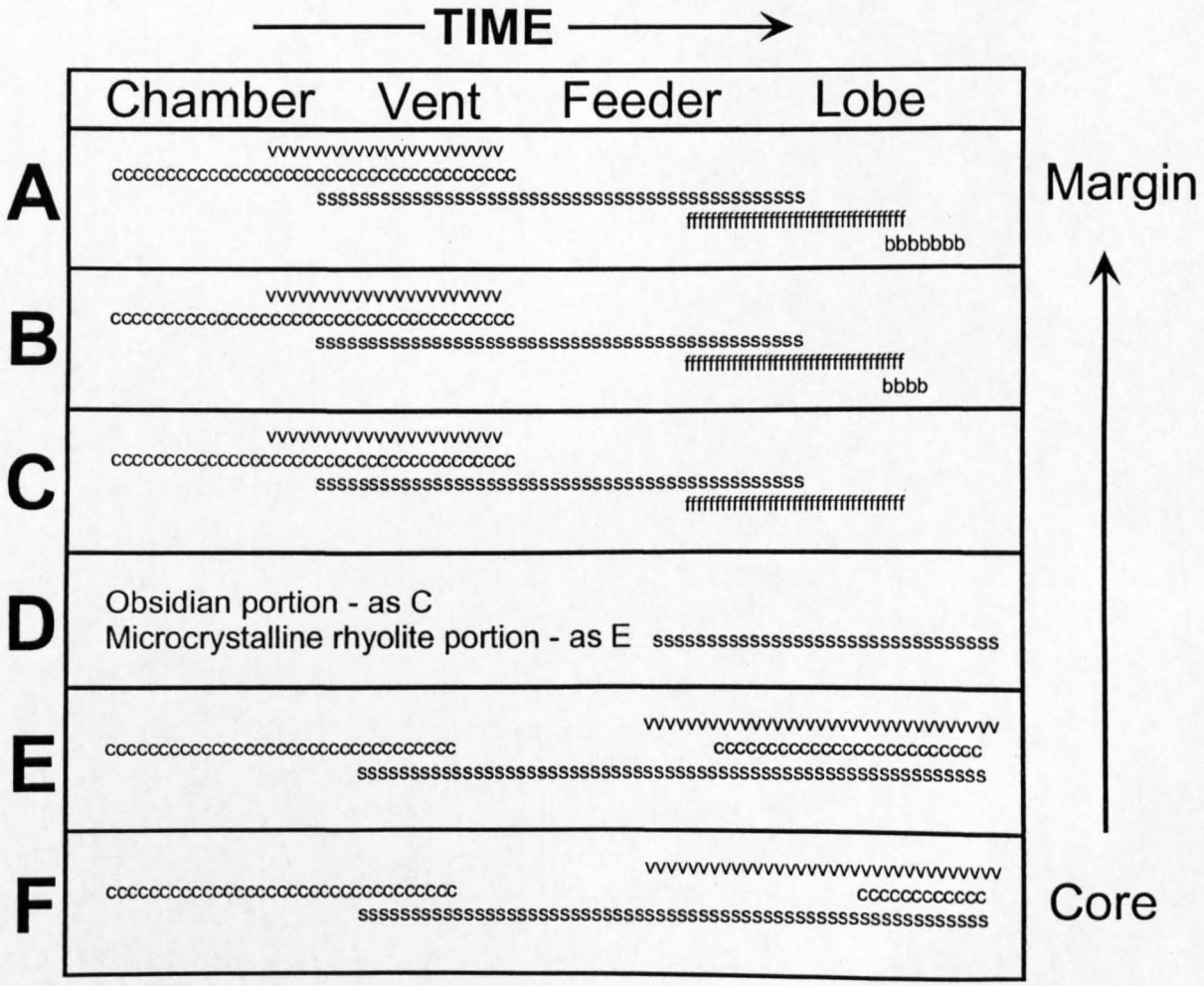

Fig. 2.12. Representation of the proposed stages in the textural development of each lobe zone. The exact timing of each event cannot be well constrained, but the relative timing of events can be reconstructed. Symbols : v - vesiculation, c - crystallisation, s - ductile shear, f - folding, b - brittle fracture. See Fig. 2.10 for a schematic diagram of zones A-F.

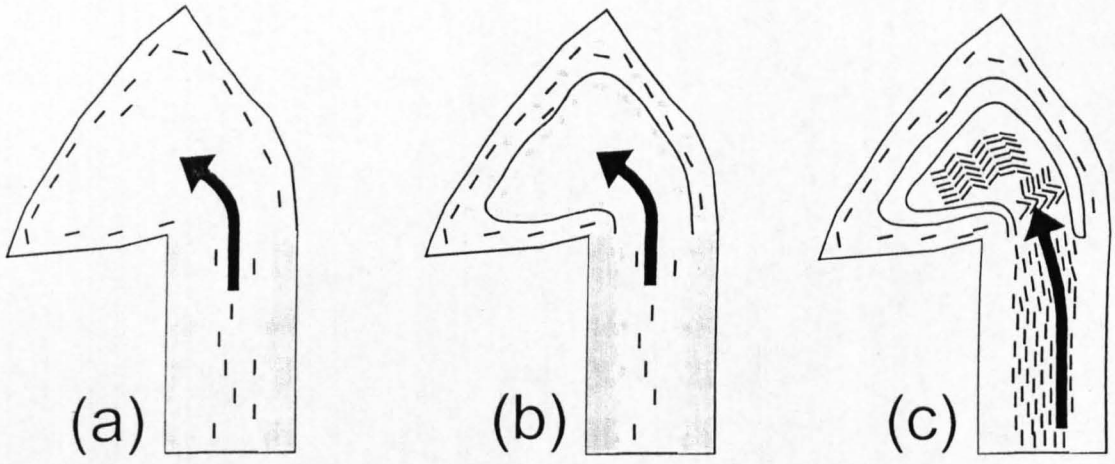

Fig. 2.13. Cartoon indicating a possible model for the formation of the suite of microtextures within lava lobes at Bláhnúkur. See text for a description of each stage.

2.5.5. Lava lobe glass compositions

Glass within a suite of samples from a single typical lobe on Bláhnúkur (textural zones B-F) was analysed using a Cameca Camebax microprobe at the Open University. Full results and analytical techniques are provided in Appendix C. In total, 95 microprobe analyses were taken, from both matrix glass and glass inclusions within clinopyroxene phenocrysts. Results are plotted in Fig. 2.14. Glass from discrete textural zones plots in distinct compositional zones. Glass within zone B appears relatively homogeneous, whereas glass from zone D is the most heterogeneous. Although the significance of these results is unclear, they may indicate minor changes in glass composition caused by variable amounts of microlite crystallisation within a small-volume closed magmatic system - supporting the view that shallow feeder bodies may have acted as 'mini magma chambers'. However, this was only a preliminary study, and further work is necessary to unravel the compositional and textural heterogeneities within the lava lobes.

2.6. Breccia B

2.6.1. Description

This lithology is best seen on the south bank of Grænagil, in cliffs 10-30 m high directly upstream of the bridge (Fig. 2.3). Much larger but less well-exposed outcrops are found on the northern and western flanks, and directly east of the summit (Fig. 2.3). In Grænagil, massive to crudely-bedded matrix- and clast- supported green breccias host elongate to lenticular ribbons and blobs of obsidian (Fig. 2.15a). Ribbons are typically 0.5-5 m long and 5-50 cm wide. The breccias consist of pumiceous, perlitised obsidian clasts, typically 0.5-5 cm across, set in an ash matrix of

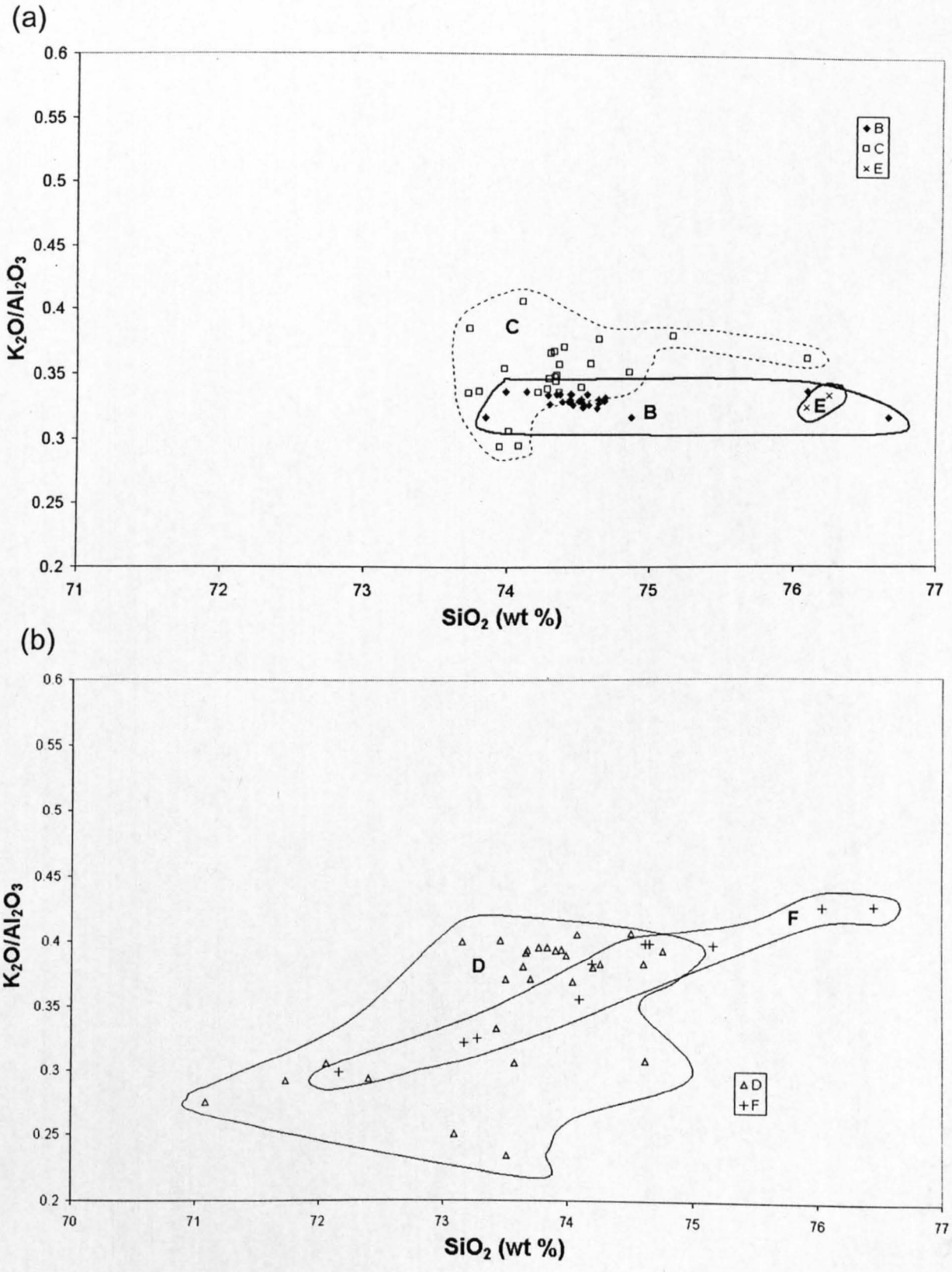

Fig. 2.14. Compositional data for glass within samples from a typical Bláhnúkur lobe. Glass from each lobe textural zone falls in a distinct compositional field, although there is considerable overlap between fields. (a) Samples from lobe zones B (fractured obsidian), C (crenulated obsidian) and E (outer microcrystalline rhyolite). (b) Samples from lobe zones D (mixed zone) and F (inner microcrystalline rhyolite). Results have been corrected to 100%. See Appendix C1 for details of analytical methods and Appendix C2 for the results of analyses.

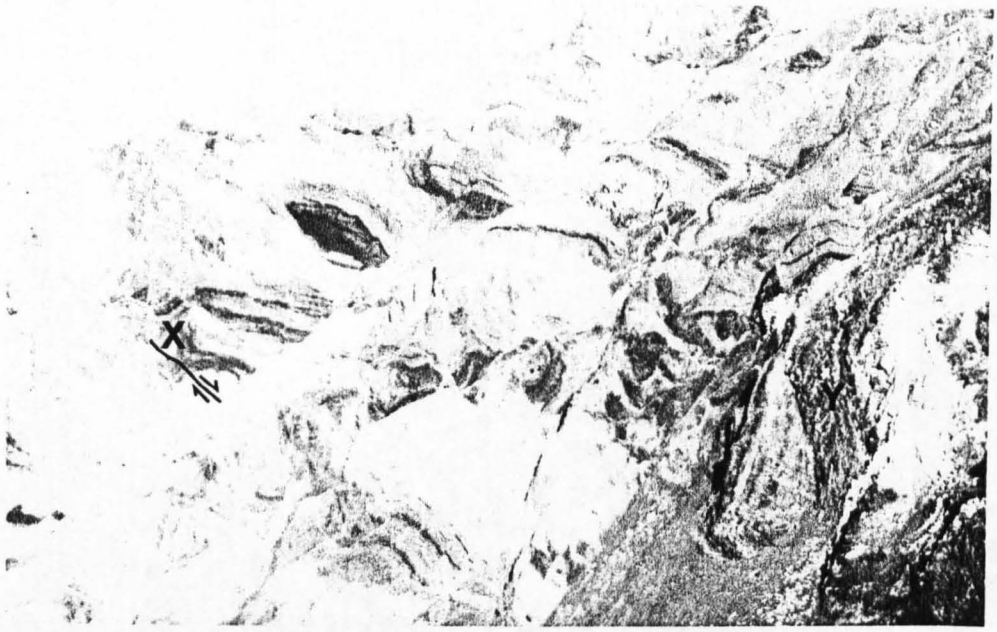

Fig. 2.15a. A 20 m-thick exposure of breccia B 50 m upstream from the bridge across Grænagil (Fig. 2.3). Massive pumiceous breccia (mid grey) hosts obsidian ribbons (dark bodies). Pale veins are filled with vesiculated ash; these cut and displace obsidian ribbons (X). The pale body at Y is the microcrystalline core of a lava lobe. From Tuffen et al. (2001).

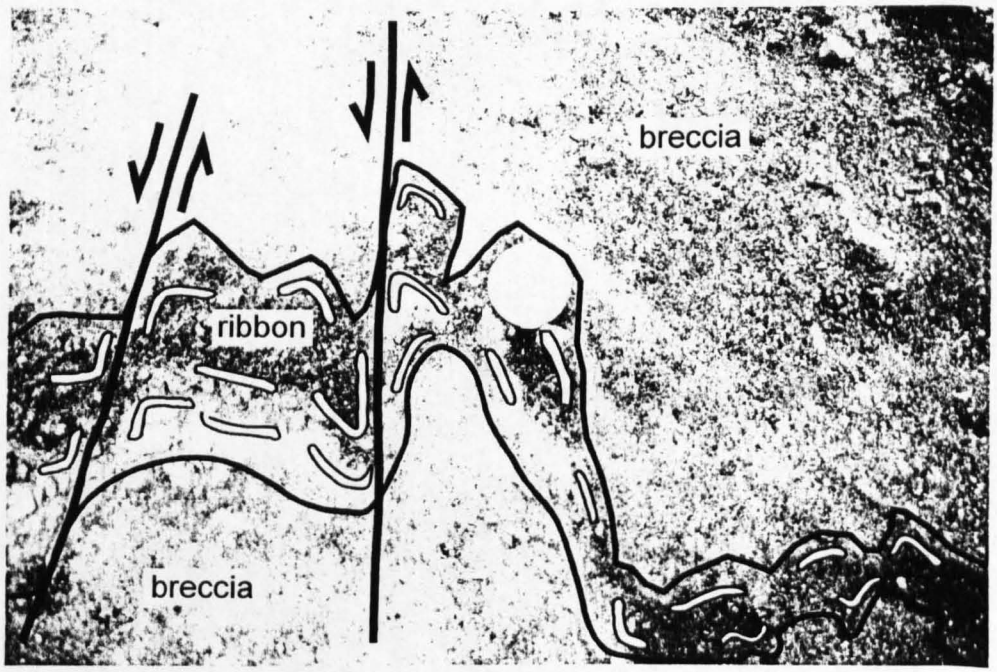

Fig. 2.15b. Close-up of an obsidian ribbon offset by small normal faults (thick black lines) within breccia B. The white deformed ellipses indicate the approximate orientation of vesicles in the obsidian and are not to scale. Vesicles have been bent along fault planes, indicating ductile deformation. Pale domains of the ribbon are perlitised, and weathering has given the intact obsidian of the ribbon a brecciated appearance. The lens cap is 50 mm in diameter. From Tuffen et al. (2001).

angular glass shards. The ash contains spherical to irregular voids 1-3 mm in diameter. Irregular, anastamosing pale green ash-filled veins 0.5-3 cm wide cut the outcrop. Obsidian ribbons are frequently displaced up to 15 cm where they are cut by these veins. Vesicles in the ribbons displaced by the veins are locally sheared parallel to the long axis of the veins (Fig. 2.15b), indicating ductile deformation. The abundance of vesicles is fairly uniform within the ribbons, and does not increase close to the sharp contact with the surrounding breccia. A centimetre-wide zone of brown, indurated ash occurs at the margin of some ribbons. Many ribbons are aligned along a plane that dips at about 10° into the modern-day slope (Fig. 2.15a). The deposit is cut by a number of low-angle minor faults, on which the sense of displacement is unclear.

2.6.2. Interpretation

Deformed vesicles adjacent to veins cutting some obsidian ribbons (Fig. 2.15b) indicate that the ribbons were deformed whilst still hot (White & Busby-Spera 1987, Hunns & McPhie 1999). However, the sharp contact between the ribbons and surrounding breccia indicates that the lobes did not generate the surrounding breccia. Rather, hot ribbons and blobs and the enclosing breccia appear to have been deposited together in a hot debris avalanche. This is likely to have been due to the syn-emplacement gravitational collapse of lava lobe-breccia A, and thus the ribbons constitute fragments of lava lobes that were still hot (above the glass transition temperature). Collapse events may have been triggered as the supporting ice melted back from around the lobes, although it is not clear how far the ice walls has receded. Fines in the breccia may have been remobilised by steam fluxing shortly after emplacement. Instability at this stage could have created numerous fault planes, into which ash was transported, generating ash-filled veins. Vesiculated ash provides

evidence for an active vapour phase (Lorenz 1974, Hunns & McPhie 1999). It is notable that the glass of the obsidian ribbons is microlite-poor, in contrast with the microlite-rich cores of lava lobes. This is consistent with the model that lava lobes fell apart whilst they were within the ice cavities, and still above the glass transition temperature, and that this disruption led more rapid cooling. Furthermore, ribbons were formed from crystal-poor magma, hence if they were generated from collapsing lobes, they must constitute fragments of crystal-poor lava lobe zones A-C. Breccia B is interpreted as a hot avalanche deposit and illustrates the instability of the subglacial rhyolite edifice during its growth.

2.7. Breccia C

2.7.1. Description

This lithology crops out in Grænagil (500-1000 m upstream of the bridge) and on the north flank, 50 m north of the summit (Fig. 2.3). In Grænagil it forms a chaotic sequence 10-20 m thick, comprising fragments of rhyolite lava lobes 1-20 m long in contact with lenses of breccia and cut by abundant small faults (Fig. 2.16). Lenses of massive, moderately well-sorted pumiceous and vesicle-poor obsidian breccia (0.2-1 m across) are faulted against lobe portions, which consist of hackly to columnar-jointed, flow-banded microcrystalline rhyolite and obsidian. Pods of breccia locally cut the microcrystalline rhyolite and are discordant to flow banding. There is a 5 cm-thick zone of clast-supported breccia at the faulted contact between obsidian and microcrystalline lobe portions. The breccia consists of obsidian clasts adjacent to the intact obsidian domains of lava lobes and microcrystalline rhyolite clasts adjacent to the microcrystalline rhyolite domains, with a zone of clast mingling ~1 cm wide on

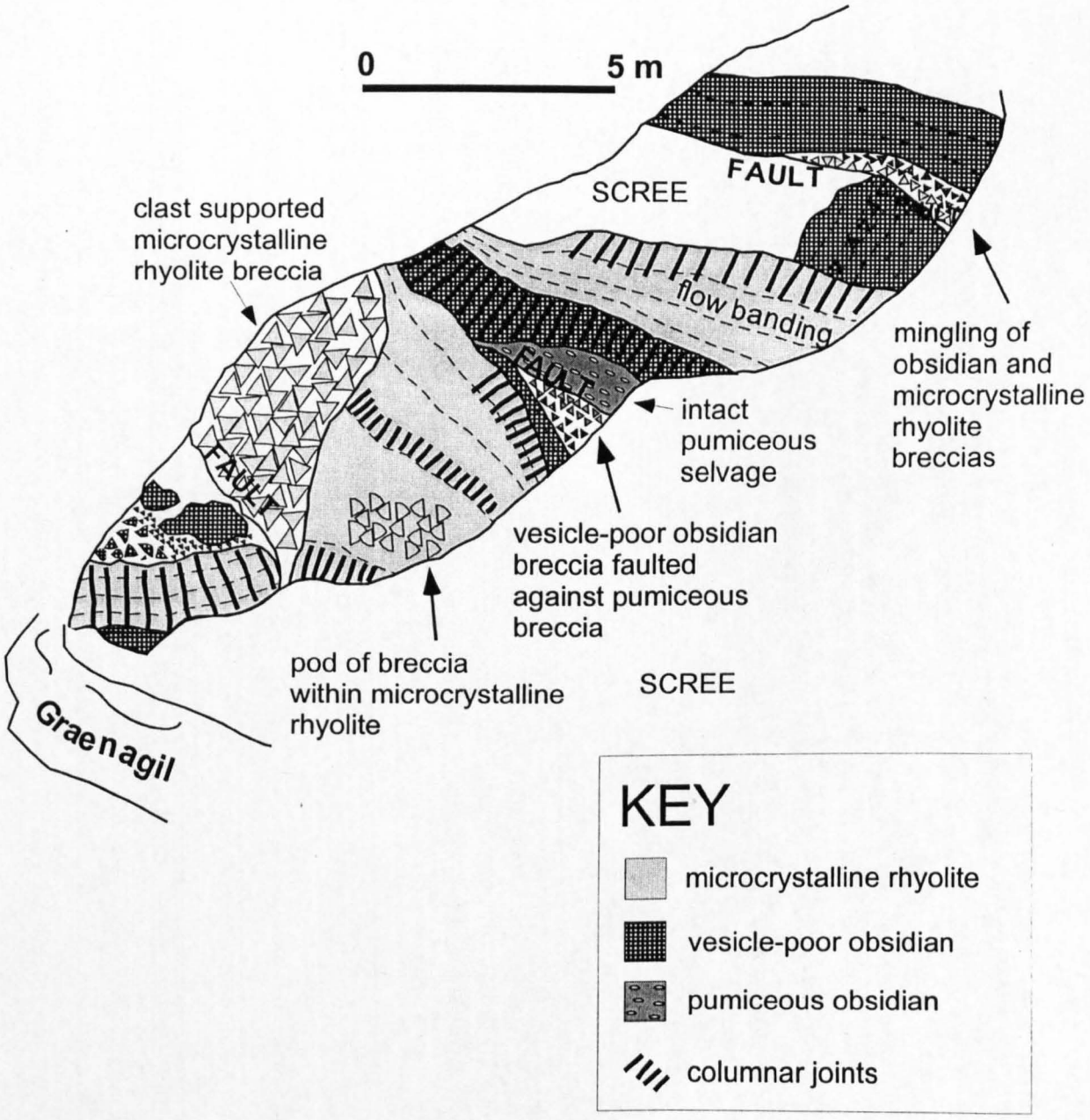

Fig. 2.16. Field sketch of breccia C in Grænagil. A stack of subparallel lobe portions 1-20 m long is cut by numerous faults, juxtaposing obsidian, microcrystalline rhyolite and pumiceous breccia. Modified from Tuffen et al. (2001).

the fault plane (Fig. 2.16). A major set of sub-parallel faults dips into the slope at 60° to 70°. These cut a second set of randomly orientated, smaller faults. Clasts in the microcrystalline rhyolite and obsidian breccias are vesicle-poor (<1% irregular vesicles <4 mm long) and blocky in shape, typically 5-20 cm across. By contrast, 0.5-5 cm angular clasts in the pumiceous breccia contain 20% elongate vesicles. On the north flank, this lithology forms a down-slope-dipping veneer <5 m thick, overlying lava lobe-breccia A. Veins of fine-grained ash in lava lobe-breccia A lithology abruptly terminate at the base of breccia C.

2.7.2. Interpretation

Breccia C consists largely of fragments of lava lobes with lesser amounts of pumiceous breccia. The faulted juxtaposition of several diverse lithologies, with brecciation and clast mingling at faulted contacts indicates lateral movement, possibly during sliding of lava lobe-breccia A down the flanks of the accumulating pile. My view is that accompanying fragmentation has been slight, resulting in the stacking of numerous near-intact lobe fragments against each other. There is no evidence for high temperatures or the presence of water during emplacement. This lithology is thus thought to record *en masse* slumping events, in which quenched, solidified lobes and breccia slid down the flanks of the edifice.

2.8. Breccia D

2.8.1. Description

This lithology crops out on the south bank of Grænagil about 150 m upstream of the bridge and on the eastern flank (locations indicated in Fig. 2.3), where it forms a prominent outcrop ~20 m high (Fig. 2.17). Breccia D is a poorly-sorted, matrix-

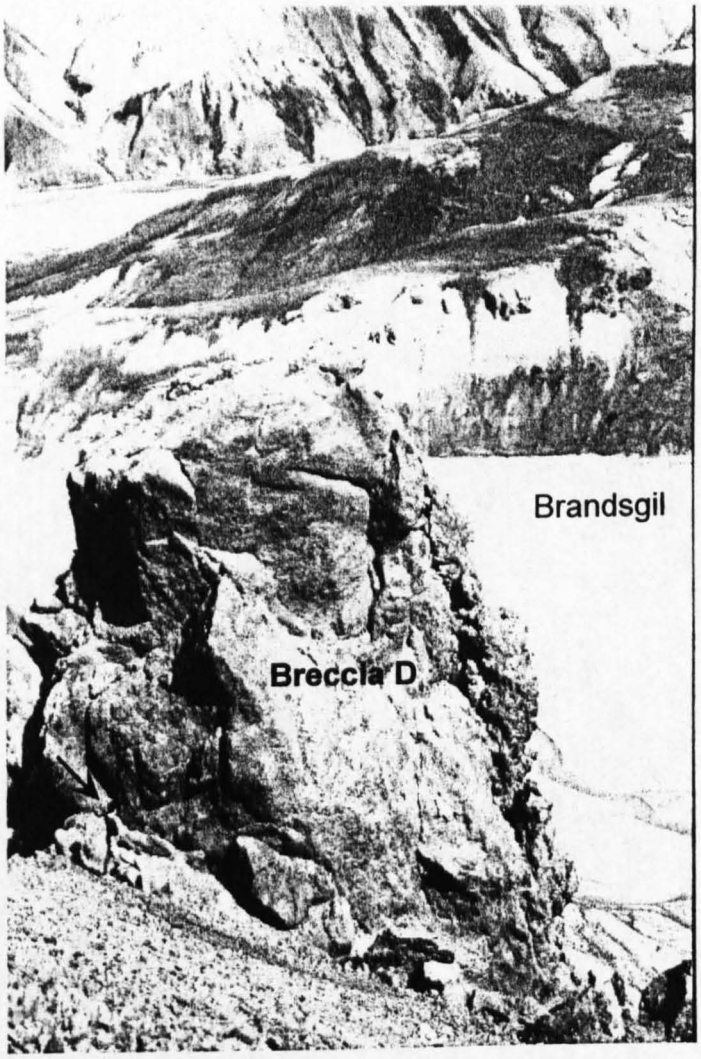

Fig. 2.17. Photograph of a prominent 20 m-high outcrop of breccia D on the east flank of Bláhnúkur. The deposit is massive and well-consolidated, with no obvious bedding structures. Figure for scale (arrow) is 1.9 m tall.

supported polymict breccia, containing 1-30 cm angular clasts of vesicle-poor microcrystalline rhyolite, vesicle-poor black obsidian and grey-white vesicular, perlitised obsidian set in an ash matrix. Faint bedding, which is picked out by trails of large clasts, dips at about 10° into the modern-day slope. Angular clasts of microcrystalline rhyolite are bounded by joint planes, which truncate flow banding. Vesicular obsidian clasts contain ~30% vesicles by volume, and ash particles resemble those found in breccia A. Irregular bodies of perlitised obsidian intrude the deposit on the east flank. These display tiny (1-2 cm wide) columns close to the contact with the breccia.

2.8.2. Interpretation

This facies corresponds to the type 2 hyaloclastite of Furnes et al. (1980), who suggested that it was formed by explosive fracture of the chilled carapace of lava lobes. Whereas such a mechanism may have generated obsidian and rhyolite clasts, it is suspected that breccia D represents remobilized lava lobe-breccia A. Poor sorting is consistent with emplacement in a cohesive mass flow (Smellie & Skilling 1994). Clasts are entirely juvenile and exactly match the range of textures observed in lava lobe-breccia A. Joint-bounded microcrystalline rhyolite clasts indicate that the core of lobes had substantially cooled prior to fragmentation. From observations of breccia B, it has already been inferred that lava lobe-breccia A was unstable during emplacement. Thus the preferred model for the emplacement of breccia D involves the gravitational collapse of quenched lava lobes and breccia, caused by the withdrawal of supporting ice walls. Accompanying fragmentation appears to have been more extensive than in breccia C, since no lobe portions have survived intact.

This may indicate a greater transport distance or a more energetic debris flow than that which generated breccia C.

2.9. Columnar-jointed lava

2.9.1. Description

Columnar-jointed lava flows occur on the eastern, southern and northern flanks of Bláhnúkur (Fig. 2.3). A lava flow 200 m long and 20 m thick drapes the steep southern flank directly south of the summit (Fig. 2.18a). It has a triangular cross section and is bounded by three sub-planar columnar-jointed surfaces: two steeply-inclined walls (~60-70° dip) and a base parallel to the modern day slope (~30° dip). Columns are 10-30 cm wide and normal to flow margins. They penetrate to the centre of the flow, a distance of up to 10 m. An obsidian selvage up to 5 m thick envelops a microcrystalline rhyolite interior, which contains <1% irregular vesicles. At the southern tip of the lava, the base grades into hydrothermally altered, perlitised obsidian breccia.

The largest lava flow observed is on the east flank (Fig. 2.3). It is sheet-like in morphology and measures ~20 m thick, 400 m long and >50 m wide. The main lava body appears to feed a number of tube-like apophyses, such as the 20 m-thick lava pictured in Fig. 2.18b, which is triangular in cross section, with a set of columnar joints normal to both the steeply inclined sides and the gently inclined base. Flow banding is parallel to the lava margins. There is a sharp contact between the microcrystalline flow interior and 4 m-thick intact obsidian selvages (Fig. 2.18b). Perlite and breccia are absent from the lava base, and there is a locally peperitic contact with the underlying poorly-consolidated till. At the south-western limit of the sheet-like lava, columnar joints describe a spectacular box-like form (Fig. 2.18c).

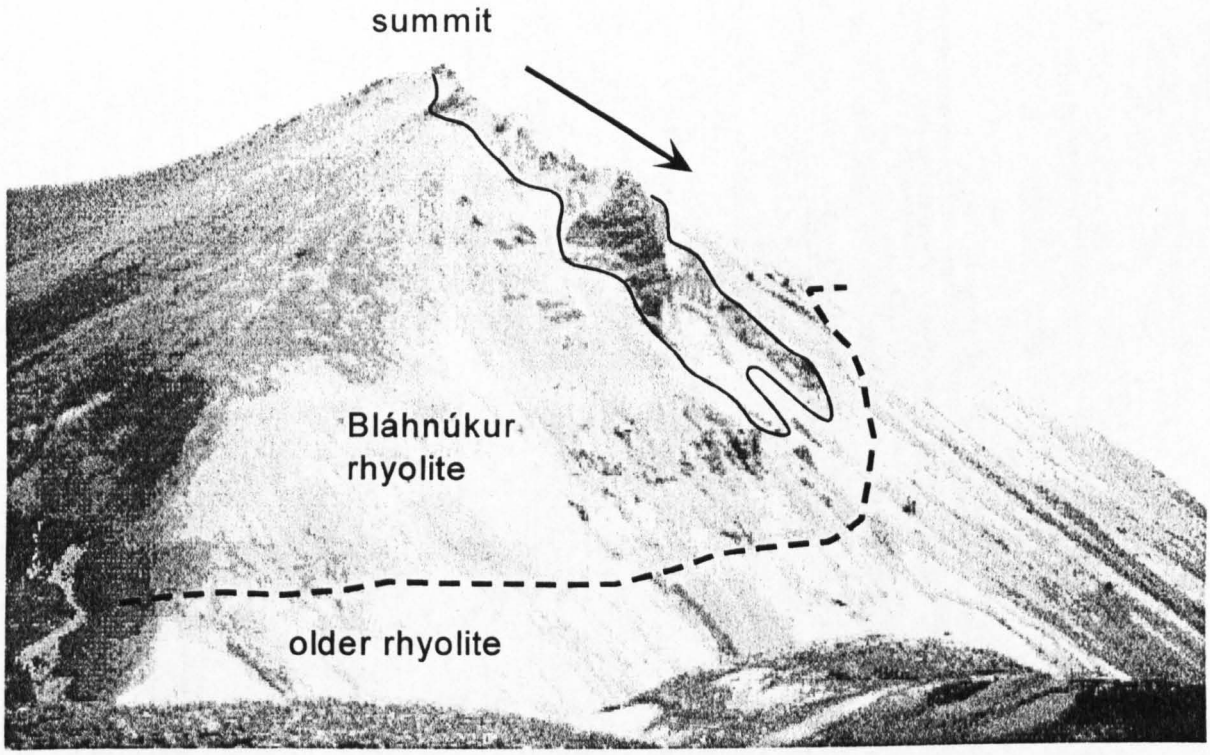

Fig. 2.18a. Columnar-jointed lava on the south flank of Bláhnúkur. The lava (black, indicated) overlies all other subglacial rhyolite lithologies.

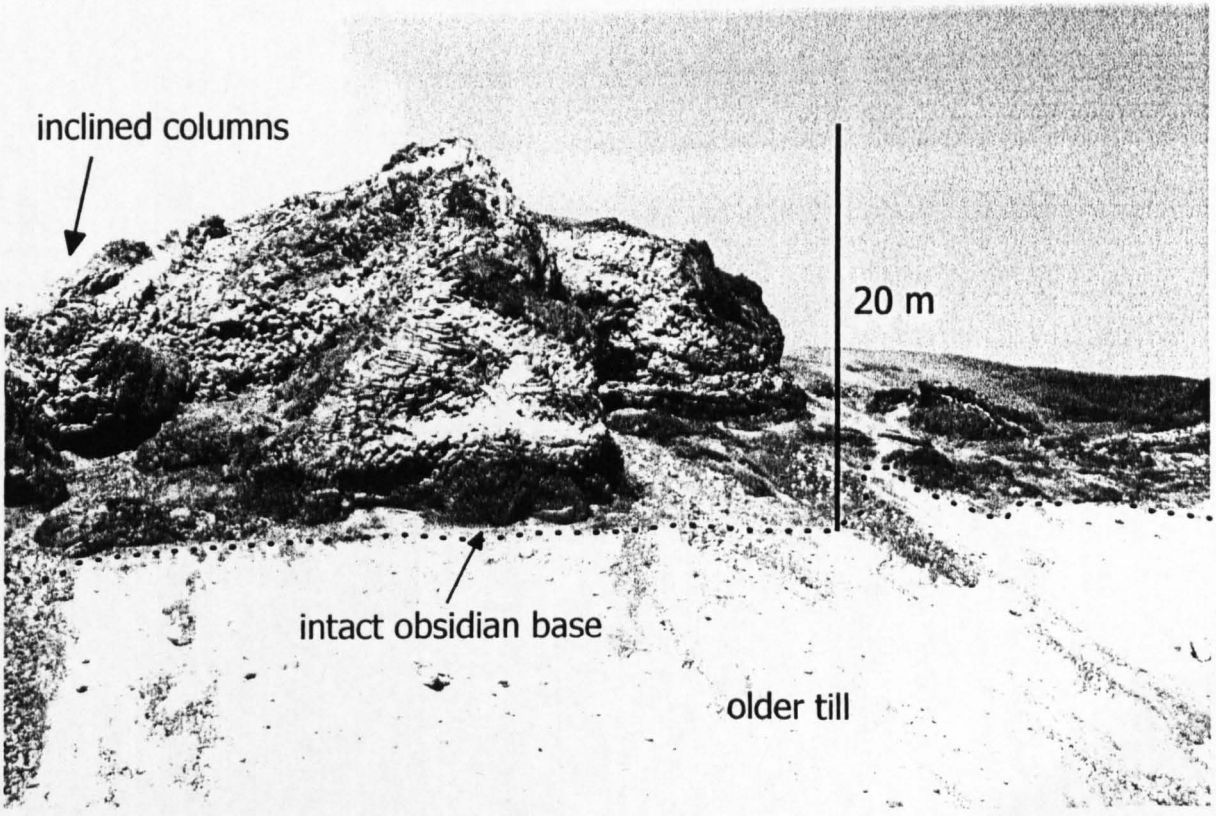

Fig. 2.18b. A 20 m-thick columnar-jointed lava flow directly overlying till on the eastern flank of Bláhnúkur. There is a 4 m-thick selvage of intact obsidian at its base. Slender columns are inclined or subhorizontal. The surface currently exposed is a cross-section of the lava flow, which flowed down a ~20° incline towards the camera. From Tuffen et al. (2001).

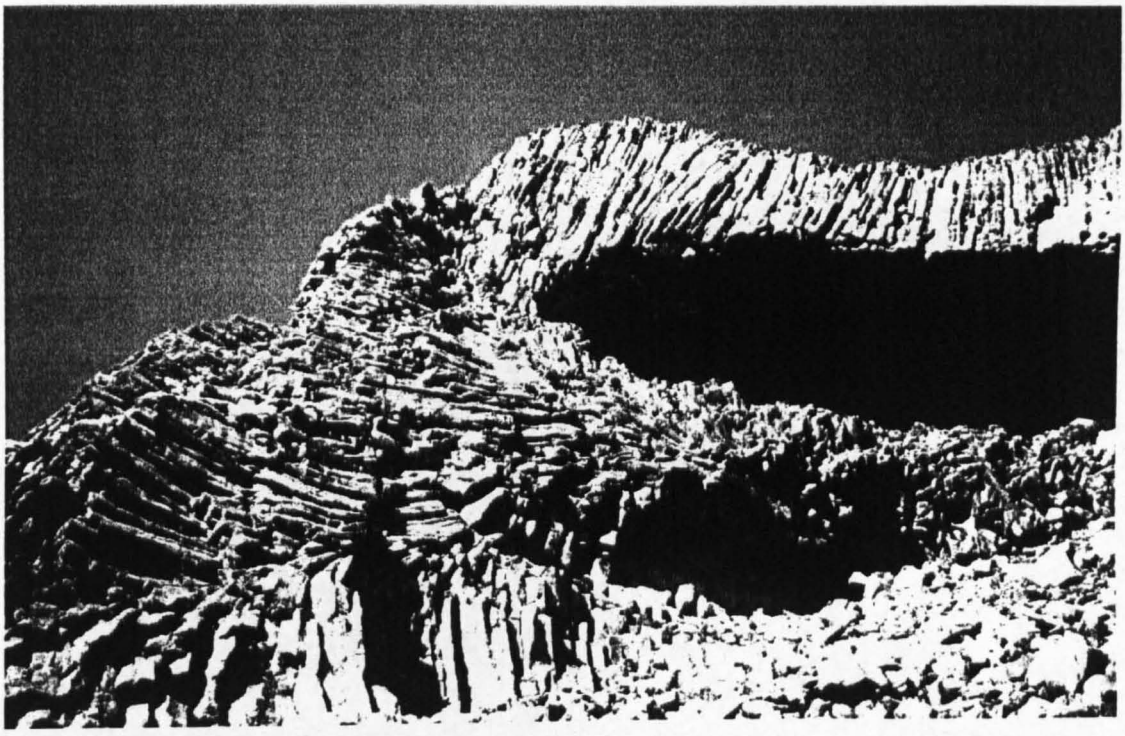

Fig. 2.18c. A 20 m-thick columnar-jointed rhyolite lava flow on the eastern flank of Bláhnúkur. Joint patterns suggest that the lava chilled against a subhorizontal ice roof (top) and steeply inclined ice walls (left). From Tuffen et al. (2001).

Columnar joints in the glassy lava top, sides and base are spaced 10-15 cm apart and are normal to flow margins.

2.9.2. Interpretation

Andesite lava flows on Mt Rainier, Washington, have similar attributes to the lava flows on Bláhnúkur: possessing steeply-inclined flow sides with subhorizontal columns and thick glassy margins (Lescinsky & Sisson, 1998). Columnar joints develop normal to cooling surfaces (Degraff et al. 1989) and therefore the orientation of columns can be used to reconstruct three-dimensional cooling patterns. Thus the columnar-jointed sides of the Mt Rainier lavas were interpreted as ice-contact features, formed as the lava flowed and chilled against ice walls. Unlike those on Mt Rainier, the lavas of Bláhnúkur also have columnar-jointed flow tops, which suggest cooling either by meltwater running over the lava (Sæmundsson 1970) or by direct contact with a subhorizontal ice roof. A subglacial setting is therefore inferred for the columnar-jointed lavas, which may have flowed and chilled within tunnel-like cavities melted into the basal ice. There is limited evidence for magma-water interaction, with perlitisation and peperite restricted to lava bases, suggesting that there was little meltwater present within the cavities during emplacement of the lavas, and any underlying materials were not water-saturated.

2.10. Evidence for the morphology of subglacial cavities

2.10.1. Evidence from lava lobes-breccia A

The joint patterns, morphologies and distribution of rhyolite lava lobes suggest that conical ice cavities were melted into the base of the glacier during, or prior to this phase of the eruption. From the sizes of the lava lobes, it can be inferred that these

cavities had roofs between 2 and 5 m high and were randomly distributed. There are three lines of evidence for magma-water interaction at lobe bases: (1) perlitic alteration of obsidian, (2) a gradational contact with breccia that contains blocky ash shards, and (3) the presence of matrix vesicles in the breccia. From this it is inferred that the cavities contained at least some meltwater, although it is impossible to tell whether they were completely filled. Such a subglacial cavity system has not been described in the glaciological literature (e.g. Fountain & Walder 1998), and may reflect localised melting of the glacier base by convecting steam or water, possibly linked to lava lobe advance (see Chapter 5 for simple mathematical models of this process).

2.10.2. Evidence from columnar-jointed lava

Later in the eruption, it appears that much larger cavities had developed in the glacier base: over 20 m high and 20 m wide. These had steeply inclined ice walls and may have contained little meltwater ('open' conditions, Hooke 1984), as the lack of evidence for magma-water interaction suggests. It may therefore be no coincidence that the orientation of the inferred tunnels (i.e. the lavas) is parallel to the maximum modern-day slope, which probably coincides with the maximum slope during the eruption. This is because the orientation of 'open' subglacial tunnels is always parallel to the bedrock slope (e.g. Syverson et al. 1994). Subglacial cavities of a similar size are thought to have carried meltwater away from the site of the 1996 Gjálp eruption (Guðmundsson et al., 1997).

2.11. Position of the ice roof and eruptive mechanisms

Initially, the rate of outward growth of the edifice may have approximately matched the rate of melting of the surrounding ice, thus maintaining the ice roof close to the volcano. At this stage, lava lobes were emplaced in isolated ice cavities formed by localised melting of the glacier base (Fig. 2.19a). Meanwhile, juvenile material was washed down the volcano flanks and redeposited by meltwater in subglacial channels. A hiatus in the eruption may then have followed, during which the ice roof receded significantly from the edifice (Fig. 2.19b). Continued heat loss from newly erupted material via steam transport of heat to the ice roof would have allowed the subglacial cavities to enlarge without continuing to be filled with debris. As the ice retreated, portions of lava lobe-breccia A were locally destabilised and cascaded down the flanks, generating debris flow deposits (Fig. 2.19c). Further instability of the breccia may be initiated by the intrusion of subsequent pulses of magma. After continued melting, a subsequent pulse of magma would have encountered larger cavities, the ice roof now up to 20 m above the edifice. Lavas then flowed down the slope within these cavities (Fig. 2.19d).

Observations from a recent subglacial basalt eruption in Iceland support aspects of this model. Melting continued above the site of the 1998 Grímsvötn subglacial eruption for weeks after the eruption had stopped, as the hyaloclastite pile slowly cooled (M. T. Guðmundsson, personal communication 1999).

2.12. Meltwater drainage and hazard implications

The presence of (a) juvenile-rich subglacial meltwater stream deposits and (b) 'dry' subglacial lava flows within the subglacial rhyolite sequence at Bláhnúkur suggests that meltwater was able to drain away during the eruption. This is consistent with the

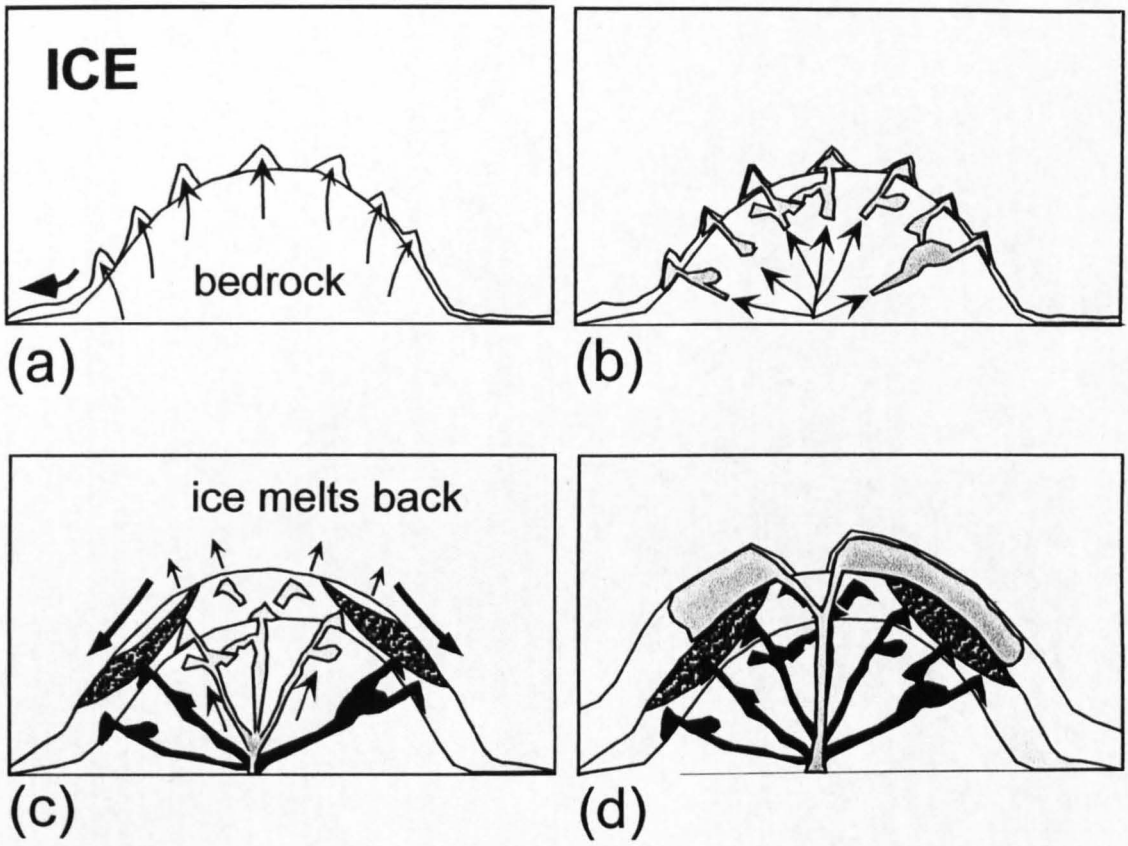

Fig. 2.19. Cartoon illustrating the proposed sequence of events at Bláhnúkur. (a) Early eruptive products are reworked by meltwater in subglacial tunnels. Steam released from cooling lavas generates cavities in the glacier base. (b) Lava lobes and breccia A are emplaced within conical cavities in the ice. (c) Hot avalanche deposits are generated as the ice melts back from lava lobes and breccia. (d) 'Dry' lava flows are emplaced within drained subglacial tunnels. Modified from Tuffen et al. (2001).

model of Hoskuldsson & Sparks (1997), which predicted that positive volume changes accompanying subglacial rhyolite eruptions would expel meltwater from the vent area. A basaltic eruption underneath thin ice (<150 m) may also be well drained (Smellie & Skilling, 1994). However, Bláhnúkur was probably emplaced beneath a glacier >400 m thick, since the lithofacies suggest an entirely subglacial setting and the edifice is 350 m high. Thus there is strong evidence for basal leakage of meltwater under a thick glacier (Smellie 1999).

The lack of development of a subglacial lake at Bláhnúkur served to decrease the volcanic hazards in two ways: (1) by limiting the volume of standing water available for explosive magma-water interaction and (2) by restricting the intensity of any resultant jökulhlaup.

2.13. Summary

Field observations of the effusive subglacial rhyolite succession at Bláhnúkur have revealed complex patterns of volcano-ice interaction. The ice roof was close to the growing edifice during the early stages of eruption, and lava lobes entered conical cavities melted in the glacier base. Only a minor volume of phreatomagmatic tephra was generated, largely at lobe bases. As the ice roof melted back, lava lobes and breccia were destabilised and cascaded down the volcano flanks. A variety of deposits indicates that avalanching occurred both during and after emplacement of the lava lobes. During the eruption, heat from the subglacial deposits enlarged existing subglacial cavities, forming moulds for subsequent lava flows that advanced and chilled against the ice walls. The presence or absence of water in the subglacial

cavities appears to have controlled the eruption mechanisms. A complex feedback between the eruption rate, the ice melting rate and the eruption mechanisms resulted in the varied lithofacies architecture observed. Meltwater was able to drain away from the vent area during the eruption, reducing the volcanic hazards.

Chapter 3.
South-east Rauðufossafjöll: a subglacial-to-emergent rhyolite tuya

3.1. Overall structure

South-east Rauðufossafjöll is the south-eastern of a group of four rhyolitic tuyas at Rauðufossafjöll (Fig. 3.1), which have a combined volume of >6 km^3. It consists of a north-east - south-west trending flat-topped ridge, 1.5 km long and 35-250 m wide, surrounded by a broad apron of scree (Fig. 3.2, Fig. 3.3). The flat top rises to 1206 m, 350-450 m above the surrounding land. The total area of the edifice is ~4 km^2, of which the flat top makes up only 0.5 km^2 (Fig. 3.3). There is a gently inclined plateau at 900 metres elevation on the south eastern flank (Fig. 3.3), which is up to 500 m wide and dips at about 5° to the south. The volcano is bounded to the north and west by neighbouring flat-topped rhyolite volcanoes of Rauðufossafjöll (Fig. 3.1), and to the south and east by subglacial and subaerial basaltic formations. Mapping of South-east Rauðufossafjöll was conducted in July-August 2000 at 1:10 000 using aerial photographs and topographic maps published by the Icelandic Geodetic Survey, although the maps presented in this chapter are at differing scales, depending upon the level of detail shown.

3.2. Evidence for a subglacial environment

The following features suggest that South-east Rauðufossafjöll was erupted under ice:

(1) The fragmental lithologies at the base of the volcano show evidence for magma-water interaction, such as perlitised obsidian and blocky ash shards. There is no

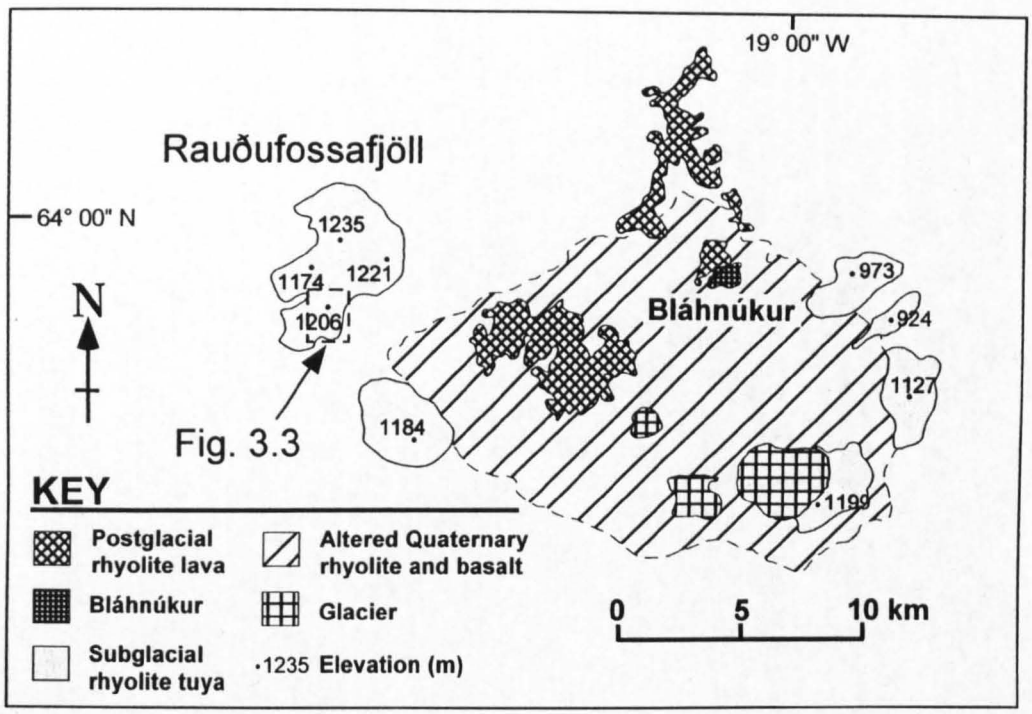

Fig. 3.1 Simplified geological map of the Torfajökull central volcano, indicating the position of South-east Rauðufossafjöll, which is shown in detail in Figure 3.3. It is one of a number of flat-topped subglacial rhyolite tuyas of the Kirkjufell formation (McGarvie 1984) that form a discontinuous ring around the outer margin of the central volcanic complex. The unshaded regions outside Torfajökull central volcano consist of subglacial and subaerial rhyolite formations from the Vatnafjöll and Veiðivötn fissure systems.

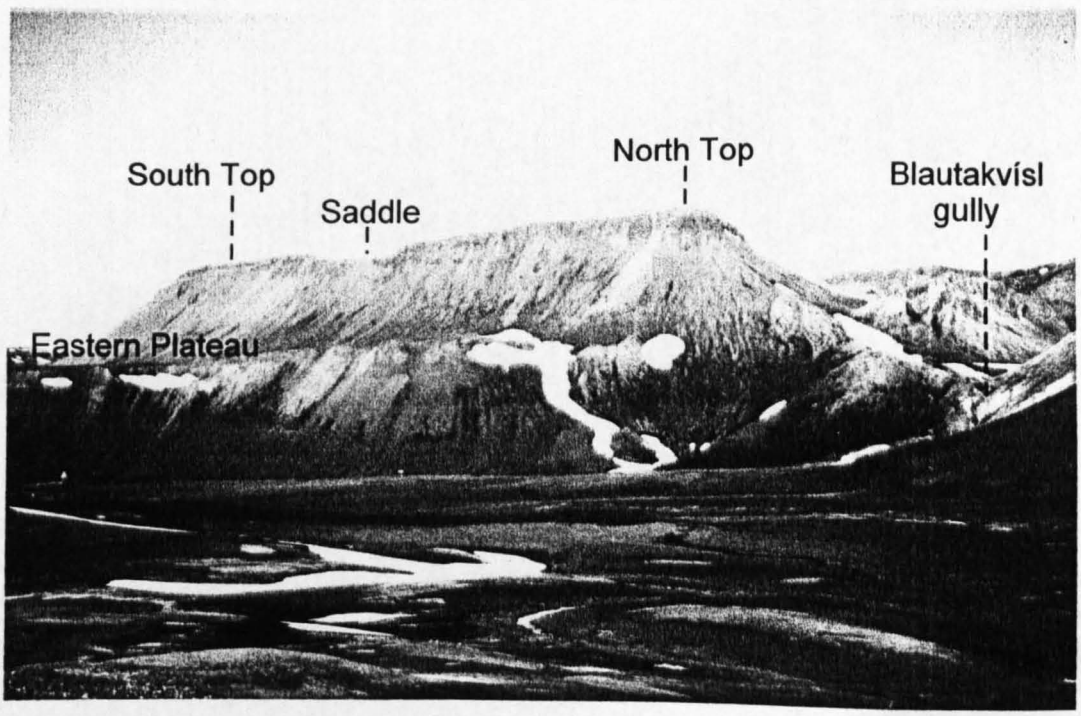

Fig. 3.2 View of South-east Rauðufossafjöll from the east. The prominent flat top, which comprises rhyolite lava flows, rises 400 m above the alluvial plain in the foreground. Much of the volcano flanks are mantled by scree.

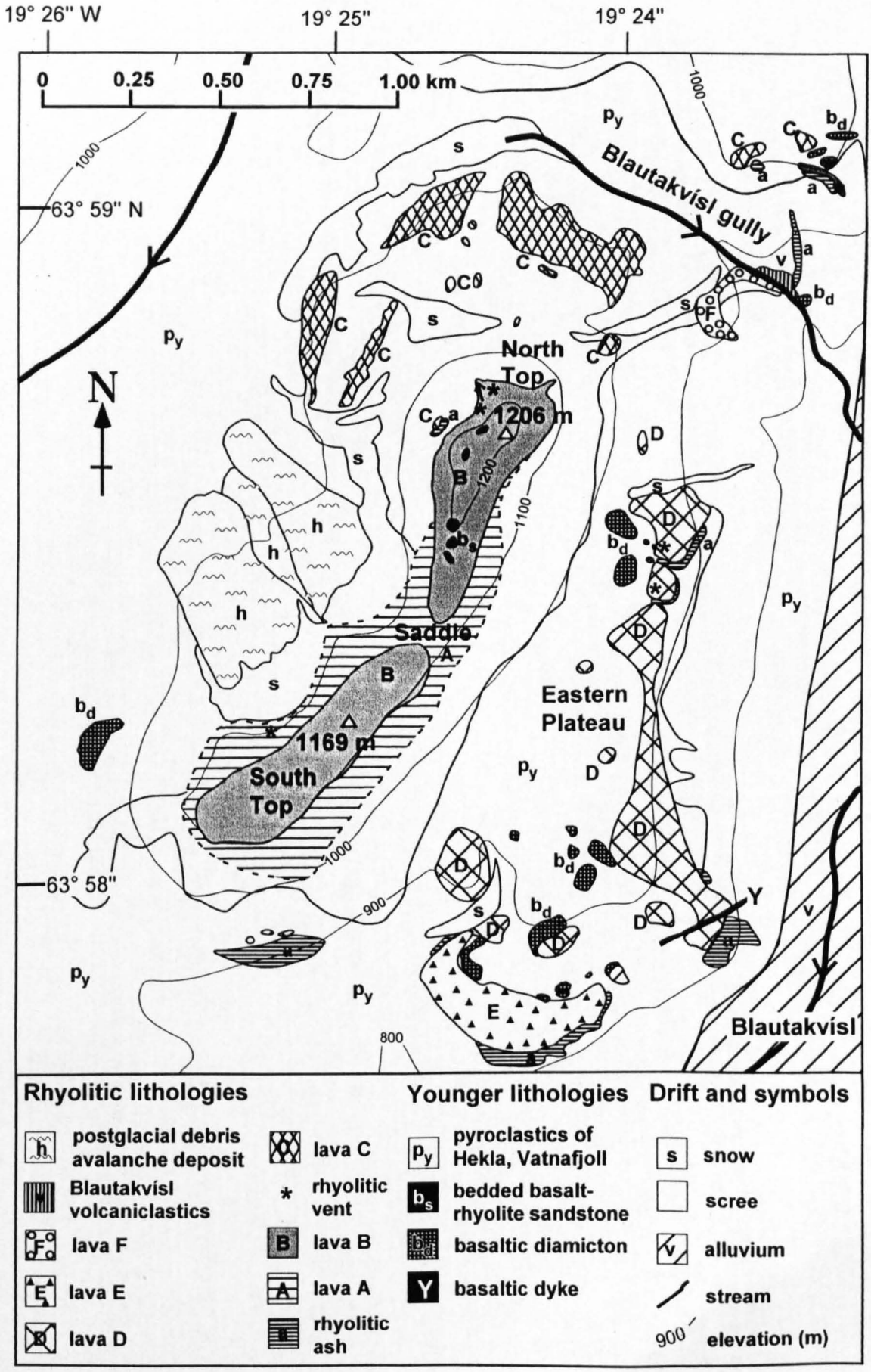
19° 26" W
19° 25"
19° 24"
0 0.25 0.50 0.75 1.00 km
63° 59" N
63° 58"
N
Blautakvísl gully
North Top
1206 m
Saddle
Eastern Plateau
1169 m
South Top
Blautakvísl
Rhyolitic lithologies
postglacial debris avalanche deposit
Blautakvísl volcaniclastics
lava F
lava E
lava D
lava C
rhyolitic vent
lava B
lava A
rhyolitic ash
Younger lithologies
pyroclastics of Hekla, Vatnafjoll
bedded basalt-rhyolite sandstone
basaltic diamicton
basaltic dyke
Drift and symbols
snow
scree
alluvium
stream
elevation (m)

Fig. 3.3.

Fig. 3.3. Simplified solid and drift geological map of South-east Rauðufossafjöll, indicating the major lithological units. Much of the map area is covered by Holocene pyroclastic fall deposits (white), principally from Hekla and Vatnafjöll. The arrow indicates the inferred flow direction of lava B from the northerly of the two vents on the north top. The regions that remained snow-covered in mid-August 2000 are indicated. Modified from Tuffen et al. (in press).

---

evidence for the existence of a palaeo-topography which could have confined a non-glacial lake (see also Jones 1968, Smellie & Skilling 1994, Smellie & Hole 1997). The current elevation of 800-1206 m, in the absence of any tectonic structures consistent with uplift, is a convincing argument against a submarine setting. Furthermore, marine fossils are absent. Glacier melting is thus the most likely source of water.

(2) Columnar-jointed rhyolite lava bodies occur at up to 1150 m elevation. Their morphologies and joint orientations are best explained by chilling against ice walls (e.g. Lescinsky & Sisson 1998).

3.3. Lithological descriptions and interpretations

Fragmental lithologies were distinguished in the field using bedding characteristics, together with the type, size, and morphology of clasts (McPhie et al., 1993). The crystallinity, morphology, vesicularity, and jointing patterns of coherent volcanic lithologies were recorded. Basaltic diamicton, till, mixed basalt-rhyolite sandstone and Holocene pyroclastics are described in addition to the rhyolitic lithologies.

3.4. Rhyolitic ash

Fragmental rhyolite deposits crop out at only a few localities at South-east Rauðufossafjöll: on the eastern flank at between 780

and 1000 m, and at 1150 m on the western flank (Fig. 3.3). Elsewhere, the flanks are covered by a veneer of scree derived from the lava cap and Holocene pyroclastic deposits. It is believed likely that ash-dominated lithologies constitute the bulk of the tuya beneath the lava cap. Hence there is only patchy exposure of the deposits that record the explosive subglacial phase of the eruption, and as a result relatively little information can be gathered about the eruptive processes. The fragmental deposits are poorly exposed due to their non-welded, unconsolidated nature.

3.4.1. Description

Over 40 m thickness of massive, well-sorted pale grey ash crops out at the south-east base of the Eastern Plateau (Fig. 3.3). Shards are mostly 10-100 μm in diameter, contain less than 20 % vesicles by volume and are blocky in morphology, with sharp corners and elongate bubble walls (Fig. 3.4a). The deposit contains up to 5 % volume of angular chips of vesicle-poor black obsidian 1-10 mm across.

The massive ash is locally overlain by 'rafts' of well-sorted pale cream ash 0.1-0.3 m thick and <2 m long. These rafts directly underlie the peperitic lavas above. Beds are typically 1-3 cm thick and describe numerous shallow channels 0.5-2 m wide. This is the only observed incidence of well-bedded fragmental deposits. Bedding planes are commonly highly folded and disrupted. Ash shards within 10 cm of the overlying peperitic lavas are frequently overgrown by cubic minerals 1-3 μm in diameter and glass surfaces have dissolution pits (Fig. 3.4b), thought to indicate hydration and interaction with high-temperature fluids.

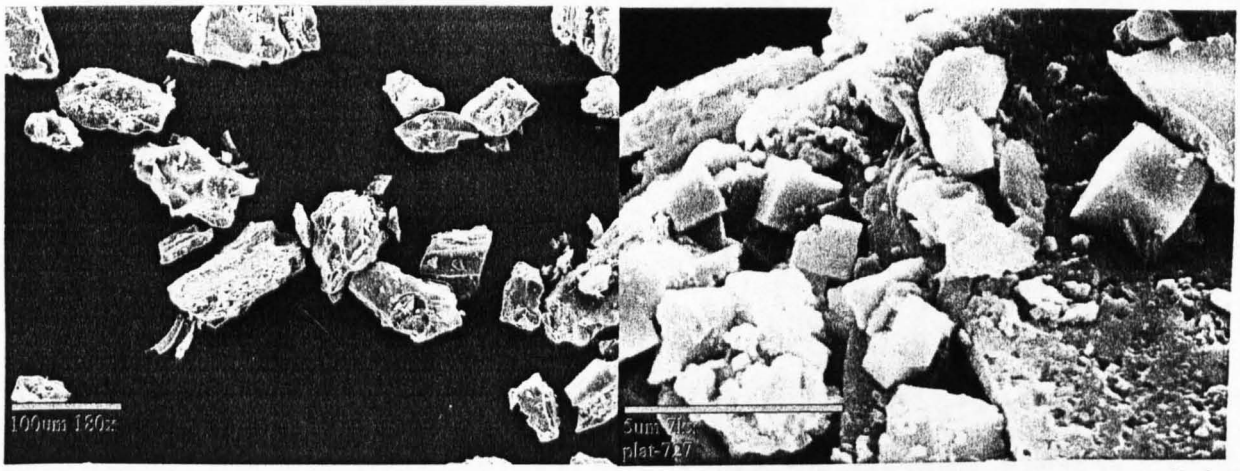
100um 180x
(a)
(b)

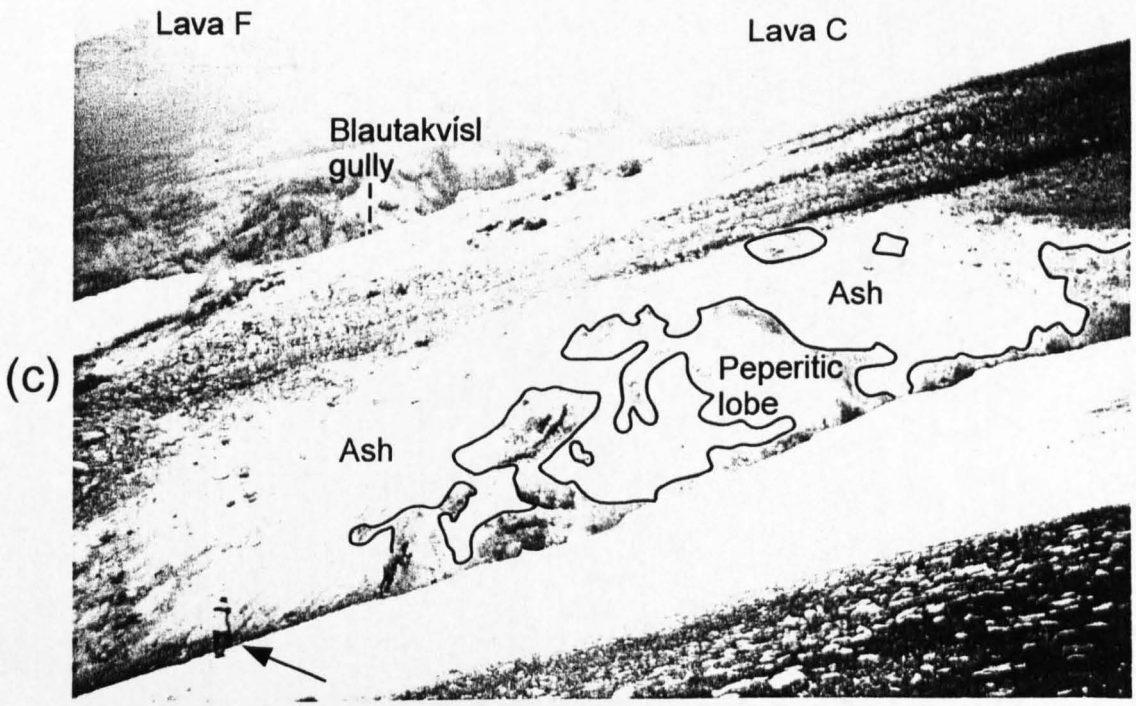
Lava F
Lava C
Blautakvísl
gully
Ash
Peperitic
lobe
Ash
(c)

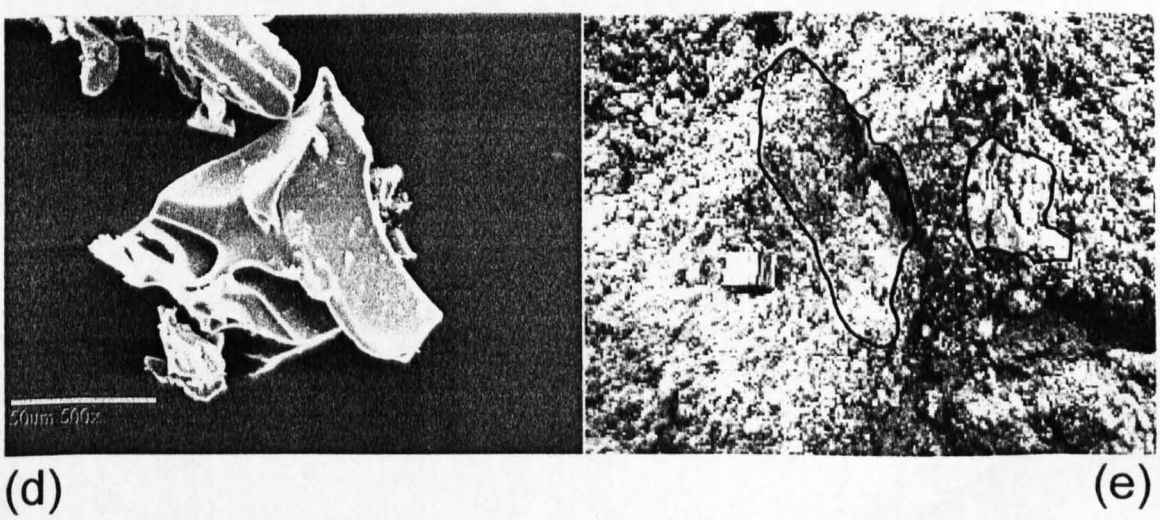
50um 500x
(d)
(e)

Fig. 3.4.

Fig. 3.4. (a) SEM image of rhyolite ash shards from the massive fine-grained ash at the base of the Eastern Plateau. Shards are blocky and angular, contain <20 % vesicles and are typically 50-100 μm across. **(b)** High-resolution SEM image of the surface of an ash shard collected from massive fine-grained ash 5 cm from the peperitic base of a lava flow on the Eastern Plateau. The 1-3 μm wide cubic crystals are suspected to be halite. Note the pitted, uneven glass surface (bottom right corner). **(c)** Overview of the gully 100 m north of Blautakvísl gully (Fig. 3.3), showing the >50 m thick deposit of pale ash. The mid-grey material elsewhere is a blanket of Holocene pyroclastics from Vatnafjöll, Hekla and other nearby volcanoes. Irregular bodies of perlitic obsidian occur the ash, their positions are indicated by solid black lines. Figure for scale is 1.7 m tall (arrow). **(d)** SEM image of a typical rhyolitic ash shard from Blautakvísl gully. Note the cuspate morphology of the shard, which is bound by smooth vesicle walls. The vesicularity of the ash in this deposit is estimated at 40 % by volume. **(e)** Clast-supported breccia exposed at 1000 m elevation to the north of Blautakvísl gully (Fig. 3.3). Angular clasts of highly sheared pumiceous obsidian contain ~40% coalescing, elongate vesicles up to 10 mm long. Large pumiceous clasts are indicated. Compass is 10 cm long.

A similar ash deposit occurs in a shallow gully 100 m north of Blautakvísl gully (Fig. 3.3, Fig. 3.4c). The ash is pale grey, massive, poorly consolidated and cut by numerous irregular, peperitic lava bodies up to 30 m long (indicated in Fig. 3.4c). The interior of lava bodies consists of grey perlitised obsidian, which grades outwards into a marginal zone of jigsaw-fit perlitic obsidian breccia ~20 cm thick. Veins filled with white ash occur between angular clasts of obsidian 1-10 cm across. This marginal zone grades outwards into pale grey massive ash. Lava bodies lack columnar jointing. Shards in the surrounding ash have cuspate morphologies, with vesicularities estimated at 40 %. These shards are noticeably more vesicular than those exposed on the Eastern Plateau, and are typically 10-150 μm in diameter (Fig. 3.4d).

Ash exposed at 900 m elevation due south of the South Top (Fig. 3.3) is similar in grain size and morphology to that north of Blautakvísl, but contains ~40 % angular clasts

of pale grey, pumiceous glassy rhyolite up to 10 cm in diameter. Some 'bomb-like' clasts have vesicle-poor margins ~3 cm thick and highly vesicular interiors (>90% vesicles), in which delicate glass spindles are surrounded by coalesced vesicles >2 cm across. No sample was taken of these clasts, due to their extreme fragility. Also within the ash are elongate, highly sheared ribbons of vesicle-poor black obsidian 0.5-1 m long and 0.1-0.2 m wide, with pale grey, pumiceous margins 1-5 cm in width. The pumiceous margins of some obsidian ribbons are highly fragmented and surrounded by a 'cloud' of angular pumiceous clasts. The textural transition from intact obsidian to matrix-supported breccia is distinct from that at lava lobe bases at Bláhnúkur (Fig. 2.5c), in that the proportion of vesicles is far higher in the fragmental material at Rauðufossafjöll (~40-50%). Furthermore, neither ash-filled veins nor matrix vesicles were observed.

The proportion of pumiceous clasts is much higher in ash exposed at 1000 m elevation on the north side of Blautakvísl gully (Fig. 3.3). This is a massive clast-supported breccia containing angular clasts of pumiceous obsidian 1-20 cm and, exceptionally, 1 m in length (Fig. 3.4e). The matrix contains blocky, low-vesicularity ash shards mostly 10-100 μm in diameter.

3.4.2. Interpretation

Ash lithologies at South-east Rauðufossafjöll are poorly exposed, cropping out only sporadically on the volcano flanks. From my observations of the other rhyolitic tuyas of Rauðufossafjöll and elsewhere in Iceland, it seems likely that much of the volcano beneath the flat lava cap consists of poorly-consolidated ash-dominated deposits. Poor exposure of fragmental deposits at rhyolitic tuyas is in direct contrast with basaltic tuyas, at which fine-grained, palagonitised breccias commonly form near-vertical cliffs many

tens or hundreds of metres high (e.g. Jones 1968, Skilling 1994, Werner et al. 1996). The reason for the lack of palagonitisation in rhyolitic deposits is not known.

The blocky morphology and low vesicularity of the majority of the ash at South-east Rauðufossafjöll suggests that fragmentation was driven principally by magma-water interaction, rather than by degassing of magmatic volatiles (Heiken & Wohletz 1985, Wohletz 1986, c.f. chapter 2 Bláhnúkur section). Glacial meltwater is the most likely source of water in the vicinity, hence I interpret the ash as the product of explosive magma-water interaction within an ice vault. However, highly vesicular (~90 %) clasts are present in some localities. Such vesicular clasts are unlikely to have interacted with meltwater, since this would have probably led to their disintegration. Thus it is possible that some eruptive pulses were principally 'dry'. Significant degassing and vesiculation of obsidian suggests that the confining pressure was low during 'dry' stages. A variation in eruption and degassing mechanisms is further suggested by the more vesicular, cuspate ash shards observed north of Blautakvísl. However, the fragmentation mechanism was probably also phreatomagmatic at this locality, since there is little vesicle coalescence and vesicle abundances are not thought to exceed 40 %.

Although no quantitative particle size measurements were made, SEM images revealed that the majority of ash shards at South-east Rauðufossafjöll are between 10 and 150 μm in diameter. Based on field relationships, it is unlikely that any of the ash observed has travelled >1 km from its source vent. The ash-dominated lithologies are therefore thought to represent the proximal deposits of a phreatomagmatic eruption(s).

Constraint by enclosing ice walls (subglacial phreatomagmatism) may have prevented fine-grained material from travelling far from the vent. These deposits are therefore likely to have been deposited within an ice vault, rather than having been widely dispersed in a subaerial plume. The massive, poorly-sorted deposits are

interpreted as the products of low-temperature pyroclastic surges (Cas & Wright 1987). Vesicle-poor clasts of obsidian observed in some outcrops may be spatter-fed material (e.g. Stevenson & Wilson 1997) that has become entrained in pyroclastic flows or surges (Mellors & Sparks 1991, Rosi et al. 1996). Well-sorted fine-grained ash on the Eastern Plateau may be either a fine-grained pyroclastic surge deposit or an epiclastic deposit (Cas & Wright 1987). I prefer the former interpretation, due to the presence of outsized clasts of vesicle-poor obsidian, which would have been likely to have been separated from the fine ash fraction if epiclastic reworking had occurred. Reworking by water only seems to have occurred locally, and after deposition of the bulk of the ash – although there is insufficient exposure to allow a complete study of the sedimentary structures in all of the ash. The bedded units directly underlying lavas on the Eastern Plateau are thought to indicate redeposition of ash in a number of ephemeral stream channels as meltwater flowed over the surface of the poorly-consolidated ash. However, the bedded units make up only a thin veneer; the bulk of the exposed ash is massive and shows no evidence for deposition by water.

Irregular, perlitised lava bodies within the ash to the north of Blautakvísl gully are interpreted as peperitic intrusions (e.g. Hanson & Hargrove 1999) which were emplaced wholly within poorly-consolidated, waterlogged ash. The presence of such intrusions may have occurred once the subglacial ice vault became entirely filled with ash, and continued explosive magma-water interaction was prevented by space problems. The evolution of the ice vault during this phase of the eruption is discussed and modelled in Chapter 5.

3.5. Lava A

3.5.1. Description

This is a 1.5 km long rhyolite lava flow that crops out at between 1000 and 1120 m elevation on the main flat-topped ridge. It is well exposed on the west flank where it forms cliffs up to 100 m high (Fig. 3.5a), but is mostly concealed by scree on the south and east flanks. Lava A is overlain by subhorizontal rhyolite lava flows (lava B), and its base is not exposed (Fig. 3.5a). The majority of the lava flow consists of non-vesicular microcrystalline rhyolite. Flow banding is well developed and steepens from near-horizontal in the lowest exposures to near-vertical at the lava top (Fig. 3.5b). The uppermost 4-5 m consists of tightly flow-folded obsidian. In this region, bands of pale pumiceous obsidian ~10 cm wide are estimated to contain ~40 % elongate vesicles, and are interbanded with non-vesicular obsidian. The pumiceous obsidian is patchily hydrothermally altered, giving it a reddish hue.

A sheet-like lava body 5 m thick and 20 m long appears to be continuous with the upper part of lava A 50 m north of the Saddle (Figure 3.5b). It has contorted flow banding and poorly-developed columnar joints that are normal to a sub-planar surface that dips at around 40° down the eastern flank. The sheet drapes over the lower parts of lava A.

3.5.2. Interpretation

Lava A has a near-horizontal, glassy upper surface with tightly folded flow banding and heterogeneous vesicularity. Such features are typical of subaerial rhyolite lava flows (e.g. Fink 1983). The downslope-dipping, columnar-jointed lava body attached to the edge of main lava flow is best interpreted as an ice-contact 'dribble' that has spilled down a gap between lava A and a nearby ice wall (Mathews 1951). This is the most compelling evidence for an ice-contact setting, although the high aspect ratio (~15:1) and near-vertical flow banding in the upper ~50 m are also consistent with a degree of topographic

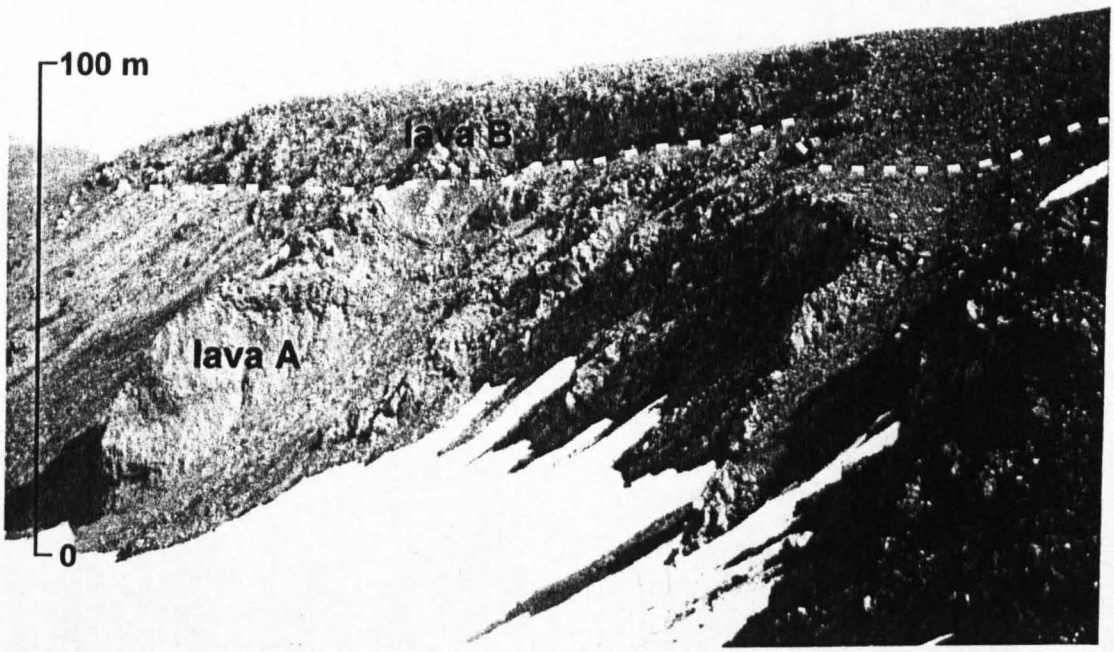

(a)

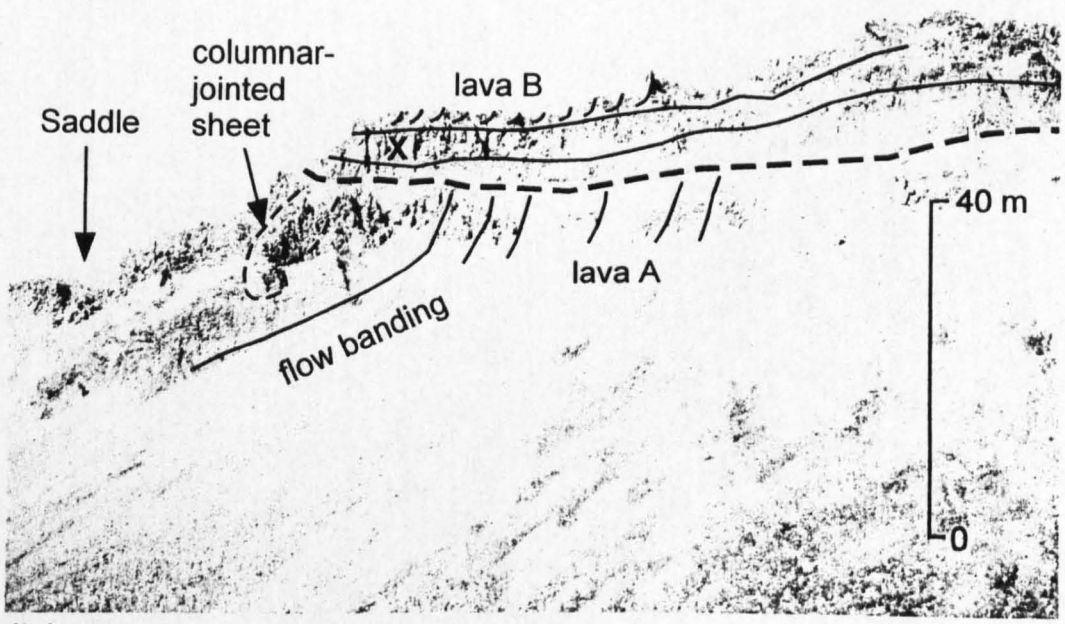

(b)

Fig. 3.5. (a) View of the southern part of the west flank of South-east Rauðufossafjöll, looking across an amphitheatre formed by postglacial flank collapse. Cliffs of lava A (bottom left) up to 90 m thick are overlain by lava B, which is subhorizontal and ~10 m thick.

(b) Close-up of lavas A and B on the eastern flank of South-east Rauðufossafjöll, looking west to the Saddle from the Eastern Plateau (Fig. 3.3). Flow banding (indicated by solid black lines) is steeply ramped in lava A and near-horizontal at the base of lava B. The heavy dashed black line indicates the contact between the lavas. X refers to detail in Fig. 3.5c.

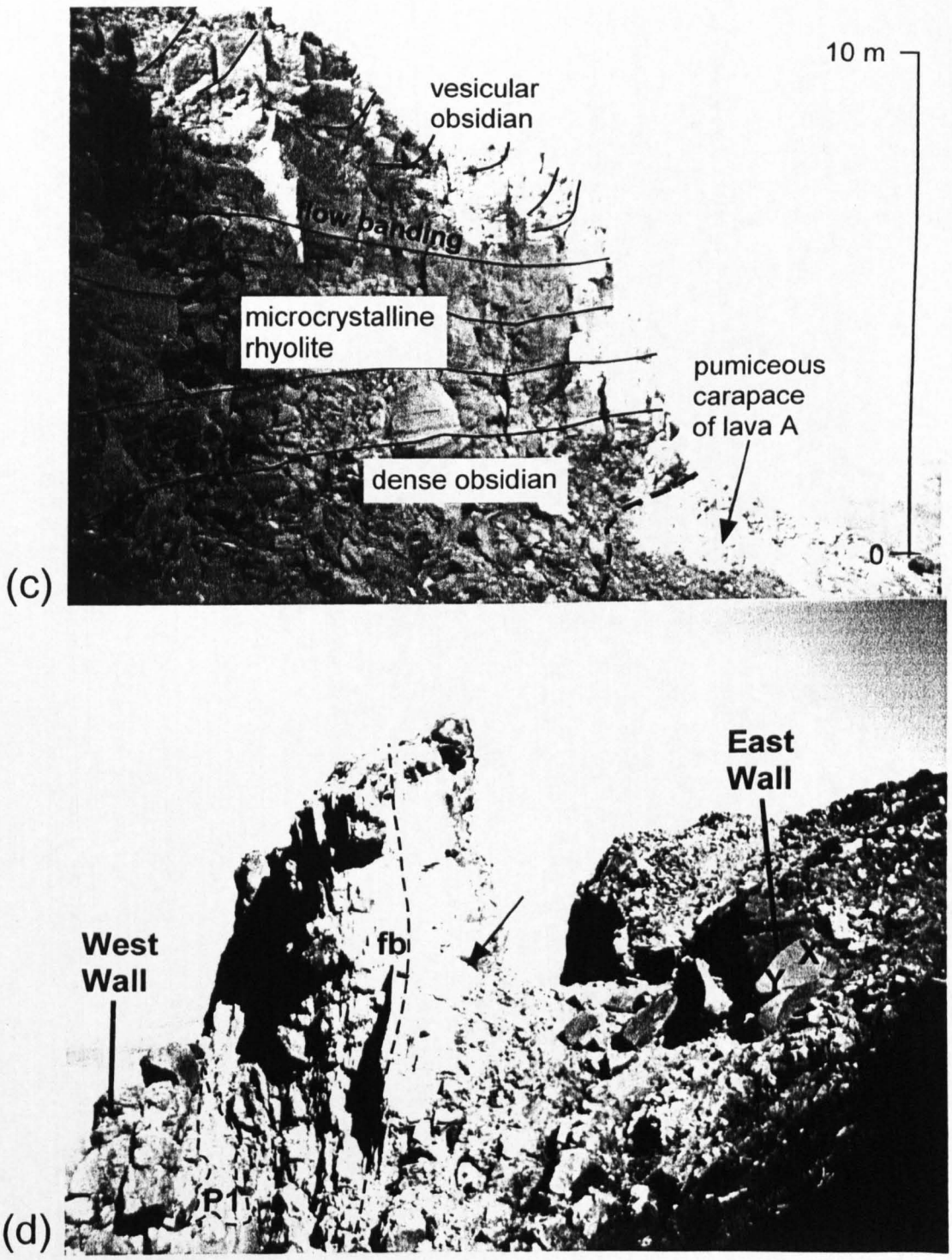

Fig. 3.5. (c) Detail at X on Fig. 3.5b. The hydrothermally altered pumiceous upper carapace of lava A is overlain by lava B. Lava B comprises a 1.5 m-thick basal zone of dense obsidian, an interior portion of microcrystalline rhyolite and a vesicular obsidian upper carapace 2 m thick. Flow banding in lava B is near-horizontal in the base and interior, and steeply ramped in the upper portion.
(d) Vent 150 m west of the North Top, viewed from the south. It crops out ~20-30 m below the upper carapace of lava B, which it appears to feed (although erosion has removed any portion of this lava that may have directly overlain the vent). Near-vertical obsidian walls (black) are ~5 m thick. Platy fracture in the mid grey interior portion of the vent is near-vertical and parallel to flow banding (fb, dashed black line). P1 is the breccia pod seen in detail in Fig. 3.6f. The ice axe is 0.6 m long (arrow).

confinement. The lava is elongate in a north-east - south-west direction (Fig. 3.3), parallel to the subglacial rhyolite fissures at Rauðufossafjöll and the regional tectonic trend. This may indicate that effusion occurred contemporaneously from a number of vents aligned north-east - south-west, and that as a result, a highly elongate ice cauldron had formed above the subglacial tephra pile. This model is consistent with the evidence that lava B was emplaced from multiple vents on the ridge of South-east Rauðufossafjöll (section 3.6).

3.6. Lava B

3.6.1. Interpretation

Lava B appears as two separate lava bodies that make up the upper part of the flat cap of South-east Rauðufossafjöll (Fig. 3.2, Fig. 3.3). Each is approximately 0.75 km long, up to 250 m wide and between 8 and 100 m thick, with an estimated combined volume of 10^7 m^3. A considerable portion of the lava flows has been removed by postglacial debris avalanches on the western flank. The sides of all the lava flows have been substantially eroded, and a blanket of scree is present beneath. Based on the estimated volume of the scree, it is speculated that these lava flows were originally up to twice their current width. Flow interiors consist of non-vesicular microcrystalline rhyolite with well-defined platy flow banding.

The northern lava flow is ~8 m thick at its most southerly exposure, with near-horizontal flow banding in the base and interior which steepens to near-vertical in the top 2 m (Fig. 3.5c). A 2 m-thick, highly sheared obsidian base is well exposed directly north of the Saddle (Fig. 3.5c). This lava flow thickens considerably to the north, where the maximum exposed thickness is ~100 m, and the base is concealed by scree. Flow banding

is steeply inclined in the thick northern portion. The upper surface of the northern lava flow is best preserved in its southern part, where the upper 2-3 m is glassy (Fig. 3.5c), and contains elongate vesicles typically 10 mm long. Elsewhere the upper carapace is either missing or obscured by Holocene pyroclastic fall deposits.

The southern lava flow is less well exposed, but exhibits many of the same characteristics as the northern flow, including a 2-3 m thick glassy upper carapace and steeply ramped flow banding in the thicker exposures. The maximum exposed thickness is ~75 m. Where exposed at its north-eastern margin, the base of the lava flow dips south-west at ~10°.

A sample of obsidian from the upper carapace of the southern lava B exposure was analysed for water content using a Fourier Transform Infra-red Spectrometer (FTIR). Ten analyses of the glass yielded mean H_2O = 0.14 wt %, σ = 0.01 wt % . The analytical methods and data are provided in Appendix D2.

Two vents were discovered on the northwest side of the northern lava flow (Fig. 3.3). The northern of the two is largely inaccessible, whereas the southern vent is easily reached and was studied in detail. It appears to have fed at least part of the northern lava flow. The southern vent is described in detail in section 3.6.3.

3.6.2. Interpretation

Lava B is interpreted as the product of subaerial lava effusion. There is no evidence for interaction with ice. The northern and southern lava flows are considered to be separate eruptive units; they appear not to have been joined. This implies that the lavas were erupted from at least three discrete vents: two which fed the northern flow, and unexposed vent(s) that fed the southern flow. These vents are likely to have been aligned parallel to the north-east - south-west axis of the ridge. Vents may have developed as a

magma rising within a fissure became focussed at a number of discrete points (Wylie et al. 1999). Low volatile contents in the obsidian carapace of lava B indicates that the lava was degassed during this effusive phase of the eruption.

It is not possible to reconstruct accurately the position of the palaeo-ice surface during the effusion of the summit lavas. Considerable hydrothermal alteration of the pumiceous upper carapace of lava A, which directly underlies lava B, suggests that there may have been a lengthy time gap between the emplacement of lava A and lava B. Indeed, lava A appears to have been thoroughly quenched when it was overlain by lava B, for there is no evidence that the upper carapace of lava A was still hot when it was overlain by lava B.

3.6.3. Effusive rhyolitic vent feeding lava B

A well-exposed rhyolitic vent crops out at c. 1170 m elevation approximately 130 m northwest of the North Top (Fig. 3.3). This is exposed due to mass wastage of the north-western portion of the northern lava B, and crops out 20-30 m vertically below the upper carapace of lava B. Continuity of flow banding indicates that the vent fed a portion of lava B, which flowed steeply down the slope to the northwest (arrow on Fig. 3.3).

The vent is ~10 m wide and near-vertical, with two 4-m-thick black obsidian outer walls enclosing an inner portion of mid-grey devitrified obsidian (Fig. 3.5d). The pale colour of the inner obsidian is due to abundant spherulites <1 mm across which make up >80 % of the rock. Near-vertical platy fractures ~10 cm apart cut this inner portion. The black obsidian walls are cut by tuffisite veins (Heiken et al. 1988, Stasiuk et al. 1996), with a wide range of characteristics. There is a textural continuum between two endmembers: angular veins and vertical bands.

Angular veins are pale grey, irregular in shape, anastamosing and 1-80 mm wide. They are bounded by angular fractures and are confined to the outer 3 m of the black obsidian walls and to within 1 m of 'pods' of breccia within the west wall (Fig. 3.6a). Individual veins can be traced over 0.1-2 m and appear to be randomly oriented. They contain complexly cross-stratified, highly-indurated grey clastic material which comprises annealed angular ash shards and angular phenocryst fragments (Fig. 3.6b, c, d, g). The outer 0.5 mm adhering to the surrounding obsidian is invariably fine-grained ash, devoid of crystal fragments. Round blebs of black obsidian 0.1-10 mm long occur in most veins >5 mm wide (Fig. 3.6b, g). These are elongated parallel to the local vein orientation. Typical aspect ratios of obsidian blebs in the planes observed range from 1:1 to 6:1.

Bedding orientations in the clastic material are parallel to the vein margins (Fig. 3.6b) in all but the widest veins, in which some subhorizontal horizons were observed, regardless of the orientation of the adjacent vein walls (Fig. 3.6c). Where veins pinch out (Fig. 3.6d) the grainsize decreases and the sedimentary features become less complex. Beds vary from poorly-sorted gravelly sandstone (in which the largest clasts are phenocryst fragments up to 2 mm long) to delicately laminated fine-grained sandstone composed entirely of glass shards (Fig. 3.6b). All veins are highly indurated and display similar patterns of fracture and weathering to the host obsidian.

Breccia pods (Fig. 3.6f) are 0.5-1 m wide and contain clast- to matrix- supported breccia with angular clasts of grey devitrified obsidian and a pale grey ash-grade matrix. The matrix is not as annealed as the tuffisite vein material, hence pods weather out (Fig. 3.6e). Angular tuffisite veins appear to originate at the intact obsidian - breccia pod contact, and propagate ~1 m into the surrounding obsidian. Fig. 3.6g is a scanned thin section of angular vein material, within which rounded obsidian blebs are seen. The 'intact' walls of the vein are themselves composed of sheared obsidian blebs (Fig. 3.6h).

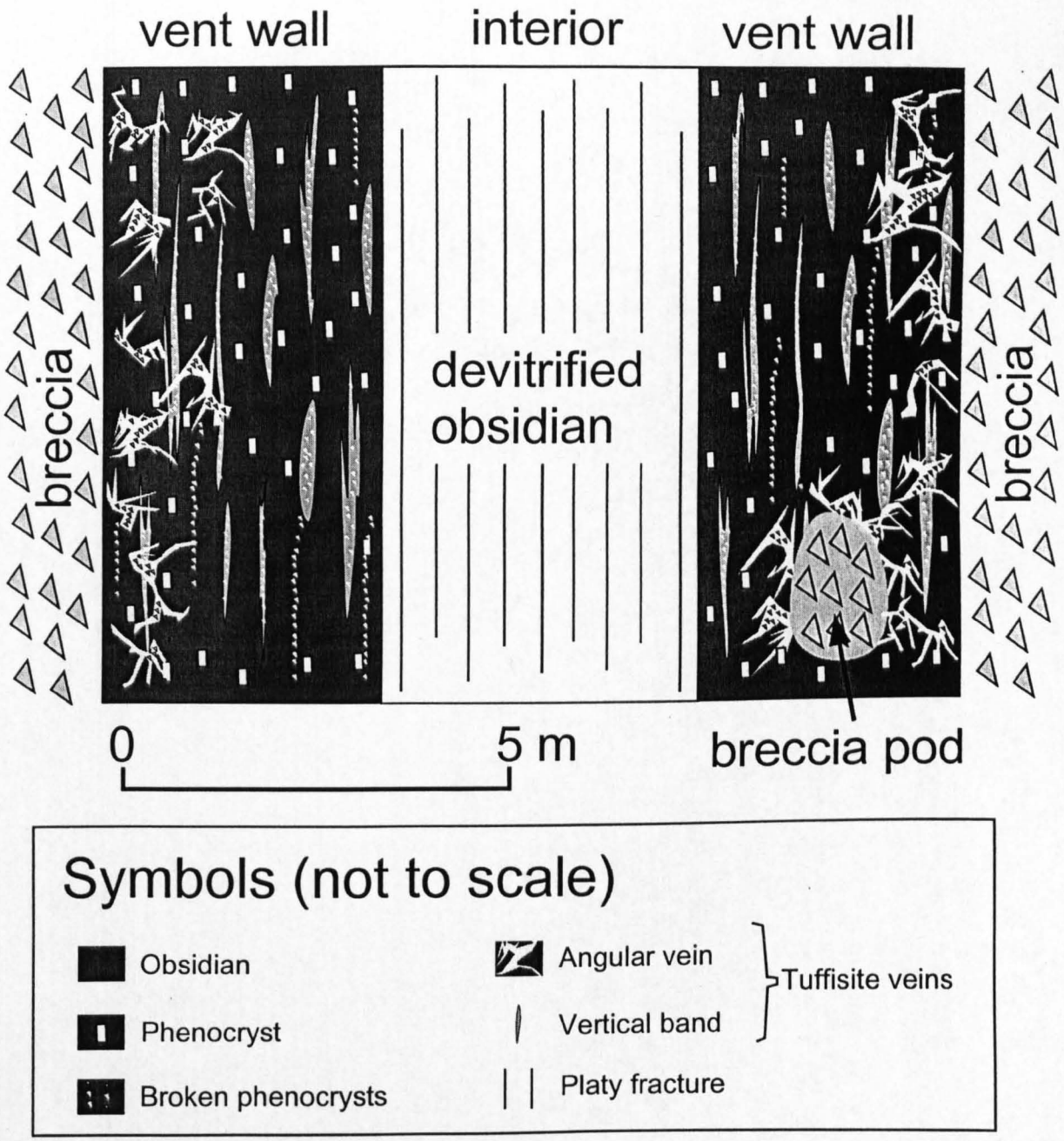

Fig. 3.6. (a) Schematic cross section of the vent (not to scale). Angular tuffisite veins are particularly common close to the outer vent walls and adjacent to breccia pods. Vertical bands, which represent sheared angular veins (see text) were observed in the vent walls. They are also present in the interior, although they are less obvious than in the walls. Trails of broken phenocrysts, indicated in the walls only, were also observed in the devitrified obsidian interior.

Fig. 3.6. continued

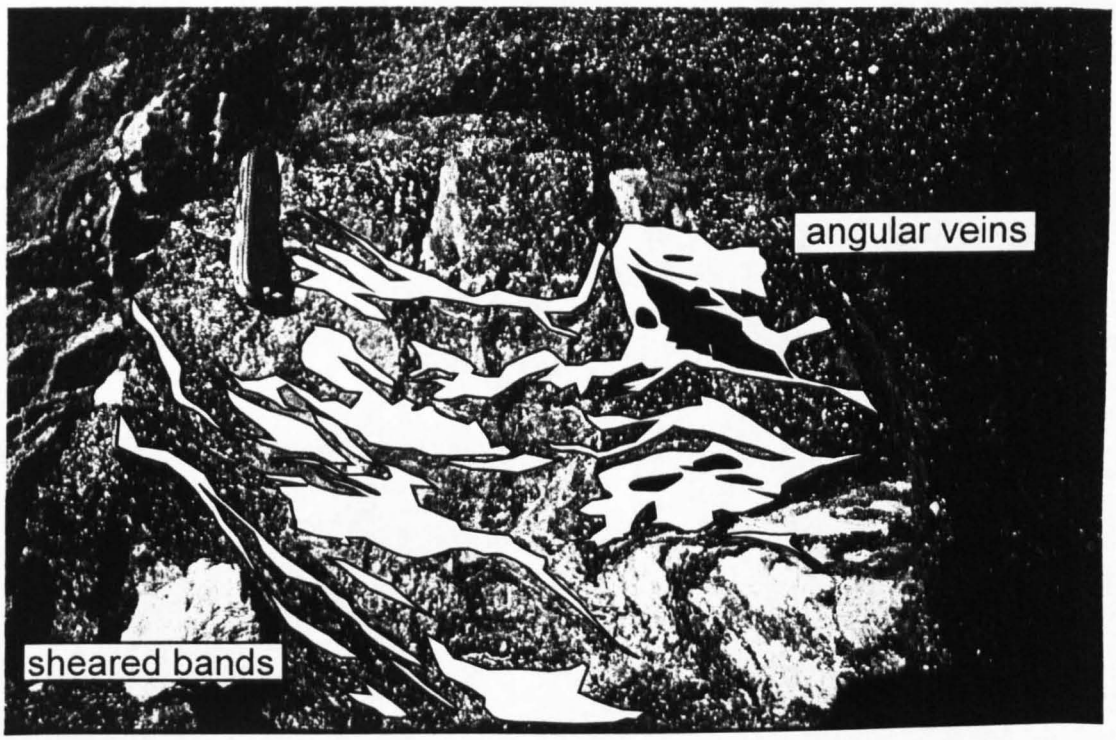

(e)

(f)

Fig. 3.6. continued

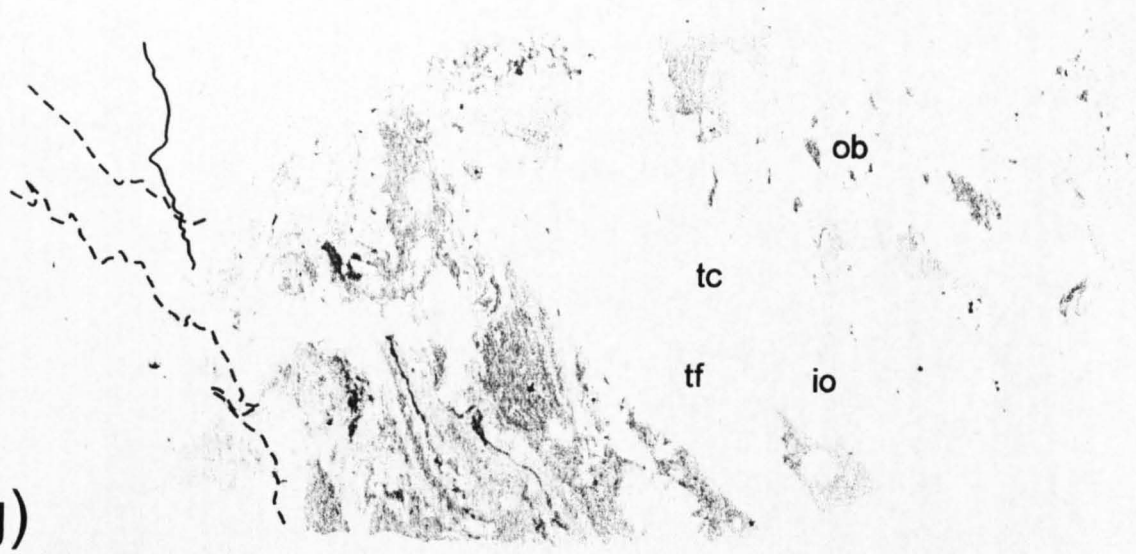

(g)

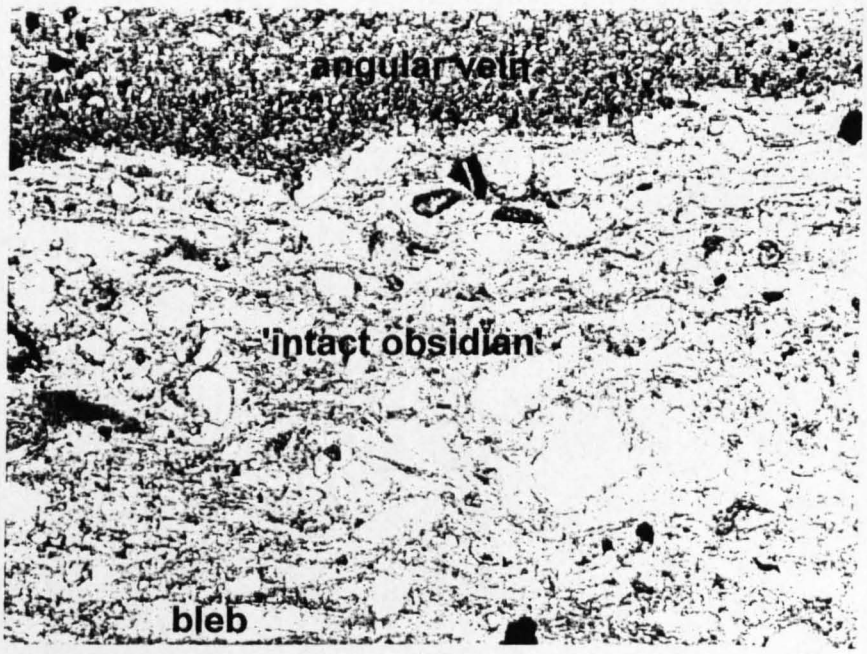

(h)

Fig. 3.6. continued

Fig. 3.6. (b) Internal structure of a typical angular tuffisite vein in the East Wall (point X on Fig. 3.5d). In the upper portion of the widest part of the vein (labelled a) the clastic material is well-sorted, with laminae 1-3 mm wide parallel to the adjacent obsidian vein wall. The interior portion the vein contains massive, poorly-sorted material rich in crystal fragments (labelled cry). Black obsidian blebs are conspicuous within the vein (labelled b). These are elongate parallel to the vein walls. The poorly-sorted unit pinches out to the left (arrow) where the vein narrows (labelled d). Vertical bands (highly sheared tuffisite veins) were observed in the intact obsidian of the vein wall (labelled e, f). **(c)** The widest angular tuffisite veins observed: on the West Wall (Fig. 3.5d). The clastic infill is intricately laminated, with regions of undisturbed planar bedding and tightly folded beds (indicated). There is locally spectacular cross-lamination (labelled cl). **(d)** Narrow angular tuffisite veins within the east vent wall (point Y on Fig. 3.5d). Veins (v) are bound by angular obsidian walls. Where veins pinch out (direction of arrows) the grainsize of the clastic infill decreases and the proportion of crystal fragments and obsidian blebs decreases to zero. Pale feldspar phenocrysts up to 5 mm across in the intact obsidian (p) are absent in the vein-filling material. **(e)** Tuffisite veins within the East Wall. There is a continuum between sheared veins (bottom left) and unsheared angular veins (top right). Some sheared veins are only apparent due to the presence of a narrow, sinuous trail of broken phenocrysts. Penknife is 8 cm long. **(f)** Breccia pod within the West Wall (labelled P1 on Fig. 3.5d). The solid black line indicates the position of the pod. Anastamosing tuffisite veins appear to originate in the breccia pod and penetrate into the surrounding intact obsidian (arrows). Near-vertical flow banding is faintly visible in the intact obsidian (dotted line, right of picture). Figure is 1.8 m tall. **(g)** A thin section of a sample from the East Wall, scanned in normal light. An angular vein (centre right, pale grey), cuts through 'intact' obsidian (io). Variations in the colour of the tuffisite vein indicate grain size variations: 'coarse tuffisite', (labelled tc), is coarse sand-grade, whereas 'fine tuffisite' (labelled tf) is fine sand-grade. Note that the coarsest material is in the centre of the vein. Obsidian blebs within the vein appear as dark patches (one is labelled ob), these measure up to 3 mm across in this section. Dotted lines on the left hand side of the photograph indicate the margins of earlier generations of tuffisite veins, some of which have highly crenulate outlines. White patches are phenocrysts, mostly of alkali feldspar. Note that these are absent in the angular veins. Although the 'intact obsidian' (io) *appears* homogeneous on this scale, a close-up (Fig. 3.6h) reveals startlingly complex internal structures. **(h)** Close-up of the 'intact obsidian' at the margin of the angular vein pictured in Fig. 3.6g. The 'intact obsidian' in fact consists of obsidian blebs (mid grey, one is labelled) which are highly elongate in one direction (approximately horizontal in the plane of view) and are surrounded by finer-grained material (darker grey). White patches are phenocrysts, mostly of alkali feldspar. Overall, this material resembles a highly-sheared tuffisite vein that is particularly rich in obsidian blebs.

Vertical bands are near-planar bands of grey material typically 1-5 mm wide and 0.1-5 m long. They are most clearly seen in the black obsidian walls (Fig. 3.6a), although similar (but less distinctive) bands were observed parallel to the planes of platy fracture

within the devitrified inner portion. The grey material is identical to that within the angular veins, and also contains black obsidian blebs and broken phenocrysts. The relics of intricate cross-laminae within the annealed grey material are visible in some of the wider vertical bands. Many bands are much darker grey in colour than angular veins, especially on the inner side of the obsidian walls, and are almost indistinguishable from the surrounding obsidian. These bands are, however, clearly picked out by trails of broken phenocrysts. There is a textural continuum between the two endmembers (Fig. 3.6e). Angular veins in the obsidian walls cut vertical bands and are clearly younger.

The volatile contents of the grey clastic material, obsidian blebs and the surrounding intact obsidian were analysed using FTIR. Results are provided in Appendix D2 and analytical techniques are given in Appendix D1. Fig. 3.7b is a 'map' of the measured volatile content within an angular vein-surrounding obsidian sample. Spatial variations in volatile content are marked. The mean volatile content of tuffisite material is lower than the intact obsidian (Table 3.1). However, the tuffisite less than 100 μm from an obsidian bleb is significantly richer in volatiles (Fig. 3.7b).

Table 3.1. H_2O contents determined by FTIR within a tuffisite vein sample from the West Wall of the vent on South-east Rauðufossafjöll. See Appendix D1 for details of the analytical techniques used.

Sample domain	Number of analyses	Mean (wt %)	Standard deviation
Vent wall obsidian	11	0.212	0.031
Obsidian bleb	5	0.250	0.011
Tuffisite <100 μm from bleb	4	0.220	0.015
Tuffisite elsewhere	5	0.140	0.016

3.5.4. Origin and significance of tuffisite veins

The angular tuffisite veins are thought to have formed as a result of brittle tensile fracturing of the vent walls (Fig. 3.7a; Heiken et al. 1988, Stasiuk et al. 1996). The textural continuum between angular tuffisite veins and vertical bands suggests that the latter is derived from ductile deformation and annealing of earlier generations of angular tuffisite veins (Sparks 1997). The vent walls thus appear to undergo episodes of brittle and ductile deformation (Dingwell 1997). The style of deformation is controlled by factors that include the strain rate, confining pressure and temperature (Smith 1996). Brittle fracture is thought to occur when the magmatic overpressure (magma pressure in vent minus lithostatic pressure in surrounding country rock) exceeds the tensile strength of the magma in the vent (Heiken et al. 1988). Cooling and degassing at the vent walls may favour brittle failure of the outer portions of the vent and tuffisite formation (Jaupart 1998), as may the presence of poorly-consolidated, permeable country rock, which lacks the mechanical strength to inhibit fracture of the adjacent vent wall (Eichelberger et al. 1986). Angular (unsheared) veins cut earlier generations of annealed vertical bands, indicating that fracture, annealing and ductile shearing are episodic processes.

The origin of the fine-grained ash within tuffisite veins is contentious. Stasiuk et al. (1996) observed tuffisite veins at the rhyolitic Mule Creek vent that appeared to originate within the vent wall and propagate outwards into the surrounding breccia. Thus brittle fracture of the vent walls was inferred to have produced the fine-grained ash. Here, the inverse may have occurred - tuffisite veins appear to have propagated inwards, from pods of breccia into the adjacent vent wall. The fine-grained ash matrix of the breccias may have been 'scavenged' from the matrix of the surrounding breccias, possibly as tensile failure (and effective inflation) of the vent walls created a transient low-pressure region, into which ash was sucked (Fig. 3.7a). Similar processes are inferred to have

occurred at the outer margins of the vent walls, which are not exposed. The sedimentary structures within angular veins are consistent with the injection of a fluidised, low-viscosity gas-solid mixture into propagating cracks (Heiken et al. 1988, Stasiuk et al. 1996). Complex bedding patterns indicate fluctuations in the vigour and clast load of the incoming fluidised mixture. A coating of fine-grained ash on angular fracture surfaces suggests that only the finest portion of the fluidised mixture was able to penetrate the infinitesimally wide tip of propagating fractures (Fig. 3.7a). This fine-grained material would be especially prone to rapid annealing, and may have helped to 'prop open' advancing cracks (Heiken et al. 1988), making way to coarser-grained clastic material as the crack widened. Although the scales are very different, the poorly-sorted beds rich in crystal fragments may be considered to be the intrusive equivalent of a pyroclastic surge deposit (Heiken et al. 1988), and indicate turbulent fluid flow within veins. Conversely, the well-sorted, planar- and cross-bedded units represent intrusive pyroclastic flow deposits, which accumulated during sedimentation from laminar fluid flow of varying intensity. Broken phenocrysts within the clastic veins may have formed as phenocrysts in the walls of opening cracks experienced short-lived shockwaves during brittle failure events and were shattered. Crystal fragments were then picked up by the incoming fluidised mixture. Elongate obsidian blebs within the wider veins appear to have been scavenged from the vent walls. Their rounded shape and elongation parallel to vein walls (Fig. 3.6b) suggest that they have undergone ductile deformation within the advancing fluidised mixture, in direct contrast with the intact obsidian walls of angular veins, which display only angular surfaces indicative of brittle deformation (e.g. Fig. 3.6d).

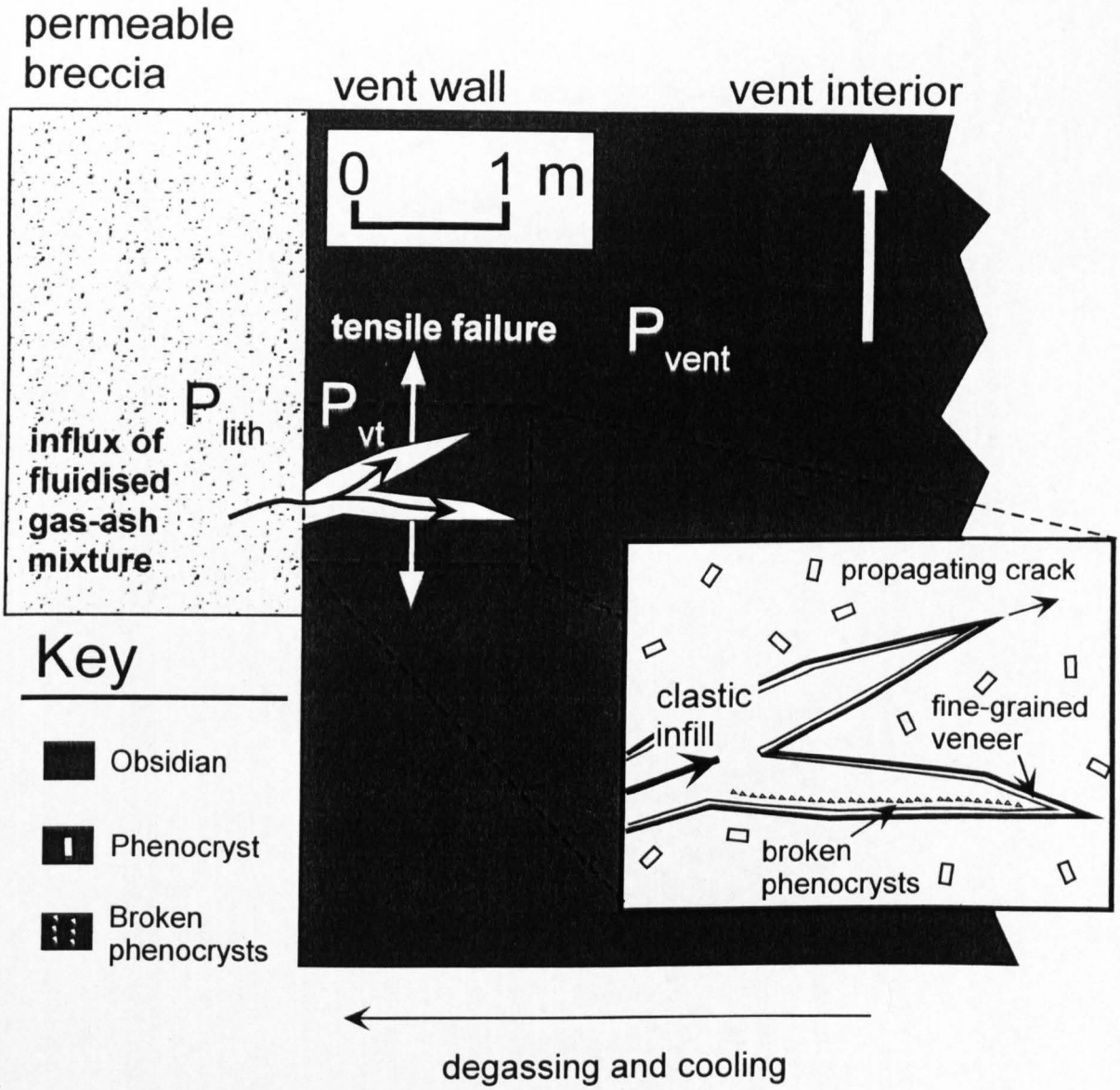

Fig. 3.7 (a) Model for the generation of tuffisite veins in the vent walls. Excess pressure within the vent (pressure in the vent P_{vent} > lithostatic pressure P_{lith}) causes brittle tensile failure of the vent walls (white arrows). Dilation during tensile failure creates a transient low pressure domain in the veins (P_{vent} <P_{lith}). Unconsolidated fine-grained material within the adjacent permeable breccia is sucked into the newly-formed void, triggered by the pressure difference P_{lith} - P_{vent}.

As the clastic material enters the propagating cracks, a fine-grained veneer on the angular obsidian fracture surfaces is formed - since only the finest portion of the clastic material can enter the infinitesimally wide crack tip (inset). The magma flow direction is indicated (large white arrow).

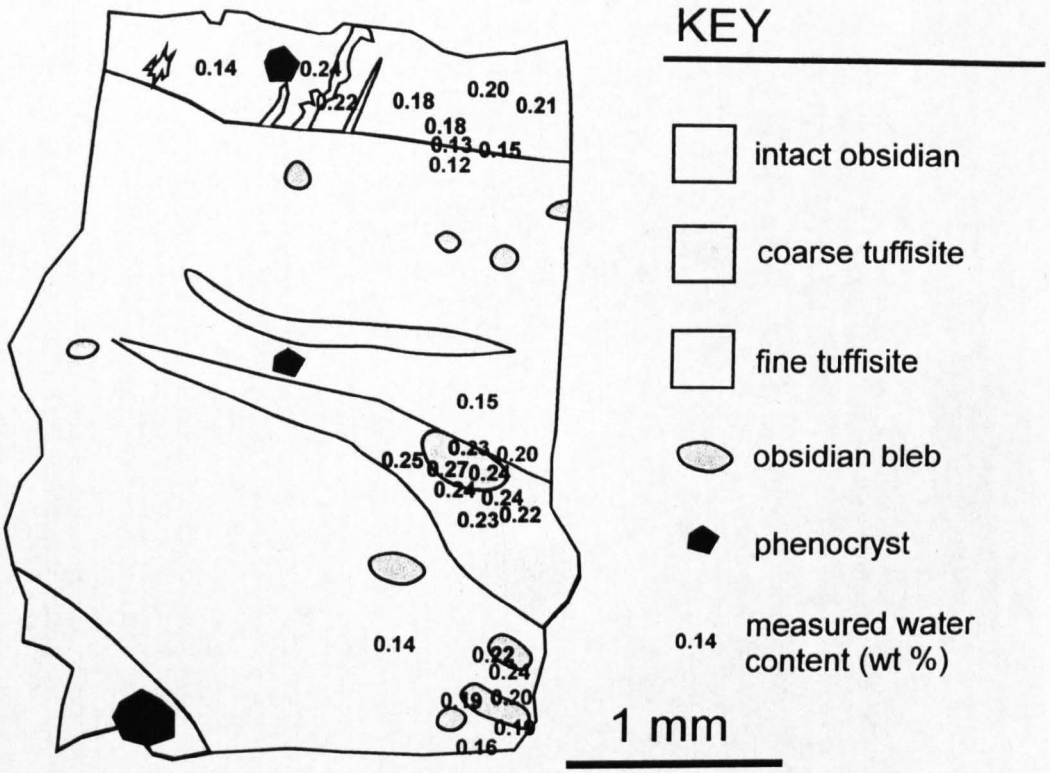

Fig. 3.7. (b) Sketch from a photomicrograph of tuffisite vein sample Vent-4, which was analysed for volatile content using FTIR (see Appendix 3.2 for data and analytical techniques). The decimal point of each water content figure on the diagram indicates the precise location of the glass measured. Note the homogeneous volatile content of the obsidian blebs, the relatively high and homogeneous volatile content of the adjacent tuffisite, and the low volatile contents measured elsewhere in the tuffisite.

Fig. 3.7. continued

Internal friction within the clast-charged fluidised mixture is a possible explanation, since 'viscous heating' during emplacement of the vein infill may have aided annealing of ash shards and ductile deformation of obsidian blebs. Such a heating mechanism may require high clast density within the fluidised mixture. The breccias adjacent to the vent represent the 'country rock' and were probably formed during an earlier explosive (phreato-) magmatic phase of the eruption. It is unclear whether the breccia pod in the west vent wall is a portion of the country rock that has become entrained in the vent, or if it formed in situ by an undetermined process.

Ductile deformation of the larger clasts within angular veins illustrates that the vein material was sufficiently hot to undergo ductile deformation at some (lower) strain rates. This is emphasised by the subsequent ductile shearing of entire angular veins parallel to the inferred [near-vertical] magma flow direction. The pale grey colour and opaque nature of angular veins may reflect incomplete annealing, as light is scattered off relic shard surfaces. This is in contrast with the surrounding black, translucent obsidian. However, certain vertical bands (sheared tuffisite veins) appear to be more thoroughly annealed, as the glass colour is almost identical to the surrounding intact obsidian. Furthermore, the 'intact obsidian' material is revealed to be a complex collage of annealed blebs of obsidian (Fig. 3.6h), and probably represents thoroughly resheared, even earlier tuffisite veins. This further suggests that vein formation and reshearing are cyclic processes within the vent walls, and that all of the rising magma has experienced a complex history of disaggregation and rewelding during its rise in the vent.

It is not easy to assess the significance of the measured volatile contents within the tuffisite-intact obsidian sample, due to uncertainties in the robustness of the acquired data. Anhydrous crystals and fracture surfaces may both serve to reduce the intensity of absorption peaks attributed to water (Ihinger et al. 1994), and may lead to false results.

Hence it is difficult to determine whether apparent differences between the volatile content of tuffisite and intact obsidian are real, or are merely an artefact of systematic measurement errors. However, it does appear that the obsidian vent wall and obsidian blebs within the tuffisite have similar and relatively high volatile contents (Table 3.1), and the measured volatile content within the pale grey tuffisite material is markedly lower. Tuffisite within 100 μm of the obsidian bleb yielded similar results to the bleb itself, whereas grey tuffisite elsewhere appears to be less volatile-rich (Table 3.1). One possibility is that the apparent lower volatile content of the tuffisite merely reflects scattering from incompletely annealed relic clast surfaces, an effect that is less pronounced adjacent to obsidian blebs, where annealing was more complete. A second possibility is that measurement errors are insignificant, and the grey clastic material is degassed relative to the vein walls. A steep gradient in water content between entrained obsidian blebs and the surrounding degassed tuffisite may have triggered volatile diffusion outwards from blebs - leading to the higher measured volatile content of tuffisite adjacent to blebs (Fig. 3.7b).

Much more work is necessary to determine whether tuffisite vein formation can introduce heterogeneous volatile contents to silicic magma within vents. However, the trails of broken phenocrysts within the 'intact' vent walls provide good evidence that textural heterogeneity can indeed be introduced to rising magma during brittle-ductile deformation and tuffisite generation. Positive feedback during subsequent laminar flow may then assist the generation of flow banding that is common in silicic and intermediate lavas (e.g. Fink 1983), but generally absent from basaltic lavas. This may occur if deformation were concentrated in low-viscosity zones, which undergo shear thinning due to viscous heating. Furthermore, episodic brittle fracture of shallow silicic vents may be

responsible for patterns of shallow seismicity recorded during recent andesitic dome eruptions (Sparks 1997).

3.7. Lava C

3.7.1. Description

Approximately ten microcrystalline lava bodies up to 250 m long and 80 m thick form a 'moat' around the northern flank of the volcano at 1000 m elevation (Fig. 3.3, Fig. 3.8a). They typically consist of a near-horizontal part on the upslope side (upper part) and a steeply-dipping part on the downslope side (lower part) which forms a crumbling cliff 50-90 m high (Fig. 3.8b). Upper parts consist of pale grey microcrystalline rhyolite with tightly folded flow banding. Flow banding in the lower parts is sub-planar and dips downslope at 40-80°. The outer 4-5 metres of the lower parts are cut by well-developed columnar joints spaced 15-20 cm apart. These dip gently into the local slope and are approximately normal to flow banding (Fig. 3.8b). The exposure of lava C 500 m west-north-west of the northern summit has an upper part which dips inwards towards the summit of South-east Rauðufossafjöll and is cut by columnar joints similar to those described above. No obsidian, perlite or tuffisite was observed at any of the lava C exposures.

3.7.2. Interpretation

The orientation of columnar joints in the lower parts of lava C suggests emplacement against steeply inclined near-planar ice walls (Mathews 1951, Lescinsky & Sisson 1998). These ice walls probably exceeded 80 m in height in places.

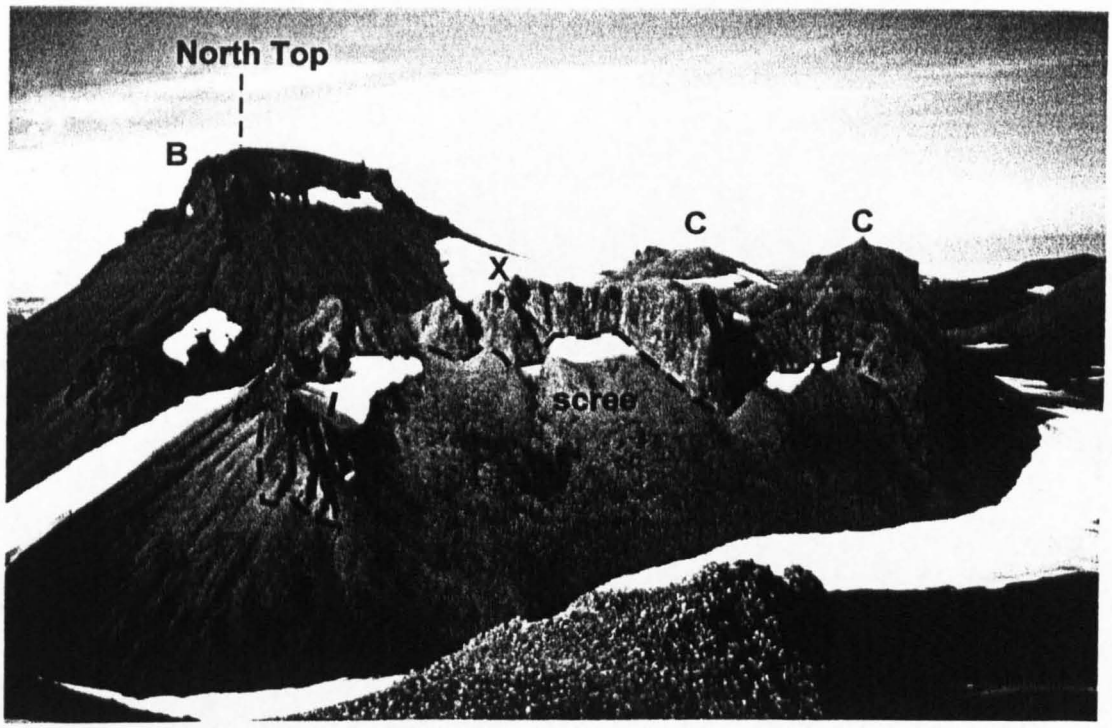

(a)

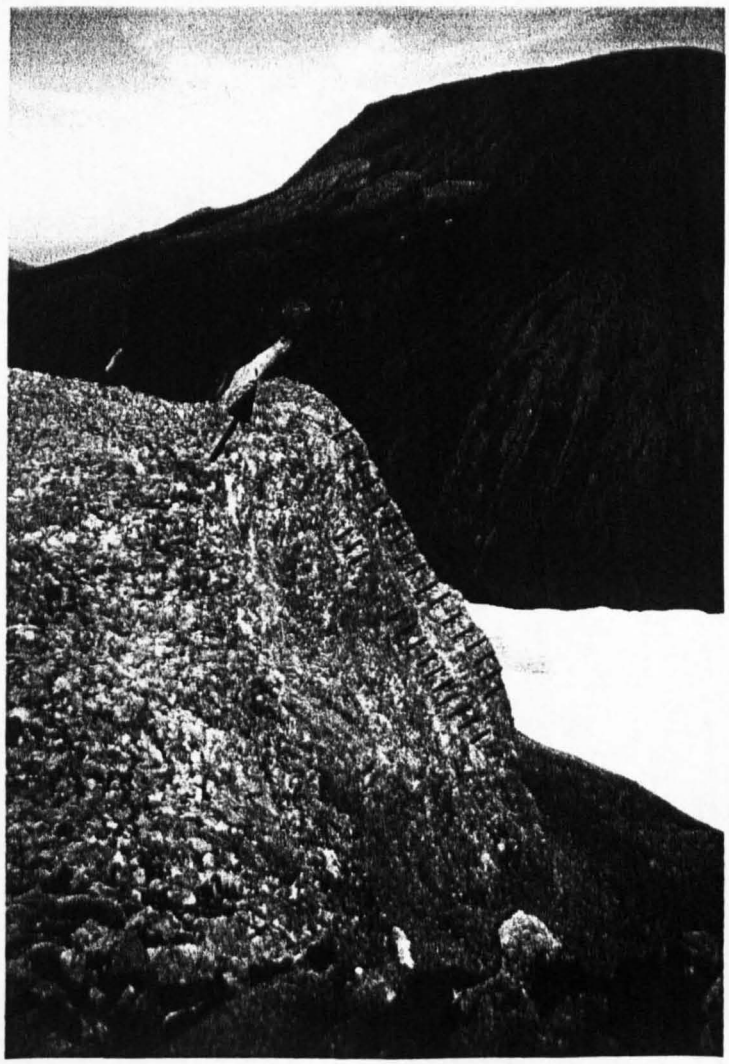

(b)

Fig. 3.8 (**a**) View of South-east Rauðufossafjöll from the north-east. Lava C, labelled as C, forms a prominent 'moat' on the tuya flank. The lava crops out as cliffs up to 100 m high (bases indicated by dotted black lines), above extensive scree slopes. B = lava B of the North Top. See Fig. 3.8b for a close-up of locality X.
(**b**) Columnar-jointed lava C 'cliff' 90 m high at locality X on Figure 3.8a. Column orientations are indicated (black lines). Figure for scale (arrow).

It is likely that chilled obsidian margins formed during emplacement of the lavas, and were subsequently removed by erosion. There is no evidence for magma-water interaction, such as perlitisation or fragmentation. It is arguable as to whether lava bodies entered pre-existing cavities in the ice, or whether cavities formed in advance of the lavas as high heat flux preceded their emplacement. The more eastern of the two lava bodies on the west flank has ice-contact surfaces on the upslope and downslope sides, suggesting that it was emplaced beneath an ice roof. There is no evidence that an ice roof was present above any of the other type C lava bodies. The relative timing of the emplacement of lava C and the main flat-topped edifice is unclear.

3.8. Lava D

3.8.1. Description

Three separate lava bodies are exposed on the Eastern Plateau, forming a prominent break in slope trending approximately north - south (Fig. 3.3). The largest exceeds 1 km in length, 250 m in width and 80 m in thickness. The distribution of lavas and orientation of flow banding and columnar joints are shown in a large-scale map of the Eastern Plateau (Fig. 3.9). Lava bases, where exposed, are peperitic (Fig. 3.10a). Matrix-supported breccia beneath the lavas consists of angular clasts of vesicle-poor black obsidian and pale grey pumiceous obsidian 1-5 cm in diameter suspended in a pale grey, massive matrix of fine-grained rhyolitic ash (Fig. 3.10a). The breccia contains localised 'rafts' of well-sorted, planar-bedded ash up to 2 m across and 0.3 m thick, which are highly sheared and disrupted. These bedded rafts were only observed within 1 m of the lava base. Lavas have a basal zone of dark grey, non-vesicular perlitised obsidian, typically 0.5 m in thickness. The lower part consists of 'clouds' of angular obsidian clasts

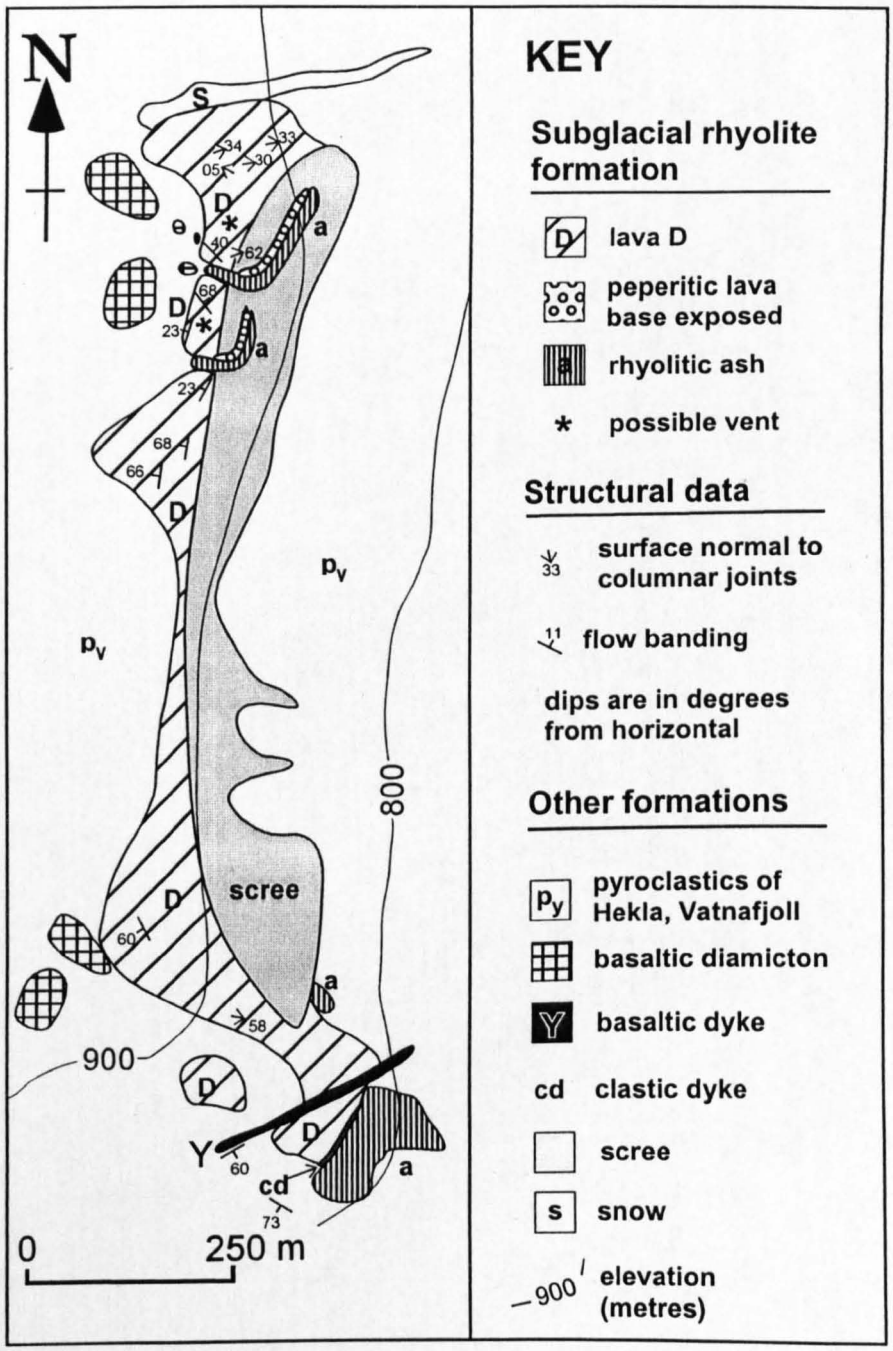

Fig. 3.9. Solid and drift geological map of the Eastern Plateau made in August 2000, showing the detailed structure of the lava D outcrops. The dip of columnar-jointed surfaces is approximately parallel with the local modern slope. The location of outcrops shown in other figures is indicated.

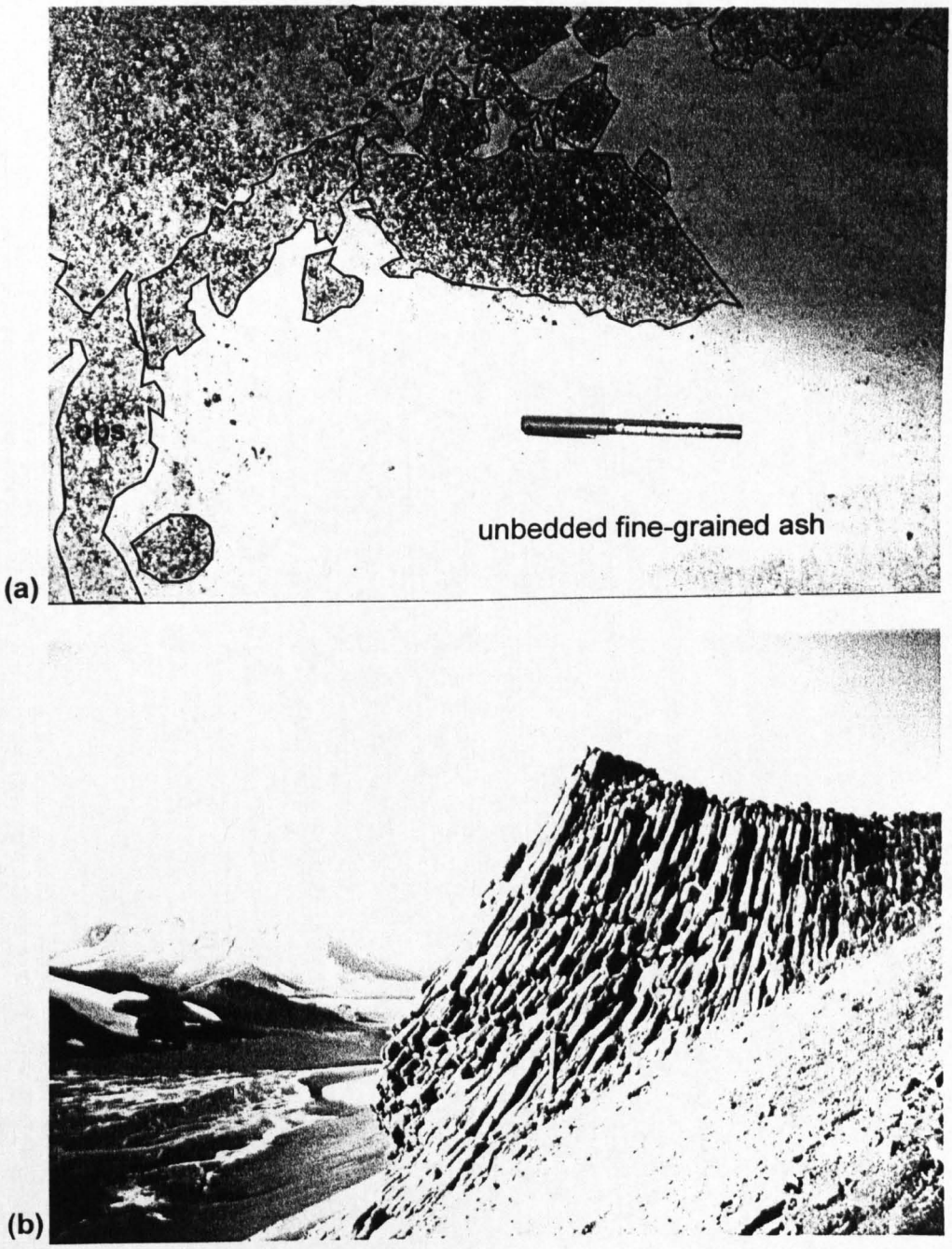

Fig. 3.10. (a) Peperitic base of lava D at the south-east limit of the Eastern Plateau. Jigsaw-fit perlitised obsidian breccia (dark grey, top and left) is in contact with well-sorted fine-grained ash (pale grey). The outline of clasts within the breccia is indicated (black lines). Pen is 10 cm long. A sample of ash was collected from point X. Fig. 3.4b is an SEM image of the surface of a typical shard from this sample. Mineral growth and dissolution are probably due to the circulation of high-temperature fluids during and after peperite emplacement. **(b)** Columnar-jointed, perlitised obsidian on the side of lava D (see Fig. 3.9 for position). Banding normal to columns is caused by variations in the degree of perlitisation. This orientation of columns, which indicates a chilling surface dipping gently to the right (upslope) is unique for lava D. Elsewhere, chilling surfaces dip at between 30 and 62° downslope (Fig. 3.9). It is likely that the portion of the lava pictured was emplaced against the near-horizontal roof of a small (c. 10 m long) ice cave that had melted into the ice wall. Formation of such a cave reflects localised heating, although the source of heat is not clear in this instance. Ice pick is 60 cm long.

1-10 cm across suspended in a poorly-sorted, unbedded ash-lapilli matrix (Fig. 3.10a). This grades upwards into a zone of jigsaw-fit obsidian breccia, cut by angular veins of unbedded pale grey ash. Above the lava base an inclined surface of mid-grey obsidian makes up the bulk of the lava D exposures. The obsidian is variably perlitised, comprising 0-80 % spherical black glass beads and 20-100 % altered pale grey glass. It is cut by columnar joints, which are locally spectacular (Fig. 3.10b). Columns are polygonal, 8-12 cm across, and aligned normal to planar surfaces mostly dipping at 30-62° down the modern day slope. In one locality, the planar surface dips gently into the slope (Fig. 3.9, Fig. 3.10b). The orientation of flow banding in the bulk of the lava is highly variable and is seldom normal to the columnar joints. The top 5-10 m of exposed lava below the plateau crest lacks columnar joints and is not perlitised. It is glassy, with near-vertical flow banding and interleaved zones of vesicle-poor black obsidian and pale pumiceous obsidian (40-50 % vesicles). A pale, clast-supported breccia consisting of angular clasts of pumiceous obsidian and vesicle-poor obsidian overlies the top of the northernmost lava flow, locally to a thickness of 2 m (Fig. 3.11a-b). The breccia grades downwards into the intact, tightly flow-folded lava flow top. Although the Eastern Plateau is mostly covered by Holocene pyroclastic fall deposits and basaltic diamicton (Fig. 3.9), intact pumiceous obsidian crops out as a number of knolls 40-50 m across.

3.8.2. Interpretation

The nature of the lava flows on the Eastern Plateau is thought to reflect an unusual emplacement environment. Peperitic flow bases may indicate that the lavas flowed over wet, poorly-consolidated breccias (Kokelaar 1982, McPhie et al. 1993). The columnar-jointed obsidian is interpreted as an ice-contact feature (Mathews 1951, Lescinsky & Sisson 1998), formed as the lavas chilled against ice walls that dipped at 30-

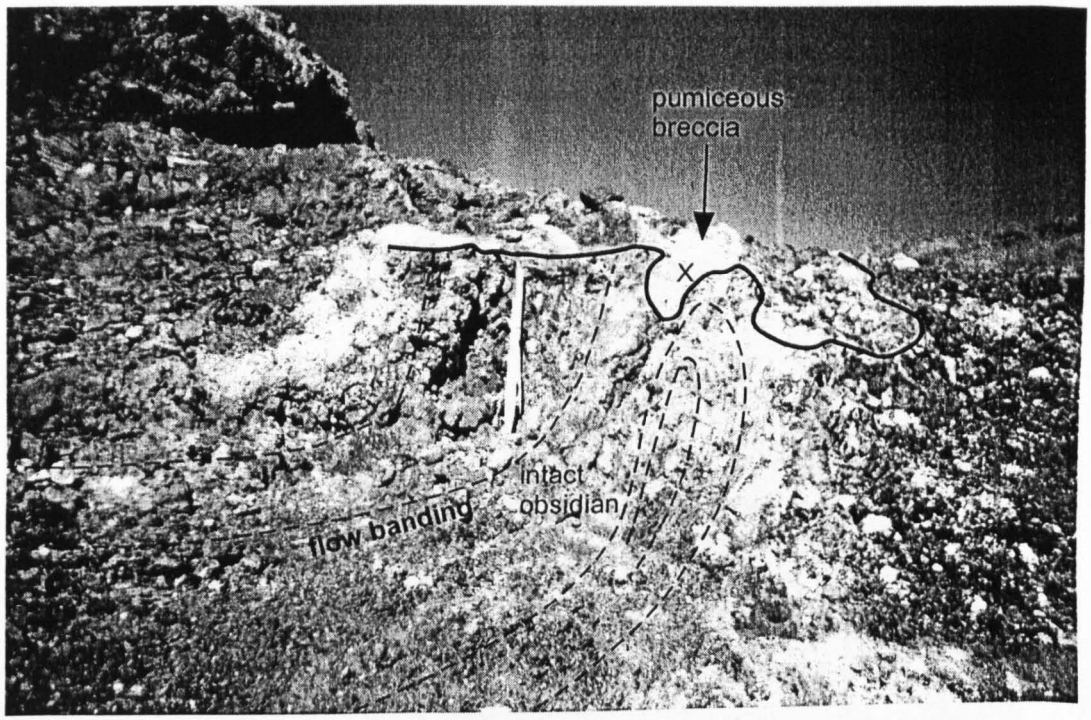

(a)

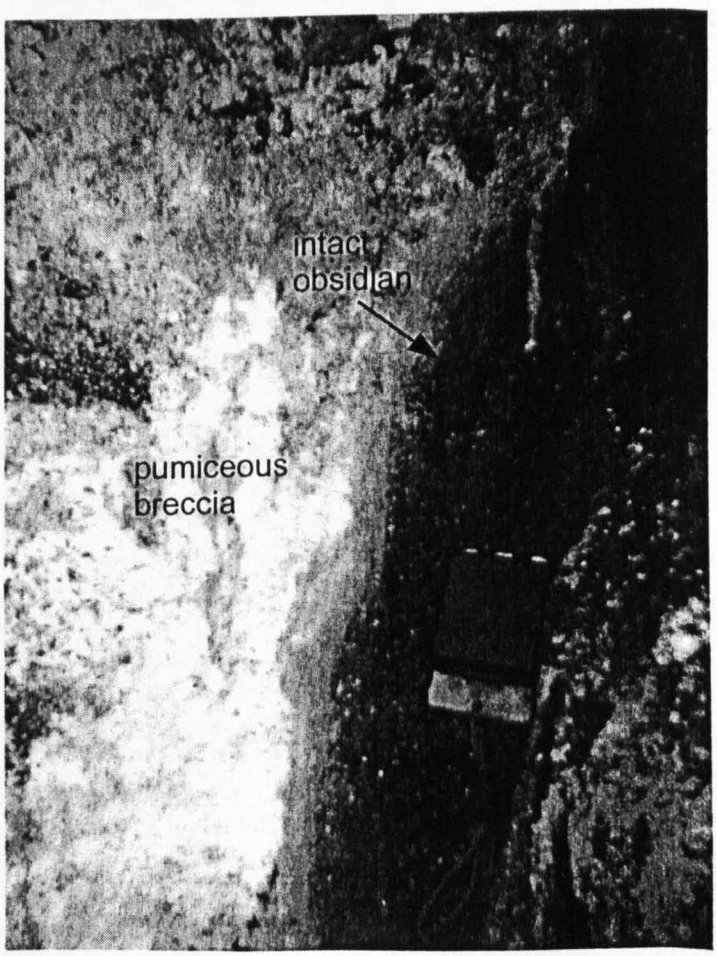

(b)

Fig. 3.11 (a) Upper carapace of the northernmost outcrop of lava D (see Fig. 3.9 for position). Flow banding in intact obsidian (dotted lines) is tightly folded and truncated. The pale material is pumiceous breccia - see (b) for a close-up photograph. Ice pick is 60 cm long.
(b) Close-up of the transition between intact obsidian and pumiceous breccia at point X on (a). Compass is 10 cm long.

62° down the local modern-day slope. Pervasive perlitic alteration indicates that water interacted with the lava body (e.g. Davis & McPhie 1996); a process that would have been greatly accelerated if the lava were still hot when permeated by water (Friedman et al. 1966). Any fragmental material generated at the ice-lava contact has not been preserved. Patterns of vesicularity and flow banding in the flow tops are characteristic of subaerial rhyolite lava flows (Fink 1983).

Lava D is interpreted to have flowed over a substrate of poorly-consolidated waterlogged ash before abutting and chilling against a steeply-inclined ice wall. The subaerial characteristics of the upper carapace suggest that the lava was either emplaced subaerially, or within an ice cave with a roof sufficiently high to prevent interaction between lava and ice or meltwater.

3.9. Lava E

3.9.1. Description

Peperitic lava E crops out on the southern flank of the Eastern Plateau (Fig. 3.3), low-lying outcrops covering an area of approximately 500 m by 250 m. The best exposure is in a gully section at the south-western margin of the Eastern Plateau. The lava is ~30 m thick, with near-horizontal top and base (Fig. 3.12). It overlies >10 m of massive, poorly-sorted matrix-supported pumice-obsidian breccia which is pale brown in colour and has a fine-grained matrix of blocky ash. A unit of well-sorted, delicately cross-laminated fine-grained sandstone ~0.5 m thick directly underlies the rhyolite lava body. The lowest part of the lava consists of non-vesicular, deformed clasts of vesicle-poor black obsidian surrounded by unbedded pale brown ash (Fig. 3.13a). Clasts are elongate, folded in a ductile manner and frequently bounded by flow-banding planes. They range from 0.5 cm

to 20 cm in length. This part is of variable thickness, but typically 0.5-1 m. It grades upwards through a zone of jigsaw-fit obsidian breccia <1 m thick into a zone of intact, vesicle-poor black obsidian. The obsidian is cut by anastomosing veins 1-30 mm wide, infilled by near-white cross-laminated ash (Fig. 3.13b). This is in turn overlain by flow-banded obsidian ~25 m thick, of which the upper 15 m is columnar-jointed. Vesicularity increases from 0 in the lava base and interior to >40 % in the uppermost 5 m. Columnar joints are 8-15 cm across and normal to a near-planar surface that dips downslope at ~45°. Joint surfaces in the upper 10 m are covered by a veneer of white ash.

In one location the columnar-jointed upper surface is cut by a fracture 10 m deep and 2 m wide (Fig. 3.12, Fig. 3.13c). The walls of the fracture are mostly parallel to joint planes (Fig. 3.13c). The fracture is filled with columns and irregularly-shaped blocks of obsidian 10 cm – 1 m across, interspersed with bedded gravelly sandstones that drape the larger obsidian blocks. A photomicrograph of a thin section of this lithology reveals that coalescing vesicles have been infiltrated by angular ash shards. Locally, extreme vesiculation has created delicate spindle-like bubble walls, some of which were in the process of rupturing when they were quenched (Fig. 3.13d). The obsidian in the upper 1 m of the fracture walls contains ~40 % coalescing, near-spherical vesicles. Vesicles within 30 cm of the fracture wall are filled with white ash. Locally, vesicle walls have ruptured, creating jagged black bubble-wall shards 1-10 mm long suspended in white ash. The lava top is covered by pale grey, poorly-sorted pumice-obsidian breccias supported by an ash matrix.

The south-eastern portion of the peperite exposure is a complex association of columnar-jointed black obsidian cut by ash-filled veins and a variety of volcaniclastic sandstones and breccias. Two separate lava bodies, each ~10 m thick were identified, displaying similar textural patterns to the 30 m-thick lava body described above. Lenses

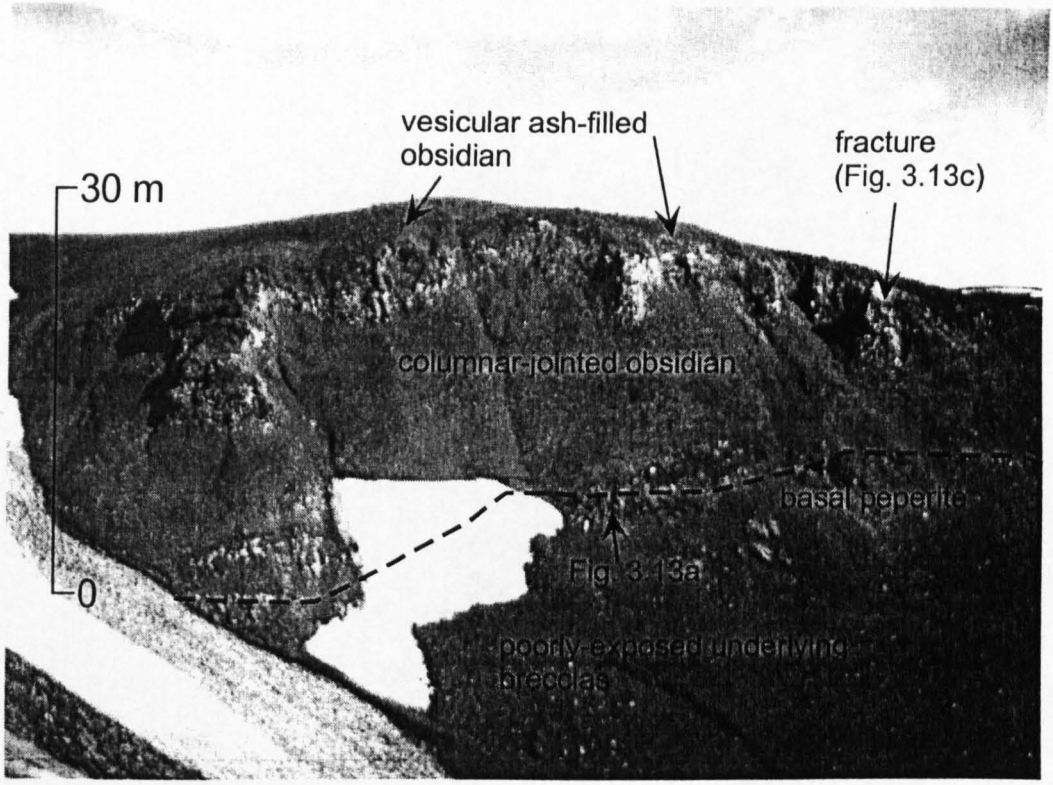

Fig. 3.12. View of the north-western outcrop of lava E on the Eastern Plateau, looking east-south-east from an altitude of 900 m. A 30-m-high vertical section through the lava is exposed. The pale colour of the upper ~5 m of the lava section is caused by the coating of columnar joint surfaces by near-white fine-grained ash (see also Fig. 3.13b-c). The dashed black line indicates the approximate position of the peperitic lava base. The location of the fracture illustrated in Fig. 3.13c is indicated.

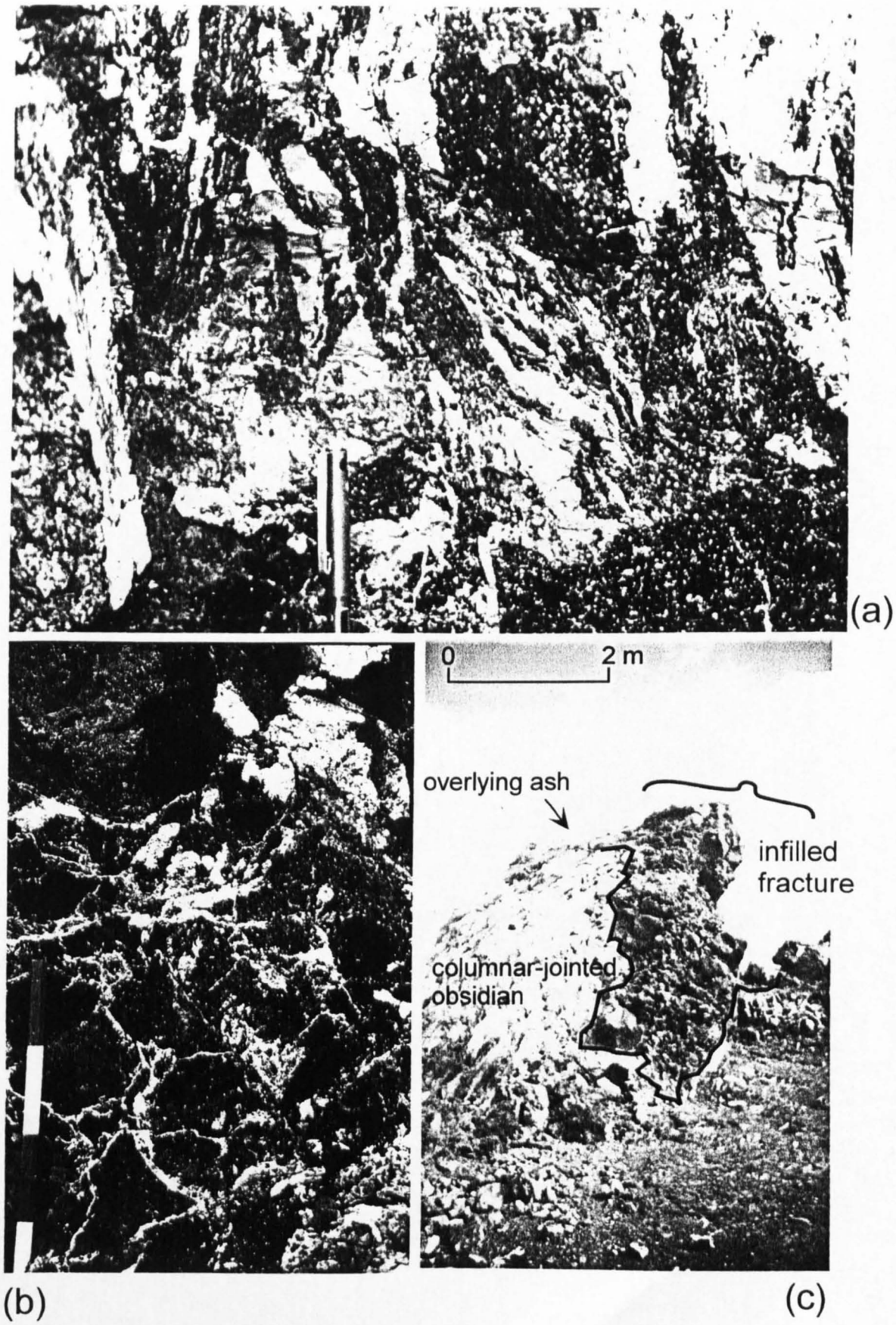
(a)
0
2 m
overlying ash
infilled
fracture
columnar-jointed
obsidian
(b)
(c)

Fig. 3.13.

(d)

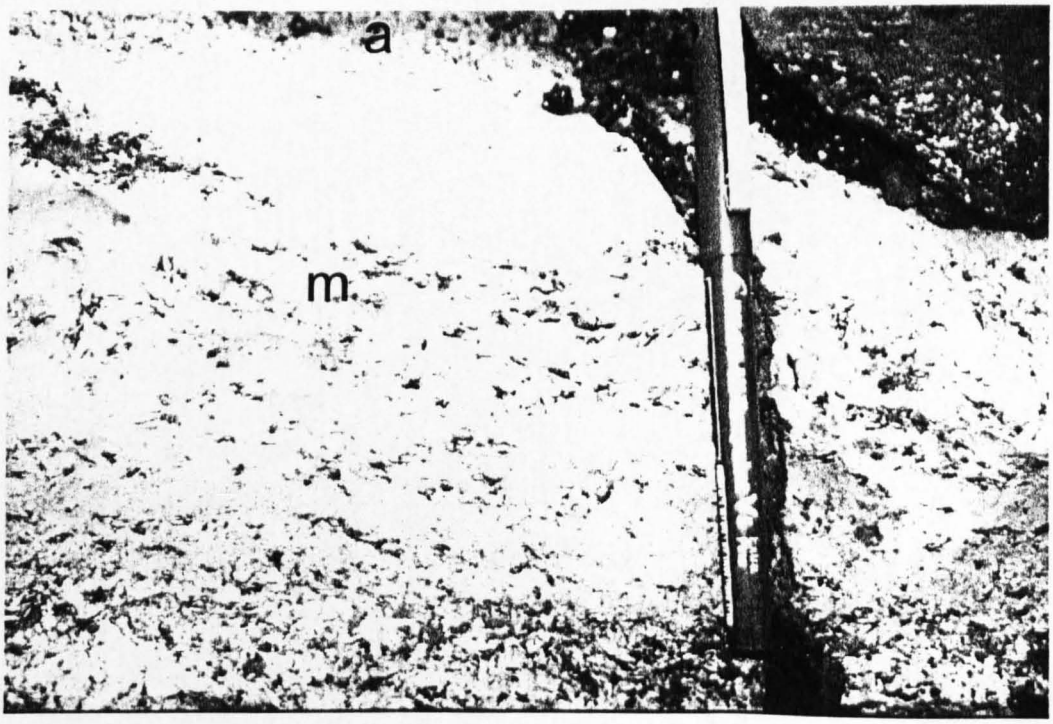

(e)

Fig. 3.13. continued

Fig. 3.13. (a) Peperite at the base of lava E (location indicated in Fig. 3.12). Vesicle-free obsidian clasts (dark grey) are surrounded by ash (white). Many obsidian clasts are platy in morphology, as fractures have exploited near-vertical flow banding. Some clasts are bent, suggesting ductile deformation. The ash in this view is structureless and fine-grained. The pen cap is 4 cm long. **(b)** Columnar-jointed obsidian of the upper carapace of lava E, looking at a section normal to the long axis of columns. The white material is fine-grained ash that has penetrated joint planes and invaded the vesiculating lava. The bars on the ruler are 10 cm long. **(c)** A view looking steeply upslope to a fracture in the columnar-jointed upper carapace of lava E (see Fig. 3.12 for location). The fracture is bounded by surfaces that have followed columnar joints. Note the massive, chaotic nature of the infilling breccia within the fracture, which contains angular boulders of black obsidian up to 0.5 m across. Laminated sandstone infills voids between large clasts, but is not seen in the photograph. The pale colour of the columnar-jointed obsidian (left of picture) is caused by a veneer of ash that coats columnar joint surfaces. The lower part of the picture is columnar-jointed, perlitised obsidian. **(d)** Photomicrograph of ash invading vesicular obsidian of the upper carapace of lava E. Many of the walls of highly elongate vesicles (mid grey, some labelled w), appear to have been undergoing brittle failure when the magma was quenched. Brittle failure may have been triggered by a sudden increase in pressure within the vesicles when water in the incoming ash was vaporised. Alternatively, quenching during ash invasion may have caused fragmentation, or otherwise 'magmatic' fragmentation may have occurred, due to degassing, and the incoming ash has fossilised the fragmentation interface. The broken vesicle walls may be the source of the angular fragments of black obsidian present in the 'mixed' sediments at the lava base (Fig. 3.13e). **(e)** Mixed fine-grained ash (white) - obsidian shard (black) sediments at the base of lava E. The proportion of obsidian shards varies between 0 and ~25 % within the pictured section. Pale domains are dominated by fine-grained ash (labelled a), whereas others are mixed (labelled m). Pen is 10 cm long.

---

of grey-brown sandstone 1-2 m thick underlie the base of the lower lava body. These comprise units of well-sorted, planar-bedded pale brown ash and units of 'mixed' sandstone. 'Mixed' sandstones contain 0-40 % black, jagged obsidian shards 1-10 mm across within a pale brown sand-grade ash matrix (Fig. 3.13e). Obsidian shards are

locally randomly orientated, although in places they display marked horizontal imbrication. Bedding in the sandstones is locally faulted and folded.

3.9.2. Interpretation

Lava bases are similar to the bases of lava D, and are typical of peperitic lavas/sills that have flowed over/through a wet, poorly consolidated clastic substrate (Kokelaar 1982, White & Busby-Spera 1987). Vesicular lava tops are suggestive of low pressure conditions (Hunns & McPhie 1999) and show evidence of infiltration of permeable, vesiculating obsidian by mobile ash. The top and sides of the lava bodies display columnar joint patterns typical of lava-ice interaction (Lescinsky & Sisson 1998).

The following argument is used to suggest that wet sediments were washed over the top of lava E whilst it was still hot:-

(1) The fracture in the lava carapace, which formed *after* the development of columnar joints, has been infilled by clastic material, including bedded fine-grained units. This shows that there were poorly-consolidated sediments above the lava at this stage, which may have been redeposited by flowing water.

(2) The ash portion of the fracture-filling sediments has penetrated the vesiculated upper metre of the fracture walls. An active gas phase (steam) was probably necessary to allow such penetration - by forming a low-viscosity particle-laden suspension capable of invading a network of interconnected vesicles < 1 mm in diameter. Thus the fracture walls were probably hot when infilling occurred, and liquid water was converted to steam.

It is thus inferred that the material infilling the void was wet or steam-charged at the time of deposition, and that there was a supply of mobile, waterlogged clastic material above the lava. Some of this material may have been derived from the vesiculated upper

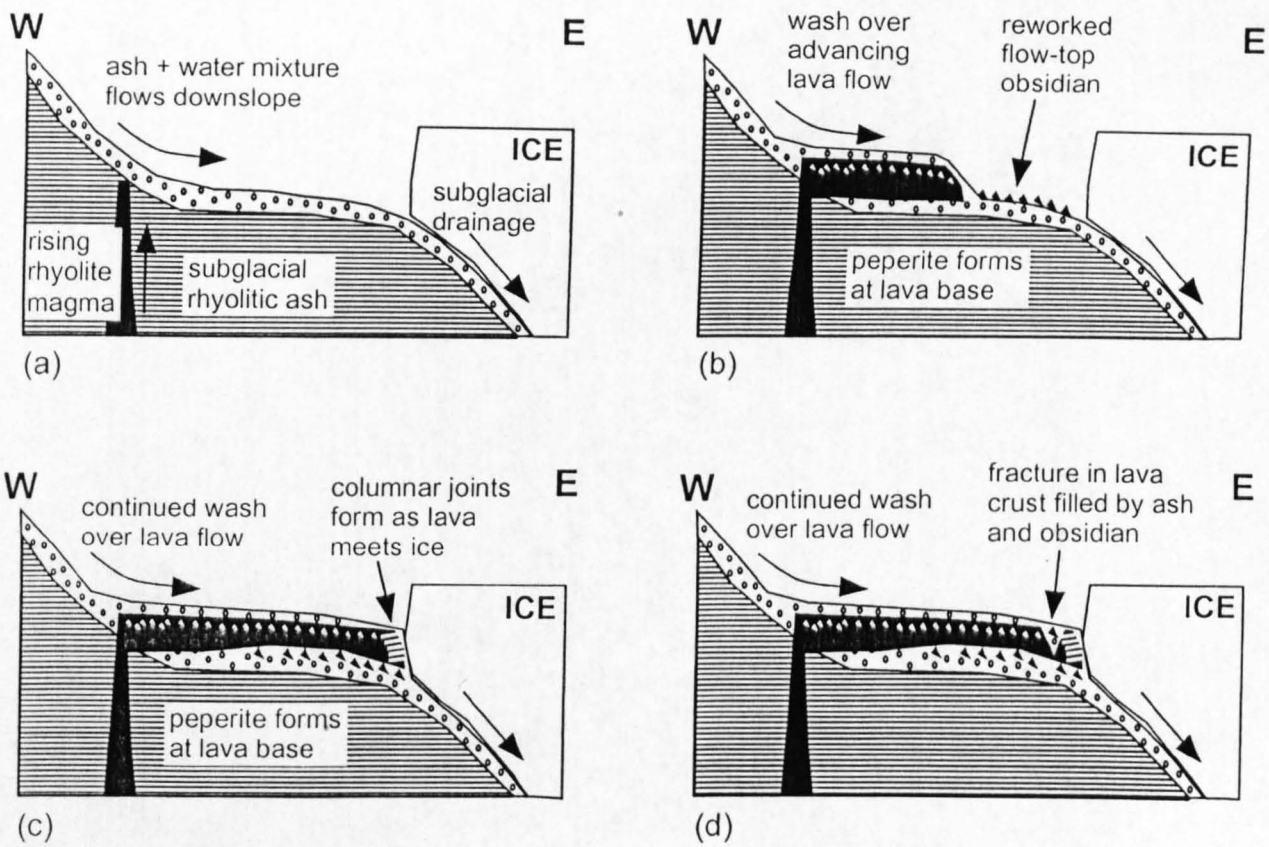

Fig. 3.14. A possible model for the emplacement of lava E. See text for a description of events. White triangles represent vesicular flow-top obsidian. From Tuffen et al. (in press).

carapace of the lava itself. Following this argument, it seems reasonable to suggest that the columnar-jointed upper carapace of the lava body burst open prior to complete quenching, creating a fracture that was filled by material spalled from its walls and by ash-dominated sediments that were washed in by flowing water. Sediments directly underlying the south-western lava, which are interpreted as water-lain, contain obsidian clasts that appear to be derived from the vesicular lava top (Fig. 3.13e). Fracturing of the lava carapace may have been triggered by (a) loading by sediments deposited on the lava surface or (b) melting and recession of the adjacent (and supporting) ice wall.

Combining the observations and inferences above, a similar scenario is envisaged for the emplacement of the peperitic lavas to that for lava D. Magma intruded subglacial rhyolite ash (Fig. 3.14a) and fed subaerial lava bodies that flowed over water-saturated sediments and chilled against an ice wall (Fig. 3.14b). Meanwhile, an ash-water mixture washed over the surface of the advancing lava, possibly flowing downslope from the main edifice 500 m to the north-west (Fig. 3.14b). This draped a thin deposit of wet ash over the top of the lava, which interacted with the hot, vesiculating upper carapace. It also picked up clasts of fragmented, vesicular obsidian from the lava surface and redeposited them at the foot of the lava (Fig. 3.14c). Brittle failure of the columnar-jointed nose of the lava, possibly triggered by recession of the adjacent ice walls, formed a fracture into which sediments were washed by flowing meltwater (Fig. 3.14d).

This peperite lithology is thought to be contemporaneous with lava D. The distribution of peperitic flow-top textures may thus indicate the position of ash-bearing currents of meltwater that drained over the lava from the main edifice above.

3.10. Lava F

3.10.1 Description

A dome-like exposure of pale grey obsidian crops out at 915 m elevation on the north-east flank of the volcano. The dome stands approximately 20 m above the surrounding slope and measures 100 m by 50 m. The obsidian contains ~20 % elongate, coalescing vesicles up to 10 mm in length, giving it a 'woody' texture. It consists of 95-100% grey, perlitised obsidian and 0-5 % spherical, unaltered black glass beads 3-5 mm across. The central part of the dome appears to consist of mostly intact obsidian and is surrounded by monomict breccia. The breccia drapes the sides of the dome and forms a sheet 1-4 m thick that extends up to 150 m downslope to the east (Fig. 3.3). It is clast-supported, crudely bedded and moderately well sorted, and contains angular clasts 5-25 cm across of woody, perlitised obsidian identical to the dome material. The Lava F breccia member of the Blautakvísl gully sequence (unit 7) overlies all other units in Blautakvísl gully.

3.10.2. Interpretation

Pervasive perlitisation of lava F suggests that the lava was thoroughly fluxed by water, possibly whilst still hot (Friedman et al. 1966, Davis & McPhie 1996); a scenario most likely to occur if the dome-like lava body cooled slowly. The apron of monomict breccia is thought to be talus derived from gravitational collapse of chilled, perlitised lava from the dome (Cas & Wright 1987). There is no evidence for subglacial or subaqueous emplacement, however perlitisation was probably caused by interaction with glacial meltwater. It is inferred that lava F represents a small-volume lava dome that is positioned directly above its (unexposed) feeder vent. This vent is colinear with the vents from which lava D and lava E were erupted (Fig. 3.3), speculatively suggesting that lavas D, E and F were formed late in the development of South-east Rauðufossafjöll, as activity became restricted to lava effusion from a north-south trending chain of vents.

3.11. Blautakvísl volcaniclastic sediments

Much information about eruptive and depositional processes can be gained from examining sequences of volcaniclastic sediments emplaced during a subglacial eruption (e.g. Smellie & Skilling 1994). Thus the complex succession of volcaniclastic sediments that crops out in the Blautakvísl stream gully, ~900 m north-east of the north summit (Fig. 3.3, Fig. 3.15a), is of fundamental importance for understanding the evolution of South-east Rauðufossafjöll. The stream gully is the lowest topographic point on the 6 km-long north-east - south-west trending ridge formed by South-east Rauðufossafjöll and the adjacent subglacial rhyolite tuya to the north-east.

3.11.1. Description

The sediments are 15 m thick and have dips of 20-30° to the south-east. They lie in an erosive channel cut into underlying subglacial ash. Only the northern side of the channel is exposed (Fig. 3.15a). The sediments comprise a succession of laterally discontinuous units, which display a wide variety of clast types, sizes, sorting and bedding characteristics, which are summarised in Table 3.2. A graphic log of the sedimentary succession is given in Fig. 3.15b, whereas Fig. 3.15c and Fig. 3.15d indicate the appearance of two units within the succession.

3.11.2. Interpretation

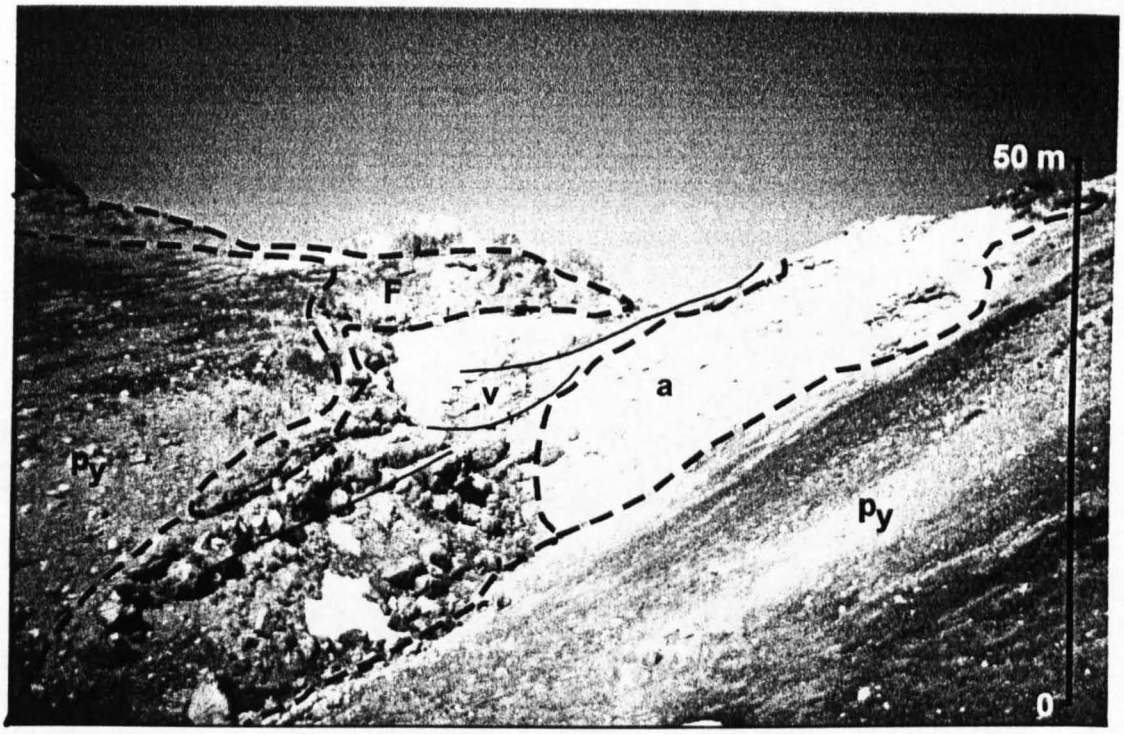

(a)

Fig. 3.15. (a) View of Blautakvísl gully, looking north-west up the stream. Volcaniclastic sediments (v) erosively overlie massive pale ash (a). Bedding in the sediments dips at approximately 20-30° to the left (i.e. south-east, solid black lines). A veneer of perlitic breccia overlying the sediments (F) is thought to be derived from collapse of lava F (top left corner). A blanket of Holocene pyroclastic deposits (py) covers the slope on the right hand side. Dotted black lines indicate approximate geological contacts.

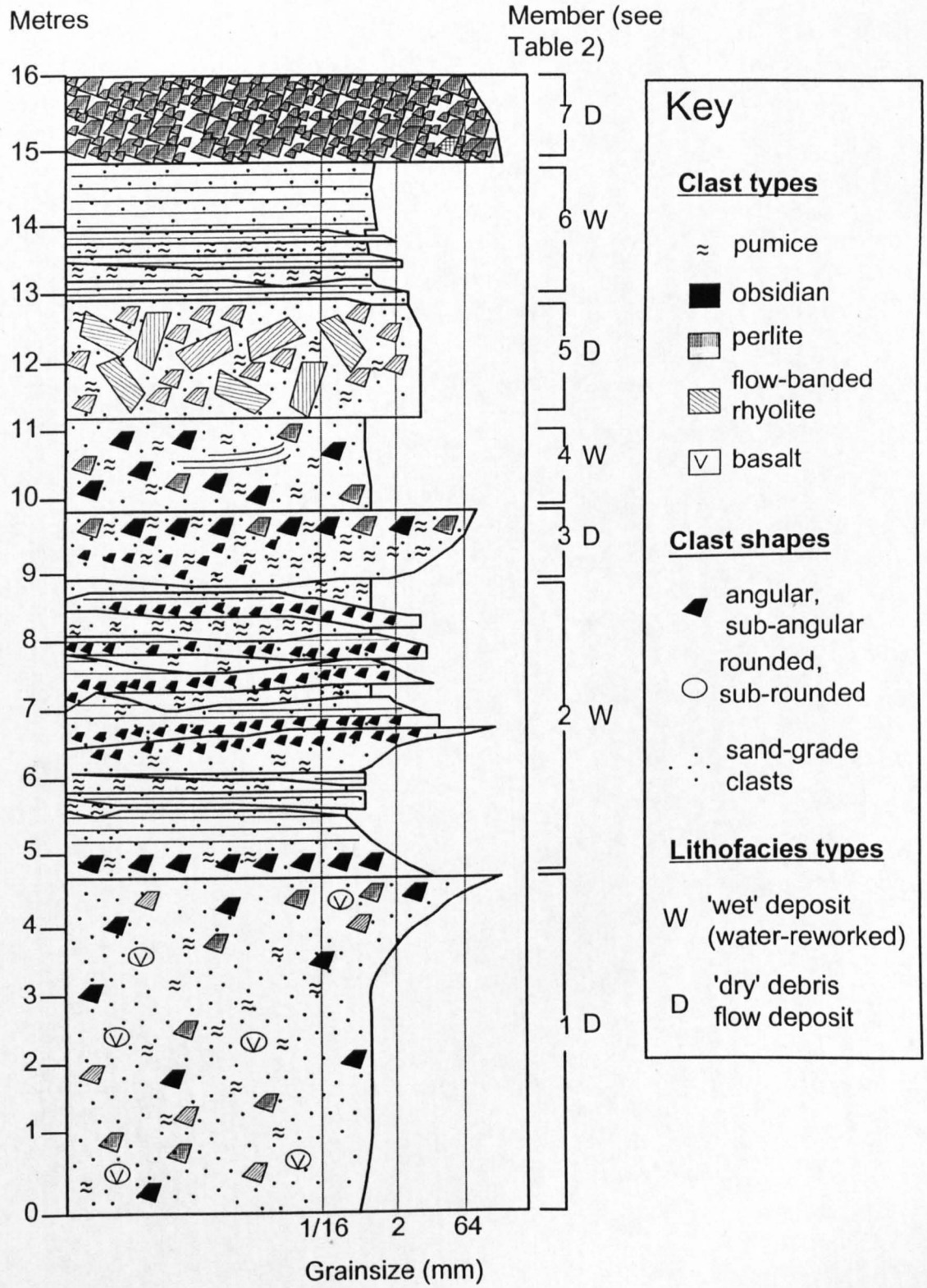

Fig. 3.15. (b) Simplified graphic log showing the major units in the Blautakvísl gully volcaniclastic sediments. See Table 3.2 for detailed descriptions and interpretations. From Tuffen et al. (in press).

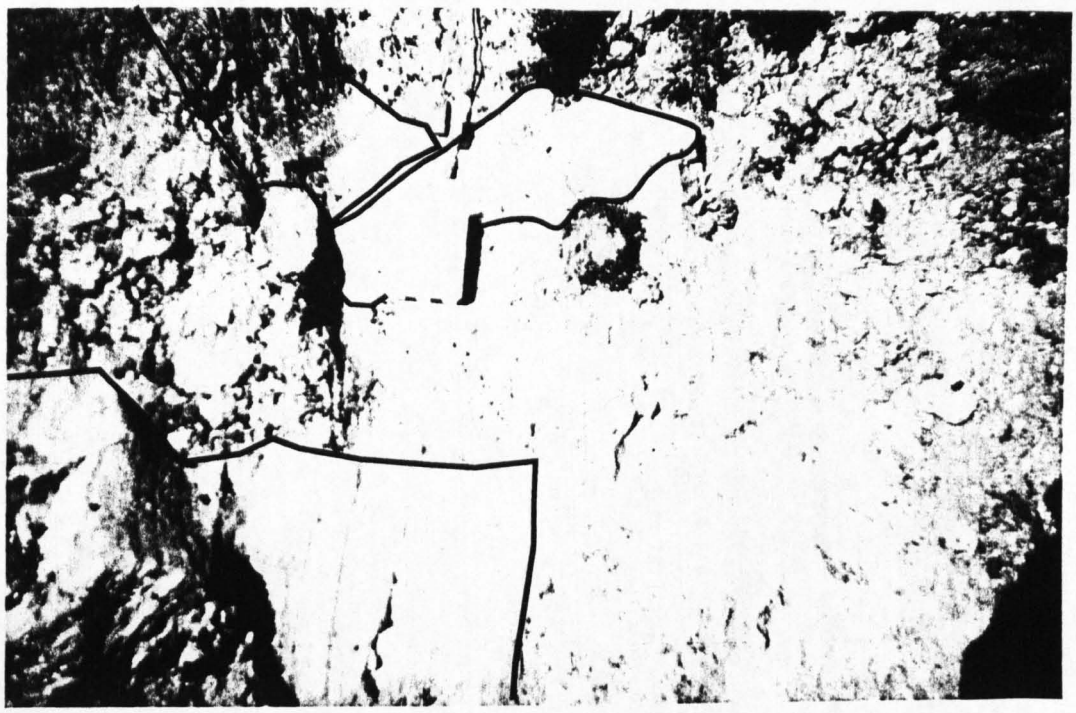

(c)

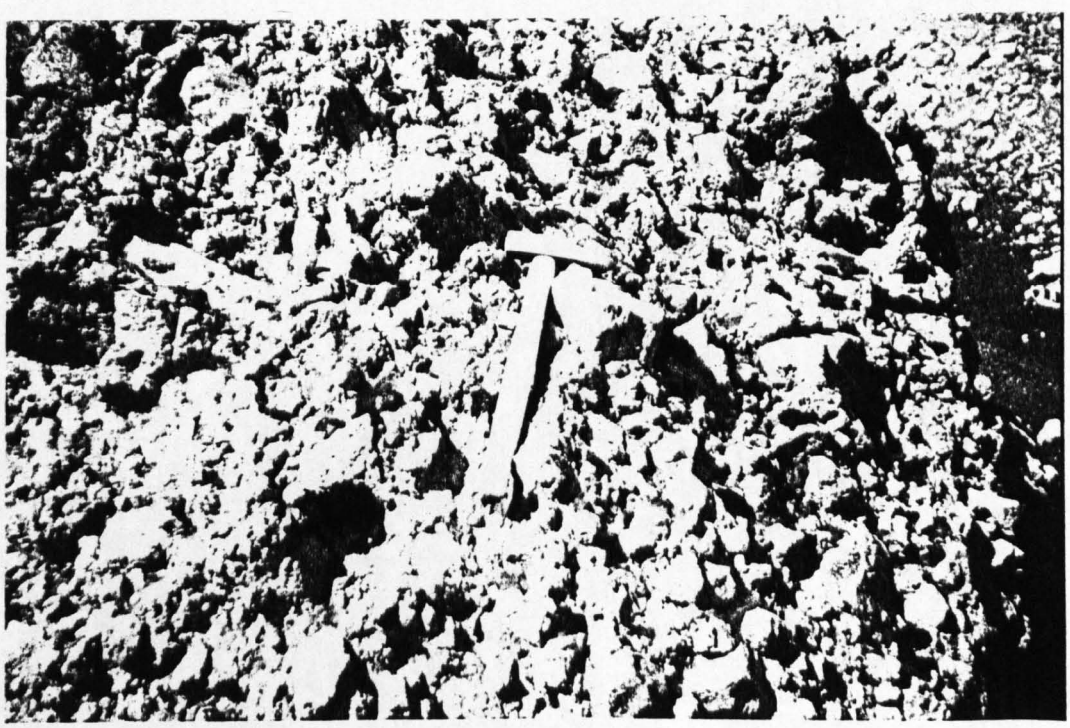

(d)

Figure 3.15. (c) Member 5 within the Blautakvísl volcaniclastic succession. The deposit is poorly sorted, with outsize clasts of flow-banded microcrystalline rhyolite (clast outlines indicated by black lines). Compass is 10 cm long. **(d)** Member 7 within the Blautakvísl volcaniclastic succession. The deposit is a moderately well-sorted clast-supported monomict breccia. Hammer is 30 cm long.

Table 3.2. Description and interpretation of the principal members within the volcaniclastic sedimentary sequence in Blautakvísl gully.
Abbreviations: bas - basalt, cry - crystal, obs - obsidian, perl - perlitic obsidian, pum - pumiceous rhyolite, rhy - microcrystalline rhyolite. Member 1 is the oldest, Member 7 the youngest. *Cas & Wright 1987, †Smellie et al. 1993, ‡McPhie et al. 1993.

Member	Description	Clast types	Other information	Interpretation
7	1-4 m-thick crudely-bedded poorly-sorted clast-supported monomict perl breccia.	Angular perl 5-25 cm.	Perl woody, 40 % vesicles, identical to Lava F perl.	Rock avalanche deposit from homogeneous body of perlitic obsidian (lava F) *.
6	2 m-thick planar-bedded well-sorted obs + pum gravelly sandstone. Beds 1-5 cm thick.	Sub-angular sand-grade obs + cry, sub-rounded pum 1-5 mm.	Laterally continuous over >10 m.	Traction current deposits, pulsing sediment supply*†.
5	1.5 m-thick massive poorly-sorted matrix + clast-supported rhy breccia.	Angular flow-banded rhy 0.1-80 cm, sub-rounded pum 1-5 cm. Matrix sub-angular coarse sand-grade obs + cry.	Laterally continuous over 10 m.	Deposit from a cohesive debris flow* derived primarily from collapse of a rhyolite lava body.
4	1.6 m-thick massive poorly-sorted matrix-supported polymict breccia, lenses of planar-laminated well-sorted gravelly sandstone.	Breccia: sub-angular perl + obs 0.5-20 cm, sub-rounded pum 1-5 cm. Gravelly sandstone: sub-angular perl 1-10 mm.	Laterally continuous over 10 m.	Episodic aggradation from debris flows, intermittent reduced particle flux and channelised water-reworking*.
3	1 m-thick reverse-graded massive poorly-sorted polymict breccia. Matrix-supported sandstone at base, clast-supported pebble breccia at top.	Base: sub-angular coarse sand-grade obs + cry. Top: sub-angular obs + perl + pum 0.5-50 cm, fine sand-grade obs + cry matrix.	Contains lenses of rounded pum.	Grain flows of obsidian and pumice followed by cohesive debris flows*‡.
2	4 m-thick sequence comprising 1-10 cm beds of matrix-supported pum + obs conglomerate, poorly-sorted obsidian breccia and lenticular-bedded gravelly obsidian sandstone.	Conglomerate: sub-rounded pum 0.5-4 cm, obs + cry <2 mm Gravelly sandstone: sub-angular obs + cry 1-5 mm. Obs breccia: sub-angular obs + cry 2 mm-5 cm.	Obs breccia grades upwards into gravelly sandstone.	Dense mass flows of obsidian, tops reworked by running water. Interspersed with pumice-bearing grain flows*‡ Fluctuating water and sediment flux.
1	5 m-thick massive poorly-sorted matrix-supported polymict breccia.	Sub-angular perl + rhy + obs + pum 0.5-20 cm. Sub-rounded bas 2-4 cm. Matrix fine sand-grade obs + cry.	Clasts coated by sand matrix, sand-filled veins 1-3 mm wide.	Fluidised debris flow deposit*, wide clast source. Matrix remobilised post-emplacement. Basalt clasts possibly derived from basement.

The wide range in sedimentology and clast types (Table 3.2, Fig. 3.15b) suggests a variety of depositional mechanisms and clast sources. The youngest member, lithology 7, is derived from gravitational collapse of perlitic lava dome lithology lava F. Lithology 7 (Fig. 3.15d), which is monomict and grades into the intact portion of the lava dome, is interpreted as a syn-eruptive unit. Thus it can be inferred that the entire volcaniclastic succession at Blautakvísl was emplaced during the eruption of South-east Rauðufossafjöll. The presence of water-lain sediments is strong evidence for meltwater drainage during the eruption, focussed at a topographic low on the subglacial rhyolite ridge. Variable clast types in different units of the sedimentary sequence point to variable eruption styles (e.g. forming pumice, microcrystalline rhyolite and perlitic obsidian), and a variable 'catchment area' from which clasts were derived. Lithologies 2, 4 and 6 show evidence for deposition by flowing water and are interbedded with lithologies 1, 3, 5 and 7, which appear to have been derived from dense gravity flows (Table 3.2, Fig. 3.15b). A possible explanation for this is that debris flow deposits may have been generated during subglacial melting events in which the recession of supporting ice walls destabilised growing piles of volcanic detritus (c.f. collapse events at Bláhnúkur, Fig 2.19c). The meltwater formed may have caused reworking of the tops of many of the debris flow deposits.

3.12. Bedded basalt-rhyolite sandstone

3.12.1. Description

Well-lithified orange-brown sandstone crops out on the north top of South-east Rauðufossafjöll, where it overlies lava B (Fig. 3.3). The sandstone forms a thin veneer (0.5-5 cm thick) that drapes over the irregular lava surface, on slopes of between 0 and

15°. Although the largest continuous exposure is a 1 × 2 m 'raft', discrete regions of patchy, discontinuous exposure have been identified, the largest measuring c. 30 × 20 m. The characteristics of this lithology are very variable, but it typically consists of planar- and cross-bedded well-sorted sandstones and gravelly sandstones. Bed thicknesses vary from <0.5 to 4 cm. Some thicker exposures include beds of massive, poorly-sorted gravelly sandstones up to 4 cm thick. Beds are commonly normally graded and seldom laterally continuous over more than 1 m. Two types of clast have been observed: ~70 % black basaltic clasts and ~30 % pale cream rhyolitic clasts. Basaltic clasts are sub-rounded, measure 1-8 mm in diameter and contain ~40 % near-spherical vesicles <0.5 mm in diameter. Rhyolitic clasts are sub-rounded, pumiceous and measure 1-4 mm in diameter. The relative proportions of clasts is variable - some beds are basalt-dominated and some are mixed, but rhyolite-only beds were not observed. The sandstone is resistant to weathering, due to the presence of an orange-brown cement between clasts.

3.12.2. Interpretation

This lithology is interpreted as mixed air-fall tephra which has been reworked and deposited by flowing water. It is thought to have been formed significantly after the emplacement of South-east Rauðufossafjöll. Laterally discontinuous beds on inclined surfaces may have been deposited by localised streams running over the lava surface. Clasts probably originated from subaerial explosive eruptions from nearby basaltic and rhyolitic volcanoes. A subglacial origin (i.e. till) is rejected, since a mud matrix is absent and there is no evidence for glacial erosion (e.g. striae). The source of water at this elevation is likely to have been snowmelt, rainfall or glacier melting.

In the preferred model, the ice level was higher than the tuya top, which was exposed as a nunatak (Fig. 3.16). Air-fall tephra from adjacent erupting volcanoes, which

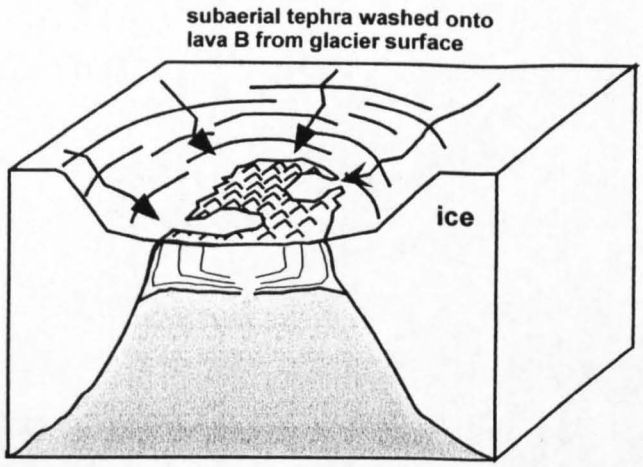

Fig. 3.16. A model for the emplacement of bedded basalt-rhyolite sandstone on the top of South-east Rauðufossafjöll. Tephra layers from neighbouring (subglacial?) volcanoes are reworked by supraglacial streams and deposited on the upper surface of the tuya-topping lava flows. Consolidation (palagonitisation?) of the tephra would be likely if the lava flow surface was still at an elveated temperature (>50 °C).

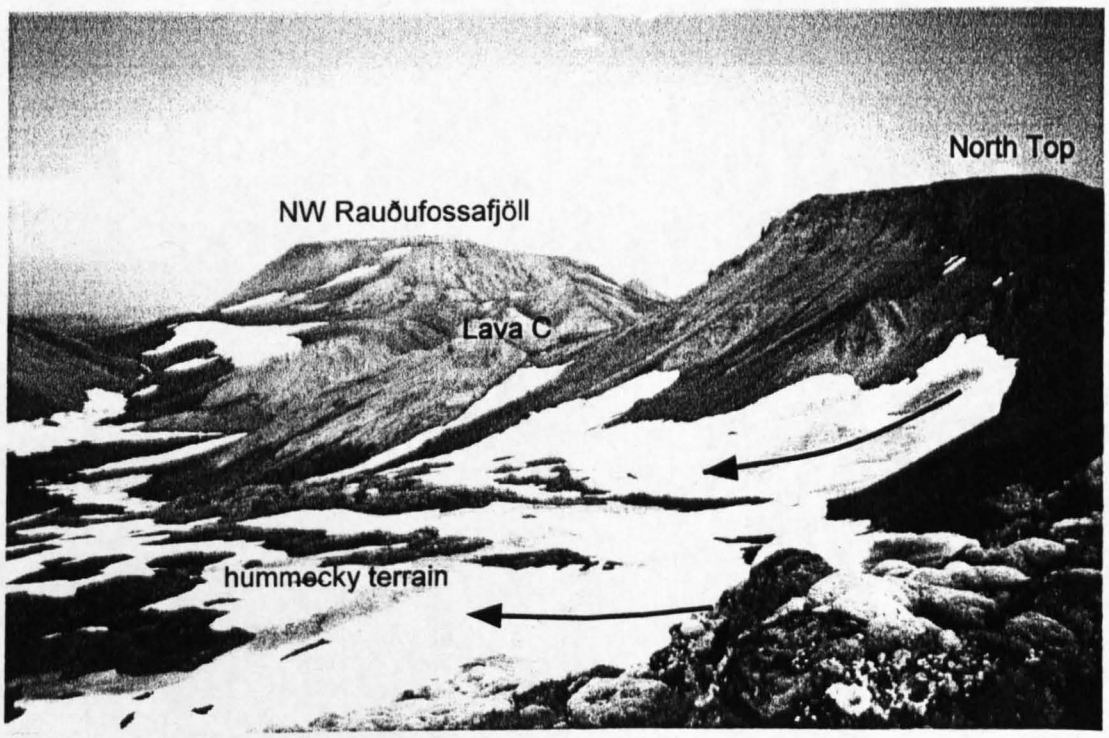

Fig. 3.17. View of the west flank of South-east Rauðufossafjöll, looking north from the west side of the South Top. The hummocky terrain (lower left) consists of postglacial debris avalanche deposits derived from collapse of the west flank of the volcano. Arrows indicate the probable directions of travel of the deposits, which spread up to 600 m from their source.

accumulated on the glacier surface, was carried by supraglacial streams and redeposited on the top of the tuya. In this case, these sandstones may be an important proximal record of subaerial eruptions in Iceland during glacial periods. Geochemical analysis of the tephra could perhaps be used to determine the source volcano. Similar basalt-rhyolite sandstones have been observed on the summit of other tuyas at Torfajökull, including Kirkjufell and North-east Rauðufossafjöll. The origin of the cementation is not clear. Palagonitisation occurs at temperatures above 50°C (Jakobsson 1978). It is unlikely that these water-lain sediments were deposited at such a high temperature, unless they were emplaced onto a still-hot lava surface (which is the scenario illustrated in Fig. 3.16).

3.13. Basaltic diamicton

3.13.1. Description

Brown-orange basaltic breccias crop out on the Eastern Plateau and on the north of Blautakvísl gully (Fig. 3.3). On the Eastern Plateau they forms rocky knolls 5-150 m across and 0.5-2 m thick. The greatest thickness observed (5 m) was at 840 m elevation on the north bank of Blautakvísl gully. The breccias overly the subglacial rhyolite formations of South-east Rauðufossafjöll. The breccias vary from well-sorted planar-bedded gravelly sandstone to massive, poorly-sorted matrix-supported breccia containing pillow fragments 1-20 cm across. Clasts are basaltic, including vesicular, glassy lapilli and holocrystalline lava. Orange-brown cement is similar to that of the basalt-rhyolite sandstone.

3.13.2. Interpretation

This nature of this lithology is similar to published accounts of fragmental, water-lain subglacial basalt formations in Iceland (*hyaloclastite* of Jones 1968, Werner et al. 1996).

A subglacial origin is also inferred here, although there is no direct evidence for a subglacial environment. The position of the source vent for the diamicton is not clear, although subglacial basalt ridges occur <1 km east of the Eastern Plateau. The presence of diamicton overlying lava D suggests that a glacier has attained at least the height of the Eastern Plateau (900 m) since the subglacial rhyolite eruption at South-east Rauðufossafjöll. However, it is not clear whether the diamicton and the rhyolitic lithologies were emplaced during the same glacial period.

3.14. Postglacial debris avalanche deposits

Two prominent amphitheatres on the west flank of South-east Rauðufossafjöll, 400 m and 500 m across (Fig. 3.3) are thought to be the source of postglacial debris avalanche deposits that extend 500-600 m to the northwest (Fig. 3.17). These amphitheatres cut deep into the lava cap of South-east Rauðufossafjöll, and expose cliffs of lavas A and B up to 150 m high. The debris avalanche deposits form three discrete 'tongues' 250-350 m wide and estimated to be >20 m thick. The deposits consist of angular blocks of microcrystalline rhyolite with minor obsidian and pumiceous material up to 5 m across. The range of lithologies observed exactly matches that within lava A and lava B. The hummocky surface of the deposits is characterised by elongate ridges 5-10 m high and 50-100 long that are commonly aligned north-east - south-west, normal to the inferred flow direction (to the northwest, Fig. 3.3). Similar ridges have been observed in debris avalanche deposits on the flanks of Andean volcanoes (e.g. Francis et al. 1985, Gardeweg et al. 1998). Volcano collapse may have been triggered by deglaciation. Similar debris avalanche deposits were observed on the east flank of North-west Rauðufossafjöll.

3.15. Discussion: emplacement mechanisms

In developing a model for the evolution of the South-east Rauðufossafjöll rhyolite tuya, it has been assumed that it is the product of one eruptive event that occurred during only one glacial period. No evidence has been found that would suggest otherwise: such as glacial or interglacial deposits intercalated with subglacial eruptive units, or major erosional horizons. Supporting evidence for a single sustained eruption comes from whole-rock geochemistry. On the basis of geochemical coherence, McGarvie (1984) argued that Rauðufossafjöll and the other rhyolite tuyas fringing Torfajökull (Fig. 3.1) constituted a single eruptive episode. The small-scale variation in whole-rock geochemistry - across the range of products of c.17 km^3 of subglacial rhyolite - supports the view that South-east Rauðufossafjöll was produced during a single eruptive event.

3.15.1. Subglacial ash-producing phase

A subglacial eruptive environment is inferred for the ash deposits on the lower flanks of South-east Rauðufossafjöll. This is because (1) they are locally intruded by perlitic and by peperitic lava bodies, suggesting that they were water-saturated, most probably by glacial meltwater, and (2) they are overlain by lava flows that show characteristic ice-marginal features. Thus it is envisaged that the ash was produced during explosive activity within an ice vault (Fig. 3.18a). Blocky shard morphologies suggest that fragmentation was mostly driven by magma-meltwater interaction, with minor degassing of magmatic volatiles (Heiken & Wohletz 1985). Although this suggests that some water was present in the vault, the lack of sedimentary structures consistent with aqueous reworking in the bulk of the ash deposits indicates that a body of standing water did not develop (c.f. Skilling 1994).

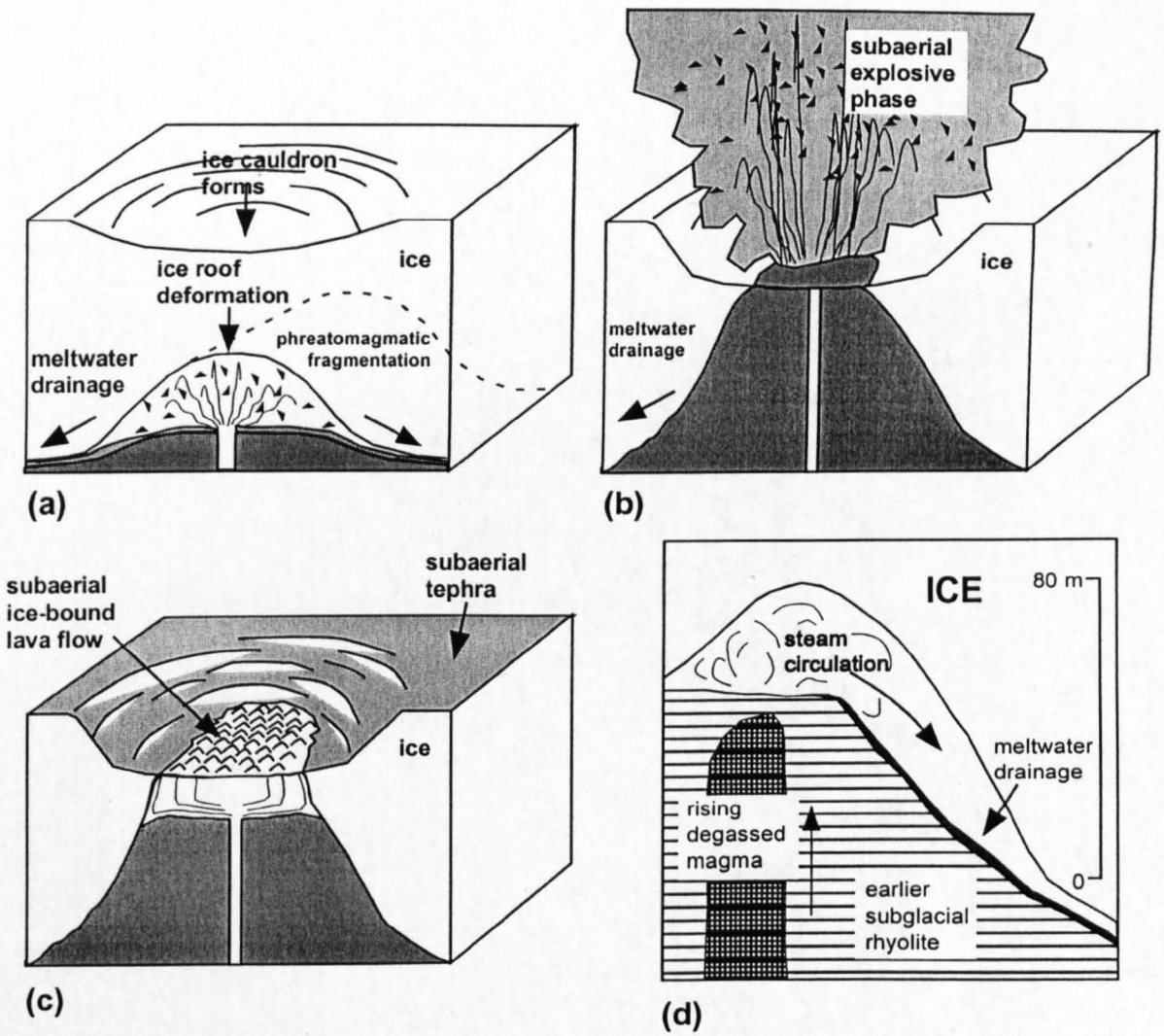

Fig. 3.18. The main stages in the proposed evolution of South-east Rauðufossafjöll. See text for discussion of each stage. Modified from Tuffen et al. (in press).

In the preferred model, meltwater drained from the vent area (as in the 'leaky vault' scenario of Smellie 1999) during confined phreatomagmatic explosions within an ice vault (Fig. 3.18a). Pressure was likely to have been near-atmospheric, as exiting meltwater formed a hydrological connection with the glacier snout (Hooke 1984, Björnsson 1988). The void space formed by melting and subsequent meltwater escape was filled by a pile of poorly-consolidated tephra. The thermal energy of the magma was transferred to the ice mostly by convecting steam, with minor mechanical abrasion as tephra collided with the ice walls. The vault volume was controlled by the comparative rates of melting and ice deformation (Kiver & Steele 1975, Cutler 1998). The vault may have become completely filled if its volume was unable to increase sufficiently rapidly to accommodate the growing pile of tephra. If this occurred, the vault pressure may have increased to near-glaciostatic (≤4 MPa for 400 m ice thickness), causing a switch to an intrusive phase of eruption. This may have been the case when peperitic intrusions were emplaced within the fine-grained ash north of Blautakvísl gully (Fig. 3.4c). Vault volumes and eruption mechanisms are discussed further in Chapter 5.

This eruption mechanism contrasts with that inferred for the small-volume subglacial rhyolite eruption at Bláhnúkur (Fig. 2.19). At Bláhnúkur, which is an order of magnitude less voluminous than South-east Rauðufossafjöll, lava bodies intruded fragmental debris generated by steam-quenching [hyaloclastite], with minor explosivity (Furnes et al. 1980). The ice roof appears to have always been <20 m above the growing edifice, and a large ice vault never developed. It is suggested that melting rates were considerably higher during the subglacial eruption at South-east Rauðufossafjöll, consistent with a greater eruption rate during a much larger eruption.

3.15.2. Transition to subaerial eruption

The only evidence that the eruption pierced the roof of the ice vault and became subaerial comes from the characteristics of the lava flows on the summit ridge. Unfortunately, the base of these lava flows and contacts with the underlying ash are not exposed. Any tephra emplaced subaerially within an ice cauldron is susceptible to erosion and unlikely to be preserved, whereas a robust, degassed lava cap has a much higher preservation potential. Therefore, the lithofacies architecture of ancient subglacial rhyolite volcanoes may be strongly influenced by the relative timing and magnitude of explosive and effusive phases of eruption (Eichelberger et al. 1986). An entirely explosive eruption may include a subaerial, plinian phase, but produce no lava cap. Thus it will form an edifice that consists entirely of fragmental material, and which is liable to be misinterpreted as entirely subglacial.

It can only speculated as to whether South-east Rauðufossafjöll produced a major subaerial explosive eruption (represented in Fig. 3.18b). Analysis of the age and composition of silicic tephra layers in ice cores (Zielinski et al. 1997), deep-sea sediments (Lacasse et al. 1995) or peat bogs (Dugmore et al. 1995) and correlation with Icelandic source volcanoes may provide the answer. However, tephra from smaller-magnitude subaerial eruptions may only accumulate on the adjacent glacier surface and not be represented in the tephrochronological record.

The summit lava flows (lava A and B) were probably emplaced within ice cauldrons (Fig. 3.18c), with ice walls ≤100 m high (Smellie 1999). In Chapter 5 ice deformation patterns are used to predict the depth of ice cauldrons that develop during the formation of rhyolitic tuyas.

3.15.3. Columnar-jointed lava phase

The columnar-jointed lava bodies that crop out at 900-1000 m elevation on the north and west flanks appear to have chilled against steeply-inclined ice walls. Lack of vesicles suggests that they were largely degassed. In the preferred model, these lavas were emplaced at a late stage of the eruption, as effusive activity began from vents situated on the flanks of the edifice. Lavas, rather than phreatomagmatic tephra may have been produced due to a low eruption rate. High heat flux preceding lava emplacement may have melted cavities in the ice above the new flank vents, creating 'moulds' into which the lavas flowed (c.f. flow lobe emplacement at Bláhnúkur, Chapter 2). Drainage of meltwater and circulation of steam may have created a steep-walled subglacial cavity (Kiver & Steele 1975), especially if the vent was located on a steep slope (Fig. 3.18d). This lithology is similar to the columnar-jointed lava lithology of Bláhnúkur (Chapter 2.9).

3.15.4. Peperitic lava phase

The upper carapace of lava D is characteristic of subaerial rhyolite lava flows, whereas its sides appear to have chilled against inclined ice walls, and its base has flowed over wet, poorly-consolidated sediments. To explain this unusual combination of features, lava D could have been formed when a series of effusive vents became active on the edge of the eastern plateau, forming lavas which flowed over waterlogged breccias before freezing against an ice wall. The presence of 'rafts' of bedded ash directly underlying the lavas suggests that the massive breccias were locally redeposited by running meltwater prior to lava effusion.

One possibility is that lava D was emplaced after the construction of the main edifice. In this scenario, the glacier may have receded to ~900 m surface elevation in the entire South-east Rauðufossafjöll area, forming a 'moat' of ice around the edifice. Lava D

then flowed subaerially before abutting the ice walls. However, it is anticipated that wholesale retreat of ice from around the lavas of the summit ridge would trigger major instability and spalling of debris, forming a talus deposit on top of the fragmental material and underlying lava D. Such a talus deposit was not observed, suggesting that the surface underlying lava D was protected from spalling debris, possibly by a roof of ice. One possibility is that the lava was emplaced within a large, drained ice vault, but this is problematic, since such a vault is likely to be rapidly closed by ice deformation.

3.16. Comparison with basaltic tuya sequences

Rhyolitic tuyas such as South-east Rauðufossafjöll are morphologically similar to basaltic tuyas. Both consist of a subglacial portion, dominated by fragmental deposits, that is overlain by near-horizontal subaerial lava flows (Table 3.3). However, the fragmental deposits have contrasting sedimentological features. These indicate that the ice vault formed during a rhyolitic eruption is well-drained of meltwater, whereas meltwater tends to accumulate during a basaltic eruption. This has profound effects on the mechanisms of magma-ice interaction and edifice construction.

It is suggested that a rhyolitic eruption will commence with an ice-confined phreatomagmatic phase. Magma-water interaction will be explosive and at low pressures, unless the melting rate wanes and the vault becomes filled with tephra. Upon transition to a subaerial eruption, there is likely to be little meltwater available for interaction with rising magma. Therefore, explosive activity may only occur if the magma is sufficiently volatile-rich to generate a 'dry' magmatic eruption. This may explain the similar morphology of distal rhyolitic ash shards formed during subaerial and subglacial-to-emergent eruptions in Iceland (Hafliðason et al. 2000).

Basaltic tuya-building eruptions typically begin with the effusion of pillow lavas. Magma-water interaction becomes increasingly energetic as the confining pressure decreases (e.g. Jones 1968, Smellie 1999). Once the ice surface is breached and a subaerial eruption ensues, meltwater ponded at the vent is likely to interact explosively with rising magma, triggering an eruption of ash and steam (Guðmundsson et al. 1997). Distal tephra from subglacial-to-emergent eruptions of basalt

Table 3.3. Differences between basaltic and rhyolitic tuyas, from Tuffen et al. (in press).

*Smellie & Hole 1997, †Smellie 1999, ‡Jones 1968, §Björnsson 1988, ¶This study.

Basaltic tuya	Rhyolitic tuya
Subaerial lava flows 1.5-20 m thick*.	Subaerial lava flows 10-150 m thick¶.
Hyaloclastite - increasingly vesicular with height, commonly bedded in turbidite sequences (Surtseyan succession)†. Pillow lava - high-pressure lithofacies (deep water/filled vault) †.	Poorly-sorted, unbedded phreatomagmatic ash¶.
Energy initially transferred from magma to ice via convecting meltwater, then by steam.	Energy transferred primarily by steam.
Fragmental subglacial deposits well exposed due to palagonitization‡.	Fragmental subglacial deposits poorly exposed and mostly scree-covered¶.
Meltwater accumulates at the vent area†.	Meltwater drains away from the vent area¶.
High-magnitude jökulhlaups likely due to meltwater accumulation§.	Low-magnitude jökulhlaups likely due to gradual meltwater release¶.
Presence of ice above volcano increases likelihood of subaerial tephra-producing eruption¶.	Likelihood of tephra-producing eruption not greatly increased by presence of ice¶.

has blocky shard morphologies consistent with phreatomagmatic fragmentation (Hafliðason et al. 2000). Since Icelandic basaltic tuyas are thought to be the subglacial

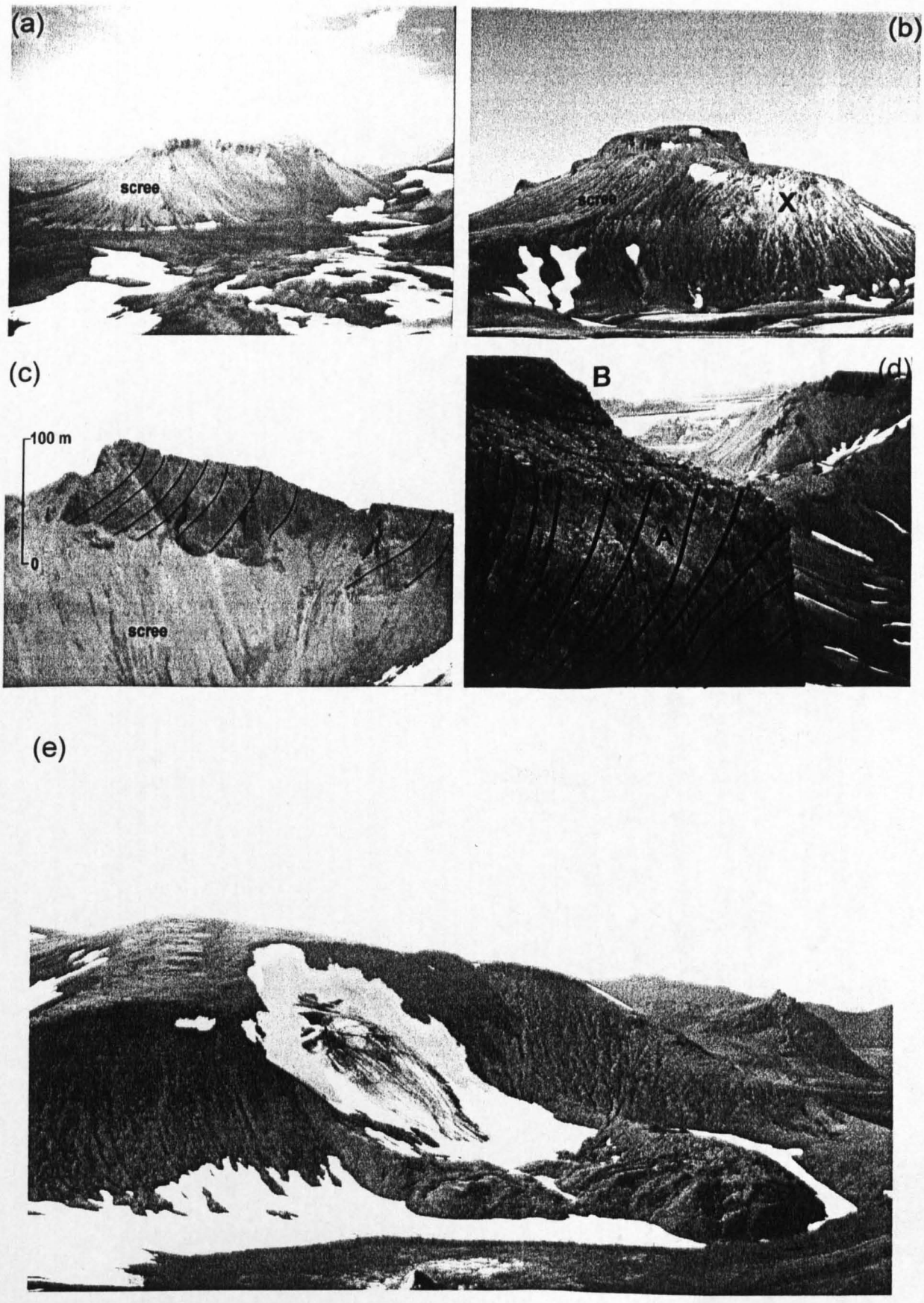

Fig. 3.19.

Fig. 3.19. **(a)** South-west Rauðufossafjöll viewed from the South Top of South-east Rauðufossafjöll. Note the scree-covered flanks and subhorizontal lava cap. The hummocky terrain in the foreground is postglacial avalanche deposits from South-east Rauðufossafjöll. **(b)** North-east Rauðufossafjöll from the east. A subhorizontal lava cap 50-100 m thick rises above scree-covered slopes. Pale deposits on the flank (X) are a veneer of downslope-dipping debris flow deposits <5 m thick which overlie unconsolidated fine-grained pale ash similar to that observed at South-east Rauðufossafjöll.
(c) The lava cap of Kirkjufell, viewed from the southwest. Flow banding within the lava steepens to near-vertical at the upper carapace. There is a 4-m-thick zone of pumiceous obsidian at the top of the lava, similar to that observed on lavas A and B of South-east Rauðufossafjöll, and characteristic of subaerial rhyolite lava flows. **(d)** Contact between a steeply-ramped lower lava flow (>100 m thick) and an overlying near-horizontal flow only 10 m thick, on a pre-Kirkjufell formation 2 km southwest of Kirkjufell. **(e)** Postglacial avalanche deposit and amphitheatre on the north-east flank of north-west Rauðufossafjöll. The avalanche deposit is 25 m thick and has travelled 400 m. Hekla is in the background.

---

equivalent of an effusive shield volcano, the presence of a overlying glacier increases the likelihood of an explosive subaerial eruption.

Field observations of rhyolitic and basaltic tuyas therefore support the simple thermodynamic models of Hoskuldsson & Sparks (1997), which predict meltwater drainage during rhyolitic eruptions and accumulation during basaltic eruptions. These models involve convecting meltwater as the energy exchange medium. The next step in the understanding of subglacial rhyolite eruption mechanisms is to place better constraints on the patterns of steam-driven melting and ice deformation in well-drained ice vaults.

3.17. Comparison with other rhyolitic tuyas at Torfajökull

The lithofacies architecture of South-east Rauðufossafjöll is similar to that observed at other rhyolitic tuyas at Torfajökull. In addition, the elevation and vertical height of South-east Rauðufossafjöll coincide with those of the other tuyas of the Kirkjufell formation

(Fig. 3.1), thought to have been emplaced during a single eruptive episode (McGarvie 1984). The summit elevation and height from base to top of South-east Rauðufossafjöll are 1206 m and 450 m respectively, comparable to North-east Rauðufossafjöll (1221 m, 400 m), South-west Rauðufossafjöll (1174 m, 380 m), North-west Rauðufossafjöll (1235 m, 450 m), Laufafell (1184 m, 500 m) and Kirkjufell (974 m, 370 m). All tuyas have basal portions dominated by poorly-exposed fragmental lithologies, scree-covered flanks and are capped by one or more subhorizontal lava flows (Fig. 3.19a-c). These lavas are generally 50-150 m thick and have steeply ramped flow banding (Fig. 3.19c-d), local development of near-horizontal columnar joints on flow sides, pumiceous flow tops and bases concealed by scree (Fig. 3.19c). Both South-east and North-west Rauðufossafjöll have suffered postglacial collapse events, which have carved amphitheatres into the flanks (Fig. 3.19e) and greatly improved the exposure of lava flows. Of the tuyas observed at Torfajökull, South-east Rauðufossafjöll has the best exposure of basal fragmental lithologies, which is nevertheless patchy. This is the fortuitous result of post-eruptive erosion patterns, and was a major factor in choosing South-east Rauðufossafjöll to study as a 'model rhyolitic tuya'.

3.18. Summary

South-east Rauðufossafjöll is typical of rhyolitic tuyas at Torfajökull. Lithofacies associations indicate distinct eruption mechanisms from those at basaltic tuyas, which are best explained by contrasting hydrological patterns caused by the temperature differences between the two magma types (Hoskuldsson & Sparks 1997).

In the initial subglacial phase, explosive magma-water interaction generated a pile of fine-grained ash within a well-drained ice vault. After the glacier surface was

breached, subaerial lava flows were emplaced within ice cauldrons above the ~2 km-long eruptive fissure. Effusive eruptions on the north and west flanks of the tuya created columnar-jointed lava flows, which were emplaced against steeply-inclined ice walls over 80 m high. Lava bodies on the east flank are interpreted as subaerial flows which travelled over wet sediments before freezing against an ice wall. A succession of volcaniclastic sediments at the northern margin of the tuya indicate channelised meltwater drainage from the vent area during the eruption. The style of eruption was probably controlled by patterns of interaction with water (e.g. Brooker et al. 1993), magma volatile content and ascent rate, constraint by ice and the effective pressure (Chapter 5). Reasons for the differences between the subglacial rhyolite sequences at South-east Rauðufossafjöll and Bláhnúkur are considered in Chapter 5, and the relative influence of eruption rate, magma volatile content and ice thickness are assessed.

Chapter 4.
Subglacial rhyolite at Dalakvísl, Rauðufossafjöll

4.1. Overall structure

Dalakvísl is a stream that flows through a deeply incised region 3 km north-east of the easternmost tuya of Rauðufossafjöll (Fig. 4.1). The terrain, which is predominantly formed by subglacial basaltic formations and till, ranges from 600 m to 900 m elevation. There is a hill bounded by Rauðufossakvísl to the west and Dalakvísl to the east that is composed of rhyolite (Fig. 4.2). This has been given the name Dalakvíslfell. It has two rounded summits at roughly 900 m elevation, gentle slopes to the west and steeper slopes to the east, with good exposure of subglacial rhyolite in valleys incised by Dalakvísl and its tributaries (Fig. 4.2).

Dalakvíslfell is prominent in views from the north-east, since the pale colour of fragmental rhyolitic lithologies exposed on its eastern flanks is conspicuous (Fig. 4.2). Based on the geological contacts exposed and the local topography, it is estimated that rhyolite has added less than 200 m to the height of Dalakvíslfell. Collectively, the rhyolitic lithologies are termed the Dalakvísl rhyolite formation. Geomorphologically, Dalakvísl is very different from the tuyas of Rauðufossafjöll, since it lacks a flat top and is considerably smaller in volume (< 0.2 km^3, compared to ~ 1 km^3). The relationship between the rhyolite at Dalakvísl and that of the neighbouring tuyas of Rauðufossafjöll is unclear. Preliminary geochemical analysis indicates that the magma erupted at Dalakvísl is of similar composition to that of the Rauðufossafjöll tuyas (D. W. McGarvie, unpublished data). However, their relative ages cannot be determined in the field, and the rocks are yet to be dated isotopically.

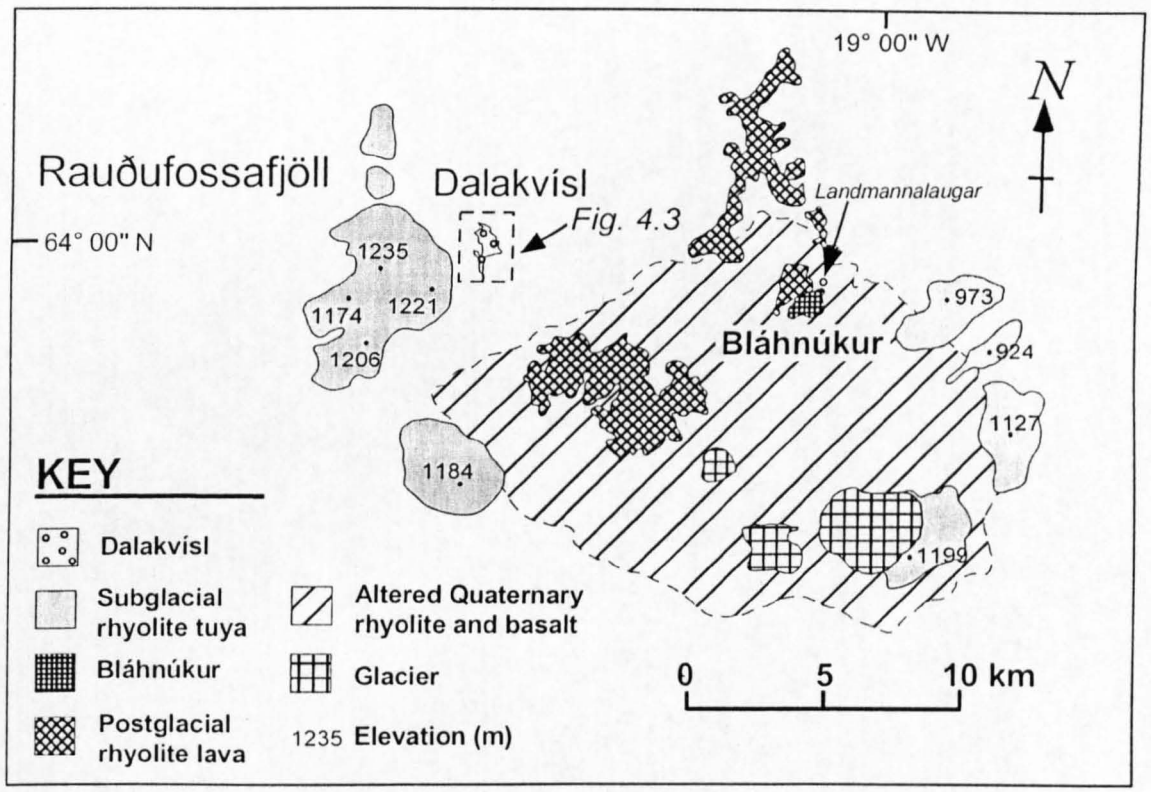

Fig. 4.1. A simplified geological map of the Torfajökull volcanic complex, showing the location of subglacial rhyolite formations at Dalakvísl, 3 km north-east of the north-eastern tuya of Rauðufossafjöll. The area covered by the detailed geological map (Fig. 4.3) is indicated.

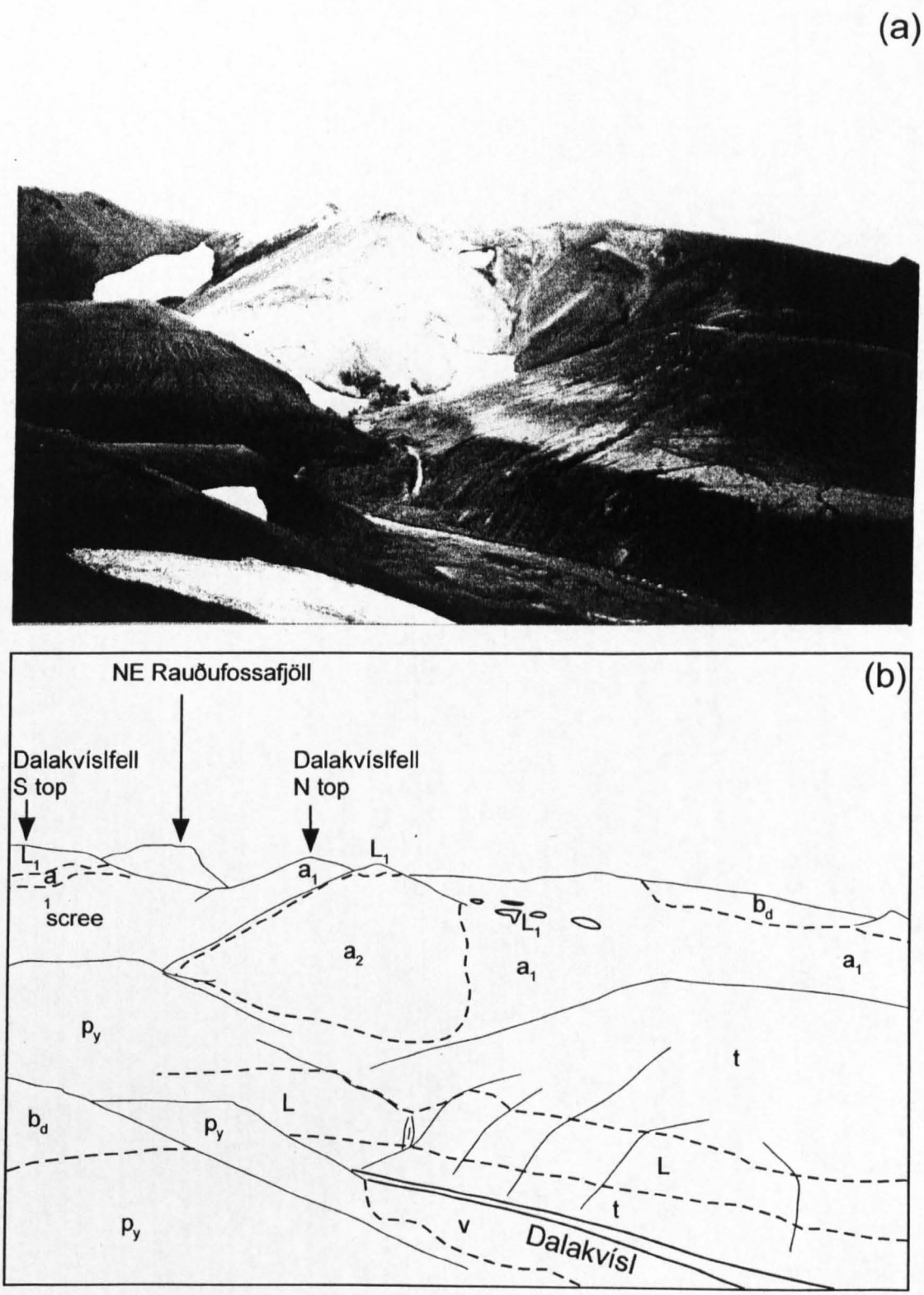

Fig. 4.2. (a) View westwards across the valley incised by Dalakvísl from point X on Fig. 4.3. The prominent pale ridge consists of poorly-consolidated ash-dominated breccias. **(b)** Annotated sketch of the view in a), indicating the major lithological units. Symbols: a_1 = breccia 1, a_2 = breccia 2, L_1 = lava 1, L = basaltic lava flow, b_d = basaltic diamicton, t = till, p_v = Holocene pyroclastics.

The rhyolite deposits at Dalakvísl were chosen for detailed study because of the relatively good exposure of fragmental lithologies, due to the deep incision by stream valleys. As at Bláhnúkur (Chapter 2) and South-east Rauðufossafjöll (Chapter 3), there is abundant evidence for a subglacial eruptive setting (e.g. columnar jointing patterns, perlitisation, magma-water interaction). A flat lava cap is absent, so there is less talus draping the volcano slopes than at South-east Rauðufossafjöll and other tuyas. Some lithologies are similar to those observed at Bláhnúkur and South-east Rauðufossafjöll, and were probably formed during similar styles of magma-ice interaction and meltwater drainage. However, some lithologies have no equivalent observed elsewhere, and may shed light on processes that occurred during the subglacial tephra-generating phase of the eruption. Overall, the eruption style at Dalakvísl appears to have been intermediate between Bláhnúkur and South-east Rauðufossafjöll.

4.2. Evidence for a subglacial environment

The following features suggest that the Dalakvísl formation was erupted under ice:

(1) The Dalakvísl formation is locally overlain by conglomerates that contain rounded and facetted clasts in a mud-grade matrix and are interpreted as subglacial tills (e.g. Bennett & Glasser 1996).

(2) Some lithologies within the Dalakvísl formation contain dykes and veins that are infilled with till-like material. To date, veins of this type have only been observed elsewhere in a subglacial setting (Rijsdijk et al. 1999).

(3) There is abundant evidence for magma-water interaction, such as perlitised obsidian, peperitic intrusions and blocky ash shards, in lithologies at elevations up to 910 m. There is no evidence for the existence of a palaeo-topography which could have confined a non-glacial lake (see also Jones 1968, Smellie & Skilling 1994, Smellie & Hole 1997). The current elevation, in the absence of any tectonic structures consistent with uplift, is a convincing argument against a submarine setting. Furthermore, marine fossils are absent. Glacier melting is thus the most likely source of water.

(4) Columnar-jointed rhyolite lava bodies occur at up to 840 m elevation. Their morphologies and joint orientations are best explained by chilling against ice walls (e.g. Lescinsky & Sisson 1998).

4.3. Lithofacies descriptions and interpretations

The geological map (Fig. 4.3) has been compiled from observations made during fieldwork in the summers of 1999 and 2000. Collectively, the rhyolitic lithologies are termed the Dalakvísl rhyolite formation. The Dalakvísl rhyolite formation has been divided into four distinct breccia lithologies and four lava lithologies, which are

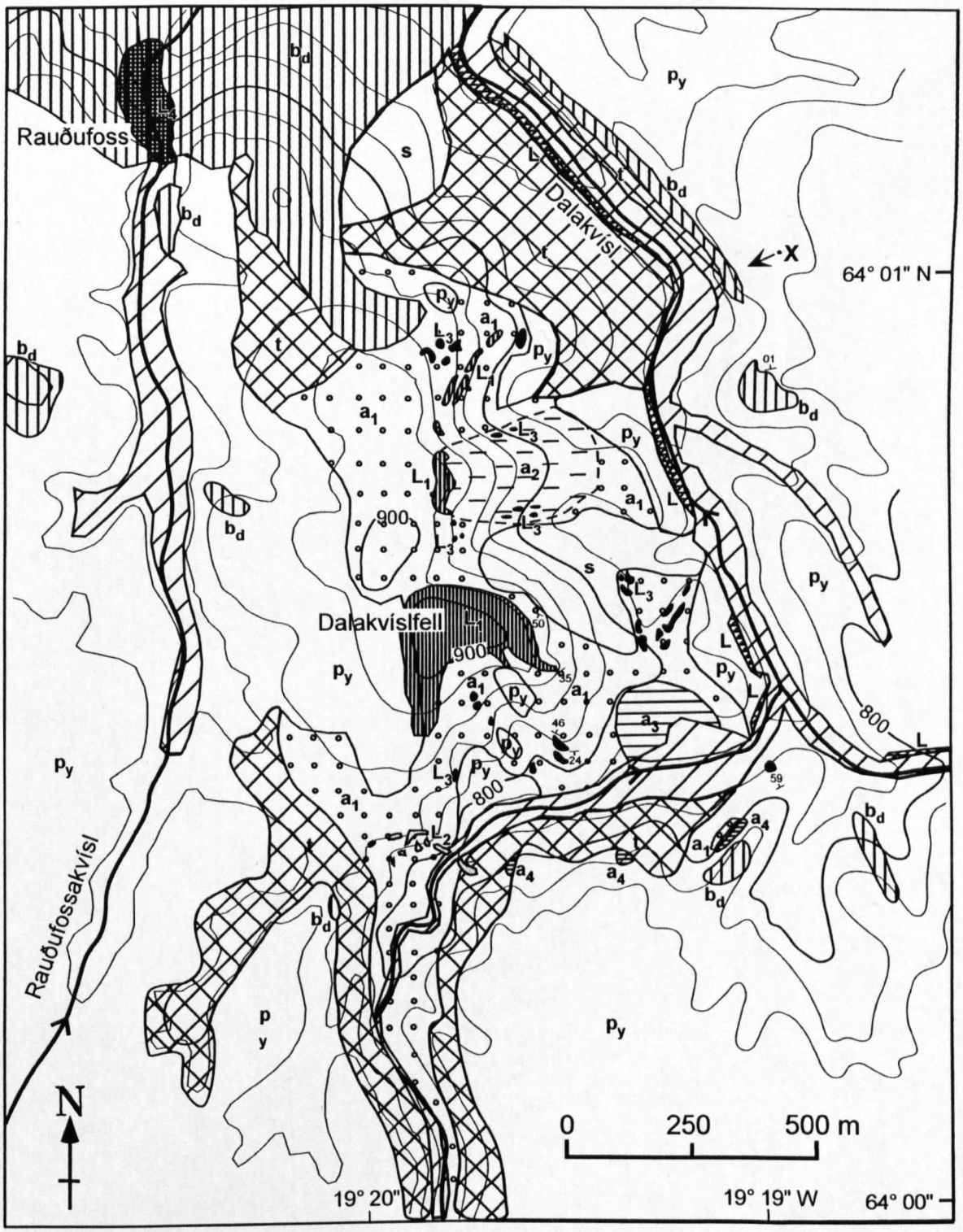
Rauðufoss
Dalakvísl
Dalakvíslfell
Rauðufossakvísl
64° 01" N
64° 00"
19° 20"
19° 19" W
0 250 500 m
N
900
800
Subglacial rhyolite formation
breccia 1
breccia 2
breccia 3
breccia 4
lava 1
lava 2
lava 3
lava 4
Younger formations
pyroclastics of Hekla, Vatnafjoll
till
basaltic diamicton
basaltic lava flow
Drift and symbols
scree
alluvium
stream
elevation (m)

Fig. 4.3.

Fig. 4.3. Geological solid and drift map of the Dalakvísl-Rauðufossakvísl area, including the Dalakvísl rhyolite formation. Most exposures of subglacial rhyolite lithologies occur on the steep slopes of incised river valleys, whereas plateau areas are mostly blanketed by Holocene pyroclastics from Hekla and elsewhere.

---

described and interpreted in sections 4.4.- 4.7. and 4.8.- 4.11., respectively. Other lithologies: clastic dykes and veins, basaltic diamicton, till and Holocene pyroclastics, are described and interpreted in sections 4.12.- 4.15.

4.4. Breccia 1 (*massive poorly-sorted obsidian - pumice breccia, a_1*)

4.4.1. Description

This is the most widespread of the fragmental rhyolite lithologies at Dalakvísl, cropping out around Dalakvíslfell summit and in the stream sections of Dalakvísl to the south (Fig. 4.2, Fig. 4.3). It is mostly poorly-exposed and unconsolidated, except for well-lithified deposits on the summit of Dalakvíslfell. The breccia varies in colour from pale grey to pale turquoise, and is poorly-sorted and structureless. Its thickness may exceed 100 m on the southern flank of Dalakvíslfell.

Low-vesicularity blocky-to-cuspate glassy ash shards typically 50-200 μm in diameter are estimated to comprise 40-80% of the breccia volume (Fig. 4.4a, b). The remainder consists of variable proportions of angular clasts. Pale grey pumiceous obsidian clasts 0.5-50 cm across are conspicuous, making up c. 10-30% of the deposit. They contain up to c. 50 % elongate vesicles by volume, which are <10 mm long. Vesicle-poor obsidian clasts 1-30 cm across are also present, varying from black fresh obsidian to mid-grey pervasively perlitised obsidian. These clasts contain <5% vesicles by volume and comprise only 5 % of the deposit volume at the southern limit

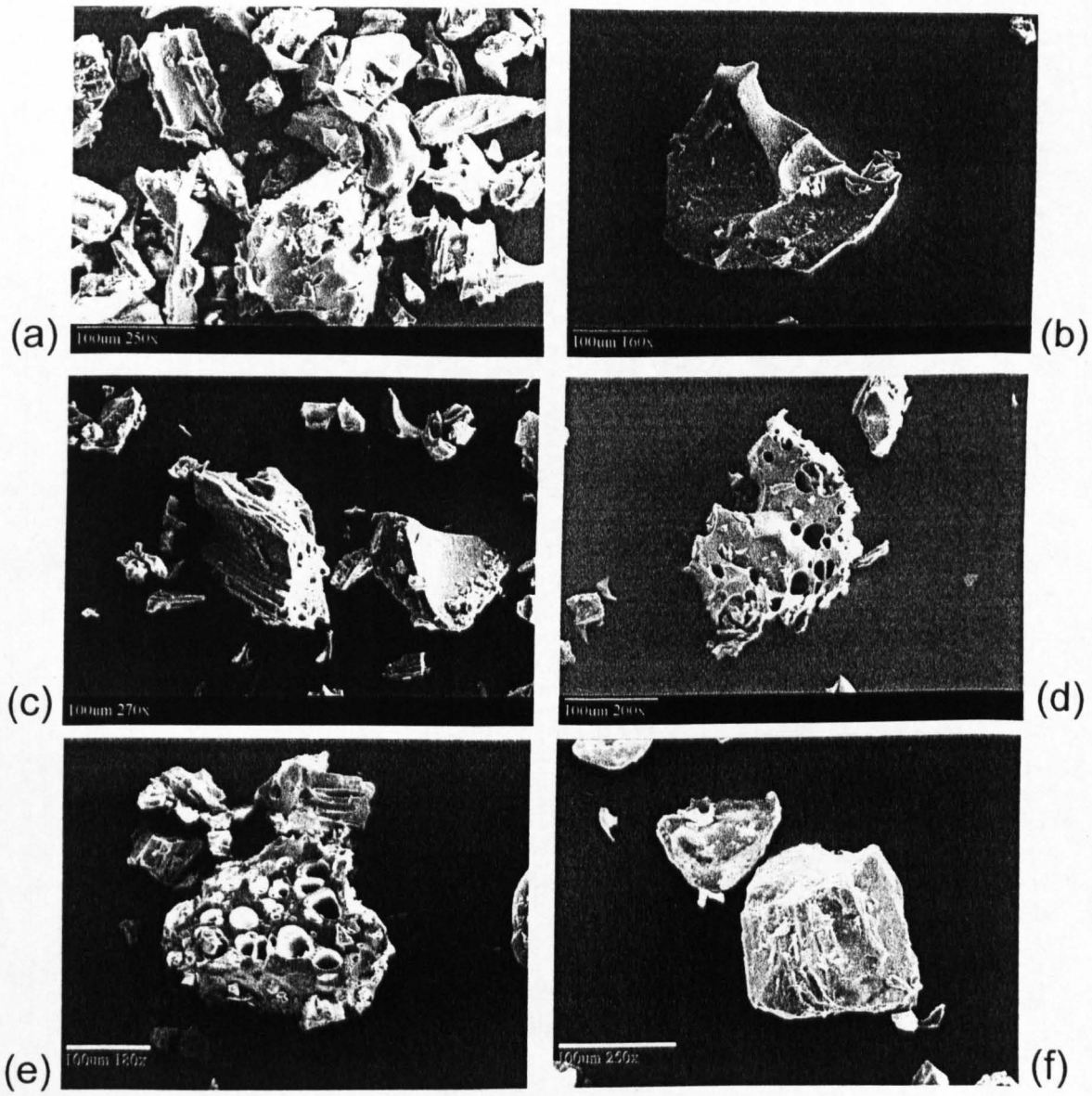

Fig. 4.4. SEM images of glassy ash shards from fragmental lithologies within the Dalakvísl rhyolite formation. **(a)** Typical ash shards from breccia 1. Shards are angular with sharp corners, and a small proportion are bounded by the walls of vesicles >50 μm long. Shards contain an estimated <20 % vesicles by volume, and mostly fall within the 50-200 μm size range. **(b)** An ash shard from breccia 1. The right hand surface of the shard consists of the walls of flattened vesicles. Note the overall blocky morphology and low vesicularity. **(c)** Typical ash shards from breccia 3, showing a mixture of contrasting shard types. Of the two large shards in the centre of the image, the left hand shard is the more vesicular, containing ~30 % tube-like vesicles <20 μm in diameter, whereas the right hand shard is blocky, and bound by the wall of a vesicle in excess of 100 μm long. Smaller shards also fall into two categories: tube-like shards and blocky vesicle poor shards. All shards have sharp corners and hydrated, pitted surfaces. **(d)** A tube-like shard within breccia 3. Vesicles <40 μm in diameter are in the process of coalescence. **(e)** Shards within breccia 4 fall into the two same main categories as those within breccia 4. This image shows tube-like ash shards with ~30 % coalescing vesicles. Note the abraded corners, possibly due to greater shard-shard interaction during epiclastic transport and redeposition. **(f)** Blocky, vesicle-poor ash shards within breccia 4.

Mixed ash types within breccias 3 and 4 reflect that the sediments are derived from reworking of more than one fragmental lithology. The simplest explanation is that blocky vesicle-poor shards are derived from breccia 1-like material, whereas the tube-like shards are derived from breccia 2-like material.

of its exposure, and up to 60 % of the deposit close to the contact with lava 1 200 m east of the south summit of Dalakvíslfell. Here, the breccia becomes increasingly clast-rich over 5 m, grading into the clast-supported perlitised obsidian breccia typical of the margin of lava 1.

Roughly 400 m south of the south summit of Dalakvíslfell, the breccia is cut by numerous anastomosing ash-filled veins 10-30 mm wide, similar to those observed in breccia A and breccia B at Bláhnúkur (Chapter 2.5, 2.6). On the summit of Dalakvíslfell, the breccia is indurated, because the ash matrix is cemented by orange-white material. All obsidian clasts are strongly perlitised, containing scarce black bead-like relicts of unaltered obsidian 2-5 mm in diameter.

4.4.2. Interpretation

The blocky, low-vesicularity nature of the ash shards suggests that fragmentation was triggered predominantly by magma-water interaction (Heiken & Wohletz 1985). Perlitisation of obsidian clasts also suggests that magma encountered water whilst still hot (Davis & McPhie 1996). Angular clasts of vesicle-poor obsidian within the breccia may have been derived from gravitational collapse or explosive decrepitation of vesicle-poor obsidian bodies (e.g. Cas & Wright 1987, Hunns & McPhie 1999), whereas pumiceous clasts were derived from more vesicular material. One possibility is that rising lava bodies with both vesicle-poor and vesicle-rich zones encountered water. Ash shards were formed by a combination of quenching and steam explosivity, whereas obsidian clasts reflect incomplete fragmentation. The poor sorting and massive nature of the breccia may indicate deposition from a dense mass flow or surge (Cas & Wright, 1987), with minimal clast size or density sorting. Alternatively, the breccia may be 'in situ', and has not been transported from the position in which it

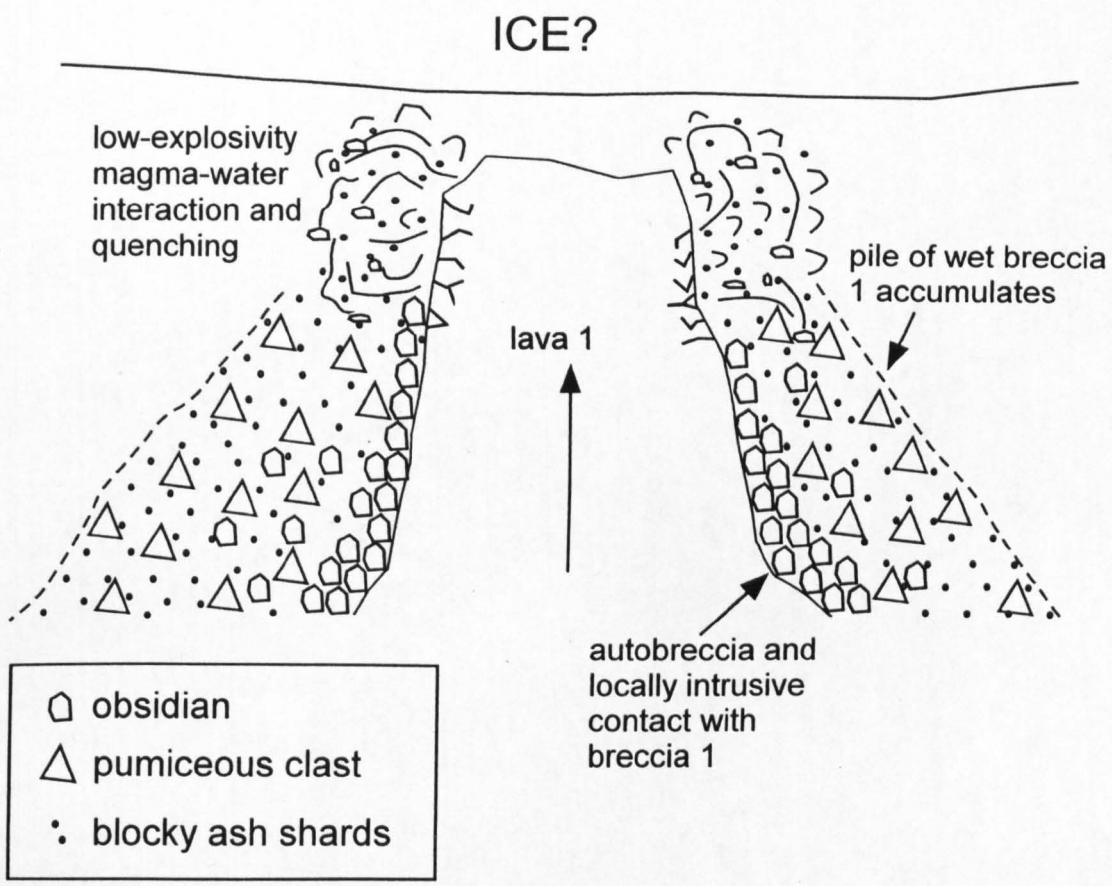

Fig. 4.5. A possible model illustrating the formation of breccia 1 and lava 1. Rising magma has encountered meltwater and generated a pile of wet breccia 1, containing blocky ash shards, obsidian fragments and clasts of pumiceous material. Lava 1 subsequently rises through the breccia, forming autobreccia at its margins and generating further breccia 1 through magma-water interaction. In this model, breccia 1 is both formed by and intruded by lava 1.

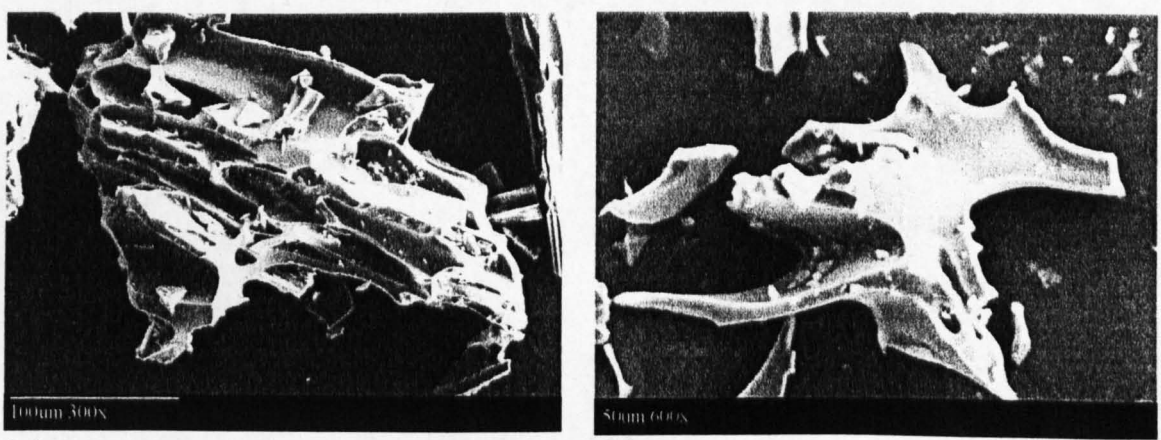

Fig. 4.6. Contrasting ash shard morphologies form the matrix of breccia 2. **(a)** Highly sheared glass shard, containing tube-like vesicles >100 μm long and <20 μm wide. **(b)** Low-shear glassy shard, which contains more equant vesicles, with some rounded embayments on vesicle walls (right-hand margin of shard), suggestive of vesicle coalescence.

was generated. If the breccia had been generated and accumulated within water, an extremely high clast concentration would be required to give the structureless deposit - perhaps akin to a dense slurry, suggesting that there was a high magma-water ratio during fragmentation.

Clast-rich zones adjacent to intact lava bodies may have formed in two ways: either by intrusion of lava within the breccia, with a zone of mechanical mixing; or from gravitational failure and spalling of talus from the lava carapace during accumulation of the breccia around the lava. It is possible that both processes occurred simultaneously (Fig. 4.5). Ash-filled veins within the breccia are interpreted as vapour-escape structures (Chapter 2.5), and suggest that the deposit contained water vapour whilst still hot. Further evidence for wetting of the breccia during or after its emplacement comes from the variety of peperitic lava bodies that subsequently intruded the deposit.

4.5. Breccia 2 (*Massive poorly-sorted breccia with obsidian stringers and vesicular bombs, a_2*)

4.5.1. Description

This lithology crops out on a prominent, well-exposed ridge that extends c. 300 m to the east from the north summit of Dalakvíslfell (Fig. 4.2, Fig. 4.3). The extent of outcrop is roughly 300 × 200 m. The deposit thickness is estimated to be 10-50 m. It consists of pale grey to pale turquoise poorly-consolidated, structureless breccia, which contains conspicuous black sheet-like bodies ('stringers') of obsidian (see next sub-section for definition and detail). The breccia is supported by a fine ash matrix, which makes up 40-80 % of the deposit. Ash shards are much more vesicular and

angular than those in breccia 1, containing an estimated 40-70 % vesicles by volume (Fig. 4.6), although the estimated modal size range is similar (50-100 μm). Shards are dominantly tube-like in morphology, with cylindrical vesicles commonly <20 μm in diameter and >100 μm long. There is little obvious vesicle coalescence (Fig. 4.6a). The remainder of ash shards preserve the walls of more equant, near-spherical vesicles > 0.1 mm across, with much evidence for vesicle coalescence (Fig. 4.6b). Angular to sub-angular clasts of pale grey or white pumiceous obsidian 0.5 mm-50 cm across are suspended in the ash matrix and typically make up c. 10-20 % of the deposit volume. Clasts are estimated to contain up to 70 % highly-elongate cylindrical vesicles by volume. Angular clasts of black obsidian 1-10 cm long are less abundant, making up <10 % of the deposit. This obsidian contains <5 % near-spherical vesicles and is not perlitised. Near-spherical or ovoid 'bombs' locally comprise c. 5 % of the breccia volume. Bombs are 15-30 cm in diameter, with mid-grey obsidian rinds 3-5 cm thick that contain <25 % vesicles. Vesicles in the rinds are pancake-shaped and <5 mm long, with long axes parallel to the outer surface of the bomb. The interior part is mostly void space, containing >95 % vesicles separated by delicate needle-like glass spindles that are the remnants of bubble walls.

4.5.2. Obsidian stringers

The breccia contains black obsidian sheets 1-20 m long and 0.15-0.5 m thick, which I have termed stringers. In morphology, these vary from near-planar to highly complex and contorted. Some stringers appear to be isolated, unconnected bodies, whereas the majority are clearly linked, near-parallel and appear to be offshoots from a number of feeder bodies (not exposed). The axes of elongation of 18 stringers were measured

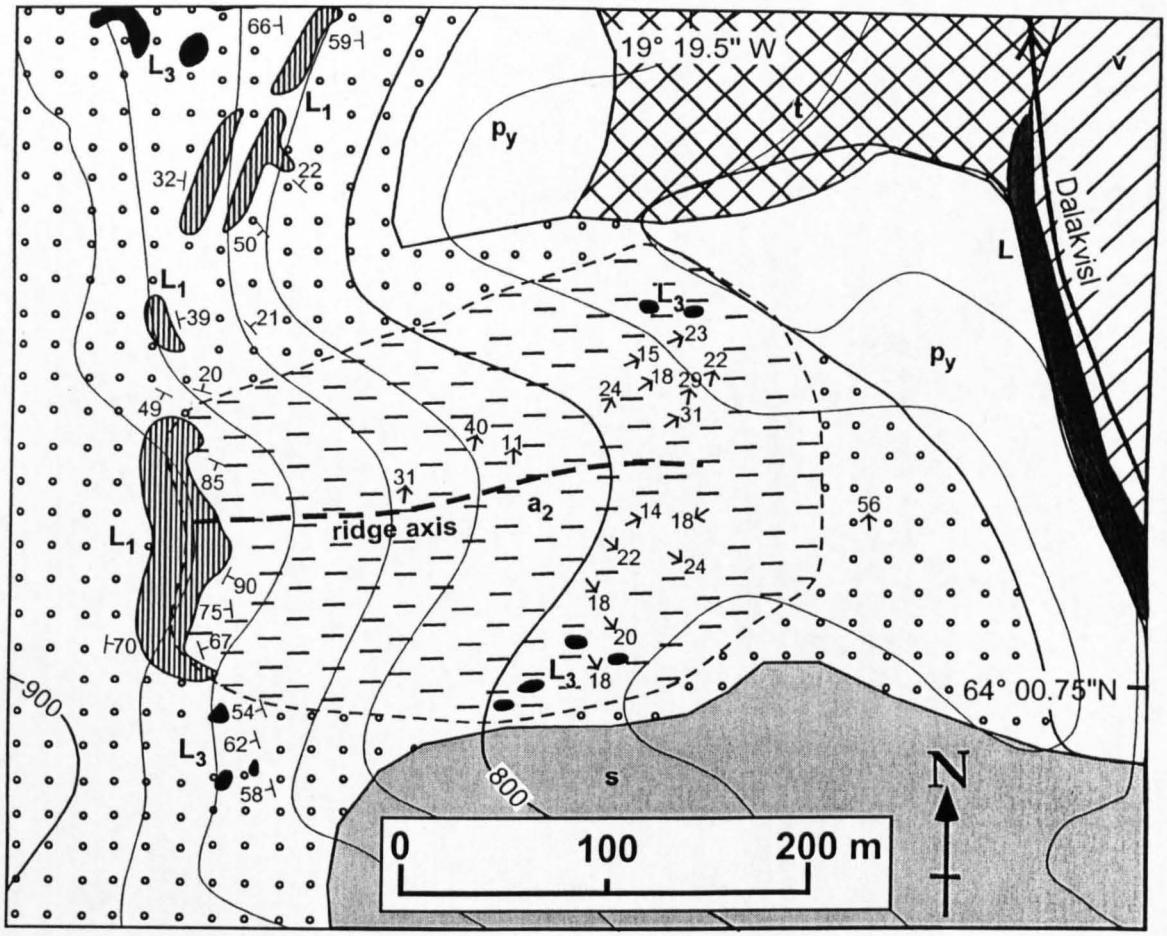

Fig. 4.7. Detailed geological map of the western flank of Dalakvíslfell, including the exposure of breccia 2. The orientations of the long axes of obsidian stringers are indicated. The thick dotted line indicates the position of the axis of the ridge. Stringer orientations are notably different on either side of the ridge axis - a similar pattern to the flow-banding and columnar-jointing orientations at Bláhnúkur (Chapter 2), where ridge axes are considered to define 'magmasheds'.

and are plotted on Fig. 4.7. On the north side of the ridge, axes dip at 10-30° to the north-east, whereas axes on the south side generally dip at 10-30° to the south-east. Stringers can be divided into two types, based upon their overall morphology and jointing patterns.

The first type of stringers are sheet-like, with length:thickness aspect ratios of 30-100:1. They lack columnar joints, are not perlitised, and occur close to the ridge axis (Fig. 4.7). The second type of stringer, exclusively found >50 m north or south of the ridge axis, is more compact (aspect ratios typically <5:1), with poorly developed columnar joints and weakly perlitised obsidian. This type of stringer shares many characteristics with lava 3 (see section 4.10) . Some stringers are cut by small normal and reverse faults, with typical displacements in the range 0.1-1 m. Many stringers exhibit open ductile folds, especially close to their margins (Fig. 4.8).

The internal structure of the stringers is complex, but typically fits into the following pattern: a near-continuous carapace of intact, near-white pumiceous obsidian 1-5 cm thick grades inwards into a black obsidian core 8-50 cm thick (Fig. 4.8). Descriptions and images of the microtextures within each textural zone are provided in Table 4.1 and Figs. 4.9, 4.10 and 4.11. The pumiceous outer carapace (Zone 3) contains c. 70 % highly sheared vesicles, with abundant evidence in thin section for incipient fragmentation, as discrete shards 100 μm-10 mm across become separated by patches of intense vesicle coalescence (Fig. 4.11). Many domains contain highly elongate cylindrical vesicles, which are approximately parallel to the outer margin of the stringer, although centimetric kink bands and folds are obvious in thin section. The breccia immediately adjacent to the outer carapace of stringers (Fig. 4.8) commonly consists of jigsaw-fit or clast-supported white pumiceous clasts resembling those of the intact carapace, within an ash-grade matrix. In many

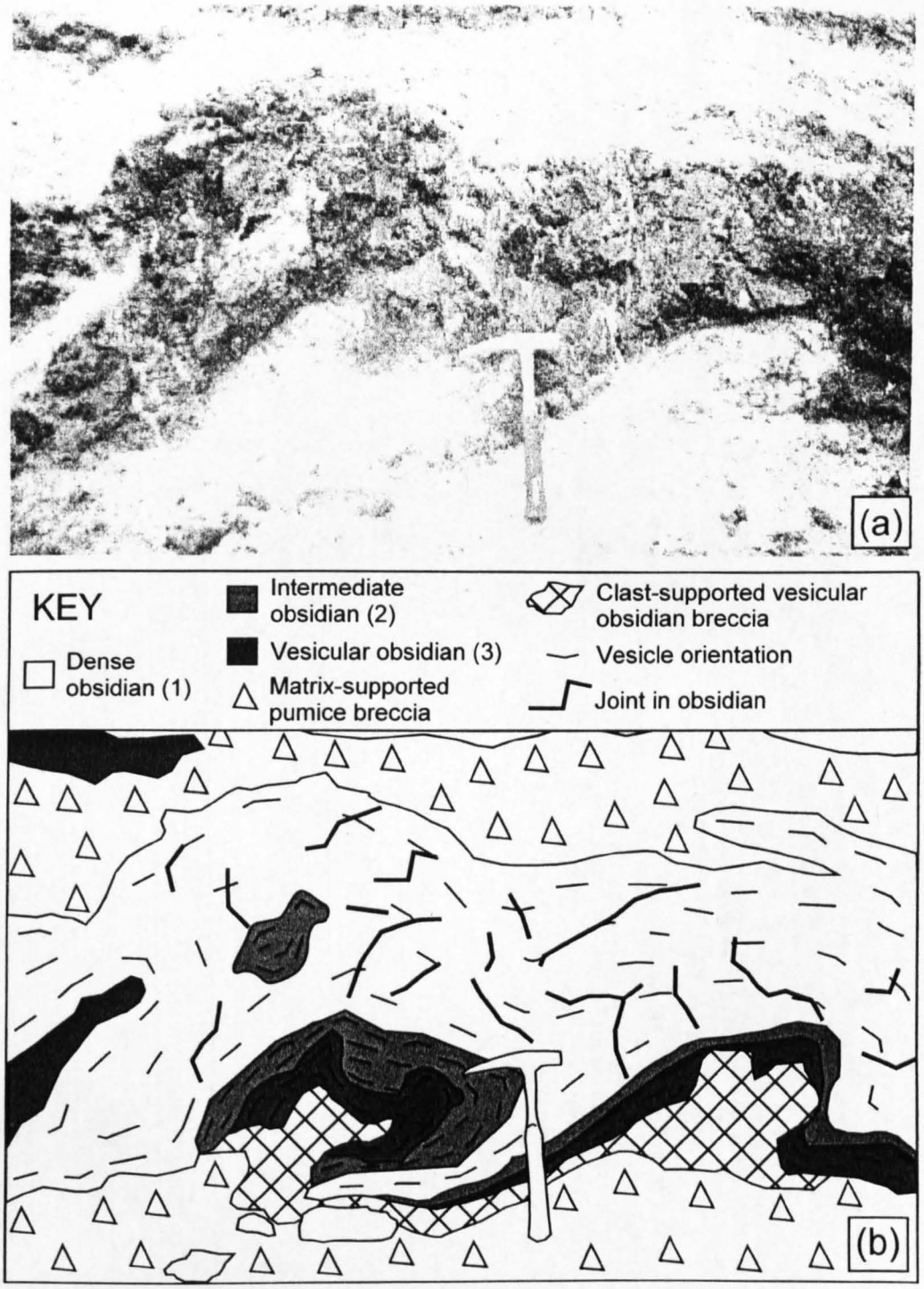

Fig. 4.8. Part of a typical stringer within breccia 2, close to the ridge axis at about 795 m elevation. **(a)** Photograph of an irregular, sheet-like stringer (grey, centre of view) surrounded by breccia 2 (yellow-grey). The hammer is 30 cm long. **(b)** Annotated field sketch of part of (a), showing the main features. There is a complete suite of textures at the base of the stringer, from zone 1 to 3 and into clast-supported vesicular obsidian breccia, which envelops much of the intact vesicular obsidian carapace. The base of the stringer is folded, with protuberances ~0.5 m across. Note that clast-supported vesicular pumiceous breccia is thickest in embayments in the stringer base, suggesting that it has been preferentially preserved due to its 'sheltered' position, having been protected from spalling and erosion during transport by the enveloping intact carapace. The upper carapace of the stringer is similarly folded, but zones 2, 3 and clast-supported vesicular obsidian breccia are absent. The zone of intermediate obsidian seemingly in the centre of the stringer is in fact part of the stringer carapace, suggesting that little of the stringer has been removed by erosion. Joints are irregular and poorly defined.

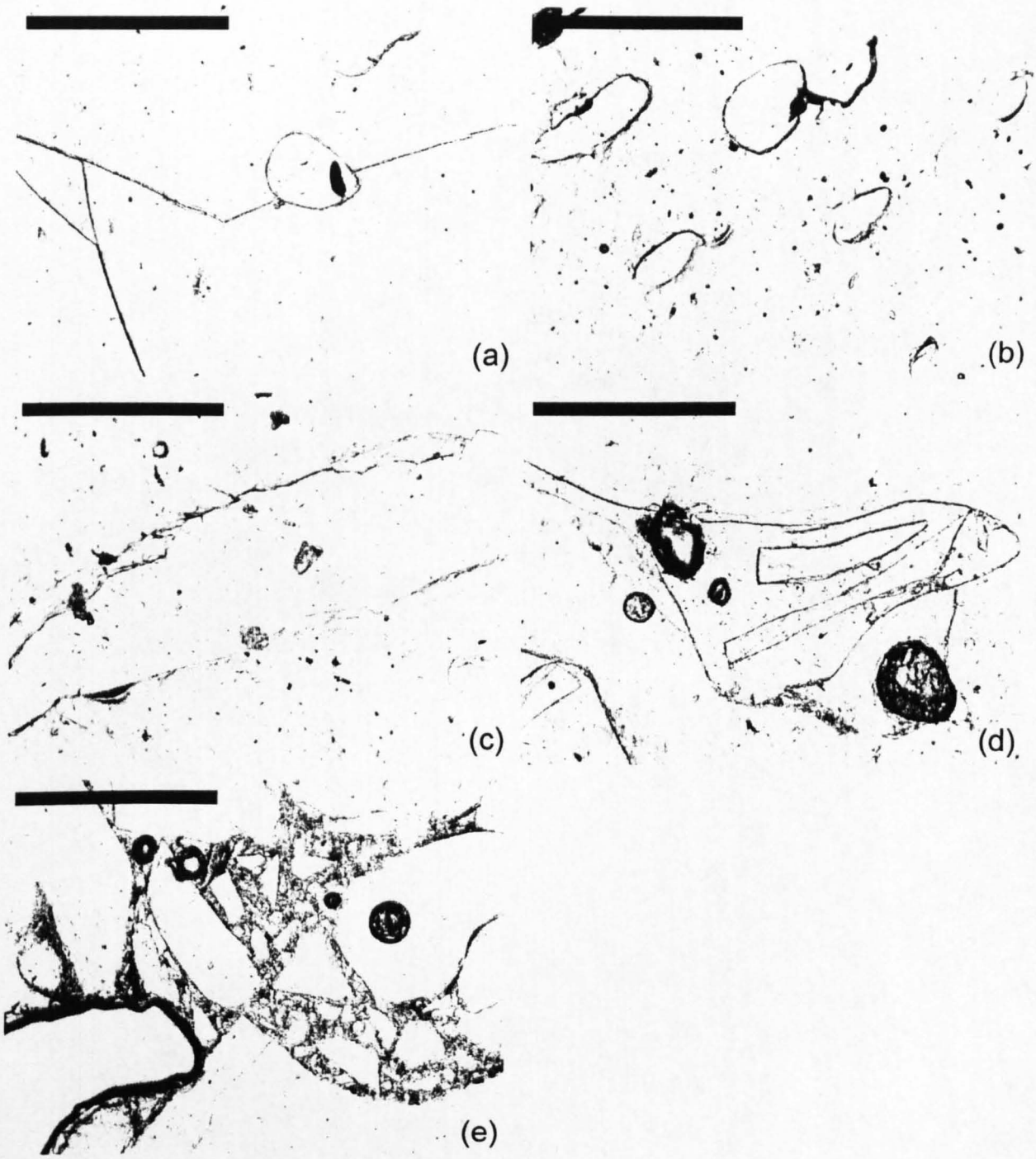

Fig. 4.9. Photomicrographs of zone 1 of an obsidian stringer (vesicle-poor obsidian core). Photographs are taken in plane-polarised light, all scale bars are 0.5 mm long. **(a)** Smooth-walled near-circular cross section of a vesicle within fractured vesicle- and crystal-free glass. **(b)** A region of slightly higher vesicle density, in which several smooth-walled vesicles between 0.15 and 0.35 mm long are seen, each elongated parallel to the others. **(c)** An elongate, rough-walled vesicle that exceeds 1.5 mm in length. **(d)** A smooth-walled vesicle >1 mm long with an unusual shape probably formed by partial collapse of an earlier, larger vesicle. Angular ash shards within the vesicle appear to have been derived from brittle failure of the vesicle walls. **(e)** Angular ash shards within a smooth-walled vesicle >2 mm long. Shards range from >0.5 mm to <0.05 mm in length.

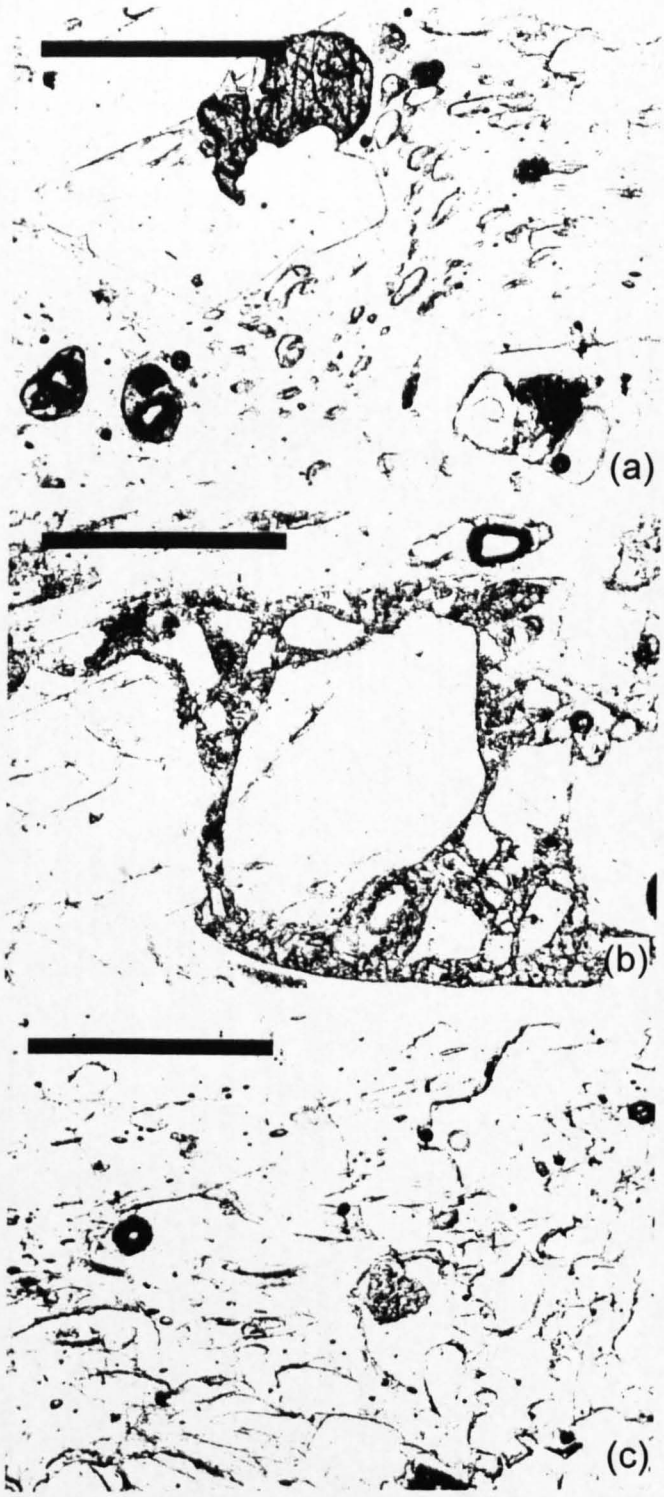

Fig. 4.10. (a) Typical textures in zone 2 (intermediate vesicular obsidian). Scale bar is 0.5 mm long. The long axes of smooth-walled vesicles 0.03-0.3 mm long are parallel to a flow line that wraps around a feldspar-fayalite phenocryst (top left). The largest vesicles are the most elongate (aspect ratios of ~5:1). **(b)** Angular ash shards within a vesicle >1 mm across (upper wall of vesicle out of field of view). Scale bar 0.5 mm long. **(c)** Close-up of heterogeneous vesicle populations. The top left corner is almost vesicle free, whereas the central and bottom left regions contain elongate, smooth-walled vesicles, some of which appear to have been in the processes of coalescence. Vesicles in the right hand side of the photograph are more equant and irregular in shape, with rough walls, and are estimated to comprise >40 % of the volume of that domain.

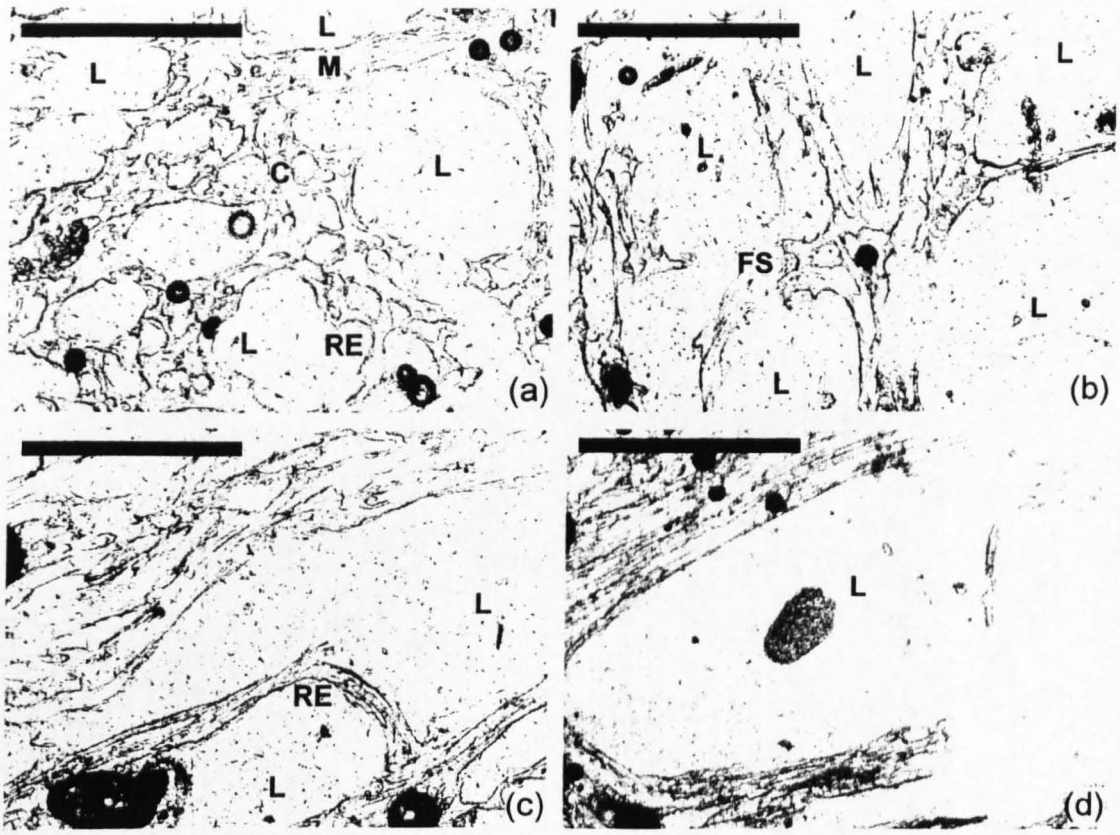

Fig. 4.11. Vesicle textures within zone 3 (pumiceous outer carapace) of a stringer. All photographs are taken in plane-polarised light; scale bars are 0.5 mm long. **(a)** Section showing the typical range of vesicle shapes and sizes present. Vesicles can be approximately divided into large vesicles (L) and smaller vesicles. Large vesicles are >0.3 mm long, and have clearly formed, on the basis of rounded embayments on walls, from the coalescence of numerous smaller vesicles (an example is labelled RE). The glass between large vesicles contains smaller vesicles mostly <0.1 mm long. Smaller vesicles in glass adjacent to large vesicles are elongate parallel to the walls of the larger vesicles. Where two large vesicles are in close proximity, the glass between the two forms a highly sheared membrane (labelled M), with elongate, tube-like small vesicles. Smaller vesicles further from large vesicles are more equant and near-circular in cross-section (labelled C). **(b)** Region with a high proportion of large vesicles (labelled L), and ruptured vesicle walls. Vesicle walls appear to have 'snapped' in a brittle manner (fracture surface labelled FS). **(c)** A region with more pervasive elongation of vesicles in a single direction. Large vesicles (labelled L) have smooth walls; rounded embayments have been almost obliterated by deformation (a relict embayment is labelled RE). Smaller vesicles are extremely highly sheared and tube-like in the lower part of the photograph, and less elongate in the top left hand corner. *Dark patches* at the bottom of the image are imperfections in the section. **(d)** Close-up of the walls of a large vesicle. No rounded embayments are visible, and the vesicle walls contain tube-like, highly elongate smaller vesicles that are parallel to the walls of the large vesicle. The walls have locally ruptured (centre right).

Textural zone	H_2O weight %	Density and vesicularity	Vesicle population	Interpretation
1 Vesicle-poor obsidian core	0.61 ± 0.08 (2 σ) Mean of 6 analyses	2.22 ± 0.10 Mg m^{-3} Vesicularity estimated at 5 vol. % Dense magma 2.34 ± 0.11 Mg m^{-3}	Smooth walled ellipsoids <2:1 aspect ratio, 0.1-0.3 mm long (Fig. 4.9a, b). Rare irregular, smooth-walled vesicles <3 mm long filled with angular ash shards (Fig. 4.9d, e).	Minor vesiculation. Large vesicles possibly formed in earlier vesiculation event. Ash shards may be formed by brittle failure of vesicle walls during shock wave propagation.
2 Intermediate vesicular obsidian	0.59 ± 0.12 (2 σ) Mean of 9 analyses	1.49 ± 0.01 Mg m^{-3} Vesicularity 36 vol. %	Heterogeneous vesicle population. Smooth-walled ellipsoidal vesicles 0.05-0.2 mm long 0-10 % volume. Locally up to 40 % volume lenticular smooth-walled <5 :1 aspect ratio vesicles < 0.5 mm long, with coalescence. Vesicle poor + rich zones on ~1 mm scale (Fig. 4.10c). Some vesicles filled with ash shards (Fig. 4.10b). Sheared vesicles are folded around phenocrysts.	Highly heterogeneous vesicle nucleation, possibly related to heterogeneous deformation during stringer emplacement. Onset of coalescence.
3 Pumiceous outer carapace	0.57 ± 0.06 (2 σ) Mean of 5 analyses	0.68 ± 0.003 Mg m^{-3} Vesicularity 71 vol. %	Highly heterogeneous vesicle population. Smooth-walled ellipsoidal vesicles <0.1 mm long. Smooth-walled irregular coalesced vesicles 0.3-1 mm long. Smooth-walled ellipsoidal vesicles >1 mm long. Small vesicles adjacent to larger coalescing vesicles are flattened tangential to the wall of the large vesicle (Fig. 4.11a, b, c, d). Highly sheared walls of coalesced vesicles commonly ruptured or in the process of rupturing (Fig. 4.11b, d). Patches of distinct texture on ~1 mm scale.	Initial heterogeneous nucleation of small vesicles (<0.3 mm). Local coalescence, expansion of coalesced vesicles dominates over nucleation of new vesicles. Walls of coalesced vesicles progressively thinned and ruptured: evolving ductile-brittle rheology.

Table 4.1a. *Data on textural zones within obsidian stringers.*

Textural zone	Description	Density kg m^{-3}	Vesicularity %
1	Black obsidian core	2.22 ±0.099	5.0 (estimated)
2	Brown inner carapace	1.49 ±0.015	36.3 ±0.33
3	Pale grey pumiceous carapace	0.68 ±0.003	70.9 ±0.15

Table 4.1b. *Density measurements for obsidian stringer within breccia 2 at Dalakvísl.* Raw data and details of analytical techniques are given in Appendix E.

Textural zone	Description	No. of analyses	H_2O_t mean	Standard deviation
1	Black obsidian core	6	0.61	0.04
2	Brown inner carapace	9	0.59	0.06
3	Pale grey pumiceous carapace	5	0.57	0.03

Table 4.1c. *Total water contents H_2O_t within an obsidian stringer, measured using FTIR.* Raw data and details of analytical techniques are given in Appendix D.

Sample	D47-1		D47-2		D47-3	
No. of analyses	27		27		28	
Species	Mean	St Dev	Mean	St Dev	Mean	St Dev
SiO2	76.86	0.12	77.09	0.12	77.28	0.25
TiO2	0.34	0.02	0.34	0.02	0.34	0.01
Al2O3	13.25	0.05	13.24	0.06	13.31	0.07
MgO	0.16	0.01	0.16	0.01	0.16	0.01
CaO	0.55	0.01	0.55	0.01	0.55	0.02
MnO	0.12	0.01	0.12	0.01	0.12	0.01
FeO	2.42	0.04	2.43	0.03	2.43	0.04
Na2O	1.89	0.09	1.65	0.11	1.41	0.23
K2O	4.13	0.04	4.14	0.04	4.13	0.03
F	0.16	0.03	0.16	0.04	0.17	0.03
Cl	0.10	0.02	0.09	0.02	0.10	0.02
P2O5	0.02	0.01	0.02	0.01	0.02	0.01

Table 4.1d. *Major element compositions of glass within a stringer.* Raw data and details of analytical techniques are given in Appendix C.

instances, the intact pumiceous carapace is partly missing (Fig. 4.8), however stringers have been observed with a continuous carapace on both upper and lower surfaces. The colour of the carapace grades inwards from near-white to mid brown-grey (Zone 2) over 1-5 cm, and the proportion of vesicles decreases to c. 20-30 %. Stringer interiors (Zone 1) consist of fresh black obsidian, with <5 % near-spherical vesicles up to 3 mm in diameter (Fig. 4.9). The densities of each textural zone were measured using a displacement method. Results are given in Table 4.1b and raw data and methods are provided in Appendix E. A preliminary analysis of the dissolved water content of stringers was made using the FTIR facility at Bristol University in October 2000. Raw data and analytical techniques are given in Appendix D. Total water contents of zones 1, 2 and 3 from a single sample are 0.61 ± 0.08, 0.59 ± 0.12 and 0.57 ± 0.06 wt % respectively (Table 4.1c). Major element compositions of glass within each of the textural zones of a stringer were analysed using an electron microprobe. The results are given in Table 4.1d, and the raw data are provided in Appendix C3. Compositions are almost identical in the different zones.

4.5.3. Interpretation

Of all the rhyolite lithofacies studied at Torfajökull, this is possibly the most enigmatic. Ash shards within the breccia are vesicular; indicating that considerable exsolution of magmatic volatiles occurred prior to fragmentation (Heiken & Wohletz 1985). Clasts of pumiceous obsidian and vesicle-poor obsidian within the breccia were probably derived from earlier generations of stringers that have completely disintegrated, as well as from spalling and brittle failure of the outer carapace of stringers that are mostly intact. Bombs may have been formed during fire-fountaining

(Mueller & White 1992), strombolian activity or spatter (Stevenson & Wilson 1997), in which volatile-rich magma was emplaced in a 'dry' environment (Fig. 4.12a). The massive, poorly-sorted nature of the breccias is best explained by deposition via dense debris flows or surges (Cas & Wright 1987), in which bombs and stringer fragments became entrained within fine-grained ash (Mellors & Sparks 1991, Valentine et al. 2000). Stringers *appear* to be intrusive within the breccia, but abundant evidence for brittle and ductile stringer deformation indicates that the breccia was poorly-consolidated and mobile when the stringers were emplaced. Due to its stratigraphic associations with lithologies interpreted as subglacial (breccia 1, lava 3), it is assumed that a 'dry' explosive eruption occurred within a well-drained, air-filled ice cave (Fig. 4.12a). With time, the cave became completely filled with tephra, and the eruption style switched to intrusive (Fig. 4.12b,c). The sheet-like morphology of stringers may have been caused by (1) the extremely low viscosity of water-rich peralkaline rhyolite magma (Dingwell et al. 1998), (2) the entrainment of stringers into a down-slope shear flow, or (3) subsequent flattening by the weight of material above. The folded, buckled shape of many stringers suggests that flattening was not entirely due to gravitational loading, hence (3) is considered unlikely. However, it is difficult to assess whether stringers were intruded within a stationary, but poorly-consolidated breccia, or whether they were entrained into a dense debris flow whilst still hot and ductile, and acquired their flattened shape during transport (Fig. 4.12c).

The sheet-like stringers appear to have been emplaced within a 'dry' environment, whereas the development of columnar joints and perlitisation in the more compact stringers near the foot of the exposed ridge of breccia 2 is suggestive of interaction with water: probably during intrusion within wet breccia 2. If the sheet-like stringers and the compact stringers were emplaced simultaneously, their different

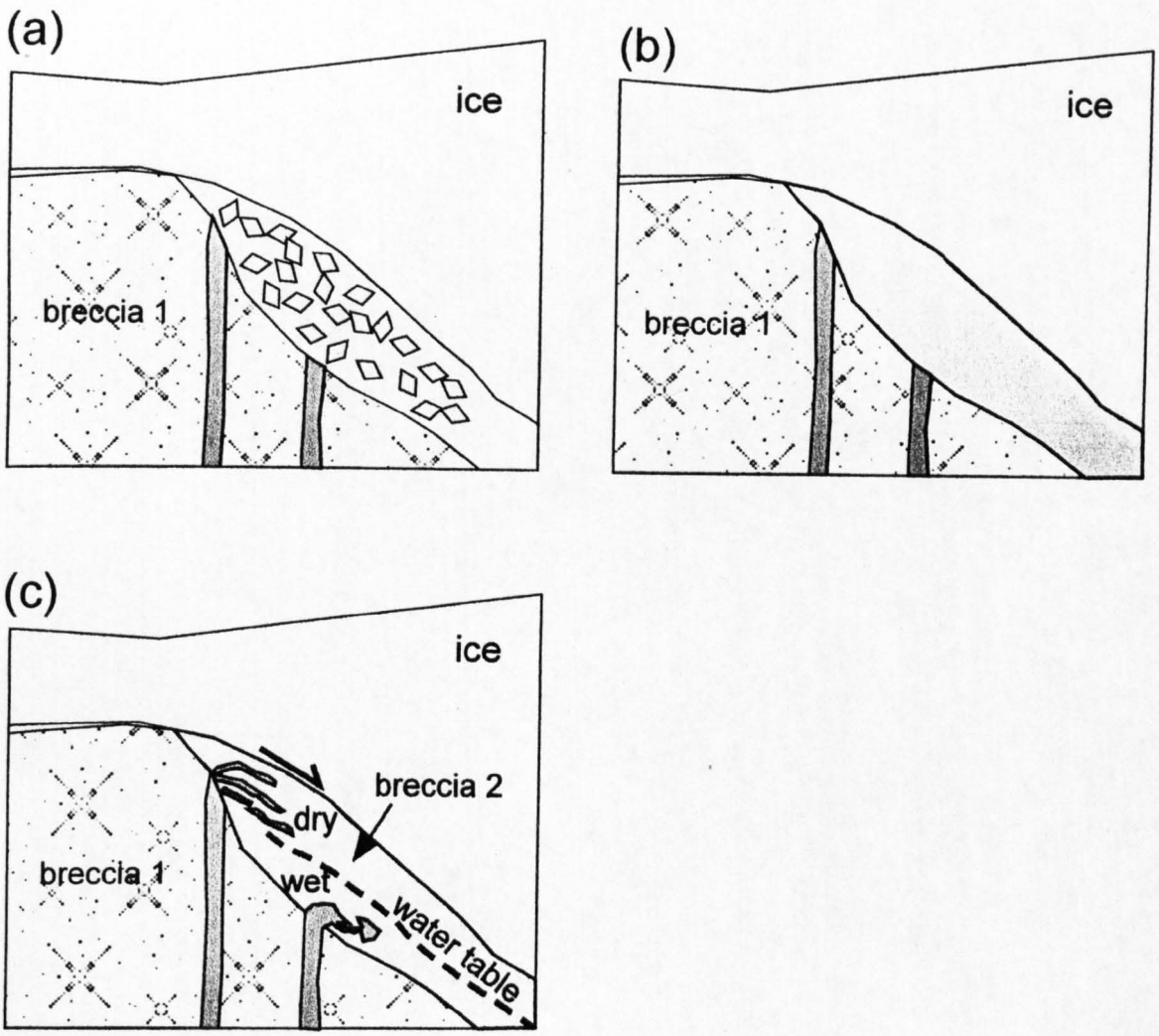

Fig. 4.12. A possible model for the formation of breccia 2 and obsidian stringers. **(a)** A 'dry' explosive eruption occurs within an air-filled cavity, forming vesicular tephra and bombs. **(b)** The cavity becomes rapidly filled with vesicular tephra, but the eruption continues. **(c)** Rising magma is now intruded into the pile of tephra filling the cavity. The upper part is 'dry' and above the water table (dashed line). Magma intruded into this part begins to vesiculate and is sheared by down-slope tephra movement (arrow), forming stringers. Down-slope movement of tephra may be triggered by the onset of cavity roof melting. Magma intruded into wet tephra beneath the water table is quenched, forming irregular intrusions of lava 3.

characteristics may be explained by the position of the water table within the pile of tephra (Fig. 4.12c).

The patterns of vesicularity in stringers have no equivalent in the published literature, and are not easily explained. Vesicle-poor obsidian within a pumiceous carapace may reflect welding and loss of vesicles from the core (Gottsmann & Dingwell 2001), or preferential vesiculation of the outer carapace. Although there is no clear textural evidence for welding and vesicle collapse in the interior, relict textures can be completely obliterated by welding and collapse (Hurwitz & Navon 1994). The arrangement of vesicles and fractures suggests that Zone 3 represents a fossilised fragmentation interface. Fragmentation appears to have been provoked by vesicle coalescence, with the transition from ductile to brittle magma deformation mediated by evolving magma rheology, rather than the influence of external water (Marti et al. 1999). Indeed, the breccia and sheet-like stringers show no evidence for interaction with water during their formation and emplacement.

Fragmentation within the outer carapace of stringers appears to be triggered by the growth of large vesicles (>1 mm). Smaller vesicles in the surrounding glass are compressed, with their long axes tangential to the walls of large vesicles (Fig. 4.11a, d). Where two or more large vesicles are in close proximity, the glass between them has become stretched into a thin membrane, which is locally seen to have ruptured. Tube pumices in the surrounding breccia exactly resemble fragments of these highly sheared membranes. The transition between ductile and brittle behaviour may have been mediated by degassing-driven cooling, which acted to increase the magma viscosity and lower the strain rate to the point at which viscous deformation was too sluggish to accommodate the imposed deformation (Sahagian & Proussevitch 1996). Furthermore, the viscosity increase due to the transition from a bubble-rich fluid to a

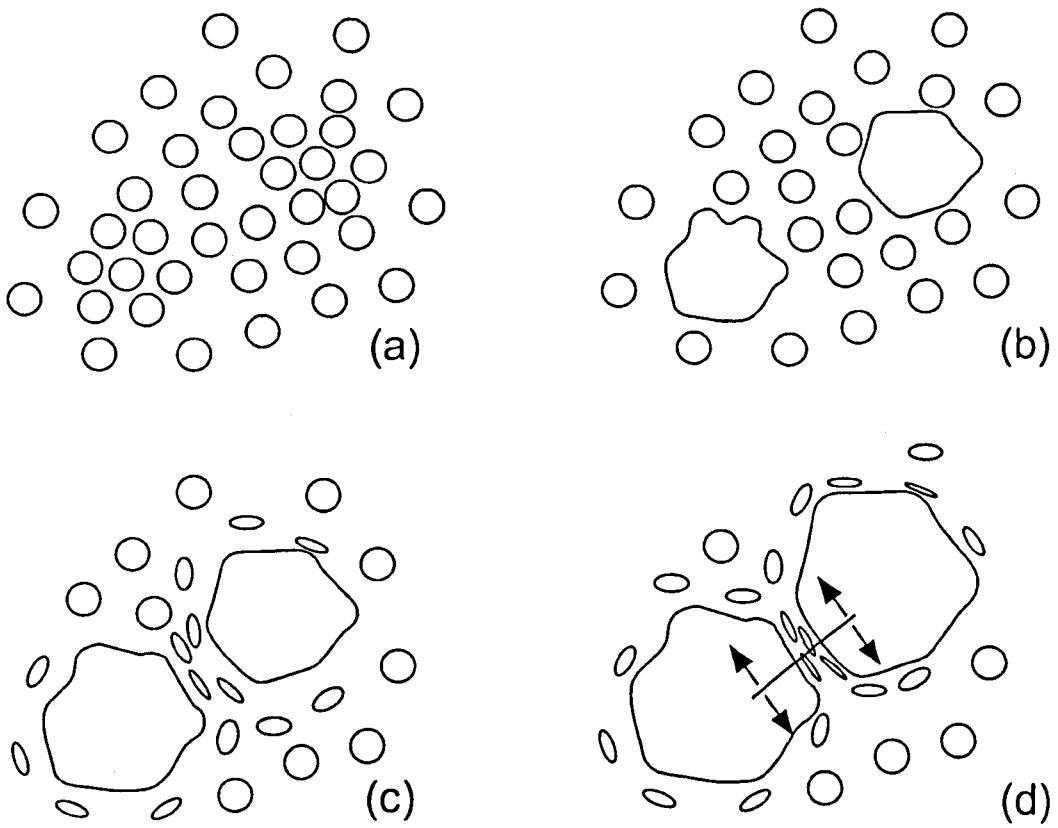

Fig. 4.13. Schematic diagrams illustrating a possible fragmentation mechanism within the outer carapace of the stringers (zone 3). **(a)** Heterogeneous nucleation of small spherical vesicles. **(b)** Coalescence of small vesicles in regions of highest number density forms large vesicles. **(c)** Expansion of large vesicles, with minimal nucleation and growth of small vesicles, leads to stretching of small vesicles parallel to the walls of large vesicles. **(d)** Further expansion of large vesicles results in rupture of the membranes separating the large vesicles, and thus the magma begins to disaggregate.

foam may have contributed to the onset of brittle deformation behaviour (Prud'homme & Khan 1993). More detailed discussion of vesiculation and fragmentation mechanisms will be given elsewhere.

Although there is a suggestion that the vesicle-poor stringer core is slightly more water-rich (Table 4.1b), all results fall within 2σ error bars, and hence no variation in water content can be statistically proven. If it is assumed that the magma of Zones 1 and 3 had the same water content prior to emplacement in a stringer, it follows that the formation of 70 % vesicles by volume had a negligible effect on the dissolved water content (i.e. less than the analytical error and hence a reduction of less than 0.10 wt % H_2O). Glass compositions within the different textural zones of the stringer are almost identical (Table 4.1c), lending weight to the suggestion that all of the stringer originated from the same body of magma.

Assuming that the vapour within the vesicles was dominated by water and that it behaved as an ideal gas, the ideal gas law $PV = nRT$ can be used to estimate the maximum pressure at which vesiculation occurred, assuming equilibrium degassing (Gardner et al. 1999). The number of moles of dissolved water per unit volume of magma n_l is given by n_l = wt % water × density of magma / molar mass of water, which gives $n_l = 6\times10^{-3} \times 2340$ kg m^{-3} / 0.018 kg mol^{-1} = 770 mol m^{-3}. Since the water content of 70 % vesicular magma is not measurably different from ~vesicle-free magma, less than 130 mol m^{-3} of water was exsolved during vesiculation (corresponding to a drop in water content of <0.10 wt %).

The maximum pressure at which vesiculation occurred can thus be estimated by using the relation $\Delta n = PV/RT$, where Δn is the number of moles of water exsolved (<130 mol m^{-3}), V is the vesicle volume per unit magma volume = 0.7 m^3, R is the universal gas constant = 8.31 J K^{-1} mol^{-1} and T is the magma temperature, estimated

at 1100 K. This yields P < 1.7 MPa, which would correspond to < 200 m ice overburden pressure, or intrusion within a pile of breccia < c.150 m thick. However, this result must be treated with caution, as non-equilibrium degassing is common in volcanic systems (e.g. Jaupart 1998, Gardner et al. 1999).

A vexed question is why stringers have opposite patterns of vesicularity to bombs, which have highly vesicular interiors and less vesicular rims. Much more study is necessary to determine the origin of the stringers.

4.6. Breccia 3 (*Crudely bedded well-sorted ash, a_3*)

4.6.1. Description

This lithology crops out on the incised north bank of Dalakvísl, 500 m ESE of the south summit of Dalakvíslfell (Fig. 4.3). The ash is pale green-blue in colour and moderately well exposed. It is well-sorted, and consists of blocky, low-vesicularity shards typically 50-100 μm across (Fig. 4.4c,d). Crude near-horizontal bedding ~5-20 cm thick is picked out by subtle variations in grainsize and sorting. Beds are planar and laterally continuous over >20 m. Clasts of black obsidian and pale grey pumice are scarce and do not exceed 1 cm in diameter. The breccia is intruded by numerous bodies of lava 1 and lava 2, which have peperitic margins.

4.6.2. Interpretation

Ash shards within breccia 3 are of similar morphology and size to those of breccia 1, and are assumed to have originally formed part of a breccia 1-type deposit. However, the sedimentary structures suggest that epiclastic redeposition has occurred. The well-

sorted, crudely bedded nature of breccia 3 is consistent with deposition within water, by either turbidity currents or grain flow (Cas & Wright 1987). The lateral extent of individual beds and lack of erosive surfaces suggests a lacustrine setting, within which pulses of sediment were deposited. Large clasts are absent, suggesting that current energies were low, and clast-rich slurries or debris flows (such as those that deposited breccia 1) were unable to reach the zone of deposition. Since breccia 3 is intruded by bodies of lava 2, which have ice-contact features, it is assumed to have been redeposited within a subglacial setting. The preferred interpretation is that an ephemeral valley-ponded lake developed at the eastern margin of Dalakvíslfell during the eruption, possibly dammed by volcanic debris. The lake was fed by meltwater running off the growing subglacial rhyolite edifice of Dalakvíslfell. This meltwater had low current energy and could carry only fine-grained ash. The deposits were wet when subsequently intruded by lava bodies.

4.7. Breccia 4 (*Well-bedded sandstone-breccia succession, a_4*)

4.7.1. Description

Three inconspicuous pale patches on the southern bank of Dalakvísl (Fig. 4.3) consist of a complex, well-preserved succession of sandstones and breccias. They are mostly covered by vegetation and Holocene tephra, and a spade is required to remove surface detritus. Planar-laminated sandstone units 0.15-0.5 m thick are intercalated with 0.1-0.2 m thick planar beds of reversely-graded, matrix-supported breccia (Fig. 4.14a). Breccias have sharp, non-erosive planar bases and irregular upper surfaces, many of which are infilled by fine-grained laminated sandstone. Sandstone units are internally complex, consisting of gravelly sandstone beds, 2-5 cm thick and laterally continuous

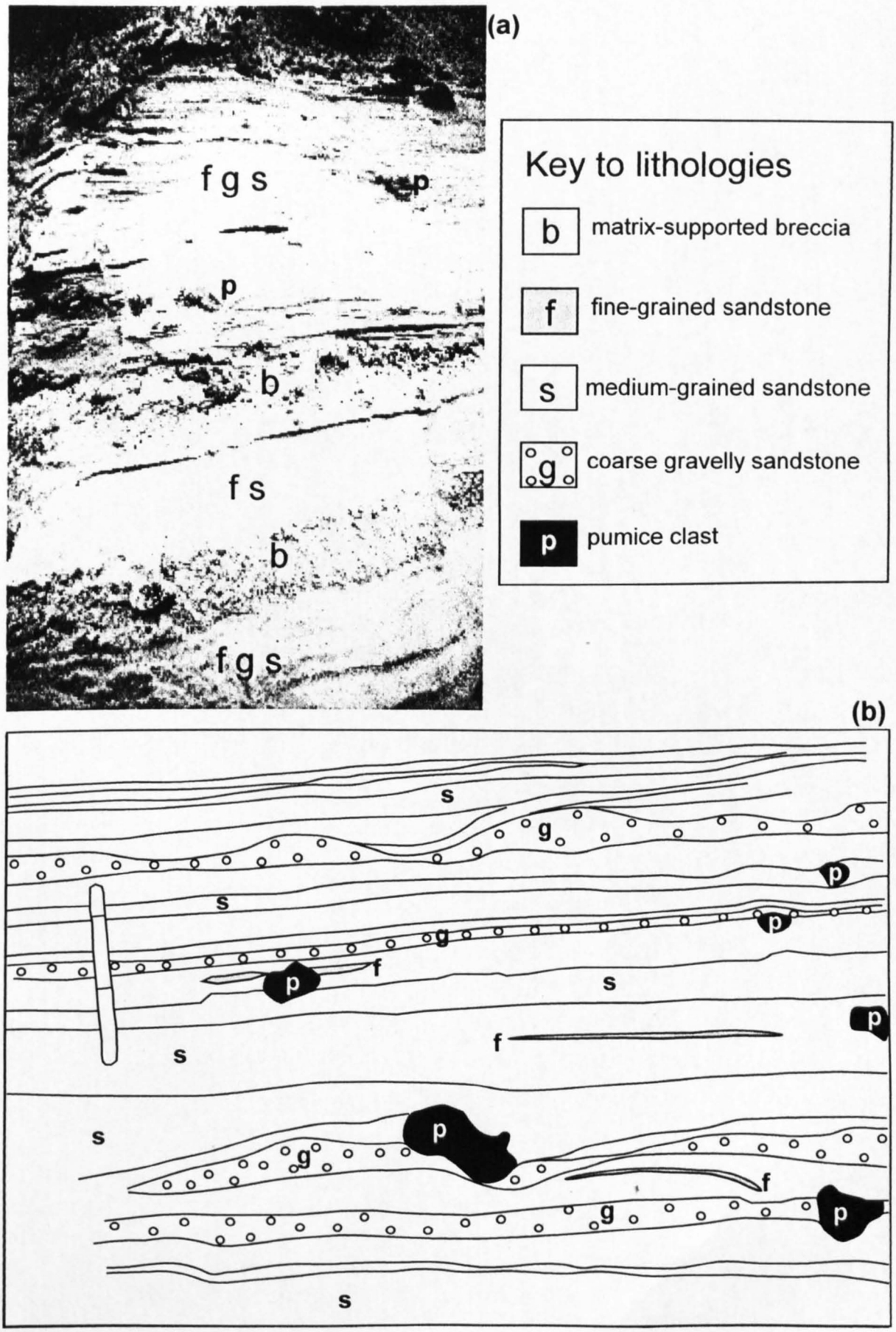
(a)
f g s
p
p
b
f s
b
f g s
Key to lithologies
b matrix-supported breccia
f fine-grained sandstone
s medium-grained sandstone
g coarse gravelly sandstone
p pumice clast
(b)
s
g
p
s
g
p
f
s
p
f
s
s
p
g
f
g
p
s

Fig. 4.14.

Fig. 4.14. (a) Photograph of part of the breccia 4. Units of laminated fine-, medium-grained and gravelly sandstones (pale, 15-50 cm thick) are interbedded with planar units of poorly-sorted breccia (dark, 10-20 cm thick). *Pen* is 15 cm long. Note the occasional outsized pumice clast (p) within the sandstone units. **(b)** Field sketch of the upper sandstone unit shown in (a). The sandstone contains beds typically 2-7 cm thick. Medium-grade sandstone beds are typically near-planar and laterally continuous over the entire section shown, whereas gravelly sandstone beds have variable thickness, commonly pinch out over <0.5 m, and have antidune ripple forms on some upper surfaces. Note the lens of fine-grained sediment immediately adjacent to the outsized pumice clast 10 cm right of the pen.

---

over 1-3 m, interbedded with laminated fine-to-medium grained sandstone (Fig. 4.14b). Gravelly beds are internally massive, with sharp, erosional bases and antidune or asymmetric ripple forms on upper surfaces. Outsized pumice clasts, commonly found within gravelly beds, are sub-rounded and up to 10 cm across. Lenses of fine-grained sandstone occur adjacent to outsized clasts. These typically pinch out laterally over <10 cm (Fig. 4.14b). The irregular upper surface of gravelly beds is draped by well-sorted, laminated fine-grained sandstone, which is thickest in depressions and 'fills in' topographic irregularities. The basal part of the westernmost exposure is intruded by perlitised, columnar-jointed lava bodies 1-5 m long, with peperitic margins.

4.7.2. Interpretation

Ash shards and clasts within breccia 4 appear to be a mixture between those of breccias 1 and 2. However, the sedimentary structures are very different. The sedimentary features of breccia 4 suggests that epiclastic redeposition occurred in a fluvio-lacustrine environment, in which sediment supply and water currents fluctuated (Cas & Wright 1987). Reversely-graded breccias were deposited by thin, small-

volume debris flows, which were interspersed with grain flow and dilute suspension deposits (sandstone units). Lenses of fine sandstone around outsized clasts were probably deposited in local regions of low current velocities around obstacles on the bed. Outsized pumices may have initially floated, before becoming water-saturated and sinking (e.g. Manville et al. 1998). The presence of fine-grained lenses around outsized pumices is evidence for progressive aggradation of sandstones from a particle-laden current.

The preferred model for the depositional environment of breccia 4 is that there was a variable meltwater flux (and occasional meltwater ponding?) at the foot of the subglacial edifice during the eruption. Pulses of poorly-sorted material containing numerous lapilli-grade clasts cascaded down the flanks of the edifice, possibly triggered by discrete gravitational collapse events. These pulses formed debris-flow deposits. Finer grained material may have been transported by low-energy flowing meltwater before being deposited during periods of low water flux. The notable difference between the environment of deposition of breccias 3 and 4 is that the current and sediment supply were much more variable during deposition of breccia 4, leading to the observed variety in bed forms, sorting and grain size characteristics.

4.8. Lava 1 (*perlitised obsidian - microcrystalline rhyolite lava)*

4.8.1. Description

This lava lithology crops out on the southern summit of Dalakvíslfell, where it forms low dark grey cliffs, and on the northern part of the eastern flank of Dalakvíslfell, where there is a chain of 20-100 m long lava bodies aligned roughly north-east -

south-west (Fig. 4.3). The three northern lava bodies are sheet-like, with tightly folded flow banding, whereas the two larger bodies to the south are irregular, and have steeply inclined flow banding. The lavas have outer carapaces of black to mid-grey vesicle-poor obsidian, which is variably perlitised. The eastern margin of the largest lava body, on the south summit of Dalakvíslfell, has a perlitised obsidian margin > 5 m thick, with patches of monomict, clast-supported perlitic obsidian breccia. The proportion of clasts in the breccia rises from 10 % to ~60 % as the breccia grades into the lava. Nearby, close to the south summit of Dalakvísl, the lava is cut by anastomosing orange veins 1-5 mm wide, giving it a brecciated appearance. The obsidian here is dark green and perlitised. Interior parts of all bodies of lava 1 are mid- to pale grey and microcrystalline or microspherulitic, with platy fractures parallel to flow banding.

The south-eastern of the four northerly lava bodies (Fig. 4.3, Fig. 4.7) is 40 m long and ~5 m thick, and flow banding dips steeply into the present day slope. A finger of lava, which is clearly connected to the main body, is c. 30 m long and <2 m thick. Flow banding in the base of the finger is parallel to and drapes over the modern day slope, but is ramped to near-vertical on the upper surface (Fig. 4.15). Rounded basaltic inclusions were discovered in the microcrystalline interior of the finger, the largest measuring 5 cm across.

The exposure at 880 m elevation 150 m north-east of the northern summit of Dalakvíslfell consists of platy-fractured microcrystalline rhyolite surrounded by a perlitised obsidian carapace. Columnar joints cut the obsidian at the north-east limit of the exposure. These are spaced 7-10 cm apart and are aligned normal to a steeply-dipping planar surface. Flow banding is mostly steep within the lava, and contacts with the surrounding breccia are not well exposed.

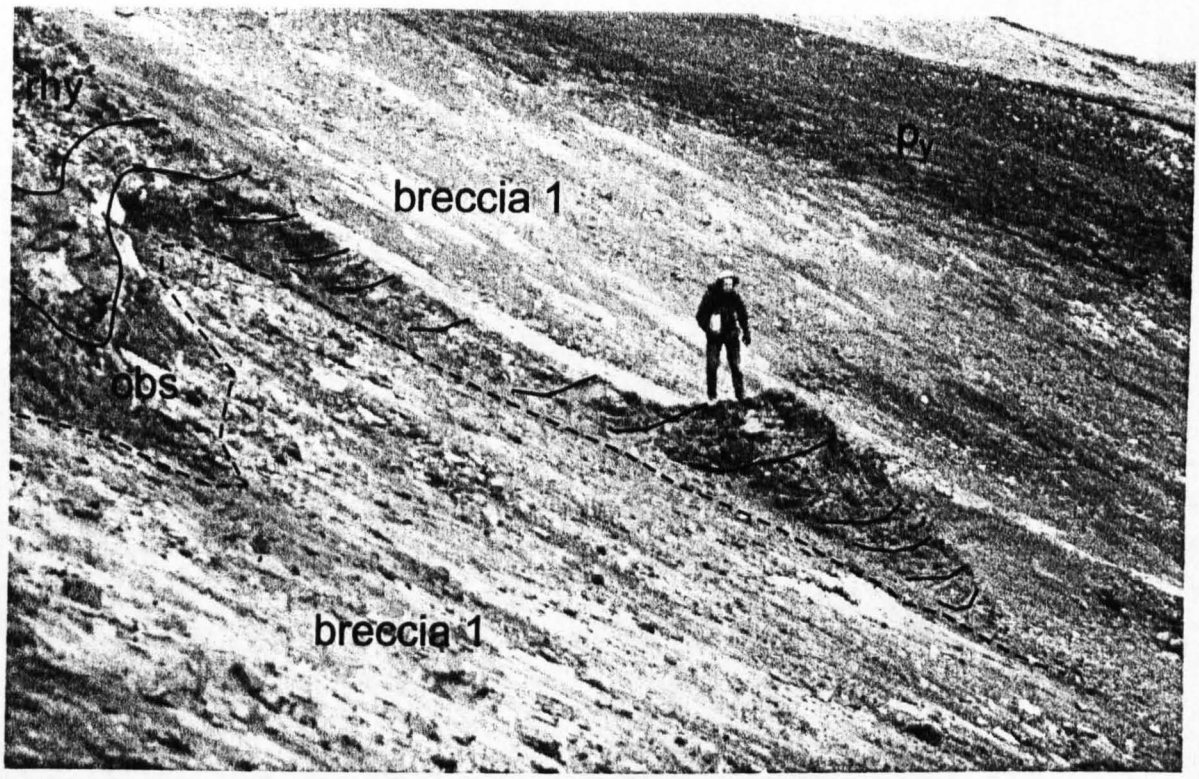

Fig. 4.15. A body of lava 1 exposed 350 m north-east of the north top of Dalakvíslfell, looking north. The figure, 1.9 m tall, is standing on a finger of lava that is oriented approximately parallel to the modern day slope (dotted line indicates the base of the finger). Flow banding within the finger is ramped (solid lines) and is contiguous with a large lava body, seen on the extreme left of the photograph. This lava body has a black obsidian margin ~2 m thick, labelled *obs*, which envelops a platy-fractured microcrystalline interior (labelled *rhy*). The lava overlies poorly-exposed breccia 1, which is mantled by dark grey Holocene pyroclastics at the top of the photograph (labelled p_y).

4.8.2. Interpretation

These are lava flows and domes with marginal autobreccia and contorted flow banding (Cas & Wright 1987). However, their mode and environment of emplacement is not easily determined, due to poorly-exposed contacts with the surrounding breccias. Perlitisation suggests that the lavas were invaded by aqueous fluids whilst still hot (Davis & McPhie 1996). The gradational contact with breccia 1 on the south summit of Dalakvíslfell is not well understood (see section 4.4). This lava body on the south summit has no ice-contact features and may be subaerial. Conversely, the lava body at 880 m elevation north-east of the north summit has columnar joints characteristic of lava-ice contact (Lescinsky & Sisson 1998). Steeply dipping flow banding and the overall morphology of this exposure is suggestive of a poorly-exposed vent, which possibly fed the breccia 2-stringer deposits down-slope to the east. The lava body to the north may have intruded the surrounding breccia, before feeding a small, ramped lava body which flowed down-slope over the breccia.

4.9. Lava 2 (*columnar-jointed lava lobes)*

4.9.1. Description

Columnar-jointed lava lobes are well exposed on the north bank of Dalakvísl about 400 m south of Dalakvíslfell south summit (Fig. 4.3). They form prominent dark protrusions that stand 5-10 m above the surrounding poorly-exposed breccia 1 (Fig. 4.16a). Lava 2 also occurs, but is less well exposed, within breccias 3 and 4. Irregular and conical lava bodies within breccia 1 are typically 5-10 m across and 3-5 m thick, but exceptionally 40 m across and 20 m thick. Good dissection reveals that the lava bodies are commonly connected (Fig. 4.16a). Lava lobes have single or multiple black

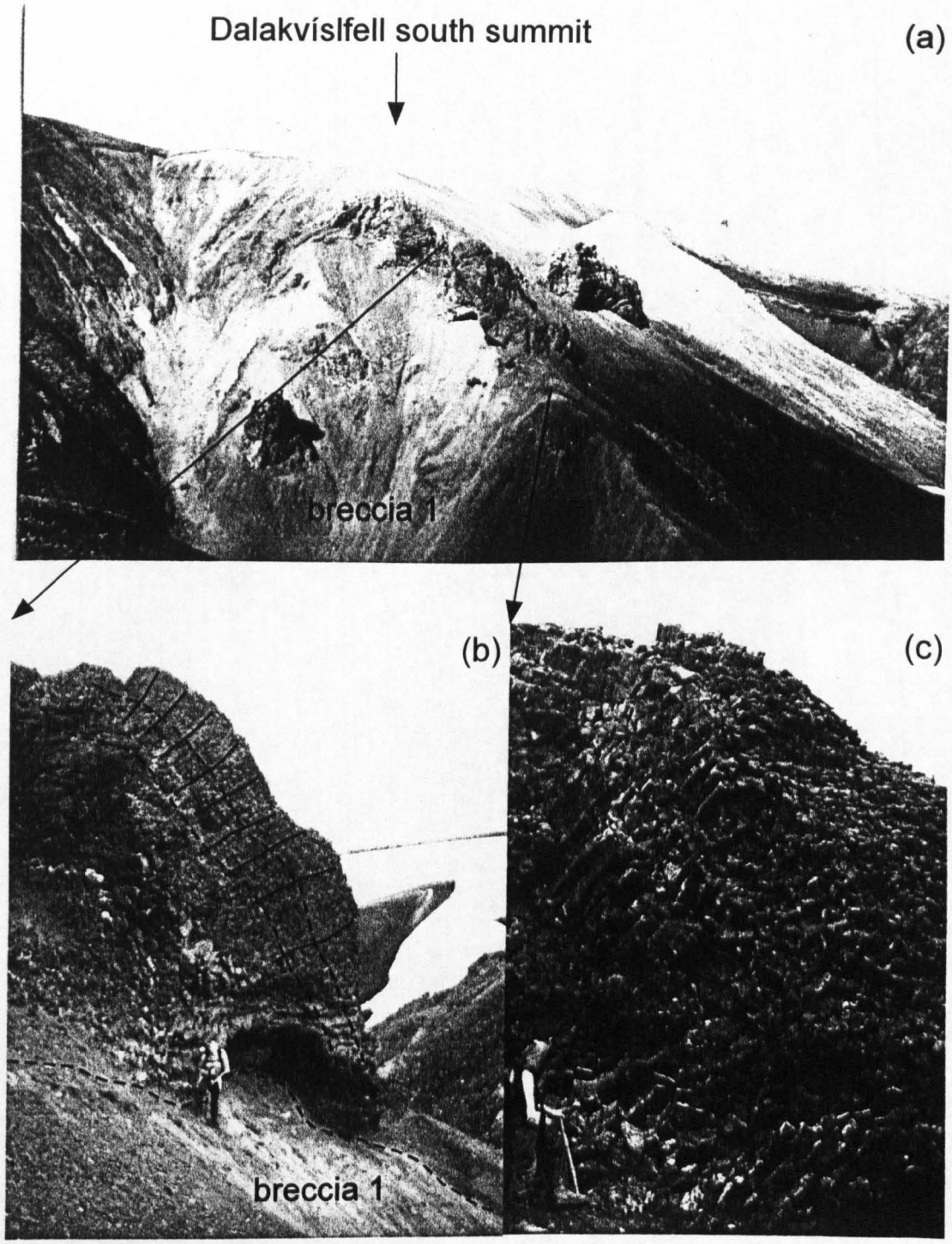

Fig. 4.16. Field photographs of columnar-jointed lava 2. **(a)** Looking northward to the exposure of lava 2 within breccia 1 of the north bank of Dalakvísl, 400 m due south of the south summit of Dalakvíslfell (Fig. 4.3). Numerous columnar-jointed lavas form dark knolls that protrude from the surrounding breccia. **(b)** Close-up of the base and sides of the largest lava body in (a), looking east-north-east. Dotted lines indicate the orientation of flow banding and the position of the basal contact with breccia 1. Solid lines indicate the orientation of columnar joints in the sides and upper surface of the lava. The pale material in the lower part of the photograph is breccia 1. The figure is 1.8 m tall. **(c)** Detail of the columnar-jointed carapace seen in (b). The regular widths and polygonal cross-section of the columns are evident. Pale material on joint planes appears to be alteration. Figure is 1.9 m tall.

obsidian carapaces typically 0.5-1 m thick, which contain <5 % volume smooth-walled vesicles up to 50 mm long. Lobe interiors consist of mid grey microcrystalline rhyolite, with <5% irregular vesicles <25 mm long. Flow banding wraps around lava bodies, and continues from one lava body to the next. The upper parts of lava lobes are cut by spectacular columnar joints (Fig. 4.16b, c). These are slender, 7-20 cm apart, and arranged normal to steeply-dipping surfaces. Joints penetrate into microcrystalline lobe interiors. Where exposed, lobe bases lack columnar joints (Fig. 4.16b). There is a zone of obsidian 0.3-0.5 m thick at lobe bases, which is increasingly fractured, perlitised and pale-coloured downwards, and grades into clast-rotated mid-grey perlitised obsidian breccia suspended in an unconsolidated matrix of blocky, low-vesicularity ash shards. Angular obsidian clasts are coated by pale ash. Locally, irregular veins of ash <5 mm wide penetrate up to 30 cm into the obsidian margin.

4.9.2. Interpretation

The columnar-jointed lava lobes of Dalakvísl are similar to those at Bláhnúkur (Chapter 2), and are interpreted as intrusive pillow-like lava bodies which rose through wet, poorly-consolidated breccias to the glacier base. Complex budding and branching of lava bodies is evident, indicating that intrusive bodies of magma within the breccia had 'burst-outs', feeding new lava bodies, when their outer carapaces failed (Yamagishi & Dimroth 1985). The lack of columnar joints at lobe bases indicates a different cooling regime from that at the top of lava lobes, with minor fragmentation driven by quenching and low-explosivity magma-water interaction (e.g. Kokelaar 1982, White & Busby Spera 1987). The arrangement of columnar joints is similar to that observed at Bláhnúkur. It is inferred that lobes chilled against steeply-inclined ice walls at the glacier base.

4.10. Lava 3 (*irregular vesicular peperitic lavas, L_3*)

4.10.1. Description

Numerous mid- to dark grey glassy lava bodies crop out within breccias 1, 2 and 3 as low-lying humps mostly concealed by scree (Fig. 4.3, Fig. 4.17a). These lava bodies are between 1 and 30 m across and often have extremely irregular shapes. Many are linked in a complex three-dimensional network. They consist of variably perlitised, crumbly obsidian with 5-30 % smooth-walled elongate vesicles up to 2 cm long, commonly parallel to the lava margin. Contacts with the surrounding breccia are peperitic, with a zone of jigsaw-fit breccia 5-10 cm thick. Within the jigsaw-fit zone, angular fractures in the intact obsidian are coated by pale grey fine-grained ash. Such fractures completely pervade the smallest lava bodies (Fig. 4.17b). Larger lavas have an internal zone of vein-free, perlitised obsidian. Microcrystalline rhyolite is absent, as are columnar joints.

4.10.2. Interpretation

The peperitic nature of these lavas indicates that they intruded poorly-consolidated wet sediments (e.g. Cas & Wright 1987, White & Busby-Spera 1987). A high proportion of vesicles suggests that the lavas were emplaced at relatively low confining pressures (Hunns & McPhie 1999). Pervasive perlitisation is consistent with interaction between hot (but solidified) magma and water (e.g. Davis & McPhie 1996). Columnar joints are absent, suggesting that the lavas did not reach the base of the glacier (c.f. lava 2). All the outcrops of lava 3 are glassy, which may indicate rapid cooling through the glass transition. This suggests that lava 3 cooled more

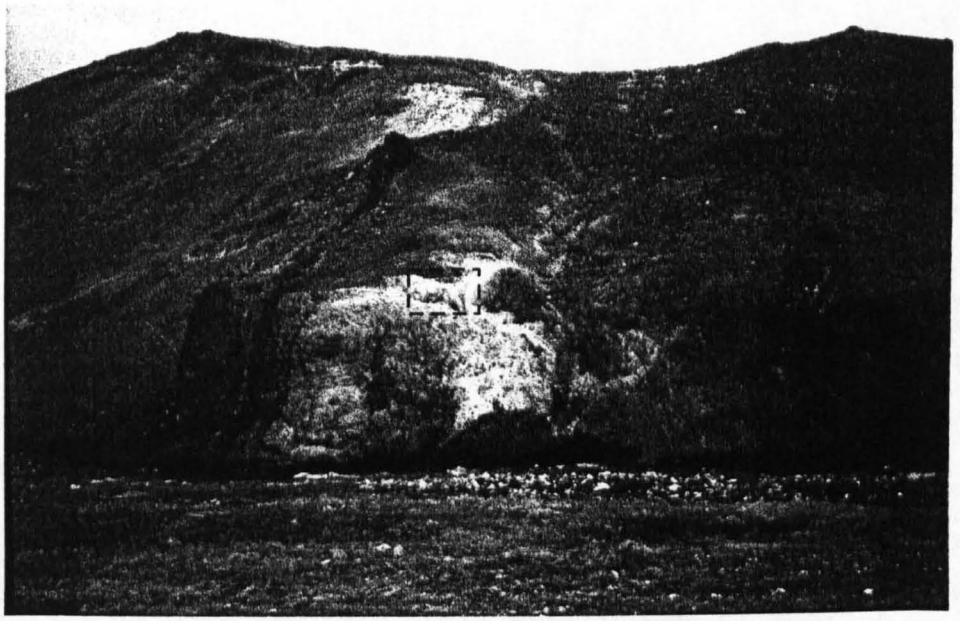

(a)

(b)

Fig. 4.17. (a) Irregular bodies of lava 3 (dark patches) within breccia 3 on the north bank of Dalakvísl, 500 m ESE of the south summit of Dalakvíslfell. Scree derived from the lava bodies conceals much of the breccia, with the exception of several pale patches. *Dashed box* indicates the field of view of Fig. 4.17b. **(b)** Close-up of the lower margin of a 15 m-long peperitic lava body. Intact perlitic obsidian (extreme top) grades downwards into jigsaw-fit obsidian and clast-rotated matrix-supported breccia (immediately above the pen). A small, irregular, dark obsidian body beneath the pen is entirely riddled by fractures, and which grades downwards into matrix-supported obsidian breccia (bottom of photograph). The small obsidian body is thought to be an apophysis from the margin of the larger peperitic body. Note the pale colour of the obsidian clasts within the breccia which is due to extreme perlitisation and fracturing. *Pen* is 15 cm long.

rapidly than the columnar-jointed lobes of lava 2. If so, the reason for more rapid cooling may be related to the irregular morphology of the bodies of lava 3, or alternatively, lava 3 was simply emplaced within wetter breccias.

4.11. (*Thick valley-filling columnar-jointed lava flows, L_4*)

4.11.1. Description

A spectacular rhyolitic lava body 90 m thick is exposed at Rauðufoss (Fig. 4.3, Fig. 4.18). It consists of orange-red altered microcrystalline rhyolite, and is cut by columnar joints spaced 15-20 cm apart. The arrangement of joints is unusually chaotic, with roseate structures in the upper 20 m of the flow. None of the margins of the flow are exposed, and the lava could not be examined closely. The lava appears to fill in a valley >80 m deep incised into basaltic diamicton and other older rocks. It cannot be traced to the north or the south, although similar lava bodies have been reported on the northern fringe of Rauðufossafjöll, some 10 km to the north-west (K. Sæmundsson, personal communication).

4.11.2. Interpretation

The lava appears to have flowed within a river valley, and been quenched by water flowing over its upper surface, which typically forms roseate jointing patterns in the upper parts of the lava (Sæmundsson 1970). It is unclear whether the valley was ice-covered at the time of lava effusion. The valley may have been incised by flowing meltwater during deglaciation (e.g. Cofaigh 1996). Similar lava flows have been observed in incised valleys on the slopes of Andean stratovolcanoes (J. S. Gilbert, personal communication).

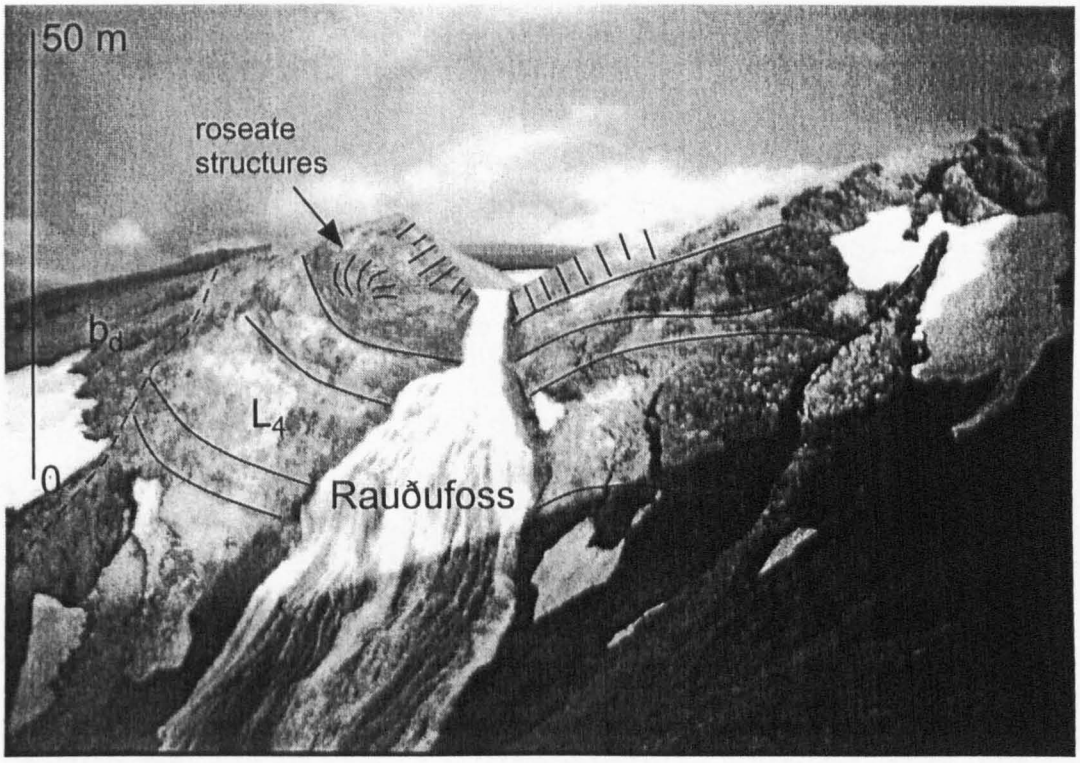

Fig. 4.18. Photograph of lava 4 exposed at Rauðufoss, looking SE. Although the lava is ~90 m thick, only the upper 50 m of the lava is visible in this view. Contacts between the sides of the lava and the surrounding basaltic diamicton are not exposed, but are inferred to be steep (inferred position indicated by dotted lines). Long solid lines within the lava indicate the orientation of flow banding. Short solid lines in the upper part of the lava are schematic and indicate the approximate orientation of columnar joints. Joint spacing is not drawn to scale.

4.12. Clastic dykes and veins

4.12.1 Description

Clastic dykes form a network of highly irregular, branching brown veins 1-50 cm thick that cut through subglacial rhyolite lithologies. Vein orientations vary from near-horizontal to near-vertical. Individual veins can be traced laterally for >50 m. They are best exposed at 780-800 m elevation 250-400 m east of the south summit of Dalakvíslfell (Fig. 4.3), where they cut breccias 1 and 3. Veins contain polymict poorly-sorted matrix-supported conglomerates, with a silt- to mud-grade matrix and sub-rounded clasts up to 10 cm in diameter in the widest veins. Clasts include vesicle-free grey basalt, scoriaceous black basalt, highly altered green and red rhyolite and rare obsidian. Clast sizes decrease and sorting is better in the narrowest veins. The outer 1-30 mm of veins is typically composed of well-sorted, finely planar-laminated fine-grained sandstone, which encloses a massive, poorly-sorted interior (Fig. 4.19). Laminae are parallel to vein margins. At 860 m elevation due north of the north summit of Dalakvíslfell, clastic dykes originate at the base of basaltic diamicton, which unconformably overlies breccia 1, and propagate downwards and laterally into the rhyolitic breccia. The proportion of scoriaceous basaltic clasts decreases from ~60 % at the base of the diamicton to 0 % within the breccia 5 m from the contact. Veins at this locality narrow, branch, and can be traced laterally >30 m into breccia 1.

4.12.2. Interpretation

Clastic dykes appear to originate at the base of till or diamicton overlying poorly-consolidated breccias of the Dalakvísl rhyolite formation. Their vein-like nature and internal sedimentary structures suggest that clast-rich material was injected

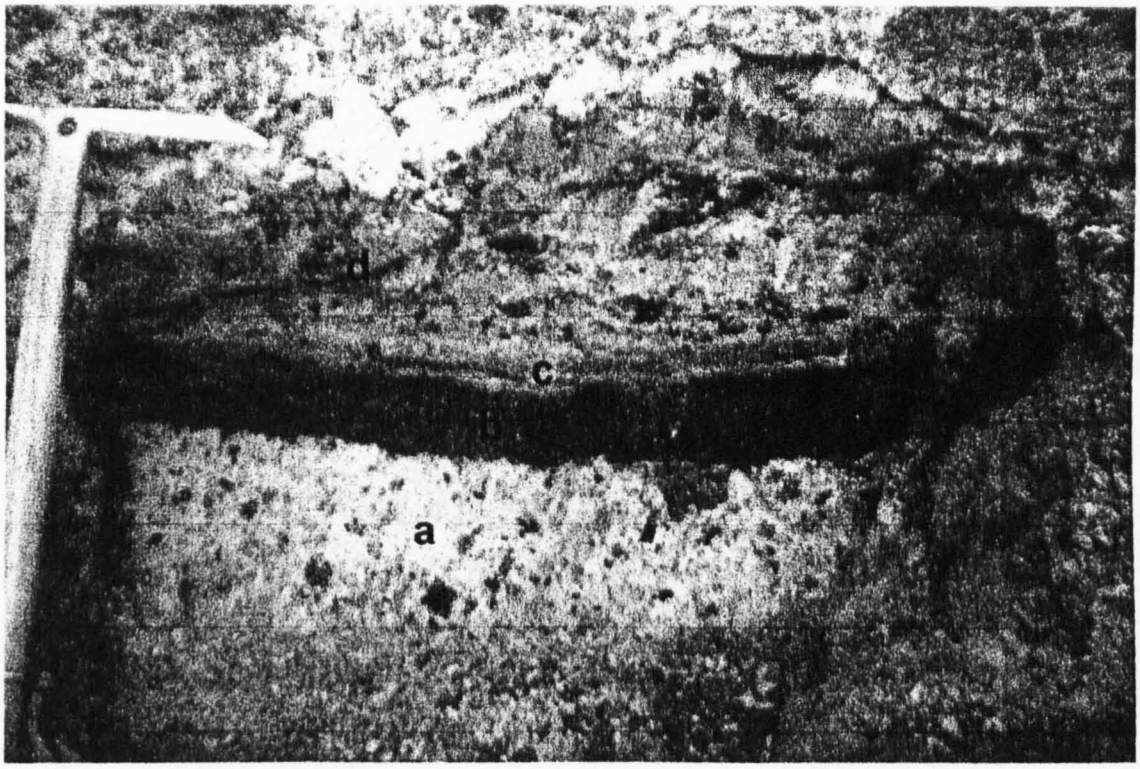

Fig. 4.19. Close-up of a typical clastic dyke, cutting breccia 1 150 m due south of the south summit of Dalakvíslfell. Breccia 1 consists of angular clasts of dark grey obsidian within a pale grey ash matrix (labelled a). The central part of the dyke, which is near-planar and inclined at ~25 degrees to the horizontal, is composed of poorly-sorted dark conglomerate (b), containing sub-rounded clasts of basalt and altered rhyolite up to 2 cm across. The upper 3 cm of the dyke consists of laminated, well-sorted gravelly sandstone (c). A narrow vein (d) branches from the main vein. It is 10 mm wide and filled with well-sorted sandstone. Grains within the narrow vein are much finer than those within the wider 'main' vein. The handle of the ice pick is 3 cm wide.

downwards and laterally into dilating cracks in the incompetent rhyolitic breccias. The presence of rounded clasts, a wide range of lithologies and a mud-grade matrix, plus the association with tills, points to a subglacial origin to the vein-filling material. Similar clastic dykes in Ireland are thought to have formed during rapid ice retreat, as glacier unloading caused rapid changes in the overburden pressure within waterlogged tills and diamicton at the glacier base (Rijsdijk et al. 1999). Clastic dykes at Dalakvísl may have a similar mode of origin.

Internal laminae within vein margins suggest that the supply of material to veins was pulsatory during the initial phase of crack widening, before the massive, poorly-sorted vein interiors were emplaced in a fluidised state. This is somewhat puzzling, since the 'host rock' needs to behave rigidly in order for a narrow crack to propagate and be sustained within it, yet the country rock in question here is poorly-consolidated breccia 1. Such rigidity may have been caused by (1) glacier overburden pressure or (2) the existence of a partially-frozen or permafrost layer in material beneath the glacier base (Kumpulainen 1994). However, there is no corroborative evidence that breccia 1 was once frozen. Further work on clastic dykes in Iceland may provide useful information about processes associated with deglaciation in Iceland.

4.13. Basaltic diamicton

4.13.1. Description

A patchy veneer of basaltic diamicton between 5 and 20 m thick overlies the Dalakvísl rhyolite formation, and is most extensive in the northern part of the mapped area, close to Rauðufoss (Fig. 4.3). Deposits are orange-brown, lithified breccias and conglomerates, consisting of variable proportions of grey vesicle-free pillow fragments and black scoriaceous lapilli within an orange-brown palagonitised fine-

grained matrix. Sedimentary structures are variable, with some exposures dominated by near-horizontal planar beds of moderately well-sorted sandstone, whereas other exposures are massive and poorly-sorted. Many exposures are cut by irregular, anastomosing pale orange veins <5 mm thick, filled with fine-grained material. Where exposed, the base of the diamicton lies upon a highly irregular topography, and clastic dykes propagate into the underlying rhyolitic breccias at one locality (see section 4.12.1).

4.13.2. Interpretation

These deposits are typical of the 'móberg' formations which are extensive throughout central Iceland, and thought to be formed during subglacial basaltic eruptions (e.g. Noe-Nygaard 1940, Jones 1966). The source of the basaltic material could not be determined from the limited area mapped in detail, but is likely to be one of numerous south-west - north-east trending subglacial basaltic ridges nearby. The well-sorted, bedded units were probably deposited in a fluvio-lacustrine environment (e.g. Skilling 1994). Although these deposits are yet to be radiometrically dated, their considerable lateral extent within Torfajökull and association with clastic dykes suggests that voluminous subglacial basaltic eruptions may have occurred at Torfajökull towards the end of the last glacial period. Hence these deposits may be less than 20 ka old.

4.14. Till

Exposures of massive, poorly-consolidated, orange-brown conglomerates in stream sections in the southern part of the mapped area are up to 40 m thick (Fig. 4.3). Deposits are interpreted as subglacial tractional or lodgement tills (e.g. Bennett & Glasser 1996). They contain rounded, facetted cobbles and boulders of various

lithologies, including basalt, rhyolite, obsidian and hydrothermally altered material, within a silt- to mud- grade matrix. Deposits appear to be thickest in the region currently dissected by Dalakvísl, and may have filled a palaeo-stream valley, but contacts are mostly obscured.

4.15. Holocene pyroclastics

Widespread non-welded, well-sorted layers of near-black basaltic scoriae 0.5-2 cm across interbedded with pale silicic pumiceous layers overlie all other lithologies at Dalakvísl, forming a blanket up to 1 m thick (Fig. 4.3). These are Holocene air-fall deposits from neighbouring volcanic systems, including Vatnafjöll, Veiðivötn and Hekla. Close to the north-western and south-eastern limits of the mapped area, black 'bombs' of vesicular basalt up to 30 cm across lie on the upper surface of the Holocene pyroclastic units, and are associated with prominent basaltic explosion craters 400-600 m in diameter, located 1 km to the north-west and south-east of the mapped area, respectively.

4.16. Discussion: emplacement mechanisms

The rhyolite formation at Dalakvísl is dominated by breccia 1, which is thought to have been formed by moderately explosive magma-water interaction at or close to the glacier base. There has been much intrusion of the breccia, by early-stage lava bodies which have almost entirely decrepitated and now form part of the breccia itself, and by lava bodies which are preserved as peperitic intrusions. Some peperitic intrusions (e.g. lava 2) appear to have reached the base of the glacier, and formed columnar-jointed upper carapaces, whereas the majority of intrusions solidified entirely within

the breccia and lack distinctive jointing patterns (lava 3). It is thus suggest that a branching network of lava bodies entered a pile of poorly-consolidated, wet subglacial breccias and some of the lava bodies reached the glacier base (Fig. 4.20). Larger-volume bodies of lava 1 have different characteristics: columnar joints are scarce, peperitic margins are not observed, marginal autobreccia is common and lava bodies are pervasively perlitised. It is difficult to determine whether these lavas were emplaced subglacially or subaerially, or indeed whether they formed during or after the accumulation of the pile of breccia 1.

In terms of sedimentology and ash shard characteristics, breccia 1 is intermediate between breccia A of Bláhnúkur (Chapter 2.5) and the ash lithology of South-east Rauðufossafjöll (Chapter 3.4). The bodies of lava 1, the like of which is not exposed at Bláhnúkur or South-east Rauðufossafjöll, may represent the initial phase of construction of a flat lava cap. If so, continued eruption at Dalakvísl would have increased the proportion of lava 1, and a more extensive lava cap may have developed.

The spectacular breccia 2-stringer lithology is similar to a poorly-exposed lithology observed on the south flank of South-east Rauðufossafjöll (Chapter 3.4). It appears to have formed in a lower-pressure, drier environment than breccia 1, since vesiculation is considerably higher and intrusive bodies within the upper part of breccia 2 are not perlitised and lack peperitic margins. Such a 'dry' and low-pressure eruption style may only occur in a subglacial environment if there is an eruption within a well-drained, low-pressure subglacial cavity. A cavity of this type is most likely to develop either (1) beneath thin ice (Smellie & Skilling 1994), or (2) if the subglacial melting rate is high and exceeds the cavity closure rate (Hooke 1984). Rapid subglacial melting will occur during periods of high eruption rate and rapid energy exchange, and will be

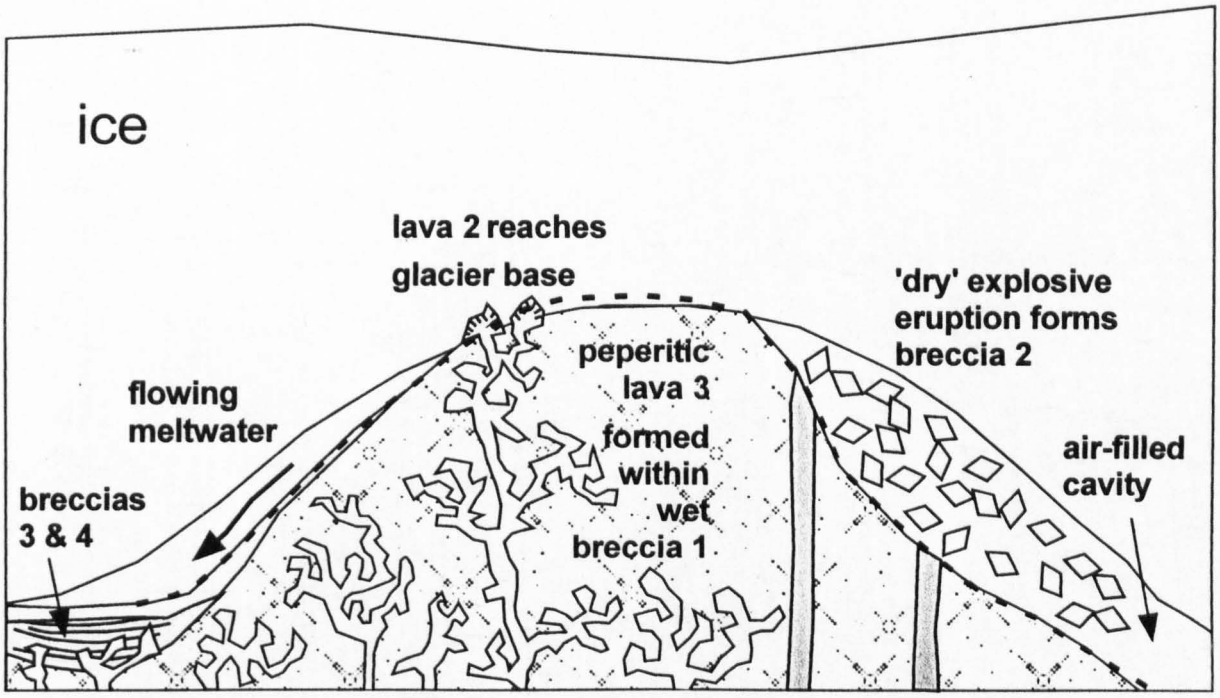

Fig. 4.20. The proposed model for some of the eruptive behaviour at Dalakvísl. The dotted line indicates the suggested position of the water table. All material beneath the line is likely to be water-saturated, whereas air gaps may develop above the line. A wet pile of breccia 1 is intruded by an anastamosing network of lava bodies. Many freeze entirely within the breccia, forming peperitic lava 2, whereas some lava bodies reach the glacier base, and columnar-jointed lava 3 is formed. Meltwater flows down the south flank of the edifice, carrying ash and pumice with it, and accumulates in a small valley-ponded lake, where deposition occurs. Meanwhile, to the north, a dry explosive eruption occurs within a well-drained cavity above the water table (see Fig. 4.12 for more details of this eruption style).

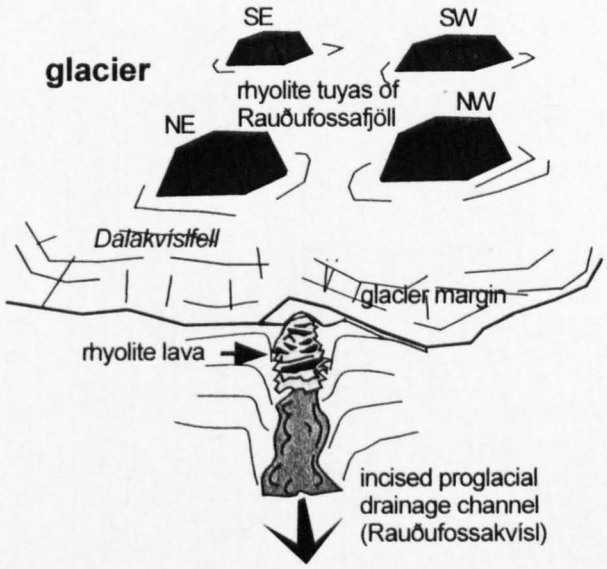

Fig. 4.21. Schematic diagram showing a possible emplacement environment for lava 4. It is assumed that the subglacial rhyolite tuyas of Rauðufossafjöll have already been formed, and are now nunataks rising above a retreating glacier. Meltwater formed during the eruption of these tuyas and of the Dalakvísl formation (not seen) has scoured a deep erosive channel in the bedrock. This feeds a proglacial stream, which occupied the approximate position of the modern-day Rauðufossakvísl. An effusive eruption from a subglacial vent close to the glacier margin fed a rhyolite lava flow, which flowed within the drainage channel and beyond the glacier snout. Flooding of meltwater over the cooling lava formed columnar joints on its upper surface (Sæmundsson 1970).

favoured by a steep bedrock slope, which will aid the drainage of meltwater. The apparent 'dryness' of parts of breccia 2 can be explained if parts of the breccia were emplaced at a position above the local water table. This scenario is most plausible if the overlying glacier were thin (<c. 100 m), or if the eruption occurred at a local peak in the bedrock topography (Björnsson 1988, Smellie & Skilling 1994). The latter explanation appears poor, since Bláhnúkur was definitely constructed on a peak in the bedrock topography and yet no such 'dry' lithologies were formed. Stringers within breccia 2 are interpreted as intrusive bodies formed during an eruption within a subglacial cavity that had become entirely filled with poorly-consolidated, hot and dry breccia. Filling of a subglacial cavity may only occur if the rate of enlargement of the cavity cannot keep pace with the input rate of material into the cavity. Conditions in which cavities may become filled are discussed in Chapter 5.

Breccias 3 and 4 show evidence for deposition in a fluvio-lacustrine environment, probably by volcanically-generated meltwater. This is thus good evidence for localised accumulation of meltwater at the eruption site during a subglacial rhyolite eruption, a scenario considered unlikely by Hoskuldsson & Sparks (1997). It may be no coincidence that meltwater accumulation occurred in what is now Dalakvísl stream valley, since this valley probably existed during the eruption and carried a subglacial meltwater stream. It would thus be a prime location for the accumulation of eruption-generated meltwater (Fig. 4.20), and for deposition of any sediment carried by the meltwater, as current energies are likely to have abruptly dropped at the break in slope. Drainage of meltwater may have been hindered by the emplacement of eruption-generated material within drainage pathways. Ripple structures within sandstones of breccia 4 provide clear evidence for flowing meltwater and localised meltwater drainage, akin to evidence gathered from the Grænagil stream

section at Bláhnúkur (section 2.4) and the Blautakvísl stream section at South-east Rauðufossafjöll (section 3.11).

Lava 4 at Rauðufoss appears to have flowed within a palaeo-stream valley that was probably eroded by meltwater generated by the subglacial eruption at Dalakvísl or the tuyas of Rauðufossafjöll (Fig. 4.21). It is not possible to tell whether the valley was covered by ice at the time of lava effusion. A larger-scale analogue is the river Jökulsá á Fjöllum in northern Iceland, which flows within a 100 m deep canyon thought to have been incised during jökulhlaups generated by volcanic eruptions beneath northern Vatnajökull (Björnsson 1988). Lava 4 was probably fed by an effusive vent close to the palaeo-valley of Rauðufossafjöll. Similar lava flows appear to have flowed over 10 km northwards from the northern margin of Rauðufossafjöll (K. Sæmundsson, personal communication).

The inferred palaeo-ice thickness at Dalakvísl is >150 m, based on the thickness and relief of the outcrops of breccia 1, and it may not have been much greater. This compares with >350 m for Bláhnúkur and >400 m for South-east Rauðufossafjöll. This may explain the presence of 'dry' facies beneath the relatively thin ice at Dalakvísl (c.f. Smellie & Skilling 1994). However, 'dry' lithofacies also appear to have been formed at South-east Rauðufossafjöll, probably beneath much thicker ice. This raises the possibility that the eruption rate can also influence the eruptive style - and this is an idea that will be explored in Chapter 5.

4.17. Summary

The subglacial rhyolite succession at Dalakvísl is intermediate in nature between Bláhnúkur and South-east Rauðufossafjöll, and fragmental lithologies are unusually well-exposed. Much of the succession consists of massive, blocky fine-grained ash that is thought to have been formed during low-explosivity magma-water interaction

within subglacial cavities. The ash appears to have been wet during the eruption, since it was subsequently intruded by a variety of peperitic lava bodies. Some lava bodies appear to have reached the glacier base, where they formed columnar-jointed carapaces as the magma chilled against ice walls. Ash at one locality is highly vesicular, and contains glassy obsidian 'stringers' and bombs. Fragmentation there appears to have been triggered by magma degassing, and there is no evidence for interaction with water. Such a 'dry' eruption style requires the existence of a well-drained subglacial cavity. The nature of the obsidian stringers suggests that the cavity became filled with dry tephra, and the eruption switched to an intrusive style. Ash exposed in the stream cutting of Dalakvísl has sedimentary features consistent with fluvio-lacustrine redeposition, and is intruded by peperitic lava bodies. This suggests that meltwater may have locally ponded within a palaeo-valley during the eruption. There is no subaerial lava cap to the succession at Dalakvísl, suggesting that the eruption did not pierce the ice surface.

The variety of eruption styles inferred from the lithologies at Dalakvísl indicates that the mechanism of eruption depends upon the conditions within the subglacial cavity and the eruption rate. Simple numerical models are constructed in the next chapter, which predict the eruption style and cavity conditions during subglacial eruptions, and which can be applied to Dalakvísl.

Chapter 5.
Numerical models of volcano-ice interaction

The varied products of subglacial rhyolite eruptions at Torfajökull suggest that contrasting patterns of volcano-ice interaction have occurred (Chapters 2-4). This chapter aims to address the basic mechanics of subglacial rhyolite eruptions, including the fundamental question of how energy is exchanged between magma and ice. It aims to predict possible patterns of melting and deformation of the glacier, and to simulate the growth of the subglacial volcanic edifice. A volcano-ice system is difficult to model, with complex feedback mechanisms between individual components, each of which behaves non-linearly. In order to bypass the seemingly intractable problems associated with such a complex multi-component system, it is necessary to make many assumptions and simplifications, each of which is introduced and discussed.

The numerical models presented in this chapter are highly simplified, and present a schematic overview of the physical evolution of the system. However, they can be used to assess the various factors which may influence the style of a subglacial rhyolite eruption, such as the ice thickness, magma discharge rate and magma vesicularity.

5.1. Outline of the models

A rhyolitic eruption is considered to behave as a point source of thermal energy at the base of a horizontal ice sheet with constant material properties. The thermal energy released from the magma causes melting of the ice, and a hemispherical cavity develops in the glacier base (Fig. 5.1). Ductile deformation of the ice roof causes closure of the cavity, in accordance with Nye's law (Nye 1953). This behaviour breaks down when the height of the cavity approaches the thickness of the ice, and brittle fracture of the roof occurs. Meltwater is assumed to drain continuously away from the cavity, in accordance with field observations. A hemispherical pile of volcanic debris accumulates within the cavity (Fig. 5.1). The model predicts the evolution of the cavity, as rates of closure by ice deformation and enlargement by melting vary with time. The symbols, suffixes and constants used in this chapter are listed in Table 5.1.

5.2. Heat exchange between magma and ice

5.2.1. Thermal energy from magma

The thermal energy released per unit volume of magma during cooling and quenching is given by

$$E_T = \rho_l(1-\theta)(c_l\Delta T_l + \Delta x L_l) \quad (1)$$

where θ denotes magma vesicularity, ρ_l magma density, c_l magma heat capacity, ΔT_l temperature change of the magma, L_l latent heat of crystallisation of magma and Δx increase in crystallinity of the magma during cooling. The heat capacity of gases

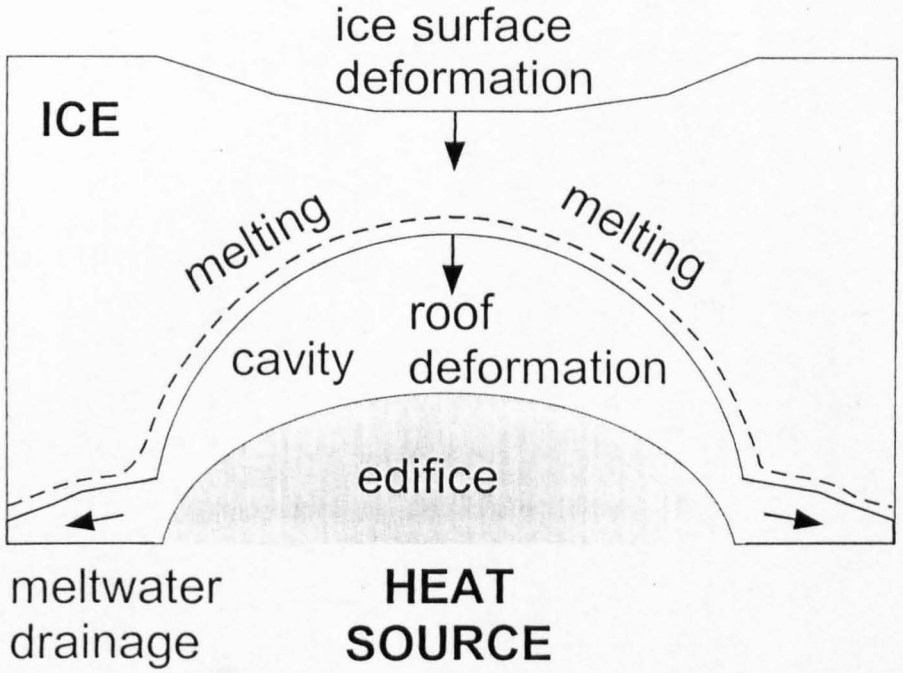

Fig. 5.1. Schematic diagram showing the volcano-ice system modelled in this chapter. Rhyolitic magma is emplaced at the base of the glacier, forming a hemispherical edifice. Thermal energy from the magma causes melting of the overlying ice, which generates a hemispherical cavity. Ductile deformation of the cavity roof and ice surface above (vertical arrows) occurs when pressure in the cavity is sub-glaciostatic. Meltwater drains continuously from the cavity in localised drainage channels (subhorizontal arrows).

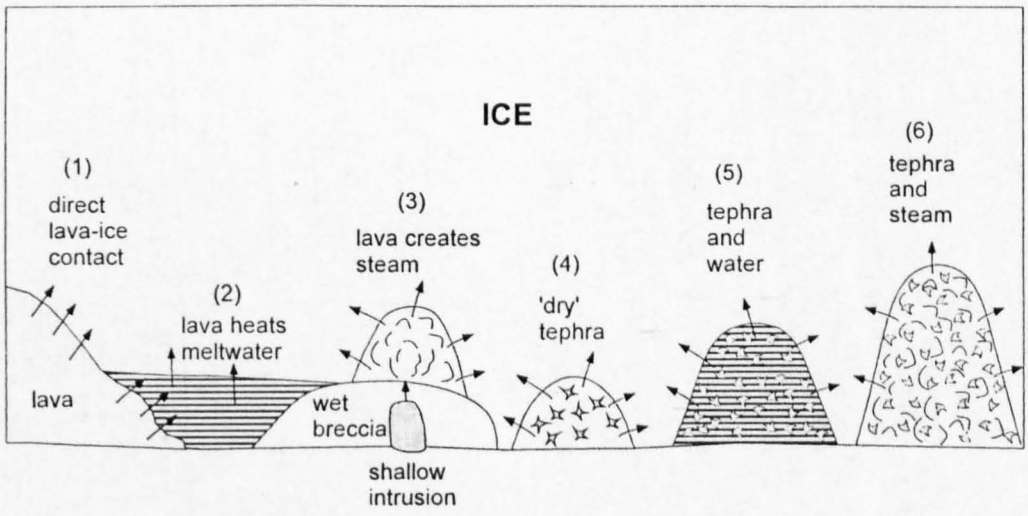

Fig. 5.2. Schematic diagram illustrating various possible mechanisms of energy exchange between magma and ice. The likely products of each mechanism are listed in Table 5.2.

Symbol		Units
Q	heat output	W
E_T	total energy per unit magma volume	J m^{-3}
V	proportion of meltwater vaporised	-
V	volume	m^3
ΔV	change in volume	m^3
D	magma rise velocity	m s^{-1}
A	surface area	m^3
M	bulk modulus	Pa
R	radius	m
Q_l	magma discharge rate	m^3 s^{-1}
r'	rate of change of radius	m s^{-1}
a	volumetric melting rate	m^3 s^{-1}
v	volume per unit volume of magma	-
X	fraction of magma heat released instantly	-
Y	rate of delayed heat release from magma	-
N	number of columns	-
s	spacing of joints	m
y	depth of penetration of joints	m
z	distance below glacier base	m
h	ice thickness	m
T	temperature	°C
ΔT	temperature change	°C
ΔP	pressure difference	Pa
α	angle from horizontal	degrees
k	thermal conductivity	W m^{-1} $°C^{-1}$
ρ	density	kg m^{-3}
μ	dynamic viscosity	kg m^{-1} s^{-1}
c	specific heat capacity	J kg^{-1} $°C^{-1}$
θ	magma vesicularity	-
t	time	s
S	packing coefficient	
L	heat of fusion	J kg^{-1}
x	magma crystallinity	-

Constants		Values
g	gravitational acceleration	9.8 m s^{-2}
n	Glen's flow law constant	3
B	ice viscosity parameter	5.3×10^7 Pa $s^{1/3}$

Suffix
c cavity
cr critical
d deformation
e edifice
e eff
eq equilibrium
f fractured
g glaciostatic
h conductive
i ice
j joint
l magma
m melting
m minimum
o initial
r roof
t time
T total
v vaporisation
w water
Properties of ice
T_i 0°C
ρ_i 917 kg m^{-3}
L_i 3.35×10^5 J kg^{-1}
k_i 2.1 W m^{-1} $°C^{-1}$
Properties of water*
T_v 100°C at 0.1 MPa
ρ_w 1000 kg m^{-3}
L_w 2.3×10^6 J kg^{-1}
c_w 4.2 kJ kg^{-1} $°C^{-1}$
M_w 2.05 GPa
Properties of rhyolite magma
T_l 900 °C
ρ_l 2300 kg m^{-3}
c_l 1.04 kJ kg^{-1} $°C^{-1}$
L_l 2.1×10^5 J kg^{-1} (crystalline), 0 (glassy)
k_l 6.9 W m^{-1} $°C^{-1}$
μ_l 10^6 kg m^{-1} s^{-1}

Table 5.1. Variables and constants used in the numerical models. Data from Hoskuldsson & Sparks 1997, except *Haar et al. 1984.

within vesicles is assumed to be negligible. The equation above is equation (1) of Hoskuldsson & Sparks (1997), modified to account for variable vesicularity of the magma, and crystallisation during cooling. Since the majority of the subglacial rhyolitic deposits studied in this project are predominantly glassy (with the exception of the lava lobes of Bláhnúkur), Δx is assumed to be 0, hence equation (1) condenses to

$$E_T = (1-\theta)\rho_l c_l \Delta T_l \qquad (2)$$

and E_T is thus the maximum thermal energy that can be transferred from the unit volume of magma to the ice. The temperature of the magma upon emplacement is estimated at 900 °C (Hoskuldsson & Sparks 1997). The products of subglacial rhyolitic eruptions at Torfajökull are estimated to contain between 0 and ~60% vesicles, hence θ varies from 0 to 0.6. E_T may thus range from 2.6×10^9 J m^{-3} for non-vesicular magma to 1.0×10^9 J m^{-3} for magma containing 60% vesicles.

5.2.2. Heat transfer mechanisms

The heat within rising magma may be all or partially transferred to the ice. Various heat exchange mechanisms are possible, depending upon the eruptive conditions (Fig. 5.2, Table 5.2). Heat exchange during fragmentation is likely to be rapid (e.g. Dobran & Papale 1993), whereas heat loss from intact lava bodies or intrusions can be orders of magnitude slower (e.g. Manley 1992).

Energy exchange system	Pressure	Probable rhyolitic products	Examples at Torfajökull	Examples elsewhere	Required conditions	References
lava → ice (1)	~Glaciostatic.	Columnar-jointed lava bodies with minor massive breccias.	Upper surfaces of lava lobes on Bláhnúkur? Lava C on SE Rauðufossafjöll?	Lava flows on Mount Rainier and elsewhere.	Effusive eruption within air-filled subglacial cavity. Meltwater drainage.	Lescinsky & Sisson 1998, Lescinsky & Fink 2000.
lava → water → ice (2)	~Glaciostatic.	Perlitised lava bodies with associated vesicle-poor glassy breccias which display evidence for deposition within water, and contain blocky ash shards.	Bláhnúkur lava lobes and associated breccias? Columnar-jointed sides of lava D on SE Rauðufossafjöll?	Pillow lavas at the base of basaltic tuya/tindar successions.	Effusive eruption within water-filled subglacial cavity. Pressure sufficiently high to prevent fragmentation of magma. Meltwater accumulation.	Hoskuldsson & Sparks 1997, Lescinsky & Fink 2000, Skilling 1994.
lava → steam → ice (3)	Atmospheric to glaciostatic, depending upon space.	Variable. If lava intrudes shallow wet sediments, may produce pumiceous peperitic lavas. Evidence for fluxing by steam.	Bláhnúkur lava lobes and associated breccias?	None described.	Drainage of meltwater from cavities into permeable bedrock. Intrusion of waterlogged material at the glacier base by lava bodies.	Kiver & Steele 1975; Chapter 2: this study.
tephra → ice (4)	Atmospheric to glaciostatic, depending upon space.	Variable. If tephra emplaced on ice surface, may produce poorly-sorted debris flow deposits with evidence for fluidisation. If tephra emplaced subglacially, may produce massive deposits of vesicular ash.	Vesicular portions of the basal ash at SE Rauðufossafjöll? Ridge C at Dalakvísl?	Lahars generated during pyroclastic flows over snow and ice.	The kinetic energy and thermal energy of tephra is transferred to ice during collision with the ice or emplacement on the ice. There is little magma-water interaction and little steam is generated. If subglacial, requires a drained cavity.	Walder 2000a, b; Major & Newhall 1989.
tephra → water → ice (5)	Glaciostatic if subglacial, hydrostatic if no ice roof.	Low-vesicularity tephra, possibly displaying evidence for deposition within water (e.g. turbidites, laminated sandstones, local channels).	None identified.	Bedded vesicle -poor 'hyaloclast - ites' at basaltic tuyas.	Explosive magma-water interaction within a water-filled cavity. Thermal and kinetic energy transferred to ice. No 'air gap' for steam formation.	Skilling 1994, Smellie 1999.
tephra → steam → ice (6)	Depends upon steam pressure.	Massive low-vesicularity tephra.	Low-vesicularity portions of basal ash at SE Rauðufossafjöll.	None described.	Explosive eruption within a partly water-filled cavity. Requires drainage of meltwater from cavity, and possibly percolation into growing pile of debris.	----------

Table 5.2. Possible energy exchange mechanisms during subglacial rhyolite eruptions.

Heat release as a function of time may be expressed by the following equation:

$$\int_0^t Q_{h(t)}dt = E_T\left[X + \int_0^t Y_{(t)}dt\right] \quad (3)$$

where Q_h is the heat flux from the volcanic deposits, X is the proportion of the total magmatic heat released instantaneously (for these models, in time $t << 10^5$ s) and Y represents gradual heat release on the order of 10^5-10^6 s. The sum of X and the integral of the Y function (within the square brackets) is 1, hence equation (3) is equal to E_T. likely to be close to 1 during phreatomagmatic fragmentation (e.g. Dobran & Papale 1993), and close to 0 during cooling of intrusive bodies and intact lava flows (e.g. Manley 1992).

During the 1996 Gjálp eruption, 3 km^3 of meltwater was generated during the 12 days of the eruption, and another ~1 km^3 in the following weeks (Guðmundsson et al. 1997). Thus the value of X was approximately 0.75.

In an eruption with a steady magma flux and near-instantaneous energy exchange (X ~ 1), steady-state conditions will apply, such that energy in = energy out = constant. An eruption with delayed energy release will emit a variable heat flux, which will increase gradually with time before diminishing. Near-steady state conditions *may* apply if the timescale of eruption far exceeds the delay time of energy release. The flux of energy into and out of the magma-ice system is shown schematically in Fig. 5.3.

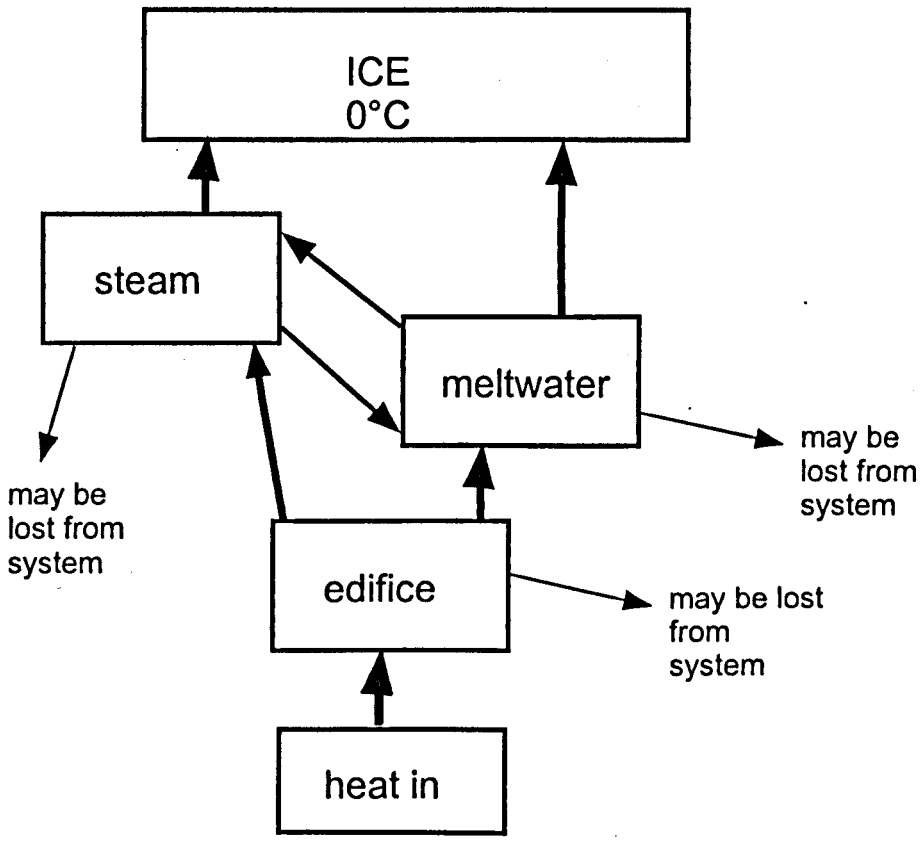

Fig. 5.3. Box diagram showing the flux of thermal energy between different 'sinks'. A known heat flux enters the system, and energy is partitioned between the edifice, meltwater and steam; all of which can cause melting of ice. The amount of heat held at any one moment within any component of the system (e.g. meltwater) depends upon the rates of heat transfer in and out.

5.2.3. Use of thermal energy

The thermal energy of the magma may cause melting of ice, and also heating and vaporisation of the meltwater formed. Some of the energy may be converted to kinetic energy during phreatomagmatic explosions, but this is likely to represent a small proportion of the total thermal energy (Wohletz 1983) and will be ignored. The volume of ice melted per unit volume of magma is given by the following equation:

$$v_i = \frac{1}{\rho_i L_i}\left[c_l \rho_l \Delta T_l (1-\theta) - v_w c_w \rho_w \Delta T_w - v_v \rho_w L_v\right] \quad (4)$$

where v_i is the volume of ice melted, ρ_i is the density of ice, L_i is the heat of fusion of ice, v_w is the volume of meltwater heated, c_w is the heat capacity of water, ρ_w is the density of water, ΔT_w is the temperature change of the meltwater, v_v is the volume of water vaporised and L_v is the heat of vaporisation. When no meltwater is heated or vaporised, (4) simplifies to

$$v_i = \frac{1}{\rho_i L_i}\left[c_l \rho_l \Delta T_l (1-\theta)\right] \quad (5)$$

and therefore $v_i = 7.01$ for vesicle-free crystal-free rhyolitic magma cooling from 900 to 0 °C. If all of the meltwater formed is heated, then

$$v_w = \frac{1}{V} v_v = v_i \rho_i / \rho_w \quad (6)$$

in which V is the proportion of meltwater vaporised.

Combining equations (5) and (6), the volume of ice melted per unit volume of magma is expressed as

$$v_i = \frac{c_m \rho_m \Delta T_m (1-\theta)}{\rho_i [L_i + \Delta T_w c_w + V L_v]} \quad (7)$$

hence less ice is melted as ΔT_w increases and as a greater proportion of the meltwater is vaporised (Fig. 5.4). The contribution of the vapour term in equations (4) and (7) is difficult to assess, as the vaporisation temperature and heat capacity of steam are strongly dependent upon the confining pressure (Fig. 5.5).

The temperature of meltwater formed during subglacial eruptions depends upon the relative rates of energy exchange (from magma to meltwater and from meltwater to ice) and the 'residence time' of meltwater in the system. These relative rates are not easily determined, and are likely to be affected by the style of magma-water energy interaction, the vigour of meltwater turbulence, and other factors. Guðmundsson et al. (1997) suggested that meltwater drained from the Gjálp eruption site at 15-20 °C. However, this estimate was based upon discrepancies between the volume of ice cauldrons on the glacier surface and the volume of meltwater discharged into Grímsvötn, which were likely to have been affected by other factors, as will be discussed later in this chapter.

5.2.4. Approximations used in the models

The models assume that the initial magma temperature is 900 °C and that all of the thermal energy of the magma is exchanged with the ice and meltwater. The effects of variable magma vesicularity and meltwater temperature are assessed, as are the effects of non-instantaneous energy exchange (using a simple function for equation (3)).

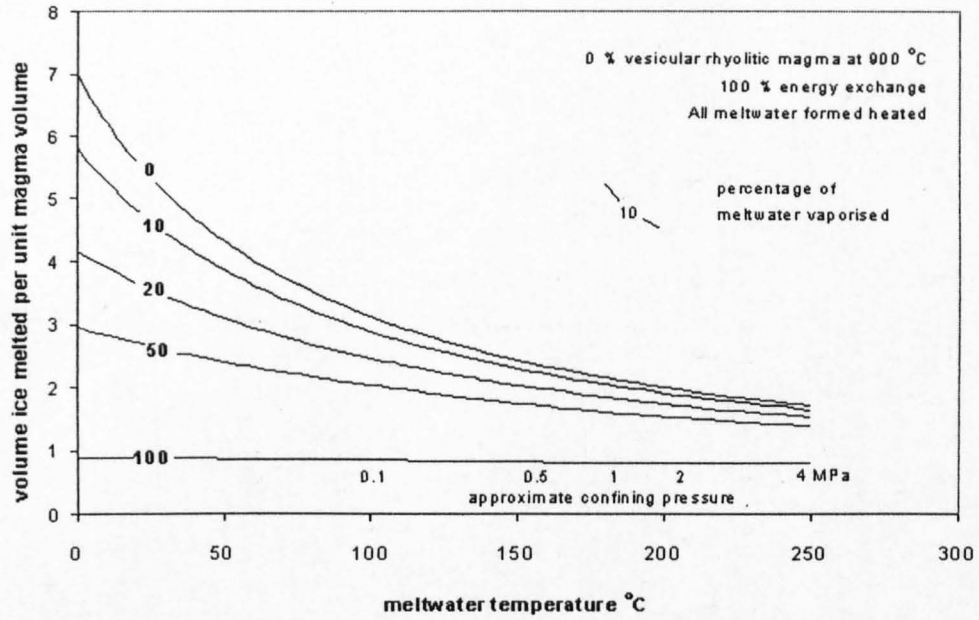

Fig. 5.4. Volume of ice melted per unit volume of rhyolite magma (v_i) as a function of meltwater temperature and amount of meltwater vaporised. The curves labelled 0, 10 etc. represent the percentage of meltwater vaporised. Magma is vesicle-free and cools from 900 ∘C to 0 ∘C. Meltwater temperatures up to 250 ∘C are considered, which may be attained at a confining pressure of 4 MPa. The value of v_i decreases with increasing meltwater temperature, and with increasing formation of steam. These calculations assume that all steam and meltwater instantly leave the cavity and cause no melting within it. However, if steam and/or heated meltwater were resident within the cavity, their thermal energy would be exchanged with the ice. Calculations use data from Haar et al. (1984) and take into account variations in the heat capacity and vaporisation energy of water with temperature.

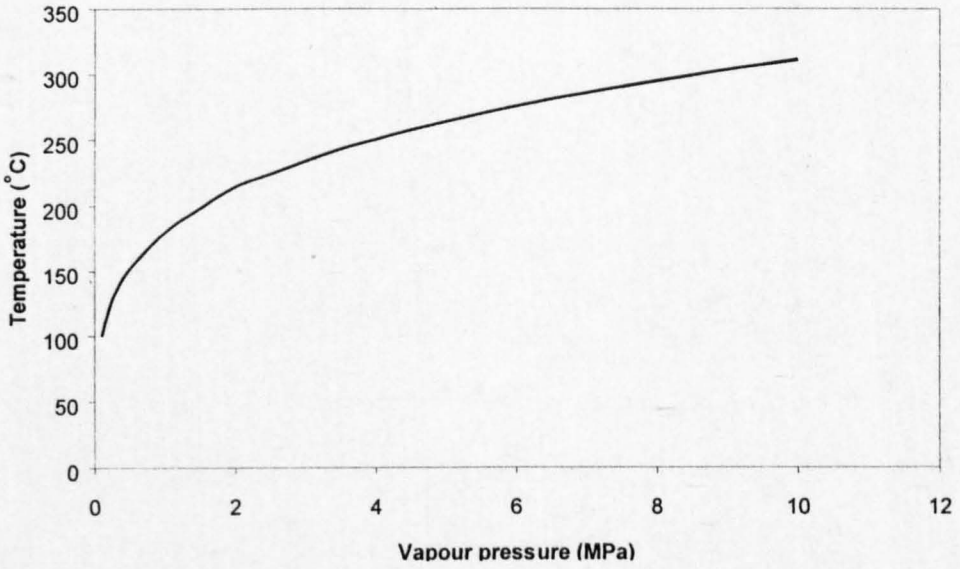

Fig. 5.5. Vapour pressure of pure water as a function of temperature. This is equivalent to the boiling point, since at a given point on the line, an increase in pressure or decrease in temperature would cause any vapour to condense. Data taken from Haar et al. (1984).

5.3. Ice melting geometry

5.3.1. Subglacial cavity geometry

The morphology of a subglacial cavity formed by basal heating depends upon the spatial distribution of heat at the glacier base (Kiver & Steele 1975) and the patterns of convection, conduction and radiation within the cavity. Hoskuldsson & Sparks (1997) carried out melting experiments using blocks of ice and PEG wax heated by a point source from below. They found that cavities within ice became pancake-shaped, as an insulating air gap developed at the top of the cavity, which greatly reduced the melting rate of the roof. This air gap developed due to the volume decrease upon melting of ice (water occupies only 92% of the volume of an equivalent mass of ice). No air gaps developed during experiments with PEG wax and conical cavities were formed. Steam-filled cavities melted by fumaroles at Mount Rainier, Washington commonly have conical or dome-like morphologies (Kiver & Steele 1975). These examples clearly show that the morphology of subglacial cavities depends upon the relative melting rates of the roof and the walls. Study of non-geothermal subglacial cavities confirms this, as partially-filled meltwater drainage channels close to the snout of temperate glaciers are commonly broad, with a low roof (Fountain & Walder 1998, Cutler 1998). This is due to relatively rapid melting of the walls, as a result of the mechanical energy (viscous drag) of flowing meltwater (Hooke 1984).

The three-dimensional morphology of cavities generated during a subglacial eruption is likely to be most strongly controlled by the geometry of the vent area (e.g. a 'point source' or a linear fissure) and the vigour of convective plumes (of steam, heated meltwater, or a tephra-fluid mixture). A time-consuming set of carefully-

designed experiments and/or numerical models would be needed to place better constraints on the melting geometry during different types of subglacial eruptions.

5.3.2. Approximation used in the models

In order to simplify the calculations, I assume that melting occurs evenly over the roof of a hemispherical cavity of radius R (Fig. 5.6). The melt-back rate r'_m is constant over the entire roof, and is given by

$$r'_m = \frac{v_i Q_l}{2\pi R^2} \qquad (8)$$

where Q_l is the magma discharge rate in $m^3\ s^{-1}$.

Unless the cavity is partially filled with meltwater and melting is mediated by meltwater-ice energy exchange, this simplification should adequately approximate the cross-section of evolving subglacial cavities. However, highly elongate cavities are likely to form during fissure-type eruptions, thus the three-dimensional geometry of melting may well be far from hemispherical.

5.4. Ice deformation

5.4.1. Brittle vs. ductile ice deformation

The deformation response of a glacier to subglacial melting will depend upon the mechanical properties of the ice and the stress field that is applied. The upper 40-60 m of temperate glaciers commonly consists of firn and snow, which is prone to brittle deformation at most strain rates, due to having a different microstructural configuration from that of ice (e.g. Hooke 1998). Polycrystalline ice, which makes up the remainder of the glacier, is a viscoelastic solid that deforms in a ductile manner at low strain rates and in a brittle manner at high strain rates (e.g. Jones 1982). The

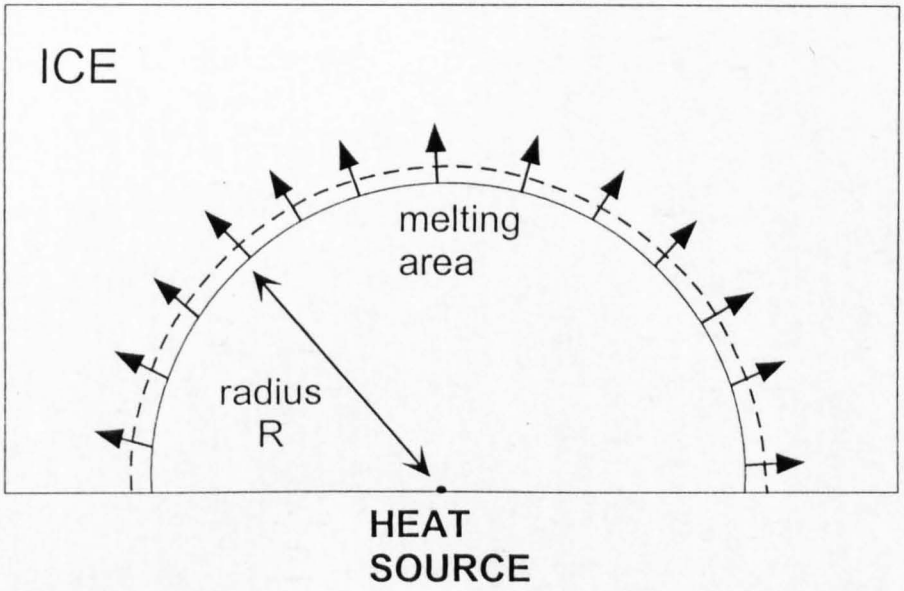

Fig. 5.6. The melting scenario assumed in the model. Radial melting from a point heat source creates a hemispherical cavity of radius R. The melting rate is assumed to be constant over the melting surface, which is of area $2_{\pi}R^2$.

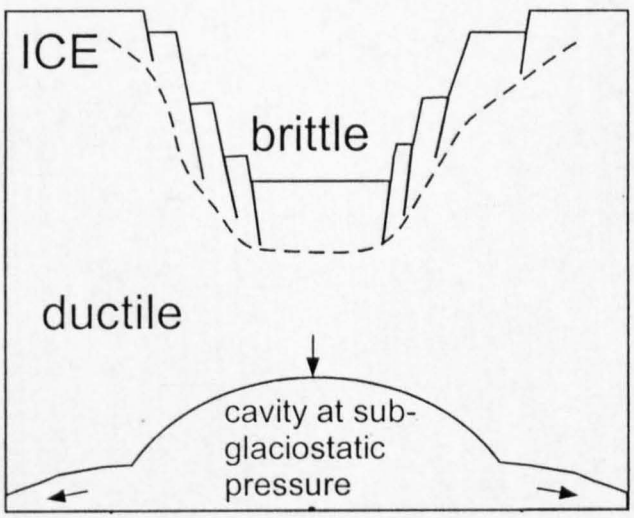

Fig. 5.7. Sketch to illustrate contrasting modes of deformation within a glacier during basal melting and formation of a low-pressure subglacial cavity. The upper portion of the glacier deforms brittly, and a set of near-vertical crevasses forms, which are arcuate or near-circular in plan view. Ductile deformation occurs in the glacier below, with creep closure of the cavity roof obeying Nye's law. The *dotted line* indicates the transition between brittle and ductile deformation.

deformation behaviour of polycrystalline ice is also sensitive to the confining pressure (e.g. Jones 1982, Mizuno 1998), with ductile deformation favoured by high confining pressures (e.g. at the glacier base) and brittle failure favoured by low confining pressures (e.g. within the upper parts of the glacier). Together, the depth-dependent rheological properties of a glacier will favour the deformation regime during subglacial melting that is illustrated in Fig. 5.7. In this model, brittle failure of the glacier surface accompanies ductile deformation of basal ice.

In recent years, many observations have been made of developing ice cauldrons above subglacial volcanoes in Iceland, both during eruptions (e.g. Björnsson 1988, Guðmundsson et al. 1997, Jónsson et al. 1998, Alsdorf & Smith 1999) and periods of increased geothermal heat flux (Björnsson 1988, Björnsson et al. 2000, Guðmundsson 2001). In general, the glacier surface remains smooth during the initial phase of cauldron development, and becomes fractured at a later stage, often once the cauldron exceeds 50 m in depth. This indicates that the depth of brittle failure is likely to increase with time during the formation of ice cauldrons. Since treatment of brittle deformation patterns is beyond the scope of this chapter, I will assume that ice deformation is predominantly ductile during cavity enlargement (section 5.4.2). Section 5.11. briefly mentions some of the possible consequences of brittle ice failure.

5.4.2. Ductile deformation: Nye's law

If it is assumed that deformation is initially purely ductile, then the roof of a hemispherical subglacial cavity of radius R will deform at a rate r'_d in accordance with Nye's law (Nye 1953):

$$\dot{r_d} = R\left[\frac{\Delta P}{nB}\right]^n \qquad (9)$$

where ΔP is the pressure difference between the cavity and the ice roof, n is Glen's flow law constant (≈ 3) and B is an ice deformation parameter, taken as 5.3×10^7 Pa $s^{1/3}$ (e.g. Hooke 1984). This relationship applies when R << ice thickness *h* (Nye 1953) and when the strain rates are sufficiently low to ensure that ductile deformation occurs. Nye's law is thus likely to break down as the cavity size approaches that of the ice thickness, when complex deformation patterns will occur, and result in brittle failure of the ice roof.

5.4.3. Vertical and horizontal deformation rates

Three-dimensional ice deformation will accompany the closure of a subglacial cavity. The relative rates of horizontal and vertical deformation are likely to vary with time, and to be controlled by the glacier morphology (Aðalgeirsdottír et al. 2000). A depression in the ice surface, caused by vertical ice deformation, will be filled by horizontal ice deformation, as the glacier seeks to return to isostatic equilibrium (Jónsson et al. 1998, Aðalgeirsdottír et al. 2000). This is shown schematically in Fig. 5.8.

The extent of horizontal deformation (into the eruption site) will depend upon the 'catchment area' for horizontal ice flow (distance from the ice divide) and the ice thickness (Aðalgeirsdottír et al. 2000). Horizontal deformation rates in the order of 10^{-5}-10^{-6} m s^{-1} were measured on Vatnajökull, Iceland between 1997 and 1999, in the vicinity of an elongate depression on the ice surface that developed during the jökulhlaup of November 1996 (Aðalgeirsdottír et al. 2000). At such low rates, horizontal ice deformation is only likely to cause substantial changes in the glacier surface profile during an eruption on the timescale of 10^7-10^8 s (1-10 years).

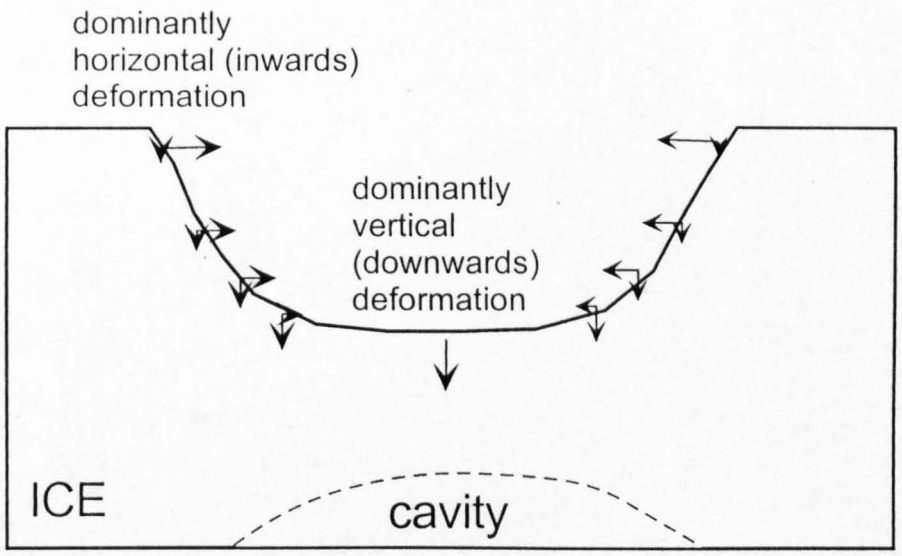

Fig. 5.8. Schematic diagram showing vectors of ice deformation (arrows) in the vicinity of an ice cauldron (see Aðalgeirsdóttir et al. 2000 for real data). Deformation is dominantly vertical (and downwards) in the central portion of the cauldron, causing deepening, whereas deformation is mostly horizontal (and inwards) near the rim of the cauldron. The relative rates of horizontal and vertical deformation will determine the cross-sectional shape of the ice cauldron. Cauldrons observed on the surface of Icelandic glaciers 400-700 m thick are typically 1-2 km across and 10-150 m deep, the deepest cauldrons are thought to occur above the regions of highest heat flux (MT Guðmundsson, personal communication).

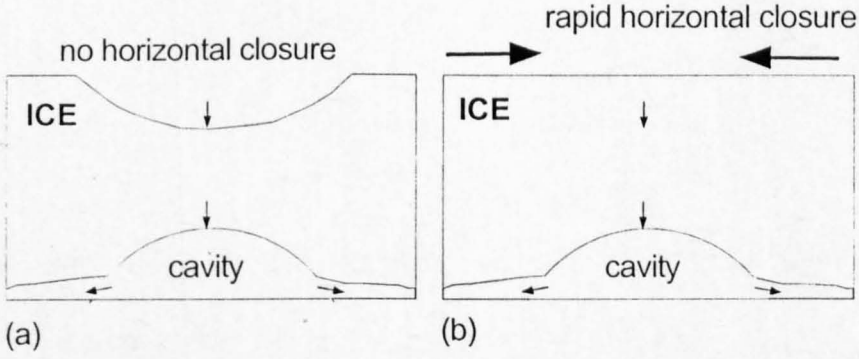

Fig. 5.9. The two endmembers used to assess the rôle of horizontal deformation. *Vertical arrows* indicate vectors of vertical (downwards) deformation of the cavity roof and the ice surface, which are assumed to be equal at all times. *Sub-horizontal arrows* indicate drainage of meltwater from the cavity. Arrow lengths are proportional to deformation rates. (a) No horizontal deformation occurs. This allows very deep ice cauldrons to form, with steep ice surface gradients. This scenario is likely to be most appropriate for high magma discharge rate eruptions beneath thin glaciers, or close to an ice divide, where horizontal deformation is less favourable. (b) Perfect horizontal deformation occurs, and the ice surface remains horizontal throughout the eruption. This scenario is unrealistic for large-volume, prolonged eruptions, as the ice surface in the 'catchment area' for infilling ice will eventually be lowered, with the formation of a broad ice cauldron.

Horizontal (and inwards) deformation in the vicinity of an ice divide (e.g. the rim of an ice-filled caldera) is likely to be insignificant.

5.4.4. Approximation used in the models

The ice is assumed to be homogeneous and deforms according to Nye's law for all cavity sizes. The ice roof is treated as an incompressible block, such that the vector of ductile deformation of the cavity roof is always equal to the vector of ice surface deformation (Fig. 5.9a), even if superficial fracturing occurs. This approximation is likely to be valid for $R << h$, but will break down at larger cavity sizes. In order to account for the viscoelastic rheology of ice, a finite-element model of ice deformation would need to be constructed, in which strain rates are mapped as a function of confining pressure, and regions of brittle or ductile behaviour predicted. Such a model is beyond the scope of this chapter. As such, the ductile deformation model presented in this chapter does not purport to simulate accurately the behaviour of the ice, however it aims to take a first step along the difficult path of modelling coupled volcano-ice systems.

Two endmembers are used to assess the rôle of horizontal ice flow (Fig. 5.9). In one endmember, no horizontal ice deformation occurs (Fig. 5.9a), and at low magma discharge rates ice cauldrons may reach 3/4 the ice thickness or more. In the other endmember (Fig. 5.9b), horizontal (inwards) ice deformation is so rapid that any depression on the ice surface is instantly filled in, and the ice surface remains horizontal throughout the eruption. Both endmembers are unrealistic in a natural setting, but give a useful insight into the probable effects of horizontal ice flow during eruptions.

5.5. Conditions in the cavity

5.5.1. Cavity pressure

Hoskuldsson & Sparks (1997) modelled a subglacial cavity during an eruption as a 'closed' system, in which effusive bodies of magma were emplaced within convecting meltwater. Meltwater was deemed unable to escape from the system, and the resultant volume change ΔV is thus given by

$$\Delta V = V_w + V_m - V_i, \qquad (10)$$

where V_w is the volume of meltwater generated, V_m is the volume of magma (or, strictly, volcanic debris) emplaced, and V_i is the volume of ice melted. The amount of ice melted per unit volume of magma has been discussed in section 5.2.

Following the analysis of Blake (1981) for magma chamber pressures, Hoskuldsson & Sparks proposed that the cavity pressure P_c can therefore be defined by the following equation:

$$\frac{\Delta V}{V_w} = \frac{P_c - P_g}{M_w} \qquad (11)$$

where P_c is the cavity pressure, P_g is glaciostatic pressure, and M_w is the bulk modulus of water. They suggested that the ice walls of the cavity may be deformed outwards if an overpressure develops (i.e. if $P_c > P_g$, which is predicted for all subglacial rhyolite eruptions). However, the following objections exist to the use of this 'closed system' model for eruptions beneath temperate glaciers:

(1) The cavity is likely to be hydraulically connected to adjacent, existing R- and N-channels at the glacier bed (section 1.8). Overpressure in the cavity will produce a local pressure gradient which will drive meltwater into these existing channels. Meltwater flow is proportional to the pressure gradient (e.g. Hooke 1998), and thus the flux of expelled meltwater should keep the cavity in approximate pressure equilibrium with the adjacent glacier bed. The meltwater flux out of the system should therefore be approximately equal to ΔV.

(2) The glacier substrate is likely to be permeable, especially if it consists of poorly-consolidated volcanic debris (e.g. Ascolese et al. 1993). If the pressure in a subglacial cavity is greater than glaciostatic, the pressure gradient will drive permeable flow of meltwater downwards into the substrate.

Due to these objections, the 'closed system' model of Hoskuldsson & Sparks (1997) is considered to be inappropriate. If it is accepted that subglacial cavities are likely to be 'leaky', and any excess meltwater will be expelled by local pressure gradients, then the cavity pressure is likely to be somewhere between atmospheric and glaciostatic. If the meltwater flux within adjacent R-channels exceeds the critical flux defined by Hooke (1984), then an air gap may develop ('open channels', section 1.8), as the rate of enlargement exceeds that of deformation. In this case, pressure in the R-channels and the adjacent, connected subglacial cavity may be atmospheric if there is a hydrological connection with the atmosphere (at the glacier surface or glacier margin). Whether this occurs depends upon the bedrock slope, ice thickness, meltwater discharge rate and, critically, the distance of the cavity from the glacier margin (Hooke 1984, Björnsson 1988). If the cavity is melted close to the glacier snout (<1 km), atmospheric pressure may become quickly established as the meltwater flux draining from the cavity is sufficient to maintain 'open', low-pressure

conditions throughout its length (Hooke 1984). If the eruption site is far from the glacier margin, atmospheric pressure may only develop once brittle fracture has opened a pathway from the cavity to the glacier surface above.

Before a connection with the atmosphere has been established, cavity pressure may be near-glaciostatic, which in the range of ice thicknesses considered in the model (100 - 1000 m) equates to 0.9-9 MPa. Similarly, the pressure within a tephra- or lava- filled cavity is assumed to be near-glaciostatic until brittle failure of the ice roof occurs. The formation of ice cauldrons during the 1996 Gjálp eruption shows that cavity pressure was less than glaciostatic (which would have been c. 4 MPa, since the ice was initially c. 450 m thick). However, water was pumped from the eruption site into Grímsvötn caldera, which requires the cavity pressure to exceed 1.8 MPa (MT Guðmundsson, personal communication 2001).

Cavity pressures used in the models

For the purposes of this study, cavities are assumed to be at atmospheric pressure when they are not entirely filled with erupted products, and at glaciostatic pressure when they are completely filled (explained fully in section 5.5.6.). Atmospheric pressure may realistically occur during prolonged eruptions, in which there is time for a hydraulic connection to be established with the glacier snout. However, cavity pressure may be closer to glaciostatic during the early phases of the eruption. Therefore, the deformation rates of the cavity roofs predicted by the model should be considered to be *maximum* rates. The possible effects of cavity pressure on eruption mechanisms are discussed in section 5.6.10.

5.5.2. Meltwater drainage patterns

Field observations at Bláhnúkur and South-east Rauðufossafjöll suggest that meltwater did not accumulate during the subglacial eruptions (Chapters 2 and 3). If the flux of meltwater expelled had been merely sufficient to maintain the cavity at glaciostatic pressure (a scenario proposed in section 5.5.1.), then the cavity may have been water-filled throughout, and thus a significant volume of meltwater may have accumulated within the growing cavity. If this scenario had occurred, field evidence for meltwater accumulation may have been expected. Thus the bulk of modelling will assume that meltwater drains *continuously* from the subglacial cavity at the same rate as it is generated by melting, and that negligible meltwater accumulation occurs. If the cavity and connected R-channels were at atmospheric pressure, meltwater would be likely to drain away at the same rate as it was formed, and drainage patterns would follow the bedrock slope. However, the development of meltwater-filled cavities is not discounted, and so the evolution of a water-filled cavity is considered in section 5.6.10. The model assumes that the rate of ice melting will be the same for water-filled and steam-filled cavities at a given magma discharge rate. This is because the rate-limiting step in the transfer of thermal energy from magma to ice is considered to be the loss of heat from the magma.

Continuous meltwater drainage during rhyolitic eruptions was predicted by Hoskuldsson & Sparks (1997) on the basis of volume changes. Similar drainage patterns are thought to have occurred during the 1918 Katla and 1996 Gjálp basalt eruptions in Iceland (Guðmundsson 2001). By contrast, meltwater is thought to have accumulated during many basaltic subglacial eruptions in Iceland and elsewhere, as suggested by the sedimentology of hyaloclastite formations (e.g. Jones 1970, Skilling 1994, Smellie 1999). The amount of meltwater in a subglacial cavity depends upon the relative rates of meltwater generation and drainage, and cannot be quantified by

the models presented in this chapter. The drainage discharge rate depends upon the size of the subglacial drainage conduits carrying meltwater and the potential gradient driving drainage (e.g. Hooke 1984), and would be greatly increased by heated meltwater, which can enlarge subglacial conduits ~ 10 times more rapidly than mechanical erosion alone (Clarke 1982).

5.5.3. Pressure driving cavity roof deformation

The glaciostatic pressure at the cavity roof at time t, $P_{g(t)}$ is given by

$$P_{g(t)} = \rho_i g h_{r(t)} \tag{12}$$

where $h_{r(t)}$ is the ice roof thickness at time t, which is expressed as

$$h_{r(t)} = h_o - R_{(t)} - \int_0^t r'_{d(t)} dt = h_o - \int_0^t r'_{m(t)} dt \tag{13}$$

where h_o is the initial ice thickness and r'_m is the melt-back rate defined in equation (8). Equation (13) is valid if the vectors of ice surface and cavity roof deformation are assumed to be equal. The pressure driving deformation of the cavity roof, $\Delta P_{(t)}$ is given by

$$\Delta P_{(t)} = \rho_i g h_{r(t)} - P_c = \rho_i g \left[h_o - \int_0^t r'_{m(t)} dt \right] - P_c \tag{14}$$

where P_c is the cavity pressure. Thus the lower the cavity pressure, the faster the ice roof deforms.

5.5.4. Cavity size balance

The rate at which the size of the subglacial cavity changes is determined by the relative rates of enlargement by melting and closure by deformation. The rate of cavity enlargement *dR/dt* is thus given by the following relation

$$\frac{dR}{dt} = r'_m - r'_d. \tag{15}$$

Substituting equation (8) for r'_m and equation (9) for r'_d into (10) yields

$$\frac{dR}{dt} = \frac{v_i Q_l}{2\pi R^2} - R\left[\frac{\Delta P}{nB}\right]^n \tag{16}$$

where Q_l is the volume flux of magma ($m^3 s^{-1}$).

Equation (16) can be combined with equations (7) and (14), for v_i and ΔP respectively, to give

$$\frac{dR}{dt} = \frac{Q_l}{2\pi R^2}\left[\frac{c_l \rho_l \Delta T_l (1-\theta)}{\rho_i [L_i + \Delta T_w c_w + V L_v]}\right] - R\left[\frac{\rho_i g\left[h_o - \int_0^t r'_{m(t)} dt\right] - P_c}{nB}\right]^n. \tag{17}$$

Equation (17) is a high-order, non-linear differential equation, which cannot be solved analytically, of the general form

$$\frac{dR}{dT} - \frac{M}{R^2} + NR = 0, \qquad (18)$$

where M and N are factors related to the temporally-variable characteristics of ice melting and deformation respectively.

However, solutions to equation (17) can be approximated numerically using a spreadsheet program. The system is set up with appropriate initial conditions (e.g. ice thickness, magma discharge rate and cavity pressure). Values of melt-back rate, ice deformation rate, cavity radius, roof thickness and ice surface deformation are then calculated incrementally for a series of timesteps which are set up such that $t^{n+1} =$ 1.01 t^n (Table 5.3). Initial timesteps of 10^{-5} s are used, in order to monitor the initially rapid enlargement of the subglacial cavity, due to its small radius. Numerical simulations are continued until the roof thickness has reduced to zero, which typically occurs over 10^6-10^7 s.

Brittle ice failure is assumed to occur when the roof is less than 50 m thick, and the eruption is likely to become subaerial at this point. It is possible to incorporate non-steady state conditions into the numerical model - for example, the magma discharge rate may be set to vary with time.

5.5.5. Cavity size evolution

When the system was run with typical values of ice thickness (100-1000 m) and volume flux of ice melted (10-1000 $m^3\ s^{-1}$) it was found that the cavity radius initially increased rapidly ($r'_m \sim 10^{-2}$ - 10^{-3} m s^{-1}). This is due to the small cavity size, which

A time t *s*	B magma flux $m^3 s^{-1}$	C heat flux $J s^{-1}$	D volume of ice melted $m^3 s^{-1}$	E cavity radius *m*	F meltback rate $m s^{-1}$	G roof deformation $m s^{-1}$	H total surface deformation *m*	I roof thickness *m*	J cavity volume m^3	K edifice volume m^3	L ice surface elevation *m*	M cavity radius *m*	N edifice radius *m*	O edifice/ cavity ---
6.63E+05	0.01	1.60E+07	0.056	16.08	3.20E-05	2.94E-05	19.96	216.17	8.71E+03	6.63E+03	430.04	16.08	14.69	0.91
6.70E+05	0.01	1.60E+07	0.056	16.10	3.19E-05	2.94E-05	20.16	215.96	8.74E+03	6.70E+03	429.84	16.10	14.73	0.92
6.77E+05	0.01	1.60E+07	0.056	16.11	3.19E-05	2.93E-05	20.35	215.75	8.76E+03	6.77E+03	429.65	16.11	14.78	0.92
6.83E+05	0.01	1.60E+07	0.056	16.13	3.18E-05	2.93E-05	20.55	215.53	8.79E+03	6.83E+03	429.45	16.13	14.83	0.92
6.90E+05	0.01	1.60E+07	0.056	16.15	3.17E-05	2.92E-05	20.75	215.32	8.82E+03	6.90E+03	429.25	16.15	14.88	0.92
6.97E+05	0.01	1.60E+07	0.056	16.17	3.17E-05	2.91E-05	20.95	215.10	8.85E+03	6.97E+03	429.05	16.17	14.93	0.92
7.04E+05	0.01	1.60E+07	0.056	16.18	3.16E-05	2.91E-05	21.15	214.88	8.88E+03	7.04E+03	428.85	16.18	14.98	0.93
7.11E+05	0.01	1.60E+07	0.056	16.20	3.15E-05	2.90E-05	21.36	214.66	8.91E+03	7.11E+03	428.64	16.20	15.03	0.93
7.18E+05	0.01	1.60E+07	0.056	16.22	3.15E-05	2.90E-05	21.56	214.44	8.94E+03	7.18E+03	428.44	16.22	15.08	0.93
7.25E+05	0.01	1.60E+07	0.056	16.24	3.14E-05	2.89E-05	21.77	214.22	8.97E+03	7.25E+03	428.23	16.24	15.13	0.93
7.33E+05	0.01	1.60E+07	0.056	16.26	3.13E-05	2.88E-05	21.98	213.99	9.00E+03	7.33E+03	428.02	16.26	15.18	0.93
7.40E+05	0.01	1.60E+07	0.056	16.27	3.12E-05	2.88E-05	22.19	213.76	9.03E+03	7.40E+03	427.81	16.27	15.23	0.94
7.47E+05	0.01	1.60E+07	0.056	16.29	3.12E-05	2.87E-05	22.40	213.53	9.06E+03	7.47E+03	427.60	16.29	15.28	0.94
7.55E+05	0.01	1.60E+07	0.056	16.31	3.11E-05	2.87E-05	22.62	213.30	9.09E+03	7.55E+03	427.38	16.31	15.33	0.94
7.62E+05	0.01	1.60E+07	0.056	16.33	3.10E-05	2.86E-05	22.84	213.07	9.12E+03	7.62E+03	427.16	16.33	15.38	0.94
7.70E+05	0.01	1.60E+07	0.056	16.35	3.10E-05	2.85E-05	23.05	212.84	9.15E+03	7.70E+03	426.95	16.35	15.43	0.94
7.78E+05	0.01	1.60E+07	0.056	16.37	3.09E-05	2.85E-05	23.27	212.60	9.18E+03	7.78E+03	426.73	16.37	15.49	0.95
7.86E+05	0.01	1.60E+07	0.056	16.39	3.08E-05	2.84E-05	23.49	212.36	9.21E+03	7.86E+03	426.51	16.39	15.54	0.95
7.93E+05	0.01	1.60E+07	0.056	16.40	3.08E-05	2.84E-05	23.72	212.12	9.24E+03	7.93E+03	426.28	16.40	15.59	0.95
Function of:		**B**	**C**	**F,G**	**D,E**	**I,E**	**G**	**E,H**	**E**	**B**	**G**	**E**	**B**	**B,E**

Parameters used: 450 m thick ice, no horizontal ice deformation, 0 °C meltwater, 20 % vesicular magma. $\dot{v}_i = 5.6$

Table 5.3. An example of a spreadsheet used to approximate the evolution of a volcano-ice system. Each quantity is calculated at discrete timesteps, with the following parameters being chosen: initial ice thickness, horizontal deformation regime, magma discharge rate and volume of ice melted per unit volume of magma. All other quantities are functions of these parameters and of each other, as indicated below each column of figures.

ensures rapid melting (the $1/R^2$ term is large in equation (18)) and slow roof deformation (R is small in equation (18)). As the cavity size increases, the melt-back rate reduces and the deformation rate increases (Fig. 5.10). The lowest ratio of melt-back/deformation typically occurs at $R \sim h_o/2$. At greater cavity sizes, thinning of the ice roof begins to reduce the rate of ice deformation, and the cavity size increases more rapidly (Fig. 5.10). Brittle ice failure is considered likely when the roof is less than 50 m thick.

In the absence of roof thinning, an equilibrium cavity radius may develop at a constant melting rate, at which melting balances deformation ($r'_m = r'_d$). This scenario may be applicable to situations when $R << h_o$ (i.e. small cavity), and is discussed in section 5.9.

5.5.6. Edifice volume and space in cavity

Having obtained the theoretical size evolution of a hemispherical cavity melted during an eruption, it is next necessary to assess the volume of the edifice growing within it. Assuming that the amount of erupted material removed by flowing meltwater is negligible, the edifice volume V_e is given by

$$V_{e(t)} = \int_0^t Q_l S dt \qquad (19)$$

where S is a packing coefficient, $S = 1$ for non-vesicular lava and $S \sim 2$ for poorly consolidated ash. Some justification for this assumption is provided by the small

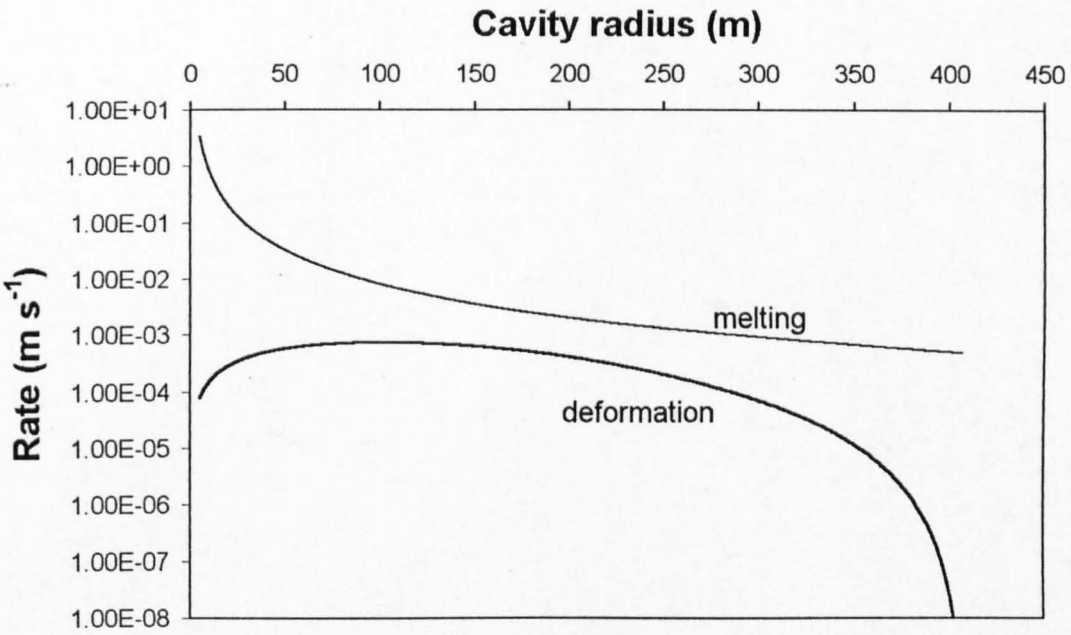

Fig. 5.10. Rates of roof meltback and deformation as a function of cavity size, with ice 450 m thick, Q_l = 100 m^3 s^{-1} , and 20 % vesicular magma giving ν_i = 5.6. Ductile deformation in accordance with Nye's law is assumed throughout, and cavities are assumed to be hemispherical and at atmospheric pressure. The meltback rate drops with increasing cavity size as the surface area of melting increases. Deformation initially rises with increasing cavity size, but falls as the effect of roof thinning becomes dominant.

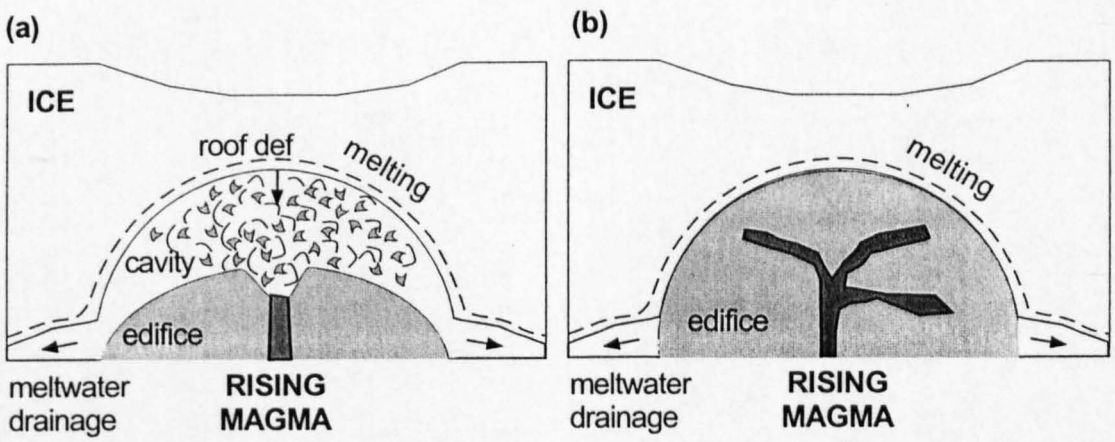

Fig. 5.11. Contrasting styles of subglacial eruption. **(a)** Edifice radius < cavity radius. Phreatomagmatic fragmentation occurs as rising magma encounters a wet pile of tephra. A highly turbulent tephra-vapour mixture enters the space in the cavity. **(b)** Edifice radius = cavity radius. The cavity is entirely filled by the edifice. Rising magma intrudes the edifice, with peperitic lava bodies formed and minor phreatomagmatic fragmentation occurring as magma encounters wet material. The melting patterns which may occur when an intrusive body reaches the glacier base are discussed in section 5.9.

proportion of the products of the 1996 Gjálp eruption (estimated at ~10 %) that were removed from the eruption site by flowing meltwater (Guðmundsson, submitted).

Assuming that the edifice is hemispherical, its radius (height) $R_{e(t)}$ is thus given by

$$R_{e(t)} = \left[\frac{3V_{e(t)}}{2\pi}\right]^{1/3} = \left[\frac{3\int_0^t Q_l S dt}{2\pi}\right]^{1/3}. \qquad (20)$$

It is interesting to compare the ratio of the edifice radius to the cavity radius during simulated eruptions. Two scenarios are envisaged:

A. Edifice radius < cavity radius

In scenario A (Fig. 5.11a), it is assumed that the cavity pressure will be sub-glaciostatic, and possibly atmospheric during prolonged eruptions. Assuming that the ice roof does not collapse, there will thus be an air- or steam-filled void above the growing edifice. Meltwater formed by melting of the roof will percolate into the growing pile of volcanic debris and drain away continuously. However, there will always be a 'reservoir' of residual meltwater within the porous debris pile. Rising magma will thus have the potential to interact with water at relatively low confining pressures, and phreatomagmatic fragmentation is possible. The presence of an air- or steam-filled void provides space for a high-velocity, turbulent plume of steam and tephra to develop, with rapid energy exchange between hot clasts and surrounding vapour (Dobran & Papale 1993). This eruptive style is likely to create a pile of massive, poorly-consolidated, poorly-sorted phreatomagmatic ash, similar to that observed at South-east Rauðufossafjöll (Chapter 3.4).

An eruption within a meltwater-filled cavity is considered in section 5.6.10. and is contrasted with one within a steam- or air- filled cavity. It is assumed (perhaps unrealistically) that the rate of melting will be the same as for an air- or steam-filled cavity, and it is the higher (near-glaciostatic) cavity pressure that causes different eruption mechanisms.

B. Edifice radius = cavity radius.

If the model predicts that the edifice height is equal to or exceeds the cavity radius, this means that the cavity will be entirely filled with volcanic deposits (Fig. 5.11b). The pressure in the cavity is thus likely to be roughly glaciostatic. There is simply no room for explosive phreatomagmatism, and the confining pressure is too high: instead, peperitic intrusions are likely to form as magma rises within waterlogged debris. Slower rates of energy transfer from magma to ice are anticipated, leading to slower melting of the ice roof. Near-glaciostatic pressure within the cavity will mean that ice roof deformation is insignificant. Once a cavity becomes entirely filled, and the eruption becomes predominantly intrusive, the cavity is assumed to remain filled for the duration of the eruption. This eruptive style is likely to create intrusive, peperitic lava bodies and breccias formed by low-explosivity quench fragmentation, similar to the lava lobe - breccia A lithofacies of Bláhnúkur (section 2.5.). If lava bodies reach the interface between volcanic debris and glacier ice, localised melting of ice is possible, on the wavelength of metres. This is explored in section 5.9.

Eruptions are generally predicted to start with explosive activity, and are most susceptible to become intrusive when the cavity radius is approximately half of the initial ice thickness (see section 5.5.5).

5.6. Models of subglacial rhyolite eruptions

In this section I present results of the numerical models. The results have been selected to illustrate the influence of various parameters which may control the style of subglacial rhyolite eruptions.

5.6.1. Choice of parameters for models

• Magma discharge rate

As a rhyolitic eruption has never been observed, the magma discharge rate must be estimated. Hoskuldsson & Sparks (1997) estimated that the magma discharge rate would be 10-100 $m^3 s^{-1}$ during a small-volume fissure-fed rhyolitic eruption. By contrast, larger volume silicic eruptions have considerably higher magma discharge rates. Adams et al. (2001) suggest that 3-4 × 10^5 $m^3 s^{-1}$ of dacitic magma was discharged during the plinian phase of the 11 km^3 Peruvian Huaynaputina eruption. Since the volume of the subglacial rhyolitic edifices under consideration in this study ranges from <0.1 to >1 km^3, a range of magma discharge rates between 10^{-1} and 10^4 $m^3 s^{-1}$ will be considered.

• Eruption duration

The eruption will be modelled as subglacial until the ice roof is <50 m thick, whereupon brittle roof failure is assumed to occur, with a resultant transition to a subaerial eruption. Melting rates during the subaerial phase will be greatly reduced, due to heat loss into the atmosphere. Depending upon the ice thickness and magma discharge rate, eruptions of between 10^4 s (3 hours) and 10^8 s (3 years) in duration are predicted.

• Ice thickness

Field evidence suggests that the ice was >350 m thick during the eruption of Bláhnúkur and South-east Rauðufossafjöll. The stratigraphy of basaltic tuyas in Iceland points to ice thicknesses of up to 1000 m during the Quaternary (e.g. Werner et al. 1996). In my model, ice thicknesses between 100 m and 1500 m are considered.

• Magma vesicularity

In accordance with field observations (Chapters 2-4), a range of vesicularities between 0 and 60 % will be considered.

• Energy transfer efficiency

The proportion of thermal energy exchanged between the magma and ice/meltwater/steam is assumed to be 1 (perfect energy exchange) during the subglacial eruptive phase, and 0 during the subaerial phase.

5.6.2. Data acquired by models

The model calculates the radius of the growing edifice and evolving subglacial cavity, and also the elevation of the ice surface (during 'perfect' horizontal deformation this will not change). Fig. 5.12 shows typical graphs produced by the model. This 'raw data' can then be processed to give information such as the relative rate of edifice and cavity growth.

5.6.3. Effects of ice thickness on eruption style

Figure 5.13 shows how the ratio of edifice radius to cavity radius changes with time at different ice thicknesses, with a constant magma discharge rate of 100 $m^3 s^{-1}$. The

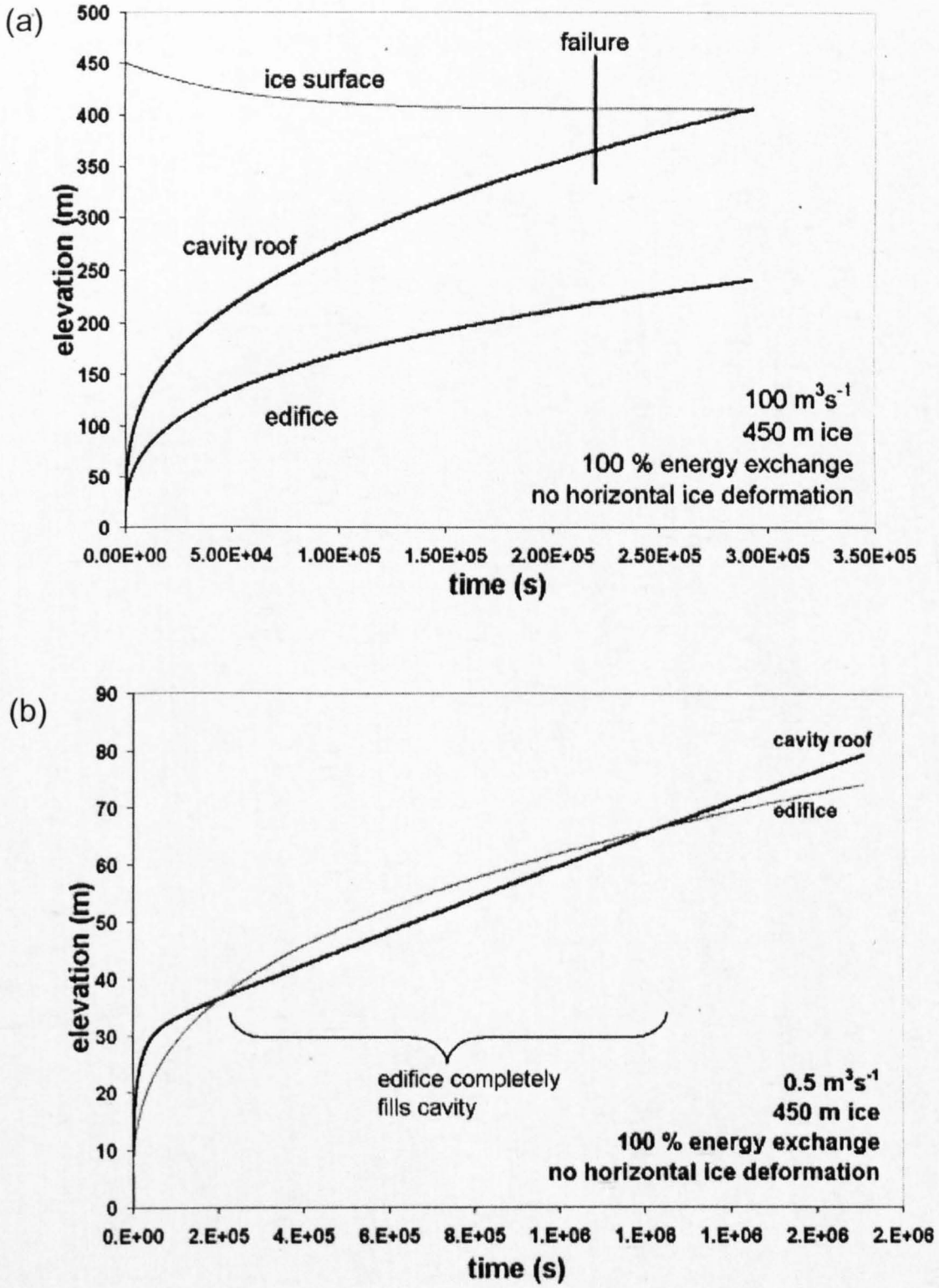

Fig. 5.12. Examples of data acquired by the model. **(a)** Ice surface elevation, cavity radius and edifice radius are plotted as a function of time with Q_I = 100 $m^3 s^{-1}$, 20 % vesicular magma giving v_i = 5.6 and h_0 = 450 m. The cavity is always considerably larger than the edifice. **(b)** Initial evolution of the same system, but with Q_I reduced to 0.5 $m^3 s^{-1}$. Note that the edifice quickly fills the cavity.

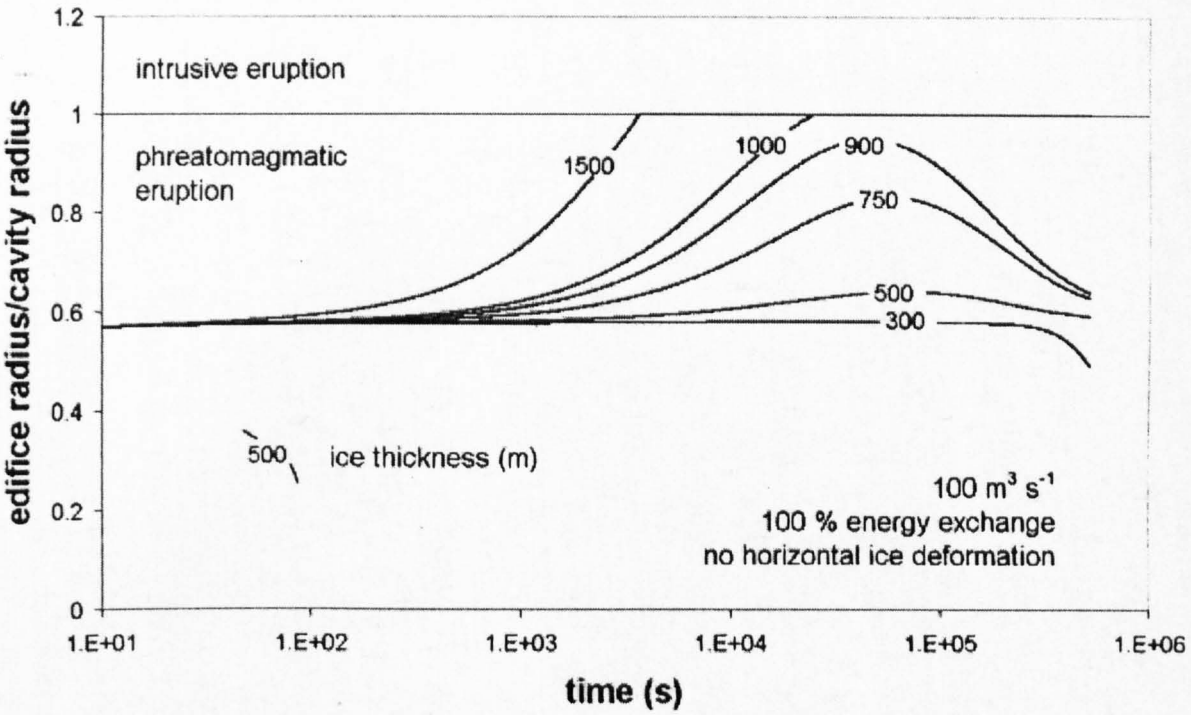

Fig. 5.13. The edifice radius : cavity radius ratio plotted as a function of time for eruptions of 100 m^3 s^{-1} rhyolite under ice of varying thicknesses (indicated by contours). No horizontal ice deformation occurs. The model predicts a phreatomagmatic eruption for ice thicknesses <900 m, and an intrusive eruption for ice >1000 m thick. At a given magma discharge rate, phreatomagmatic eruptions are thus more likely to occur beneath thin glaciers.

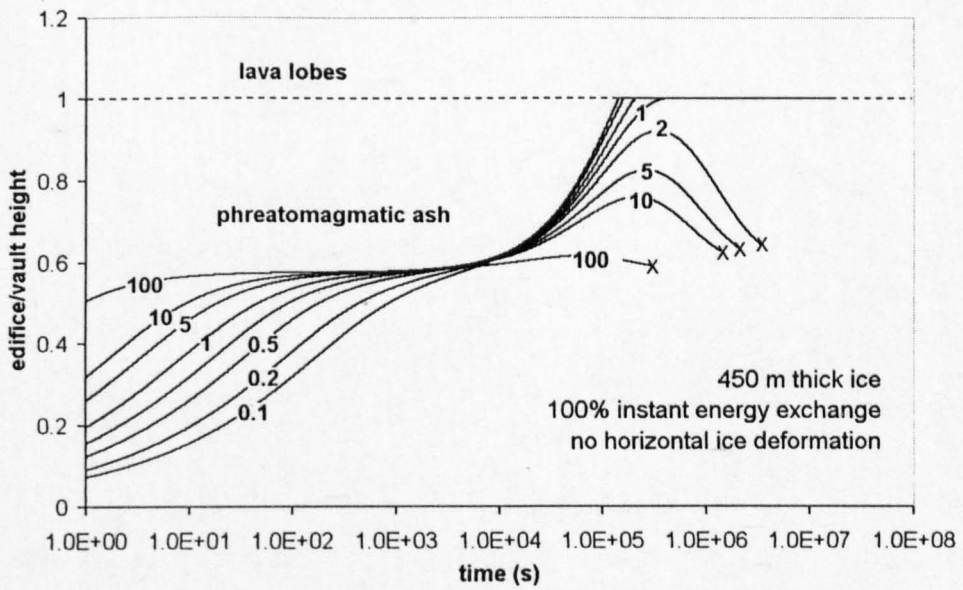

Fig. 5.14. The edifice radius : cavity radius ratio plotted as function of time for eruptions of varying magma discharge rate under ice 450 m thick, with no horizontal deformation. The cavity size always exceeds the edifice size (ratio < 1) at eruption rates above 2 m^3 s^{-1}, and phreatomagmatic fragmentation is the likely eruption mechanism. At $Q_I \leq 1$ m^3 s^{-1}, the ratio reaches 1 at time ~ 10^5 - 10^6 s. Once the cavity becomes completely filled, it is assumed to remain so for the remainder of the duration of the eruption. *Crosses* indicate the termination of the subglacial eruption, when the ice roof is <50 m thick and is assumed to collapse.

graph demonstrates that, at a given magma discharge rate, thick ice favours an intrusive eruption (scenario B), whereas an explosive eruption (scenario A) is favoured by thin ice. This is due to the more rapid deformation of the cavity roof when the ice is thick, as the glaciostatic pressure is higher.

5.6.4. Effects of magma discharge rate on eruption style

Figure 5.14 shows the evolution of the edifice/cavity system at a constant ice thickness and different magma discharge rates. A high magma discharge rate favours a phreatomagmatic eruption style, and an intrusive eruption is more likely at low discharge rates.

5.6.5. The style of eruption at different magma discharge rates and ice thicknesses

A solving technique within the spreadsheet programme was used to determine the critical magma discharge rate Q_{cr} for a chosen ice thickness. Below Q_{cr}, the system always evolves to edifice/cavity ratio >1, and thus the eruption is considered to become intrusive. Above Q_{cr}, the edifice never completely fills the cavity, and the eruption is assumed to be explosive throughout. This process was iterated for a range of ice thicknesses, and the results plotted on Fig. 5.15. An intrusive eruption style is favoured by thick ice (high h_o) and low magma discharge rate (low Q_l). Combinations of h_o and Q_l which plot below the line are likely to erupt intrusively and produce Bláhnúkur-style edifices. The line indicates *minimum* values of Q_{cr}, since it uses 0 % magma vesicularity, 0 °C meltwater and 100 % instant energy exchange (ν_i optimum).

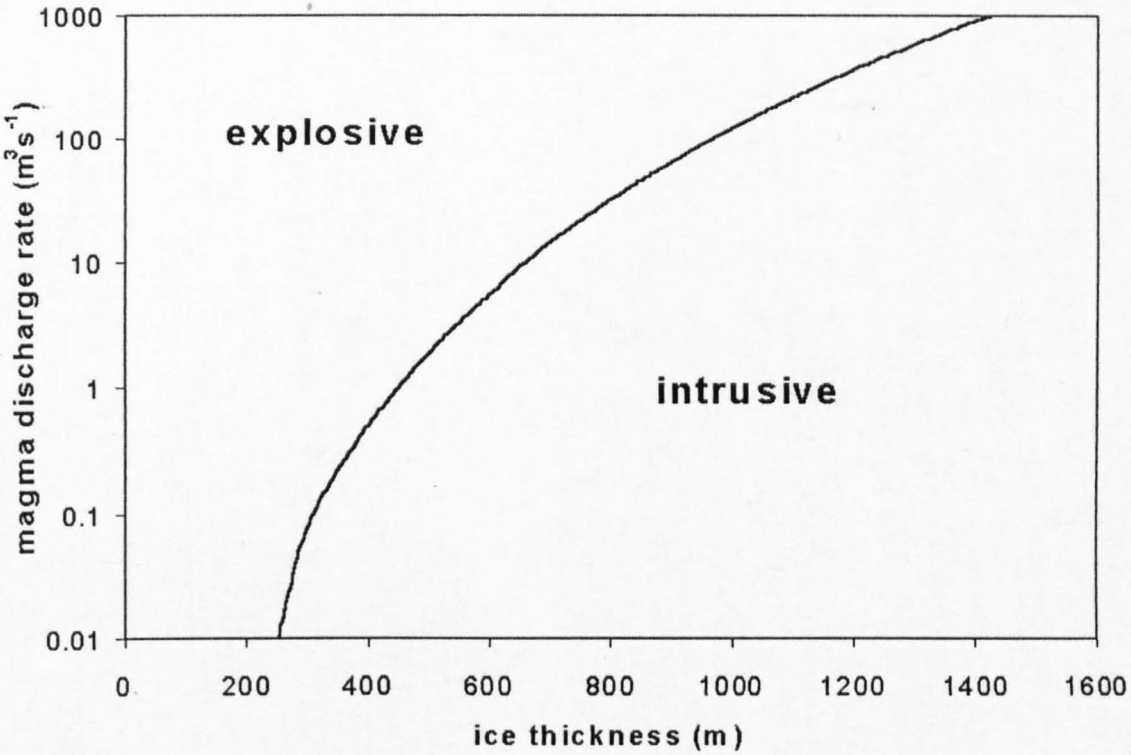

Fig. 5.15. Critical magma discharge rate as a function of ice thickness for eruptions with ν_i = 5.6 (20 % vesicular magma) and no horizontal ice deformation.

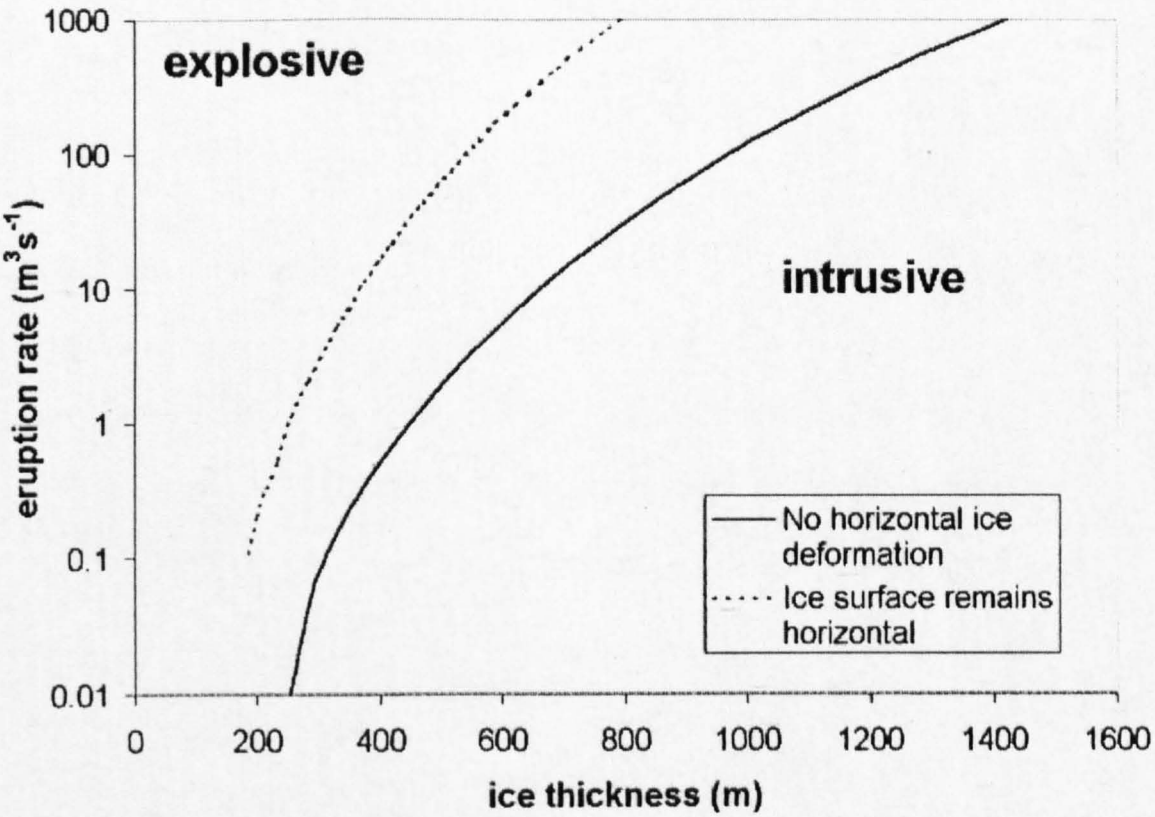

Fig. 5.16. Critical magma discharge rate (Q_{cr}) for eruptions beneath horizontally deforming and non-deforming glaciers. Q_{cr} is 1 or 2 orders magnitude greater when the glacier deforms horizontally, because no ice cauldron forms, and the eruption has to melt through more ice.

5.6.6. Effects of horizontal ice deformation

The effects of horizontal deformation patterns can be assessed by comparing values of the critical magma discharge rate for the two deformation endmembers - one in which no horizontal deformation occurs, and one in which 'perfect' horizontal deformation occurs, such that the ice surface remains horizontal. It is seen that, for a given ice thickness (Fig. 5.16), an eruption rate 1-2 orders of magnitude higher is necessary to sustain an explosive eruption during perfect horizontal deformation than during no horizontal deformation. This is because roof thinning plays a reduced rôle during perfect horizontal deformation, meaning that the glaciostatic pressure (and thus the cavity closure rate) is higher. The possible significance of horizontal ice deformation is discussed further in section 5.7.3.

5.6.7. Effects of magma vesicularity

An example of the potential effects of magma vesicularity on the eruption style is illustrated in Fig. 5.17. A 'borderline' magma discharge rate, at which Q_l is just sufficient to maintain an explosive eruption, was chosen for an ice thickness of 500 m, to emphasise the influence that variable magma vesicularity may exert. The eruption remains phreatomagmatic for magma vesicularities below 40 %, whereas an intrusive eruption is likely for vesicularities above 60 %, because the magma is unable to melt the cavity roof back sufficiently quickly. This is because v_i is reduced as the vesicularity θ increases (equation 7). In other words, if the magma is too vesicular, it may fill the cavity up.

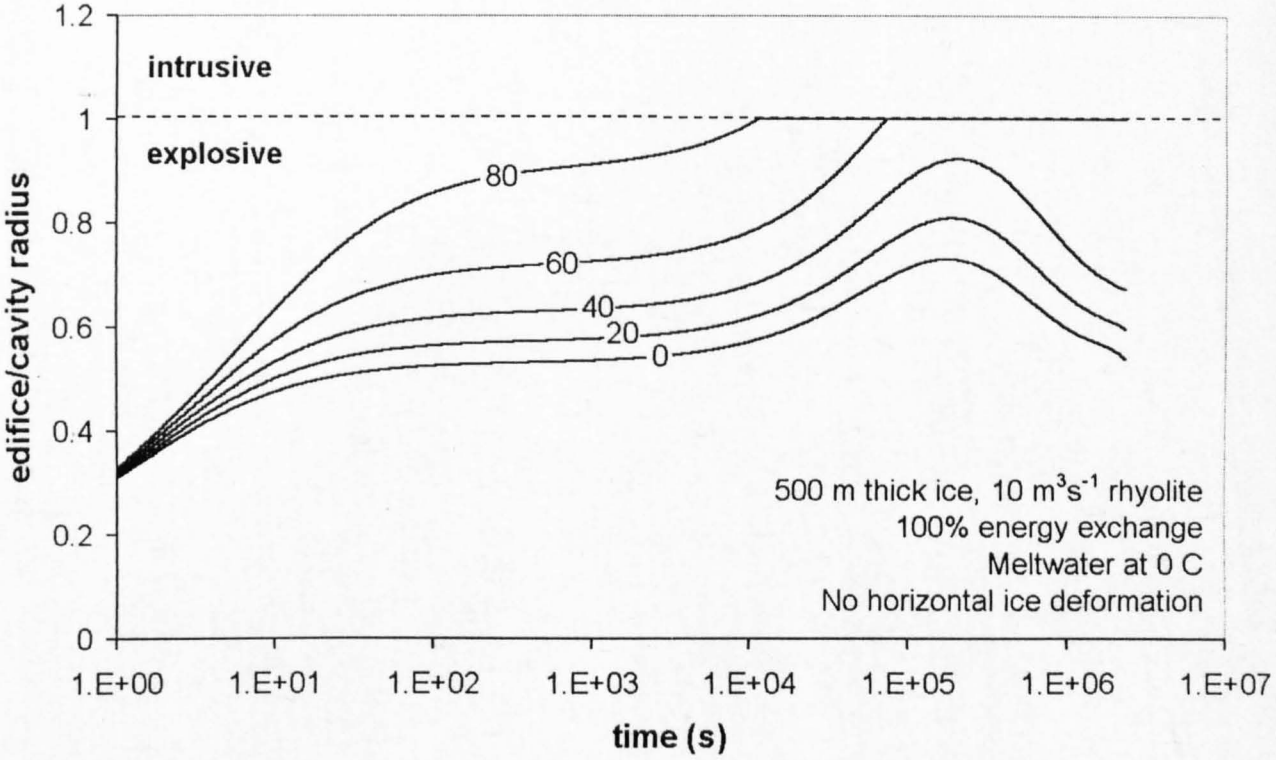

Fig. 5.17. The edifice radius : cavity radius ratio plotted against time for eruptions of 10 m^3 s^{-1} of variably vesicular magma beneath ice 500 m thick.

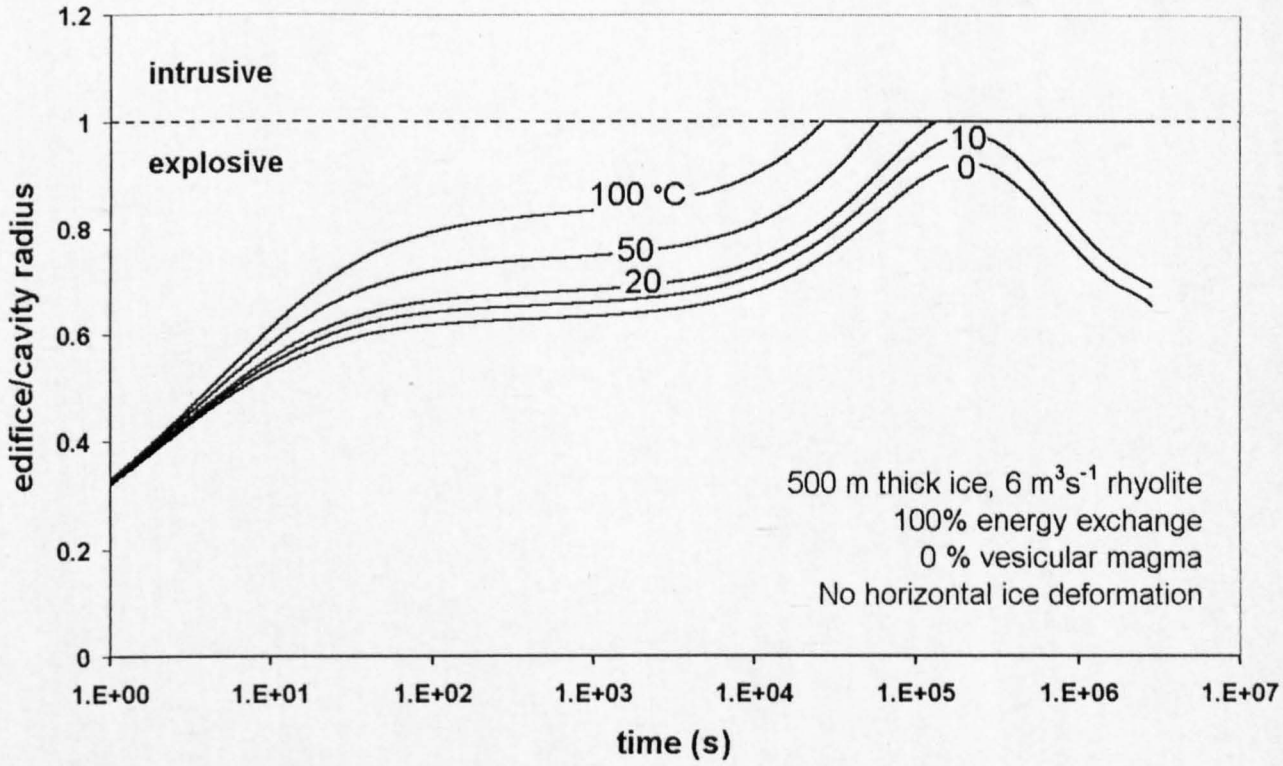

Fig. 5.18. The edifice radius : cavity radius ratio plotted against time for $Q_l = 6$ m^3 s^{-1}, $h_o =$ 500 m, 20 % vesicular magma giving $v_i = 5.6$, and variable meltwater temperatures.

In reality, the vesicularity of the rising magma is determined by the magma volatile content and the extent of degassing during magma ascent and decompression. Small-volume eruptions with a low magma discharge rate are commonly degassed and produce low-vesicularity material, whereas larger-volume eruptions are commonly more volatile-rich and produce relatively vesicular material (e.g. Eichelberger et al. 1986, Fink et al. 1992). The vesicularity of magma emplaced during a subglacial eruption may be sensitive to the (variable) confining pressure, since glaciostatic pressures in the order of 5-10 MPa may be sufficient to inhibit vesiculation. However, the influence of cavity pressure on magma vesicularity has not yet been incorporated into the model.

5.6.8. Effects of meltwater temperature

Again, a 'borderline' eruption rate was selected for the chosen ice thickness. ΔT_w was varied in equation (17) and the resultant values of v_i fed into the eruption model. The model predicts that at high meltwater temperatures, a significant proportion of the thermal energy of the magma fails to melt the ice of the cavity roof, and the cavity enlarges less rapidly. This means that the cavity is more likely to fill with debris, and an intrusive eruption style is predicted. In the case illustrated (Fig. 5.18), the eruption is explosive at meltwater temperatures <10 °C, and becomes intrusive at temperatures >20 °C.

5.6.9. Effects of variable energy exchange rate during eruptions

One simulation was set up to examine the effects of a variable energy exchange rate, which may occur during cyclic or periodic phreatomagmatic explosions (e.g. Kokelaar 1986). Fig. 5.19 shows the resultant growth of the edifice and vault. The

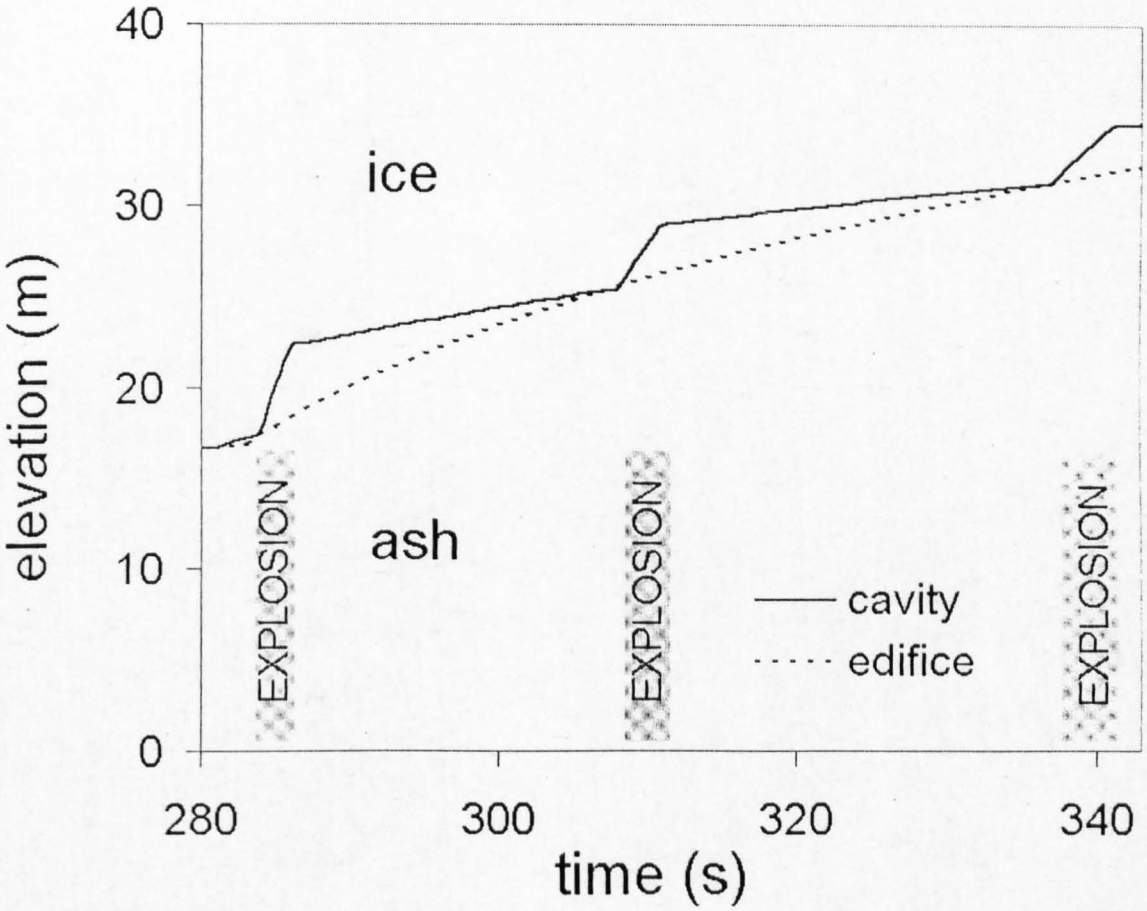

Fig. 5.19. Evolution of the edifice and cavity during the early stages of a phreatomagmatic eruption with Q_f= 100 m^3 s^{-1} and h_w = 450 m. The heat energy causing melting of ice is 100 % of the heat input to the system from the rising magma during three explosions, each of two seconds duration. Thus the cavity rapidly enlarges during explosions. It is estimated that only 20 % of this energy causes melting between explosions, hence the edifice begins to refill the cavity.

model predicts that rapid melting and cavity enlargement will be triggered by short-lived explosions. Energy exchange and melting is much slower between explosions, and the cavity may almost fill up with material. In continuous uprush-type behaviour, the heat flux is likely to be near-constant (e.g. White & Houghton 1999), whereas more episodic explosions may also occur during Surtseyan eruptions (e.g. Kokelaar 1986).

Periodic pressure waves?

Dobran and Papale (1993) show that pressure waves in the order of 10-100 MPa can be generated within lava tubes by the injection of water onto the molten lava surface. This is due to rapid expansion of steam formed by magma-water interaction. The pressures generated are sufficient to cause brittle failure of the solidified lava roof and destruction of the lava tube. Similar processes may occur during magma-water interaction within a subglacial cavity, and possibly crack the ice roof. However, this is merely noted as a possibility, and not incorporated into the eruption models, as the resultant fracture patterns are not straightforward to predict.

5.6.10. Effects of non-atmospheric cavity pressure

Fig. 5.20 shows the predicted evolution of the edifice/cavity radius with time for the eruption of 1 $m^3 s^{-1}$ of magma beneath 450 m of ice, with a range of different cavity pressures. The lower the cavity pressure, the more rapid the deformation of the ice roof - and the cavity is more likely to become filled by the edifice. Therefore an intrusive eruption style is favoured by low cavity pressure.

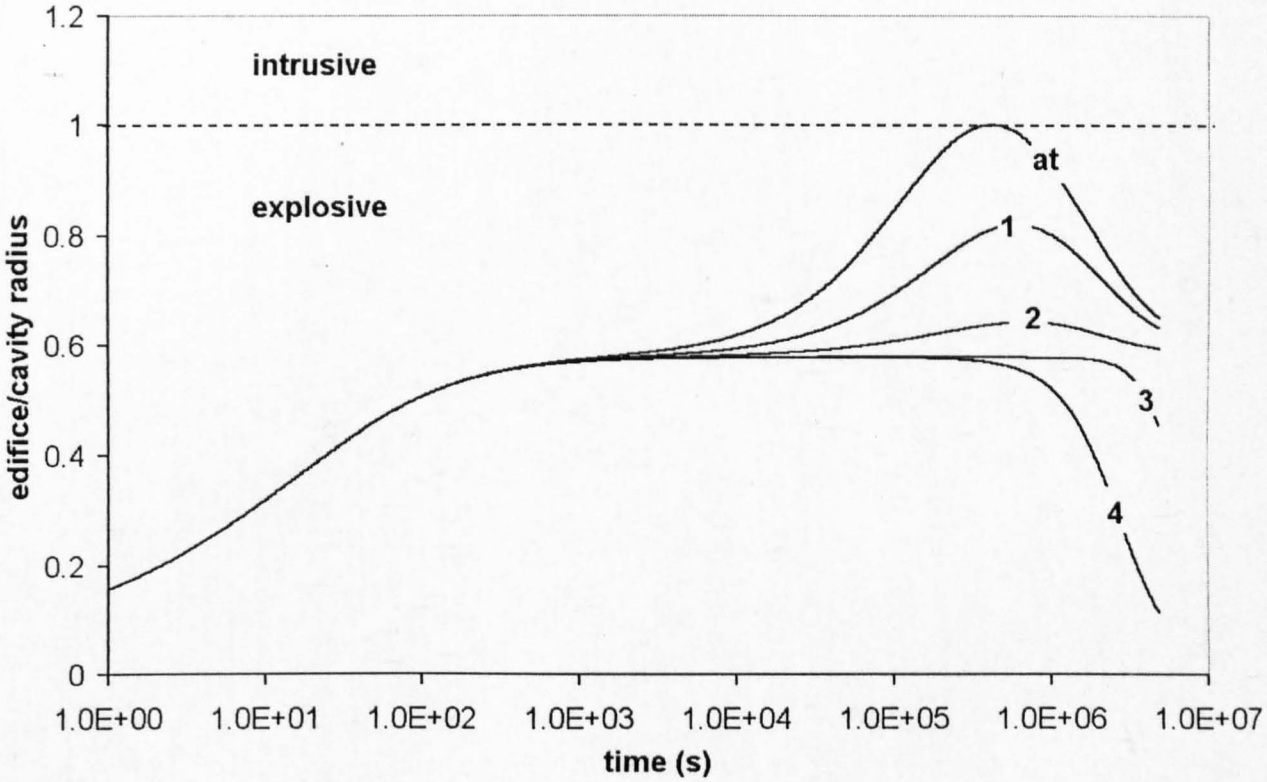

Fig. 5.20. The predicted evolution of the edifice/cavity radius with time for the eruption of 1 $m^3 s^{-1}$ of magma beneath 450 m of ice, with a range of different cavity pressures. Cavity pressures in MPa are indicated, 'at' represents atmospheric pressure (0.1 MPa). Although the model predicts that *high* cavity pressure will favour *explosive* eruptions (due to less rapid closure of the ice roof), in reality high pressure may stifle the explosivity of eruptions by reducing the vigour of magma-water interaction.

5.7. Ice surface deformation

What causes deformation of the ice surface?

An important point is that basal melting will *only* trigger ice surface deformation if the pressure in the region of melting is sub-glaciostatic, leading to closure of the ice roof. In an entirely brittle deformation regime, this will lead to block subsidence of the ice above the melting site, in a similar process to caldera collapse (Branney 1995). Were ductile deformation to occur, complex 3-D deformation fields are likely to develop (e.g. Aðalgeirsdottír et al. 2000).

5.7.1. Depth of ice cauldrons formed (Scenario A: no horizontal ice deformation)

Fig. 5.21 shows the depth of ice cauldron that would develop on the surface of a 450 m-thick glacier during eruptions with varying magma discharge rates. It is assumed that no horizontal ice deformation occurs, deformation is purely ductile, and ice surface deformation is equal to cavity roof deformation. Considerably deeper ice cauldrons are expected to develop during prolonged eruptions with a low magma discharge rate. This is because there is simply more time for the ice roof (and surface) to deform. If horizontal ice deformation were significant, ice cauldron depths would reflect the relative rates of horizontal and vertical ice deformation, and could only be simulated using a finite-element technique (Aðalgeirsdottír et al. 2000).

5.7.2. Effects of non-atmospheric cavity pressure on ice cauldron depths

The rate of vertical ice deformation depends upon the pressure difference driving closure of the cavity roof. If pressure in the cavity is greater than atmospheric, this pressure difference will be reduced, and ice deformation rates will be lower. Fig. 5.22

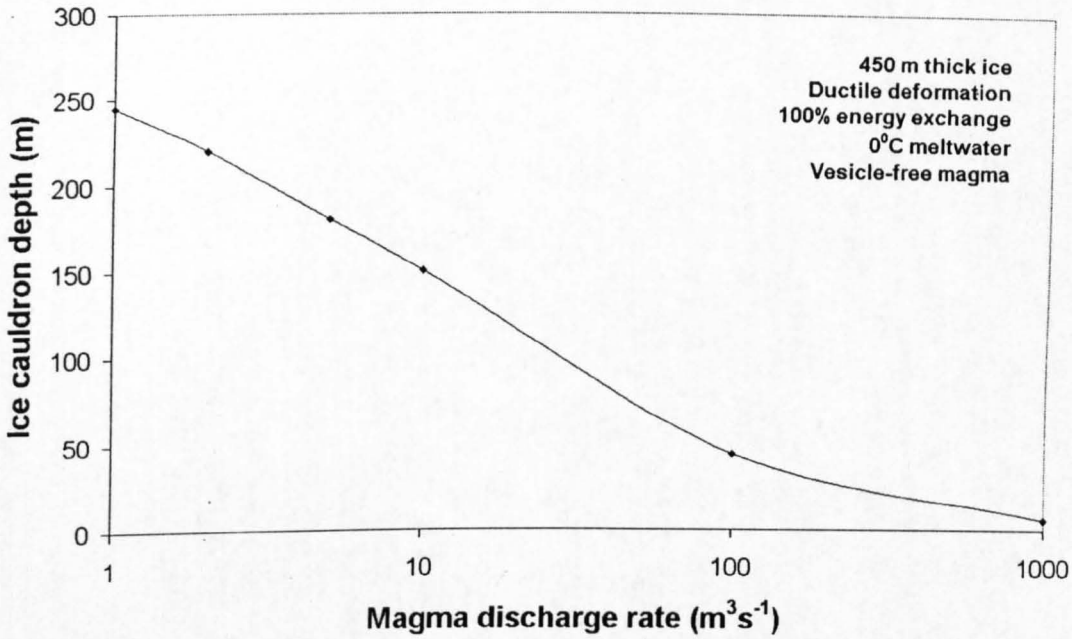

Fig. 5.21. Model predictions for the depth of ice cauldron formed as a function of the magma discharge rate for eruptions of vesicle-free rhyolite beneath 450 m-thick ice, with no horizontal ice deformation. The ice cauldron is considered to have reached its maximum depth when the ice roof is less than 50 m thick and fails, leading to a subaerial eruption. Deeper ice cauldrons develop when the eruption rate is low. This is because there is more time for vertical (downward) deformation of the ice before the eruption becomes subaerial.

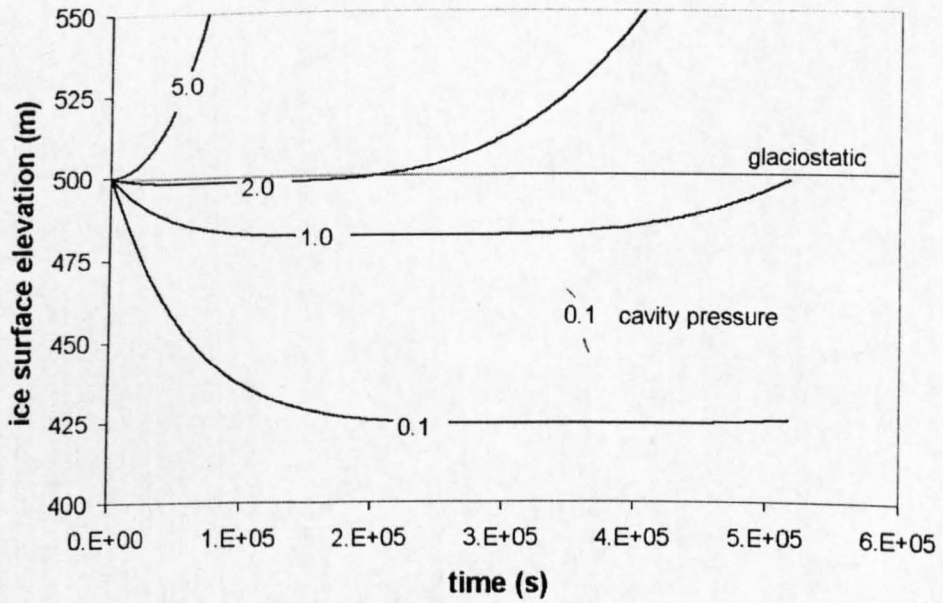

Fig. 5.22. Predicted changes in the elevation of the ice surface for eruptions within cavities at different pressures, with $Q_l = 100\ m^3\ s^{-1}$ and $h_o = 500$ m, 20 % vesicular magma giving $v_i = 5.6$. Curves indicate the elevation of the ice surface for different cavity pressures (MPa). Cavity pressures are assumed to be constant throughout the eruption. The glaciostatic pressure is 4.5 MPa. The model predicts that the ice surface will be deformed upwards when the cavity pressure exceeds glaciostatic pressure (e.g. 5 MPa). An ice cauldron is predicted to form when the cavity pressure is less than glaciostatic (e.g. 1 MPa), but as the roof thins, cavity pressure exceeds glaciostatic pressure, and the ice surface is predicted to deform upwards. However, upward deformation of the ice surface is unlikely due to 'pumping' of meltwater out of pressurised cavities (section 5.5.1).

is used to compare the predicted depths of ice cauldrons that develop during eruptions with variable cavity pressures.

5.7.3. Total ice thickness melted (Scenario B: perfect horizontal ice deformation)

If horizontal ice deformation were to fill in any ice surface depression, there would be an influx of ice into the region of melting. As a result, the eruption would have to melt through a total ice thickness that is considerably greater than the bedrock-to-surface glacier thickness. When the cavity is not filled, the total thickness of ice melted can be calculated using the numerical model. If the cavity remains filled during the eruption, the total thickness melted can be calculated analytically, as shown below.

At a magma discharge rate Q_l, the radius R of the hemispherical edifice is given by

$$R = \left[\frac{3Q_l t}{2\pi}\right]^{1/3} \tag{21}$$

and the melting rate over the surface of the edifice r'_m, which is in contact with the overlying ice roof, and of equal area, is defined as

$$r'_m = \frac{v_i Q_l}{2\pi R^2}. \tag{22}$$

Substituting (21) into (22) yields

$$r'_m = \frac{v_i Q_l}{2\pi}\left[\frac{3Q_l t}{2\pi}\right]^{-2/3} = v_i\left[\frac{Q_l}{18\pi}\right]^{1/3} t^{-2/3} \tag{23}$$

which expresses the melting rate as a function of time. This can then be integrated with respect to time to obtain the total thickness of ice melted. The time period over

which melting occurs (t_1 - t_0) is equal to the time taken for the edifice to grow to be as high as the surrounding glacier (assuming that no brittle ice fracture occurs). Since

$$t_1 - t_0 = \frac{2\pi R^3}{3Q_l} \tag{24}$$

and $t_0 = 0$, the total melting h_T is thus

$$h_T = \int_{t_0}^{t_1} r'_m \, dt = v_i \left[\frac{Q_l}{18\pi}\right]^{1/3} \int_{t_0}^{t_1} t^{-2/3} dt$$

$$= 3v_i \left[\frac{Q_l}{18\pi}\right]^{1/3} r \left[\frac{2\pi}{3Q_l}\right]^{1/3}$$

$$= 3v_i \left[\frac{Q_l}{18\pi}\right]^{1/3} \left[t^{1/3}\right]_{t_0}^{t_1}$$

$$= v_i R. \tag{25}$$

Hence the total melting is equal to the ice thickness multiplied by v_i, the volume of ice melted per unit volume of magma. As shown in Fig. 5.4, typical values of v_i range between 4 and 6 for vesicle-poor magma and cool meltwater (<20 °C). Fig. 5.23 shows the total thickness h_T of ice melted during eruptions of varying magma discharge rate (Q_l) beneath a glacier 450 m thick. At low Q_l, h_T approaches $v_i R$, whereas h_T is considerably lower at high values of Q_l, and approaches R. These results show that, if horizontal ice deformation is significant on the timescale of the

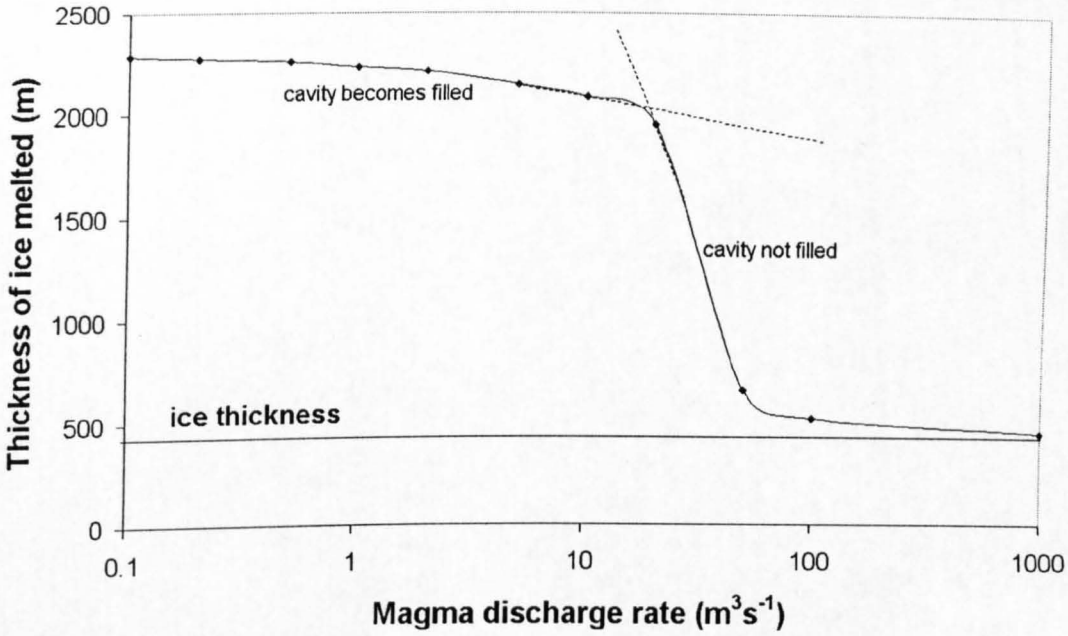

Fig. 5.23. The total vertical thickness of ice melted plotted against time plotted against magma discharge rate during eruptions beneath a glacier with 'perfect' horizontal deformation (i.e. ice surface remains horizontal). The plotted line is the combination of two distinct segments: in which the cavity is never filled (at high Q_l) and in which the cavity becomes filled (at low Q_l). *Dotted lines* indicate the probable extension of each segment.

subglacial phase of the eruption, the volcano may have to melt through considerably more ice than the thickness of the glacier suggests.

5.8. Lithofacies associations created

5.8.1. Theoretical examples

The model presented provides information on the growth of an idealised hemispherical edifice within a well-drained hemispherical subglacial cavity. Since the eruption style is predicted, it is possible to predict approximately the lithofacies associations formed. Fig. 5.24 shows the results of such predictions for three different magma discharge rates beneath ice 450 m thick. The model assumes that all newly-erupted material is emplaced on the outer surface of the growing hemispherical edifice, whereas in reality considerable auto-intrusion will probably occur. A subaerial eruption is deemed to begin when the ice roof is reduced to 50 m in thickness, and fails in a brittle manner. Any fragmental subaerial deposits generated will be prone to reworking and are not expected to increase the size of the edifice. Subaerial lava thus directly overlies subglacial deposits. The thickness of the subaerial lavas depends upon the volume of lava extruded subaerially. Since, in general, the total volume erupted is roughly proportional to the magma discharge rate (e.g. Pyle 1999), large volume lava caps are likely to form during eruptions with high Q_l. It is considered unlikely that the height of the preserved subaerial lava cap will exceed that of the surrounding ice surface, as any lava that flows over the ice surface has a low preservation potential.

During 'perfect' horizontal deformation, low values of Q_l produce intrusive edifices. The 'passage zone' (i.e. contact between subglacial deposits and subaerial

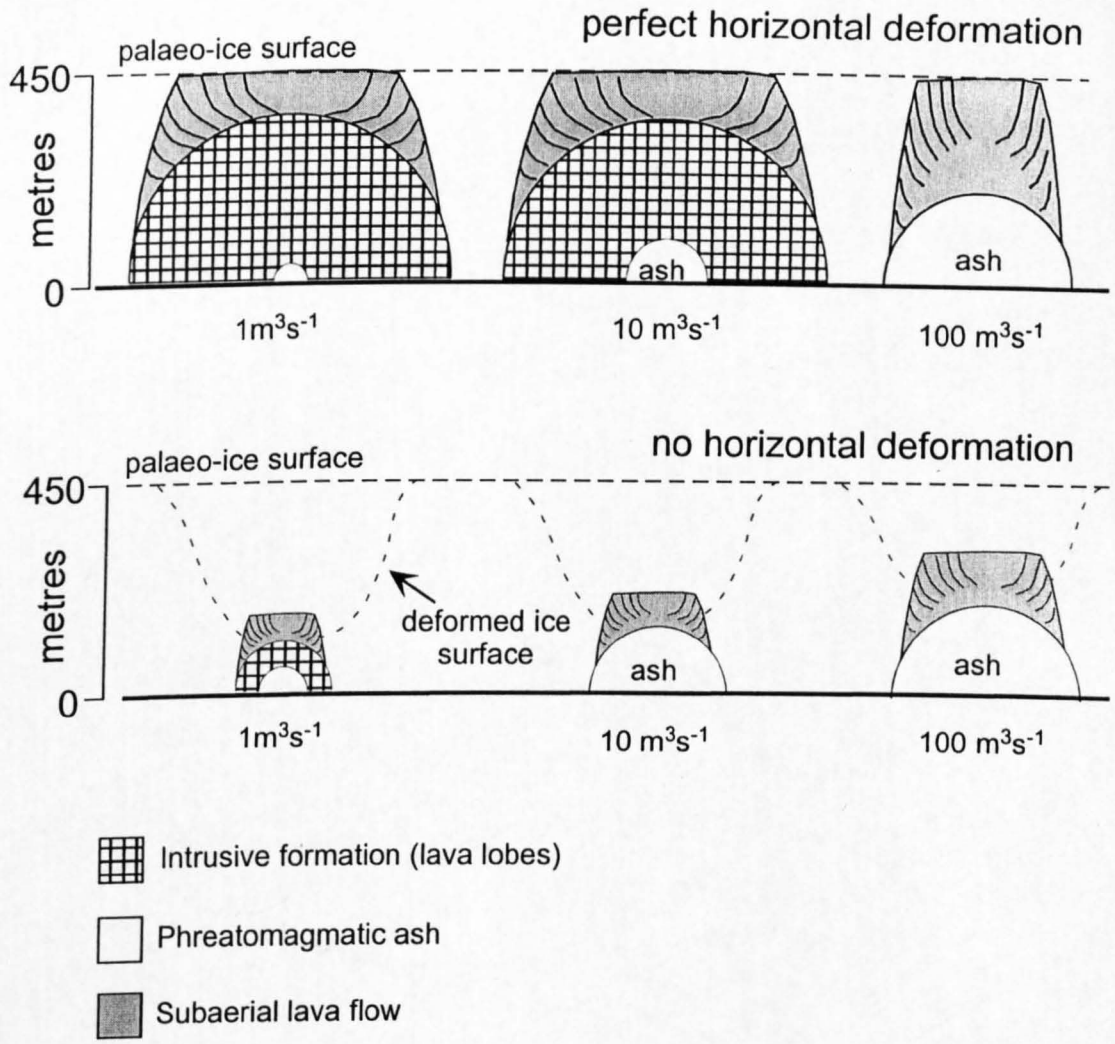

Fig. 5.24. Schematic diagram of the stratigraphy predicted to be formed by the model during eruptions beneath ice 450 m thick. It is assumed that phreatomagmatic ash (white) is formed when the cavity is not entirely filled by the edifice, and that intrusive lava lobes are formed when the edifice completely fills the cavity. It is assumed that the ice roof fails when less than 50 m thick, and that subaerial lava then drapes over the subglacial edifice. The shape of the deformed ice surface in the 'no horizontal deformation' scenario is shown schematically and not to scale. The diagram illustrates that the elevation of the subglacial-subaerial transition at rhyolitic tuyas is an unreliable palaeo-ice thickness indicator, since it depends upon the magma discharge rate and horizontal deformation patterns. Lava lobes may dominate the stratigraphy when there is perfect horizontal ice deformation, but only a small thickness of lava lobes can be generated if there is no horizontal ice deformation, even at low magma discharge rates.

lava, Smellie 1999) is 50 m beneath the palaeo-ice surface. At higher values of Q_l, the passage zone may be considerably lower, as the glacier is 'blasted through', and the subaerial lava cap may be twice as thick as the underlying subglacial phreatomagmatic ash deposits. Conversely, when no horizontal ice deformation occurs, the elevation of the passage zone *increases* with increasing Q_l, but is always >200 m beneath the palaeo-ice surface. At high eruption rates, patterns of ice deformation exert less influence on the volcanic stratigraphy, hence the similarity between the two edifices formed at the highest magma discharge rate, $Q_l = 100\ m^3\ s^{-1}$.

The stratigraphy formed by subglacial rhyolite eruptions clearly depends upon patterns of magma discharge rate with time and ice deformation, as well as the ice thickness. Unless these patterns can be reconstructed from the geological record, it is unwise to use passage zones to infer *absolute* palaeo-ice thicknesses. All that they provide is a *minimum* value of ice thickness at the time of eruption.

5.8.2. The models applied to Bláhnúkur, South-east Rauðufossafjöll and Dalakvísl

The numerical models provide an estimate of the magma discharge rate that would produce 'explosive' or 'intrusive' subglacial deposits beneath ice of varying thicknesses. If the approximate ice thickness during an ancient subglacial eruption is known, it is thus possible to estimate the magma discharge rate. This can now be applied to Bláhnúkur, South-east Rauðufossafjöll and Dalakvísl. The eruption at Bláhnúkur was mostly 'intrusive', that at South-east Rauðufossafjöll mostly 'explosive', whereas Dalakvísl is intermediate between the other two. Firstly, it is necessary to estimate the ice thickness.

Estimating the ice thickness

The subaerial lavas of South-east Rauðufossafjöll lie approximately 400 m above the base of the volcano, suggesting an ice thickness of >400 m. However, the depth of ice cauldron is unknown, since it depends upon the magma discharge rate (Fig. 5.21), and the rate of horizontal ice deformation. A range of ice thicknesses between 400 and 600 m is taken. Bláhnúkur was erupted beneath ice >350 m thick, and it is assumed that the ice thickness was in the same range as South-east Rauðufossafjöll (400-600 m). The ice thickness at Dalakvísl is assumed to be 300-500 m.

Estimating the eruption rate

Fig. 5.25 indicates the approximate magma discharge rate at each volcano, based on the estimates of ice thickness and the subglacial lithologies. The models predict that the magma discharge rate at South-east Rauðufossafjöll was 5-1000 $m^3 s^{-1}$. This suggests that the ice cauldron depth was in the range 0-150 m (see Fig. 5.21). The magma discharge rate at Bláhnúkur was lower - possibly between 0.1 and 10 $m^3 s^{-1}$, whereas the magma discharge rate at Dalakvísl may have been between 0.5 and 100 $m^3 s^{-1}$. The amount of horizontal ice deformation during the eruptions is not known, thus the range of possibly magma discharge rates is broad, to allow both 'perfect' and no ice deformation. The estimates of Q_l from these models are consistent with those of Hoskuldsson & Sparks (1997), who estimated a magma discharge rate of 10-100 $m^3 s^{-1}$ during intrusive subglacial rhyolite eruptions, using a model of buoyant rise of magma within a dyke.

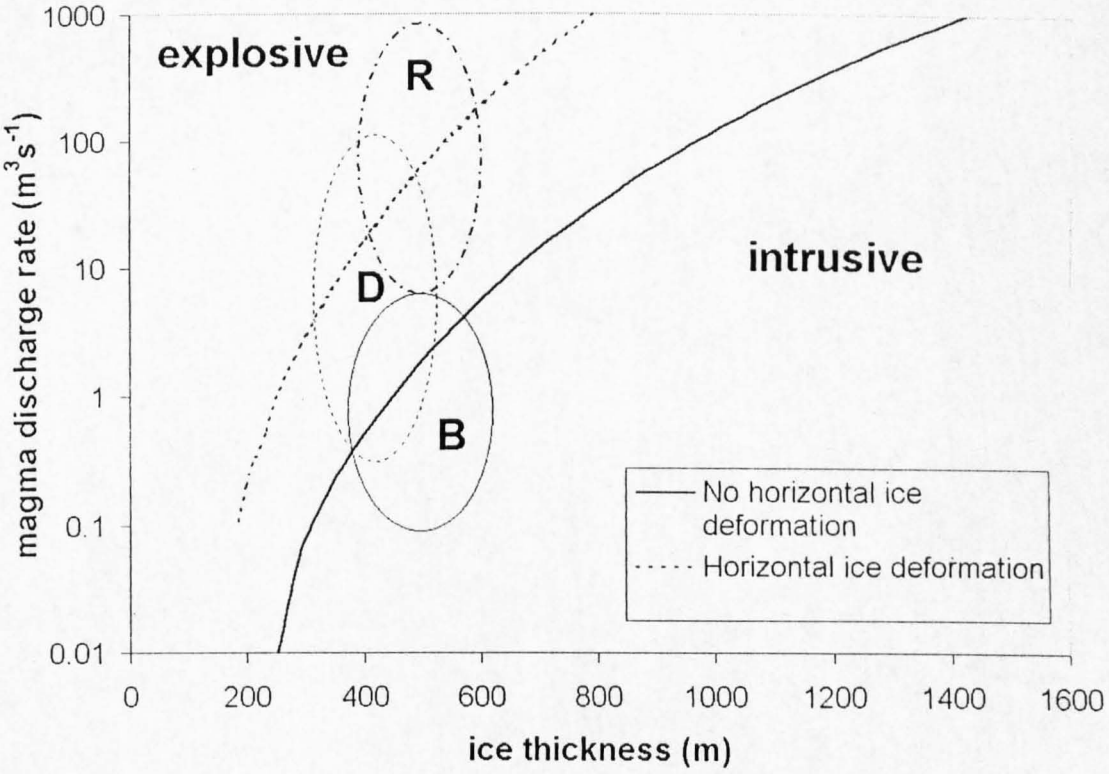

Fig. 5.25. Possible ranges of magma discharge rate and ice thickness during the subglacial rhyolite eruptions of Bláhnúkur (B), South-east Rauðufossafjöll (R) and Dalakvísl (D). The solid line indicates Q_{cr} as a function of ice thickness if there is no horizontal ice deformation, the dotted line indicates Q_{cr} if there is perfect ice deformation. See text for discussion.

5.9. Localised subglacial melting during intrusive rhyolite eruptions: a model to explain the formation of columnar jointed lava lobes at Bláhnúkur

As discussed above, a subglacial cavity may become completely filled with volcanic debris during an eruption, especially if the ice is thick, or the magma discharge rate is low. Activity is likely to be characterised by the intrusion of magma within the debris (Fig. 5.11b). This is thought to have occurred at Bláhnúkur, and have formed the lava lobes (section 2.5). The patterns of melting differ from those considered earlier in this chapter, in that melting is localised and individual magma bodies act as transient heat sources. Furthermore, thinning of the ice roof is assumed to be negligible.

5.9.1. Lava lobes at Bláhnúkur and the inferred melting mechanisms

Columnar-jointed lava lobes at Bláhnúkur (section 2.5) are thought to have risen through wet breccias to the glacier base, where they chilled against steeply-inclined ice walls. Most ice walls were probably orientated at between 45 and 80° from the horizontal (Fig. 2.6c), and dip down the modern-day slope. The scenario envisaged for their emplacement is illustrated in Fig. 5.26, and described below.

Emplacement scenario

A cylindrical body of magma rises within wet breccia. Heat release by conduction to the surrounding breccia is retarded by chilling of the carapace but accelerated by the formation of joints in the carapace. Water in the breccia adjacent to the magma body is vaporised, and vapour travels rapidly along veins in the breccia. A hemispherical

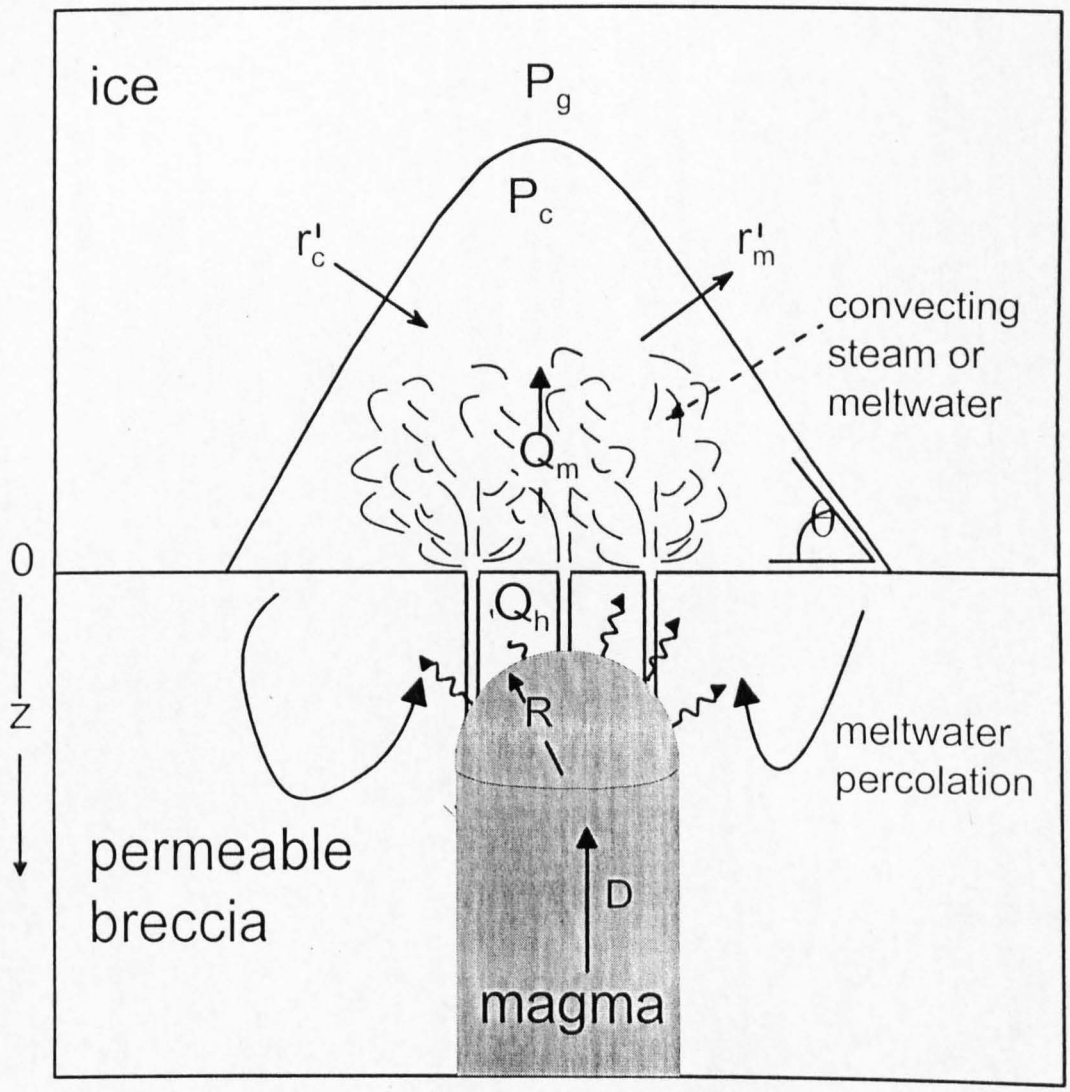

Fig. 5.26. Cartoon illustrating a model for the melting of an ice cavity during the ascent of a cylindrical magma body to the glacier base. Q_h = conductive heat flux, R = cylinder radius, D = lava rise velocity, ΔT = temperature difference between lava margin and surrounding breccia, Q_m = heat flux that causes melting of ice, P_g = glaciostatic pressure, P_c = cavity pressure, r'_c = closure rate due to ice deformation, r'_m = melting rate, θ = orientation of ice wall.

cavity is melted into the glacier base during the last 10 metres of ascent of the magma body. The rising magma body enters the cavity, and is chilled against the ice walls, which are effectively stationary during movement of the magma. Columnar cooling joints then develop normal to the steeply-inclined ice walls.

The dynamics of the system described above are examined in the following sections the heat flux from rising magma (section 5.9.2), the transfer of thermal energy from magma to ice (5.9.3.) and the magma ascent rate (5.9.4.) are considered. The evolving size of the subglacial cavity is modelled by simulating the rate of melting (5.9.5.) and closure by ice deformation (5.9.6.), leading to estimates of equilibrium cavity radii (5.9.7. and 5.9.8). The applicability of the model to the lava lobes at Bláhnúkur is discussed in section 5.9.9.

The model uses the following assumptions:

1. Ice is incompressible and deforms in accordance with Nye's law.
2. Ice is at 0 °C.
3. Rising magma loses heat through conduction, aided by the formation of joints.
4. Convecting steam carries this heat to the glacier base in vapour-escape pipes.
5. Vapour-escape pipes develop during the final 10 m of magma ascent to the glacier base, and localised melting of ice occurs, forming subglacial cavities which may be steam- or water- filled, depending upon the position of the water table and the proximity of low-pressure meltwater conduits.
6. The cavity is enlarged by melting, and closed by ductile deformation of the ice roof, which will occur if the cavity pressure is less than glaciostatic.
7. Cavities have attained approximate size equilibrium, at which the rates of melting and closure are balanced, when they are entered by lava bodies.
8. All of the thermal energy of heated meltwater is transferred to the ice (i.e.

meltwater leaves the system at 0 °C).

9. The ice roof does not thin significantly during basal melting, hence glaciostatic pressure is constant.
10. The rate of loss of thermal energy from magma to steam is equal to the heat flux causing melting of the ice.
11. The meltwater formed may either drain away through the permeable bedrock and into any connected R-channels, leaving a steam-filled cavity (e.g. Mount Rainier firn caves, Kiver & Steele 1975). Alternatively, meltwater may accumulate in the cavity until it is filled with water, and then pressure in the cavity would be equilibrated with any hydraulically connected R- and N-channels and the bedrock by 'pumping' of water in or out of the cavity. It is thus considered unlikely that cavity pressure could exceed glaciostatic pressure. Cavity pressure may therefore be less than or equal to glaciostatic pressure, and possibly as low as atmospheric pressure.

5.9.2. Heat flux from magma

In order to simulate the rise of lava lobes to the glacier base, I consider the rise of a cylindrical magma body of radius R with a hemispherical upper surface towards isothermal ice at 0 °C (Fig. 5.26). In order to simplify calculations, the magma body is assumed to be isothermal (T_m = 900 °C) and loses heat by conductive cooling from the hemispherical upper portion (Fig. 5.26). An isothermal magma body is deemed appropriate because it is likely to have lost only a fraction of its heat on the timescales considered. Furthermore, the magma temperature is likely to have been buffered by latent heat released during microlite crystallisation, which can be shown texturally to have occurred during lobe emplacement (section 2.5.4).

The conductive heat flux Q_h from an isothermal hemispherical magma body is given by

$$Q_h = Sk_l\Delta T, \quad (26)$$

where S is a shape term, k_l is the thermal conductivity of magma, and ΔT is the temperature difference between the magma and surrounding breccia (Holman 1997). Estimating the effective ΔT is not straightforward. It is assumed that the breccia was maintained close to 100 °C, the temperature of steam at atmospheric pressure, because of the field evidence for steam fluxing through the breccia. Field observations suggest that the magma body developed a fractured, chilled rind during its ascent and emplacement. The effect of this rind on the conductive heat flux is twofold:- its lower temperature will reduce the temperature contrast between the magma and the breccia (ΔT), but fracturing will increase the surface area available for energy exchange, hence increasing S. The relative magnitudes of these two effects can be estimated:-

a) Chilled rind

It is assumed that the fractures in the obsidian rind propagated inwards as far as magma at the glass transition temperature (~400 °C, Stevenson et al. 1995), and the outermost part of the rind was in thermal equilibrium with the surrounding breccia (T = 100 °C, Fig. 5.27). Assuming a linear temperature gradient within the obsidian, the average temperature of the fractured obsidian surfaces is therefore roughly (400 °C + 100 °C) / 2 = 250 °C. Hence ΔT, the temperature difference between the obsidian rind and the surrounding breccia, is 150 °C. Without a chilled rind, ΔT is 800 °C. Since the conductive heat output Q_h is proportional to ΔT, the presence of a chilled rind reduces Q_h by a factor of about 5.

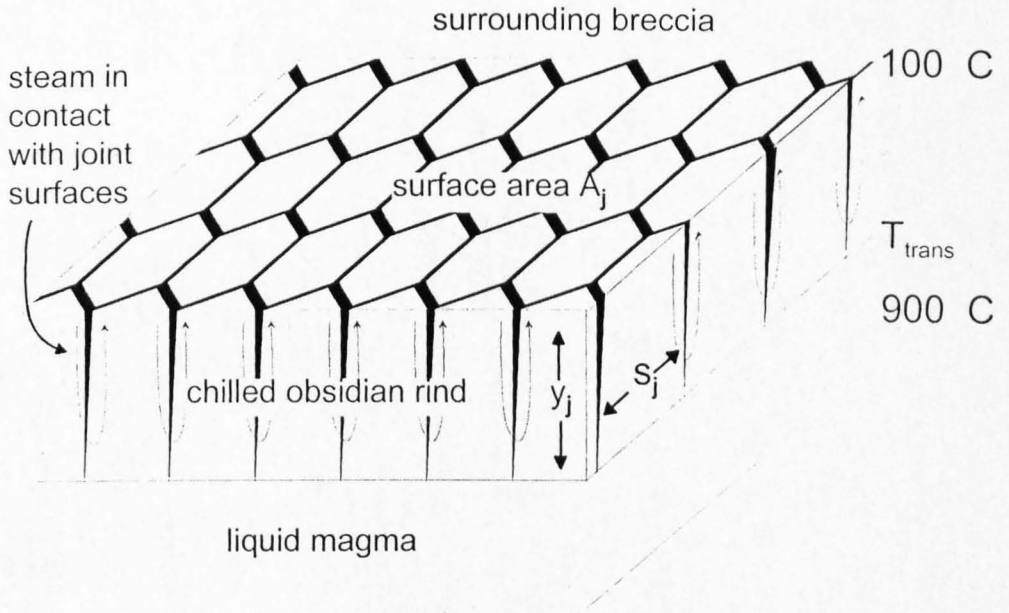

Fig. 5.27. Schematic diagram illustrating a columnar jointed lava margin. Joints spaced s_j apart have propagated distance y_j into the lava. It is assumed that convecting steam at 100°C percolates into fracture surfaces, thus increasing the effective cooling area.

b) Fractured rind

In accordance with field observations, it is assumed that fractures propagated a distance $y_j = 0.1$ m into the obsidian rind, and were spaced a distance $s_j = 0.1$ m apart (Fig. 5.27). The number of regular hexagonal columns of side length s_j on a hemispherical surface, W, is given by hemisphere surface area / column surface area

$$W = \frac{2\pi R^2}{3\sqrt{3}s_j^2/2} \tag{27}$$

where R is the hemisphere radius. The total surface area of each column is thus

$$A_{column} = 6y_j s_j + 3\sqrt{3}s_j^2/2 \tag{28}$$

and the total surface area of the fractured hemisphere

$$A_f = \frac{2\pi R^2}{3\sqrt{3}s_j^2/2}\left[6y_j s_j + 3\sqrt{3}s_j^2/2\right] = 2\pi R^2\left[1 + \frac{4y_j}{\sqrt{3}s_j}\right]. \tag{29}$$

Therefore, as

$$\frac{A_f}{A_0} = 1 + \frac{4y_j}{\sqrt{3}s_j} = 3.3 \quad (30)$$

where $s_j = y_j = 0.1$ m, fracturing of the obsidian rind is expected to increase the conductive heat flux by a factor of 3.3.

Combining the two effects, rind cooling and fracturing will reduce the heat flux by a factor of 5/3.3 = 1.5. Many parameters in the heat flux model have been only roughly estimated, hence it is assumed that the effects approximately cancel out, and ignore the chilled rind in our heat flux calculations. Instead, I consider the conductive cooling of an isothermal magma body at 900 °C, with $\Delta T_{eff} = T_l - T_v \approx 800$ °C. The conductive heat flux Q_h from a hemisphere with radius R = 2.5 m is thus ~ 0.17 MW.

5.9.3. Energy transfer from magma to ice

The presence of vapour-escape pipes within breccia A at Bláhnúkur (section 2.5) suggests active and locally focussed steam flux through the breccia during lava emplacement. It is therefore suggested that conductive heat released from magma generated a steam envelope in the adjacent breccias, and that the steam formed travelled within vapour-escape pipes to the base of the glacier. From the length of vapour-escape pipes observed at Bláhnúkur, it is anticipated that this process began to operate efficiently once the magma bodies had risen to within 10 metres of the glacier base. From this point, the heat released from the magma was transferred almost instantaneously to the overlying ice via convecting meltwater or steam. The rate of

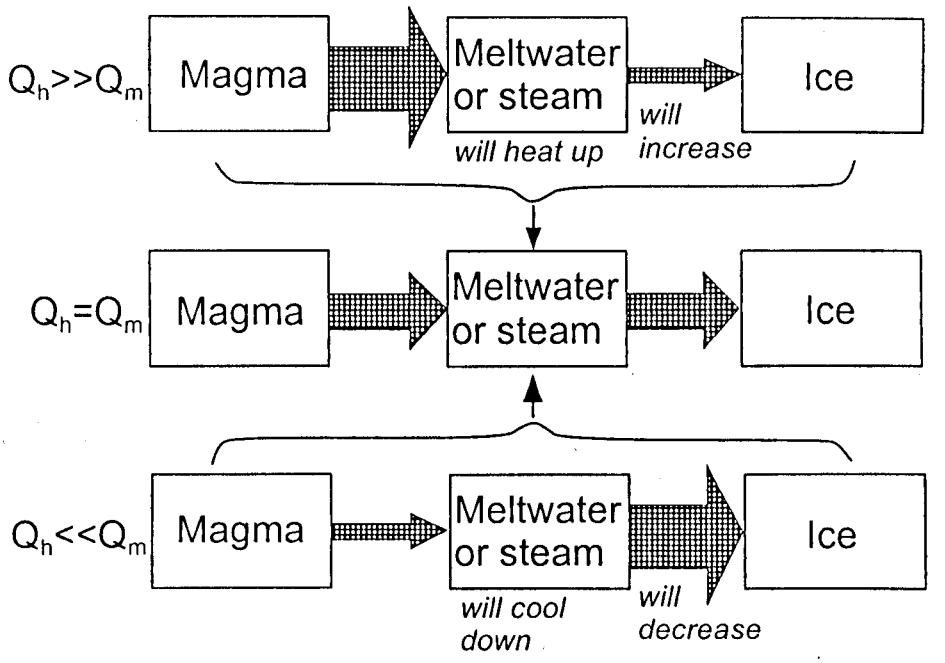

Fig. 5.28. Box diagram indicating the transfer of heat from magma to ice. The widths of shaded arrows are a schematic indication of the magnitude of heat fluxes. Q_h indicates the heat flux from magma to meltwater or steam, Q_m is the heat flux from meltwater or steam that causes melting of ice. In the models, Q_h and Q_m are assumed to be equal (centre). If Q_h were much greater than Q_m (top), the temperature of the meltwater/steam would increase, and thus Q_m would increase. If Q_h were much less than Q_m (bottom), the meltwater/steam would lose thermal energy and may refreeze, greatly reducing Q_m. Therefore it is assumed that Q_h and Q_m will be roughly balanced.

heat transfer from meltwater to ice has been examined by Hoskuldsson & Sparks (1997), who predicted that only a small proportion of the thermal energy released from the magma to the meltwater would be stored within the meltwater. This is assumed to apply here to either meltwater- or steam- filled cavities, and hence the heat flux from meltwater or steam to ice is assumed to be equal to the heat flux from the magma (Fig. 5.28).

The fraction of released heat that causes melting of ice is assumed to change from 0 at $z > 10$m (no heat reaches the glacier base) to 1 at $z \leq 10$ m (all the heat reaches the glacier base), where z is the distance below the glacier base.

5.9.4. Magma ascent rate

It is necessary to estimate the ascent rate (D) of magma bodies, in order to calculate how long cavities may be melted before they are entered by the magma. Since the magma is denser than the surrounding breccia, its rise must be triggered by a connection to an underlying over-pressured magma chamber. A lower limit on the magma rise rate can be obtained by considering the dimensions of lava lobes. Lobes are typically 100 m^3 in volume. The length of feeder lobes suggests that magma bodies have risen ~10 m through breccia to the glacier base. The minimum ascent rate D_{min} is thus the distance travelled/cooling time. Taking 10^5-10^6 s as a reasonable cooling time (c.f. Hoskuldsson & Sparks 1997), I acquire $D_{min} = 10^{-4}$-10^{-5} m s^{-1}.

5.9.5. Rate and distribution of ice melting

As discussed above, it is anticipated that heat from the rising lava lobes will be carried by convecting steam to the glacier base. If all the thermal energy of the magma is used to melt ice, the volume of ice melted per second a is given by

$$a = \frac{Q_h}{L_i \rho_i}, \tag{31}$$

where L_i is the heat of fusion of ice. The mean meltback rate of the ice walls

$$r'_m = a / A_i \tag{32}$$

where A_i is the ice wall area. For simplicity, the ice cavity is assumed to be hemispherical, thus for a cavity of radius R,

$$A_i = 2\pi R^2. \tag{33}$$

Hence the melting rate is proportional to the inverse square of the cavity radius

$$r'_m = \frac{a}{2\pi R^2} = \frac{Q_h}{2\pi r^2 L_i \rho_i}. \tag{34}$$

5.9.6. Cavity closure by ice deformation

If glaciostatic pressure exceeds cavity pressure, the cavity walls are likely to close by visco-plastic deformation (Nye 1953), as discussed earlier. The deformation rate r'_c is given by Nye's law (equation (9)). An equilibrium radius r_{eq} can be thus be calculated,

at which the melting and closure rates are equal and opposite. This is obtained by combining equations (9) and (34) and setting r'_c to be equal to r'_d, giving

$$r_{eq} = \left[\frac{Q_h (nB)^n}{\Delta P^3 2\pi L_i \rho_i} \right]^{1/3} \tag{35}$$

which reduces to

$$r_{eq} = \left[\frac{Q_h C}{\Delta P^3} \right]^{1/3} \tag{36}$$

where C is a constant, of value $(nB)^n / 2\pi L_i \rho_i = 2.1 \times 10^{15}$ J kg^{-3} s^5, where $n = 3$. Cavity radii are predicted to reach equilibrium in this model because the ice roof is assumed not to thin, leading to a constant ΔP. This is why the equilibrium cavity radius can be solved analytically, whereas an equivalent solution does not exist when the ice roof thins (equation (17)). The equilibrium cavity radius is thus weakly dependent on the basal heat input and inversely proportional to the effective pressure. The summit firn caves of Mount Rainier appear to be close to equilibrium, and r'_c is estimated at 10^{-7} m s^{-1} from measurements of the ablation rate (Kiver & Steele 1975). Deformation rates of glacier ice at Bláhnúkur are likely to have been orders of magnitude higher, since the effective pressures were probably greater and ice deforms more readily than firn (Paterson 1994).

5.9.7. Equilibrium cavity radii

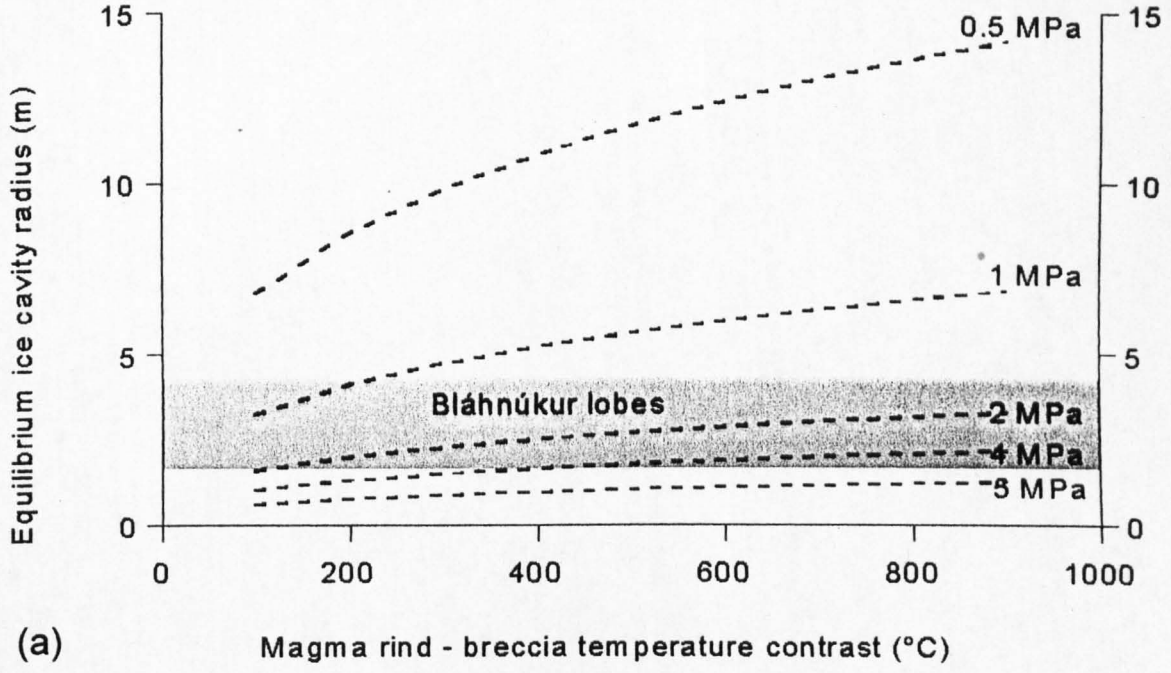
Equilibrium ice cavity radius (m)
15
10
5
0
0.5 MPa
1 MPa
Bláhnúkur lobes
2 MPa
4 MPa
5 MPa
0
200
400
600
800
1000
(a)
Magma rind - breccia temperature contrast (°C)

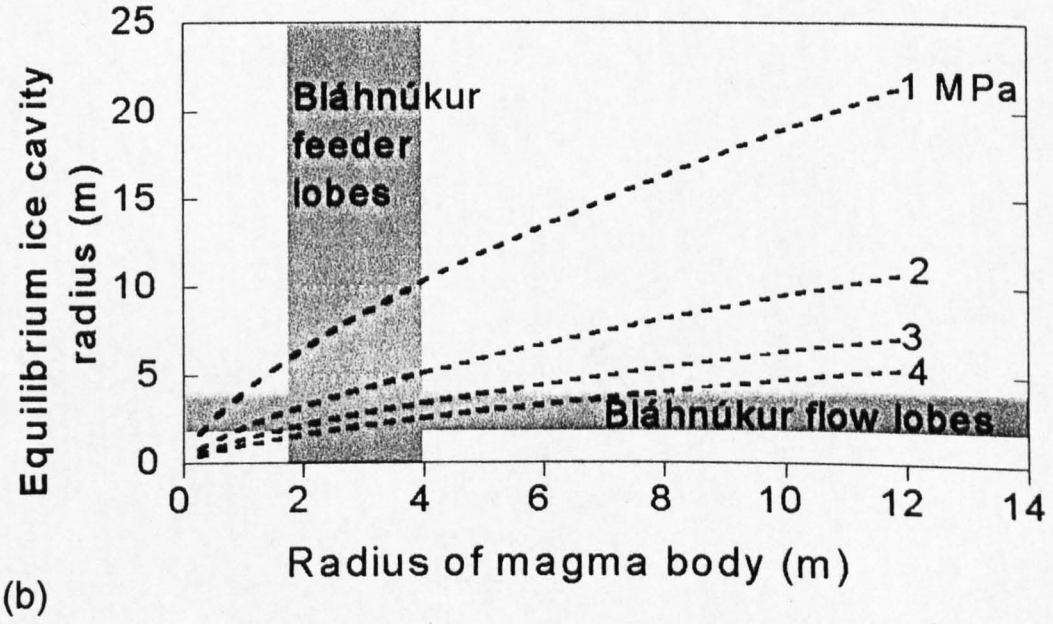
Equilibrium ice cavity radius (m)
25
20
15
10
5
0
Bláhnúkur feeder lobes
1 MPa
2
3
4
Bláhnúkur flow lobes
0
2
4
6
8
10
12
14
Radius of magma body (m)
(b)

Fig. 5.29.

Figure 5.29c

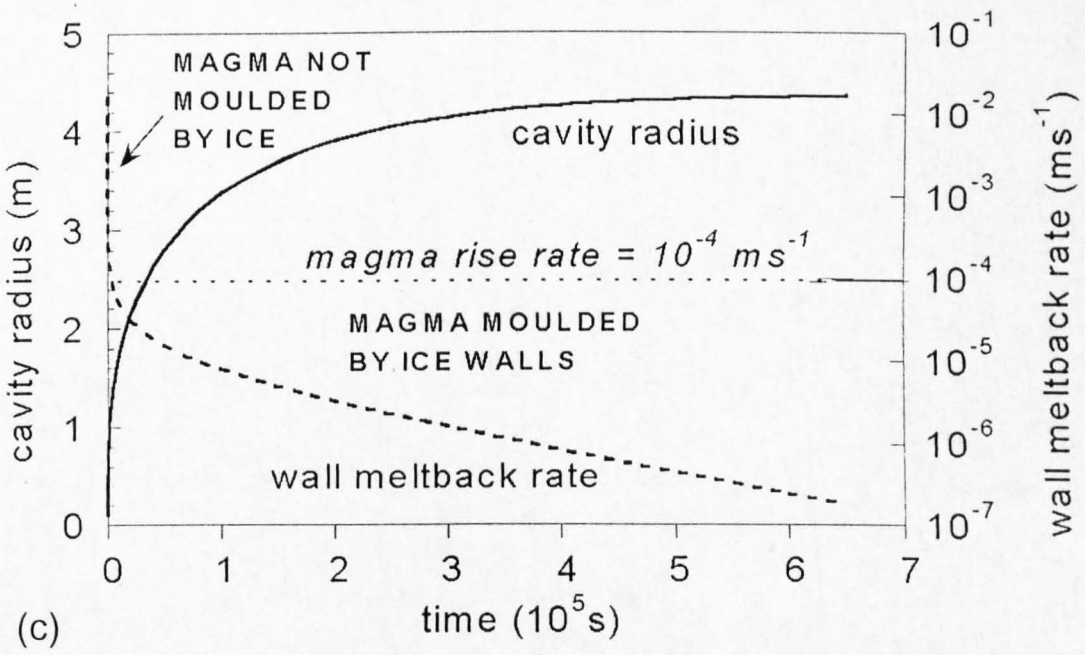

Fig. 5.29. (a) Equilibrium ice cavity radius as a function of effective outer surface temperature. R = 2.5 m. **(b)** Equilibrium ice cavity radius as a function of magma hemisphere radius for $_{\Delta}T$ = 750 ∘C, E_h =1. **(c)** Evolution of an ice cavity with time. Effective pressure = 4 MPa, magma body radius = 2.5 m. The cavity radius (solid curve) increases rapidly until about 10^5 s, whereupon it increases asymptotically towards an equilibrium value. The rate at which the cavity walls melted back (dotted curve) decreases sharply from an initial value of ~10^{-2} ms^{-1} to < 10^{-4} ms^{-1} after less than 10^4 s. It is anticipated that magma bodies entered cavities ~10^5 s after melting began. Thus cavities would have been close to equilibrium, with effectively stationary ice walls, at the moment that they were entered by magma bodies. This is the scenario in which ice-moulded lava lobes were formed within cavities.

Fig. 5.29 continued

The equilibrium cavity radius is only weakly proportional to the lava-breccia temperature contrast ΔT (Fig. 5.29a). Cavity sizes applicable to Bláhnúkur develop at effective pressures of 2-4 MPa for all reasonable values of ΔT. Fig. 5.29b shows equilibrium cavity radii as a function of effective pressure and the radius of spherical lava bodies at ΔT.= 800 °C. Equilibrium radii are only weakly proportional to lava body size, but strongly influenced by the effective pressure. For a range of magma sphere sizes consistent with the volume of Bláhnúkur feeder lobes (1.5-4 m), equilibrium cavity radii of 2-4 m, inferred from flow lobes, require effective pressures of 2-4 MPa.

5.9.8. Timescales of cavity enlargement and magma rise

The rate of change of the cavity radius is obtained by combining equations (9) and (34):

$$\frac{dR}{dt} = r'_m - r'_c = \frac{Q_h}{2\pi R^2 L_i \rho_i} - R\left[\frac{\Delta P}{nB}\right]^n, \qquad (37)$$

which is a second order differential equation of the form

$$\frac{dR}{dt} - \frac{M}{R^2} + NR = 0 \qquad (38)$$

where M is a melting term of value $Q_l/2\pi L_i\rho_i$ and N is a deformation term of value $[\Delta P/nB]^n$. Thus the cavity radius at time t, R_t is given by

(39)

$$R_t = R_0 + \int_0^t \frac{dR}{dt} dt$$

and R_0 is assumed to be zero. Analytical solutions of (37) indicate that approximate equilibrium is attained within 5×10^5 s (Fig. 5.29c). This results is in accordance with the response time of subglacial cavities to changes in meltwater flux obtained by finite element modelling (Cutler 1998). Assuming that magma bodies rise at a velocity of 10^{-4} m s^{-1}, melting will occur during the 10^5 s that a magma body takes to rise the final 10 metres to the glacier base, and the lava lobe will then enter the cavity. At 10^5 s, the rate of wall recession (dR/dt) has fallen to $<10^{-5}$ m s^{-1} (Fig. 5.29c), which is an order of magnitude slower than the lava lobe advance rate. Ice walls with thus be effectively stationary when flow lobes enter cavities, and advancing lavas will be moulded and chilled against the ice. It is assumed that the melting rate will not greatly increase once the lava has enter the cavity, and that the lava will solidify against the near-stationary ice wall (Vinogradov & Murav'ev 1988; Lescinsky & Sisson 1998).

5.9.9. Application of the model to Bláhnúkur lava lobes

The formation of steep-walled steam- or water-filled subglacial cavities is consistent with many features of the lava lobe lithofacies, including lobe morphologies, joint patterns, magma-water interaction at lobe bases, and the presence of vapour-escape pipes. It is suggested that lobes were emplaced within cavities with an effective pressure in the range 2-4 MPa. This may correspond to a cavity at atmospheric pressure beneath ice 200-400 m thick. If the cavity pressure were much greater than atmospheric, this may imply that the ice was considerably thicker. Thus the model predicts that the cavity pressure was significantly less than glaciostatic, possibly caused by the high permeability of the substrate, and the steep slope of the glacier

base, which may favour the development of low-pressure meltwater conduits (Hooke 1984). The palaeo-ice thickness has been independently estimated at >350 m from the volcanic stratigraphy (Chapter 2). An obvious problem is that there is no clear relationship between the stratigraphic position (elevation) of lava lobes at Bláhnúkur and their size, which the model predicts. An alternative explanation for the size of lava lobes at Bláhnúkur is simply their composition: Friðleifsson et al. (1992) have found that the dimensions of subglacially-erupted lava pillows and lobes in Iceland are related to the magma composition. However, an explanation is needed for the apparent size and shape of the ice cavities within which the lobes at Bláhnúkur are inferred to have been emplaced, since the lobes are thought to have been moulded against ice walls.

5.10. Applying the model to subglacial basaltic eruptions

5.10.1. The 1996 Gjálp eruption

Approximately 0.4 km^3 of basaltic magma was erupted beneath ice 400-600 m thick between 30th September and 12th October 1996. Details of the eruption relevant to the model are listed in Table 5.4a, whereas a complete chronology of the eruption is provided in Table 1.2c. The eruption was initially subglacial, with an ice cauldron 150 m deep and 2 km across forming within the first 36 hours, whereupon the ice roof was broken and a subaerial eruption ensued (Guðmundsson et al. 1997, Guðmundsson, submitted). Considerable fracturing of the ice surface was observed from the second day of the eruption onwards. Water accumulated in the nearby Grímsvötn caldera at 0.5 km^3 per day during the first three days of the eruption, giving a minimum value for the subglacial melting rate.

Parameter	Value	How determined	References
¶ice melting rate	†*6000 $m^3 s^{-1}$	rate of meltwater accumulation in Grímsvötn	[1]
¶ice thickness	~ 600 m	radar-echo sounding	[1]
¶magma discharge rate	*730 $m^3 s^{-1}$	estimated from melting rate	------this study------
total eruption duration	10^6 s	observations and remote sensing	[1], [2]
total magma volume	4×10^8 m^3	estimated from meltwater volume	[1]
initial magma temperature	1090 ± 50 °C	geothermometry of samples	[1]
magma vesicularity	~ 0	sample analysis	[3]
meltwater temperature	15-20 °C	estimated from ice cauldron and meltwater volumes	[1], [2]
meltwater accumulation	negligible	direct observation: no large lake formed	[1], [2]
A (instant release)	0.75	comparing instant to delayed melting	[1]
‡time to pierce roof	1.1×10^5 s	observations and remote sensing	[2]
‡depth of ice cauldrons	100 m (16 h) 150 m (30 h)	observations and remote sensing	[2], [4]
cavity pressure	>1.8 MPa	Meltwater flushed into Grímsvötn caldera	[3]

Table 5.4a. Data on the Gjálp eruption. Compiled from [1] Guðmundsson et al. 1997, [2] Guðmundsson in review, [3] Guðmundsson unpublished data, [4] Jónsson et al. 1998. *During initial 36 hours of eruption. †Hence melting *per bowl* is 3000 $m^3 s^{-1}$. ¶Parameters fed into the numerical model. ‡Values that are simulated by the model.

Cavity pressure	0.1 MPa	1 MPa	2 MPa
Depth of ice cauldrons (m)	120	55	16
Time to pierce roof (s)	2.5×10^5	3.5×10^5	4.8×10^5

Table 5.4b Results acquired when data from Table 5.4a is fed into the melting-ice deformation model.

The ice melting-deformation model was applied to Gjálp, to examine how closely predictions matched the true course of events. Parameters used in the model were chosen to best accord with measurements and likely values for Gjálp (Table 5.4a). Results are listed in Table 5.4b. The ductile deformation model can roughly approximate the depth of ice cauldron and duration of the subglacial phase of the eruption. However, the best fit with the real data for Gjálp was acquired when cavity pressure was assumed to be atmospheric, whereas there is convincing evidence for cavity pressure in excess of 1.8 MPa (Table 5.4a). Assuming that cavity pressure was indeed 1.8 MPa, the model underestimates the ice surface subsidence at Gjálp by an order of magnitude. Brittle ice deformation thus appears to have greatly increased the rate of vertical subsidence, and shortened the duration of the subglacial phase of the eruption.

5.10.2. Palaeo-ice thicknesses during tuya construction in Iceland

Subglacial-to-subaerial basaltic tuyas in Iceland are thought to be the subglacial equivalent of shield-building eruptions (e.g. Rossi 1996, Jull & McKenzie 1996). The 'passage zone' (transition from subglacial to subaerial lithofacies) commonly occurs at 500 – 1000 m above the base of the edifice (e.g. Jones 1970, Werner et al. 1996). The palaeo-ice surface elevation is thought to be up to 100-150 m above the passage zone, depending upon the depth of the ice cauldron formed (Smellie 1999, see also section 5.7.1.). At Kalfstindar (Jones 1970), a pile of pillow basalt 500 m thick is overlain by 200 m of hyaloclastite and thin subaerial lava flows (Fig. 1.4b,c). The ice thickness is thus inferred to be 700-850 m. However, the heat given off by cooling of a pile of pillows 500 m thick is sufficient to melt >2000 m of ice, if meltwater were at 0 °C and melting were confined to a subglacial cavity. Even if meltwater drained

away at a reasonable temperature (20 °C) and energy exchange were only 75 % efficient (as is proposed for the Gjálp eruption), the pillows could still have melted >1000 m thickness of ice. Thus there is clearly a problem. Unless extremely hot meltwater drained away, or energy exchange was very inefficient, the eruption of the pillows alone should have been sufficient to melt through to the surface of the glacier, and subaerial lavas ought to overlie the pillows. A possible explanation is that ice deformed horizontally during the eruption of pillows, and increased the total thickness of ice melted by the volcano (section 5.7.2.). Such a scenario is highly probable for basaltic tuyas, since Rossi (1996) suggests that magma discharge rates were as low as 5-10 $m^3 s^{-1}$, and thus the duration of eruptions may have exceeded 10^9 s for the most volumetric tuyas. Even if horizontal deformation rates were as low as the 10^{-6} $m s^{-1}$ measured by Aðalgeirsdottír et al. (2000), horizontal deformation of ice is likely to be significant during such sustained eruptions. Deformation at 10^{-6} $m s^{-1}$ over 10^9 s would allow ice to travel 1 km horizontally during the eruption. Tuyas and ice cauldrons in Iceland seldom exceed 1 km in radius, hence ice at the margins of an ice cauldron may have had time to flow into the central, deepest part of the cauldron, and increased the thickness of the ice roof above the eruption.

5.11. Eruptions in the real world: complex processes during volcano-ice interaction

Due to the currently limited understanding of the physics of subglacial eruptions, it has been necessary to make many assumptions and oversimplifications in order to construct the numerical models presented in this chapter. Therefore, many complex

(and intriguing) facets of volcano-ice interaction have been overlooked. These include the following points, none of which are so far adequately developed in the models:

1. The trajectory and rise rate of magma at shallow crustal levels is influenced by pressure gradients (Pinel & Jaupart 2000). Therefore, the spatial distribution and discharge rate of rising magma during a subglacial eruption may be influenced by the pressure patterns at the glacier base. Magma may preferentially rise into low-pressure subglacial cavities.

2. The vesicularity of magma erupted beneath a glacier may also be influenced by the pressure in subglacial cavities, which may vary rapidly.

3. The real cavity pressures during subglacial eruptions depend upon the water potential gradient at the glacier base. This in turn depends upon the arrangement of subglacial drainage channels, the nature of the bedrock, and is likely to vary with time.

4. The explosivity and rate of heat transfer during magma-water interaction are pressure-dependent, thus the cavity pressure may influence the melting rate during explosive magma-water interaction. The melting rate may in turn influence the cavity pressure, and these two parameters are not easily decoupled.

5. It is very difficult to model the temperature of meltwater generated in subglacial eruptions, since both the rate of heat transfer from magma to meltwater and from

meltwater to ice are poorly constrained. The temperature of meltwater exerts an important influence on the hydrology of the vent area.

6. The brittle-ductile behaviour of glaciers during basal melting is poorly understood, and brittle failure of ice may greatly increase the depth of ice cauldrons formed during subglacial eruptions. Much depends upon the distribution of stress within a glacier that is caused by melting a basal cavity.

7. Nye's law may be inappropriate for (a) irregular subglacial cavities and (b) subglacial cavities with a radius comparable to the ice thickness. However, no better estimate of ice deformation rates is currently available.

8. The division of eruption styles into 'intrusive' and 'explosive' is oversimplified - because there is likely to be intrusion of magma into the base of the edifice at the same time as explosive magma-water occurs higher in the edifice. The energy output from such a 'mixed' eruption style cannot be easily estimated.

5.13. Summary

Although the numerical models presented in this chapter are highly simplified, and assume ductile ice deformation, the results are consistent with many features of the subglacial rhyolite sequences described in Chapters 2-4. Different eruption mechanisms are predicted, depending upon the magma discharge rate and the ice thickness.

At low eruption rates, subglacial cavities may become completely filled with volcanic debris, favouring an intrusive style of eruption, which was inferred at Bláhnúkur and part of Dalakvísl. This is due to the relatively low melting rate, which is assumed to be proportional to the magma discharge rate. If rising lava bodies reach the glacier base, their heat may melt a steep-sided cavity, which acts as a mould for the lava. The sizes of cavity melted depend upon the ice thickness and cavity pressure, and are consistent with an ice thickness of 200-400 m during the eruption at Bláhnúkur.

At higher eruption rates, there is always space in the cavity for an explosive eruption, due to the high rate of melting caused by a high heat flux. Fragmentation of rising magma may be triggered by either magma-water interaction or magma degassing, and is likely to form a thick pile of variably vesicular ash, similar to that observed at South-east Rauðufossafjöll.

The models predict that the style of subglacial eruption (intrusive or explosive) depends primarily upon the magma discharge rate and ice thickness. Thus the magma discharge rates during the eruptions at Bláhnúkur, Dalakvísl and South-east Rauðufossafjöll can be estimated, and the figures produced by the models are consistent with independent estimates of magma discharge rate.

Chapter 6.
Conclusions

A concise summary of the main findings of this thesis is given below. Points 1-8 refer to the mechanisms of volcano-ice interaction, whereas point 9 refers to processes at rhyolitic vents.

1. Rhyolitic eruptions under glaciers can produce a vast range of lithologies, characterised by differing magma-water interaction mechanisms, constraint by ice and instability.

2. The eruption at Bláhnúkur was dominantly intrusive, with quench fragmentation during interaction between rising lava bodies and meltwater, and only minor explosivity. Meltwater drained away from the vent area during the eruption in one or more subglacial drainage channels. Lava bodies rose through a pile of wet breccia, some reached the glacier base, where they were moulded within steep-sided cavities in the ice. The edifice was unstable both during and after the eruption, possibly due to the recession of supporting ice walls caused by melting. The eruption style varied with time, and was linked to the nature of the subglacial cavity system.

3. The eruption at South-east Rauðufossafjöll began with an explosive subglacial phase, with fragmentation triggered by a varying combination of magma-water interaction and degassing of magmatic volatiles. Subaerial lava flows up to 150 m thick were emplaced once the glacier surface was pierced, presumably within ice cauldrons, and some lavas 'dribbled' down the sides of the edifice, in contact with the adjacent ice walls. Peperitic lava flows on the volcano flanks are thought to have formed when advancing lavas were washed by meltwater laden with volcanic debris, before chilling against restraining ice walls. Meltwater drained away from the volcano during the eruption in localised subglacial drainage channels.

4. The style of the eruption at Dalakvísl was transitional between those at Bláhnúkur and South-east Rauðufossafjöll, and was characterised by both intrusive and explosive behaviour. In one locality, an initially explosive eruption within a subglacial cavity appears to have become intrusive when the cavity became filled with debris. Meltwater ponded within a stream valley during the eruption, possibly when subglacial drainage channels became blocked by volcanic debris.

5. There was a different style of eruption at each of the three subglacial rhyolite volcanoes, although the ice thickness may have been comparable during the eruptions (>350 m). Bláhnúkur is considered to have been formed by the subglacial equivalent of an effusive eruption, whereas South-east Rauðufossafjöll was formed during an explosive eruption, with an effusive final phase. Thus the volatile content and magma discharge rate are likely to have been considerably higher at South-east Rauðufossafjöll than at Bláhnúkur, and Dalakvísl was transitional between the other two. The magma discharge rate and volatile content control the eruption mechanism in subaerial eruptive environments. The same is thought to apply to subglacial eruptive environments, but in addition, different magma discharge rates lead to

different melting rates and thus varying conditions at the glacier base. This serves to accentuate the differences between the products of effusive and explosive eruptions, as the style of eruption mediates the eruptive environment itself - providing positive feedback that is lacking from subaerial systems.

6. Numerical models of the evolution of subglacial cavities and edifices during eruptions suggest that two main styles of eruption may occur: intrusive, when the cavity is completely filled by the edifice, and explosive when the cavity is not completely filled. Explosive eruptions are favoured by high magma discharge rates and thin ice. Intrusive eruptions are shown to be favoured by a low magma discharge rate and thick ice, as closure of the cavity by deformation of the ice roof is more important. Horizontal ice deformation can have a large effect on the depths of ice cauldrons that develop and the total vertical thickness of ice melted.

7. There are major differences between the subglacial rhyolite described in this thesis and subglacial basalt volcanoes reported elsewhere. Rhyolitic lava lobes are considerably larger (~7 m) than their basalt equivalents (pillows, ~1 m), and are accompanied by more fragmental material than basaltic pillows. The fragmental lithologies at subglacial rhyolitic volcanoes are predominantly massive and poorly-sorted and show no evidence for deposition within standing water, unlike those at subglacial basaltic volcanoes. Rhyolitic fragmental deposits are poorly-consolidated and poorly-exposed, whereas basaltic fragmental deposits are well-consolidated and well-exposed, due to palagonitisation.

8. The magnitude of jökulhlaups triggered by melting during subglacial rhyolite eruptions was probably lower than those triggered by basaltic eruptions, as there is no evidence for the accumulation of substantial bodies of meltwater during rhyolitic eruptions. The presence of an overlying glacier may little affect the capacity of a rhyolitic volcano to disperse widespread tephra in an explosive subaerial eruption, whereas magma-water interaction during basaltic eruptions is likely to increase the potential for tephra dispersal.

9. Tuffisite veins at an effusive rhyolite vent at South-east Rauðufossafjöll are thought to have been formed by episodic brittle fracture of the vent walls, and propped open by the injection of poorly-consolidated country rock into the fractures formed. Vertical bands in the vent walls are shown to represent earlier tuffisite veins that were sheared in a ductile manner parallel to the flow direction. The process of episodic brittle and ductile deformation of the vent walls may be responsible for creating heterogeneous volatile contents in the rising magma, and thus be a primary mechanism for the generation of flow banding. Tuffisite formation is shown to be a repeatable, non-destructive process, and may be linked to the generation of long-period earthquakes during effusive eruptions of silicic magma.

References

Adams NK, de Silva SL, Self S, et al (2001) The physical volcanology of the 1600 eruption of Huaynaputina, southern Peru. Bull Volcanol 62:493-518.

Águstsdóttir AM, Brantley SL (1994) Volatile fluxes integrated over 4 decades at Grímsvötn volcano, Iceland. J Geophys Res 99: 9505-9522.

Allen CC (1979). Volcano-ice interactions on Mars. J Geophys Res 84:8048-8059.

Allen CC (1980) Icelandic subglacial volcanism: thermal and physical studies. J Geol 88:108-117.

Allen CC, Jercinovic MJ, Allen, JSB (1982) Subglacial volcanism in north-central British Columbia and Iceland. J Geol 90:699-715.

Alsdorf DE, Smith LC (1999) Interferometric SAR observations of ice topography and velocity changes related to the 1996, Gjálp subglacial eruption, Iceland. Int J Remote Sens 20:3031-3050.

Ascolese, E., Aurisicchio, A., Briggssmith, M., Mita, D.G., Perna, G., Rossi, S., Gaeta, F.S., 1993. Thermodynamics of water-permeated unwelded pyroclasts. 1. Equilibrium properties. J Volcanol Geotherm Res 57:219-233.

Aðalgeirsdóttir G, Guðmundsson GH, Björnsson H (2000) The response of a glacier to a surface disturbance: a case study on Vatnajökull ice cap, Iceland. Ann Glaciol 31:104-110.

Bennett MR & Glasser NJ (1996) Glacial geology - ice sheets and landforms. John Wiley, Chichester, 364 pp.

Benson C, Bingham D, Wharton G (1975). Glaciological and volcanological studies at the summit of Mt. Wrangell, Alaska. Snow and ice symposium-Proceedings of the Moscow Symposium, August 1971, IASH-AISH Pub 104:95-98.

Benson CS, Follett AB (1986) Application of photogrammetry to the study of volcano-glacier interactions on Mount Wrangell, Alaska. Photogram Eng Rem Sens 52:813-827.

Benson CS, Motyka RJ (1978) Glacier-volcano interactions on Mt. Wrangell, Alaska. Geophys Inst Univ Alaska Ann Report 1977-1978, 1-25.

Björnsson H (1975) Subglacial water reservoirs, jökulhlaups and volcanic eruptions. Jökull 25:1-14.

Björnsson H (1988) Hydrology of ice caps in volcanic regions. Vis Is Soc Sci 45:1-139.

Björnsson H (1992) Jökulhlaups in Iceland: prediction, characteristics and simulation.

Ann Glaciol 16:95-106.

Björnsson H, Björnsson S, Sigurgeirsson T (1982) Penetration of water into hot rock boundaries of magma at Grímsvötn. Nature 295: 580-581.

Björnsson H, Guðmundsson MT (1993) Variations in the thermal output of the subglacial Grímsvötn caldera, Iceland. Geophys Res Lett 20:2127-2130.

Björnsson H, Pálsson F, Guðmundsson MT (2000). Surface and bedrock topography of the Mýrdalsjökull ice cap, Iceland: the Katla caldera, eruption sites and routes of jökulhlaups. Jökull 49:29-46.

Björnsson H, Rott H, Guðmundsson S, et al. (2001) Glacier-volcano interactions deduced by SAR interferometry. J Glaciol 47:58-70.

Blake S (1981) volcanism and the dynamics of open magma chambers. Nature 289:783-785.

Blake S (1984) Magma mixing and hybridization processes at the alkalic, silicic, Torfajokull central volcano triggered by tholeiitic Veidivotn fissuring, south Iceland. J Volcanol Geotherm Res 22:1-31.

Blankenship DD, Bell RE, Hodge SM, Brozena JM, Behrendt JC, Finn CA (1993) Active volcanism beneath the west Antarctic ice sheet and implications for ice-sheet stability. Nature 361:526-529.

Bourgeois O, Dauteuil O, VanVlietLanoe B (1998) Pleistocene subglacial volcanism in Iceland: tectonic implications. Earth Plan Sci Lett 164:165-178.

Bourgeois O, Dauteuil O, Van Vliet-Lanoe B (2000) Geothermal control on flow patterns in the last glacial maximum ice sheet of Iceland. Earth Surf Proc Landform 25: 59-76.

Branney MJ (1995) Downsag and extension at calderas - new perspectives on collapse geometries from ice-melt, mining, and volcanic subsidence. Bull Volcanol 57:303-318.

Brooker MR, Houghton BF, Wilson CJN, Gamble JA (1993) Pyroclastic phases of a rhyolitic dome-building eruption - Puketarata tuff ring, Taupo volcanic zone, New-Zealand. Bull Volcanol 55:395-406.

Budd WF, Jacka TH (1989) A review of ice rheology for ice-sheet modelling. Cold Reg Sci Technol 16:107-144.

Carslaw HS, Jaeger JC (1959) Conduction of heat in solids, 2nd ed. Oxford University Press, Oxford.

Cas RAF, Allen RL, Bull SW, Clifford BA, Wright JV (1990) Subaqueous, rhyolitic dome-top tuff cones - a model based on the Devonian Bunga beds, southeastern Australia and a modern analog. Bull Volcanol 52:159-174.

Cas RAF, Wright JV (1987) Volcanic successions: modern and ancient. Chapman Hall, London, 528 pp.

Clarke GKC (1982) Glacier outburst floods from Hazard Lake, Yukon Territory, and the problem of flood magnitude prediction. J Glaciol 28:3-21.

Cofaigh CO (1996) Tunnel valley genesis. Prog Phys Geog 20: 1-19.

Cutler PM (1998) Modelling the evolution of subglacial tunnels due to varying water input. J Glaciol 44:485-497.

Davis BK & McPhie J (1996) Spherulites, quench fractures and relict perlite in a Late Devonian rhyolite dyke, Queensland, Australia. J Volcanol Geotherm Res 71:1-11.

DeGraff JM, Long PE, Aydin A (1989) Use of joint-growth directions and rock textures to infer thermal regimes during solidification of basaltic lava flows. J Volcanol Geotherm Res 38:309-324.

Dingwell DB (1997) The brittle-ductile transition in high-level granitic magmas: Material constraints. J Petrol 38:1635-1644.

Dingwell DB, Hess KU, Romano C (1998) Extremely fluid behavior of hydrous peralkaline rhyolites. Earth Planet Sci Lett 158: 31-38.

Dixon HJ, Murphy MD, Sparks SJ, Chavez R, Naranjo SA, Dunkley PN, Young SR, Gilbert JS, Pringle MR (1999) The geology of Nevados de Chillan volcano, Chile. Rev Geol Chile 26:227-253.

Dobran F, Papale P (1993) Magma-water interaction in closed systems and application to lava tunnels and volcanic conduits. J Geophys Res 98:14041-14058.

Dugmore AJ, Larsen G, Newton AJ (1995) 7 tephra isochrones in Scotland. Holocene 5: 257-266.

Edwards BR (1997) Field, kinetic and thermodynamic studies of magmatic assimilation in the Northern Cordilleran Volcanic Province, northwestern British Columbia. PhD thesis, Univ. B. C., Vancouver.

Eichelberger JC, Carrigan CR, Westrich HR et al. (1986) Non-explosive silicic volcanism. Nature 323:598-602.

Einarsson T (1966) Physical aspects of sub-glacial eruptions. Jökull 16:167-174.

Einarsson GT (1975) Jarðfræði Prestahnúks (The Geology of Prestahnúkur) BS thesis, University of Iceland, 45 pp.

Fink JH (1983) Structure and emplacement of a rhyolitic obsidian flow - Little Glass

Mountain, Medicine Lake Highland, Northern California. Geol Soc Am Bull 94:362-380.

Fink JH, Anderson SW, Manley CR (1992) Textural constraints on effusive silicic volcanism - beyond the permeable foam model. J Geophys Res 97: 9073-9083.

Fountain AG, Walder JS (1998) Water flow through temperate glaciers. Rev Geophys 36:299-328.

Fowler AC (1999) Breaking the seal at Grímsvötn, Iceland. J Glaciol 45:506-516.

Francis PW, Gardeweg M, Ramirez CF, et al. (1985) Catastrophic debris avalanche deposit of Socompa volcano, northern Chile. Geology 13: 600-603.

Fridleifsson IB (1970) The Stora-Laxa igneous complex, S. Iceland, BSc thesis, University of St Andrews, 88 pp.

Fridleifsson IB (1973) Petrology and structure of the Esja Quaternary volcanic region, southwest Iceland. D Phil thesis, Oxford University, 208 pp.

Fridleifsson IB, Furnes H, Atkins FB (1982) Subglacial volcanics - on the control of magma chemistry on pillow dimensions. J Volcanol Geotherm Res 13:103-117.

Friedman I, Smith RL, Long WD (1966) Hydration of natural glass and formation of perlite. Geol Soc Am Bull 77:323-328.

Furman T, Frey FA, Meyer PS (1992) Petrogenesis of evolved basalts and rhyolites at Austurhorn, southeastern Iceland - the role of fractional crystallization. J Petrol 33:1405-1445.

Furnes H, Fridleifsson IB, Atkins FB (1980) Subglacial volcanics - on the formation of acid hyaloclastites. J Volcanol Geotherm Res 8:95-110.

Gardeweg MC, Sparks RSJ, Matthews SJ (1998) Evolution of Lascar Volcano, Northern Chile. J Geol Soc Lond 155: 89-104.

Gardner JE, Hilton M, Carroll MR (1999) Experimental constraints on degassing of magma: isothermal bubble growth during continuous decompression from high pressure. Earth Planet Sci Lett 168: 201-218.

Geirsdóttir A, Hardardóttir J, Sveinbjörnsdóttir AE (2000) Glacial extent and catastrophic meltwater events during the deglaciation of Southern Iceland. Quat Sci Rev 19:1749-1761.

Gerlach TM (1986) Exsolution of H_2O, CO_2 and S during eruptive episodes at Kilauea volcano, Hawaii. J Geophys Res 91:12,177-12,185.

Gilbert JS, Stasiuk MV, Lane SJ, Adam CR, Murphy MD, Sparks RSJ, Naranjo JA

(1996) Non-explosive, constructional evolution of the ice-filled caldera at Volcan Sollipulli, Chile. Bull Volcanol 58:67-83.

Glen JW (1955) The creep of polycrystalline ice. Proc Roy Soc Lond A 228:519-538.

Gonzalez-Ferran O (1984) Descriptions of volcanic events - Chile. SEAN Bull 9-11:2.

Gonzalez-Ferran O (1985) Descriptions of volcanic events - Chile. SEAN Bull 10-1:3.

Gordon S, Sharp M, Hubbard B, Smart C, Ketterling B, Willis I (1998) Seasonal reorganization of subglacial drainage inferred from measurements in boreholes. Hydrol Process 12:105-133.

Gottsmann J, Dingwell DB (2001) Cooling dynamics of spatter-fed phonolite obsidian flows on Tenerife, Canary Islands. J Volcanol Geotherm Res 105:323-342.

Grönvold K (1972) Structural and petrological studies in the Kerlingarfjöll region, central Iceland. D Phil thesis, Oxford University, 237 pp.

Guðmundsson A (2000) Dynamics of volcanic systems in Iceland: Example of tectonism and volcanism at juxtaposed hot spot and mid-ocean ridge systems. Ann Rev Earth Planet Sci 28:107-140.

Guðmundsson MT & Björnsson H (1991) Eruptions in Grímsvötn, Vatnajökull, Iceland 1934-1991. Jökull 41:21-45.

Guðmundsson MT, Sigmundsson F, Björnsson H (1997) Ice-volcano interaction of the 1996 Gjálp subglacial eruption, Vatnajökull, Iceland. Nature 389:954-957.

Guðmundsson MT (2001) Subglacial volcanic activity in Iceland. J Quat Sci, in review.

Gunnarsson B, Marsh BD, Taylor HP (1998) Generation of Icelandic rhyolites: silicic lavas from the Torfajokull central volcano. J Volcanol Geotherm Res 83:1-45.

Haar L, Gallagher JS, Kell GS (1984) Steam tables. Hemisphere Publishing Corp.

Hafliðason H, Eiríksson J, VanKreveld S (2000) The tephrochronology of Iceland and the North Atlantic region during the Middle and Late Quaternary: a review. J Quat Sci 15:3-22.

Hanson RE (1991) Quenching and disruption of andesitic to rhyolitic intrusions in a submarine island-arc sequence, northern Sierra Nevada, California. Geol Soc Am Bull 103:804-816.

Hanson, RE & Hargrove, US (1999) Processes of magma/wet sediment interaction in

a large-scale Jurassic andesitic peperite complex, northern Sierra Nevada, California. Bull Volc 60:610-626.

Harbor J, Sharp M, Copland L, et al. (1997) Influence of subglacial drainage conditions on the velocity distribution within a glacier cross section. Geology 25:739-742.

Hards VL, Kempton PD, Thompson RN, Greenwood PB (2000) The magmatic evolution of the Snæfell volcanic centre; an example of volcanism during incipient rifting in Iceland. J Volcanol Geotherm Res 99:97-121.

Heiken G (1972) Morphology and petrography of volcanic ashes. Geol Soc Am Bull 83:1961-1988.

Heiken G, Wohletz K (1985) Volcanic ash. University of California Press, Berkeley, 246 pp.

Heiken G, Wohletz K, Eichelberger J (1988) Fracture fillings and intrusive pyroclasts, Inyo Domes, California. J Geophys Res 93:4335-4350.

Helgason J, Duncan RA (2001) Glacial-interglacial history of the Skaftafell region, southeast Iceland, 0-5 Ma. Geology 29: 179-182.

Hickson CJ (2000) Physical controls and resulting morphological forms of Quaternary ice-contact volcanoes in western Canada. Geomorphology 32:239-261.

Holman JP (1997) Heat Transfer (8^{th} ed.) McGraw-Hill, 696 pp.

Hooke RL (1984) On the role of mechanical energy in maintaining subglacial water conduits at atmospheric pressure. J Glaciol 30:180-187.

Hooke RL, Wold B, Hagen JO (1985) Subglacial hydrology and sediment transport at Bondhusbreen, southwest Norway. Geol Soc Am Bull 388-397.

Hooke RL (1998) Principles of glacier mechanics. Prentice Hall, New Jersey, 248 pp.

Hoskuldsson A, Sparks RSJ (1997) Thermodynamics and fluid dynamics of effusive subglacial eruptions. Bull Volcanol 59:219-230.

Hubbard B, Nienow P (1997) Alpine subglacial hydrology. Quat Sci Rev 16:939-955.

Hunns SR, McPhie J (1999) Pumiceous peperite in a submarine volcanic succession at Mount Chalmers, Queensland, Australia. J Volcanol Geotherm Res 88:239-254.

Huppert HE, Sparks RSJ (1988) Melting the roof of a chamber containing a hot, turbulently convecting fluid. J Fluid Mech 188:107-131.

Hurwitz S, Navon O (1994) Bubble nucleation in rhyolitic melts: experiments at high pressure, temperature and water content. Earth Planet. Sci. Lett. 122:267-280.

Iken A, Röthlisberger H, Flotron A, Haeberli W (1983) The uplift of Unteraargletscher at the beginning of the melt season - a consequence of water storage at the bed? J Glaciol 29:28-47.

Iken A, Bindschadler RA (1986) Combined measurements of subglacial water pressure and surface velocity of Findelengletscher, Switzerland: conclusions about drainage system and sliding mechanism. J Glaciol 32:101-119.

Ihinger PD, Hervig RL & McMillan, PF (1994) Analytical methods for volatiles in glasses. In: Volatiles in Magmas (Carroll MR & Holloway JR, eds.), Rev Mineral 30:67-121.

Ivarsson G (1992) Geology and petrochemistry of the Torfajökull central volcano in central south Iceland, in association with the Icelandic hot spot and rift zones. Unpublished PhD thesis, University of Hawaii.

Jakobsson SP (1978) Environmental factors controlling the palagonitisation of the Surtsey tephra, Iceland. Bull Geol Soc Denmark 27:91-105.

Jakobsson SP (1979) Outline of the petrology of Iceland. Jökull 29:57-73.

Jaupart C (1998) Gas loss from magmas through conduit walls during eruption. In: Gilbert JS, Sparks RSJ (eds) The physics of explosive volcanic eruptions. Geol Soc London Spec Publ 145, 73-90.

Jóhannesson H & Sæmundsson K (1998) Geological map of Iceland. 1:500 000. Bedrock Geology. Nátturúfræðistofnun Íslands, Reykjavík.

Jónasson K, Holm PM, Pedersen AK (1992) Petrogenesis of silicic rocks from the Króksfjörður central volcano, NW Iceland. J Petrol 33:1345-1369.

Jónasson K (1994) Rhyolite volcanism in the Krafla central volcano, northeast Iceland. Bull Volcanol 56:516-528.

Jones JG (1966) Intraglacial volcanoes of south-west Iceland and their significance in the interpretation of the form of the marine basaltic volcanoes. Nature 212:586-588.

Jones JG (1968) Intraglacial volcanoes of the Laugarvatn region, south-west Iceland, I. J Geol Soc London 124:197-211.

Jones JG (1970) Intraglacial volcanoes of the Laugarvatn region, southwest Iceland, II. J Geol 78:127-140.

Jones SJ (1982) Confined compressive strength of polycrystalline ice. J Glaciol 28:171-177.

Jónsson S, Adam N, Björnsson H (1998) Effects of subglacial geothermal activity observed by satellite radar interferometry. Geophys Res Lett 25:1059-1062.

Jull M, McKenzie D (1996) The effect of deglaciation on mantle melting beneath Iceland. J Geophys Res 101:21815-21828.

Kavanaugh JL, Clarke GKC (2000) Evidence for extreme pressure pulses in the subglacial water system. J Glaciol 46: 206-212.

Kiver EP, Mumma MD (1971) Summit firn caves, Mount Rainier, Washington. Science 173, 320-322.

Kiver EP, Steele WK (1975) Firn caves in the volcanic craters of Mount Rainier, Washington. Nat Spel Soc Bull 37:45-55.

Kokelaar BP (1982) Fluidization of wet sediments during the emplacement and cooling of various igneous bodies. J Geol Soc 139:21-33.

Kokelaar P (1986) Magma-water interactions in subaqueous and emergent basaltic volcanism. Bull Volcanol 48:275-289.

Kjartansson G (1964) Isaldarlok og eldfjoell a Kill--The retreat of the last glacial ice-sheet and some volcanoes in the Kjoelur area, central Iceland. Náttúrufræðingurinn arg, 1:9-38.

Kristmannsdottír H, Björnsson A, Palsson S, Sveinbjornsdottír AE (1999) The impact of the 1996 subglacial volcanic eruption in Vatnajökull on the river Jökulsá a Fjöllum, North Iceland. J Volcanol Geotherm Res 92:359-372.

Kumpulainen RA (1994) Fissure-fill and tunnel-fill sediments - expressions of permafrost and increased hydrostatic-pressure. J Quat Sci 9:59-72.

Lacasse C, Garbe-Schonberg CD (2001) Explosive silicic volcanism in Iceland and the Jan Mayen area during the last 6 Ma: sources and timing of major eruptions. J Volcanol Geotherm Res 107:113-147.

Lacasse C, Carey S, Sigurdsson H (1998) Volcanogenic sedimentation in the Iceland Basin: influence of subaerial and subglacial eruptions. J Volcanol Geotherm Res 83:47-73.

Lacasse C, Sigurdsson H, Carey S, Paterne M, Guichard F (1996) North Atlantic deep-sea sedimentation of Late Quaternary tephra from the Iceland hotspot. Marine Geol 129:207-235.

Langley K (2000) A morphological investigation of volcanic activity beneath Vatnajökull, Iceland, interpreted from radio echo sounding data. Unpublished MS thesis, Univ Iceland, 129 pp.

Larsen G, Gudmundsson MT, Björnsson H (1998) Eight centuries of periodic volcanism at the center of the Iceland hotspot revealed by glacier tephrostratigraphy. Geology 26:943-946.

LeMasurier WE, Harwood DM, Rex DC (1994) Geology of Mount Murphy volcano - an 8-My history of interaction between a rift volcano and the west Antarctic ice-sheet. Geol Soc Am Bull 106:265-280.

Lescinsky DT, Sisson TW (1998) Ridge-forming, ice-bounded lava flows at Mount Rainier, Washington. Geology 26:351-354.

Lescinsky DT, Fink JH (2000) Lava and ice interaction at stratovolcanoes: use of characteristic features to determine past glacial extents and future volcanic hazards. J. Geophys. Res. 105, 23711-23726.

Lliboutry L (1968) General theory of subglacial cavitation and sliding of temperate glaciers. J Glaciol 7:21-58.

Lorenz V (1974) Vesiculated tuff and associated features. Sedimentology 21:273-291.

Macdonald R, McGarvie DW, Pinkerton H, Smith RL, Palacz ZA (1990) Petrogenetic evolution of the Torfajökull volcanic complex, Iceland. 1. Relationship between the magma types. J Petrol 31:429-459.

McGarvie DW (1984) Torfajökull - a volcano dominated by magma mixing. Geology 12:685-688.

McGarvie DW (1985) Volcanology and petrology of mixed magmas and rhyolites from the Torfajökull volcano, Iceland. Unpublished PhD thesis, University of Lancaster, UK.

McGarvie DW, Macdonald R, Pinkerton H, Smith RL (1990) Petrogenetic evolution of the Torfajökull volcanic complex, Iceland. 2. The role of magma mixing. J Petrol 31:461-481.

Maclennan J, McKenzie D, Gronvold K, et al. (2001) Crustal accretion under northern Iceland. Earth Planet Sci Lett 191:295-310.

McPhie J, Doyle M, Allen R (1993) Volcanic textures. A guide to the interpretation of textures in volcanic rocks. Tasmanian Government Printing Office, Tasmania, pp 1-196.

Major JJ, Newhall CG (1989) Snow and ice perturbation during historical volcanic eruptions and the formation of lahars and floods. Bull Volcanol 52:1-27.

Malthe-Sorenssen A, Walmann T, Jamtveit B, et al. (1998) Modelling and characterization of fracture patterns in the Vatnajökull glacier. Geology 26:931-934.

Manga M (1998) Orientation distribution of microlites in obsidian. J Volcanol Geotherm Res 86:107-115.

Manley CR (1992) Extended cooling and viscous flow of large, hot rhyolite lavas:

implications of numerical modelling results. J Volcanol Geotherm Res 53:27-46.

Manville V, White JDL, Houghton BF, et al. (1998) The saturation behaviour of pumice and some sedimentological implications. Sediment Geol 119: 5-16.

Maria A, Carey S, Sigurdsson H, et al. (2000) Source and dispersal of jökulhlaup sediments discharged to the sea following the 1996 Vatnajökull eruption. Geol Soc Am Bull 112:1507-1521.

Marti J, Soriano C, Dingwell DB (1999) Tube pumices as strain markers of the ductile-brittle transition during magma fragmentation. Nature 402:650-653.

Mathews WH (1947) "Tuyas", flat-topped volcanoes in northern British Columbia. Am J Sci 245:560-570.

Mathews WH (1951) The Table, a flat-topped volcano in southern British Columbia. Am Jour Sci 249:830-841.

Mellors RA, Sparks RSJ (1991) Spatter-rich pyroclastic flow deposits on Santorini, Greece. Bull Volcanol 53:327-342.

Miller TP (1994) Dome growth and destruction during the 1989-1990 eruption of Redoubt volcano. J Volcanol Geotherm Res 62:197-212.

Mizuno, Y (1998) Effect of hydrostatic confining pressure on the failure mode and compressive strength of polycrystalline ice. J Phys Chem B 102:376-381.

Moore JG, Phillips RL, Grigg RW, Peterson DW, Swanson DA (1973) Flow of lava into the sea, 1969-1971, Kilauea volcano, Hawaii. Geol Soc Am Bull 84:537-546.

Moore JG (1976) Mechanism of formation of pillow lava. Am Sci 63:269-277.

Moore JG, Calk LC (1991) Degassing and differentiation in subglacial volcanoes, Iceland. J Volcanol Geotherm Res 46:157-180.

Moore JG, Hickson CJ, Calk LC (1995) Tholeiitic-alkalic transition at subglacial volcanoes, Tuya region, British Columbia, Canada. J Geophys Res 100:24577-24592.

Morel JM, Gourgaud A, Vincent PM (1992) A climactic hydromagmatic eruption in the Aiguiller massif (Mont-Dore stratovolcano, French Massif Central) Bull Soc Geol France 163: 625-634.

Moreno H, Fuentealba G (1994) The May 17-19 1994 Llaima volcano eruption, southern Andes (38° 42' S - 71° 44' W). Rev Geol Chile 21:167-171.

Mueller W, White JDL (1992) Felsic fire-fountaining beneath Archean seas -

pyroclastic deposits of the 2730-Ma Hunter-Mine-Group, Quebec, Canada. J Volcanol Geotherm Res 54: 117-134.

Mungall JE, Bagdassarov NS, Romano C, Dingwell DB (1996) Numerical modelling of stress generation and microfracturing of vesicle walls in glassy rocks. J Volcanol Geotherm Res 73:33-46.

Newman S, Stolper EM, Epstein S (1986) Measurement of water in rhyolitic glasses - calibration of an infrared spectroscopic technique. Am Mineral 71:1527-1541.

Nienow P, Sharp M, Willis I (1996a) Temporal switching between englacial and subglacial drainage pathways: Dye tracer evidence from the Haut Glacier d'Arolla, Switzerland. Geogr Ann. Ser A-Phys Geogr 78:51-60.

Nienow PW, Sharp M, Willis IC (1996b) Velocity-discharge relationships derived from dye tracer experiments in glacial meltwaters: Implications for subglacial flow conditions. Hydrol Process 10:1411-1426.

Noe-Nygaard A (1940) Sub-glacial volcanic activity in ancient and recent times (studies in the palagonite system of Iceland, no. 1). Folia Geog Dan 1:1-67.

Nye JF (1953). The flow law of ice from measurements in glacier tunnels, laboratory experiments and the Jungfraufirn borehole experiment. Proc R Soc Lond Series A 219:477-489.

Nye JF (1976) Water flow in glaciers: jökulhlaups, tunnels and veins. J Glaciol 17:181-207.

Paterson WSB (1994) The physics of glaciers (3rd ed.) Pergamon Press, Oxford, 480 pp.

Pierson TC, Janda RJ, Thouret JC, Borrero CA (1990) Perturbation and melting of snow and ice by the 13 November 1985 eruption of Nevado-del-Ruiz, Colombia, and consequent mobilization, flow and deposition of lahars. J Volcanol Geotherm Res 41:17-66.

Pierson TC, Janda RJ (1994) Volcanic mixed avalanches - a distinct eruption-triggered mass-flow process at snow-clad volcanoes. Geol Soc Am Bull 106:1351-1358.

Pinel V, Jaupart C (2000) The effect of edifice load on magma ascent beneath a volcano. Phil Trans Roy Soc A 358:1515-1532.

Pjetursson H (1900) The glacial palagonite-formation of Iceland. Scottish Geol Mag 16:265-293.

Prud'homme RK & Khan SA (1993) Experimental results on foam rheology. In: Foams: theory, measurements and applications, Prud'homme RK & Khan SA (eds.), Marcel Dekker, pp. 217-241.

Pyle DM (1999) Sizes of volcanic eruptions. In: Sigurdsson H. (Ed.) Encyclopaedia of volcanoes. Academic Press, pp 263-269.

Rijsdijk KF, Owen G, Warren WP, et al. (1999) Clastic dykes in over-consolidated tills: evidence for subglacial hydrofracturing at Killiney Bay, eastern Ireland. Sed Geol 129: 111-126.

Roberts MJ, Russell AJ, Tweed FS, Knudsen O (2000) Rapid sediment entrainment and englacial deposition during jökulhlaups. J Glaciol 46:349-351.

Roberts MJ, Russell AJ, Tweed FS, et al. (2001) Ice fracturing during jökulhlaups: Implications for englacial floodwater routing and outlet development. Earth Surf Proc Land 25:1429-1446.

Rodolfo KS (1999) The hazard from lahars and jökulhlaups. In: Sigurdsson H. (Ed.) Encyclopaedia of volcanoes. Academic Press, pp 973-995.

Rosi M, Vezzoli L, Aleotti P, et al. (1996) Interaction between caldera collapse and eruptive dynamics during the Campanian Ignimbrite eruption, Phlegraean Fields, Italy. Bull Volcanol 57:541-554.

Rossi MJ (1996) Morphology and mechanism of eruption of postglacial shield volcanoes in Iceland. Bull Volcanol 57:530-540.

Russell AJ, Knudsen O, Fay H, et al. (2001) Morphology and sedimentology of a giant supraglacial, ice-walled, jökulhlaup channel, Skeiðarárjökull, Iceland: implications for esker genesis. Global Planet Change 28:193-216.

Saemundsson K (1970) Interglacial lava flows in the lowlands of southern Iceland and the problem of two-tiered columnar jointing. Jökull 20:63-77.

Sæmundsson K (1972) Jarðfræðiglefsur um Torfajökulssvæðið. Natturufræðingurinn 42:81-99 (in Icelandic).

Sæmundsson K, Noll H (1974) K/Ar ages of rocks from Husafell, western Iceland, and the development of the Husafell central volcano. Jökull 24:40-58.

Sæmundsson K (1988) Jarðfræðiþattur um Torfajökulsöræfi. Arbok Ferðafelag Islands 164-180 (in Icelandic).

Sahagian DL, Proussevitch AA (1996) Thermal effects of magma degassing. J Volcanol Geotherm Res 74:19-38.

Sakai H, Casadevall TJ, Moore JG (1982) Chemistry and isotope ratios of sulfur in basalts and volcanic gases at Kilauea Volcano, Hawaii. Geochim Cosmochim Acta 46:729-738.

Salamatin AN, Murav'yev YD, Shiraiwa T, et al. (2000) Modelling dynamics of glaciers in volcanic craters. J Glaciol 46:177-187.

Schneider T (1999) Water movement in the firn of Storglaciaren, Sweden. J Glaciol 45: 286-294.

Scutter CR, Cas RAF, Moore CL, Derita D (1998) Facies architecture and origin of a submarine rhyolitic lava flow-dome complex, Ponza, Italy. J Geophys Res 103:27551-27566.

Seaman SJ, Scherer EE, Standish JJ (1995) Multistage magma mingling and the origin of flow banding in the Aliso lava dome, Tumacacori Mountains, southern Arizona. J Geophys Res 100:8381-8398.

Sharp M, Richards K, Willis I, Arnold N, Nienow P, Lawson W, Tison JL (1993) Geometry, bed topography and drainage system structure of the Haut Glacier D'Arolla, Switzerland. Earth Surf Proc Landform 18:557-571.

Sheridan MF (1970) Fumarolic mounds and ridges of the Bishop Tuff, California. Geol Soc Am Bull 81:851-868.

Shreve RL (1972) Movement of water in glaciers. J Glaciol 11:205-214.

Sigvaldason GE, Annertz D, Nilsson M (1992) Effect of glacier loading/deloading on volcanism: postglacial volcanic production rate of the Dyngjufjöll area, central Iceland. Bull Volcanol 54:385-392.

Skilling IP (1994) Evolution of an englacial volcano: Brown Bluff, Antarctica. Bull Volcanol 56:573-591.

Slater L, Jull M, McKenzie D, Gronvold K (1998) Deglaciation effects on mantle melting under Iceland: results from the northern volcanic zone. Earth Planet Sci Lett 164:151-164

Smellie JL, Hole MJ (1997) Products and processes in Pliocene-Recent, subaqueous to emergent volcanism in the Antarctic Peninsula: examples of englacial Surtseyan volcano construction. Bull Volcanol 58:628-646

Smellie JL, Hole MJ, Nell PAR (1993) Late Miocene valley-confined subglacial volcanism in northern Alexander Island, Antarctic Peninsula. Bull Volcanol 55:273-288.

Smellie JL, Skilling IP (1994) Products of subglacial volcanic eruptions under different ice thicknesses - 2 examples from Antarctica. Sed Geol 91:115-129.

Smellie JL (1999) Subglacial eruptions. In: Sigurdsson H. (Ed.) Encyclopaedia of volcanoes. Academic Press, pp 403-418.

Smellie JL (2001) Lithofacies architecture and construction of volcanoes erupted in englacial lakes: Icefall Nunatak, Mount Murphy, eastern Marie Byrd Land, Antarctica. In: 'Lacustrine Volcaniclastic Sedimentation' (White JDL, Riggs N, Eds.) Spec Publs int Ass Sediment 30:9-34.

Smellie JL (in press) The 1969 subglacial eruption on Deception Island (Antarctica): events and processes during an eruption beneath a thin glacier and implications for volcanic hazards. In: Smellie JL & Chapman MG (eds) Volcano-ice interaction on Earth and Mars. Geol Soc Lond Special Publication.

Smith JV (1996) Ductile-brittle transition structures in the basal shear zone of a rhyolite lava flow, eastern Australia. J Volcanol Geotherm Res 72:217-223.

Smith LC, Alsdorf DE, Magilligan FJ, et al. (2000) Estimation of erosion, deposition, and net volumetric change caused by the 1996 Skeiðarársandur jökulhlaup, Iceland, from synthetic aperture radar interferometry. Water Resour Res 36:1583-1594.

Sparks RSJ (1997) Causes and consequences of pressurisation in lava dome eruptions. Earth Planet Sci Lett 150:177-189.

Stasiuk MV, Barclay J, Carroll MR, Jaupart C, Ratte JC, Sparks RSJ, Tait SR (1996) Degassing during magma ascent in the Mule Creek vent (USA). Bull Volcanol 58:117-130.

Steinthorsson S, Harðarson BS, Ellam RM, et al. (2000) Petrochemistry of the Gjálp-1996 subglacial eruption, Vatnajökull, SE Iceland. J Volcanol Geotherm Res 98:79-90.

Stevenson RJ, Dingwell DB, Webb SL, Bagdassarov NS (1995) The equivalence of enthalpy and shear stress relaxation in rhyolitic obsidians and quantification of the liquid-glass transition in volcanic processes. J. Volcanol. Geotherm. Res. 68, 297-306.

Stevenson RJ, Wilson L (1997) Physical volcanology and eruption dynamics of peralkaline agglutinates from Pantelleria. J Volcanol Geotherm Res 79:97-122.

Sturm M (1995) Short-period velocity fluctuations of 2 glaciers on Mt Wrangell, Alaska. Phys Geog 16: 42-58.

Syverson KM, Gaffield SJ, Mickelson DM (1994) Comparison of esker morphology and sedimentology with former ice-surface topography, Burroughs Glacier, Alaska. Geol Soc Am Bull 106:1130-1142.

Thorarinsson S (1967) Surtsey: the new island in the North Atlantic. Viking, New York.

Till AB, Yount ME, Bevier ML (1994) The geologic history of Redoubt volcano, Alaska. J Volcanol Geotherm Res 62:11-30.

Tómasson H (1996) The jökulhlaup from Katla in 1918. Ann Glaciol 22:249-254.

Trabant DC, Waitt RB, Major JJ (1994) Disruption of Drift Glacier and origin of

floods during the 1989-1990 eruptions of Redoubt volcano, Alaska. J Volcanol Geotherm Res 62:369-385.

Tuffen H, Gilbert JS, McGarvie DW (2001) Products of an effusive subglacial rhyolite eruption: Bláhnúkur, Torfajökull, Iceland. Bulletin of Volcanology 63:179-190.

Tuffen H, McGarvie DW, Gilbert JS, Pinkerton H (in press) Physical volcanology of a subglacial-to-emergent rhyolitic tuya at Rauðufossafjöll, Torfajökull, Iceland. In: Smellie JL & Chapman MG (eds) Volcano-ice interaction on Earth and Mars. Geol Soc Lond Special Publication.

Valentine GA, Perry FV, WoldeGabriel G (2000) Field characteristics of deposits from spatter-rich pyroclastic density currents at Summer Coon volcano, Colorado. J Volcanol Geotherm Res 104: 187-199.

Vernon RH (1987) A microstructural indicator of shear sense in volcanic rocks and its relationship to porphyroblast rotation in metamorphic rocks. J Geol 95:127-133.

Vinogradov VN, Murav'yev YD (1988) Lava-ice interaction during the 1983 Klyuchevskoi eruption. Volcanology and Seismology 7:39-61.

Waitt RB, Gardner CA, Pierson TC, et al. (1994) Unusual ice diamicts emplaced during the December 15, 1989 eruption of Redoubt volcano, Alaska. J Volcanol Geotherm Res 62:409-428.

Walder JS, Driedger CL (1995) Frequent outburst floods from South Tahoma Glacier, Mount-Rainier, USA - relation to debris flows, meteorological origin and implications for subglacial hydrology. J Glaciol 41: 1-10.

Walder JS (2000a) Pyroclast/snow interactions and thermally driven slurry formation. Part 1: Theory for monodisperse grain beds. Bull Volcanol 62:105-118.

Walder JS (2000b) Pyroclast/snow interactions and thermally driven slurry formation. Part 2: Experiments and theoretical extension to polydisperse tephra. Bull Volcanol 62:119-129.

Waller RI, Russell AJ, van Dijk TAGP, Knudsen O (2001) Jökulhlaup-related ice fracture and supraglacial water release during the November 1996 Jökulhlaup, Skeiðarárjökull, Iceland. Geogr Ann Ser A-Phys Geogr 83:29-38.

Warburton J, Fenn CR (1994) Unusual flood events from an alpine glacier - observations and deductions on generating mechanisms. J Glaciol 40:176-186.

Werner R, Schmincke HU, Sigvaldason G (1996) A new model for the evolution of table mountains: Volcanological and petrological evidence from Herdubreid and Herdubreidartogl volcanoes
(Iceland). Geol Rundshau 85:390-397.

White JDL, Busby-Spera CJ (1987) Deep marine arc apron deposits and syndepositional magmatism in the Alisitos group at Punta Cono, Baja California, Mexico. Sedimentology 34:911-927.

White JDL, Houghton BF (1999) Surtseyan and related phreatomagmatic eruptions. In: Sigurdsson H. (Ed.) Encyclopaedia of volcanoes. Academic Press, pp 495-511.

Whitten DGA, Brooks JRV (1972) Dictionary of Geology. Penguin, London.

Wohletz KH (1983) Mechanisms of hydrovolcanic pyroclast formation - grain-size, scanning electron-microscopy, and experimental studies. J Volcanol Geotherm Res 17:31-63.

Wohletz KH (1986) Explosive magma-water interactions: thermodynamics, explosion mechanisms and field studies. Bull Volcanol 48:245-264.

Wylie JJ, Helfrich KR, Dade B, et al. (1999) Flow localization in fissure eruptions. Bull Volcanol 60:432-440.

Yamagishi H, Dimroth E (1985) A comparison of Miocene and Archean rhyolite hyaloclastites - evidence for a hot and fluid rhyolite lava. J Volcanol Geotherm Res 23:337-355.

Yount ME, Miller TP, Emanuel RP, Wilson FH (1985) Eruption in an ice-filled caldera, Mount Veniaminof, Alaska peninsula. In: Bartsch-Winkler S, Reed KM (eds) The USGS in Alaska: accomplishments during 1983. US Geol Surv Circ 945:59-60.

Yount ME, Miller TP, Gamble BM (1987) The 1986 eruptions of Augustine volcano, Alaska: hazards and effects. In Hamilton TD, Galloway JP (eds) Geologic studies in Alaska by the USGS during 1986. US Geol Surv Circ 998:4-13.

Zhang YX (1999) H_2O in rhyolitic glasses and melts: Measurement, speciation, solubility, and diffusion. Rev Geophys 37:493-516.

Zielinski GA, Mayewski PA, Meeker LD, Whitlow S, Twickler MS (1996) A 110,000-yr record of explosive volcanism from the GISP2 (Greenland) ice core. Quat Res 45:109-118.

Zielinski GA, Mayewski PA, Meeker LD, Gronvold K, Germani MS, Whitlow S, Twickler MS, Taylor K (1997) Volcanic aerosol records and tephrochronology of the Summit, Greenland, ice cores. J Geophys Res 102:26625-26640.

Zimbelman DR, Rye RO, Landis GP (2000) Fumaroles in ice caves on the summit of Mount Rainier - preliminary stable isotope, gas, and geochemical studies. J Volcanol Geotherm Res 97:457-
473.

Zobin VM (1999) The fault nature of the M-s 5.4 volcanic earthquake preceding the

1996 subglacial eruption of Grimsvotn volcano, Iceland. J Volcanol Geotherm Res 92:349-358.

Appendix A1.
Commonly-used terms in volcano-ice interaction

autobreccia	**Monomict** breccia formed by spontaneous brittle failure of a lava carapace
central volcano	A long-lived volcanic complex in Iceland, commonly forming a near-circular field of silicic rocks
clastic	(Of a fragmental rock) formed by the transport and deposition of rock fragments. Includes **epiclastic** and **volcaniclastic** rocks
cold-based glacier	A glacier with a frozen bed, currently confined to high-latitude regions (c.f. **temperate glacier**)
columnar joint	Polygonal body in lava bounded by planar fractures formed during cooling contraction
country rock	The older, non-**primary** material that surrounds rising magma
debris flow deposit	General term for a poorly-sorted clastic rock deposited by a dense, often fluidised flow of debris (also termed mass flow deposit)
decrepitation	Spontaneous fragmentation in a vesicular magma triggered by brittle failure of vesicle walls (literally: crackling)
devitrification	Development of crystalline texture within metastable volcanic glass, below the **glass transition**
diamicton	Non-genetic term for poorly-sorted clastic aggregates (including **till** and **debris flow deposits**)
emergent	Of an eruption, making the transition from a **subglacial** to a **subaerial** environment
englacial	Entirely surrounded by ice (frequently misused)
epiclastic	Of **volcaniclastic** deposits: redeposited by weathering, erosion, wind, ice or water (i.e. not **primary**)
firn	Intermediate between snow and ice - typically comprises the upper 40-60 m of **temperate glaciers**

glass transition	The temperature range over which magma changes from liquid-like to solid-like behaviour
hyaloclastite breccia	A **hydroclastic** volcanic rock composed of glassy angular fragments formed by **magma-water interaction**.
hydroclastic	A fragmental volcanic rock formed during **magma-water interaction**
ice cauldron	Depression in the glacier surface above a region of melting (also known as subsidence bowl)
ice-contact	(Of volcanic deposits) formed beneath or adjacent to ice
ice-dammed lake	A standing body of meltwater confined by ice but open to the air
ice divide	The glacial equivalent of a watershed
ice sheet	A large body of ice, typically >20 km across and >400 m thick (c.f. valley glacier)
jökulhlaup	A catastrophic glacial meltwater flood, often triggered by melting due to volcanic heat (Icelandic: *glacier leap*)
juvenile	Eruption-derived material within a **volcaniclastic** sequence (c.f. **lithic**)
lava lobe	Pillow-like bodies of lava, usually silicic, which often exhibit evidence for **magma-water interaction**, such as **peperitic** margins
lithic	Material within a **volcaniclastic** sequence not generated by the eruption (e.g. fragments of country rock)
lithofacies	A rock type formed in a given environment
magma-water interaction	Physical contact between hot magma and liquid water, which may provoke explosive **phreatomagmatic** fragmentation or less violent **quench fragmentation**
microcrystalline	Applied to lava: with a groundmass entirely or dominantly composed of **microlites**
microlite	A crystal <0.1 mm long typically formed during the late stage of magma ascent and cooling
monomict	(Of any **clastic** rock) containing only one clast type

móberg	A general name for **subglacial** basaltic deposits (Icelandic: *brown rock*)
palaeo-ice thickness	The thickness of ice beneath which an ancient **subglacial** eruption occurred
palagonite	Loosely applied to basaltic **hyaloclastite** that is cemented by palagonitic mineralisation
passage zone	Contact between steeply-dipping **hyaloclastite** breccia and subhorizontal **subaerial** lavas, thought to indicate water level in an **ice-dammed lake** during an eruption
peperitic	Of or pertaining to a volcanic deposit formed by the intrusion of magma within wet sediment, characterised by **quench fragmentation** of magma and **fluidisation** of sediment
perlite	A texture formed by hydration of obsidian, in which spherical, dark obsidian beads are surrounded by pale, altered glass
polymict	(Of a **volcaniclastic** rock) containing more than one clast type
phreatomagmatic	Formed by or pertaining to explosive **magma-water interaction** (c.f. **quench fragmentation**)
pillow lava	lava, usually basaltic, occurring in pillow-shaped masses and formed in a **subaqueous** environment
primary	Of a **volcaniclastic** deposit: emplaced during an eruption and not subsequently affected by **epiclastic** reworking
quench fragmentation	Disaggregation of magma by cooling contraction during non-explosive **magma-water interaction** (c.f. **phreatomagmatic**)
stapi	Non-genetic Icelandic term for a **table mountain**
subaerial	Formed within air: of volcanic deposits or eruptions, formed once the ice surface has been pierced
subaqueous	An environment that is beneath water. In a subglacial setting, typically a **subglacial** or **ice-dammed lake**
subglacial	Occurring at the base of a glacier (c.f. **englacial, ice-dammed, subaerial, subaqueous**)

subglacial cavity	A cavity at the base of a glacier with an ice roof and bedrock floor
subglacial mound	A conical volcanic edifice formed by an entirely **subglacial** eruption
table mountain	Non-genetic geomorphological term for any steep-sided, flat-topped mountain, including **tuyas**
temperate glacier	A glacier with a non-frozen bed, found in Iceland and other mid-to-low latitude regions today.
till	A genetic term for a poorly-sorted, commonly **polymict** breccia or conglomerate with a muddy matrix formed at the base of a glacier
tindar	steep-sided, linear ridge of **hydroclastic** rocks formed during a **subglacial** fissure-type eruption
tuya	flat-topped landforms formed by flat-lying **subaerial** lavas overlying fragmental **subglacial** deposits
valley glacier	An elongate, tongue-like glacier confined by steep valley sides, some are offshoots from **ice sheets**
volcaniclastic	A general term for fragmental deposits generated by a volcano: including **primary** and **epiclastic** deposits

Definitions from Cas & Wright (1987), Penguin Dictionary of Geology (Whitten & Brooks 1972), Smellie 1999, Hickson 2000.

Appendix A2.
Glossary of selected Icelandic geographical terms

askja.....caldera
blá.....blue
Bláhnúkur.....Blue Peak
dal-..... valley (dale: Cumbrian)
Dalakvísl..... stream valley (Dale Beck: Cumbrian)
fell..... hill, mountain (fell: Cumbrian)
foss..... waterfall (force: Cumbrian)
fjöllum.....of the mountains
gjálp.....mythical giant
gil.....ravine (gill/ghyll: Cumbrian)
græn.....green
Grænagil.....Green ravine (Green Gill: Cumbrian)

hnúkur..... peak
hraun..... lava
jarðfræðikort..... geological map
jökull..... glacier
jökulhlaup..... glacier outburst flood(s)
jökulsá..... glacier river
Jökulsá a fjöllum..... Glacier river of the mountains
kirkja.....church(es)
Kirkjufell.....Church Mountain (Kirk Fell: Cumbrian)
kvísl.....stream (Cumbrian: beck)
Landmannalaugar.....
laug.....warm spring
móberg.....palagonite
rauður.....red
Rauðufoss..... Red Waterwall (Cumbrian: Red Force)
Rauðufossakvísl.....Stream of the red waterfall (Cumbrian: Redforce Beck)
Rauðufossafjöll.....Mountains of the red waterfall (Cumbrian: Redforce Fells)
sandur.....glacial outwash plain

Appendix B1 Blahnukur sample inventory

Each sample locality is indicated in Figure B1

Sample	Location	Description
B18	600 m S of bridge	obs, lava lobe margin
B25a	750 m S of bridge	green perl obs-ash (breccia D)
B25b	750 m S of bridge	green perl obs-ash (breccia D)
B34	20 m S of summit	pale grey rhy, 8mm pyx
B45a	400 m NW of summit	interior vesicular portion of 5m lava lobe
B45b	400 m NW of summit	sheared obs margin of 5m lava lobe
B51	250 m NW of summit	cinder toffee texture black pumice
B65	50m S of bridge	green pum-ash breccia B
B67	100 m SSW of bridge	5cm granitoid inclusion in breccia B
B72	125 m SSW of bridge	75cm basaltic inclusion in breccia B
B72b	125 m SSW of bridge	cemented green pum-ash breccia B
B75	150 m SW of bridge	pum from breccia B
B77	175 m SW of bridge	matrix supported pum ash breccia, Grænagil
B120a	400 m W of summit	pum ash breccia A at margin of 10m lobe (zone A)
B120b	400 m W of summit	perlitic obs, lobe margin (zone B)
B120c	400 m W of summit	black obs, lobe margin (zone C)
B120d	400 m W of summit	banded obs-rhy (zone D)
B120e	400 m W of summit	white rhy, lobe interior (zone E)
B120f	400 m W of summit	grey rhyolite, lobe interior (zone F)
B121	400 m W of summit	fibrous perl obs, lobe margin (zone B)
B126	400 m W of summit	pale grey rhy with 8mm
B133	790m elevation on NW flank	banded obs-rhy (zone D) of 7m lobe,
B134	790m elevation on NW flank	obs clasts in rhy, (zone D) of 5 m lobe
B154a	830 m elevation on W flank	obs-ash breccia A
B154b	830 m elevation on W flank	net-veined green obsidian clast, lava lobe margin
B167	200 m S of bridge	obs with basaltic inc, breccia A
B172	500 m S of bridge	white-grey rhy (zone E), lava lobe
B182	250 m E of summit	sph obs, breccia B
B183	210 m E of summit	grey rhy, breccia B
B194a	250 m S of summit	ms altered ves obs breccia, base of cj lava
B194b	250 m S of summit	cs altered ves obs breccia, base of cj lava
B195a	250 m S of summit	varying perl obs, base of cj lava
B195b	250 m S of summit	intact ves obs, base of cj lava

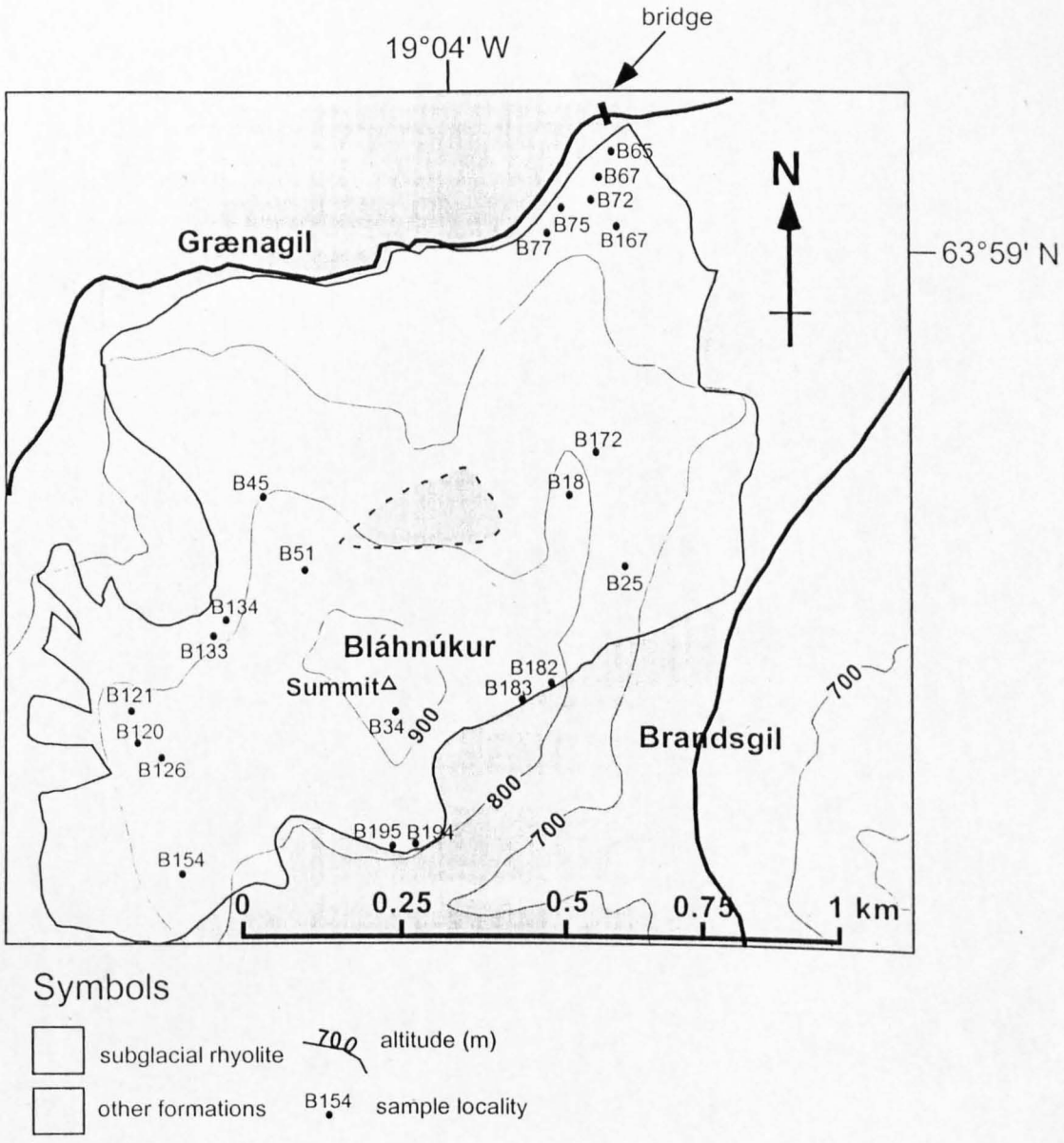

Figure B1. Map of Bláhnúkur, indicating the localities from which samples were collected.

Appendix B2 South-east Raudufossafjoll sample inventory

Each sample locality is indicated in Figure B2

Sample	Location	Description
D00-13	North of Blautakvisl gully	Ash with pale grey ves obs
D00-14	North of Blautakvisl gully	Palagonitised basaltic breccia
D00-15	North of Blautakvisl gully	Cemented obs/pum/ash breccia
D00-16	East Plateau, SE limit	Green ash
D00-17	S-e R south flank	Pale grey ash
D00-18	S-e R south flank	Pale grey pumice
D00-19	S-e R south flank	brown pumice
TCO-1	S-e R S top	obs from lava B top
TCO-2	S-e R saddle	obs from lava A top
TCO-3	S-e R saddle	obs from lava B base
TCO-4	S-e R N top	obs from lava A top
TCO-5	S-e R N top	mixed basalt-rhyolite sandstone
TCO-6	S-e R N top	obs with ves bands from lava B top
TCO-7	S-e R North Top vent	obs with angular tuffisite veins, West Wall
TCO-8	S-e R North Top vent	basaltic inc from East Wall
TCO-9	S-e R North Top vent	sph obs from West Wall
TCO-10	S-e R North Top vent	obs with angular tuffisite veins, East Wall
TCO-11	S-e R North Top vent	grey clast from breccia pod, West Wall
TCO-12	S-e R North Top vent	obs with grey streaks from West Wall
TCO-13	700 m N of North Top	Rhy from lava C
TCO-14	S-e R North Top vent	devit obs from vent interior
TCO-15	S-e R North Top vent	obs with angular tuffisite veins, West Wall
3AV-1	Vent NE of Blautakvisl gully	unsheared breccia pod within lava feeder
3AV-2	Vent NE of Blautakvisl gully	high shear streaked breccia
3AV-3	Vent NE of Blautakvisl gully	low shear sph obs breccia
3AV-4	Vent NE of Blautakvisl gully	high shear streaked breccia
3AV-5	Vent NE of Blautakvisl gully	medium shear breccia
3AV-6	Vent NE of Blautakvisl gully	low shear breccia
3AV-7	Vent NE of Blautakvisl gully	unsheared breccia pod
3AV-10	Lower vent NE of B gully	sph + perl obs
3AV-11	Lower vent NE of B gully	sheared obs 'clasts' from vent wall
SV-1	400 m NNW of N top	perl obs in rhy, lava C feeder
SV-2	S-e R scavenging vent	lumpy rhy clast in obs lava C feeder
SV-3	S-e R scavenging vent	rhy, lava C feeder interior
SV-4	S-e R scavenging vent	banded rhy-obs, lava C feeder
GD-1	650 m NE of N top	100% perl obs clast from lava F breccia
GD-2	S-e R gully 'dome'	98% perl obs, intact lava F
TCOG-1	North of Blautakvisl gully	ash
PLAT-1	EP, 700 m ESE of N top	intact ves obs from lava D flow top
PLAT-2	EP, 700 m ESE of N top	brown pum from lava D flow top
PLAT-3	EP, 700 m ESE of N top	white 'ash' from lava D flow top
PLAT-4	EP, 700 m ESE of N top	perl obs from lava D
PLAT-5	EP, 650 m ESE of N top	pep base of lava D
PLAT-6	EP, 700 m SE of N top	Rhy from lava D with contorted streaks
PLAT-7	810 m elevation SE limit of EP	fine ash from pep lava base above hot springs
PLAT-8	810 m elevation SE limit of EP	obs of lava D base 10 mm from PLAT-7
PLAT-10	600 m SE of S top	ash invading platy obs, base of lava E
PLAT-11	600 m SE of S top	ash-obs breccia, lava E base
PLAT-12	600 m SE of S top	cross laminated ash infill, lava E base
PLAT-13	600 m SE of S top	ash penetrating ves obs, fracture in lava E
PLAT-14	1000 m SE of S top	bedded ash-reworked shard transtion, base of lava E
PLAT-15	1100 m SE of S top	bedded ash, base of lava E
PLAT-16	1100 m SE of S top	ash penetating joint of lava E
PLAT-17	820 m elevation SE limit of EP	fb obs with sph
TEPH-1	250 m SW of N top	mixed basalt-rhyolite sandstone

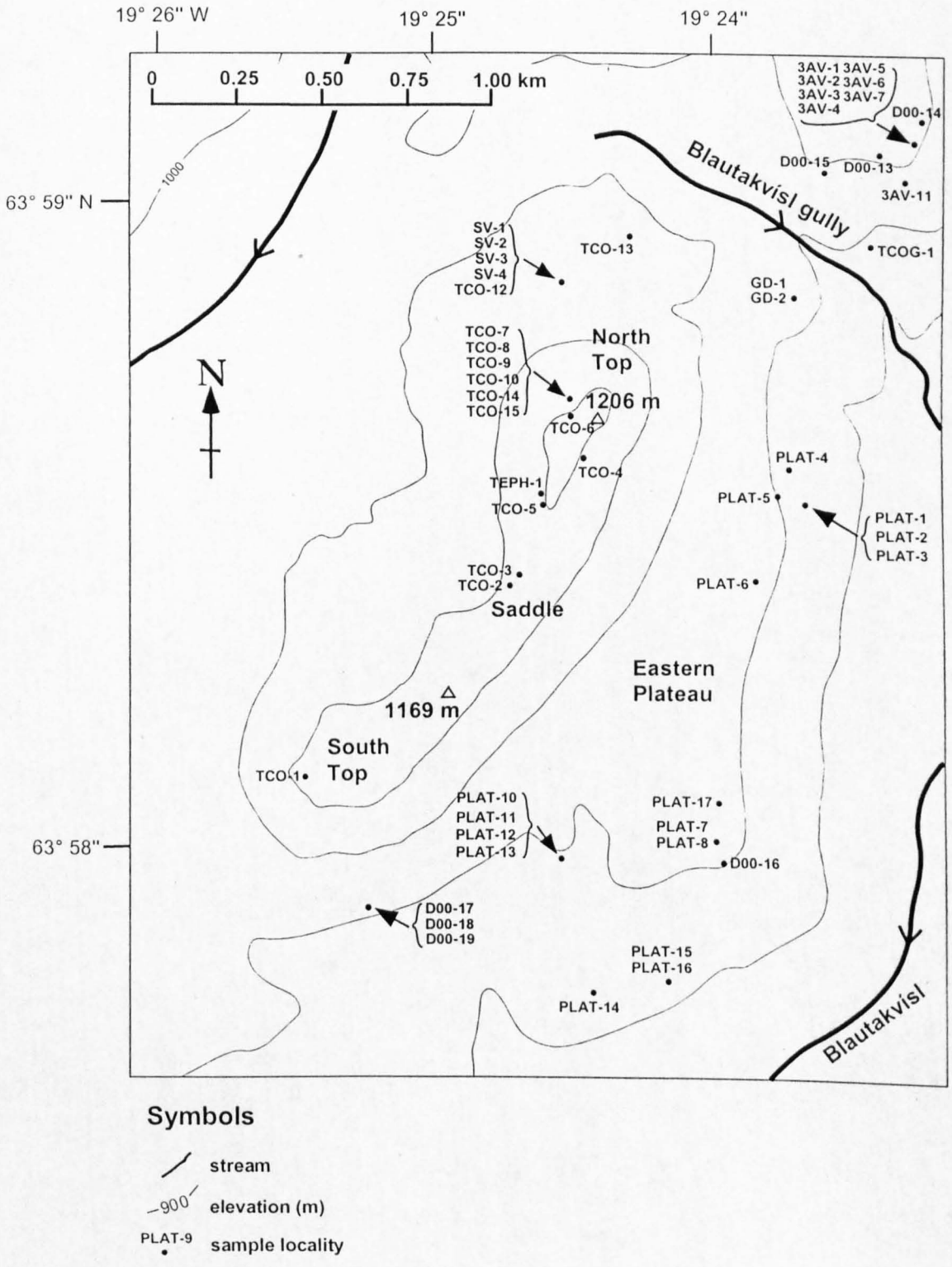

Figure B2. Map of South-east Rauðufossafjöll, indicating the localities from which samples were collected.

Appendix B3 Dalakvisl sample inventory

Each sample locality is indicated in Figure B3

Sample	Location	Description
Dalakvisl		
D00-1	South of Dalakvislfell	Ash/pum breccia from lava 2 margin
D00-2	South of Dalakvislfell	Ash/lobe fragment breccia, lava 2 margin
D00-3	South of Dalakvislfell	Ash-pum-obs (breccia 1)
D00-4	South of Dalakvislfell	Ash/obs from breccia 1
D00-5	Dalakvislfell SW top	Green obs lava 1
D00-6	Dalakvislfell SW top	Green indurated ash/obs/pum breccia
D00-7	Dalakvislfell SW top	Perlitic net veined obs lava 1
D00-8	Dalakvislfell SW top	Perlitic obs/pum breccia, lava 1-breccia 1 contact
D00-9	Dalakvislfell SW top	Ash/pum/obs breccia 1
D00-10	Dalakvislfell NE top	Perlitic, indurated ash/pum/obs breccia 1
D00-20	Dalakvisl campsite seds	ash from fine bedded unit of breccia 4
RIDGE C-	Ridge of breccia 2	breccia 2 0.5 m from stringer margin
RIDGE C-	Ridge of breccia 2	bomb within breccia 2 0.5 m from stringer margin
RIDGE C-	Ridge of breccia 2	stringer zone 1-3 transition
RIDGE C-	Ridge of breccia 2	vesicle-poor obs core of stringer (zone 1)
D47-1	Ridge of breccia 2	vesicle-poor obs core of stringer (zone 1)
D47-2	Ridge of breccia 2	zone 2 of stringer (brown vesicular obs)
D47-3	Ridge of breccia 2	zone 3 of stringer (intact white pumice)
D47-4	Ridge of breccia 2	ash-pum breccia at margin of stringer
D47-5	Ridge of breccia 2	greypumice streaked with obs bands 1m from stringer
D47-6	Ridge of breccia 2	fragment of bomb 4m from stringer
D47-7	Ridge of breccia 2	ash matrix of breccia 2, 2m from stringer
D57a	350 m NE of Dalakvislfell N top	black obs 5% perl, lava 1 margin
D57b	350 m NE of Dalakvislfell N top	banded obs-rhy 1m from lava 1 margin
D57c	350 m NE of Dalakvislfell N top	perl obs from core of lava 1
D58	350 m NE of Dalakvislfell N top	basaltic inclusion from lava 1
D62	350 m NE of Dalakvislfell N top	grey/black streaked obsidian, lava 1
D66	Ridge of breccia 2	3 cm thick transition from stringer zone 1-3
D72	350 m E of Dalakvislfell S top	clastic dyke infill
D74a	300 m E of Dalakvislfell S top	ves obs core, of lava 3
D74b	300 m E of Dalakvislfell S top	brown perl obs, lava 3
D74c	300 m E of Dalakvislfell S top	ash matrix of breccia 1, lava 3 margin
D81a	500 m ESE of Dal S top	perl obs sheared ves lava 2
D81b	500 m ESE of Dal S top	non-perl obs lava 2
D81c	500 m ESE of Dal S top	small ves non-perl obs, lava 2
D83a	480 m ESE of Dal S top	obs core, lava 3
D83b	480 m ESE of Dal S top	perl obs, lava 3 margin
D84	480 m ESE of Dal S top	perl obs lava 3
D85a	450 m ESE of Dal S top	green breccia 3, poorly consolidated
D85b	450 m ESE of Dal S top	green breccia 3, cemented

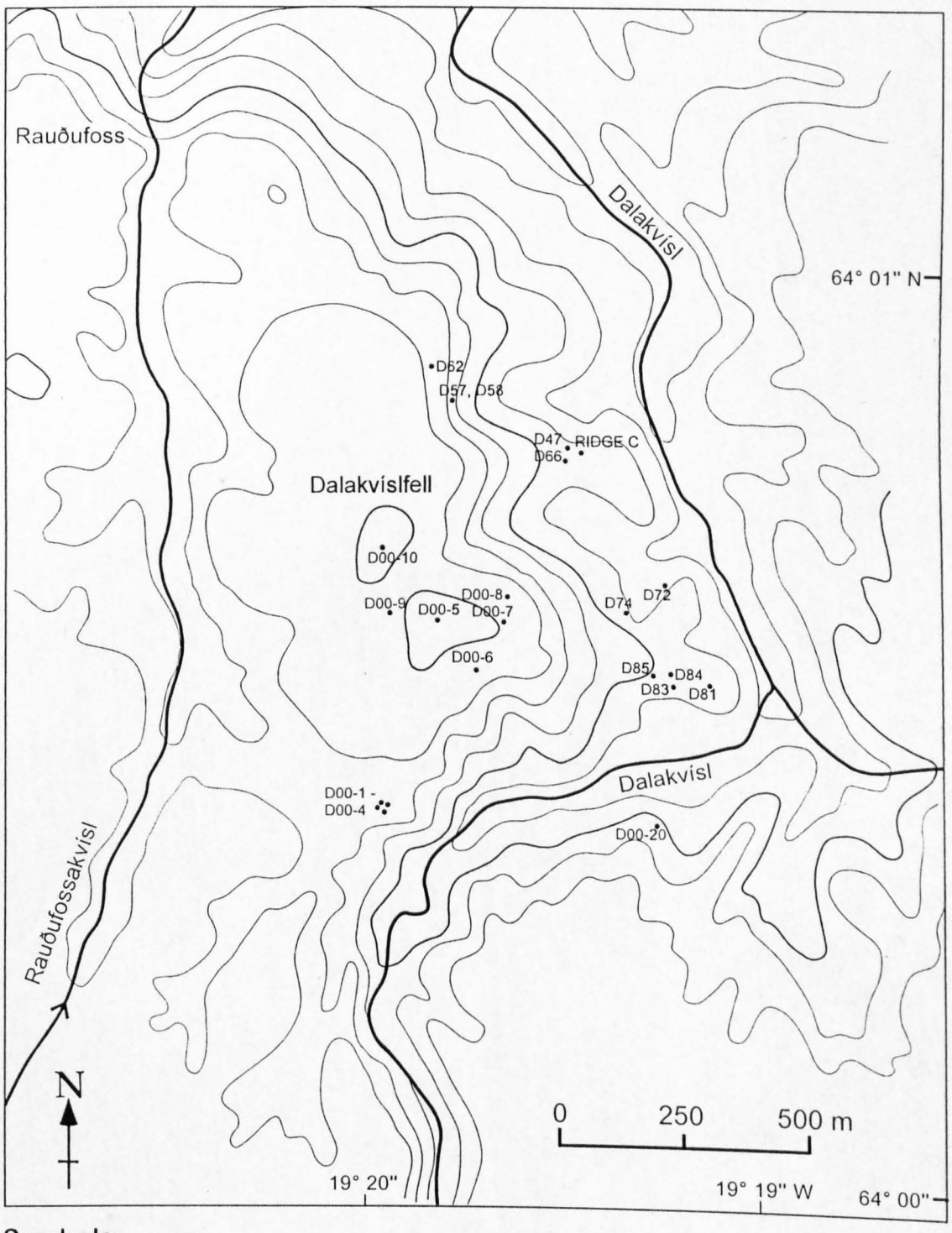

Symbols

stream

900 elevation (m)

D00-6 sample locality

Figure B3. Map of Dalakvísl, indicating the localities from which samples were collected.

Appendix C1
Microprobe analytical technique

Carbon-coated, 30 μm thick polished thin sections were analysed using a Cameca Camebax electron microprobe at the Department of Earth Sciences, Open University, with the assistance of Dr. Andy Tindle. An accelerating voltage of 20 kV, beam current of 20 nA and beam width of 20 μm was used, to minimise sodium loss.

Appendix C2

Blahnukur lava lobe glass analyses

p=pale glass, red=red glass, I=inclusion

Sample	Analysis	Type	P2O5	SiO2	TiO2	Al2O3	MgO	CaO	MnO	FeO	Na2O	K2O	F	Cl	Total
b120b	be	p	0.024	72.679	0.211	13.869	0.136	0.578	0.054	2.343	2.764	4.6	0.211	0.171	97.64
b120b	bf	p	0.003	72.722	0.224	14.07	0.06	0.479	0.071	2.308	2.653	4.613	0.154	0.173	97.53
b120b	bh	p	0.014	72.681	0.175	13.976	0.093	0.551	0.072	2.353	2.625	4.622	0.196	0.205	97.563
b120b	bi	p	0	71.082	0.188	13.701	0.096	0.501	0.063	2.341	2.595	4.531	0.216	0.197	95.511
b120b	bm	p	0.015	72.466	0.197	14.029	0.084	0.484	0.07	2.323	2.699	4.718	0.219	0.176	97.48
b120b	bn	p	0.011	73.422	0.214	14.027	0.065	0.531	0.073	2.3	2.664	4.64	0.207	0.17	98.324
b120b	bq	p	0.026	73.481	0.183	14.062	0.065	0.506	0.069	2.212	2.765	4.478	0.15	0.157	98.154
b120b	br	p	0.007	72.012	0.201	13.871	0.077	0.485	0.071	2.293	2.948	4.65	0.18	0.154	96.949
b120b	bs	p	0.007	72.799	0.186	13.963	0.074	0.477	0.07	2.317	2.649	4.636	0.205	0.16	97.543
b120b	bt	p	0.003	72.633	0.194	13.974	0.094	0.501	0.06	2.402	2.69	4.619	0.234	0.189	97.593
b120b	bv	p	0.033	72.636	0.199	13.962	0.09	0.523	0.071	2.364	2.654	4.692	0.175	0.178	97.577
b120b	bv	p	0.013	72.766	0.209	14	0.093	0.524	0.058	2.32	2.746	4.587	0.226	0.191	97.733
b120b	by	p	0.01	73.11	0.197	13.991	0.084	0.512	0.078	2.35	2.795	4.615	0.194	0.176	98.112
b120b	bg	r	0.027	73.245	0.19	14.084	0.065	0.478	0.058	2.246	2.711	4.634	0.215	0.183	98.136
b120b	bj	r	0.005	72.306	0.189	13.865	0.071	0.511	0.079	2.267	2.728	4.656	0.146	0.166	96.989
b120b	bk	r	0.008	72.611	0.21	13.953	0.076	0.503	0.068	2.359	2.614	4.535	0.197	0.169	97.303
b120b	bl	r	0.003	72.666	0.191	14.065	0.075	0.478	0.062	2.286	2.67	4.622	0.213	0.171	97.502
b120b	bo	r	0.023	72.806	0.194	13.878	0.08	0.496	0.071	2.249	2.686	4.625	0.204	0.18	97.492
b120b	bp	r	0.003	73.003	0.219	13.999	0.087	0.847	0.07	2.551	3.268	4.45	0.211	0.15	98.858
b120b	bu	r	0.018	72.874	0.219	13.935	0.087	0.495	0.077	2.313	2.739	4.628	0.258	0.155	97.798
b120b	bw	r	0	72.27	0.214	13.887	0.086	0.515	0.065	2.413	2.914	4.563	0.164	0.189	97.28
b120b	bx	r	0.01	71.866	0.205	13.905	0.078	0.479	0.065	2.343	2.677	4.677	0.155	0.185	96.645
b120b	bz	r	0.016	72.468	0.205	14.003	0.087	0.465	0.044	2.336	2.72	4.567	0.188	0.139	97.238
b120b	1bv	r	0.01	72.711	0.206	14.031	0.084	0.516	0.08	2.388	3.176	4.745	0.126	0.203	98.276
b120b	1bk	I	0.015	72.96	0.243	14.097	0.025	0.424	0.059	2.287	2.777	4.738	0.174	0.208	98.007
b120b	1bl	I	0.022	73.641	0.216	14.229	0.025	0.435	0.062	2.256	0.672	4.812	0.192	0.218	96.78
b120b	1bm	I	0.032	74.675	0.221	14.346	0.031	0.41	0.06	2.382	0.299	4.554	0.196	0.202	97.408
b120b	1bt	I	0.029	73.236	0.202	14.236	0.025	0.418	0.095	2.382	2.765	4.705	0.178	0.192	98.463
b120b	1bu	I	0.013	72.412	0.209	14.018	0.048	0.522	0.062	2.349	2.944	4.742	0.176	0.19	97.685

Appendix C2 continued															
Sample	Analysis	Type	P2O5	SiO2	TiO2	Al2O3	MgO	CaO	MnO	FeO	Na2O	K2O	F	Cl	Total
b120c	cd	p	0.02	72.873	0.185	14.11	0.076	0.456	0.068	1.97	3.115	4.763	0.213	0.154	98.003
b120c	ch	p	0.014	72.066	0.201	13.778	0.141	0.856	0.075	2.574	3.027	4.641	0.221	0.159	97.753
b120c	ci	p	0.012	72.905	0.191	13.965	0.093	0.496	0.059	2.307	2.797	4.871	0.201	0.191	98.088
b120c	cj	p	0.02	71.721	0.173	13.848	0.07	0.351	0.056	2.256	2.741	4.851	0.23	0.163	96.48
b120c	cl	p	0.011	71.786	0.232	13.215	0.089	0.4	0.083	2.616	2.671	4.907	0.24	0.247	96.497
b120c	1cj	p	0	73.215	0.182	14.151	0.048	0.335	0.054	1.946	3.418	4.807	0.21	0.207	98.573
b120c	1cl	p	0.013	72.948	0.205	13.857	0.064	0.398	0.068	2.144	2.92	5.082	0.267	0.215	98.181
b120c	ca	r	0.018	72.817	0.185	14.012	0.059	0.382	0.066	2.238	2.739	4.782	0.231	0.194	97.723
b120c	ca	r	0.019	72.403	0.183	13.982	0.062	0.349	0.061	2.137	2.919	4.832	0.256	0.202	97.405
b120c	cb	r	0.016	72.47	0.206	13.938	0.069	0.401	0.057	2.253	2.855	4.848	0.242	0.201	97.556
b120c	ce	r	0.022	72.618	0.214	13.443	0.093	0.447	0.073	2.471	2.744	4.831	0.204	0.212	97.372
b120c	ce	r	0.009	73.278	0.22	13.553	0.089	0.476	0.057	2.514	0.798	4.922	0.18	0.217	96.313
b120c	cg	r	0.021	72.567	0.22	13.515	0.105	0.526	0.077	2.484	2.745	4.978	0.18	0.22	97.638
b120c	cm	r	0.009	71.922	0.243	12.757	0.07	0.354	0.073	2.622	2.433	4.855	0.18	0.19	95.708
b120c	cn	r	0.022	71.727	0.201	13.651	0.119	0.554	0.072	2.573	2.778	4.85	0.222	0.191	96.96
b120c	co	r	0.01	72.548	0.193	13.996	0.089	0.409	0.087	2.363	2.951	4.72	0.212	0.184	97.762
b120c	cp	r	0.018	72.173	0.197	13.643	0.073	0.528	0.061	2.243	4.356	4.024	0.145	0.14	97.601
b120c	cr	r	0.017	72.462	0.199	13.428	0.082	0.391	0.068	2.473	2.654	4.737	0.134	0.171	96.816
b120c	cs	r	0	70.658	0.172	15.355	0.054	0.707	0.044	1.846	4.912	3.991	0.148	0.114	98.001
b120c	cx	r	0.009	72.656	0.219	14.006	0.049	0.322	0.06	2.26	2.777	5.026	0.161	0.172	97.717
b120c	1cm	r	0.03	73.285	0.217	13.35	0.075	0.44	0.07	2.429	2.814	5.04	0.239	0.204	98.193
b120c	ct	l	0.03	71.584	0.227	12.824	0.131	0.526	0.077	2.816	3.484	4.945	0.214	0.232	97.09
b120c	cu	l	0.005	71.469	0.242	12.98	0.146	0.429	0.083	2.84	2.481	5.279	0.198	0.293	96.445
b120c	cv	l	0.034	71.507	0.227	12.836	0.134	0.482	0.096	2.945	3.858	4.34	0.187	0.249	96.895
b120d	dj	p	0.027	71.079	0.179	14.328	0.059	0.485	0.066	2.085	5.392	4.206	0.146	0.129	98.181
b120d	dp	p	0.017	70.301	0.196	13.77	0.022	0.289	0.038	1.804	3.488	5.102	0.41	0.213	95.65
b120d	dp	p	0.026	71.07	0.145	13.617	0.055	0.355	0.059	2.057	3.214	5.24	0.437	0.211	96.486
b120d	dv	p	0.009	71.477	0.193	13.561	0.029	0.237	0.048	1.901	2.949	5.478	0.398	0.217	96.497
b120d	da	r	0.015	71.177	0.177	13.598	0.034	0.234	0.056	2.085	2.521	5.182	0.535	0.229	95.843
b120d	db	r	0	71.079	0.194	13.79	0.024	0.284	0.04	1.955	3.249	5.107	0.521	0.203	96.446
b120d	dc	r	0.011	71.133	0.214	13.775	0.023	0.261	0.051	1.909	3.225	5.236	0.531	0.227	96.596
b120d	dl	r	0.021	70.474	0.182	13.688	0.034	0.286	0.046	1.8	2.582	5.313	0.589	0.237	95.252

Appendix C2 continued															
Sample	Analysis	Type	P2O5	SiO2	TiO2	Al2O3	MgO	CaO	MnO	FeO	Na2O	K2O	F	Cl	Total
b120d	dm	r	0.022	71.468	0.184	13.433	0.039	0.25	0.047	1.834	2.408	5.433	0.578	0.221	95.917
b120d	dn	r	0.018	71.084	0.205	13.548	0.024	0.26	0.04	1.893	3.202	5.348	0.454	0.203	96.279
b120d	dq	r	0.006	70.691	0.195	13.623	0.024	0.242	0.057	1.961	2.839	5.375	0.537	0.283	95.833
b120d	ds	r	0.012	70.508	0.175	13.399	0.022	0.214	0.051	1.638	2.233	5.241	0.542	0.277	94.312
b120d	dt	r	0	70.725	0.178	13.44	0.018	0.187	0.042	1.699	2.692	5.128	0.468	0.215	94.792
b120d	1da	l	0.019	71.535	0.186	14.035	0.022	0.509	0.058	2.181	3.092	5.614	0.331	0.216	97.798
b120d	1db	l	0.017	71.715	0.209	14.027	0.018	0.272	0.057	2.273	2.876	5.612	0.338	0.216	97.63
b120d	1dc	l	0.001	72.011	0.179	14.096	0.003	0.268	0.063	2.043	3.093	5.533	0.261	0.196	97.747
b120d	1dd	l	0.026	72.137	0.19	14.134	0.024	0.292	0.058	2.181	2.951	5.522	0.208	0.207	97.93
b120d	1de	l	0.006	72.257	0.215	14.095	0.024	0.253	0.036	2.029	2.825	5.533	0.255	0.183	97.711
b120d	1dr	l	0.019	70.314	0.207	13.458	0.107	0.565	0.065	2.307	2.278	5.272	0.337	0.219	95.148
b120d	1ds	l	0.013	70.791	0.217	13.18	0.117	0.568	0.079	2.44	2.481	4.991	0.293	0.23	95.4
b120d	1dt	l	0.016	72.748	0.242	13.171	0.108	0.551	0.061	2.465	3.63	4.848	0.173	0.242	98.255
b120e	ek	l	0.041	72.951	0.132	13.575	0.004	0.237	0.043	1.52	2.339	4.549	0.09	0.2	95.681
b120e	el	l	0.022	73.109	0.175	13.791	0.022	0.294	0.049	1.422	2.345	4.483	0.163	0.21	96.085
b120f	fe	p	0.004	72.925	0.187	14.417	0.031	0.488	0.045	2.037	4.496	4.638	0.215	0.188	99.671
b120f	ff	p	0.001	73.08	0.203	13.602	0.037	0.432	0.073	2.334	3.49	4.813	0.292	0.273	98.63
b120f	fn	r	0.01	73.593	0.198	13.476	0.05	0.37	0.08	2.41	2.372	5.343	0.374	0.298	98.574
b120f	fp	r	0.016	73.14	0.18	13.335	0.063	0.4	0.066	2.464	2.39	5.285	0.422	0.253	98.014
b120f	1fc	l	0.024	74.96	0.253	11.6	0.05	0.367	0.081	2.798	2.495	4.942	0.177	0.306	98.053
b120f	1fd	l	0.044	74.849	0.289	11.91	0.08	0.399	0.084	3.019	2.064	5.062	0.367	0.275	98.442
b120f	1fe	l	0.009	72.346	0.238	12.656	0.071	0.411	0.083	2.888	1.889	5	0.353	0.308	96.252
b120f	1ff	i	0.006	73.601	0.198	13.923	0.049	0.424	0.079	2.462	2.524	5.307	0.369	0.26	99.202

Appendix C3

Glass analyses of Dalakvisl stringer.

D47-1 low-ves obs core (zone), D47-2 transitional obs, D47-3 pumice.

Sample	Analysis	Type	P2O5	SiO2	TiO2	Al2O3	MgO	CaO	MnO	FeO	Na2O	K2O	F	Cl	Total
d47-1	1a	p	0.014	75.612	0.322	13.031	0.149	0.568	0.118	2.349	1.795	4.081	0.14	0.095	98.274
d47-1	1b	p	0.022	75.283	0.312	13.088	0.147	0.553	0.123	2.342	2.079	4.105	0.119	0.073	98.246
d47-1	1c	p	0.014	75.449	0.333	13.068	0.155	0.536	0.098	2.356	1.794	4.108	0.229	0.089	98.229
d47-1	1d	p	0.014	75.263	0.311	13.071	0.156	0.526	0.121	2.405	1.783	4.05	0.181	0.11	97.991
d47-1	1e	p	0.02	75.399	0.36	12.914	0.158	0.563	0.13	2.373	1.845	4.052	0.13	0.075	98.019
d47-1	1f	p	0.015	75.241	0.316	13.031	0.157	0.527	0.124	2.37	1.848	4.103	0.177	0.097	98.006
d47-1	1g	p	0.005	75.685	0.344	12.96	0.16	0.551	0.127	2.348	1.865	4.067	0.167	0.094	98.373
d47-1	1h	p	0.022	75.253	0.31	13.127	0.153	0.56	0.11	2.343	2.101	4.012	0.166	0.067	98.224
d47-1	1k	p	0.022	75.558	0.334	12.98	0.16	0.542	0.11	2.317	1.815	3.977	0.12	0.14	98.075
d47-1	1m	p	0.032	75.214	0.322	12.988	0.137	0.529	0.112	2.342	1.896	3.99	0.187	0.111	97.86
d47-1	1n	p	0.026	75.521	0.31	12.987	0.146	0.54	0.113	2.385	1.829	4.087	0.144	0.096	98.184
d47-1	1o	p	0.008	75.605	0.359	12.978	0.168	0.544	0.125	2.401	1.83	4.063	0.18	0.072	98.333
d47-1	1p	p	0.014	75.573	0.318	13.073	0.164	0.528	0.125	2.38	1.837	4.061	0.206	0.093	98.372
d47-1	1q	p	0.003	75.356	0.351	13.039	0.146	0.56	0.115	2.388	1.848	4.066	0.115	0.081	98.068
d47-1	1r	p	0.029	75.438	0.332	13.015	0.138	0.519	0.113	2.427	1.835	4.014	0.175	0.101	98.136
d47-1	1s	p	0.022	75.487	0.306	13.032	0.154	0.566	0.129	2.415	1.847	3.998	0.104	0.098	98.158
d47-1	1t	p	0	75.531	0.326	12.964	0.153	0.558	0.115	2.318	1.9	4.01	0.121	0.085	98.081
d47-1	1v	l	0.031	75.587	0.341	12.916	0.161	0.536	0.12	2.422	1.666	4.09	0.196	0.123	98.189
d47-1	1x	p	0.014	75.551	0.326	12.965	0.148	0.548	0.131	2.366	1.791	4.06	0.117	0.093	98.11
d47-1	1y	p	0.021	75.658	0.326	13.033	0.156	0.556	0.105	2.37	1.787	4.038	0.171	0.114	98.335
d47-1	1z	p	0.022	75.191	0.327	13.061	0.181	0.54	0.12	2.411	1.903	4.077	0.176	0.1	98.109
d47-1	11k	r	0.007	75.472	0.349	12.959	0.169	0.537	0.114	2.356	1.864	4.074	0.188	0.123	98.212
d47-1	11l	r	0.023	75.554	0.309	12.991	0.147	0.538	0.12	2.354	2.018	4.016	0.198	0.123	98.391
d47-1	11q	p	0.016	75.629	0.363	13.025	0.152	0.554	0.127	2.475	1.892	4.073	0.15	0.117	98.573
d47-1	11s	p	0.019	75.434	0.343	13.061	0.143	0.546	0.108	2.474	1.861	4.058	0.17	0.097	98.314
d47-1	11t	p	0.026	75.703	0.327	13.049	0.161	0.544	0.124	2.383	1.783	4.066	0.169	0.093	98.428
d47-1	11u	p	0.02	75.612	0.33	13.011	0.15	0.531	0.116	2.393	1.765	4.021	0.118	0.083	98.15

Appendix C3 continued															
Sample	Analysis	Type	P2O5	SiO2	TiO2	Al2O3	MgO	CaO	MnO	FeO	Na2O	K2O	F	Cl	Total
d47-2	2a	p	0	75.2	0.305	12.779	0.16	0.54	0.129	2.366	1.593	4.028	0.156	0.082	97.338
d47-2	2b	p	0.011	75.517	0.344	12.915	0.147	0.555	0.119	2.349	1.597	4.057	0.145	0.082	97.838
d47-2	2c	p	0.009	75.276	0.338	12.844	0.154	0.539	0.123	2.352	1.63	4.098	0.16	0.092	97.615
d47-2	2d	p	0.012	75.692	0.338	13.056	0.145	0.528	0.113	2.412	1.65	4.096	0.178	0.081	98.301
d47-2	2e	p	0.022	75.4	0.307	12.892	0.171	0.554	0.123	2.38	1.57	4.032	0.075	0.047	97.573
d47-2	2f	p	0.009	75.038	0.344	12.841	0.164	0.548	0.109	2.346	1.732	4.086	0.172	0.073	97.462
d47-2	2g	p	0.027	75.419	0.318	12.908	0.155	0.537	0.11	2.376	1.597	4.013	0.148	0.11	97.718
d47-2	2h	p	0.017	75.456	0.335	13.024	0.165	0.523	0.128	2.346	1.585	4.096	0.111	0.118	97.904
d47-2	2i	p	0.031	74.972	0.319	12.948	0.159	0.521	0.117	2.369	1.586	4.081	0.138	0.093	97.334
d47-2	2j	p	0.006	75.265	0.324	12.975	0.141	0.528	0.111	2.372	1.603	4.002	0.167	0.084	97.578
d47-2	2k	p	0.019	74.921	0.325	12.843	0.158	0.548	0.107	2.359	1.561	4.016	0.126	0.048	97.031
d47-2	2q	p	0.015	75.087	0.33	12.965	0.155	0.556	0.102	2.404	1.579	4.012	0.179	0.106	97.49
d47-2	2r	p	0.024	75.637	0.32	12.967	0.158	0.526	0.112	2.4	1.627	4.01	0.155	0.095	98.031
d47-2	2s	p	0.024	75.35	0.311	12.832	0.14	0.518	0.123	2.349	1.606	4.056	0.187	0.101	97.597
d47-2	2t	p	0.036	75.564	0.352	12.926	0.149	0.542	0.127	2.36	1.604	4.027	0.199	0.075	97.961
d47-2	2u	p	0.037	75.378	0.327	12.862	0.151	0.538	0.13	2.407	1.555	4.045	0.194	0.094	97.718
d47-2	2v	p	0.018	75.522	0.341	12.992	0.15	0.55	0.123	2.446	1.603	4.081	0.103	0.119	98.048
d47-2	2w	p	0.02	75.421	0.322	12.943	0.151	0.53	0.129	2.409	1.578	4.087	0.225	0.095	97.91
d47-2	21a	p	0.023	75.573	0.298	12.924	0.15	0.564	0.122	2.343	1.605	4.137	0.189	0.11	98.038
d47-2	21b	p	0.023	75.372	0.298	12.968	0.154	0.564	0.131	2.459	1.592	3.985	0.159	0.115	97.82
d47-2	21g	p	0.017	75.46	0.329	13.05	0.154	0.525	0.116	2.353	1.534	4.055	0.12	0.095	97.808
d47-2	21h	p	0.01	75.291	0.353	12.946	0.155	0.543	0.122	2.361	1.522	4.011	0.165	0.091	97.57
d47-2	21i	p	0.022	75.144	0.351	12.937	0.146	0.523	0.11	2.325	1.509	3.982	0.181	0.11	97.34
d47-2	21n	p	0.041	75.681	0.324	13.002	0.157	0.537	0.124	2.372	1.51	3.995	0.139	0.114	97.996
d47-2	21o	p	0.014	75.428	0.321	13.088	0.152	0.531	0.128	2.367	1.608	4.061	0.179	0.059	97.936
d47-2	21p	p	0.032	74.999	0.333	12.895	0.158	0.553	0.13	2.394	2.073	3.992	0.135	0.092	97.786
d47-2	21q	p	0.026	75.67	0.335	13	0.149	0.546	0.12	2.391	1.591	4.079	0.242	0.07	98.219

Appendix C3 continued															
Sample	Analysis	Type	P2O5	SiO2	TiO2	Al2O3	MgO	CaO	MnO	FeO	Na2O	K2O	F	Cl	Total
D47-3	3a	p	0.017	74.443	0.317	12.775	0.147	0.534	0.12	2.387	1.254	3.992	0.11	0.108	96.204
D47-3	3b	p	0.038	74.403	0.324	12.754	0.167	0.527	0.122	2.288	1.228	3.988	0.12	0.094	96.053
D47-3	3c	p	0.017	73.29	0.329	12.618	0.161	0.5	0.111	2.34	1.259	3.96	0.167	0.099	94.851
D47-3	3d	p	0.007	73.363	0.296	12.509	0.132	0.536	0.103	2.251	1.165	3.924	0.149	0.096	94.531
D47-3	3e	p	0.011	73.244	0.316	12.51	0.151	0.521	0.113	2.307	1.193	3.921	0.165	0.115	94.567
D47-3	3f	p	0.019	74.714	0.336	12.862	0.149	0.54	0.122	2.403	2.087	4.014	0.214	0.09	97.55
D47-3	3g	p	0.017	74.334	0.314	12.787	0.147	0.544	0.12	2.386	1.37	3.968	0.147	0.1	96.234
D47-3	3h	p	0.015	75.501	0.349	12.992	0.141	0.543	0.113	2.313	1.495	4.029	0.147	0.077	97.715
D47-3	3i	p	0.018	74.305	0.34	12.758	0.146	0.536	0.114	2.294	1.387	3.954	0.168	0.082	96.102
D47-3	3l	p	0.024	73.438	0.315	12.668	0.144	0.515	0.108	2.294	1.292	3.976	0.186	0.078	95.038
D47-3	3p	p	0.026	74.532	0.325	12.93	0.163	0.522	0.119	2.371	1.442	3.943	0.172	0.118	96.663
D47-3	3q	p	0.021	75.699	0.34	13.148	0.163	0.525	0.134	2.372	1.566	4.05	0.102	0.101	98.221
D47-3	3r	p	0.018	74.86	0.318	13.003	0.163	0.568	0.094	2.327	1.415	4.037	0.132	0.101	97.036
D47-3	3s	p	0.013	73.355	0.323	12.692	0.165	0.536	0.105	2.286	1.137	3.942	0.168	0.082	94.804
D47-3	3u	p	0.012	75.029	0.313	12.846	0.151	0.549	0.111	2.322	1.236	3.937	0.154	0.085	96.745
D47-3	3t	p	0.016	73.809	0.291	12.679	0.155	0.502	0.114	2.231	0.804	3.874	0.16	0.086	94.721
D47-3	3v	p	0.018	74.286	0.324	12.796	0.158	0.522	0.116	2.357	1.221	3.984	0.167	0.092	96.041
D47-3	3w	p	0.017	75.148	0.315	13.054	0.155	0.56	0.118	2.377	1.522	3.952	0.181	0.103	97.502
D47-3	3x	p	0.015	75.007	0.34	12.956	0.151	0.527	0.114	2.415	1.533	3.995	0.173	0.092	97.318
D47-3	3y	p	0.017	74.859	0.336	13.009	0.154	0.52	0.122	2.345	1.415	4.048	0.186	0.087	97.098
D47-3	3z	p	0.035	74.684	0.347	12.976	0.162	0.516	0.118	2.399	1.484	3.962	0.132	0.085	96.9
D47-3	31a	p	0.027	74.712	0.317	12.981	0.173	0.528	0.102	2.381	1.567	4.028	0.182	0.086	97.084
D47-3	31b	p	0.011	72.442	0.336	12.359	0.149	0.543	0.12	2.198	1.016	3.845	0.13	0.139	93.288
D47-3	31c	p	0.03	73.745	0.327	12.577	0.146	0.518	0.115	2.317	1.42	3.909	0.161	0.068	95.333
D47-3	31d	p	0.001	73.609	0.312	12.674	0.161	0.544	0.105	2.299	1.458	3.898	0.257	0.07	95.388
D47-3	31e	p	0.011	75.302	0.334	12.951	0.148	0.516	0.11	2.403	1.524	4.044	0.168	0.064	97.575
D47-3	31f	p	0.023	75.094	0.323	12.844	0.156	0.527	0.103	2.374	1.488	4.035	0.178	0.071	97.216
D47-3	31g	p	0.028	75.231	0.327	12.991	0.142	0.54	0.108	2.327	1.08	3.993	0.233	0.092	97.092

Appendix D1.
Fourier transform infra-red spectroscopy - analytical techniques

Fourier transform infra-red spectroscopy (FTIR) analysis was conducted at the Department of Earth Sciences, University of Bristol, with the assistance of Dr. Richard Brooker. Pea-sized samples of obsidian were mounted on a glass slide with dental resin, and double-polished to thicknesses of 100-600 μm. Thicknesses were measured with a digital micrometer, with an accuracy of 5 μm. Analyses were carried out in a chamber purged with nitrogen, and background counts were made between every 3-4 analyses. A beam width of 50 μm was used.

The height of the absorbance peak at 3550 cm^{-1} (total water, e.g. Zhang 1999), was used to calculate the water content, using the correlation coefficient of Newman et al. (1988). Due to the low water contents of the samples analysed (<0.7 %), the 3550 cm^{-1} peak was only saturated when the thickest samples were used, in which case the combined height of the 4520 cm^{-1} OH peak and the 5250 cm^{-1} molecular H_2O were used. However, most samples had very low OH and molecular H_2O peaks, and no attempt has been made to study the speciation of water in the glasses.

Appendix D2

Sample TCO-1 obsidian from upper carapace of lava B

Analysis no.	Thickness microns	Thickness centimetres	Density kg m^{-3}	3550 cm^{-1} peak height	H_20 total weight %
TCO101	178	0.0178	2300	0.22	0.14
TCO102	186	0.0186	2300	0.22	0.13
TCO103	184	0.0184	2300	0.21	0.13
TCO104	171	0.0171	2300	0.21	0.14
TCO105	180	0.018	2300	0.2	0.12
TCO106	244	0.0244	2300	0.33	0.15
TCO107	245	0.0245	2300	0.3	0.14
TCO108	242	0.0242	2300	0.33	0.15
TCO109	243	0.0243	2300	0.36	0.17
TCO110	244	0.0244	2300	0.28	0.13
				Mean	**0.14**
				Standard dev	**0.01**

H_20 total =25.7*peak height (cm)/(thickness (cm)*density (kg m^{-3})

Appendix D3

Sample TCO-7 from West Wall of vent on South-east Rauðufossafjöll

Key: x = estimated proportion of microlites, obs = obsidian, tuff = tuffisite

Analysis n	Comments	Thickness microns	Thickness centimetres	Density kg m^{-3}	3550 cm^{-1} peak height	H_20 total weight %
VENT4A	pale obs<5x	74	0.0074	2300	0.14	0.21
VENT4B	pale obs<5x	87	0.0087	2300	0.16	0.21
VENT4C	pale obs<5x	114	0.0114	2300	0.18	0.18
VENT4D	red obs ~10x	175	0.0175	2300	0.22	0.14
VENT4E	red obs ~20x	130	0.013	2300	0.28	0.24
VENT4F	red obs ~20x	130	0.013	2300	0.26	0.22
VENT4G	pale obs<5x	81	0.0081	2300	0.11	0.15
VENT4H	red obs <10x	82	0.0082	2300	0.14	0.19
VENT4I	red obs <10x	77	0.0077	2300	0.13	0.19
VENT4J	tuff red >20x	82	0.0082	2300	0.12	0.16
VENT4K	tuff red >20x	77	0.0077	2300	0.14	0.20
VENT4L	red obs bleb ~5x	88	0.0088	2300	0.20	0.25
VENT4M	red obs bleb ~5x	88	0.0088	2300	0.21	0.27
VENT4N	red obs bleb ~5x	88	0.0088	2300	0.19	0.24
VENT4O	pale obs bleb <5x	88	0.0088	2300	0.19	0.24
VENT4P	pale obs bleb <5x	87	0.0087	2300	0.19	0.24
VENT4Q	tuff 100 μm from bleb	88	0.0088	2300	0.16	0.20
VENT4R	tuff 100 μm from bleb	88	0.0088	2300	0.18	0.23
VENT4S	tuff 100 μm from bleb	88	0.0088	2300	0.18	0.23
VENT4T	Centre of obs bleb	88	0.0088	2300	0.17	0.22
VENT4U	fine pale tuffisite	109	0.0109	2300	0.15	0.15
VENT4V	fine pale tuffisite	118	0.0118	2300	0.15	0.14
VENT4W	pale obs 200 μm from tuff	99	0.0099	2300	0.13	0.15
VENT4X	half obs half tuff	107	0.0107	2300	0.12	0.13
VENT4Y	all tuff	110	0.011	2300	0.12	0.12
VENT4Z	red obs, flattened vesicles?	86	0.0086	2300	0.17	0.22
VENT4AB	red obs, flattened vesicles?	87	0.0087	2300	0.19	0.24

H_20 total =25.7*peak height (cm)/(thickness (cm)*density (kg m^{-3})

Appendix D4

D47 stringer from breccia 2, Dalakvisl

Analysis no.	Zone	Thickness microns	Thickness centimetres	Density kg m^{-3}	3550 cm^{-1} peak height	H_20 total
HTDO 2	1	217	0.0217	2300	1.14	0.59
HTDO 3	1	218	0.0218	2300	1.28	0.66
HTDO 4	1	202	0.0202	2300	1.02	0.57
HTDO 5	1	200	0.02	2300	1.03	0.58
HTDO 6	1	202	0.0202	2300	1.1	0.61
HTDO 14	1	317	0.0317	2300	1.69	0.60
					Mean	**0.61**
					SD	**0.04**
HTPUM1a	2	170	0.017	2300	0.81	0.53
HTPUM1b	2	163	0.0163	2300	0.87	0.60
HTPUM1c	2	168	0.0168	2300	0.79	0.53
HTPUM1d	2	166	0.0166	2300	0.92	0.62
HTPUM1e	2	174	0.0174	2300	0.81	0.52
HTPUM3a	2	183	0.0183	2300	0.96	0.59
HTPUM3c	2	183	0.0183	2300	1.05	0.64
HTPUM3d	2	182	0.0182	2300	1.07	0.66
HTPUM3e	2	183	0.0183	2300	1.09	0.67
					Mean	**0.59**
					SD	**0.06**
HTPUM2a	3	168	0.0168	2300	0.85	0.57
HTPUM2b	3	170	0.017	2300	0.92	0.61
HTPUM2c	3	171	0.0171	2300	0.87	0.57
HTPUM2d	3	171	0.0171	2300	0.81	0.53
HTPUM2e	3	171	0.0171	2300	0.9	0.59
					Mean	**0.57**
					SD	**0.03**

H_20 total =25.7*peak height (cm)/(thickness (cm)*density (kg m^{-3})

Appendix E1

Analytical techniques: measuring the density of obsidian samples.

The mass of blocks of obsidian was determined using a precision balance at the Department of Environmental Science, Lancaster University. Each block was weighed three times. These blocks were then coated with cling film and immersed in a measuring cylinder of water, and the volume of water displaced was recorded. Care was taken to prevent air pockets forming between the cling film and the sample.

Appendix E2

Results of density measurements of stringer from Dalakvisl

Sample	Zone 1	Zone 2	Zone 2	Zone 3
Weight (g)	262, 262, 262	12.8, 12.8, 12.8	19, 19, 19	13.2, 13.2, 13.2
Mean weight (g)	262	12.8	19	13.2
Measurement error	5g (2 %)	0.01 g (0.1 %)	0.01 g (0.05 %)	0.01 g (0.1 %)
Volume (cm^3)	120, 120, 115, 115	8.4, 8.5, 8.7, 8.7, 8.9	9.5, 10, 10, 10, 10.5	19.4, 19.4, 19.2, 19.7, 19.5
Mean volume (cm^3)	118	8.6	10	19.4
Error	5 cm^3 (4 %)	0.1 cm^3 (1 %)	0.1 cm^3 (1 %)	0.1 cm^3 (1 %)
Density (g cm^{-3})	2.22	1.49	1.9	0.68
Vesicularity (%)	**5 (estimated)**	**36**	**18**	**71**
Combined error	4%	1.00%	1.00%	0.50%

Appendix F.
Scanning electron microscope (SEM) analytical techniques

I used a scanning electron microscope at the Open University, with assistance from Naomi Williams. Ash was carefully removed from sample bags with a spatula and gently sprinkled on the surface of a target, before being gold coated. This was to minimise grinding of ash shards on the target head. A range of magnifications between 100:1 and 23000:1 was used, and images were saved in .tiff format using the image export software of the SEM.

Appendix G.
Selected conference abstracts

List of conferences attended

*†Volcano-ice interaction workshop, Reykjavík, Iceland, August 2000.
*Iceland 2000 (Keele University)
*Ice-marginal Landsystems and Processes 2000 (Keele University)
*Yorkshire Geological Society Special Session: Iceland (Sheffield University)
*‡Volcanic and Magmatic Studies Group 2000 (Lancaster University)
†Volcanic and Magmatic Studies Group 1999 (Birmingham University)
†Quaternary Climate Change 1998 (Cambridge University)

*oral presentation given
† poster presentation given
‡ awarded the Bob Hunter Prize for best student talk

Selected abstracts

Volcano-ice interaction workshop, Reykjavík, Iceland, August 2000

Abstract 1.

VOLCANO/ICE INTERACTION AT BLÁHNÚKUR, TORFAJÖKULL, ICELAND: A QUATERNARY SUBGLACIAL RHYOLITE ERUPTION. H. Tuffen[1,2], J. S. Gilbert[2], D. W. McGarvie[1]. [1]Department of Earth Sciences, Open University, Milton Keynes MK7 6AA, UK. [2]Department of Environmental Science, Lancaster University, Lancaster LA1 4YQ, UK.

Bláhnúkur is a 350 m high subglacial rhyolite volcano emplaced during the last glacial period at the Torfajökull volcanic complex, south central Iceland. We present field evidence for complex volcano/ice interaction beneath a glacier >400 m thick. Reworked basal till is intercalated with juvenile-dominated sandstones in an incised subglacial meltwater channel at the base of the sequence. This suggests that meltwater was draining from the vent area during the eruption, as predicted for subglacial rhyolite eruptions [1].

Much of the subglacial deposits consist of 5-10 m lava lobes set in pumice breccia [2,3]. Columnar jointing patterns may indicate that some lobes reached the glacier base, where they were moulded within steep-sided conical cavities in the ice [3]. Explosive magma-water interaction probably contributed to fragmentation at lobe margins, forming blocky ash shards typically 10-100 μm in diameter. Mass flow deposits on the volcano flanks consist of portions of lava lobes and pumice breccia [3]. They appear to have been hot when emplaced and were possibly formed by syn-eruptive instability of lava lobes and breccia, triggered by melting of the supporting ice walls (e.g. [4]).

Larger lava flows (>20 m thick) were extruded towards the end of the eruption. The orientation of columnar joints suggests that lava flowed within subglacial tunnels [3,4,5]. The lack of fragmentation at lava flow margins may indicate that these tunnels were largely empty of meltwater. We propose that the eruption mechanism was strongly influenced by the evolving subglacial cavity system. This emphasizes that an understanding of subglacial hydrology is the key to hazard assessment at active ice-covered volcanoes.

References: [1] Hoskuldsson A., Sparks R. S. J. (1997) *Bull. Volcanol. 59*:219-230 [2] Furnes H., Fridleifsson I. B., Atkins F. B. (1980) *J. Volcanol. Geotherm. Res. 8*:95-110. [3] Tuffen H., Gilbert J. S., McGarvie D. W. (2000) *Bull. Volcanol.*, sub judice. [4] Hickson C. J. (2000) *Geomorphology 32*:239-261. [5] Lescinsky D. T., Sisson T. W. (1998) *Geology 26*:351-354.

Abstract 2.

RHYOLITE TUYAS AT TORFAJÖKULL, ICELAND. H. Tuffen[1,2], D. W. McGarvie[1], J. S. Gilbert[2]. [1]Department of Earth Sciences, Open University, Milton Keynes MK7 6AA, UK. [2]Department of Environmental Science, Lancaster University, Lancaster LA1 4YQ, UK.

A large subglacial eruption of peralkaline rhyolite at Torfajökull, Iceland has created at least ten tuyas with a total volume of 11-17 km3 [1,2]. These tuyas, which rise 370-520 m above the surrounding land, are the rhyolitic equivalent of basaltic tuyas such as Herðubreið [3].

Lithofacies record three distinct phases: (1) an early subglacial phase, (2) an ice-constrained subaerial lava phase, and (3) an unconstrained subaerial lava phase. The products of the early subglacial phase (1), which consist of lava lobes and pumice breccia [c.f. 4,5] are mostly concealed by scree. Products of the next eruptive phase (2) consist of steeply ramped lava flows up to 1.2 km long and 150 m thick. Where preserved, flow tops are pumiceous and glassy; closely resembling those of subaerial rhyolite lava flows nearby. The nature of these lava flows appears consistent with subaerial emplacement within an ice cauldron. The final eruptive phase (3) occurs on volcanoes above 1000 m in elevation, where the ice-constrained lava flows (2) are overlain by subhorizontal and unramped lava flows only 10-25 m thick, which locally drape down the volcano flanks (c.f. [6]). These may have flowed above the glacier surface, before entering a bergshrund-like gap between the volcano and the encapsulating glacier.

The high viscosity of rhyolite lava has lead to the development of ramped structures not seen in the subaerial lava flows of less silicic tuyas. The morphology and stratigraphic position of the ice-constrained rhyolite lava flows reported here may provide evidence for both ice cauldron geometries and palaeo-ice thickness. We estimate that the subaerial lava cap of one rhyolite tuya at Torfajökull (Kirkjufell) was emplaced within an ice cauldron 150 m deep and ~1.2 km in diameter that had developed in a glacier ~400 m thick. These dimensions are strikingly similar to those of the ice cauldrons that developed during the Gjálp eruption - but is this purely a coincidence?

References: [1] McGarvie D. W. (1984) *Geology 12:*685-688. [2] McGarvie D. W., Tuffen H., Tindle A. G. (2000) *Volcano/Ice Interaction on Earth and Mars, Reykjavik.* [3] Werner R., Schmincke H.-U., Sigvaldason G. (1996) *Geol. Rundsch. 85:*390-397. [4] Tuffen H., Gilbert J. S., McGarvie D. W. (2000) *Bull. Volcanol.*, sub judice. [5] Furnes H., Fridleifsson I. B., Atkins F. B. (1980) *J. Volcanol. Geotherm. Res. 8:*95-110. [6] Mathews W. H. (1951) *Am. J. Sci. 249:*830-841.

Abstract 3.

FRAGMENTATION MECHANISMS IN ICELANDIC SUBGLACIAL RHYOLITE ERUPTIONS: EVIDENCE FROM ASH SHARD MORPHOLOGIES. H. Tuffen[1,2] , D. W. McGarvie[1], J. S. Gilbert[2]. [1]Department of Earth Sciences, Open University, Milton Keynes MK7 6AA, UK. [2]Department of Environmental Science, Lancaster University, Lancaster LA1 4YQ, UK.

Rhyolitic ash shards from Quaternary subglacial volcanoes at Torfajökull, Iceland have distinctive shapes and surface textures that relate to a variety of fragmentation mechanisms and alteration processes. Ash shards from the margins of in-situ subglacial lava lobes at Bláhnúkur [1] are relatively vesicle-poor and have blocky morphologies typical of magma-water interaction [2,3]. From field observations we postulate that small-scale phreatomagmatic explosions occurred when lava lobes encountered meltwater-saturated breccias under ice >300 m thick. Arrested vesiculation may attest to a high glaciostatic confining pressure (c. 3 MPa). Ash shards within green, indurated debris flow deposits on Bláhnúkur [1] are similar, but have abraded corners and pitted surfaces, suggestive of transport and alteration [3].

Very different ash has been found in northern Rauðufossafjöll, in a thick (>10 m) sequence of bedded ash which we interpret to have been deposited in an ice-dammed lake at the northern margin of a large (>6 km^3) subglacial-to-emergent volcano. Shards are highly vesicular, with delicate bubble walls, and show no sign of alteration or abrasion. In this case, fragmentation was probably driven by volatile exsolution in a 'dry' magmatic eruption [3]. Assuming that this ash came from the Rauðufossafjöll

massif, we infer that the rhyolite magma was sufficiently volatile-rich to generate an explosive eruption once the glacier surface had been breached and meltwater was no longer available [4]. This raises the possibility that Rauðufossafjöll generated a widespread tephra layer.

A recent study of historic basaltic tephra layers in Iceland [5] has found a quantitative difference between the morphology of subglacially and subaerially erupted ash shards. However, rhyolitic tephra appears more difficult to interpret. Our preliminary observations at Torfajökull suggest that rhyolitic ash shard morphologies may indeed yield information on eruption mechanisms.

References: [1] Tuffen H., Gilbert J. S., McGarvie D. W. (2000) *Bull. Volcanol.*, sub judice. [2] Wohletz K. (1986) *Bull. Volcanol. 48:*245-264. [3] Heiken G., Wohletz K. (1985) *Volcanic Ash.* University of California Press, Berkeley. [4] Skilling I. P. (1994) *Bull Volcanol 56:*573-591. [5] Hafliðason H., Eiríksson J., van Kreveneld S. (2000) *J Quat Sci 15:*3-22.

Appendix H.

Abstracts of papers derived from work presented in this thesis

1. Tuffen H, Gilbert JS, McGarvie DW (2001a) Products of an effusive subglacial rhyolite eruption: Bláhnúkur, Torfajökull, Iceland. Bulletin of Volcanology 63, 179-190.

Abstract We present field observations from Bláhnúkur, a small volume (< 0.1 km^3) subglacial rhyolite edifice at the Torfajökull central volcano, south-central Iceland. Bláhnúkur was probably emplaced during the last glacial period (c. 115-11 ka). The characteristics of the deposits suggest that they were formed by an effusive eruption in an exclusively subglacial environment, beneath a glacier > 400 m thick. Lithofacies associations attest to complex patterns of volcano-ice interaction. Erosive channels at the base of the subglacial sequence are filled by both eruption-derived material and subglacial till, which show evidence for deposition by flowing meltwater. This suggests that meltwater was able to drain away from the vent area during the eruption. Much of the subglacial volcanic deposits consist of conical-to-irregularly-shaped lava lobes typically 5-10 m long, set in poorly-sorted breccias with an ash-grade matrix. A gradational lava-breccia contact at the base of lava lobes represents a fossilised fragmentation interface, driven by magma-water interaction as the lava flowed over poorly consolidated, waterlogged debris. Sets of columnar joints on the upper surfaces of lobes are interpreted as ice-contact features. The morphology of the lobes suggests that they chilled within conically shaped subglacial cavities 2-5 m high. Avalanche deposits mantling the flanks of Bláhnúkur appear to have been generated by the collapse of lava lobes and surrounding breccia. A variety of deposit characteristics suggests that this occurred both prior to and after quenching of the lava lobes. Collapse events may have occurred when the supporting ice walls were melted back from around the cooling lava lobes and breccias. Much larger lava flows were emplaced in the latter stages of the eruption. Columnar joint patterns suggest that these flowed and chilled within subglacial cavities 20 m high and 100-200 m in length. There is little evidence for magma-water interaction at lava flow margins which suggests that these larger cavities were drained of meltwater.
As rhyolite magma rose to the base of the glacier, the nature of the subglacial cavity system played an important role in governing the style of eruption and the volcanic facies generated. We present evidence that the cavity system evolved during the eruption, reflecting variations in both melting rate and edifice growth that are best explained by a fluctuating eruption rate.

Key words Subglacial · Rhyolite · Magma-ice interaction · Columnar jointing · Obsidian · Phreatomagmatic

---

Hugh Tuffen
Department of Earth Sciences, The Open University, Milton Keynes, MK7 6AA, UK and
Department of Environmental Science, Lancaster University, Lancaster LA1 4YQ, UK
E-mail: h.tuffen@lancaster.ac.uk

Jennie Gilbert
Department of Environmental Science, Lancaster University, Lancaster LA1 4YQ, UK

Dave McGarvie
Department of Earth Sciences, The Open University, Milton Keynes, MK7 6AA, UK

2. Tuffen H, McGarvie DW, Gilbert JS, Pinkerton H (2001b) Physical volcanology of a subglacial-to-emergent rhyolitic tuya at Rauðufossafjöll, Torfajökull, Iceland. Journal of the Geological Society of London special edition: Volcano-ice interaction on Earth and Mars (ed. J.L. Smellie), in press.

Abstract: We present the first modern volcanological study of a subglacial-to-emergent rhyolite tuya, at SE Rauðufossafjöll, Torfajökull, Iceland. A flat-topped edifice with a volume of ~1 km^3 was emplaced in Upper Pleistocene time beneath a glacier >350 m thick. Although it shares morphological characteristics with basaltic tuyas, the lithofacies indicate a very different eruption mechanism.

Field observations suggest that the eruption began with vigorous phreatomagmatic explosions within a well-drained ice vault, building a pile of unbedded ash up to 300 m thick. This was followed by a subaerial effusive phase, in which compound lava flows were emplaced within ice cauldrons. Small-volume effusive eruptions on the volcano flanks created several lava bodies, with a variety of features (columnar-jointed sides, subaerial tops, peperitic bases) that are used to reconstruct spatially-heterogeneous patterns of volcano-ice interaction. Volcaniclastic sediments exposed in a stream section provide evidence for channelised meltwater drainage and fluctuating depositional processes during the eruption.

We develop models for the evolution of SE Rauðufossafjöll, and discuss the differences between subglacial rhyolitic and basaltic eruption mechanisms, which are principally caused by contrasting hydrological patterns.

3. Tuffen H, Pinkerton H, Gilbert JS, McGarvie DW (2001c) Ice-melting patterns during small-volume subglacial volcanic eruptions: evidence from Bláhnúkur, Iceland. Submitted to Sedimentary Geology Special Issue: Modern and Ancient ice-marginal landsystems.

Abstract
Although observations of recent volcanic eruptions beneath Vatnajökull, Iceland have improved understanding of ice deformation and meltwater drainage, little is known about the processes that occur at the glacier base. We present observations of the products of a small-volume, effusive subglacial rhyolite eruption at Bláhnúkur, Torfajökull, Iceland. Lava bodies, typically 7 m long, have unusual conical morphologies and columnar joint orientations that suggest emplacement within cavities melted into the base of a glacier. Cavities appear to have been steep-walled and randomly distributed. These features can be explained by a simple model of conductive heat loss during the ascent of a lava body to the glacier base. The heat released melts a cavity in the overlying ice. The development of vapour-escape pipes in the waterlogged, permeable breccias surrounding the lava allows rapid heat transfer between lava and ice. The meltwater formed percolates into the breccias, recharging the cooling system and leaving a steam-filled cavity.

The slow ascent rates of intrusive rhyolitic magma bodies provides ample time for a cavity to be melted in the ice above, even during the final 10 m of ascent to the glacier base. An equilibrium cavity size is calculated, at which melting is balanced

by creep closure. This is dependent upon the heat input and the difference between glaciostatic and cavity pressure. The cavity sizes inferred from Bláhnúkur are consistent with a pressure differential of 2-4 MPa, suggesting that the ice was at least 200 m thick. This is consistent with the volcanic stratigraphy, which indicates that the ice exceeded 350 m in thickness.

Although this is the first time that a subglacial cavity system of this type has been reconstructed from an ancient volcanic sequence, it shares many characteristics with the modern firn cave system formed by fumarolic melting within the summit crater of Mount Rainier, Washington. At both localities it appears that localised heating at the glacier base has resulted in heterogeneous melting patterns. Despite the different rheological properties of ice and firn, similar patterns of cavity roof deformation are inferred. The development of low-pressure subglacial cavities in regions of high heat flux may influence the trajectory of rising magma, with manifold implications for eruptive mechanisms and resultant subglacial volcanic landforms.

Appendix I.
Speculation about eruptions beneath frozen-based glaciers

In normal conditions, no meltwater is present within or beneath frozen-based glaciers, and basal ice temperatures may be tens of degrees below freezing (Paterson 1994, Hooke 1998). Rothlisberger channels would not exist, and there is little or no erosion at the glacier base. Given these different starting conditions, how might the course of events during eruptions beneath frozen-based glaciers differ from that beneath temperate glaciers? Here are some tentative suggestions:

1. Subglacial meltwater drainage would be impossible, and intraglacial meltwater lakes would always form.

2. If volume changes are negative, an ice cauldron will form above the eruption site. If volume changes are positive, the ice may be uplifted (Hoskuldsson & Sparks 1997), allowing some meltwater to escape at the glacier base, and increasing the basal diameter of the lake.

3. The volume of intraglacial lakes would be determined by the balance between the thermal output of the volcano and heat loss to the ice walls and atmosphere.

4. There would be little deformation of ice into the eruption site unless either an ice cauldron had formed, or the rate of regional ice flow were high enough for considerable deformation to occur within the timescale of the eruption.

5. If the ice roof were melted through and an intraglacial lake formed, its level may rise until meltwater escapes by percolation through the upper firn and snow layers (Smellie 1999, Smellie 2001).

6. If the ice surface in the vicinity of the eruption site were lower than the surrounding ice (e.g. if an ice cauldron had formed, or there were a depression in the ice surface

prior to eruption), permeable flow through firn may be uphill. This may reduce the efficiency of drainage through firn, and the lake level may rise until meltwater accumulated on the ice surface, where it would rapidly refreeze, forming an impermeable layer on the glacier surface. This may encourage further raising of the water level. Subaqueous lithologies may thus be formed at a level close to the glacier surface in the vicinity.

7. I speculate that magma may be quenched within the meltwater lake during Surtseyan-type eruptions, yet be entrained in a turbulent plume and deposited outside the lake. Thus the thermal energy stored in the lake would increase, but not the level of the lake itself, which would only rise if the magma were deposited within the lake. If the thermal energy and volume of the magma were thus decoupled, the lake volume may *drop* as the ice walls melted further back, due to the negative volume change upon melting. However, this scenario may only occur during the emergent surtseyan phase, perhaps when the water column is <50 m deep above the vent. Lowering of the water level at this stage would accelerate the emergence of the growing edifice and may reduce the explosivity of the eruption, reducing the ejection of tephra outside the lake and encouraging a rise in the meltwater level. The water level may be coupled to the eruption mechanism, leading to cyclic surtseyan activity and accompanying lake level changes. However, it is not clear whether this is a viable mechanism which would have any effect on the timescale of most eruptions (days).

8. Meltwater accumulation would occur regardless of the magma composition, and all subglacial-to-subaerial eruptions would form volcanic edifices similar to the basaltic tuyas described by Jones (1970), Smellie & Skilling (1994) and others.

9. The lower temperature of ice would mean that less meltwater would be melted per unit volume of magma than during 'temperate' subglacial eruptions, encouraging positive volume changes (Hoskuldsson & Sparks 1997), although this is likely to be a marginal effect.

10. As the heat flux from the volcano decreased, the lake would refreeze, starting at the ice walls and surface. Freezing onto the ice walls would raise the lake level, possibly breaking the ice crust on the surface. Meltwater may thus 'prograde' onto any

subaerially-formed edifice, increasing its cooling rate and heating meltwater, leading to more melting. If volcanic activity continued at this stage, and 'dry' subaerial lava flows were emplaced, progradation of the lake would 'drown' the lavas, and columnar joints would form. Flooding of the vent feeding the lavas may cause a return to a phreatomagmatic eruption, although the vent is likely to be protected by a cinder cone or spatter rampart, thus requiring a large rise in lake level.

11. Once the glacier had largely refrozen, many years after the eruption terminated, the ice level might be considerably higher around the volcano than before, due to the addition of the volume of the edifice. This would drive ice flow from around the edifice.